



Investigation into Additive Manufacturing for Controlling
Thermal Expansion in Optical Applications

By Steven Milward

Submitted to Swansea University in fulfilment of the
requirements for a Degree of Doctor of Philosophy

Swansea University

2019

This thesis is dedicated to my mum Carol.

Abstract

The design of components for the optical industry requires a consideration into the thermal expansion co-efficient of the materials used. Often the body material of an optical system exceeds the thermal expansion of the lens material. This can lead to lens decentre and misalignment. This thesis will investigate the use of additive manufacturing to tailor the thermal expansion co-efficient of the parts produced so that they match the thermal expansion co-efficient of the lens material. Several state-of-the-art additive manufacturing methods are investigated to achieve this. These include metal laser powder bed fusion, polymer fused deposition modelling, and continuous fibre re-enforced polymer fused deposition modelling. A method used to tailor the co-efficient of thermal expansion focuses on the design of the components, while another method focuses on the adjustment of the materials used.

The design of an optical system features two metals with different thermal expansion co-efficients which work together to produce a different overall thermal expansion co-efficient similar to the lens material. Another method investigates the use of the low expansion invar alloy, and the controlled expansion aluminium - silicon alloy. Adjusting the elemental constituents by mixing the alloy powders with elemental powders has shown to successfully change the overall constituents of the printed alloy, opening up the avenue for tailoring thermal expansion in-situ with the build process. A promising method of controlling thermal expansion with polymers is shown by introducing inclusions into the polymer filament feedstock material. The introduction of carbon and glass fibres as well as metal and organic particles shows a remarkable ability to adjust the co-efficient of thermal expansion over a wide range. Using a fibre polymer printer, a composite can be printed with a layer of carbon, glass, or Kevlar fibre laid in a predetermined orientation. This method provides the widest range of thermal expansion control.

Declaration

This work has not previously been accepted in substance for any degree and is not being concurrently submitted in candidature for any degree.

Signed (candidate)

Date

STATEMENT 1

This thesis is the result of my own investigations, except where otherwise stated. Where correction services have been used, the extent and nature of the correction is clearly marked in a footnote(s).

Other sources are acknowledged by footnotes giving explicit references. A bibliography is appended.

Signed (candidate)

Date

STATEMENT 2

I hereby give consent for my thesis, if accepted, to be available for photocopying and for inter-library loan, and for the title and summary to be made available to outside organisations.

Signed (candidate)

Date

Acknowledgments

This work was partially supported by the Welsh Government and Higher Education Funding Council for Wales through the Sêr Cymru National Research Network in Advanced Engineering and Materials and by the Materials Advanced Characterization Centre (MACH1) at Swansea University.

I would like to thank Prof Nicholas Lavery and Prof Stephen Brown for their continued support throughout this research. I would also like to thank the encouragement and support provided by Dr Helen Swygart, and Lee Eccles. You have both always remained supportive at every meeting we had, which was a huge source of motivation for me. I would also like to thank Dr Feras Korkees, and Prof Richard Johnston for donating their time and equipment in aid of my research.

I have met many friends at my time here that I would also like to thank for their support. Stuart Sillars, for his research ideas and overall help, Andre Giordimaina for his humour and friendship, and Adam Philo with his guidance and ideas throughout. The support of fellow doctorate students has been essential. I would also like to thank many friends who have been supportive in the later stages, Dan, Sha, Jordan, and Jon.

And finally, but by no means least, I would like to thank my family, Colin, Tracy, Ruby, and Rebecca for their continued support and patience during not only my PhD, but my whole education. I am very for the opportunities both parents have provided for me.

Contents

Abstract	3
Declaration	4
Acknowledgments.....	5
Contents	6
List of Figures	11
List of Tables	22
1 Introduction	25
1.1 Technical objectives	28
1.2 Design Considerations for an optical system	28
1.3 Thesis objectives	31
1.4 Publications	31
2 Literature review of thermal expansion control	32
2.1 Introduction	32
2.2 Controlling thermal expansion through material properties	33
2.2.1 Controlled thermal expansion metals	33
2.2.2 Controlled thermal expansion polymers	39
2.3 Controlling thermal expansion bi-material structures	42
2.3.1 Three-phase topology optimisation	42
2.3.2 Analytically derived metamaterial structures	46
3 Literature review of the additive manufacturing process	53
3.1 Introduction	53
3.2 Metal Additive Manufacturing	53
3.2.1 Powder Bed Fusion	53
3.2.2 Directed Energy Deposition	58
3.2.3 Material Jetting.....	60
3.2.4 Binder Jetting.....	61
3.2.5 Fused Deposition Modelling.....	62
3.2.6 Sheet Lamination	63
3.2.7 Specification summary table for metal AM processes	64
3.3 Plastic and Polymer Additive Manufacturing	66
3.3.1 Powder Bed Fusion	66

3.3.2	Material Jetting	68
3.3.3	Binder Jetting (BJ)	68
3.3.4	Stereolithography Apparatus (SLA)	69
3.3.5	Fused Deposition Modelling	70
3.4	Geometric Tolerances of Additive Manufacturing	74
3.4.1	Summary	74
3.4.2	Introduction	74
3.4.3	Method	83
3.4.4	Rectangular slot resolution	84
3.4.5	Cylinder slot resolution	85
3.4.6	Wall thickness resolution	87
3.4.7	Hole-size resolution	88
3.4.8	Hollow cylinders diameter and circularity resolution	90
3.4.9	Conclusions on the geometric tolerances of additive manufacturing	100
4	Experimental Methods	101
4.1	Summary.....	101
4.2	Dilatometer	101
4.3	Density.....	115
4.4	Microhardness	116
4.5	Tensile.....	116
4.6	Composition.....	117
4.7	Design of Experiments and Orthogonal Arrays	119
4.8	Thermal expansion test bench design	120
4.8.1	Digital Image Correlation (DiC) camera system	122
4.8.2	Co-ordinate measuring machine	128
5	Thermal Expansion Control in Metal AM by Design	132
5.1	Introduction.....	132
5.2	Simulation setup.....	134
5.3	Bi-material bonded cylinder	135
5.4	Tuneable Auxetic Structure	141
5.4.1	Thermal Expansion Simulation.....	144
5.4.2	Stiffness Simulation	147
5.4.3	Discussion on tuneable auxetic structure simulations	149
5.5	Tuneable porosity structure	149
5.5.1	Design 1 – Single array.....	150
5.5.2	Design 2 –Stacked array.....	155

5.5.3	Stiffness Simulation	159
5.5.4	Discussion on the tuneable porosity structure	161
5.6	Manufacture	163
5.6.1	Primary Material – LPBF.....	163
5.6.2	Secondary Material - DED	166
5.7	Thermal Expansion Test Bench Results	166
5.8	Discussion on thermal expansion control in metal AM by design.....	169
5.9	Conclusion on thermal expansion control in metal AM by design	170
6	Thermal Expansion Control in Metal AM by Alloy Selection	171
6.1	Summary.....	171
6.2	Introduction	171
6.3	Manufacturing Setup	172
6.4	Powder Characterisation	175
6.4.1	Optical Classification.....	176
6.4.2	Scanning Electron Microscopy	177
6.4.3	Particle Size Distribution (PSD).....	179
6.4.4	Rheometry.....	180
6.4.5	Tap Density.....	182
6.4.6	Conclusion of powder characterisation	183
6.5	Iron-Nickel (Fe-Ni) Alloys	184
6.5.1	Optimum laser parameters for full densification.....	186
6.5.2	Invar induction melted compositional adjustments	189
6.5.3	Invar in-situ compositional adjustments	193
6.5.4	Adjustment of Invar laser processing parameters.	220
6.5.5	Discussion on the Iron-Nickel alloys	235
6.5.6	Conclusion on the Iron-Nickel alloys	237
6.6	Aluminium-Silicon Alloys	239
6.6.1	Introduction.....	239
6.6.2	Method.....	239
6.6.3	Results.....	240
6.6.4	Discussion.....	253
6.6.5	Conclusions on Al-Si alloys	255
6.7	Conclusions on thermal expansion control with metal AM using alloy selection.....	255
7	Thermal Expansion Control in Plastic AM	258
7.1	Summary.....	258

7.2	Introduction.....	258
7.3	Plastic feedstock material.....	258
7.3.1	Manufacture.....	261
7.3.2	Thermal Expansion	262
7.3.3	Discussion on plastic feedstock material.....	265
7.3.4	Conclusion on plastic feedstock material	266
7.4	Controlled thermal expansion plastic feedstock.....	266
7.4.1	Manufacture.....	269
7.4.2	Thermal Expansion	274
7.4.3	Discussion on controlled thermal expansion plastic feedstock.....	276
7.4.4	Conclusions on controlled thermal expansion plastic feedstock.....	276
7.5	Multi-material triangular concept	277
7.6	Multi-material polymer combinations.....	280
7.6.1	Manufacture.....	283
7.6.2	Curvature Calculations.....	283
7.6.3	Rule of Mixtures analysis	285
7.6.4	Simulation	286
7.6.5	Thermal Expansion	291
7.6.6	Discussion on multi-material polymer combinations.....	293
7.6.7	Conclusion on multi-material polymer combinations.....	294
7.7	Discussion on thermal expansion control in polymer AM	294
7.8	Conclusion on thermal expansion control in polymer AM.....	296
8	Thermal Expansion Control in Polymer AM using Fibre Reinforced Material	297
8.1	Summary.....	297
8.2	Introduction.....	297
8.3	Design.....	298
8.4	Manufacture	299
8.5	Results	301
8.5.1	CT Scans	302
8.5.2	Thermal Expansion	305
8.6	Discussion on thermal expansion control in polymer AM using fibre reinforced material.....	311
8.7	Conclusions on thermal expansion control in polymer AM using fibre reinforced material.....	313
9	Final Discussion	313
9.1	Thermal expansion control by design	313

9.2	Thermal expansion control using metal AM	314
9.3	Thermal expansion control using polymer AM	315
9.4	Thermal expansion control using fibre-reinforced polymer AM	315
9.5	Controlling thermal expansion in optical applications.....	316
10	Conclusions	317
10.1	Summary of outcome of work	317
10.2	Future work requirements	319
	References.....	321

List of Figures

Figure 1. CAD image provided by sponsor company Qioptiq showing the required areas to match CTE in a cylindrical lens and rectangular lens system.....	26
Figure 2. Images showing the orientations of axial shift, lens tilt, and lens decentre.....	29
Figure 3. Lens and body cross-section showing exploded view of the parts inside, notably the location of the potting pads which seat the lens to the body.....	30
Figure 4. Physical alpha curves for invar as the nickel percentage changes [40].....	34
Figure 5. Thermal expansion values for spray formed AlSi alloys (Al-27-70%Si), AA6061 Al Alloy, [48], [49].	36
Figure 6. Yield strength and UTS, for AlSi alloys manufactured by Sandvik, and AlSiC composite by Materion [48], [49].	37
Figure 7. The Sandvik Osprey Spray forming process for creating AlSi alloys with high silicon content for controlled thermal expansion.....	38
Figure 8. Phase diagram for AlSi binary alloy [51].	38
Figure 9. CTE of CFRC composites after a cryogenic thermal cycle from -120 to 120°C of; a) along the length of the fibres and, b) across the length of the fibres [22].....	40
Figure 10. Graph showing CTE's in a CFRP Epoxy Resin mix for different volume fractions. Measurement taken along the length of the fibres (left) and across the length of the fibres (right) Data taken from (B.Yates,1978 et al.) [23].	41
Figure 11. A unit cell of a three-material composite with macroscopic negative thermal expansion. The red denotes the higher CTE material, while the blue denotes the lower CTE material. a) shows the generated geometry, b) shows the simplified geometry allowing for DMD toolpath application. [63].....	43
Figure 12. Toolpath image for DMD where blue denotes the low CTE material chromium, and green denotes the high CTE material, Nickel.[63]	43
Figure 13. a) Image showing multiple connected Ni-Cr negative CTE structures after manufacture using DMD. b) Graph showing the experimental results for change in length as temperature increase [63].	44
Figure 14. Optimal configurations and 2D view of the STL model. (a) Original topology optimization result. Pink dotted lines indicate the optimized domain. Gray dotted lines indicate the forced void domain for maintaining the deformation range. (b) 2D view of the STL model generated from the topology optimization result. The hinge-like part of the stiff material on the corner was replaced with thicker soft material as shown in blue dotted circles. (c) Thermal deformation shape obtained from the reanalysis of the STL model. The green lines indicate the original shape.....	45
Figure 15. Negative CTE structure created on an Objet Conex 500 [64].....	45
Figure 16. Thermal deformation of test pieces measured by a laser scanning dilatometer. The temperature rising rate is 1 °C/min. The temperature range is between RT and 50 °C. RTs of measurements No. 1, 2, and 3 are 17.45, 19.45, and 22.85 °C, respectively. Approximation lines are plotted for the data within the temperature range between RT and 34°C.	45
Figure 17. (a) Metastructure with unbounded CTE designed by Lakes [7]. (b) Metastructure with low CTE designed by Steeves et al. [2]. High and low CTE materials are indicated by blue (darker) and orange (lighter) colors, respectively.	46
Figure 18. (a) Shows a structure by Lakes with an included angle θ . (b) shows angle θ geometry.....	47
Figure 19. (a) Bend dominated arrangement. (b) Stretch dominated arrangement.	48
Figure 20. Metastructure patented by Jefferson et al. showing high CTE constituents in grey, and low CTE constituents in yellow [6].	48

Figure 21. (a) A sketch of the lattice structure showing the key geometric parameters. The low CTE type 1 members are blue while the high CTE type 2 members are red. The key parameters are the lattice skewness h and the ratio of thermal expansions $= \alpha_2/\alpha_1$ [3] (b) Contours of normalized net thermal expansion coefficient a of the planar lattice for a range of skewness [3]. 49

Figure 22. 3D structures theorised possible, but not yet additively manufactured [2]...... 51

Figure 23. Schematic s of how powder based direct deposition can achieve gradient 3D metallic structures, and an example of a compositionally graded structure [67]–[70]. 52

Figure 24. Laser Powder Bed Fusion process schematic [74]...... 54

Figure 25. Diagram illustrating the operation of an EBM machine, and an image of the build in operation [74]...... 56

Figure 26. Schematic showing a Laser Metal Deposition process being used to create a compositionally graded component [67]–[70]...... 58

Figure 27. a) Diagram of the LENS process, b) Diagram of the EBAM process [74]...... 59

Figure 28. Figures showing the metal MJ process and an example part produced [93]...... 61

Figure 29. Diagram of the binder jetting process, an image of the sintered part metal infiltration layout [93] [74]...... 62

Figure 30. Image of a typical UAM material feed, and an operational diagram ¹¹ [103]. 64

Figure 31. Selective Laser Sintering process schematic [107]. 67

Figure 32. Selective Heat Sintering process schematic [107]. 68

Figure 33. Two modes of operation for SLA include a) Scanning-Based SL (SSL) or Direct Writing b) Projection-based SL (PSL) featured in the DLP method [122]. 69

Figure 34. Typical FDM extrusion process and overhang support requirements [74] [26]...... 71

Figure 35. Images showing two FDM nozzles, the single nozzle, and multiple nozzle design with a diagram of the nozzle alignment value position. 71

Figure 36. Ultimaker 3 multi-material solution, showing primary nozzle stowed and secondary nozzle lowered for printing. Leapfrog’s independent dual extruder multi-material solution. 72

Figure 37. Ultimaker 3 high temperature core by Solex 3D provides capability to change the nozzle to a hardened steel or ruby tipped design. 73

Figure 38. Mark One Composite 3D printer (left). The fibre is introduced from the spool into the print head that lays the fibre onto the preceding nylon layer, thus allowing continuous fibre composites to be manufactured, layer by layer (right). 73

Figure 39. Benchmark model by J.-P.Kruth et al. [134]. 77

Figure 40. Benchmark model and a manufactured hole size benchmark by J. Kranz et al. [135] 77

Figure 41. Benchmark model by M.G.Teeter et al. [136]. 78

Figure 42. Benchmark parts for wall thickness (1A, 1B) and rectangular slot resolution (2A 2B) by V. Matilainen [132]. 78

Figure 43. Benchmark model by K.Kamarudin et al.[137] 79

Figure 44. Benchmark parts for wall thickness at various angles to the recoater by Y.L.Yap et al. [131]. 79

Figure 45. Benchmark test piece (left) showing measured area and the results for circularity of a) an EBM process and b) a LPBF process, by A. Cooke et al. [138]. 80

Figure 46. Rectangular slot deviation found in literature for benchmark parts [132], [137]. 80

Figure 47. Cylinder slot deviation found in literature for benchmark parts [136]. 81

Figure 48. Wall thickness deviation found in literature for benchmark parts [131], [132], [134], [136], [137]. 82

Figure 49. Hole size deviation found in literature for benchmark parts [134]–[136]. 83

Figure 50. Build plate assembly showing part orientation and recoater direction. Parts are; a) Wall thickness resolution, b) Cylindrical slot resolution, c) Square slot resolution, and d) Hole-size resolution.	84
Figure 51. Images of the flat plane slot resolution benchmark CAD drawing and final printed part in Ti64Al.	84
Figure 52. Graph showing deviation using shadow graph results for the slot resolution benchmark for Ti64Al (RenAM500), 316L (AM400), PLA (Ultimaker 3), and Nylon & Onyx (Markforged Desktop 2).	85
Figure 53. Cylinders ranging from 1mm to 0.05mm gaps.....	86
Figure 54. Graph showing deviation using shadow graph results for the cylinder resolution benchmark for Ti64Al (RenAM500), 316L (AM400), PLA (Ultimaker 3), and Nylon & Onyx (Markforged Desktop 2).	86
Figure 55. CAD image from with wall of thicknesses between 1-0.1mm (left) and to the right are images of the 316L part and the Ti64Al part.	87
Figure 56. Graph showing wall thickness deviation from nominal for each nominal thickness in Ti64Al (RenAM500), 316L(AM400), PLA (Ultimaker 3), and Nylon & Onyx (Desktop 2).	88
Figure 57. Hole sizes ranging from 1mm to 0.1mm in diameter.	89
Figure 58. Graph showing holes size deviation for a Ti64Al (RenAM500), 316L (AM400), PLA (Ultimaker 3), and Nylon & Onyx (Markforged Desktop 2) for horizontally built samples.	89
Figure 59. Figure showing CAD for circularity and tolerance benchmarking for a 250x250mm build plate.	90
Figure 60. Graph showing Ti64Al deviation from nominal for each ring and the percentage difference compared to its nominal size.	91
Figure 61. Graph showing Ti64Al circularity for each ring, and as a percentage to its nominal size.	92
Figure 62. Plot showing Ti64Al circularity for the largest diameter ring 10 inside measurement with 10X magnification, and 100X magnification, respectively.....	93
Figure 63. Plot showing Ti64Al circularity for ring 1 inside measurement with 10X magnification, and 100X magnification, respectively.	93
Figure 64. Graph showing PLA deviation from nominal for each ring and the percentage difference compared to its nominal size. Printed on a Ultimaker 3.....	94
Figure 65. Graph showing PLA circularity for each ring, and as a percentage to its nominal size. Printed on a Ultimaker 3.....	94
Figure 66. Plot showing PLA circularity for the largest diameter ring (number 8) inside measurement with 10X magnification, and 100X magnification, respectively.	95
Figure 67. Plot showing PLA circularity for the smallest diameter ring (number 1) inside measurement with 10X magnification, and 100X magnification, respectively.	95
Figure 68. Graph showing Onyx +CF deviation from nominal for each ring and the percentage difference compared to its nominal size.	96
Figure 69. Graph showing Onyx + CF circularity for each ring, and as a percentage to its nominal size.	96
Figure 70. Plot showing Onyx + CF circularity for the largest diameter ring (number 5) inside measurement with 10X magnification, and 100X magnification, respectively.....	97
Figure 71. Plot showing Onyx + CF circularity for the smallest diameter ring (number 1) inside measurement with 10X magnification, and 100X magnification, respectively.	97
Figure 72. Onyx concentricity benchmark showing artefacts on ring five circled in yellow.....	98
Figure 73. Comparison in diameter deviation between Ti64Al, PLA, and Onyx, printed on the AM400, Ultimaker 3, and Markforged Desktop Two respectively.	99

Figure 74. Comparison in circularity deviation between Ti64Al, PLA, and Onyx, printed on the AM400, Ultimaker 3, and Desktop Two respectively.	99
Figure 75. Netzsch 402 push-rod dilatometer photograph [148].	102
Figure 76. Schematic of the operation of a push-rod dilatometer.	102
Figure 77. Graph comparing different methods of dilatometer thermal expansion analysis; physical and technical alpha curves. Physical Alpha is smoothed at a level 8.	103
Figure 78. Graphs showing Physical Alpha smoothing levels from 1-8 and A-H in the Netzsch proteus software. Material used is AlSi10Mg from -120°C to 480°C.	104
Figure 79. First dilatometer test run and analysis for a set of various FeNi alloys. a) Invar 36 temperature and change in length with correction applied, b) <i>Al2O3</i> correction; temperature and change in length, c) <i>Al2O3</i> correction; physical alpha curve with highlighted anomaly, d) the physical alpha curves for all invar variants. Physical alpha curves in graphs c and d have a smoothing level of 8.	107
Figure 80. Second dilatometer test run and analysis for a set of various FeNi alloys. a) Invar 36 temperature against change in length with correction applied, b) <i>Al2O3</i> correction; temperature and change in length c) <i>Al2O3</i> correction; physical alpha curve, d) and the physical alpha curves for all invar variants. Alpha curves on graphs c and d have a smoothing level of 8.	109
Figure 81. Final dilatometer test program showing change in length and temperature over time, for a) invar 36 with correction applied, and b) the <i>Al2O3</i> correction run.	111
Figure 82. Temperature profile over time for the entire heating and cooling cycle, compared with the target 5k/min. Deviation is highlighted.	111
Figure 83. Temperature profile over time for the heating and cooling cycle from ambient to cryogenic temperatures. Target 5k/min compared.	112
Figure 84. Dilatometer heating and cooling cycle showing physical alpha curves for invar 36 with level 8 and F smoothing.	113
Figure 85. Measured length change as a function of temperature of a platinum reference specimen using a 20K/min rate interrupted by a 30min isothermal at 1273K for; a) alumina pushrods, b) fused silica pushrods. Measured with the DIL 805 A/D induction dilatometer from Texas Instruments [149].	114
Figure 86. Measured length change as a function of temperature of <i>Al2O3</i> specimen using a 5K/min rate interrupted by a 1hr isothermal at 480°C.	114
Figure 87. ImageJ threshold analysis.	115
Figure 88. Vickers hardness indent showing where the measurements are taken.	116
Figure 89. EDS operational diagram [150].	117
Figure 90. EDS Spectrum for an iron-nickel alloy.	118
Figure 91. Comparison of a T4 EDS scan (left) and a T2 EDS scan (right) for an iron-nickel alloy. 512x384, 5 sweeps, dwell time 1.0msec, mag x100.	119
Figure 92. Comparison of a single sweep EDS scan (left) and a 5 sweep EDS scan (right) for an iron-nickel alloy. 1024x768, T2, dwell time 1.0msec, mag x100.	119
Figure 93. Step by step process for designing a L9 array. For density optimisation, the relative density percentage will be the result. Output in step 5 gives the response each laser parameter has on the density. Step 6 provides a rank for the maximum result.	120
Figure 94. Heated baseplate featuring a grid array for analysis of temperature distribution. Image shows setup with IR camera, Baseplate with thermocouple reading locations, and IR image where the white box shows the plate boundary.	121
Figure 95. Schematic showing the DiC test rig setup.	123
Figure 96. Image of the DiC test rig setup, and Infra-red image from the Ti64Al test plate.	123

Figure 97. DiC images of a flat Ti64Al plate at 100°C showing the displacement contours for the X,Y, and XY combined directions respectively.	124
Figure 98. DiC images of a flat Ti64Al plate at 230°C showing the displacement contours for the X,Y, and XY combined directions respectively.	124
Figure 99. DiC images of a flat Ti64Al plate at 230°C showing the strain contours for the overall strain, and the normalised overall strain. Strain represents error.....	125
Figure 100. Four Ti64Al test plates with a Stochastic pattern applied with white and black spray paint.	126
Figure 101. DiC images of a flat Ti64Al plate at 220°C showing the displacement contours and values(mm) for the four speckled plates in the X, Y, and combined XY direction, respectively.	126
Figure 102. Schematic of CMM test bench setup.	128
Figure 103. Image of the CMM test bench.....	129
Figure 104. Temperature profile for hotplate and structure for the CMM test rig measuring a Ti64Al cylinder.	130
Figure 105. CMM Readings for the diameter of a Ti64Al cylinder at 24°C. Trendline shows increase of 1µm over 85 readings.	130
Figure 106. CMM Readings for the diameter of a Ti64Al cylinder at 101.75°C. Trendline shows increase of 1.8µm over 85 readings.....	131
Figure 107. CMM readings comparing ambient against heated diameter for a Ti64Al cylinder. Change in diameter normalised against average ambient readings.	131
Figure 108. Figure showing the two arrangements, a) tuneable auxetic lattice type, and b) tuneable porosity type.	133
Figure 109. The bi-material ring arrangement, and mesh at 1.6mm body sizing (top image) followed by 1.4mm and 1mm body sizing.	135
Figure 110. Graph showing sensitivity study for a bi-material ring of equal thickness ($T_o/T_i=1$) for Ti64Al inside and INVAR outside.	136
Figure 111. Simulation showing Stress on the left, and strains on the right. The outside material is INVAR whilst the inside is Ti64Al. The top two images simulate from 22°C to 70°C, whilst the bottom two simulate from -30°C to +22°C ($t_c/t_v=1$).	136
Figure 112. Graph showing CTE and Von-Mises strains as the INVAR to Ti64Al thickness ratio changes where t_c is the constant thickness material, and t_v is the thickness of the material being varied. Temperature range is +100°C.....	137
Figure 113. Scatter Plot showing FEA data for a bonded 2D ring of varying outside INVAR thickness and varying inside Ti64Al thickness and its corresponding CTE.....	138
Figure 114. Scatter Plot showing FEA data for a bonded 2D ring of varying outside INVAR thickness and varying inside 316L thickness and its corresponding CTE.	138
Figure 115. Demonstration of the greatest negative CTE the structure can produce. Simulation of Ti64Al Auxetic structure bonded with Invar showing before and after temperature change. Total Deformation image at 140x the true scale. Arrangement shown is at $\theta = 38^\circ, L_i = L_o = 1mm, L_a = 2mm$	141
Figure 116. Shows both equal angles theta on its most efficient tangential line. All other variables are outlined.	142
Figure 117. Diagram showing the angle change across the tangent line and its subsequent effect on the position of adjacent members.	142
Figure 118. Fixed radius at both the inside and outside. These locations will be used determine the CTE in simulation and testing.	142
Figure 119. Series of CAD drawings showing the effect of angle change on the radius of the adjoining members.....	143

Figure 120. Series of CAD images showing the angle change for auxetic arrangement concept where the 38° minimum to 66° median and the 88° maximum angle.....	143
Figure 121. ANSYS Image showing the deformation probe location where the y-direction movement is measured.....	144
Figure 122. Mesh sensitivity study showing percentage change in deformation compared to a 0.5mm element size baseline. Invar structure with 316L clad.	144
Figure 123. Graph displaying the simulated angle change against CTE for each member thickness L for materials 316L structure , with an Invar clad . $L_i = L_o = 1mm$. $L_a = 2mm$	145
Figure 124. Graph displaying the simulated angle change against CTE for each member thickness L for materials Ti64Al structure , with an Invar clad . $L_i = L_o = 1mm$. $L_a = 2mm$	145
Figure 125. Graph displaying the simulated angle change against CTE for each member thickness L for materials Invar structure , with an 316L clad . $L_i = L_o = 1mm$. $L_a = 2mm$	146
Figure 126. Graph displaying the simulated angle change against CTE for each member thickness L for materials Invar structure , with a Ti64Al clad . $L_i = L_o = 1mm$. $L_a = 2mm$	146
Figure 127. ANSYS Images showing radial forces applied to attain deformations for calculation of stiffness.	147
Figure 128. Simulation Image showing von-mises stresses and deformations at 22 times the true scale for visualisation purposes.....	147
Figure 129. Plot of simulated results for stiffness against force applied for confirmation of force linearity with deformation result. $L = 1mm$, $\theta = 38^\circ$	148
Figure 130. Graph showing the Stiffness for L=1,1.5, and 2mm for each possible angle for 316L clad invar structure.	148
Figure 131. Rendered image of a single and multi-array tailored porosity structure fully integrated inside an optical system body.	150
Figure 132. Dimensions for Single array in millimetres.....	151
Figure 133. Von-mises stress plots in MPa with 130X scaled deformation, showing CTE probe locations with Invar clad with 316L (left) and 316L clad with Invar (right).	151
Figure 134. Simulated CTE difference caused by deformation differences between probes 1 and 2 for the single porosity array after a 100°C temperature change.	152
Figure 135. Thermal Expansion simulation for the single array for Invar and 316L combinations.....	153
Figure 136. Thermal Expansion simulation for the single array for Invar and Ti64Al combinations... ..	153
Figure 137. Dimensions for Stacked array in millimetres.....	156
Figure 138. Von-mises stress plots with 130X scaled deformation, showing CTE probe locations with Invar clad with 316L (left) and 316L clad with Invar (right).	156
Figure 139. Simulated CTE difference caused by deformation differences between probes 1 and 2 for the stacked porosity array.....	157
Figure 140. Thermal Expansion simulation for the stacked array for Invar and 316L combinations... ..	157
Figure 141. Thermal Expansion simulation for the stacked array for Invar and Ti64Al combinations.	158
Figure 142. Ansys mech and support locations for the single array (left) and the stacked array (right). .	159
Figure 143. Single array stiffness for Invar, Ti64Al, and 316L.....	160
Figure 144. Single array stiffness for Invar, Ti64Al, and 316L, as a percentage of the materials elasticity modulus.	160
Figure 145. Stacked array stiffness for Invar, Ti64Al, and 316L.....	161
Figure 146. Stacked array stiffness for Invar, Ti64Al, and 316L, as a percentage of the materials elasticity modulus.	161

Figure 147. Single and stacked array designs showing percentage effectiveness for each material arrangement.....	162
Figure 148. Manufactured tuneable auxetic structure in invar using LPBF. Angles shown are 38°, 66°, and 88° respectively.....	163
Figure 149. CAD drawings for single and stacked porosity designs.....	164
Figure 150. Optical microscopy of single array with 4mm diameter holes.	165
Figure 151. Optical microscopy of stacked array with 1mm diameter holes.	165
Figure 152. Schematic of CMM test bench setup.	167
Figure 153. Deviation between clad and un-clad inside diameters.	167
Figure 154. Thermocouple temperature readings over each test for the auxetic structure at 38°.....	168
Figure 155. CMM diameter readings for the auxetic structure at 38°	169
Figure 156. Standard build volume stages. Stage 1 shows the dosing of the powder from the hopper, stage 2 shows the machine applying the first layer of powder.	172
Figure 157. Reduced Build Volume (RBV) stages. Stages 1 shows the manual compaction of the powder, stage 2 shows the machine applying the first layer of powder.....	172
Figure 158. The configuration of the Renishaw LPBF pulse modulated laser scanning.	173
Figure 159. Laser power vs scanning speed graph – how process outcomes vary with laser parameters. Zones (a-d) relate to the weld-pool behaviour.	174
Figure 160. Cross-section diagram of laser weld behaviour.....	174
Figure 161. Reference for optical classification for flowability using LPBF [152].	176
Figure 162. Optical classification of all used ALM powder feedstocks.	177
Figure 163. SEM images of all metal powders used in manufacture. EDS maps show distribution of the two greatest elemental constituent.....	178
Figure 164. Graph of the basic flowability energy of the powder feedstock.	181
Figure 165. Graph of the compaction percentage of the powder feedstock.....	181
Figure 166. Flow Rate Index (FRI) for the powder feedstock.	182
Figure 167. Tap density results for a selection of gas atomised powders.....	183
Figure 168. Invar36 build 1 and 2 Archimedes density plotted.	188
Figure 169. Tensile and density arrays used to determine optimum laser parameters (left), and the successful build completed using the parameters for Thales Alenia.	189
Figure 170. Fe-Ni(x) induction melted alloy deviation in target nickel composition.....	191
Figure 171. Dilatometry results showing physical alpha for induction melted Invar alloys cooling from 450°C to -120°C at 5K/min.....	191
Figure 172. Dilatometry cooling cycle results. CTE's plotted for induction melted Invar alloys. Cryogenic and above ambient temperature ranges, as function of the nickel percentage measured using EDS.....	192
Figure 173. Process diagram for the experiment.	196
Figure 174. Build components and dimensions for in-situ blended powders.	196
Figure 175. Plotted Ni wt.% target for each invar base alloy.	197
Figure 176. Heating and cooling cycle for invar36 heat treatment.	199
Figure 177. Images of powders before and after blending.	200
Figure 178. Image of RBV build in progress (left) and the finished build (right).....	200
Figure 179. Density cube cut orientations for microscopy and EDS.....	201
Figure 180. Deviation of nickel wt.% measured using EDS, from the target Ni content.	202
Figure 181. Build 1 & 4 – EDS map images for Invar batch 1 and 2 with no in-situ additions.....	203
Figure 182. Builds 2 & 3 – EDS map images for invar batch 1, with 1 & 2wt.% Ni carbonyl fine powder (3-7µm diameter) added in-situ.	203

Figure 183. Builds 5 & 6 – EDS map images for invar batch 2, with 1 & 2wt.% Fe carbonyl fine powder (6-8µm diameter) added in-situ.....	204
Figure 184. Builds 7 & 8 – EDS map images for invar batch 2, with 1 & 2wt.% Ni gas atomised powder (15-45µm diameter) added in-situ.....	205
Figure 185. Optical porosity for invar builds with in-situ Fe and Ni additions.....	205
Figure 186. Optical porosity images showing porous locations for the in-situ blended compositions using the build number notation.....	206
Figure 187. Archimedes density for increasing nickel content for the in-situ blended compositions.....	207
Figure 188. Optical and Archimedes density for each build in the in-situ blended compositions. Normalised against density for EDS measured composition.....	207
Figure 189. Box-plot for Vickers hardness values for invar in-situ additions.....	208
Figure 190. Scatter plot of Vickers hardness values against nickel content measured using EDS, for invar in-situ additions.....	209
Figure 191. Image of all tensile bars printed after pulling.....	210
Figure 192. Stress against strain curves for all invar blended powders tensile pulls.....	210
Figure 193. Blended in-situ invar additions tensile performance with and without heat treatment. Showing the percentage elongation until the tensile bar breaks for batch 1(B1) and batch 2 (B2).....	211
Figure 194. Blended in-situ invar additions tensile performance with and without heat treatment. Showing the percentage elongation until the ultimate tensile strength is achieved for batch 1(B1) and batch 2 (B2).	211
Figure 195. Blended in-situ invar additions tensile performance with and without heat treatment. Showing the elasticity modulus for batch 1(B1) and batch 2 (B2).	212
Figure 196. Blended in-situ invar additions tensile performance with and without heat treatment. Showing the ultimate tensile strength for batch 1(B1) and batch 2 (B2).....	212
Figure 197. Physical alpha curves plotted for all in-situ compositionally adjusted invar alloys using the dilatometer cooling cycle . Nickel percentages taken from averaged EDS results.....	214
Figure 198. Physical alpha curves plotted for all heat treated in-situ compositionally adjusted invar alloys using the dilatometer cooling cycle . Nickel percentages taken from averaged EDS results.....	215
Figure 199. Physical alpha curves plotted for all as-built and heat treated in-situ compositionally adjusted invar alloys using the dilatometer cooling cycle . Nickel percentages taken from averaged EDS results.....	216
Figure 200. Physical alpha curves comparing instantaneous CTE at 25°C for a range of Ni content measured from EDS. Guillaume et al. added for reference.....	216
Figure 201. Instantaneous CTE measurements for a range of temperatures for as built and heat-treated parts for the invar blended powders.....	218
Figure 202. Thermal expansion of (a) Invar 36 and (b) stainless steel samples after increasing temperature to 50 °C [163].	220
Figure 203. Contour plots for the thermal expansion of Invar 36 samples at temperature of 200 °C. The plots show the effect of laser power and scanning speed on thermal expansion at hatch spacings of 0.08, 0.10, and 0.12 mm [163].....	221
Figure 204. Each L25 parameter plotted for the experiment to be conducted (left), and the conversion to scanning speed plotted, and compared against those completed by Yakout et al. [163] (right).	223
Figure 205. Comparison between energy density and scanning speeds for the experiment and Yakout et al.'s work.....	223
Figure 206. Invar high laser energy QuantAM build layout.....	224
Figure 207. Physical CTE curve from -100°C to 200°C for invar as a function of volumetric laser energy density.....	224

Figure 208. Graph showing the CTE and measured nickel content for 25 samples of increasing input energy density. Energy density is increased by adjusting both exposure time and power of the modulated laser.	225
Figure 209. Final change in length over -100°C to 200°C for invar as a function of volumetric laser energy density.....	226
Figure 210. Yakout et al. comparison to Figure 209 over 23 to 50°C [163].....	226
Figure 211. Measured nickel content using EDS for invar as a function of volumetric laser energy density.	227
Figure 212. Thermal expansion and EDS compared over -100°C to 200°C. Crosses represent thermal expansion, circles represent EDS measurements.	227
Figure 213. Final change in length over -100°C to 200°C for invar against scanning speed.....	228
Figure 214. Final change in length over -100°C to 200°C for invar against laser power.	229
Figure 215. Contour plot of scanning speed against power for thermal expansion ranges in the present work (left). Yakout et al. contour plot (right) [163].....	229
Figure 216. Graph showing the density measured by Archimedes and by optical microscopy.	230
Figure 217. Build layout showing where the other components are in relation to the dilatometers cross-section.	231
Figure 218. Hardness box plot for 24 linear points on a cross-section of each invar dilatometer rod against its corresponding laser energy density.	233
Figure 219. Hardness max, median, and minimum, for 24 linear points on a cross-section of each invar dilatometer rod against its corresponding laser energy density.	234
Figure 220. AlSi LPBF Build plate.....	240
Figure 221. Optical porosity for each AlSi alloy manufactured by LPBF and spray forming. LPBF exposure time of 10µs has been omitted to make results comparable.	243
Figure 222. Dilatometer rod showing hardness indent locations and imaging location.	244
Figure 223. AlSi40 phase area compared to the quantity of phases.....	246
Figure 224. AlSi40 LPBF x500 SEM BEC & EDS overlaid showing finer microstructure around weld melt pools. Red is Al, green is Si, overlaid using 50% transparency.....	247
Figure 225. HV2 indent in AlSi30 producing clear shape (left). HV2 indent applied to AlSi80 showing significant cracking (right).	248
Figure 226. AlSi30 Vickers HV2 hardness data for a LPBF component at various laser exposure times.	248
Figure 227. AlSi35 blended Vickers HV2 hardness data for a LPBF component at various laser exposure times.	249
Figure 228. Vickers HV2 hardness data for a spray formed component AlSi42, and a LPBF AlSi40 component at various laser exposure times.	249
Figure 229. AlSi30, AlSi35, and AlSi40 median Vickers hardness comparison over a range of exposure times.	250
Figure 230. Thermal expansion for all AlSi LPBF printed materials, showing the effect of exposure time and silicon content.	251
Figure 231. Physical alpha values for all AlSi LPBF printed materials, and spray formed materials.	252
Figure 232. Image from the Cura build software showing the extrusion paths for a horizontal sample (left) and a vertical sample (right).	261
Figure 233. PLA dilatometer results showing CTE and averaged linear expansion rates.	262
Figure 234. ABS dilatometer results showing CTE and averaged linear expansion rates.	263
Figure 235. CPE dilatometer results showing CTE and averaged linear expansion rates.	263

Figure 236. CPE+ dilatometer results showing CTE and averaged linear expansion rates.....	264
Figure 237. Nylon dilatometer results showing CTE and averaged linear expansion rates.	264
Figure 238. Image showing process for plastic impregnation with inclusions.....	266
Figure 239. Image of 2.85mm diameter filaments used to manufacture dilatometer rods using Ultimaker 3.	269
Figure 240. Optical images taken with a DSLR camera of the horizontally printed samples, from the top (left) and side (right).	270
Figure 241. Optical microscopy images of the side of a printed 7x7x25mm sample showing the layers and inclusions at x1010 and x200.....	272
Figure 242. CTE curves for a PLA and PETG with a range of inclusions. Printed on the Ultimaker 3 with Cura's predefined PLA and PETG material parameters. 3 rd party Solex3D heating core and hardened steel nozzle used.	275
Figure 243. Triangular concept structure showing calculated CTE as the angle changes for a pin-jointed arrangement for CPE (low CTE constituent) and ABS (high CTE constituent).....	277
Figure 244. Figure showing the location of the connection radius.	278
Figure 245. Triangular concept structure showing simulated CTE as the angle changes for varying outside member thicknesses, where r=2mm, L=50mm.	278
Figure 246. Simulation results showing comparison between the measured connection radius (Rc) from the values on Table 63, and where the connection radius is kept at 1mm.	280
Figure 247. Images showing a potential arrangement for a graded composite plastic material in the form of an optical system body. The overall thermal expansion would be a value in between both materials.....	281
Figure 248. Build image showing the orientation of each patterned dilatometer rod. Light green represents ABS while dark green represents CPE.	281
Figure 249. Images of the completed lattices in black CPE and white ABS.....	282
Figure 250. Selection of images and measurements of the dilatometer plastic composites. The reflective black is CPE whilst the matte black is ABS.....	283
Figure 251. Two bonded layers with different elastic properties and their mechanical behaviour [213].	284
Figure 252. Calculated upper and lower bounds of thermal expansion.	286
Figure 253. a) Showing boundary conditions to be applied to the H1, H2, and H5 composite dilatometer samples. A and B are nodes held at a fixed displacement. A is fixed in XYZ, B is fixed in YZ. b) boundary conditions to be applied to H3 and H4 composite dilatometer sample.	287
Figure 254. Simulation views for all dilatometer composite rods	287
Figure 255. Displacement locations and notation example for the composite dilatometer rod H1_1-2...	287
Figure 256. Simulations showing deformation with 30x scaler to visibly show swelling locations. View 1 shows displacement values whilst view 2 shows Von-mises stresses.....	288
Figure 257. Simulated CTE results for dilatometer composites.	290
Figure 258. Dilatometer Results for H1_1, and H1_2 Composite Samples.	291
Figure 259. Dilatometer results for H1_3, and H1_4 Composite Sample.....	291
Figure 260. Dilatometer results for H2_1, and H2_2 Composite Sample.....	292
Figure 261. Dilatometer results for H3_1-2 and H4_1 Composite Sample.....	292
Figure 262. Dilatometer results for H5_1 Composite Sample.	292
Figure 263. Co-efficient of thermal expansion results for all printed plastic composites compared against simulated expansion, and theoretical upper and lower bounds.	293
Figure 264. Fibre orientations for the three samples. Images from Markforged's Eiger.io print software.	299

Figure 265. Top down view of two dilatometer samples with the fibre laid longitudinally , and transverse to the test direction. Image shows the CAD, then layer 1, and layer 2 respectively.....	300
Figure 266. Top down view of a dilatometer sample with the fibre rotated at 45° each layer. This is to attempt to make a material with isotropic thermal expansion. Image shows the CAD, then layer 1, layer 2, layer3, and layer 4, respectively.	303
Figure 267. Images of 3D printed continuous fibre composites showing fibre orientation.	301
Figure 268. CT scan of a nylon polymer with longitudinally oriented carbon-fibre filament. All views are taken from a middle cross-section.	303
Figure 269. CT scan showing a rendered 3D view outside with a 3.5x3.5x7mm block removed (left) and the inside layers of carbon-fibre and nylon with the walls removed (right) of the longitudinally oriented carbon-fibre nylon dilatometer sample.....	304
Figure 270. High resolution CT scan imagery of a 1mm diameter by 1mm length section of fibres in the centre of the longitudinally oriented carbon-fibre nylon dilatometer sample.	304
Figure 271. Image of the Nylon Kevlar fibre orientated transverse to the test direction.	305
Figure 272. CTE curves for nylon matrix material and orientated carbon-fibre	306
Figure 273. CTE curves for nylon matrix material and orientated glass-fibre	306
Figure 274. CTE curves for nylon matrix material and orientated Kevlar fibre	307
Figure 275. CTE curves showing thermal expansion for three identical Onyx samples, tested three times each. Shows stability of material over multiple temperature cycles.	308
Figure 276. CTE curves for Onyx matrix material and orientated carbon-fibre	309
Figure 277. CTE curves for Onyx matrix material and orientated glass-fibre	309
Figure 278. CTE curves for Onyx matrix material and orientated Kevlar fibre	310
Figure 279. CTE values for instantaneous CTE at -40°C for all nylon and onyx with all fibre types and orientations.....	311

List of Tables

Table 1. Typical materials used for optical system body and lens.	30
Table 2. CTE ranges for common invar variants in $\mu m/mK$	35
Table 3. CTE's for different fibre reinforced composites [22], [23], [60]–[62].	41
Table 4. Specifications comparing both Renishaw and EOS LPBF machines.	55
Table 5. Specifications comparing the current EBM systems by ARCAM .	57
Table 6. Specifications comparing three different DED machines .	59
Table 7. Metal Material Jetting machines specification comparison [93].	61
Table 8. Metal Binder Jetting machines specification comparison.	62
Table 9. Comparison between both Metal FDM printers.	63
Table 10. Specifications of a common UAM Machine.	64
Table 11. Summary of the most common metal AM processes accumulated from references in this chapter	65
Table 12. Selective Laser Sintering Plastic Machine Specifications.	67
Table 13. The most common three multi-material FFF printers with different nozzle arrangements.	72
Table 14. Benchmarks featured in the present work	75
Table 15. Specification of manufacturing parameters for benchmark parts from literature.	76
Table 16. Nominal diameters for each ring used to determined circularity and diameter deviation.	91
Table 17. Table showing the percentage difference in thermal expansion of the measured <i>Al2O3</i> against reference values.	106
Table 18. Table showing temperature uniformity from thermocouple readings across the baseplate. Hotplate temperature is set to 200°C, but the hotplate thermocouple reads a steady 156°C. 1:1 is at the top left edge, and 6:6 is at the centre.	122
Table 19. Table showing displacement and CTE data for a flat Ti64Al plate at 230°C from annotations in Figure 98.	125
Table 20. Table showing displacement and CTE data for a flat Ti64Al speckled plate at 220°C from annotations in Figure 101 above.	127
Table 21. CMM test bench measured CTE against reference CTE showing accurate thermal expansion measurement for Ti64Al and Invar.	131
Table 22. Linear material properties for determined ALM manufactured components and used in the simulation.	134
Table 23. Data showing simulation results for 1-2mm bonded INVAR around a Ti64Al and 316L ring. Linear interpolation used to show required inside thickness to match the CTE of the lens material. Data showing simulation results for 1-2mm bonded 316L and Ti64Al around an Invar ring. Linear interpolation used to show required inside thickness to match the CTE of the lens material.	139
Table 24. Reference CTE for 5mm thick ring with clad material, without any porosity added	150
Table 25. Simulated percentage CTE change for the single array design, compared with simulated values with no porosity.	154
Table 26. Proposed single array hole diameter to produce a matched CTE.	155
Table 27. Simulated percentage CTE change for the stacked array design, compared with simulated values with no porosity.	158
Table 28. Proposed stacked array hole diameter to produce a matched CTE.	159
Table 29. Geometric deviation from the nominal dimensions for the auxetic structure.	164
Table 30. Nominal compared to measured dimensions for single and stacked arrays.	166

Table 31. Simulated and measured CTE for the Auxetic and designed porosity structures manufactured in invar with a 316L clad, and measured with the CMM test bench.	169
Table 32. Metal powders used - Manufacturing methodology and target PSD.	176
Table 33. Particle Size Distribution for all gas atomised powders obtained using a Malvern Mastersizer. Powder sizes outside of nominal highlighted red.	180
Table 34. Tap density results.	183
Table 35. Laser parameters investigation ranges for LPBF of invar36.	185
Table 36. CTE's for invar36 LPBF manufactured samples.	186
Table 37. L9 input parameters for invar36 build 1. Level 1 build 1 is the settings for 316L provided by Renishaw. Level 1 build 2 is an estimated optimum setting from build 1.	187
Table 38. Laser parameters and corresponding relative densities obtained. Red signifies higher energy density while green is lower.	187
Table 39. Response and density result analysis for steps 4,5 and 6 outlined in experimental Chapter 4.7.	188
Table 40. Fe-Ni(x) induction melted alloy target and EDS measured composition.	190
Table 41. Literature references for in-situ LPBF composition, PSD, and manufacturing setup.	195
Table 42. Build plan showing percentage of in-situ Fe and Ni additions added.	197
Table 43. Invar in-situ blended powders mass proportions.	198
Table 44. Chemistry for the powders used measured using ICPMS.	198
Table 45. EDS scan settings used.	201
Table 46. Build numbers with the EDS map wt.% of nickel for density cube side and top cross-sections.	202
Table 47. Tabulated tensile data for the blended in-situ invar additions.	213
Table 48. Invar blended powders instantaneous CTE's every 50°C for the whole temperature range, units are $\mu\text{m}/\text{mK}$.	217
Table 49. Instantaneous CTE measurements for a range of temperatures for as-built parts for the invar blended powders.	218
Table 50. L25 array parameter variables.	222
Table 51. High laser energy input invar - optical porosity data.	231
Table 52. AlSi Optical porosity results table. The black dots are the porosity in the optical of the cross-section of the dilatometer rod.	241
Table 53. Microstructure of spray formed AlSi alloys. Centreline images compared.	244
Table 54. SEM BEC & EDS images showing phase sizes and distribution for AlSi40 manufactured with LPBF with 40ns ET, and AlSi42 spray formed. Magnification is x1000.	246
Table 55. Co-efficient of thermal expansion of the aluminium-silicon alloys averaged over -40 to 70°C.	253
Table 56. Plastic mechanical data as printed from Ultimaker technical data sheets.	259
Table 57. Plastic thermal data from Ultimaker technical data sheets	260
Table 58. Cura default material profile parameters for a 0.1mm layer thickness.	261
Table 59. Dilatometer results for thermal expansion of FDM plastics.	265
Table 60. Plastics with inclusions and their claimed features.	268
Table 61. Filament inclusion measurements from optical microscopy.	273
Table 62. Plastic CTE values and corresponding percentage reduction from inclusions.	275
Table 63. Table of figures displaying Triangular lattice concept manufactured in CPE and ABS at different angles. The connected interface is measured and compared to the nominal value.	279
Table 64. Plastic experimental composite layouts and their corresponding CTE ratio.	282

Table 65. Homogenised CTE's for composite dilatometer rods H3 H4.	284
Table 66. Curvature and radius for a bi-material strip composed of CPE and ABS.	285
Table 67. Boundary conditions for simulated composites.	287
Table 68. Table of simulated deformation data and calculated CTE's for the dilatometer composite samples.	290
Table 69. CTE's for oriented fibre reinforced nylon and the percentage reduction compared to the matrix polymer without the orientated fibres.	307
Table 70. CTE's for oriented fibre reinforced onyx and the percentage reduction compared to the matrix polymer without the orientated fibres.	310

1 Introduction

Additive manufacturing (AM) has seen an increasing level of investment over the last ten years, as companies look to investigate the unique opportunities it presents for their industry. There has been a significant increase in budget allocated by companies for the production of parts using additive manufacturing worldwide, from approximately \$200M in 2010 to \$1.4bn in 2019. In the United States the number of patents has also increased from 109 in 2010 to 1142 in 2017. Global predictions show an increase in market size from \$16bn worldwide in 2019 to \$40.8bn by 2024 [1]. The increase in investment occurs as companies are noticing the benefits of producing prototype and functional parts using additive manufacturing. AM provides the ability to rapidly produce small quantities of components without the need for complex and expensive tooling. The ability to rapidly change the design after each prototype enables engineers to shorten the development lifecycle of their products. Functional parts can be manufactured featuring complex geometries with multiple materials in a single print. The ability to print complex structures provides advantages over conventional manufacturing techniques.

To determine if additive manufacture can provide a competitive edge for a company, an assessment of the individual design challenges is needed. The sponsor company Qioptiq has determined that an improvement in the dimensional stability of its products over a range of temperatures would provide a significant technological improvement to their optical systems. Qioptiq have identified that their optical systems can experience a mismatch in the thermal expansion rates of the components in their assemblies. An example of this would be an assembly of a glass, germanium, or polymer lens inside a metal optical system casing. In this scenario it is likely that the metal will expand at a different rate with temperature compared to the lens material, creating expansion gaps in hotter or colder climates. Figure 1 shows a diagram of a cross-section of a typical lens housing, one symmetric and the other asymmetric. The locations highlighted are subjected to movement unless the co-efficient of thermal expansion of the surrounding casing is matched. Currently the thermal expansion mismatch is mitigated by the company using materials designed to absorb any contact stresses between the lens and its casing.

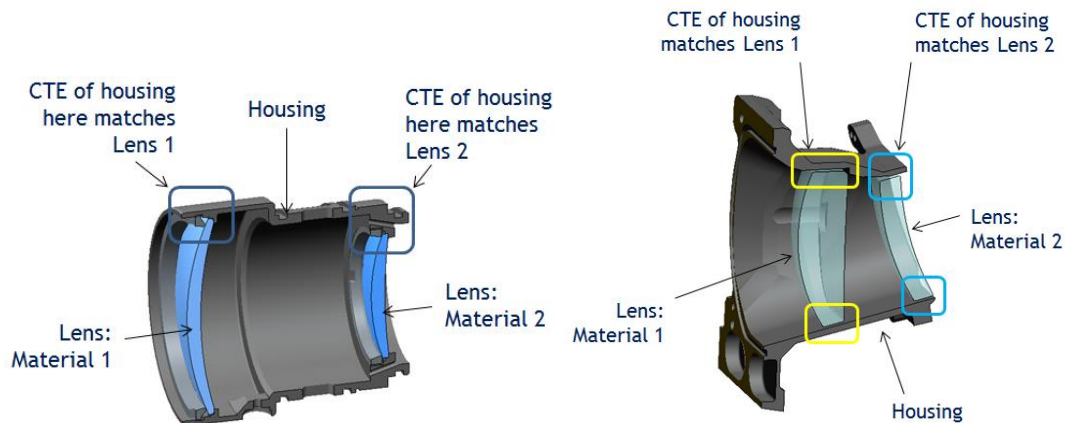


Figure 1. CAD image provided by sponsor company Qioptiq showing the required areas to match CTE in a cylindrical lens and rectangular lens system.

There are many ways to adjust the thermal expansion of a component. One method is to produce a structural design, whereby the movement of one member in the structure effects the surrounding members of the structure. There are several structural arrangements in literature where the material selection can cause movement within the structure when the temperature changes [2]–[11]. By selecting two materials with different thermal expansions and carefully choosing their location, the structure can emulate a lower coefficient of thermal expansion at key points on its structure. Work in this thesis suggests a layout for the best structural arrangement to control the thermal expansion around a cylindrical lens, using materials available for additive manufacture. These materials can be printed by multi-material additive manufacturing machines. Many companies have released machines on the market that have the capability to use a secondary material. The machines are designed to print using polymer materials, using either a fused deposition modelling technique, material jetting, or binder jetting process [12]. The most frequent use of a secondary material is to print the support structures using a material that is easily broken away from the main material. Some materials exist that can dissolve in liquid, meaning the supports can be printed in hard to reach areas. A secondary material of a different colour is used in industries to improve the aesthetics of the part [13]. In this investigation the secondary material will be used as a structural material to impart force or restrain members within the printed structure. It has a significantly different coefficient of thermal expansion to achieve movement with a change in temperature. It is printed using a fused deposition modelling process with a machine using a second nozzle for the secondary material. Other processes are also investigated to try and manufacture a structure with two metals. At the present time, the additive manufacturing technologies available for printing two metallic materials together at the same time are limited [14]. To achieve a similar result, laser powder bed fusion is used to create the structure, and a secondary metallic material is applied to the outside circumference using a laser cladding technique. The secondary material acts to constrain the primary material inside the

cylinder and creating movement within the structure. The approach of obtaining a tailored co-efficient of thermal expansion using two materials in a structure has a benefit and a disadvantage. It allows an engineer to tailor the thermal expansion by adjusting the dimensions of the structure in a computer aided design, speeding up development time. It also requires significant volume for the structure to exist, adds manufacturing complexity, and could be prone to fatigue issues as the structure frequently bends. Other methods of tailoring thermal expansion exist where only a single material needs to be printed. For the fused deposition modelling process, this can be achieved by adding inclusions such as short-chopped glass and carbon fibres, or metallic particles into the polymer. The introduction of short-chopped carbon and glass fibres are known to improve the mechanical strength of the printed components [15]–[18]. Literature shows that the coefficient of thermal expansion of glass and carbon fibres (-0.5 to $5\mu\text{m/mk}$) is significantly lower than most polymers (60 - $100\mu\text{m/mk}$), and when homogenously blended with a polymer can act to reduce the overall thermal expansion of the material to match that of glass or germanium (6 - $7\mu\text{m/mK}$) [19]–[24]. This opens the possibility for adjustment of the volume fraction of fibres depending on the desired co-efficient of thermal expansion which is a route of optimisation explored in the present work. The alignment of the glass or carbon fibres have also been shown to affect the thermal expansion. The co-efficient thermal expansion along the length of a carbon fibre (-0.5 to $0.1\mu\text{m/mk}$) is significantly less than the thermal expansion across it (4 to $5\mu\text{m/mK}$) [22]. To take full advantage of this behaviour, the thesis manufactures several parts using an additive manufacturing technique known as continuous fibre fabrication, where a fibre is deposited used the FDM process on top of each polymer layer in the build [25]–[29]. Four types of fibre are printed, kevlar, glass fibre, and carbon fibre. These fibres are deposited in between layers of nylon or nylon impregnated with short-chopped carbon fibres. The effects of the orientation of the fibre, the type of fibre, and the choice of matrix material all effect the co-efficient of thermal expansion. It is shown that with certain combinations a co-efficient of thermal expansion of close to glass and germanium is achieved.

Metal base additive manufacture also presents opportunities for thermal expansion adjustment. The powdered metallic alloy used in the laser powder bed fusion process can be adjusted to suit a range of thermal expansion requirements. The co-efficient of thermal expansion is determined by the elemental composition of the alloy used. Alloys such as Invar (FeNi36) and aluminium-silicon have their thermal expansion determined by the amount of nickel or silicon they have. Adjusting the amount of nickel in invar above 36wt.% can adjust the co-efficient of thermal expansion between 1 and $12\mu\text{m/mK}$. With aluminium-silicon alloys increasing the silicon content up to 87wt.% is shown to reduce the thermal expansion from 24 to $4.9\mu\text{m/mK}$. In this thesis Invar36 powder is blended with nickel powder and printed to produce a component with a higher nickel content and

a higher co-efficient of thermal expansion. The printing of two aluminium silicon alloys of 30 and 40wt.% are shown to be possible. The two powders are also blended together in even amounts to produce an alloy with 35wt.% silicon and a co-efficient of thermal expansion in between both. This opens up the possibility for laser powder bed fusion to become a manufacturing option for companies that wish to adjust the elemental expansion by composition of their alloys with each component printed. A study into the effect of adjusting the lasers scanning parameters on the thermal expansion is also conducted. It is determined that there is a small effect on the co-efficient of thermal expansion of invar36, increasing it from 2.05 to 2.3 $\mu\text{m}/\text{mK}$ as the laser parameters are varied to increase the energy density of the melt pool. This study demonstrates the need to maintain a consistent set of laser parameters to achieve a stable co-efficient of thermal expansion.

1.1 Technical objectives

The technical objectives for the additively manufactured optical system are as follows:

- Perform over all climates from -40 to 70 °C
- Exhibit a CTE for the lens casing of between 6-7 $\mu\text{m}/\text{mK}$ to match glass or germanium lens material, or 60-70 $\mu\text{m}/\text{mK}$ to match a range of polymer lenses.
- Suitable stiffness for the lens casing within the working temperature.
- Design for the tolerances available using additive manufacturing.

1.2 Design Considerations for an optical system

In an optical system there are many design requirements in order to produce the correct quality image. The quality of the image can be attributed to the mechanical design and material choice.

The design requirements Qioptiq are looking to achieve are as follows;

- Working temperature range -40 °C + 70 °C
- Germanium \varnothing 50mm lens: Decentre: \pm 0.02mm
- Schott N-BK7 \varnothing 150mm lens: Decentre \pm 0.15mm
- Lens tilt 2-5 mins
- Axial Shift 0.1-0.2 mm

A typical cylindrical lens design is shown in Figure 2 and Figure 3. The system is a typical system presented by Qioptiq that would benefit from thermal expansion control of the body components.

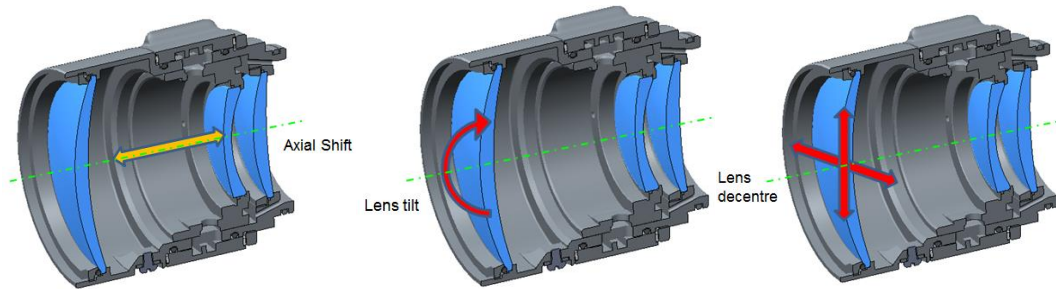


Figure 2. Images showing the orientations of axial shift, lens tilt, and lens decentre.

To satisfy the design requirements of axial shift, lens tilt and lens shift, considerations have to be made for the changes in thermal expansion rates between the lens material and its casing.

Currently potting pads are used in between the lens and the casing. These pads allow for the manufacturer to align the lens appropriately, by adjusting their thickness and position. These pads are manufactured from a rubber or silicon material, and provide an important barrier between the lens and its casing. The pads are assembled to make a tight fit, so that changes in diameter of the lens or casing will not reduce the applied pressure to a point where the lens is able to move, and conversely will not increase the pressure to a point where the lens can be damaged. These pads provide an important means to absorb any thermal expansion changes during its lifetime, and provide an even distribution of pressure to hold alignment. Figure 3 shows the cross-section lens and its housing from a 3-lens optical system. Materials used in the body of the optical system are typically metals or high strength polymers depending on their application. The lenses used most frequently by Qioptiq are germanium for Infra-red applications, and borosilicate glass for visible light applications. For an optical design engineer, the choice of material is important for not only its stiffness and density, but also its thermal behaviour. It can be seen that the polymers typically used by Qioptiq have a CTE of approximately ten times higher than all others. If a polymer body is used, it would be advantageous to use a polymer lens also, since the CTE mismatch will be too high with any other combination.

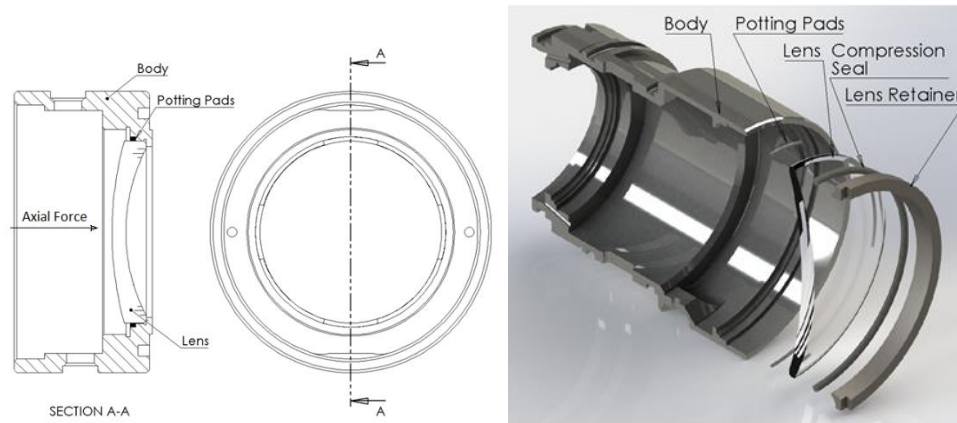


Figure 3. Lens and body cross-section showing exploded view of the parts inside, notably the location of the potting pads which seat the lens to the body.

		Density (g/cc)	Young's Modulus (GPa)	Coefficient of Thermal Expansion ($\mu\text{m/mK}$) @ 20°C	Specific Stiffness ($10^6\text{m}^2\text{s}^{-2}$)
Body	Stainless Steel	8	200	17.3	25
	Aluminium	2.7	69	23.6	25.6
	Titanium	4.43	114	8.6	25.7
	PEEK	1.31	5.75	55	4.4
	GF Nylon (30%)	1.29	5	50	3.9
Lens	Germanium	5.32		6.1	
	Schott® N-Bk7 Borosilicate Glass Lens	2.51	82	7.1	32.67
	ZEONEX® 480R Plastic Lens	1.01	2.2	60	2.18

Table 1. Typical materials used for optical system body and lens.

1.3 Thesis objectives

This thesis will aim to understand the abilities of Additive Manufacturing in producing CTE tailored meta-material structures for optical systems by;

- i) Investigate the latest advancements in additive manufacturing for deployment of tailored thermal expansion solutions.
- ii) Benchmarking current additive manufacturing processes to assess feasibility for production of components in the optical industry.
- iii) Investigate thermal expansion control structures with multi-material additive manufacturing techniques.
- iv) Investigate methods of controlling thermal expansion with laser powder bed fusion using controlled expansion alloys.
- v) Investigate controlled expansion plastics for printing using fused deposition modelling.
- vi) Investigate additively manufactured controlled expansion fibre reinforced polymers.

1.4 Publications

- S.S.Milward, H.Swygart, L.Eccles, S.G.R.Brown, and N.P.Lavery, "Controlling thermal expansion with laser powder bed fusion." [30]
- N. Lavery, S. Milward, S. Brown, S. Mehraban, "Laser Powder Bed Fusion processing of Invar 36® (Fe-36%Ni) for thermal expansion control in Space Satellite Components", Additive International, Nottingham, United Kingdom, 7th July 2019.

2 Literature review of thermal expansion control

2.1 Introduction

Most engineering materials expand in response to heating, and contract in response to cooling. From an atomic perspective, thermal expansion is caused by an increase in the average distance between atoms. The rate at which this occurs is called the Co-efficient of Thermal Expansion (CTE) of the material. If there is a greater atomic bonding energy in the material, the result will be a lower CTE. If a material expands with temperature change the CTE will be positive, if it contracts with temperature change then the CTE will be negative. The CTE is defined as:

$$a_L = \frac{l_f - l_o}{l_o(\Delta T)} \quad (1.1)$$

Where l_o is original length, l_f is final length after temperature change, ΔT is the temperature change, and a_L is the linear co-efficient of thermal expansion. The CTE has units of reciprocal temperature (k^{-1}) such as ($X10^{-6}/K$) which can also be expressed more commonly as; ($\mu m/m.K$), and ($ppm/^\circ C$).

Similarly, it is possible to define a volumetric coefficient a_V as:

$$a_V = \frac{\Delta V}{V_o(\Delta T)} \quad (1.2)$$

Where V_o is the initial volume, ΔV is the change in volume, and a_V is the volume coefficient of thermal expansion. There are two methods of controlling co-efficient of thermal expansion (CTE), by the selection of an alloy, plastic, or geometric arrangement of two materials with different thermal expansions.

2.2 Controlling thermal expansion through material properties

2.2.1 Controlled thermal expansion metals

Considerations for the thermal expansion of a metal is important when designing many mechanical systems. An optical system is very sensitive to the changes in dimensions of the metal that surrounds the optical systems lenses, as these changes can affect the optical alignment. Controlling the thermal expansion of the metals so that all the materials in the optical system thermally expand at the same rate is beneficial for performance. This is achieved by matching the CTE of all the materials in the optical system. An optical system will typically use either a borosilicate glass, germanium, or polymer lenses. The coefficient of thermal expansion of all three materials can vary from $6\text{-}7\mu\text{m/mK}$ for glass and germanium to $60\text{-}70\mu\text{m/mK}$ for polymer lenses. The thermal expansion of the metal casings that hold the lenses in the optical system can vary from $12\mu\text{m/mK}$ for steel to up to $24\mu\text{m/mK}$ for aluminium. When designing an optical system, engineers will understand the differences in thermal expansion will create contact stresses and alignment issues and try to design compensation features to mitigate the issue. Another method is to adjust the thermal expansion of the metal itself to match that of the lens material. The elemental composition of the alloy can also be adjusted to reduce the thermal expansion of the metal. There are several examples of low coefficient of thermal expansion materials such as INVAR, Super INVAR, Zerodur®, and ULE™. Each material has a different application. Super INVAR has a lower CTE than INVAR since the nickel percentage has been tweaked, and cobalt has been added. Zerodur® and ULE™ are glass ceramics used in the space industry for mirrors and reflectors. They have been widely applied as mirrors in large telescopes, such as Keck I and Keck II [31].

Some commercially available controlled expansion alloys include FeNi30-46 (Invar), FeNi29Co17 (Kovar), and AlSi7-70. Composite pseudo-alloys also exist; Cu-W, Cu-Mo which are widely used for controlled expansion in electric applications. The low expansion alloy Invar (FeNi36) can achieve the lowest CTE at around $1\mu\text{m/mK}$ but can also be adjusted by increasing or decreasing the nickel content. FeNi30, and FeNi46 can both achieve a CTE of $9\mu\text{m/mK}$, when adjusting the nickel content either side of the lowest point of 36wt.% nickel. Choosing approximately 40% and 43% nickel tailors the metal to match the CTE of germanium and NBK-7 glass, respectively. Adding cobalt into the alloy to create FeNi29Co17 (Kovar) exhibits a thermal expansion curve to match that of borosilicate glass [32]. The material also bonds to the glass via an intermediate oxide layer of nickel oxide and cobalt oxide. It is used extensively in cathode ray tubes [33].

Iron-Nickel (Fe-Ni) Alloys

Fe-Ni36 is also known by the name Invar. It is a very low thermal expansion iron nickel alloy discovered by Charles Guillaume in 1897. In his initial discovery he determined the lowest CTE of approximately $1.2\mu\text{m/mK}$ when the nickel content is approximately 35.5wt.%. He drew attention to the possibility that this was not a precise limit because of impurities in industrial materials, for example manganese, or chromium etc. [34]. The name 'invar' derives from the property invariability of the alloy to thermal expansion. While his work focussed on the volume changes Guillaume was aware that the effect was strongly related to thermo-magnetic transformations, based on earlier work in 1890 by Jon Hopkins. In this work it was shown there was an anomaly in the magnetisation of alloys with Ni constant between 30-33wt.% at low temperatures [35]. It has been found that the effect vanishes at a temperature near to the curie temperature further confirming that magnetism plays a role in the low thermal expansion. The exact reason for the low thermal expansion is still not fully understood, although some good theories backed up with data have been presented since its discovery. After years of intensive research, the first widely accepted theory was that the effect is attributed to face-centered-cubic alloys being close to the phase boundaries between fcc and bcc [36]. It was later discovered in the late 1970's that it could occur in bcc, hcp, and even amorphous metals [37]. The current held theory is that the invar effect is caused by Ising magnetism. It has been shown that this theory accurately reproduces several well-known properties of these materials, including Guillaume's famous plot of the thermal expansion coefficient as a function of the concentration of nickel [38], [39].

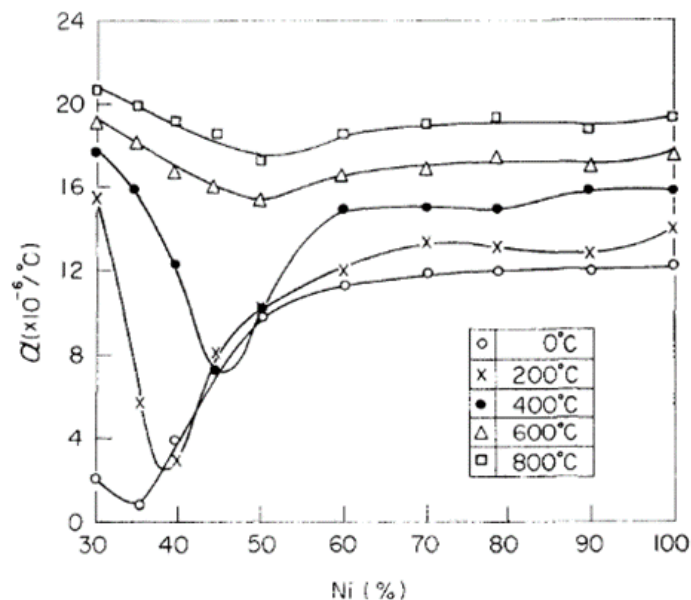


Figure 4. Physical alpha curves for invar as the nickel percentage changes [40].

The level of impurities can affect the CTE of invar. Several different grades of invar exist with optimised chemical compositions dependant on the applications; mechanical properties, weld ability, structural stability, and thermal expansion effects at cryogenic or elevated temperatures.

Grade	Material use	- 180°C	20°C to 100°C	20°C to 200°C	20°C to 300°C
Invar	General use, including cryogenic.	1.8	1.2	2.3	4.8
Invar-93	Developed specifically for cryogenic use with improved weldability.	1.5	1.3	2.4	4.9
Inovar	Low residuals, low CTE.	1.4	0.65	1.9	4.8
Microvar	Inovar with lower cobalt and improved mechanical properties.	1.4	0.65	1.7	4.6
Inovco	Invar with cobalt, very low CTE and enhanced mechanical properties.		0.55	1.5	4.4
Hardened Invar36	Elevated mechanical properties, hardened by 750°C for 30mins.	4.5	2.8	4.0	9.0

Table 2. CTE ranges for common invar variants in $\mu\text{m}/\text{mK}^1$

It is also noted that the level of carbon must be kept below 0.05wt.% to keep the low thermal expansion properties. When processing the material through additive manufacturing, the chemical composition needs to be tightly controlled in the gas atomised powder. The manufacturing method of LPBF creates a unique microstructure that experiences different cooling rates to conventionally manufactured materials.

Aluminium Silicon

Aluminium-Silicon (AlSi or ‘Silumin’) alloys have significant potential in the design of optical systems due to their low density and reduced thermal expansion when compared with elemental Aluminium [41]. They have seen rapid deployment in electronics as a package material for controlled expansion, and in engine blocks and pistons due to the high wear resistance and hardness provided by a high silicon content [42]. An increase in silicon content corresponds with a decrease in thermal expansion, providing an excellent ground for a tailoring the silicon content depending on the co-efficient of thermal

¹ Carpenter Invar, Inovar, Microvar, Inovco, Invar-93 [Online]. Available: <http://www.matweb.com>. [Accessed: 21-May-2017]

expansion required. Manufacturing the alloy in a conventional method employs chill-casting. In high silicon alloys, this method of manufacture creates in large columnar grains of silicon throughout the cast. This produces a fragile, brittle component not suitable for use. One way to increase the mechanical strength is to create an Aluminium silicon carbide (Al/SiC) metal matrix composite (MMC). Here, a matrix of Al is reinforced with fine 2-3 μm SiC particles using pressure casting and stir casting techniques incorporating up to 70 wt% SiC in an Al matrix [43], [44]. The incorporation of high levels of SiC leaves the composites virtually unmachinable with conventional tools [45]. An improved method of manufacture called spray forming has been developed by Sandvik Osprey that features a finer, isotropic microstructure. The process works by induction melting the Al-Si pre-requisite alloy, and directing the molten alloy through a nozzle where it is atomised by nitrogen at high velocity, creating droplets which are typically 40 μm in diameter. The droplets condense onto a cold rotating plate. The coalescing droplets undergo rapid cooling as they are added to the plate layer by layer [46]. It is the combination of rapid cooling in the spray, and the generation of a large population of solid nucleants in the impacting spray that leads to a fine isotropic microstructure. The process can be used to create an Al-Si alloy with high silicon content up to 70 wt% Si that is stronger than conventionally casted Al-Si alloy, and can be easily machined compared with Al/SiC composites which cannot [47].

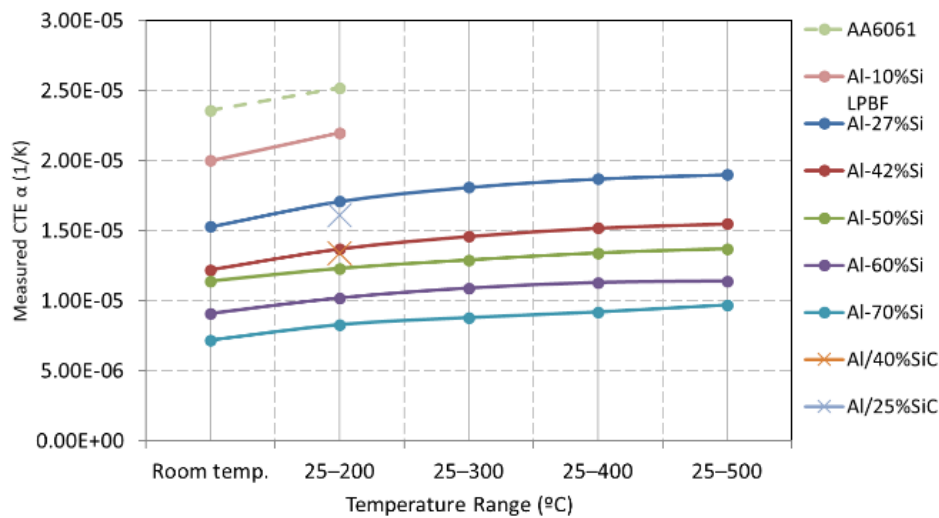


Figure 5. Thermal expansion values for spray formed AlSi alloys (Al-27-70%Si), AA6061 Al Alloy, [48], [49].

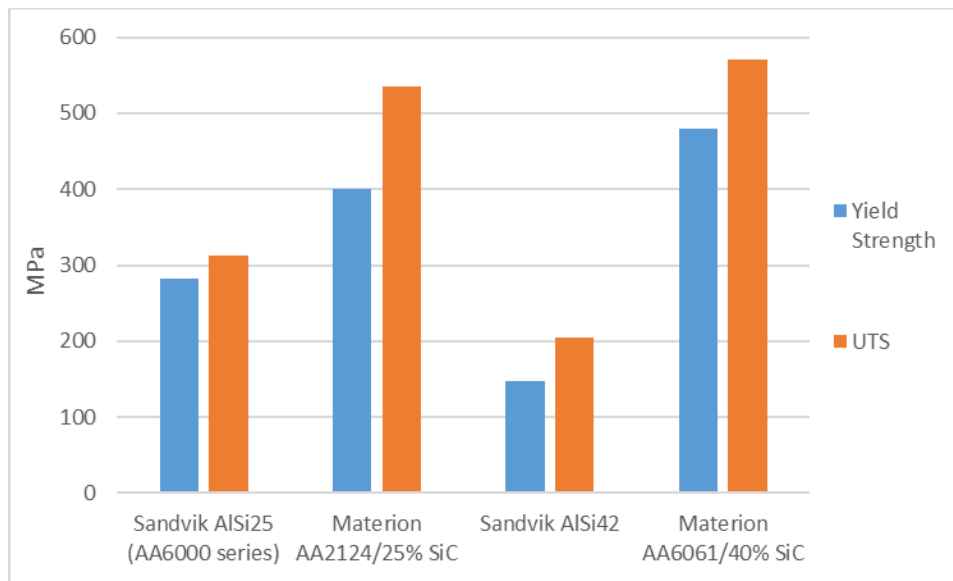


Figure 6. Yield strength and UTS, for AlSi alloys manufactured by Sandvik, and AlSiC composite by Materion [48], [49].

This chapter will look at the possibility of creating high silicon aluminium alloys using LPBF instead of spray forming. It will look to compare the grain size and distribution, mechanical, and thermal properties of produced parts, with parts produced using the spray forming process.

There are several similarities between spray forming process and the LPBF process, that may create a similar fine isotropic microstructure if parameters are suitably controlled. Both processes use a gas atomised feedstock powder, and both processes deposit the material layer by layer. During spray forming the molten droplets are cooled onto a plate, and subsequent molten droplets are added on top. This creates rapid heating and cooling similar to what is experienced during the LPBF process. To mimic the spray forming processes as best as possible using LPBF, the laser processing parameters must limit the build-up of heat in the component, so that each layer has time to cool before the subsequent layer is added. This will create a fine microstructure. Spray forming has a porosity level ranging from 1-2%, with a pore size depending on the alloy freezing range, however LPBF has shown that high silicon AlSi components can be manufactured with 99.8% density [46], [50]. Although it is normal to find the optimum laser parameters based on density, it may be more advantageous to optimise based on mechanical strength and microstructure, considering the process to replicate already has porosity, and is deemed mechanically superior to cast components with no porosity.

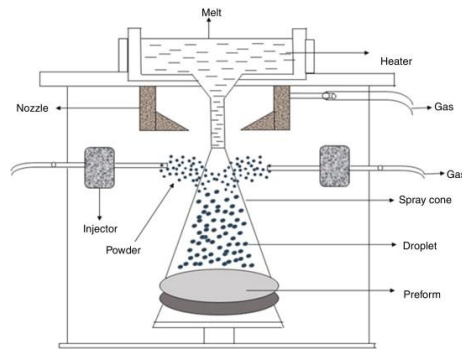


Figure 7. The Sandvik Osprey Spray forming process for creating AlSi alloys with high silicon content for controlled thermal expansion.

The maximum silicon alloy Al-Si40 has been chosen to be characterised using LPBF due to its low CTE of approximately $13.7\mu\text{m/mK}$ between 25-200 °C, and good mechanical properties, plotted in Figure 6. The Al phase in an AlSi alloy is continuous up to 85%, and the Si phase is continuous over approximately 40%, so AlSi40 is advantageous because it will offer a co-continuous duplex alloy. Such an alloy exists from Sandvik, ‘CE13F’ a cold sprayed Al-42%Si alloy. The continuous Si phase produces a stiff alloy with low thermal expansion, and low internal stresses, whereas a continuous Al phase improves thermal conductivity, toughness, and lowers electrical resistance. There is minimal solubility of Si into Al (<0.3%), and even less solubility of Al into Si.

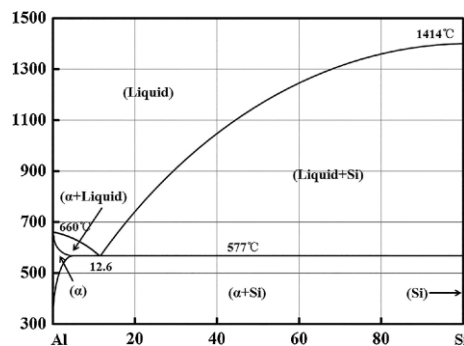


Figure 8. Phase diagram for AlSi binary alloy [51].

The most successful AlSi alloys manufactured using LPBF are those with silicon content near to the eutectic point, where the melting point is lower, and the solidification temperature is narrower. This creates less shrinkage porosity and improved processing using LPBF. Alloys such as AlSi10Mg and AlSi12 fall into this category [51]. The fine grain strengthening and solid solution strengthening means they exhibit superior yield strength (YS) and ultimate tensile strength (UTS) with LPBF compared with those fabricated through conventional alloy casting [52], [53]. AlSi10Mg exhibits a hardness rating of between 130-150HV, double that of die cast EN 1706. Success has also been achieved with hypereutectic high silicon alloy AlSi50 using *in-situ* melting of gas atomised aluminium and silicon alloys. *In-situ* meaning aluminium and silicon powders

have been blended together and melted. A dense component with ultrafine microstructure was created, with components featuring high hardness values of 188HV [54]. Macro-segregation of the primary Si is observed due to Marangoni convection and the temperature difference between the interior and exterior of the molten pool [50], [55]. This could present issues during manufacture, however it has been shown to have completed successfully with in-situ melting, so a gas atomised powder may have more success. Kimura et al. [56] used LPBF to manufacture AlSi alloys with up to 20wt% Si, and achieved up to 99.5% density, but the samples contained many microcracks. Franhoufer university has printed AlSi40 using LPBF and fully characterised the thermal and mechanical properties, achieving a relative density of above 99.5%. They investigated the effects of heat treatment and hot isostatic pressing on the properties [57]. Later the team demonstrated its applicability for use as a mirror substrate to be coated with electroless nickel for cryogenic space applications [58].

To the best of the authors knowledge there is no literature available that investigates the feasibility of blending different silicon amounts in pre-alloyed AlSi powders and manufacturing using LPBF. In chapter 6.6 this work focuses on the printing of AlSi30 and AlSi40 and comparing it to conventionally made material. To make the work novel, AlSi30 and AlSi40 are blended and printed together to form a silicon content in-between both.

2.2.2 Controlled thermal expansion polymers

Plastics have a weight advantage over metals but lack their strength, stiffness, and dimensional stability. Re-enforcing them with carbon fibres (CF) or glass fibres (GF) has been used to bridge the properties gap. When it comes to thermal expansion plastics have a relatively large CTE (60-100 $\mu\text{m}/\text{mK}$) compared with metals (1-24 $\mu\text{m}/\text{mK}$), but research has shown that adding CF and GF inclusions can significantly reduce the CTE [59]. This opens up the possibility to tailor the CTE depending on the volume fraction (V_f) of inclusions either mixed homogeneously or laid with a matrix to form a composite. Carbon Fibres have shown to have a negative CTE in the fibre direction [19], [20]. There is little data for CTE of carbon fibres across the fibre direction [21]. The Carbon-Fibre Reinforced Polymers (CFRP) have been shown to be stronger than Aluminium 6061 and 40% lighter. The strength is highly dependent on the fibre orientation, whereby a unidirectional fibre in the direction of load will be stronger. This makes the comparison between an anisotropic composite and an isotropic metal challenging. An isotropic metal has a Young's modulus, and Poisson's ratio is the same in all directions, where as a composite will require a greater number of constants to describe its elastic behaviour [60]–[62].

3D printing of plastics and polymers with inclusions such as glass or carbon fibre can be achieved by adding the short-chopped strands into the feed filament and printed in a conventional manner, as outlined in chapter 3.3.5. The printing of oriented fibres is achieved using a process called continuous filament fabrication which uses two nozzles, one for the polymer and the other for printing the filament. CFF allows you to directionally orientate the fibres according to the mechanical and thermal requirements. A typical CFF machine is shown in chapter 3.3.5 and in Figure 38.

For comparison against the 3D printed CFRP's it is useful to understand similar composites manufactured by conventional means. A Carbon Fibre Reinforced Carbon (CFRC) composite is a material consisting of carbon fibre reinforcement in a matrix of graphite. It is the same material used on the space shuttle thermal insulation panels. There is no literature of CFRC's being 3D printed. This unique material exhibits a negative CTE of -0.5 to $-0.1 \mu\text{m/mK}$ in the direction of the fibre, and 4 to $5 \mu\text{m/mK}$ across the length of the fibre for the temperature range of between 20 and 200°C . The CTE is highly dependent on the number of thermal cycles, for which it exhibits a non-linear relationship over 1 - 100°C cycles. This data is useful for comparison and guidance in relationship to carbon fibre reinforced polymers [22].

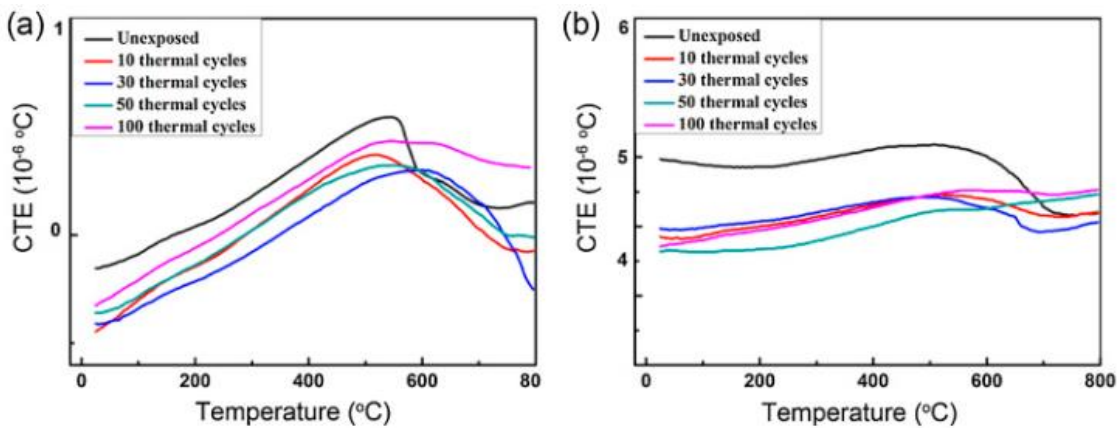


Figure 9. CTE of CFRC composites after a cryogenic thermal cycle from -120 to 120°C of; a) along the length of the fibres and, b) across the length of the fibres [22].

Research performed by B.Yates et al. analyses the transverse and longitudinal CTE's in a carbon fibre epoxy resin mix with varying volume fractions (Vf). The composite is constructed with unidirectional fibres. It is observed that CTE is significantly affected by the direction of measurement across these fibres [23]. The data presented in this paper has been plotted for analysis in Figure 10.

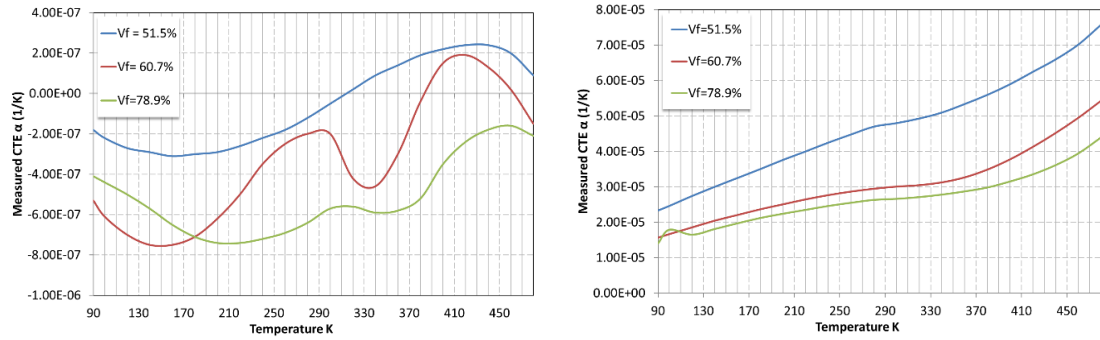


Figure 10. Graph showing CTE's in a CFRP Epoxy Resin mix for different volume fractions. Measurement taken along the length of the fibres (left) and across the length of the fibres (right) Data taken from (B.Yates,1978 et al.) [23].

The data presented shows that measurements along the length of the fibre have a below zero CTE for much of the temperature range, however measurements across the fibres have a much higher CTE. The data is very similar to that of CFRC composites, showing a negative CTE along the length of the fibre, and a higher CTE across the length of the fibres, although a magnitude higher in due to the plastic matrix material. In both directions, the increased volume fraction of glass fibres has reduced the CTE. These findings are useful as they suggest that the CTE can be reduced in 3D printed composite, and tailored depending on the direction of the fibre. Alternatively, randomly orientated short-chopped fibres could be impregnated into the material to produce a material with isotropic thermal expansion directions.

Materials	Co-efficient of thermal expansion ($\mu\text{m/mK}$) @ 20-100°C	Materials	Co-efficient of thermal expansion ($\mu\text{m/mK}$) @ 20-100°C
Fibre Glass Composite	5.3	Carbon Fibre Reinforced Plastics	-1 to 70
Kevlar Fibre Reinforced Plastics	-6.3	Carbon Fibre Reinforced Carbon	-0.5 to 6

Table 3. CTE's for different fibre reinforced composites [22], [23], [60]–[62].

For comparison for the mark forged machine, it is useful to look at the effect of inclusions in nylon. Looking at the matrix polymer Nylon 6, it is shown that adding e-glass fibre inclusions of 30% by volume, reduces CTE by 57% at 300K [24]. It is reasonable to assume that carbon fibre will restrict thermal expansion further due to its lower CTE. The

effect of short-chopped carbon fibres added into PETG in chapter 7.4 shows a reduction of up to 74.7%. It is useful to attempt to reduce the CTE as much as possible when dealing with plastics and polymers, as their thermal expansion is already high (around $85\mu\text{m/mK}$ for nylon). If a reduction of more than 90% for nylon can be achieved, then the CTE could come close to that of the glass or germanium lens material at $6\text{--}7\mu\text{m/mK}$. Polymer lenses such as the ZEONEX[®] are easily tailorable using polymer composites at $60\mu\text{m/mK}$ [22], [23], [60]–[62].

To the best of the authors knowledge there is no literature on the effect of fibre orientation in 3D printed carbon, glass, or kevlar within a nylon matrix, on the linear co-efficient of thermal expansion of the composite. Chapter 8 completes this work by determining thermal expansion curves separately when fibres are orientated with or tangential to the test direction.

2.3 Controlling thermal expansion bi-material structures

This chapter will perform a literature review into the different types of tailored co-efficient of thermal expansion (CTE) lattice structures available. To tailor any co-efficient of thermal expansion, two materials must be used. The geometry and arrangement of these two materials amongst the structure, will determine its stiffness and efficiency. Several arrangements have been developed by computation modelling using three-phase topology optimisation, and analytically using numerical derivation.

2.3.1 Three-phase topology optimisation

Three-Phase Topology optimisation is a method of generating a structure with a pre-defined co-efficient of thermal expansion (CTE), first proposed by Sigmund and Torquato. The composite structure is made of two different material phases and a void phase. The method works by finding the distribution of material phases that optimises an objective function, for example its thermoelastic properties. The optimisation is subject to certain constraints such as elastic symmetry or volume fractions of the constituent phases, within a periodic base cell. The operation is solved using sequential linear programming. This method can produce organic looking structures with symmetry depending on the side looking to be controlled [4]. For example, control on all four sides would produce a geometry whereby it is symmetric across four planes. In a situation where two sides are being controlled instead of four, there is symmetry on two sides.

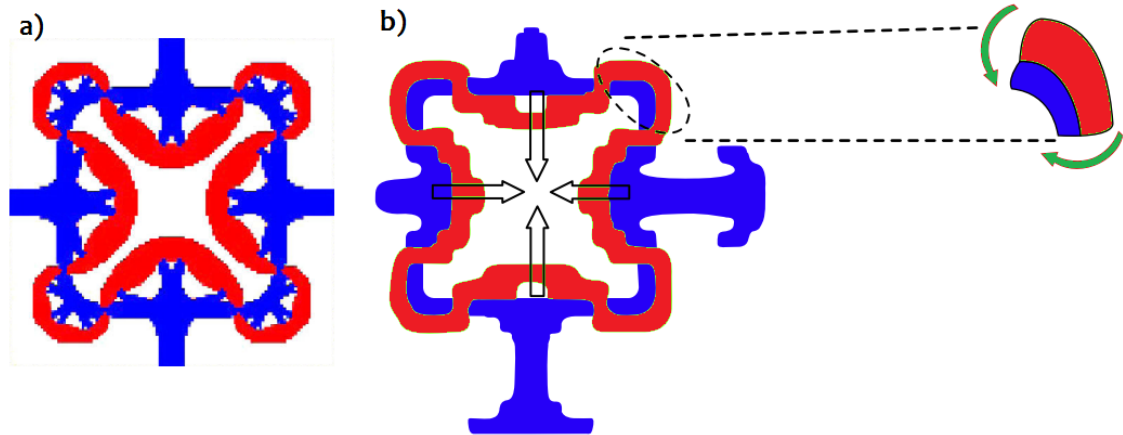


Figure 11. A unit cell of a three-material composite with macroscopic negative thermal expansion. The red denotes the higher CTE material, while the blue denotes the lower CTE material. a) shows the generated geometry, b) shows the simplified geometry allowing for DMD toolpath application. [63]

Due to its complex geometry, this has traditionally been too difficult to manufacture but due to advancements in additive manufacturing, it has also been realised experimentally. The generated structures have been printed using various ALM techniques, including Direct Metal Deposition (DMD), and Photo polymerisation Material Jetting (MJ). The main advantage of the method is that it describes a general approach to design for any CTE for any set of material properties. It is effectively unbound given stiffness is not an objective function.

To manufacture using DMD, Mazumder, J et al. [63] used two powdered materials which were jetted into a laser on a pre-determined tool path. The tool path had to be carefully controlled to allow for overlap and mixing of the metals, but to not cause reduction in the effective geometry. The materials chosen had to both be miscible with one another, and also feature a large enough CTE ratio. To achieve this, the team used Chromium ($6.5 \mu\text{m}/\text{mK}$) and Nickel ($13 \mu\text{m}/\text{mK}$), providing a CTE ratio of 2. This was proven to provide a negative CTE when tested using a dilatometer.

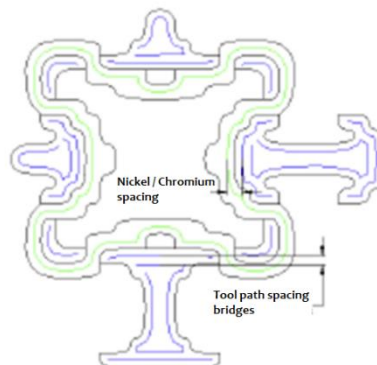


Figure 12. Toolpath image for DMD where blue denotes the low CTE material chromium, and green denotes the high CTE material, Nickel.[63]

The best toolpath overlap was found to be 50% nickel /chromium spacing where a 600um layer width features a 300um. This provided a consistent connection between the two materials.

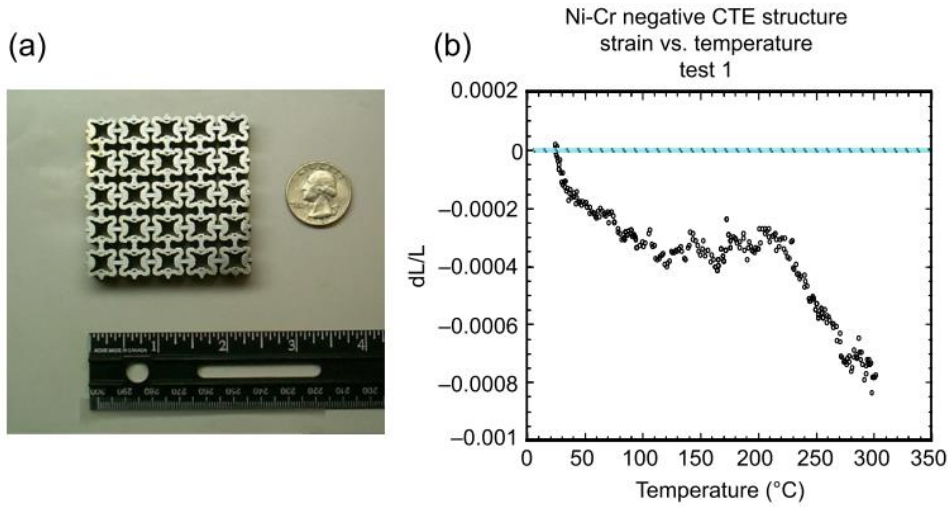


Figure 13. a) Image showing multiple connected Ni-Cr negative CTE structures after manufacture using DMD. b) Graph showing the experimental results for change in length as temperature increase [63].

For construction using photopolymer additive manufacturing Akihiro Takezawa, et al. used the same 3-phase topology optimisation method to create an STL of a similar negative CTE arrangement [64]. Manufacture was carried out using a Stratasys Objet Connex 500 which allows for multi-material printing using two photopolymers named VeroWhitePlus RGD835 and FLX9895-DM, which is an admixture of VeroWhitePlus and TangoBlackPlus. This secondary material is flexible in nature, but also exhibits a different CTE. The CTE and Young's Modulus of these materials were used in the optimisation model, as the following;

$$E1 = 290 \text{ MPa}, \quad E2 = 5.0 \text{ MPa}, \quad a_1 = 1.0 \times 10^{-4} \text{ K}^{-1}, \\ a_2 = 1.2 \times 10^{-4} \text{ K}^{-1}$$

To maintain a certain level of effective stiffness while reducing the CTE, a multi-objective function can be set;

$$\text{minimize } \varphi_1, \varphi_2 \quad J(\varphi_1, \varphi_2) = -w * C_{iii}^H + (1 - w) * \beta_{ii}^H \quad (i = 1, 2) \quad (2.1)$$

Where β^H is the thermal stress tensor, and C^H is the effective in-plane elastic tensor and CTE tensor [64].

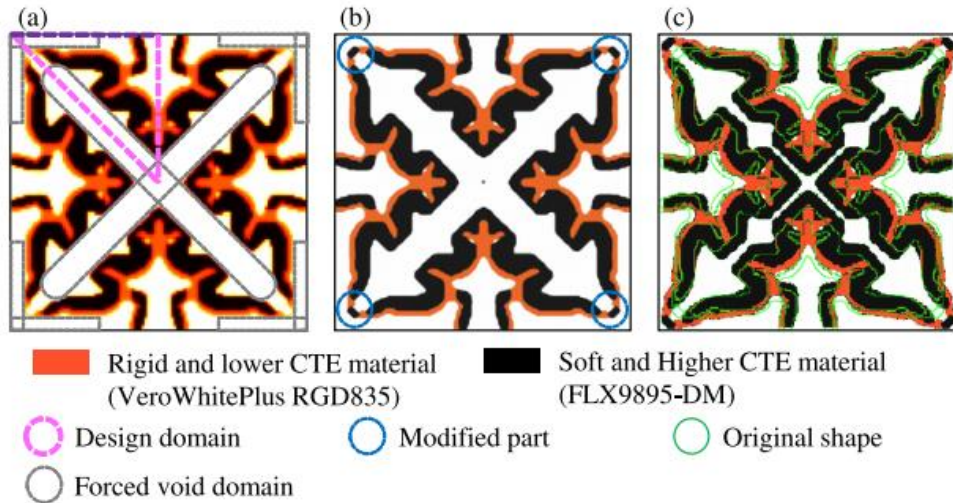


Figure 14. Optimal configurations and 2D view of the STL model. (a) Original topology optimization result. Pink dotted lines indicate the optimized domain. Gray dotted lines indicate the forced void domain for maintaining the deformation range. (b) 2D view of the STL model generated from the topology optimization result. The hinge-like part of the stiff material on the corner was replaced with thicker soft material as shown in blue dotted circles. (c) Thermal deformation shape obtained from the reanalysis of the STL model. The green lines indicate the original shape.

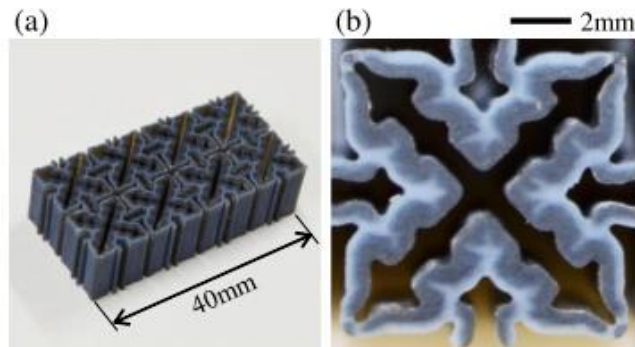


Figure 15. Negative CTE structure created on an Objet Conex 500 [64]

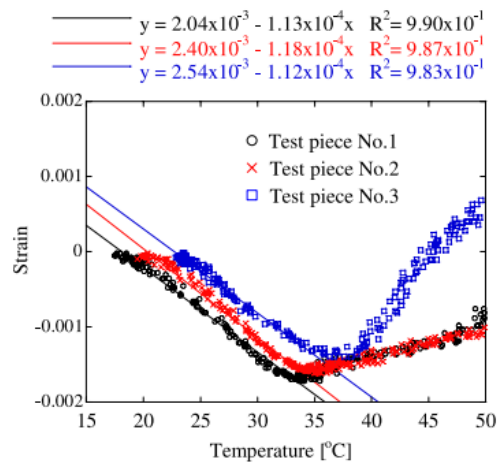


Figure 16. Thermal deformation of test pieces measured by a laser scanning dilatometer. The temperature rising rate is 1 °C/min. The temperature range is between RT and 50 °C. RTs of measurements No. 1, 2,

and 3 are 17.45, 19.45, and 22.85 °C, respectively. Approximation lines are plotted for the data within the temperature range between RT and 34°C.

The results show CTE's of as low as $-3 \times 10^{-4} K^{-1}$ which is a reduction of -300% compared to its bulk modulus [64]. This research proves that topology optimisation works and can be manufactured using Material Jetting additive manufacturing. Although the structure can produce a tailored CTE, the low homogenised Young's modulus of the combined material is too low for the optical industry. When compared to the lens material, it is too soft and would not provide adequate stiffness.

2.3.2 Analytically derived metamaterial structures

Analytically deriving the best approach to creating a tailored CTE structures requires thought into structural stiffness, efficiency, and ease of manufacture. There are many forms of bi-material structure proposed by Lakes, Steeves, and Jefferson [3], [6], [8]. These structures use two materials with different CTE's to create bending or stretching of members in the structure to create a positive or negative CTE. Figure 17 shows the first arrangements proposed by Gibiansky and Torquato, and Lakes.

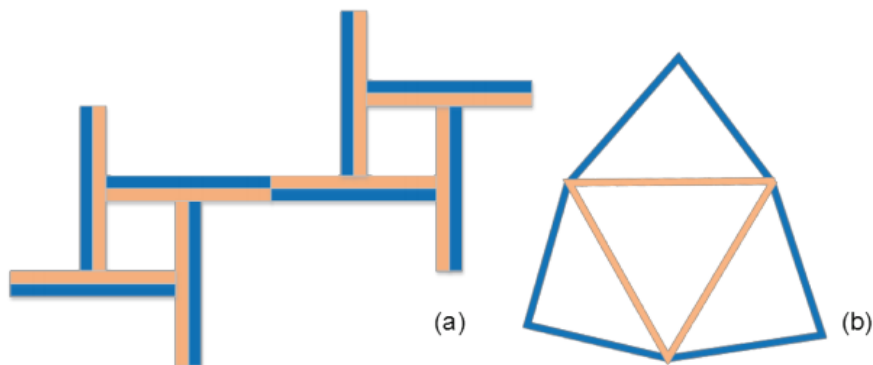


Figure 17. (a) Metamaterial with unbounded CTE designed by Lakes [7]. (b) Metamaterial with low CTE designed by Steeves et al. [2]. High and low CTE materials are indicated by blue (darker) and orange (lighter) colors, respectively.

As a first step in calculating the CTE of any structure, first there must be an understanding of how to calculate the bending moment of the structure. The bi-material design proposed by Lakes (Figure 17a) uses a series of bi-material strips to undergo bending when experiencing temperature change. The bending causes contraction on one side of the beam, causing a rotation effect into the open space and causing an overall reduction in thermal expansion.

The curvature, k , of a single bi-material beam as a result of thermal bending can be calculated with the equation 2.2.

$$k = \frac{6(a_2 - a_1)\Delta T}{(h_1 + h_2)} \frac{\Delta T \left(1 + \frac{h_1}{h_2}\right)^2}{3 \left(\left(1 + \frac{h_1}{h_2}\right)^2 \right) + \left(1 + \frac{h_1 E_1}{h_2 E_2}\right) \left(\left(\frac{h_1}{h_2}\right)^2 + \frac{h_2 E_2}{h_1 E_1} \right)} \quad (2.2)$$

Where subscripts 1 and 2 denote materials 1 and 2 respectively, a denotes CTE, h denotes beam height, E denotes elastic modulus and ΔT denotes temperature change. To calculate the overall CTE of the metastructure designed by Lakes, calculation of the curvature increment δk is required.

$$\varepsilon = \left(\frac{1}{2} \cot\left(\frac{\theta}{2}\right) - \frac{1}{\theta} \right) l_{arc} \delta k \quad (2.3)$$

Where l_{arc} is the length of a bi-material beam, and θ is the initial angle of the beam shown in Figure 18.

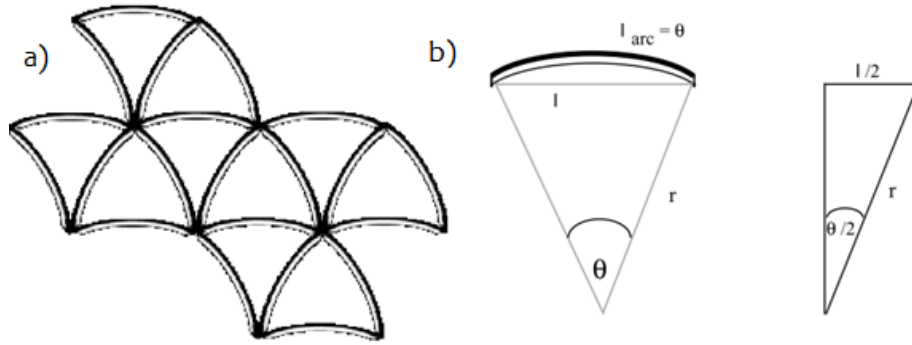


Figure 18. (a) Shows a structure by Lakes with an included angle θ . (b) shows angle θ geometry. The CTE a can now be expressed as equation 2.4.

$$a_{net} = \frac{l_{arc}}{(h_1 + h_2)} \frac{6(a_2 - a_1) \left(1 + \frac{h_1}{h_2}\right)^2}{3 \left(\left(1 + \frac{h_1}{h_2}\right)^2 \right) + \left(1 + \frac{h_1 E_1}{h_2 E_2}\right) \left(\left(\frac{h_1}{h_2}\right)^2 + \frac{h_2 E_2}{h_1 E_1} \right)} \left(\frac{1}{2} \cot\left(\frac{\theta}{2}\right) - \frac{1}{\theta} \right) \quad (2.4)$$

The geometric and material parameters in equation (4.3) can be manipulated to achieve higher and lower CTE values. Negative CTE values can also be realised by switching the higher and lower CTE materials in the bimaterial beam.

To simplify the equation further, let's assume the beam thickness ratio; $m = a_1/a_2$, CTE ratio; $n = E_1/E_2$ and total thickness $t = h_1 + h_2$ re-write the equation to make it simpler.

$$a_{net} = (a_1 - a_2) \frac{l_{arc}}{t} \left(\frac{\theta}{12} \right) \frac{6(1 + m^2)}{3(1 + m)^2 + (1 + mn) \left(m^2 + \frac{1}{mn} \right)} + \frac{a_1 + a_2}{2} + (a_2 - a_1) \left[\frac{4m^2 + 3m + \frac{1}{mn}}{nm^3 + 4m^2 + 6m + \frac{1}{mn} + 4} - \frac{1}{2} \right] \quad (2.5)$$

The structure exhibits 2D cubic symmetry which results in isotropic thermal expansion but anisotropic elasticity. However, hexagonal structures which are elastically isotropic are also possible. The main advantage of this design over others is that it can achieve theoretically unbound CTE. This design by Lakes has been experimentally realised by Lakes et al. using thin bonded metal strips, but it has not yet been achieved with Additive Manufacturing [65].

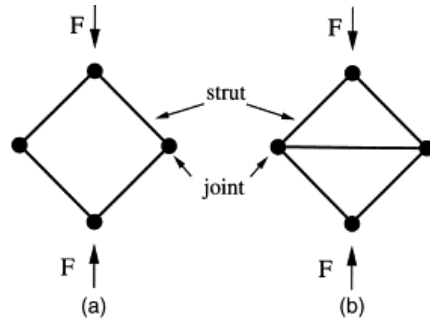


Figure 19. (a) Bend dominated arrangement. (b) Stretch dominated arrangement.

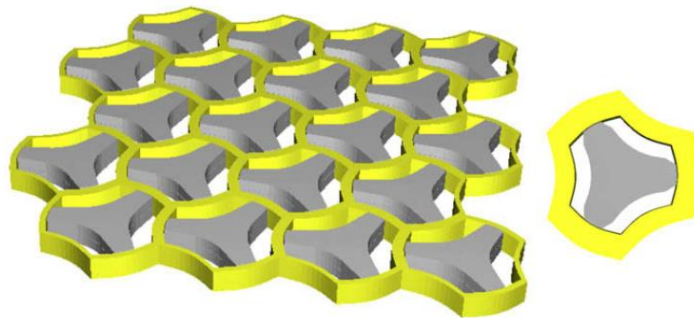


Figure 20. Metastructure patented by Jefferson et al. showing high CTE constituents in grey, and low CTE constituents in yellow [6].

A patented structure designed by Jefferson et al. is similar, but it is not known whether it has been experimentally realised [6], [65]. The main limitation of the design is that the metastructure is dominated by bending, and thus exhibits low in-plane stiffness and strength which limits its use cases. Figure 19 shows the differences between these two

mechanisms. By comparing the structure shown in Figure 20 to Figure 21, it can be observed that Figure 20 is stretch dominated, and Figure 21 is bend dominated.

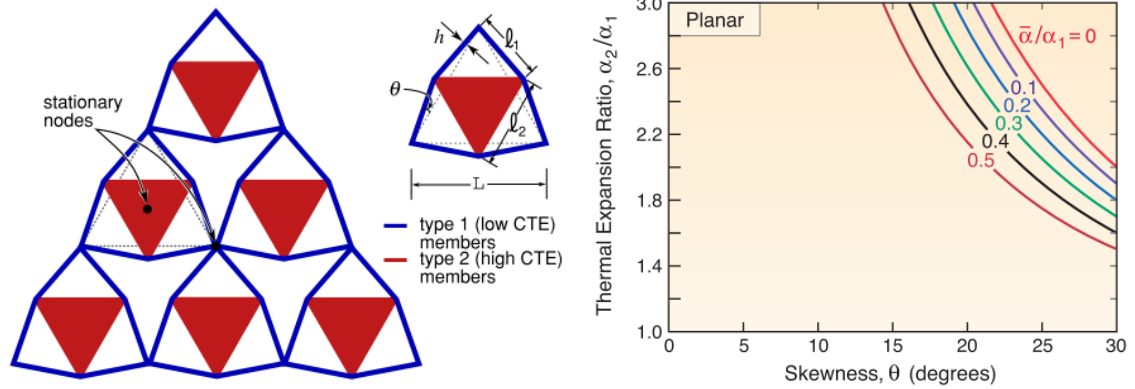


Figure 21. (a) A sketch of the lattice structure showing the key geometric parameters. The low CTE type 1 members are blue while the high CTE type 2 members are red. The key parameters are the lattice skewness h and the ratio of thermal expansions $\Sigma = \alpha_2/\alpha_1$ [3] (b) Contours of normalized net thermal expansion coefficient $\bar{\alpha}$ of the planar lattice for a range of skewness [3].

Steeves et al. [2] describes a structures whereby a negative CTE has been achieved using 2D linear beams bending at a joint [2], [3], [10]. To describe this arrangement when using pin joints (no resistance to rotation) the following equation can be derived.

$$a = a_1 \frac{1 - \frac{1}{2} \left(\frac{a_2}{a_1} \right) \sin(2\theta) \left(\frac{1}{\sqrt{3}} + \tan(\theta) \right)}{1 - \frac{1}{2} \sin(2\theta) \left(\frac{1}{\sqrt{3}} + \tan(\theta) \right)} \quad (2.6)$$

Where subscripts 1 and 2 denote material 1 and 2, a denotes the material CTE and θ denotes the angle shown in Figure 21.

It can be seen that adjusting the skewness angle θ can tailor the CTE to a pre-determined value. It is apparent that the lattice has zero net thermal expansion within a realizable window of skewness, θ , and thermal expansion ratio, $\Sigma = \alpha_2/\alpha_1$. Specifically, when $\Sigma \approx 2.5$, zero thermal expansion emerges for skewness $\theta \approx 25^\circ$. Using this model, the CTE can be tailored to match that of Borosilicate glass, or Germanium.

Since the joints are pin jointed however, they undergo no axial stress. To include a bonded joint taking into account the stresses in the outer beams, equation 2.7 is formed.

$$a = a_1 \left(1 - \frac{(c_1 \tan(\theta)(\sin(2\theta) + \sqrt{3} \cos(2\theta) + \sqrt{3} \sin(\theta)^2 \left(\frac{a_2}{a_1} - 1\right))}{c_1 (\sqrt{3} \cos(\theta) - \sin(\theta))^2 + 12 (\cos(\theta) + \sqrt{3} \sin(\theta)) (\cos(\theta) + \sqrt{3} \sin(\theta) + 2 \frac{E_1 A_1}{E_2 A_2})} \right) \quad (2.7)$$

Where $C_1 = \frac{A_1 l_1^2}{l_1}$ and denotes the area, E , the elastic modulus, l_1 the length of the low CTE side member (material 1), and I is the second moment.

We can see that Steeves et al. and Berger et al. also provide expressions for the biaxial stiffness, S_b (such that $S_b = \frac{\varepsilon}{N_b}$, where N_b is the force applied) of the pin-jointed metastructures [2], [11]:

$$S_b = \frac{\frac{E_2 A_2}{L} \cos\left(\frac{\pi}{6} + \theta\right) \left(3 - 2 \sqrt{3 \sin(\theta) \sin\left(\frac{\pi}{6} + \theta\right)}\right)}{3Q + 2 \sin^2(\theta) \sin\left(\frac{\pi}{6} + \theta\right)}, \quad Q = \frac{E_2 A_2}{E_1 A_1} \quad (2.8)$$

Equation 3.7 is shown to fall closely within the Gibiansky-Torquato et al. bounds for the area fraction of a three-phase system (two materials and gaps) when the biaxial stiffness is prescribed [66]. The closeness to this bound suggests that, from a stiffness perspective, this may be an optimal design. Steeves et al.'s and Berger et al.'s design performs comparably against this bound to the designs obtained with shape optimization by Sigmund and Torquato [4], [11]. They have also manufactured and tested the designs using pin-joints and bonded joints, and demonstrated the correlation between computation modelling, and experimental results [3], [11].

The work by Steeves et al.[2], [3], [10] and Berger et al. [11], has significantly advanced the state of the art field of low CTE metastructures. They experimentally showed, for the first time, the manufacturability of such metastructures and also developed theoretical principles for predicting their CTE and stiffness. However they have only demonstrated the ability of the design principles in application for laser cut thin sections of Aluminium and Titanium alloys.

More work is required in the field of additive manufacturing, to assess the ability for manufacture of such structures, and their accuracy to the theory. Their viability to be manufactured in two materials in the same process needs to be accessed. It would pose a challenge with metal AM given the current technology, but could be realised with plastic AM. This would significantly advance the field, by using a Direct from Digital approach. This would allow analytical and computational methods to be used to create the

structures, and then to be directly printed from these simulations, without the need of assembly. This allows for the structures to be fitted directly into the CAD of an optical system component, and printed as one unit.

Steeves et al. has also proposed a 3D design (Figure 22). This has been theoretically derived for a pin-jointed structure, but not experimentally realised due to previous manufacturing complexities. Multi-material Additive Manufacturing could be used to manufacture 3D structures if the correct ALM method is chosen. Studying chapter 3, it can be seen that; Plastic Fused Deposition Modelling and Plastic Material Jetting are the most promising multi-material ALM methods for this application.

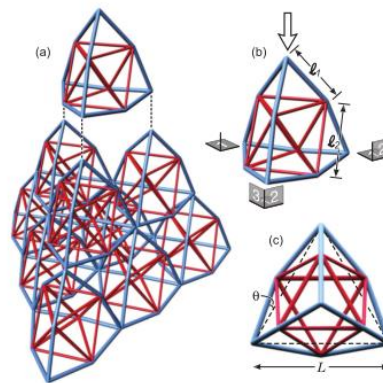


Figure 22. 3D structures theorised possible, but not yet additively manufactured [2].

For metal AM, the DED LENS based system would be a useful system for multi-material printing 3D thermal expansion controlling structures. The attraction with a LENS system is for its ability to print two metals at the same time, adjoining the metals in situ throughout the build. This ability allows for the possibility to create 2D multi-material lattice structures that can exhibit unique properties. The lattice structures will need to be assessed for their accuracy to the original CAD data, and assumptions will need to be made to account for overbuild, layer thickness and the multi-material boundary weld. A similar study has been completed to create a negative co-efficient of thermal expansion lattice using a 2D Chromium and Nickle lattice structure using a LENS system [63]. Another use is to clad the outside of a cylinder containing the lattice structure. It is common practice to clad piping using DED for additional wear resistance. Cladding a low thermal expansion metal such as Invar onto a cylindrical structure made from another material would also provide a graduated dual material configuration.

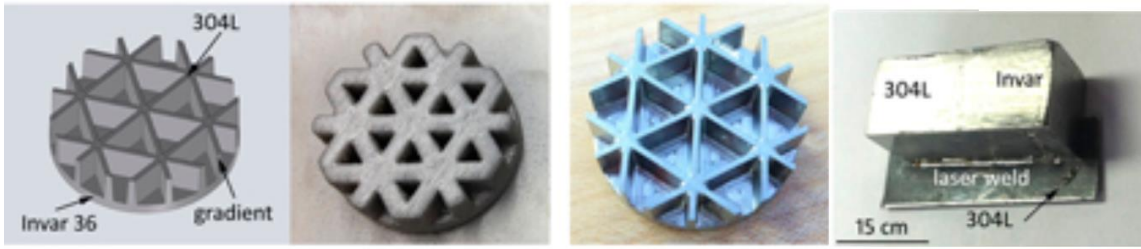


Figure 23. Schematics of how powder based direct deposition can achieve gradient 3D metallic structures, and an example of a compositionally graded structure [67]–[70].

3 Literature review of the additive manufacturing process

3.1 Introduction

This chapter outlines all the additive manufacturing process methods available. The additive manufacturing methods are placed into categories based on their feedstock material and method of manufacture. All process methods have been standardised by ASTM during committee F42, which convenes once every two years to update the process methods should a new method be invented. Every process method for metals will be outlined in section 3.2, and again for plastics or polymers in section 3.3. The features of each process method are highlighted, and a review of commercial system available is outlined. Section 3.3 contains present work on benchmarking the geometric capabilities of the additive manufacturing machines used in later chapters. The section discusses the deviations in dimensions compared to the specified dimensions and compares the values to literature. Conclusions are made to determine any geometric offsets required for each machine and material.

3.2 Metal Additive Manufacturing

ASTM F42 structures all types under the following 7 categories:

- Powder Bed Fusion (PBF)
- Directed Energy Deposition (DED)
- Material Jetting (MJ)
- Binder Jetting (BJ)
- Material Extrusion
- Sheet Lamination
- Vat Photopolymerisation

3.2.1 Powder Bed Fusion

Powder Bed Fusion (PBF) is type of Additive Layer Manufacturing categorised under ASTM-F42. It defines all processes that deposit a layer of powder into a build chamber ready for another process to selectively fuse the powder together. Powders are typically fused by Laser, Electrons, or a heated print head.

Processes that use a laser for fusion come under the category of Laser Powder Bed Fusion (LPBF) processes. Depending on whether the laser is fully melting the powder or sintering it will depend on the type of machine in this category. When selectively sintering the powder, the method is known as Selective Laser Sintering (SLS) or Direct Metal Laser Sintering (DMLS). When fully melting the powder, it is called Selective Laser Melting (SLM). Metal is the most common powdered material used, but can also extend to Plastics

and Ceramics [71]. Electron Beam Melting (EBM) is a similar process as LPBF, except an electron beam is used instead of a laser [72]. Selective Heat Sintering (SHS) utilises a similar system for plastic powders, except a heated print head is used to selectively melt the powder [73].

Laser Powder Bed Fusion

Laser Powder Bed Fusion (LPBF) can produce sintered or melted parts depending on the process used. A layer of metallic powder between 20µm to 100µm is deposited over a metal base plate by a wiper arm. The powder is then selectively melted or sintered depending on the geometry required. The process is then repeated to build the component. Typically powder size distribution is between 15-60µm with the average size being 45µm. Figure 24 shows an image of the process, and a table of the most common machines and their specifications.

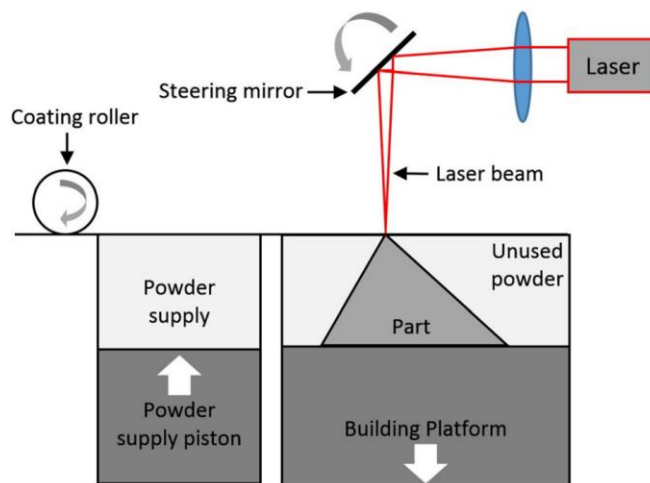


Figure 24. Laser Powder Bed Fusion process schematic [74].

	AM250	AM 400	RenAM 500 ²	EOS M 100 ³	EOSINT M 280 ⁴	EOS M 400 ⁵
Process Type	DMLM	DMLM	DMLM	DMLS	DMLS	DMLM
Manufacturer	Renishaw	Renishaw	Renishaw	EOS	EOS	EOS
Build Volume (mm)	250x250x300	250x250x300	250x250x350	100 x 95(Ø/H)	250x250x325	400x400x400
Build Rate	-	-	-	-	-	-
Max Laser Power	200W	400W	500W	200W	400W	1KW
Focus Diameter	70µm	70µm	75µm	40µm	100-500µm	90µm
Layer Thickness	20-100µm	20-100µm	20-100µm	30µm	20-50µm	N/A
Min.Wall Thickness	150µm	150µm	150µm	80µm	300-400µm	N/A
Max Scan Speed	2 m/s	2 m/s	2 m/s	7 m/s	7 m/s	7 m/s
Inert Gas	Argon	Argon	Argon	Argon	Nitrogen Generator	Nitrogen Generator
Features	Standard	Increased Output	Automatic Sieving.	R&D Versatility	Variable focus for sintering	High Output Volume

Table 4. Specifications comparing both Renishaw and EOS LPBF machines.

It can be seen there is a great variety of machines when it comes to LPBF. Shown in Table 4 there is an R&D, mid-range industrial, and high output industrial machine from the four manufacturers with the highest market share [1]. The overall operation of most machines remains the same, with scan speeds of 7m/s. Layer thickness is largely dependent on the most common powder size between 15-45µm. Most machines chose to use a typical layer thickness of between 20-100µm depending on machine and part requirements. Smaller powder sizes can be purchased for use with machines such as the Mlab Cusing which

² Manufacturers Technical Data - Renishaw RenAM 500M.” [Online]. Available: <http://www.renishaw.com/en/renam-500m--30939>. [Accessed: 15-May-2017]

³ Manufacturers Technical Data - EOS M 100 - Ideal entry level model for industrial 3D printing.” [Online]. Available: <https://www.eos.info/eos-m-100>. [Accessed: 15-May-2017].

⁴ Manufacturers Technical Data - EOSINT M 280 – EOS.” [Online]. Available: https://www.eos.info/systems_solutions/metal/systems_equipment/eosint_m280. [Accessed: 15-May-2017].

⁵ “Manufacturers Technical Data - EOS M 400 for Additive Manufacturing for the Industrial Production of High-Quality Large Metal Parts. – EOS.” [Online]. Available: https://www.eos.info/systems_solutions/metal/systems_equipment/eos_m_400. [Accessed: 15-May-2017].

focuses on 15-30 μm layer thicknesses for R&D. Higher Laser powers can be seen on large scale industrial machines aimed at a higher output. Higher power lasers can also be used with an increased spot size for sintering. LPBF can see a typical dimensional accuracy of $\pm 50\mu\text{m}$ and surface roughness of 9-16 μm [75]–[77]. Literature shows minimum wall thickness or feature size can be as low as 150 μm when creating fine lattice structures; however as a general design rule for functional parts should be between 200-300 μm [78], [79]. Typical build rate will not exceed 25 cm^3/h for a single laser system (SLM125). The maximum build rate currently available is 120 cm^3/h (M2 X LINE 200R) using two 1KW lasers, which no machine has stated to exceed (2017).

Electron Beam Melting

Electron Beam Melting is a powder bed process that allows for the whole bed to be sintered with each layer, removing the need for any support material. Sintering the whole bed reduces residual stress, and has been proven not to affect powder quality once the sintered powder is recycled [80]. This is a quicker process than LPBF and is generally used for larger components [81]. Due to the conductive requirements of the material, only a small range of materials can be used. Stainless steels, Inconel 718, Ti6Al4V, and Copper materials have all been manufactured with relative densities above 99.7% [72], [82]–[84]. The process is similar to LPBF, except an electron beam is used instead of a laser. The system works by using a coil to focus the electrons down to 140 μm and then deflection coils to deflect the electrons to the scan location required on the powder bed [85].

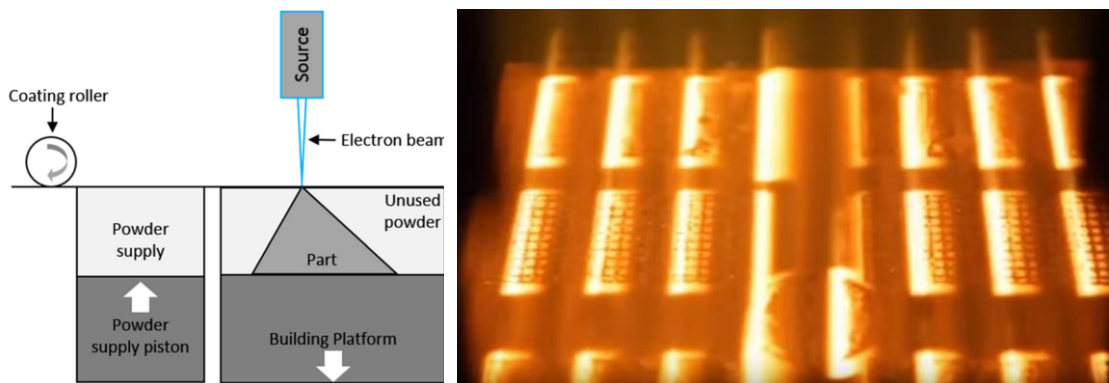


Figure 25. Diagram illustrating the operation of an EBM machine, and an image of the build in operation [74].

Currently the EBM patent is held by ARCAM. ARCAM do not lease their patent, choosing instead to produce their own line of commercial machines listed in Table 5. ARCAM was purchased by GE as part of a \$1.4bn deal in 2015. Since then many other companies are entering the market. The company Freemelt established in 2017 gained \$1.6 million in investment for the development of an opensource EBM machine. The machine named the Freemelt One is designed for smaller builds requiring a low material investment. Other companies such as Wayland Additive have raised £3m to produce a

machine for the aerospace and medical industries. Furthermore, Ruselectronics, a Russian holding company which is a subsidiary of state-owned Rostec, has begun developing their own EBM machine for aerospace applications. The R&D work for Ruselectronics will be carried out by the Toriy Scientific Production Association [86].

	ARCAM Q10plus	ARCAM Q20plus	ARCAM A2X
Process Type	EBM	EBM	EBM
Build Volume (mm)	200x200x180	350x380 (Ø/H)	200x200x380
Build Rate	-	-	55-80 cm ³ /h
Max. Beam Power	3KW	3KW	3KW
Cathode Type	Single Crystalline	Single Crystalline	Tungsten Filament
Max. EB Speed	8000m/s	8000m/s	8000m/s
Min. Beam Diameter	140µm	140µm	250µm
Layer Thickness	50 - 100µm	50 - 100µm	50 - 100µm
Min. Wall Thickness [87]	0.6 - 1.0mm	0.6 - 1.0mm	0.6 - 1.0mm
Features	For Orthopaedic implant manufacturing. Build size designed for optimal stacking.	For cost efficient aerospace components.	Able to process temperatures up to 1100°C. Good for TiAl & Inconel 718. For Aerospace Production & R&D
Manufacturer Features	Holds the patent for EBM technology		

Table 5. Specifications comparing the current EBM systems by ARCAM ⁶.

The EBM process takes place in a vacuum of 5×10^{-5} mbar or better, and Helium is introduced to 4×10^{-3} mbar. The helium reduces oxidation, allows partial cooling, and provides beam stability. The build platform is heated to 700°C before the build. Each layer is pre-heated by a high-speed electron scan keeping the temperature at 600°C (between 40-60% of the melt temperature) before the melting stage begins. This temperature is maintained throughout out the build, and results in stress relieved components after about 5 hours of maintained heat. During the melting stage, a lower current low speed scan is used to melt the powder. The A2X has a build plate capable of being heated to 1100°C for TiAl & Inconel 718 producing similar results [88]. The heating of each layer sinters the bed, meaning supports are only required on horizontal surfaces such as the bottom edge, or those vulnerable to over melting. EBM also has the ability to penetrate further into the substrate underneath. It is the preferred method for the

⁶ EBM Hardware - Arcam AB.” [Online]. Available: <http://www.arcam.com/technology/electron-beam-melting/hardware/>. [Accessed: 24-Oct-2017].

aerospace industry due to the higher density and reduced residual stress on larger components.

3.2.2 Directed Energy Deposition

Directed Energy Deposition (DED) is a manufacturing process that fuses materials by melting them as they are being deposited. The material can be a solid wire or in powder form, and melted using a laser, electron beam, or plasma arc. The material and heat affected zone are moved together on a 2D plane to create one layer. This method can also be used on a multi-axis system for Laser Cladding of a materials surface to provide a functional metal coating [63]. Many powder fed machines have the capability to print in multiple materials by switching between multiple metal powder injection sources, to produce graded materials [89]. In some applications a 4-5 axis arm with nozzle moves around a fixed object, to clad or build on an existing component.

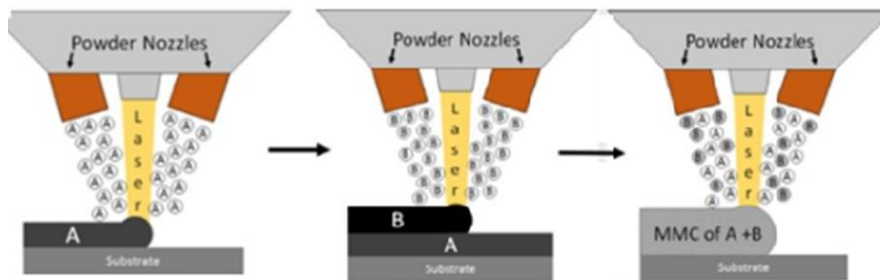


Figure 26. Schematic showing a Laser Metal Deposition process being used to create a compositionally graded component [67]–[70].

Common areas for DED include;

- Cladding of existing parts to improve wear resistance.
- Additive manufacture of new features onto existing components.
- Direct manufacture of new components.
- Repair of defects in existing components.
- Creation of multiple metallic materials in one print.

Several types of DED technologies exist. Each uses a different energy sources and material injection methods. These include;

- Laser Engineered Net Shaping (LENS) is a form of Laser Metal Deposition (LMD) using a laser to melt a feedstock of metal powder [90].
- Laser Metal Deposition (LMD-w) is a process that uses a laser to melt a wire feedstock. Also known as Wire Feed Metal Deposition (WFMD) [91].
- Electron Beam Additive Manufacturing (EBAM®) uses an electron beam to melt a wire feedstock instead of a conventional laser. Patent holder Sciaky Inc. claim it is the world's fastest metal 3D printing process with deposition rates three times higher than LENS and LMD-w [89].

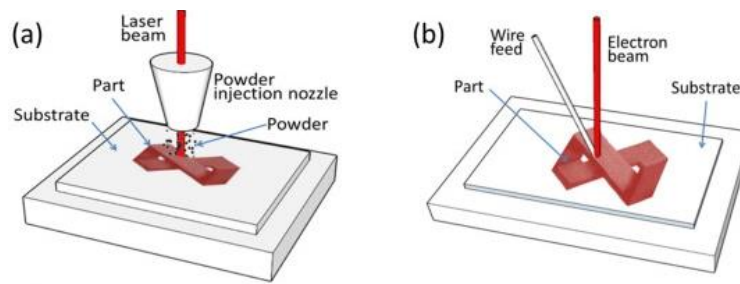


Figure 27. a) Diagram of the LENS process, b) Diagram of the EBAM process [74].

All processes are similar in requiring an inert gas to surround the weld pool to prevent oxygen exposure and oxidation by keeping it below 5 to 10 $\mu\text{m}/\text{mK}$. There are two methods of achieving this. One method is to use a completely sealed build chamber filled with argon. The other method is to use a shielding gas applied directly to the melt pool. This option can be more flexible and practical in allowing the building of larger parts with robot arms and retrofitted hybrid machines. One problem with this method is that the shielding gas only works when the nozzle is directly over the melt pool; when it moves away the material still at a high temperature tends to oxidise. Table 6 below shows the different machines and their specifications.

	BeAM Magic 2.0	EBAM [®] 300	Optomec 850-R
Description	5-Axis LENS [®]	5-Axis Sciaky Electron Beam AM	5-Axis LENS [®]
Feed Material	Powder	Wire	Powder
Build Volume (mm)	1200x800x800	5791x1219x1219	900x1500x900
Build Rate	20 – 300 cm^3/h	705-1510 cm^3/h ⁷	110 cm^3/h ⁸
Gas System	Closed Atmosphere O ₂ <40ppm	Vacuum	Closed Atmosphere O ₂ <10ppm
Layer Thickness	200-800 μm	3mm	-
Minimum Wall Thickness	0.8 - 4mm	10mm	-
Beam Type	IPG 2KW Fibre Laser. 2 outputs	Electron Beam 42KW	IPG 1KW Fibre Laser
Features	Versatile mid-range industrial, multiple material powders in single print.	Patented EBAM [®] technology for higher deposition rates.	Versatile, multiple material powders in single print.

Table 6. Specifications comparing three different DED machines⁹.

⁷ Calculated from manufacturer Sciaky's assumption for a build rate of 7- 15lb/h of titanium.

⁸ Calculated from the manufacturer OPTOMECC's assumption of 0.5kg/h of titanium.

⁹ "Efesto | EBAM Machines Overview." [Online]. Available: <http://www.efesto.us/products/ebam/>. [Accessed: 16-May-2017]. "OPTOMECC - LENS 850-R Systems." [Online]. Available:

There are several different machines in the range between high output and mid-range industrial. All processes presented use a closed atmosphere. LMD-w systems are most commonly used in open atmosphere systems with a shielding gas, such as those used on robotic arms. These can be designed for purpose by companies such as Atec.

3.2.3 Material Jetting

An additive manufacturing process where the build material is selectively deposited in liquid form by a drop on demand (DOD) process, in a similar mode of operation to a 2D inkjet printer. Due to the nature of the DOD process, the material must be able to form a droplet. Different materials can be combined and graded throughout the print to form different mechanical properties [92] .

Material jetting is a similar technique to that of inkjet printing. It has traditionally been used to print plastics and ceramics only, but a new Israeli startup company named XJet has produced a machine capable of jetting liquid metal. This is achieved by suspending nano-sized metal particles into a liquid jetting agent. In 2016 they unveiled the world's first metal 3D printer capable of jetting droplets of metal directly at the location required. The company has patented their technology as NanoParticle Jetting™. The process works by jetting two materials independently, one for support and one for the metal build material. As the liquid metal drops fall into the 300°C heated build envelope the liquid 'jacket' around the nanoparticles evaporate, leaving a dense and ultrafine layer of build material. Layer thicknesses can be as low as 1µm. The company claims the fabricated parts have the same chemical composition of traditionally made parts, but still require sintering after printing. Xjet have demonstrated the use of Stainless Steel and Silver metals. The technology is suited to rival that of conventional micro-SLS systems and has been made for the mass production of small to medium sized parts. The process has a limited build height of up to 11mm [93].

<https://www.optomec.com/3d-printed-metals/lens-printers/metal-component-repair-3d-printer/>. [Accessed: 16-May-2017]. BeAM - Fabricant de Solutions Additives DED." [Online]. Available: <https://www.beam-machines.fr/> [Accessed: 16-May-2017].

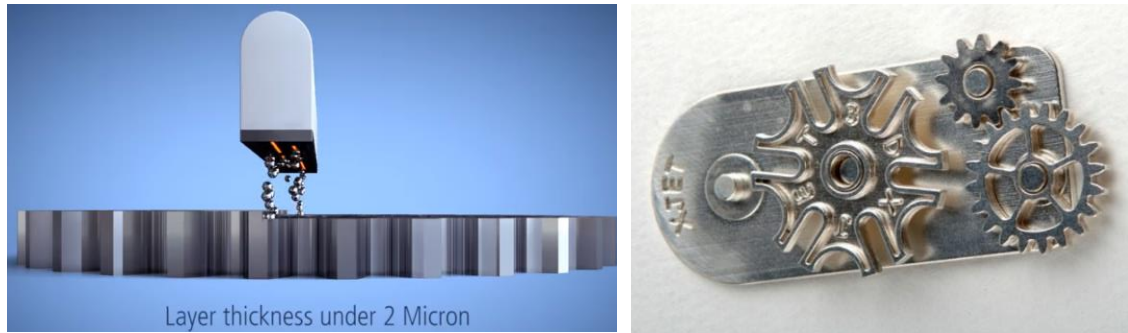


Figure 28. Figures showing the metal MJ process and an example part produced [93].

	Xjet Xcarmel 1400	Xjet Xcarmel 700
Material	Stainless Steel and Silver	Stainless Steel and Silver
Max Build Rate	-	-
Build Volume (mm)	500x280x11	500x180x5.5
Layer Thickness	1 μ m	1 μ m
Gas Required	Air Pressure 6bar	Air Pressure 6bar

Table 7. Metal Material Jetting machines specification comparison [93].

3.2.4 Binder Jetting

Binder jetting is an additive layer manufacturing process where a liquid bonding agent is selectively deposited onto a layer of powder. This results in two materials present in the final part, the bonding agent, and the powder. Due to the method of binding, the material characteristics are not always suitable for structural components [94].

Binder jetting is usually done in a single pass in what is known as Single Pass Jetting (SPJ) where the powder and then the binder is deposited by the same single wiper arm movement. The arm can perform the same task on the return movement back to its original position, reducing print times. Desktop metal claims their binder jetting system is 100x faster than LPBF and 10x faster than their metal FDM process, and is therefore marketed as a production system. No support structures are required. The parts are not as dense as those created with PBF because there is a binder that is removed during the sintering process, but the voids left behind are not entirely closed [95]. Traditionally they have not been considered suitable for structural applications. Work is being done in the material development to create parts that are up to 99.6% dense, which could see the process start to be adopted for structural applications in the future [96]–[99]. This is achieved by using Hot Isostatic pressing in combination with sintering additives including 0.5 wt% of boron compounds [100]. The parts can also be infiltrated with a secondary material such as bronze or steel, depending in the application [74].

	ExOne M-Flex	Desktop Metal Production System
Material	Stainless Steel, Iron, Bronze, Tungsten, and Alloy IN 625.	316L, IN625
Max Build Rate	12000 cm ³ /h	8200°Cm ³ /h
Build Volume (mm)	400x250x250	330x330x330
Layer Thickness	100 μm	-
Features	Flexible prototype production	High output functional component manufacture

Table 8. Metal Binder Jetting machines specification comparison.¹⁰

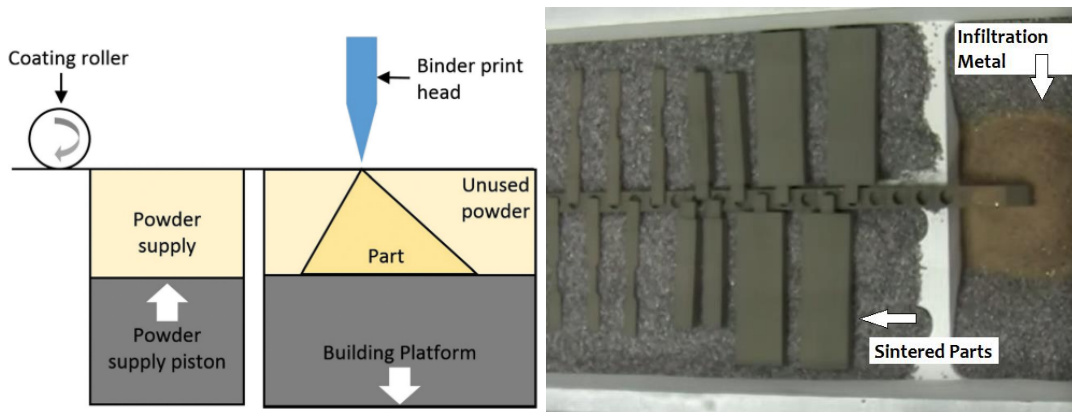


Figure 29. Diagram of the binder jetting process, an image of the sintered part metal infiltration layout [93] [74].

3.2.5 Fused Deposition Modelling

Fused Deposition Modelling (FDM) has traditionally been used with plastic materials, but recent technology improvements make it possible to print metallic materials. The technology describes the ability to create a 3D printed metal object by including a metal powder with a polymer binder, which is then extruded at 250°C and selectively placed layer by layer to create the desired part. The printed part then moves to a washing stage to remove some of the binder, and then to a sintering phase where it is heated in a furnace by a combination of microwaves and conventional heating. Each stage requires a separate machine.

Currently there are two manufacturers of metal FDM printers. These include Desktop Metal (2015) Markforged Ltd (2017). Markforged introduced a new process name to their machine called ‘Atomic Diffusion Additive Manufacturing (ADAM)’. This process name is not shared with that of Desktop Metal. The technology is currently in its infancy, but development is moving fast with rapid investment in Desktop Metal of over \$200 million

¹⁰ “M-Flex 3D Printer | ExOne.” [Online]. Available: <http://www.exone.com/Systems/Production-Printers/M-Flex>. [Accessed: 23-Nov-2017]. “Production | Desktop Metal.” [Online]. Available: <https://www.desktopmetal.com/products/production/>. [Accessed: 23-Nov-2017]

from big companies like BMW and General Electric [101]. Both companies claim relative densities in the range of 95.7% and 99.7%. There will always be a level of porosity in the parts because the temperature of the sintering process never reaches the melting point of the metal. This means the component would have less strength than LPBF or EBM part, but would have less internal residual stress as a result. The process has the ability to support many metals, including 17-4 Stainless Steel, Tool Steels, Titanium, Aluminium, and Inconel. For safe office friendly handling, powders are loaded into the machine in safe-to-handle cartridges. Another benefit of the technology is its office friendly small form factor, with a lower overhead cost compared to LPBF. The technology is claimed to be ten times faster than that of LPBF. It also allows for lattice infill structures to be printed in metal without worrying about powder removal.

Markforged has stated that the shrinkage can be up to as much as 20% after sintering. Trial and error investment by the team has led them to develop specific algorithms in their software to predict the behaviour of shrinkage so that the final part is to the required specifications. The minimum wall / feature size is not provided by either manufacturer, but design guidelines published by Stratasys suggest a typical FDM printer using ABS can achieve 0.4mm as a minimum wall / feature size when printing with 100 µm layers and a 0.4mm diameter nozzle [100]. Markforged has developed several patents protecting their core metal AM technologies for binding and sintering [102].

	Desktop Metal	Markforged Metal-X
Feed Material	Metal Powder & Binder	Metal Powder & Binder
Build Rate	16 cm ³ /hr	-
Build Volume (mm)	300x200x200	250x220x200
Layer Thickness	50µm	50µm
Nozzle Diameter	0.4mm	-
Build Plate Temperature	70°C	-
Build Volume Temperature	50°C	-

Table 9. Comparison between both Metal FDM printers.¹¹

3.2.6 Sheet Lamination

Ultrasonic Additive Manufacturing (UAM) is a Sheet Lamination process, whereby a layer of thin metal foil (typically 100-200µm) is selectively placed on a metal and ultrasonically welded in place using a rotating sonotrode travelling along the length of the film. The sonotrode oscillates transversely to the direction of motion, at a constant 20 kHz frequency and user-set oscillation amplitude. This procedure is repeated until a

¹¹ “Studio | Desktop Metal.” [Online]. Available: <https://www.desktopmetal.com/products/studio/>. [Accessed: 01-Nov-2017].

complete layer is placed. The next layer is bonded to the previously deposited layer using the same procedure. This causes the metals to join via state disruption of surface oxide films between the metals. There is no melting formation between the two metals. This means dissimilar metals can be joined if required. A milling operation is carried out periodically with each layer to form the net shape required. The surface roughness can be varied depending on the CNC spindle speeds, but is considered one of the lowest in metal AM of between $3.7\mu\text{m}$ - $4.35\mu\text{m}$ [103].

The technology was first commercialised by Solidica Inc. in 2000. Bonded materials are normally used for aesthetic and visual purposes, and not normally suitable for structural use.

FABRISONIC SonicLayer 7200	
Feed Material	Metal foils
Build Rate	$245\text{ cm}^3/\text{h}$ – $327\text{ cm}^3/\text{h}$
Build Volume (mm)	$1828.8 \times 1828.8 \times 914.4$
Layer Thickness	$200\mu\text{m}$
Surface Roughness	$3.7\mu\text{m}$ - $4.35\mu\text{m}$
Features	Integrated 3-Axis CNC Machining.

Table 10. Specifications of a common UAM Machine¹².

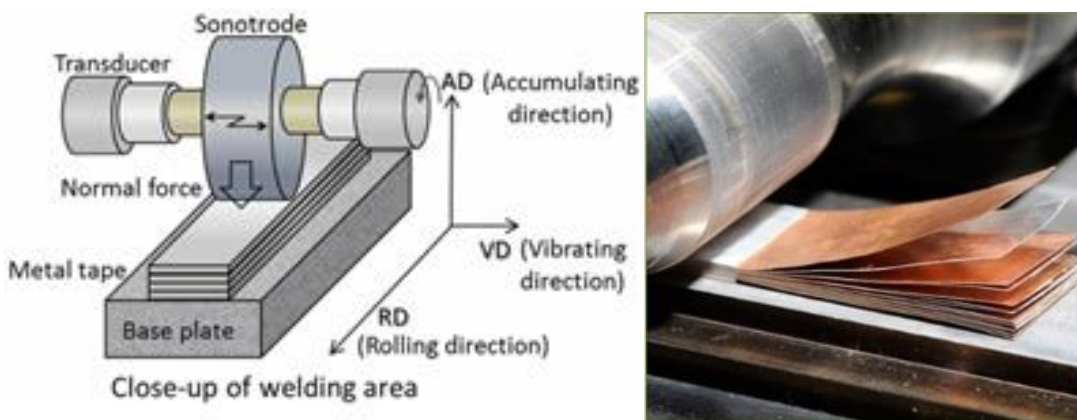


Figure 30. Image of a typical UAM material feed, and an operational diagram ¹¹ [103].

3.2.7 Specification summary table for metal AM processes

A summary of the specifications for metal AM machines is put together in Table 11 overleaf.

¹² Fabrisonic-Patented Solid-State Ultrasonic Additive Manufacturing.” [Online]. Available: <https://fabrisonic.com/>. [Accessed: 23-Nov-2017]

	LPBF	EBM	DED	UAM	ADAM	BJ	MJ
Multi-Material	No	No	Yes	Yes	Yes	No	Yes
Materials available	Most metal powders (Stainless steel, Titanium, Aluminium, etc)	Only conductive materials (Ti6Al4V, CrCo, etc)	Most metal powders and wires (Stainless steel, Aluminium, Titanium, Cobalt etc)	Most metal foils even if dissimilar (Steels, Copper, Aluminium, Titanium etc)	17-4 Stainless Steel. (Beta testing; Aluminium, Titanium, and Incolnel)	Stainless Steel, Iron, Bronze, Tungsten, and Alloy IN 625.	Stainless Steel and Silver demonstrated so far.
Build Volume (m ³)	0.00195 – 0.16	0.0072 – 0.0152	0.768 – 8.605	0.378	0.011 -0.012	0.025 -0.036	0.0000495 – 0.000099
Build Rate (cm ³ /h)	25-130	55-80	20– 1510	245– 327	16	<12000	-
Layer Thickness (µm)	25 - 100	50 - 100	200-3000	100	50	100	1
Min.Feature Size (µm)	100	600-1000	1000	-	-		
Surface Roughness Ra (µm)	5-15	20-30	13-51	3.7 - 4.35	-		
Support Required?	Yes – Bottom edge and all surfaces ~45°	Yes – Bottom edge and horizontals	Must be self-supporting	No Supports available. Overhangs ~45° cannot be built.	Yes - – Bottom edge and all surfaces ~45° or less from platform	No supports required. Self-supporting	Yes

Table 11. Summary of the most common metal AM processes accumulated from references in this chapter

3.3 Plastic and Polymer Additive Manufacturing

This chapter will look into the different types of plastic and polymer additive manufacture which are outlined by ASTM-42. It will investigate the multi-material abilities, features, and advantages and disadvantages of each method.

3.3.1 Powder Bed Fusion

Powder bed fusion systems are categorised by their method of fusion. For polymer powder bed sintering machines, a laser is used to sinter the polymer powder together in a process known as selective laser sintering. This works much in the same way as laser powder bed fusion is applied to metals. Selective Heat Sintering (SHS) utilises a similar system for plastic powders, except a heated print head is used to selectively melt the powder. Multi-material printing has not been reliably achieved with PBF. The requirement of a bed of powder would mean any efforts to selectively place a powder for the application of heat would result in the mixing of powders around the component, making it impossible to recycle [104].

Selective Laser Sintering

Selective Laser Sintering (SLS) is an additive manufacturing process whereby a laser is used to sinter layers of powdered thermoplastic. To start the process the powder bed moves down and an automated wiper adds a layer of powder. The powder is selectively sintered with a laser scanning strategy that fills the whole cross-section. The process is repeated for the next layer of powder. The process has a narrow variety of available plastics, almost exclusively using Polyamide (PA) 12. PA 11 has seen moderate success, demonstrating some improved part properties [105]. Other 'exotic' plastics like Nylon, elastomeric types (TPE, TPU, PEBA), and other polyamides (PA 6) are commercialised and with growing but still limited achievement [106]. Most commercial systems use a spot size of 400µm, much greater than a metal-based laser fusion system which uses a typical 70µm spot size. The particle size distribution of a typical SLS plastic powder is between 20 µm and 80 µm, compared with 15 µm to 45 µm in gas atomised metal powders.

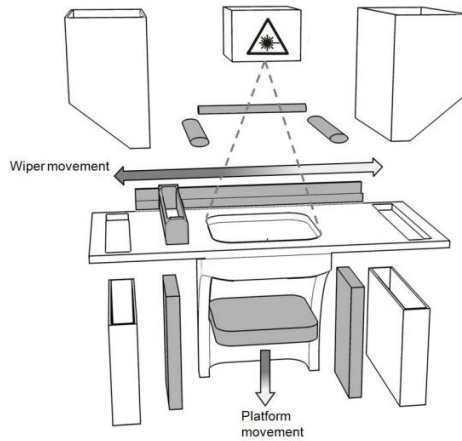


Figure 31. Selective Laser Sintering process schematic [107].

	EOS P 500	Formlabs Fuse 1
Material	PA12	PA 12
Manufacturer	EOS	Formlabs
Build Volume (mm)	500x330x400	165x165x320
Maximum Build Rate	40 mm/h	10 mm/h
Max Laser Power	2x 70W	10W
Laser Spot Size	-	200 μm
Layer Thickness	100 μm	100 μm
Min. Wall Thickness	700 μm	750 μm
Max Scan Speed	2 x 10 m/sec	2 m/sec
Inert Gas	N/A	N/A
Features	Industrial high-output	Desktop Sized R&D

Table 12. Selective Laser Sintering Plastic Machine Specifications.

Selective Heat Sintering

Selective Heat Sintering (SHS) is an additive manufacturing process whereby a thermal printhead is used to apply heat to layers of powdered thermoplastic. To start the SHS process, the powder bed moves down and an automated wiper adds a layer of powder. The powder is selectively sintered to form the cross-section of the component with the thermal printhead, and then the process is repeated for the next layer.

SHS is better for rapid prototyping for concept evaluation, rather than as a functional component. The process is much cheaper and quicker than a laser based SLS solution, making it ideally suitable for scaled down desktop units [107]. The technology is patented by Blueprinter, who are the sole manufacturer of the machines. In September 2016, the company filed for bankruptcy, and to date there are no investors have been willing to salvage the technology. This is partly due to economic conditions favouring cheaper laser-based systems over more complicated and bespoke thermal print heads.

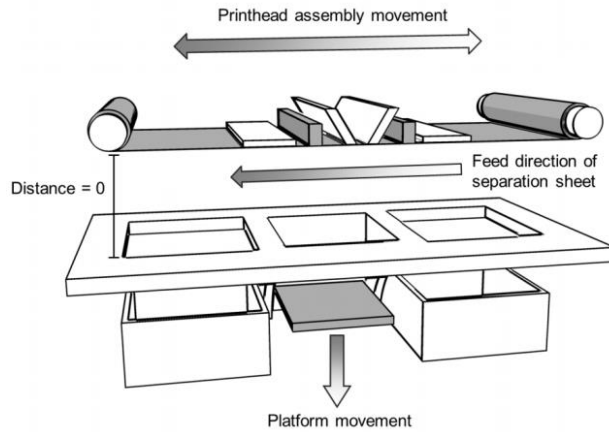


Figure 32. Selective Heat Sintering process schematic [107].

3.3.2 Material Jetting

An additive manufacturing process where the build material is selectively deposited in liquid form by a drop on demand (DOD) process, in a similar mode of operation to a 2D inkjet printer. It uses piezoelectric nozzles to dispense the plastic droplets, which are then cured by UV light [74], [108]. PolyJet printing is the common name used for this technology used by Stratasys. Stratasys use materials named Tango Black + (TB+) and Vero White+ (VW+). TB+ is a rubber like material capable of large elongation, and VW+ is a rigid material that simulates the behaviour of Acrylonitrile Butadiene Styrene (ABS). Mixing these materials can produce material combinations ranging from 40 to 95 on the Shore A hardness rating. Different materials can be actively combined and graded throughout the print [108]–[111]. This is been demonstrated in many applications for controlled CTE structures, where the combination of materials create an overall change in CTE [64].

MJ is faster than similar technologies such as SLA, however it typically has a higher initial cost. It can achieve high resolution layers from $15\mu\text{m}$, minimum wall thicknesses down to $300\mu\text{m}$ and a dimensional error of 2.14% [109]. Another advantage over SLA includes the ability to print large scale objects without having to compromise on resolution. The produced components are able to be used as a functional industrial prototype [110].

3.3.3 Binder Jetting (BJ)

Binder Jet printing is an additive manufacturing technique that dispenses liquid binding agent on powder to form a two-dimensional pattern on a layer. The layers are stacked to build a physical component. Binder Jetting (BJ) can be adapted to almost any powder with high production rates and the BJ process utilizes a broad range of technologies including printing techniques, powder deposition, dynamic binder/powder interaction,

and post-processing methods. Limited work has been done with BJ of polymers. A part of this problem is because polymers are rarely fabricated from a powder, therefore there are limited formulations available [112]. Polymers such as polylactic acid (PLA), polyglycolic acid (PGA), polycaprolactone (PCL) and polyethylene oxide (PEO) have been printed when using a solvent as a binder [113]. Other formulations with wax and epoxy binders have been commercialised by companies such as Voxeljet, that use polymethyl methacrylate (PMMA) [114]. A process developed by Hopkinson et al.[115] and commercialised by HP is the multijet fusion process which uses a radiation absorber as the binder, and an additional step where a heat lamp bonds the binder after depositing [112]. This is slightly different from the BJ process because a final part is produced as an additional sintering step is not required.

3.3.4 Stereolithography Apparatus (SLA)

Vat Photo polymerisation, also known as Stereolithography Apparatus is an additive layer manufacturing method that requires a vat of photopolymer resin which is cured by UV light as the platform moves down layer by layer. Stereolithography, like other additive manufacturing (AM) methods, has the ability to create parts with complex geometries, and has been used for a wide range of applications in both medical and dental industries [116]–[119].

A low power solid-state yttrium vanadate (Nd: YVO₄) laser is used in modern machines, ranging between 1000 and 2000mW. Digital Light Projection (DLP) is an emerging method of illuminating the resin. In this technology a digital mirror device (DMD) is used to move several millions of mirrors that can be rotated independently to an on or off state, is used. These mirrors correspond to each individual pixel in a 1920x1080 resolution high definition image, which is the highest available resolution [120][121].

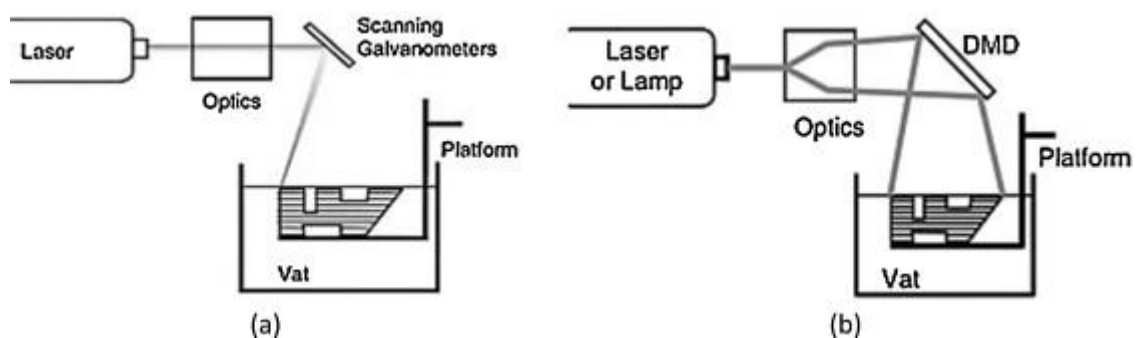


Figure 33. Two modes of operation for SLA include a) Scanning-Based SL (SSL) or Direct Writing b) Projection-based SL (PSL) featured in the DLP method [122].

One of the main advantages of stereolithography is the degree of precision that can be achieved using this method. For a micro platform (9.6mm x 5.4mm) the minimum feature

size can be as small as $5\mu\text{m} \times 5\mu\text{m}$, but for a standard volume ($384\text{mm} \times 216\text{mm}$) the minimum feature size is $200\mu\text{m} \times 200\mu\text{m}$ due to the magnification pattern [123]. The higher resolution of SLA is the main advantage over technologies such as FDM [124]. One of the disadvantages with stereolithography is that a typical stereolithography system requires several litres of material to fill its print tray. The material costs for operating a stereolithography are so much higher than that of other systems that the cost of operations exceeds that of other plastic-based additive manufacturing methods [125].

For the production of components for the optical industry the process might seem like a great option due to its high resolution, however there are a number of issues that may affect its adoption in this industry. There is a limited range of materials available to use, all of which must be able to cure with ultraviolet light. The material used for stereolithography is also susceptible to degradation from environmental factors such as humidity, temperature, and light. As a result, the parts made from stereolithography are quite good for making prototypes, but not well suited for final part production [126]. The process cannot print in multiple materials, meaning the manufacture of tailored CTE structures is not possible.

3.3.5 Fused Deposition Modelling

Fused Deposition Modelling (FDM) is a material extrusion process whereby a plastic filament typically between $1.75\text{mm} - 3.0\text{mm}$ in diameter is fed into a hot nozzle between $0.1\text{mm} - 1\text{mm}$ where it is melted and selectively deposited into layers ranging from $0.1\text{mm} - 0.4\text{mm}$ depending on nozzle diameter. The process can be used to create functional parts and prototypes from a range of plastics.

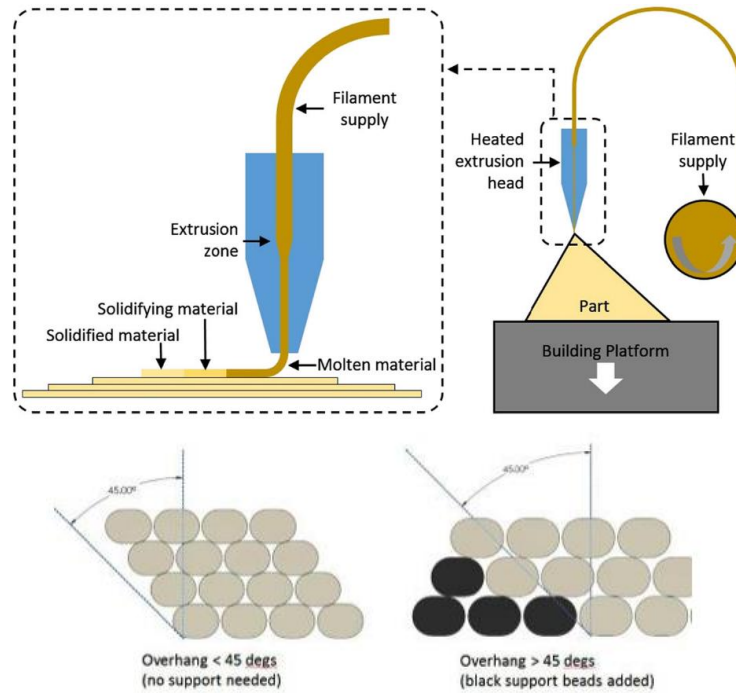


Figure 34. Typical FDM extrusion process and overhang support requirements [74] [26].

There are two methods of printing multiple materials simultaneously; these include the single nozzle, and the dual nozzle arrangement.

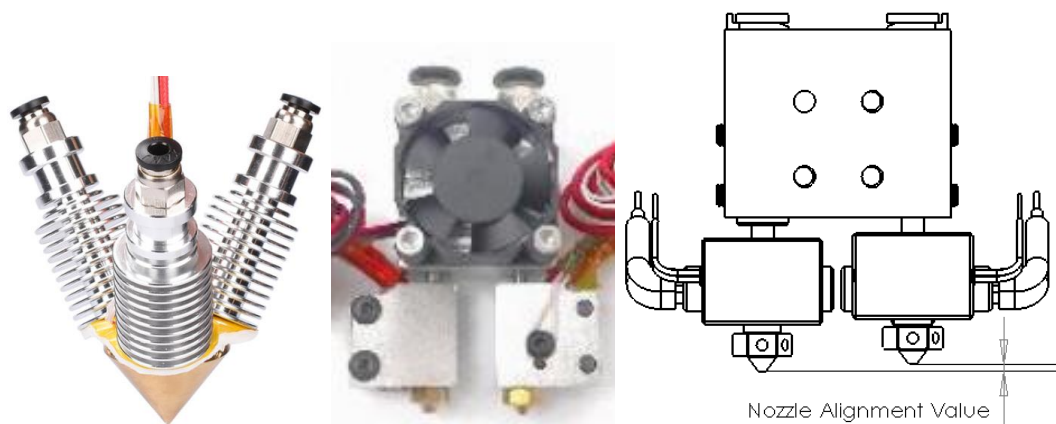


Figure 35. Images showing two FDM nozzles, the single nozzle, and multiple nozzle design with a diagram of the nozzle alignment value position.

A single nozzle design easily allows for more than two materials to be extruded; however, a nozzle purge is required when switching materials, resulting in material wastage and increased printing time. Using a dual nozzle arrangement increases print speed but is almost impossible to get high quality prints if the ‘nozzle alignment value’ is not exactly zero. When perfectly aligned, the print quality can still be degraded due to material oozing from one nozzle and being dragged across the print. The Ultimaker 3 avoids the alignment value problem by raising and lowering the nozzle when each material is used [127].

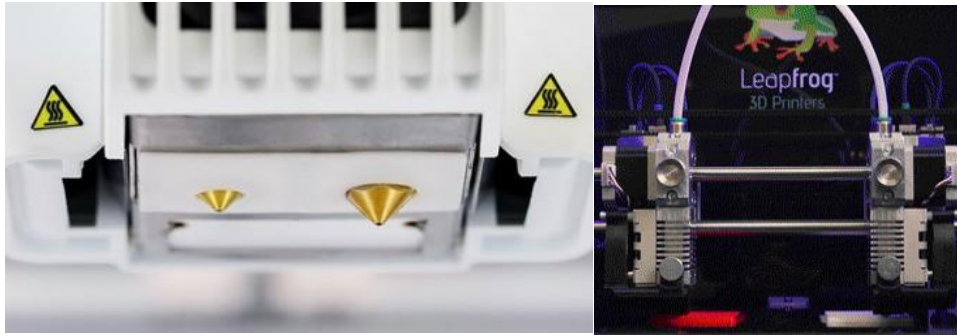


Figure 36. Ultimaker 3 multi-material solution, showing primary nozzle stowed and secondary nozzle lowered for printing. Leapfrog’s independent dual extruder multi-material solution.

	Ultimaker 3	Prusa i3 MK3	Leapfrog BOLT
Number of materials	2	4	2
Nozzle Type	Dual	1x Single	2x Single separate nozzles
Extruder Type	Bowden	Bowden	Bowden
Build Volume (mm)	197x215x200	210x210x250	723x831x801
Filament Diameter (mm)	2.85	1.75	1.75
Layer Thickness (µm)	60	50	50
Max Nozzle Temperature	280°C	280°C	360°C
Max Bed Temperature	110°C	100°C	90°C
Enclosed Heating	No	No	Yes
Auto Bed Levelling	Yes	Yes	Yes
Features	Dual Nozzle Auto-Material Switch.	4 Materials into one nozzle.	2 separate nozzles printing independently.

Table 13. The most common three multi-material FFF printers with different nozzle arrangements.

The Ultimaker 3 can be used to produce multi-material structures. Inclusions such as carbon and glass fibres are sometimes added to the plastic filament to improve mechanical properties. These inclusions can wear the Ultimakers brass nozzle. The use of a 3rd party heating core is required so that hardened steel and ruby tipped nozzles can be used. One such system is the Solex3D high temperature core for the Ultimaker 3 [128]. Figure 37 shows an image of the Solex3D core which replaces the Ultimaker 3’s core to allow abrasive filaments to be processed at higher temperatures.



Figure 37. Ultimaker 3 high temperature core by Solex 3D provides capability to change the nozzle to a hardened steel or ruby tipped design.

Continuous Filament Fabrication (CFF)

Fused deposition modelling can also be used for printing fibre composites. This is a process known as continuous filament fabrication (CFF). The process works using two nozzles, one for the placement of the filament and the other for the extrusion of the polymer. The Desktop Mark Two by Markforged is a commercial machine with the ability to print with either carbon, glass, or kevlar fibres. The feed filament consists of woven thin hairs of continuous fibres encased in nylon, instead of a thicker single continuous strand. This enables the filament to be more flexible and less brittle, and provides it with a means to adhere to the substrate [28]. The fibres can be laid in a specified direction to produce a composite that can be stronger and less thermally expansive in one direction than the other [25]–[27]. The printer has a choice of Nylon or Onyx as the printing material. Onyx is nylon, impregnated with short-chopped carbon fibres. The company owns several patents protecting their core technologies [129]. Orientation of the fibres is completed in the online slicer provided by Markforged called eiger.io.[60][61][62].

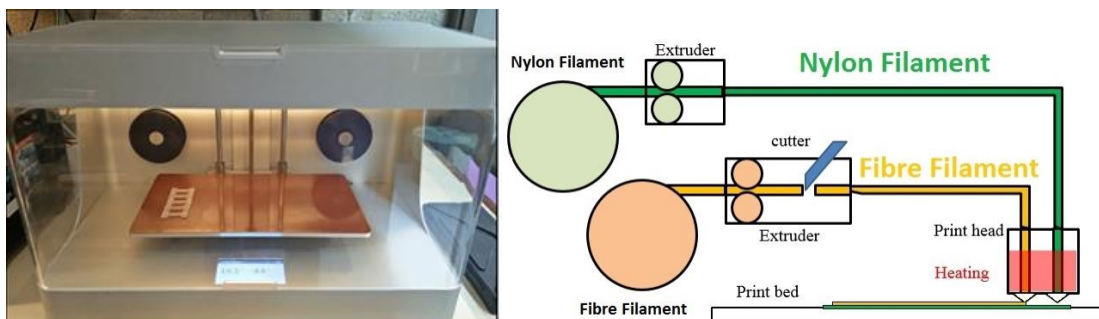


Figure 38. Mark One Composite 3D printer (left). The fibre is introduced from the spool into the print head that lays the fibre onto the preceding nylon layer, thus allowing continuous fibre composites to be manufactured, layer by layer (right).

3.4 Geometric Tolerances of Additive Manufacturing

3.4.1 Summary

This chapter has identified the geometric tolerances of both metal and plastic AM parts. It has measured dimensions such as the wall thicknesses, gaps between features, hole diameters, and cylinder diameters. It has also looked at the concentricity of the cylinders. These lengths were measured using an array of high precision techniques such as shadow graph measuring and 5-axis co-ordinate measuring. The measured lengths are all considered to be essential when considering the high tolerances required in the manufacture of an optical system body.

3.4.2 Introduction

Traditional standards for tolerances have been developed based on the capabilities of conventional manufacturing. Due to increasing interest in AM by industry, specific AM standards through ASTM International and ISO have been formed to characterise each process. There is a standard in development ‘ISO/ASTM DIS 52902’ a part of ‘ASTM F42’ which specifies a standard guideline for measuring the geometric capability of an AM system [130]. The Nation Institute of Standards and Technology (NIST) has commenced a program called AM-BENCH, which attempts to provide a framework of additive manufacturing benchmarks for completion across all additive manufacturing methods. The aim of the program is to provide modelers with rigorous, highly controlled AM benchmark test data to validate their models with. The first round of benchmark data was completed in 2018, with the next due in 2022. The 2018 does not contain dimensional tolerances of AM processes. Many researchers have formed their own benchmarks and are reported in literature, the lack of standardisation across all the benchmarks used by the researchers provides difficulty when comparing across multiple additive manufacturing methods. The benchmarks in this chapter include the ‘flat plane slot resolution’ which assess the tolerance of a series of increasing distance gaps, the ‘cylindrical slot resolution’ which is the same but measuring the distance between each cylinder, the ‘wall thickness resolution’ which measures the tolerance of a series of increasing thickness walls, and finally the ‘hole size resolution’ which measures the diameter of a series of bore holes. Further benchmarks are completed using a co-ordinate measuring machine to obtain the diameter, and circularity, of a series of increasing diameter rings. The benchmarks completed in the present work are tabulated in Table 14 with a label for easier reference.

Label	Benchmark feature
A	Square slot resolution - distance between square features
B	Cylindrical slot resolution - distance between cylindrical features
C	Wall thickness resolution - thickness of the wall itself
D	Hole size resolution - diameter of the hole itself
E	Hollow cylinder - diameter inside and outside
F	Hollow cylinder - circularity inside and outside

Table 14. Benchmarks featured in the present work

The benchmarks in the present work are compared to equivalent benchmarks in literature. Table 15 shows which benchmarks have been completed for comparison, and also the manufacturing method and parameters used to make it. Consideration has been made so that the build orientation in chosen literature matches that of the printed benchmarks in the present work. The tolerances of the benchmark parts will be affected by the orientation of the benchmark parts in relation to the build direction and the recoater [131]–[133]. The orientation of the parts printed are shown in Figure 50.

No.	Reference	Benchmark label	Equipment	Process type	Material	Layer thickness / Laser power
1	J.-P. Kruth et al. [134]	C, D	3D systems DTM	SLS	Polymer coated stainless steel	80µm / 10W
2			Concept Laser	LPBF	Hot work tool steel	30µm / 100W
3			Tumph	LPBF	Stainless Steel 316L	50µm / 200W
4			MCP-HEK	LPBF	Stainless Steel 316L	50µm / 100W
5			EOS	SLS	Bronze based	20µm / 221W
6	J. Kranz et al. [135]	A, D	EOS M270 XT	LPBF	TiAl6V4	30µm / 170W
7	M.G. Teeter et al. [136]	A,B,C	3D Systems DM125	LPBF	Stainless Steel 316L	50µm / 200W
8	V. Matilainen et al. [132].	A,C	EOSINT M-Series	LPBF	Stainless Steel PH1	30µm / 200W
9	K. Kamarudin et al. [137]	A,C	SLM 125HL	LPBF	AlSi10Mg	30µm / 350W
10	Y.L. Yap et al. [131]	C	Polyjet Objet500 Connex3	Material Jetting	VeroWhitePlus RSD835	32µm
11	A. Cooke et al. [138]	E, F	-	LPBF, EBM	-	-

Table 15. Specification of manufacturing parameters for benchmark parts from literature.

Each reference in Table 15 uses a unique benchmark design to discover the tolerances of process they are benchmarking. Kruth et al. [134] produced a benchmark design to combine many benchmarks into one piece shown in Figure 39. The model consists of a series of holes (5,2,1 and 0.5mm diameters) and thin walls (1, 0.5, and 0.25mm thickness). They manufactured the benchmark piece using laser powder bed fusion and sintering processes.

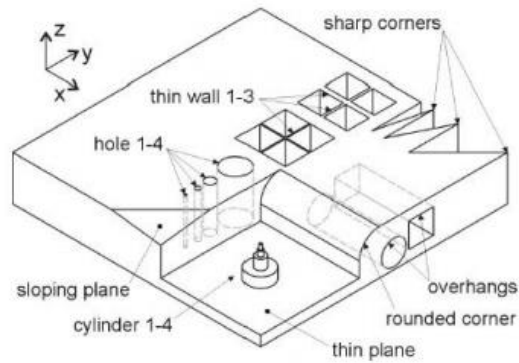


Figure 39. Benchmark model by J.-P.Kruth et al. [134].

J. Kranz et al. [135] uses a benchmark designs to test the bore hole size with a similar benchmark to present work, with the hole axis in the same direction as the build direction. Hole sizes range from 2, 3, 4, 5, 6, 7, 8, 9, 10 and 12mm diameters, measured using optical microscopy.

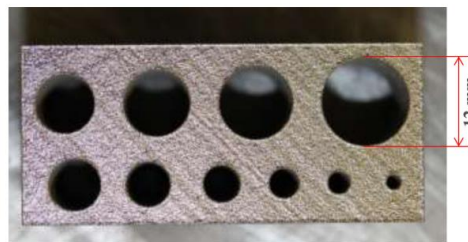


Figure 40. Benchmark model and a manufactured hole size benchmark by J. Kranz et al. [135]

M.G.Teeter et al. [136] has constructed a benchmark that includes a wide range of thin walls and bore holes . The thin walls are printed at 45° and 135° to the recoater, compared to the 90° in the present work. They range from 1mm to 0.1mm decreasing by $100\mu\text{m}$ per wall. The bore hole diameters are 8, 5, 3, 1, 0.7, 0.5, and 0.3mm. Six cylinders are also printed with decreasing gaps between them of 1, 0.7, 0.5, 0.3 and 0.1mm. The distance between the cylinders is compared to nominal. The 0.1mm gap in this benchmark could not be distinguished. The benchmark also features a series of squares with various gaps, but this is not comparable to present work because they are printed parallel to the build direction rather than perpendicular in the present work.

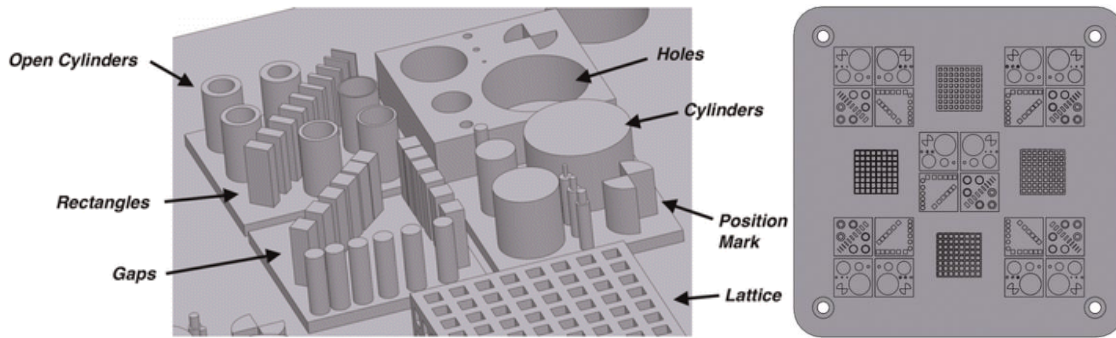


Figure 41. Benchmark model by M.G. Teeter et al. [136].

V. Matilainen [132] provides benchmarks in a thesis for the wall thickness and rectangular slot resolution at 0° and 45° to the recoater. The wall thicknesses vary from 1.4mm to 0.1mm decreasing by $100\mu\text{m}$ per wall. The rectangular slot gap distances are between 1mm and 0.1mm decreasing by $100\mu\text{m}$ each gap.

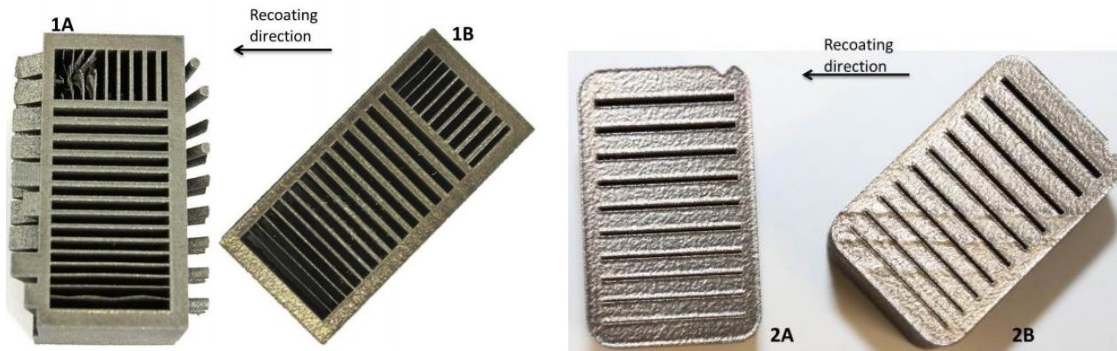


Figure 42. Benchmark parts for wall thickness (1A, 1B) and rectangular slot resolution (2A 2B) by V. Matilainen [132].

K. Kamarudin et al. [137] features a benchmark test piece with a series of rectangular slots with gaps of 8, 3, 2, 1.5, 1, and 0.5mm between each, printed perpendicular to the build direction as in present work. The wall thickness benchmark varies from 3, 2, 1, and 0.5mm.



Figure 43. Benchmark model by K.Kamarudin et al.[137]

Y.L.Yap et al. [131] prints a series of thin walls at 15° angles to the recoater. Measurements are average over all the heights for each angle, with angles 0° , 45° , and 90° plotted in Figure 48. The angle of 90° is directly comparable to LPBF builds in the results of present work.

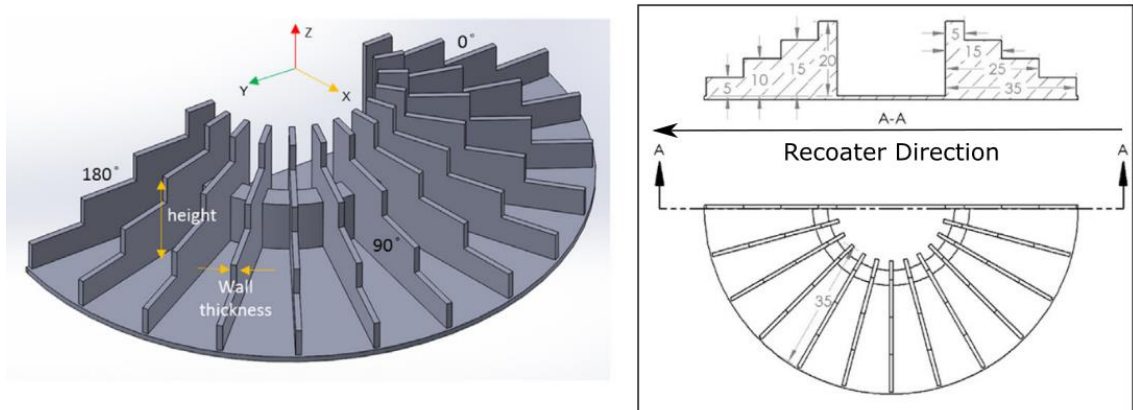


Figure 44. Benchmark parts for wall thickness at various angles to the recoater by Y.L.Yap et al. [131]

A. Cooke et al. [138] provides a benchmark test called the National Aerospace Standard, NAS 979 circle diamond square with and inverted cone [139]. This part was developed in 1966 as a test part for CNC machining centres. Parts are printed in Ti-6Al-4V using the LPBF process and stainless steel 316L using the EBM process. Parts 1 and 2 shown in Figure 45 are printed using the same machine using the same process parameters. The results indicate a relatively high degree of repeatability, providing opportunities for compensation. The work indicates that the residual stresses in both processes are the likely contributor to the error in the form of the circle compared to nominal.

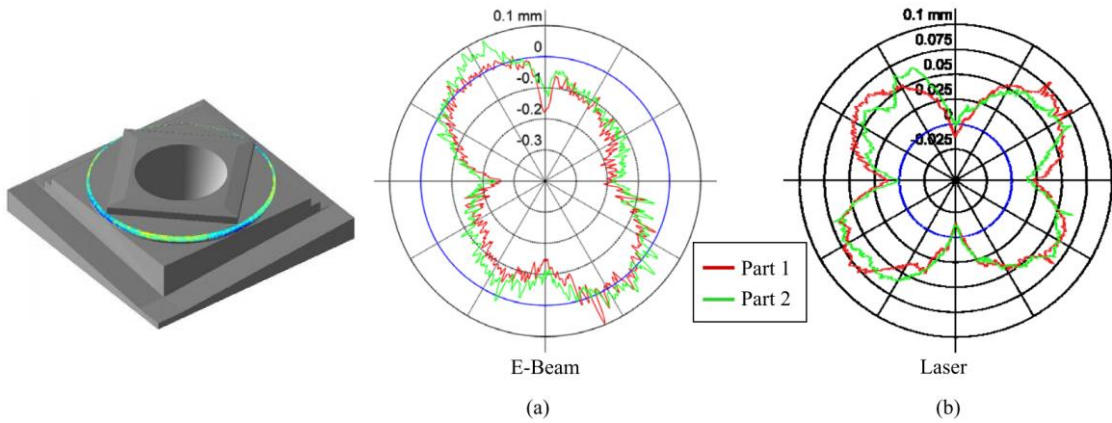


Figure 45. Benchmark test piece (left) showing measured area and the results for circularity of a) an EBM process and b) a LPBF process, by A. Cooke et al. [138].

The rectangular slot deviation is plotted in Figure 46 from literature. V. Matilainen [132] shows that the slots are a between 0.1 and 0.2mm less than nominal between 1 and 0.6mm gap spacing. A fixed offset can be applied to bring the gap spacing closer to nominal. As the gap decreases in size to less than 0.6mm the deviation in gap distance becomes positive, increasing to 0.08mm for those printed at 45° to the recoater. The difference between the angles of 0° and 45° shows that 0° produces values at or below nominal (between -0.12 to 0.01mm), whilst 45° produces a wider range (between 0.19 to 0.08mm). K. Kamarudin et al. provides a set of data of 8, 3, 2, 1.5, 1, and 0.5mm gaps. There is no information provided about the angle to the recoater.

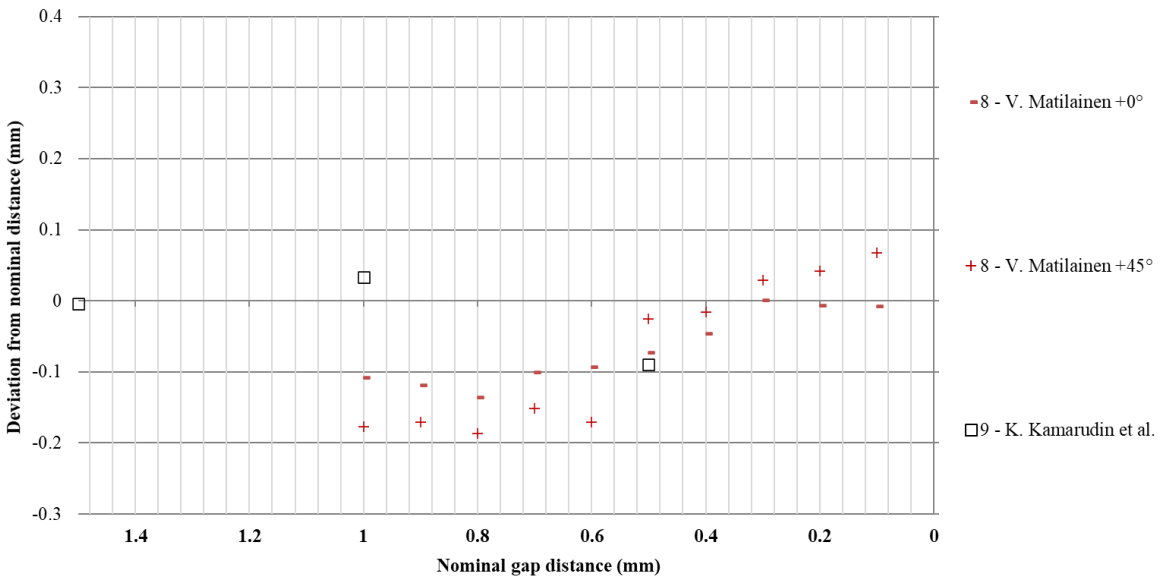


Figure 46. Rectangular slot deviation found in literature for benchmark parts [132], [137].

The cylinder slot resolution has been provided by M.G.Teeter et al. [136] and plotted in Figure 47. It has been manufactured on a 3D systems LPBF machine using 316L. The deviation from nominal distance between the cylinders is very tight of between only -

1 μ m and +5 μ m on average. Compared the rectangular slot deviation found by V. Matilainen [132] of between -190 μ m and +80 μ m, this is significantly less deviation. The lower deviation found by M.G.Teeter et al. [136] is also noticed across their other benchmarks, such as the wall thickness deviation (Figure 47), where a deviation up to only +6 μ m was observed from 1 to 0.4mm. A similar benchmark by Y. L. Yap et al. [131] was completed using a material jetting polymer process, but did not provide a cylinder gap deviation measurements, only the allowable minimum gap of 0.4mm before the feature becomes closed.

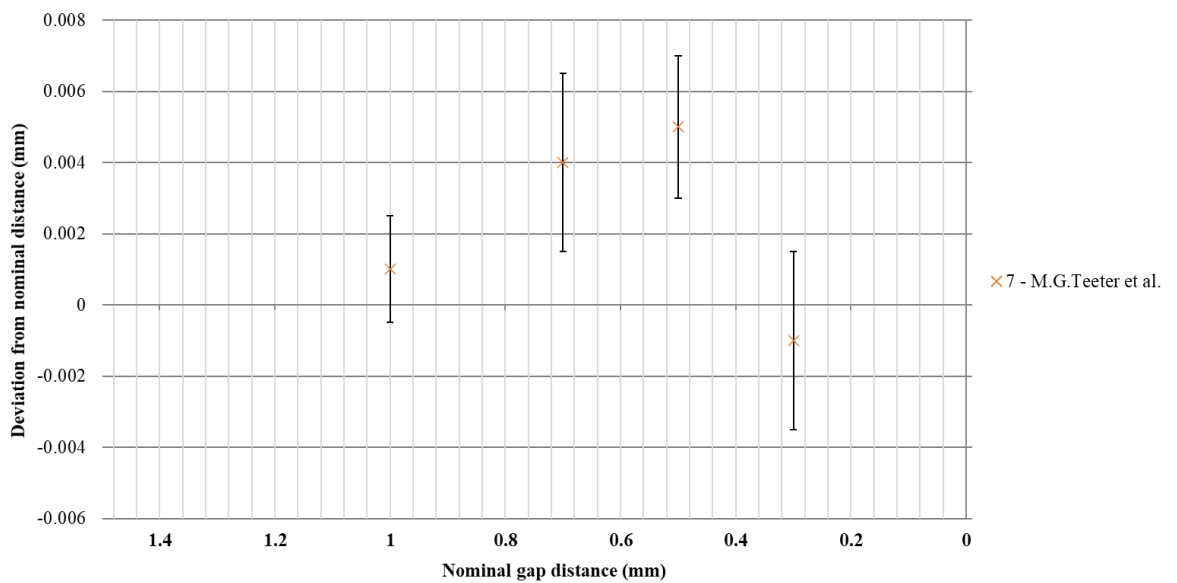


Figure 47. Cylinder slot deviation found in literature for benchmark parts [136].

The wall thickness deviation is gathered and plotted from five authors shown in Figure 48. J.-P.Kruth et al. [134] finds that the wall thickness of 0.25mm could not be printed on part numbers 1 and 2, and 0.5mm could also not be printed on part number 2. The angle to the recoater was not provided by authors for parts 1-5 and 9. Looking at parts 8 and parts 10, the deviation is closer to nominal when the recoater is at 0° to wall. For parts 10 there is an increasing deviation with the angle from 45° and to 90°. Both authors for parts 8 and 10 have discussed the effect of the angle of the benchmark parts to the recoater and discussed that the deviation is caused by the overspreading of the material across the wall thickness which increases as the recoater come closer to being perpendicular with the wall [131], [132]. Another theory is that the wall flexes more with the increased surface area in contact with the recoater as the angle comes closer to being perpendicular. The flexing of the wall causes a greater variance in thickness throughout causing a larger maximum deviation will be measured.

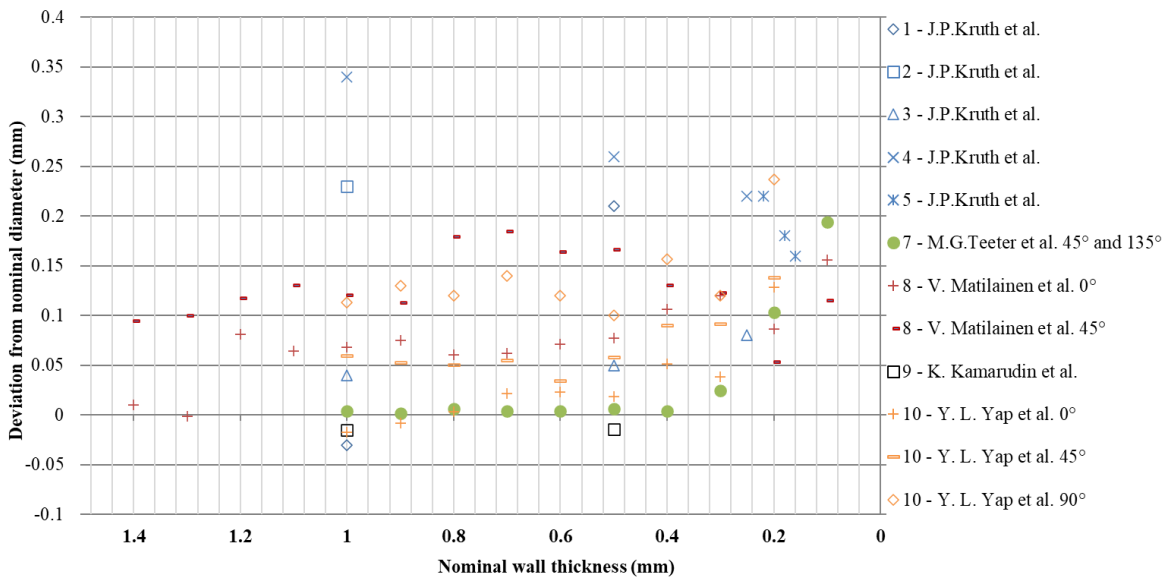


Figure 48. Wall thickness deviation found in literature for benchmark parts [131], [132], [134], [136], [137].

J. Kranz et al. [135] provides data for hole size deviation when printing Ti64Al with an EOS M270XT in the same orientation as printed in the present work. They have heat treated the component to relieve residual stresses, whereas the present work has not [135]. J.-P.Kruth et al. [134] has printed a benchmark component and measured 5, 2, 1 and 0.5mm holes diameters printed in the same orientation as the present work, using a range of binder jetting and LPBF printers [134]. Hole diameters of 0.5mm were not distinguishable on all process methods, and 1mm diameter holes were only distinguishable on part numbers 3 and 5, with the remaining three process types showing a badly built hole where the diameter could not be established. M.G.Teeter et al. [136] prints 316L using a LPBF machine by 3D systems. Six repeats are printed across the build plate producing relatively small error in each reading of up to ± 0.021 m. All methods of measurement in literature is by optical image analysis. The hole diameter deviation in the literature is plotted in Figure 49. The plot shows that most hole diameters were less than nominal for the processes by J.-P.Kruth et al. [134] of up to 0.38mm, compared to those by J.Kranz et al. [135], which were larger than the intended diameter by up to 0.3mm. M.G.Teeter et al. [136] produced the highest accuracy parts with as little as 18 μ m below nominal. The higher accuracy of the benchmarks by J.Kranz et al. [135] and M.G.Teeter et al. [136] compared to J.-P.Kruth et al. [134] could be due to the advancements in additive manufacturing process technology over the decade from when J.-P.Kruth et al. [134] was published in 2005 to 2015 for J.Kranz et al. [135] and M.G.Teeter et al [136]. Author D. Thomas [133] finds holes printed in the same orientation have a minimum hole diameter of 0.7mm before the feature becomes closed, disagreeing with M.G.Teeter et al. finding a minimum of 0.5mm is achievable with LPBF [136].

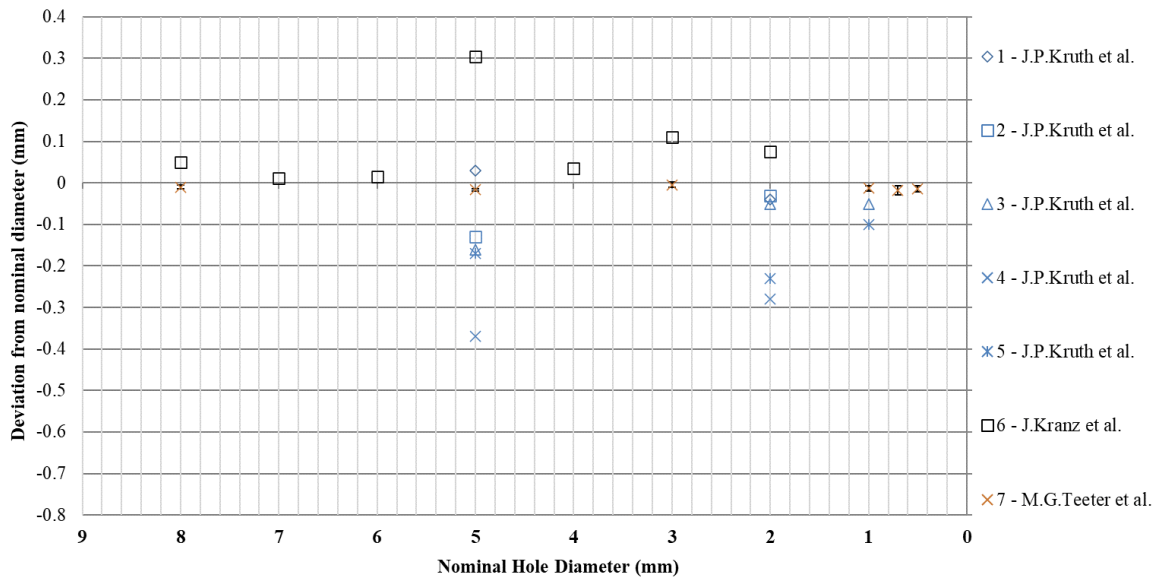


Figure 49. Hole size deviation found in literature for benchmark parts [134]–[136].

3.4.3 Method

The benchmarking has been completed with 316L on the Renishaw AM400 and Ti64Al on the Renishaw RenAM500. Both machines have used a 200W manufacturer provided material laser setting. For plastic benchmarking, the Ultimaker 3 has been used to benchmark PLA material since it is the most common plastic used in FDM printers. For the fibre reinforced AM polymers, the Markforged Desktop Mark Two will be used. It will print two matrix polymers available; these are nylon, and nylon impregnated with short-chopped carbon fibres which Markforged are calling ‘Onyx’.

To determine dimensional accuracy; the flat plane slot resolution, cylindrical slot resolution, and hole size resolution are all be measured using a shadowgraph machine called the Starrett HE400 comparator. The wall thickness resolution is measured using a Mitutoyo micrometer with a resolution and accuracy of 1µm. Diameter and circularity measurements of a cylinder over the build plate is measured using the Renishaw Revo5-axis CMM touch probe machine. All parts were tested as-built, without any form of heat treatment. Any incorporated adhering powder is removed with the application of compressed air only. No other post surface treatments are used. The build parameters used for each material are taken from the recommended values by the machine manufacturer.

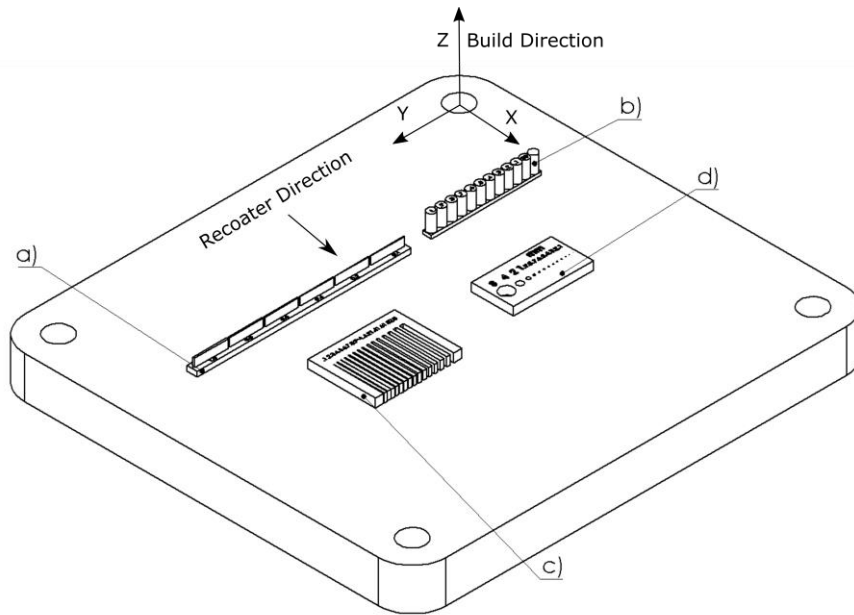


Figure 50. Build plate assembly showing part orientation and recoater direction. Parts are; a) Wall thickness resolution, b) Cylindrical slot resolution, c) Square slot resolution, and d) Hole-size resolution.

3.4.4 Rectangular slot resolution

To benchmark the accuracy of a periodic gap, a piece has been designed with the dimensions of increasing size shown in Figure 51, where the gap dimensions are 0.1, 0.2, 0.3, 0.4, 0.5, 0.6, 0.7, 0.8, 0.9, 1, 1.2, 1.4, 1.6, 1.8, 2mm. The parts are printed flat to the plate and removed using a wire EDM machine.

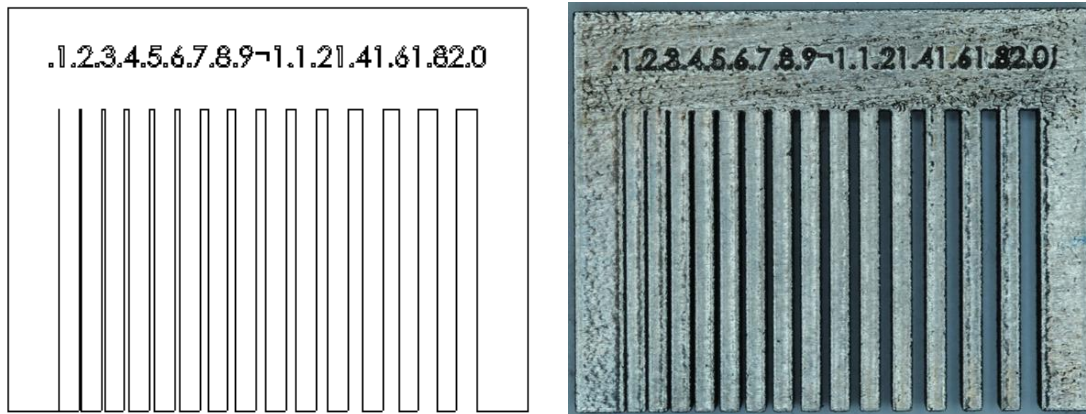


Figure 51. Images of the flat plane slot resolution benchmark CAD drawing and final printed part in Ti64Al.

The measurements made from the shadowgraph are averaged over three cross-sections from the base, middle and top section of the gap. The averaged result is plotted in Figure 52. Nylon produces the only deviation with positive deviation values, meaning the gap is larger than nominal. The deviation becomes larger as the gap size decreases from 2 to 0.1mm. Despite the material onyx (nylon with short-chopped carbon fibres) using the

same machines for manufacture, then deviations are negative with features 0.2 and 0.1mm closed. The material has a steady deviation between $-150\mu\text{m}$ and $-280\mu\text{m}$ with no increasing or decreasing trend with nominal diameter. For onyx, a fixed millimetre offset of approximately $210\mu\text{m}$ would be appropriate. Ti64Al, 316L and PLA could also be offset by $130\mu\text{m}$, $210\mu\text{m}$, and $180\mu\text{m}$, respectively. Nylon requires a $+15\%$ increase in each nominal gap size, and a fixed -0.2mm offset, although its gap to gap variation will remain higher than the other materials.

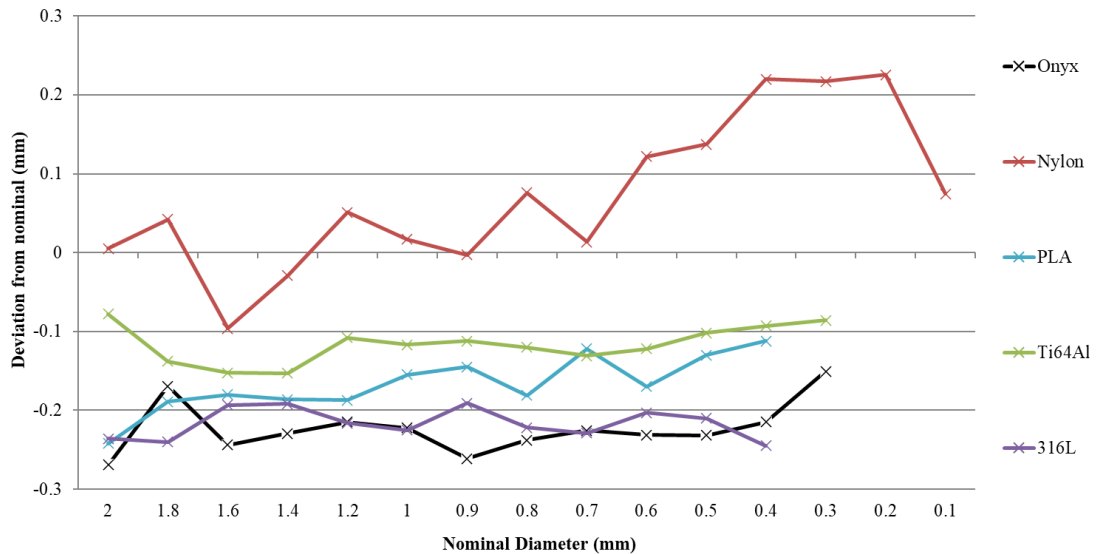


Figure 52. Graph showing deviation using shadow graph results for the slot resolution benchmark for Ti64Al (RenAM500), 316L (AM400), PLA (Ultimaker 3), and Nylon & Onyx (Markforged Desktop 2).

Literature from V. Matilainen et al. [132], and K.Kamarudin et al. [137] print a similar benchmark design with the same orientation as the present work. Both authors have printed parts at 0° to the recoater and flat to the plate as shown in Figure 50. Figure 46 has the deviation plotted for both authors, showing 0° and 45° for part 8 (316L) and part 9 (AlSi10Mg) as 0° . Both authors have printed using the same process of LPBF. Part 8 shows a negative deviation of between 100 and $200\mu\text{m}$ from 1 to 0.6mm , similar to 316L and Ti6Al4 in the present work. As the gap size decreases the deviation reduces closer to nominal and continues the increasing trend until at $+85\mu\text{m}$ at 0.1mm gap distance. In the present work an increase in deviation lower than a 0.6mm gap for Ti64Al and 316L could not be obtained because the features were closed. It is observed that 0° to the recoater had the least deviation overall.

3.4.5 Cylinder slot resolution

The cylinder resolution is a benchmark used to determine the gap between a series of cylinders printed vertically with the build direction. The gaps are $1, 0.9, 0.8, 0.7, 0.6, 0.5, 0.4, 0.3, 0.2, 0.1,$ and 0.05mm . They are measured using a shadow graph at three places,

the top, middle, and bottom section. The three measurements are averaged and plotted for each process in Figure 54. The minimum gap before the feature appears closed is also obtained.



Figure 53. Cylinders ranging from 1mm to 0.05mm gaps.

Inspecting Figure 54 it is observed that nylon has a larger positive deviation compared to any other process of between 220 and 480 μ m. It has also printed the smallest feature at only 50 μ m, where all other processes have not. This is because the deviation is 220 μ m higher than the 50 μ m it should be; therefore the gap has not become small enough to appear closed. Onyx which is nylon with short-chopped carbon fibre added has performed well between only 45 and 105 μ m. PLA had the most accurate gaps between only -5 and 50 μ m with an average deviation closest to nominal of 10 μ m. Both Ti64Al and 316L had the highest negative deviation of between -90 and -150 μ m and subsequently gaps 0.05, 0.1, and 0.2mm were closed. Recommended offsets for 316L, Ti64Al, PLA, Nylon, and Onyx, are +150 μ m, +110 μ m, +20 μ m, -60 μ m, and -420 μ m, respectively.

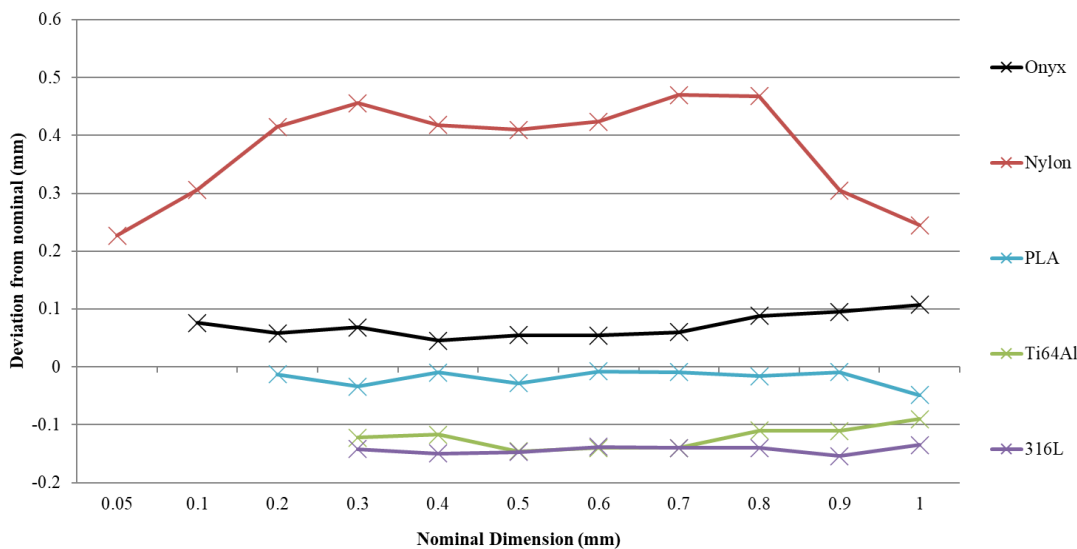


Figure 54. Graph showing deviation using shadow graph results for the cylinder resolution benchmark for Ti64Al (RenAM500), 316L (AM400), PLA (Ultimaker 3), and Nylon & Onyx (Markforged Desktop 2).

Literature by M.G.Teeter et al. [136] provides a comparable benchmark plotted in Figure 47 to measurements in the present work. They have very tight deviations of between only -1 μ m and +5 μ m with errors of up to \pm 2.5 μ m. In the present work, only PLA comes close to such low deviations.

3.4.6 Wall thickness resolution

The wall thickness is benchmarked to obtain the deviation compared to the specified thickness. Thicknesses of 1, 0.8, 0.6, 0.4, 0.2, and 0.1mm are printed on a 5mm substrate and at 90° to the recoater. The wall thickness was measured using a Mitutoyo micrometre with a resolution and accuracy of 1µm.

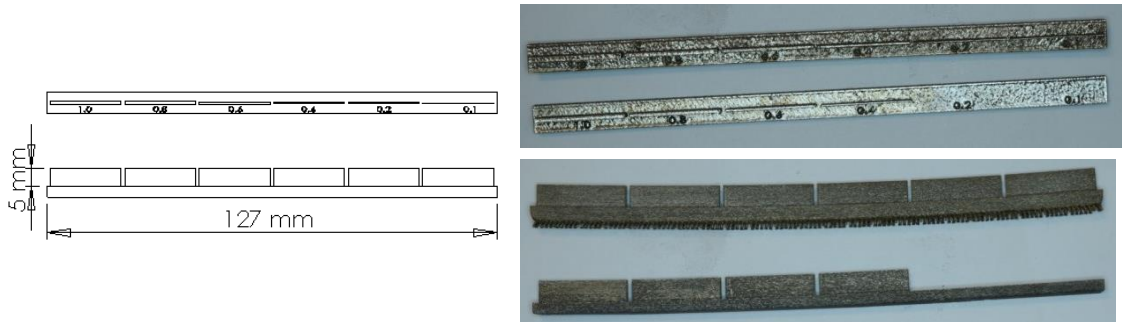


Figure 55. CAD image from with wall of thicknesses between 1-0.1mm (left) and to the right are images of the 316L part and the Ti64Al part.

The wall thicknesses shown in Figure 56 are all thicker than the nominal thickness. Stainless Steel 316L has printed with the highest deviation across all wall thicknesses of between 320µm and 465µm. Ti64Al has printed with the second highest deviations in wall thickness of between 170 and 260µm. The FDM polymer and plastics processes are within a similar range of one another of between 2µm and 85µm. The increased accuracy of FDM processes compared to LPBF processes could be due to the adhesion of metal particles to the outside walls of the LPBF parts. Parts specified as 0.2 and 0.1mm the machines did not attempt to print for Ti64Al and PLA. Nylon and Onyx both did not print from 0.1 to 0.6mm. For 316L, Ti64Al, PLA, Nylon, and Onyx, the recommended offsets to the nominal wall thickness are -400µm, -210µm, -70µm, -40µm, and -85µm, respectively.

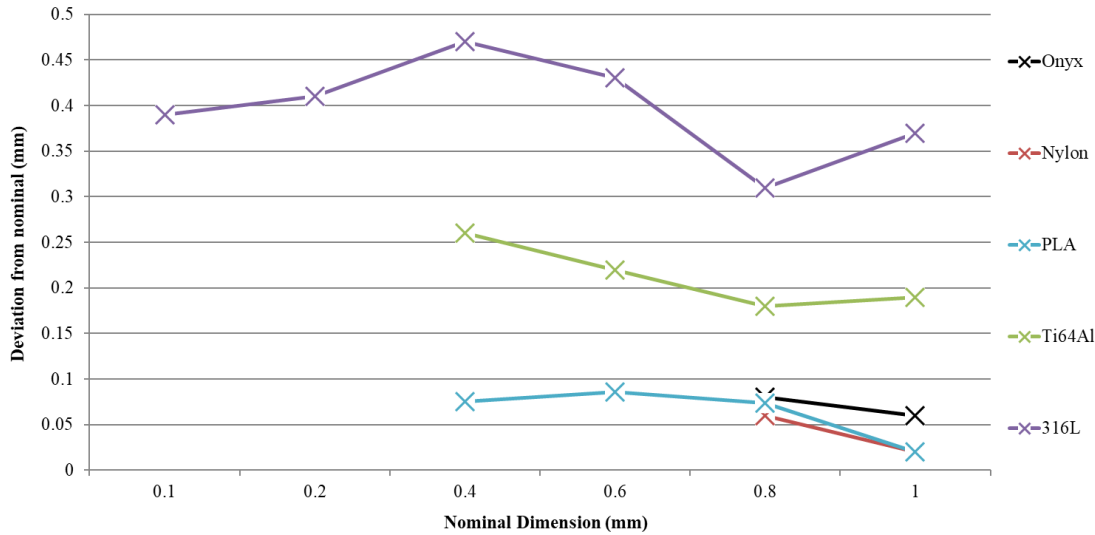


Figure 56. Graph showing wall thickness deviation from nominal for each nominal thickness in Ti64Al (RenAM500), 316L(AM400), PLA (Ultimaker 3), and Nylon & Onyx (Desktop 2).

Literature plotted in Figure 48 shows an equivalent benchmark for comparison with the LPBF processes. Y.L. Yap et al. [131] prints a set of walls that are also 90° to the recoater and has nominal deviations of between 100 and 230µm for wall thicknesses of 1 to 0.2mm. These results are slightly closer to nominal than the present work for Ti64Al of 170µm to 265µm. The deviations measured for 316L are higher than most in literature. Most LPBF processes in literature have been able to print wall thicknesses down to 200µm, with some achieving 100µm. Literature shows that deviation decreases as the wall length comes closer to being perpendicular to the recoater, labelled as 0° to the direction of recoater movement. Y.L. Yap et al. [131] shows a deviation of between only -2µm and 5µm at 0° to the recoater. J.-P.Kruth et al. [134] provides measurements of from 1mm walls with deviations of between 340µm to -3µm showing wall thickness deviation varies widely depending on the material and the machine. The majority of measurements from literature are positive in deviation, meaning the wall are wider than the specified nominal amount [131], [132], [134], [136], [137].

3.4.7 Hole-size resolution

It is important to understand the diameter and shape of bore holes printed using AM. The deviation in diameter is established across a series of changing diameters. A series of holes are printed with the bore axis orthogonal to the build plate and dimensions measured across the X and Y direction shown in Figure 57.

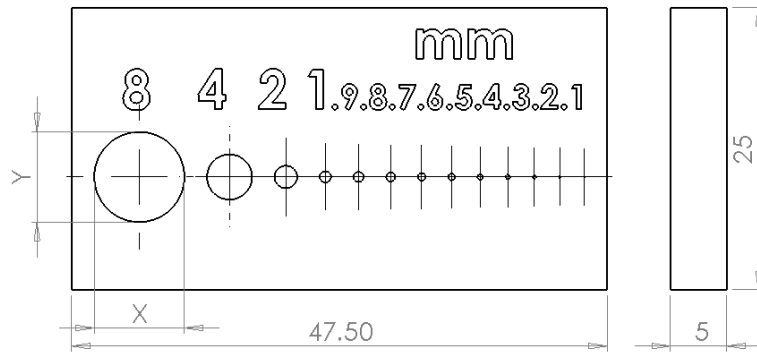


Figure 57. Hole sizes ranging from 1mm to 0.1mm in diameter.

A range of hole diameters are measured, with particular focus on the smallest diameter possible for the 3D printing method and material. For Onyx, Nylon, and 316L there were no diameters below 0.7mm that could be determined, the features appear closed. For PLA the minimum is 0.9mm before features appear closed. The work in Figure 58 shows that with the exception of nylon, there is a trend of increasing deviation with decreasing hole size. The differences between X and Y are larger for Nylon compared to nylon mixed with short-chopped carbon fibre (Onyx). Stainless steel shows large differences in X and Y for larger hole sizes of 8,4 and 2mm. Suggested fixed nominal offsets to the hole sizes for 316L, PLA, and Onyx of $+310\mu\text{m}$, $+550\mu\text{m}$, and $+200\mu\text{m}$, respectively. Nylon is difficult to make a fixed recommendation for because the deviation has a wide range between $+210\mu\text{m}$ and $-500\mu\text{m}$.

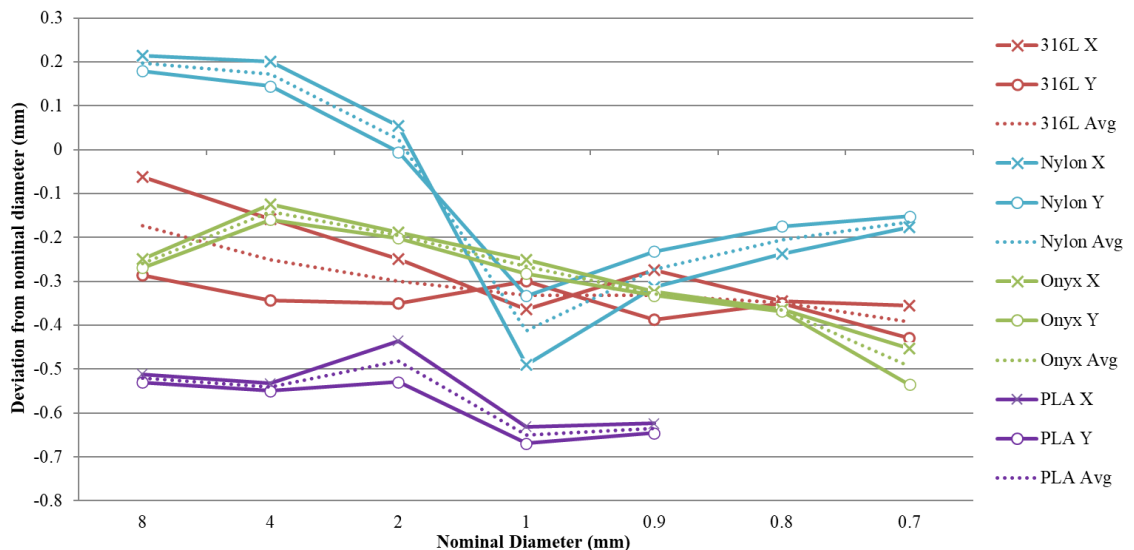


Figure 58. Graph showing holes size deviation for a Ti64Al (RenAM500), 316L (AM400), PLA (Ultimaker 3), and Nylon & Onyx (Markforged Desktop 2) for horizontally built samples.

Comparing present work in Figure 58 with literature plotted in Figure 49 it is observed that holes measured by manufacture from six different machines report by J.-P.Kruth et al. and M.G.Teeter et al. were all undersized, whereas the holes manufactured by one LPBF machine and measured by J.Kranz et al. were oversized [134]–[136]. J.Kranz et al. heat treated the samples before measurement, whereas the others did not [135]. The heat treatment and subsequent reduction of residual stress could have removed distortion and increased the hole size, as literature shows removal of residual stress removes distortion in printed parts [140]–[146]. The distortion shown in 316L parts by the increased X diameter compared to the Y diameter for hole diameters 8, 4, and 2mm shown in Figure 58, could also be caused by residual stresses. It would be recommended to perform a stress relieving heat treatment cycle to produce a part without distortion. Distorted parts will be harder to produce a nominal offset for because distortion is a function of the shape and volume of the component.

3.4.8 Hollow cylinders diameter and circularity resolution

The circularity of an optical system is important to ensure that the lenses can be mounted with minimal lens shift, lens decentre, or lens misalignment. To understand the tolerances and circularity capabilities of the machines, a benchmark has been created as shown in Figure 59. This will be measured on the Renishaw REVO-2 5-Axis CMM machine. The machine has a resolution of up to $1nm$. A program has been written to scan the inside surface taking 100 points a second at $10mm/sec$. The scan path is placed $10mm$ up from the baseplate in the centre of each ring.

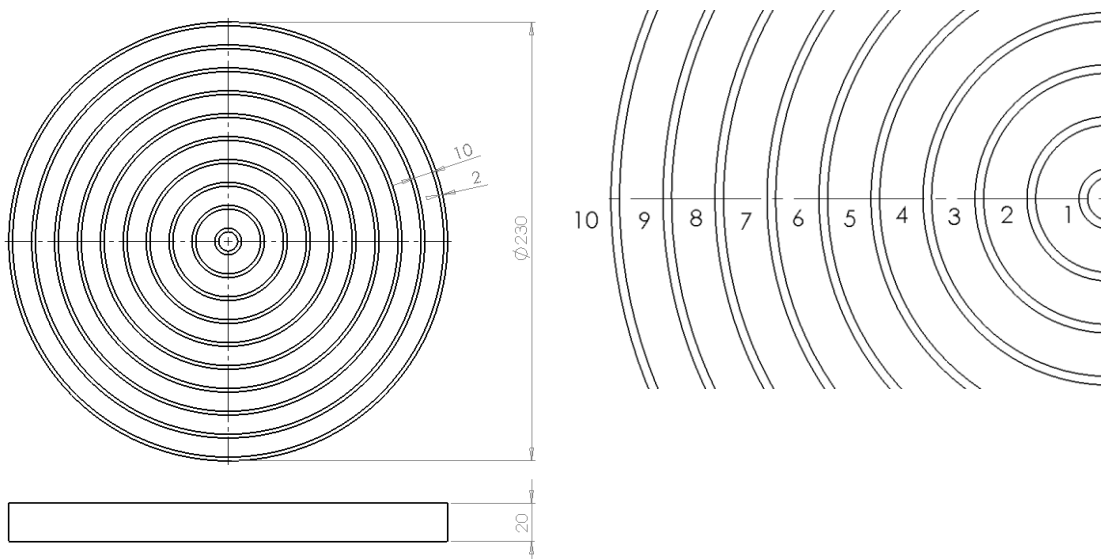


Figure 59. Figure showing CAD for circularity and tolerance benchmarking for a 250x250mm build plate.

	Ring Number									
	1	2	3	4	5	6	7	8	9	10
Inside Diameter (mm)	10	34	58	82	106	130	154	178	202	226
Outside Diameter (mm)	14	38	62	86	110	134	158	182	206	230

Table 16. Nominal diameters for each ring used to determined circularity and diameter deviation.

Metal Laser Powder Bed Fusion

The benchmark has been manufactured on the AM400 in Ti64Al on a 200mm x200mm baseplate using the manufacturer optimised 200W material profile. The build volume size means 10 rings can be printed on the plate. The benchmark data is presented in a series of graphs showing the circularity and deviation. Figure 60 shows the absolute deviation from nominal and the relative deviation as a percentage of the nominal.

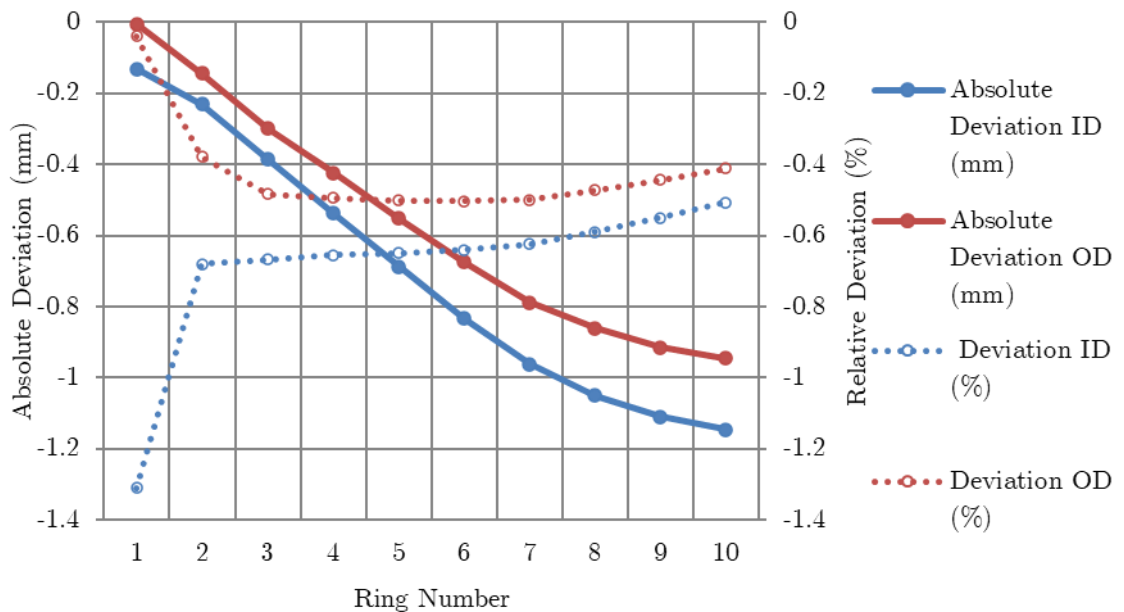


Figure 60. Graph showing Ti64Al deviation from nominal for each ring and the percentage difference compared to its nominal size.

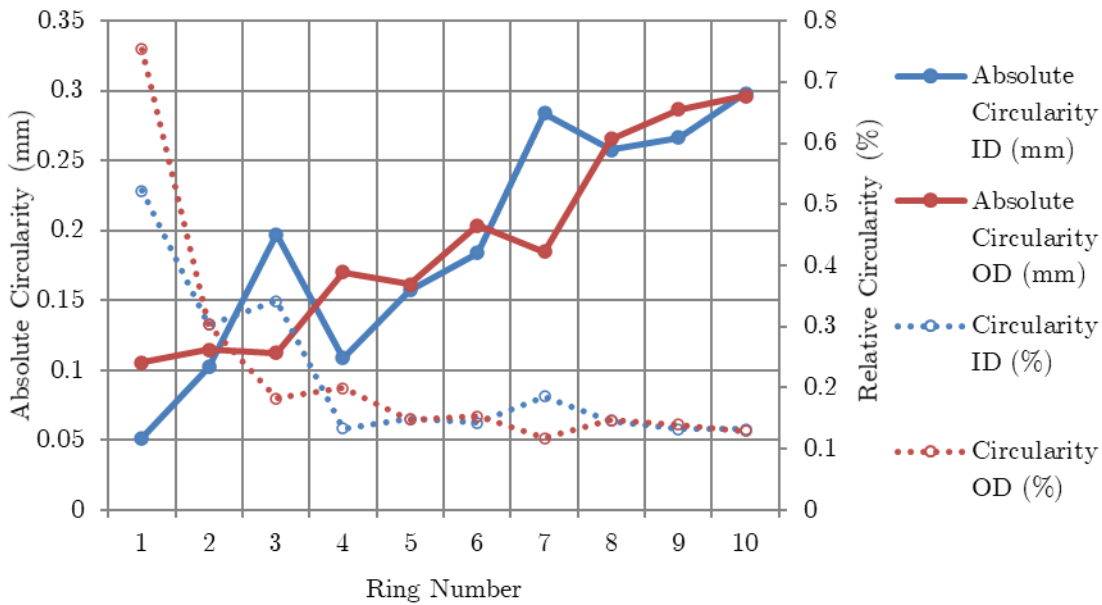


Figure 61. Graph showing Ti64Al circularity for each ring, and as a percentage to its nominal size.

It is observed by looking at Figure 60 that as the diameter of the ring increases, the absolute deviation in millimetres from the nominal diameter also increases. It is observed however that the relative deviation in percentage from the nominal inside diameter decreases by a small margin from -0.68% to -0.5%. This suggests that setting a percentage offset from the nominal diameter specified in CAD, is a suitable method of correcting the deviation. Figure 61 shows that a relative percentage offset to the diameter can also be applied to improve circularity. If the shape causing the change in circularity is also known, then a relative percentage change to the shape can be applied. Figure 62 and Figure 63 below show circularity plots from a co-ordinate measuring machine, providing the regions of deviation across its circumference. A new circumference in CAD can be created using the relative offset and applied in a similar shape as Figure 62.

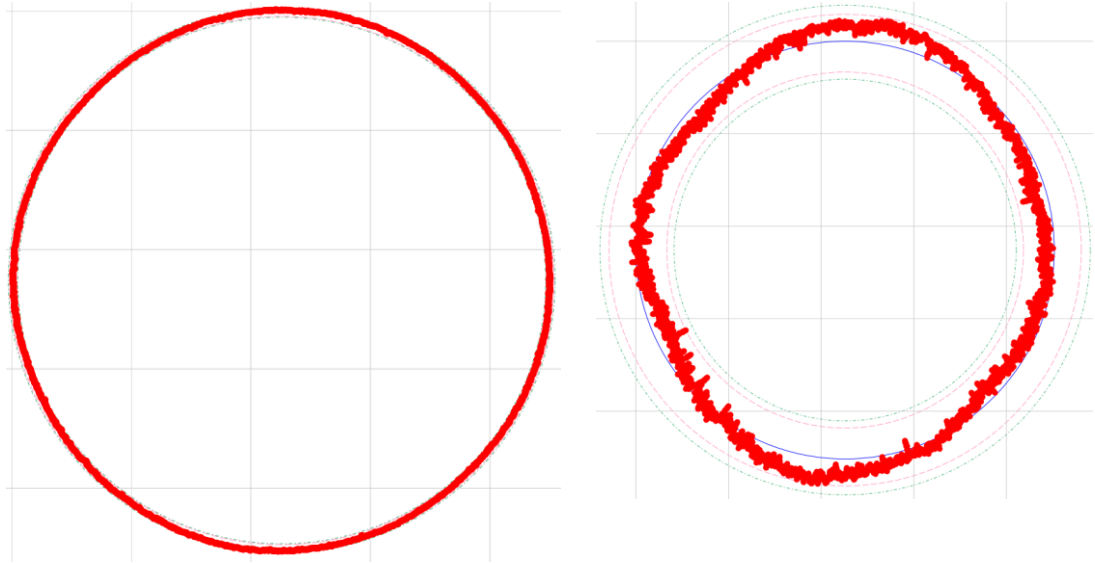


Figure 62. Plot showing Ti64Al circularity for the largest diameter ring 10 inside measurement with 10X magnification, and 100X magnification, respectively.

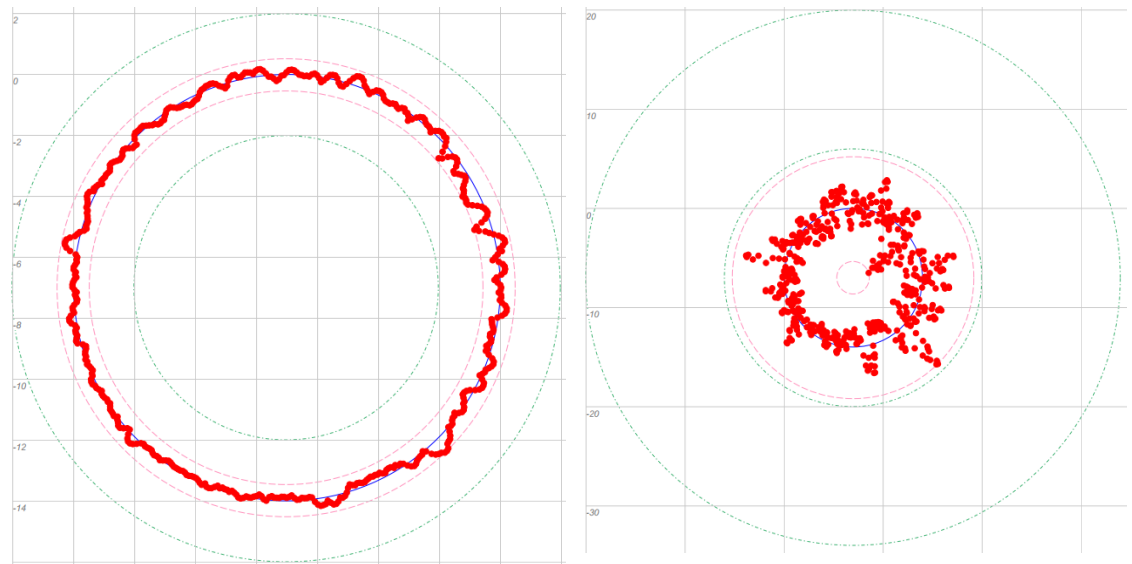


Figure 63. Plot showing Ti64Al circularity for ring 1 inside measurement with 10X magnification, and 100X magnification, respectively.

Plastic Fused Deposition Modelling

To benchmark the diameter and circularity using FDM, the Ultimaker 3 will print in PLA. PLA has been chosen as it exhibits the best print quality out of all FDM materials [147]. Compared to the benchmark using in LPBF, only 8 rings could be printed due to print bed size limitations.

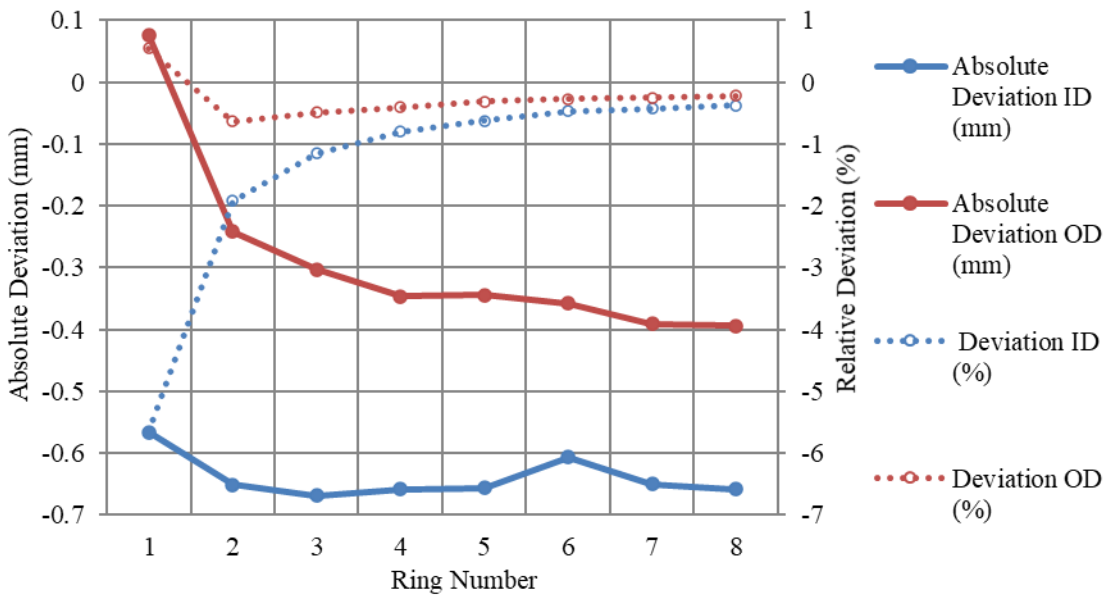


Figure 64. Graph showing PLA deviation from nominal for each ring and the percentage difference compared to its nominal size. Printed on a Ultimaker 3.

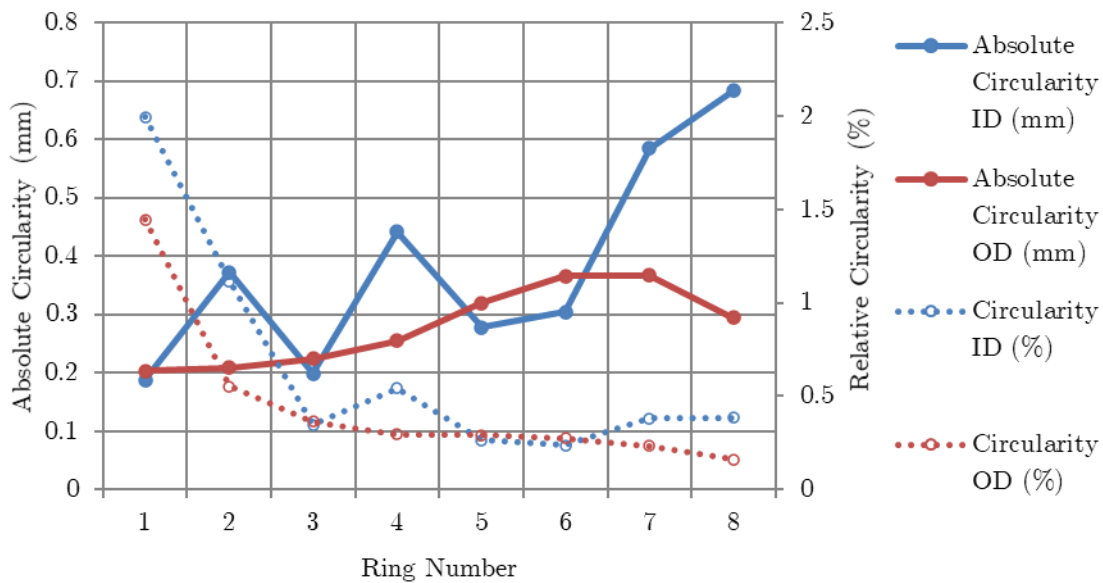


Figure 65. Graph showing PLA circularity for each ring, and as a percentage to its nominal size. Printed on a Ultimaker 3.

It is observed by looking at Figure 64 that there is more deviation on the inside compared to the outside diameter. It can be seen that the inside diameter displays a consistent absolute deviation of between -0.65 and -0.68mm with the exception of rings 1 and 6. To produce a nominal result, the data suggests that an average offset of approximately 0.655mm could be applied to the inside diameter of all ring sizes. For the outside diameter, using the relative percentage change would be more appropriate because the

absolute deviation changes with the diameter. The circularity graph in Figure 65 shows that circularity decreases with increasing diameter. This could be offset with a relative percentage change to the nominal shape in key regions shown in the circularity plot in Figure 66.

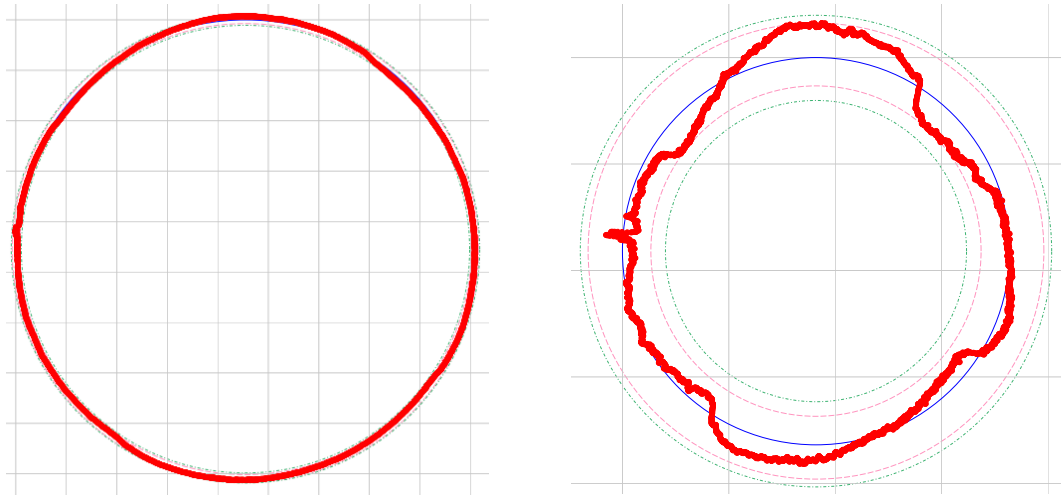


Figure 66. Plot showing PLA circularity for the largest diameter ring (number 8) inside measurement with 10X magnification, and 100X magnification, respectively.

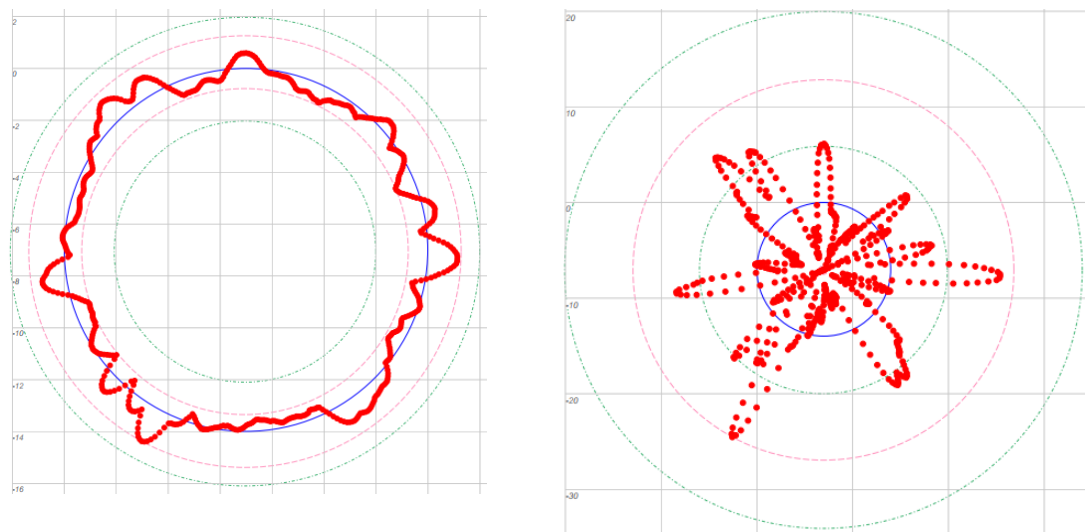


Figure 67. Plot showing PLA circularity for the smallest diameter ring (number 1) inside measurement with 10X magnification, and 100X magnification, respectively.

Polymer-Fibre Composite Fused Deposition Modelling.

To benchmark the diameter and circularity using Plastic-Fibre Composite FDM, the Markforged will print in Onyx with a continuous carbon fibre laid concentrically in the centre of each ring, per layer, with a separate nozzle. The software will automatically decide how many continuous strands to place based on its algorithm to determine to optimum placement. Onyx is a nylon plastic with short-chopped carbon fibre mixed in. Compared to previous benchmarks, only 5 rings could be printed due to print bed size limitations.

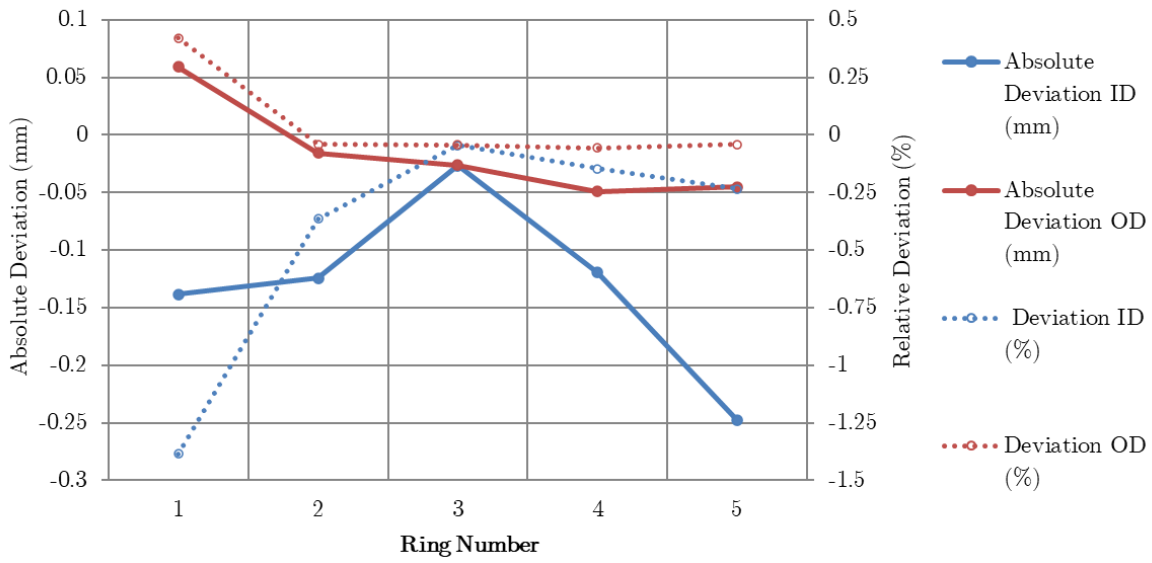


Figure 68. Graph showing Onyx +CF deviation from nominal for each ring and the percentage difference compared to its nominal size.

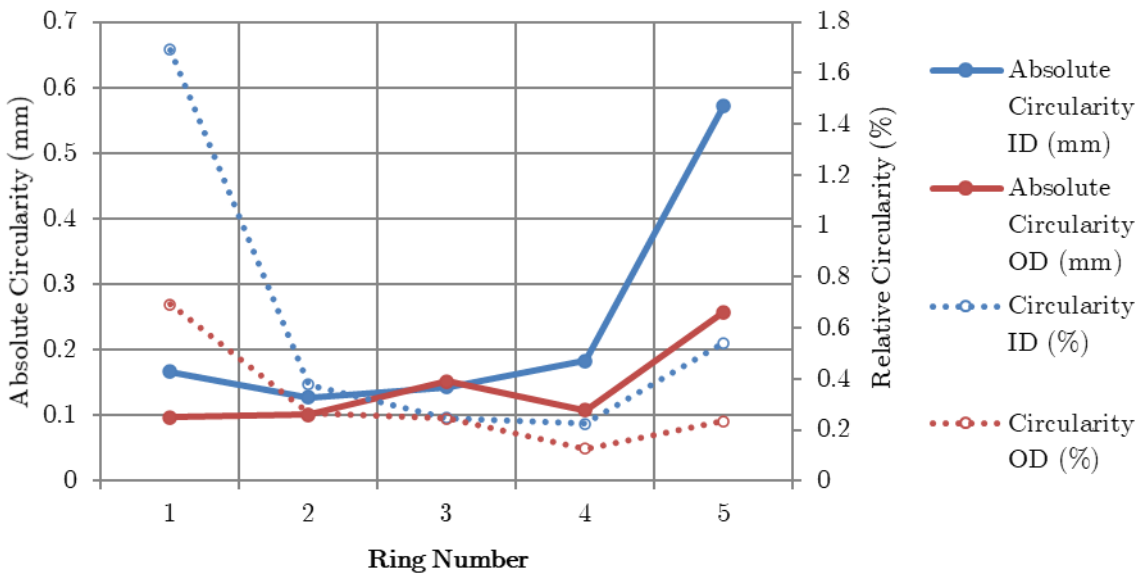


Figure 69. Graph showing Onyx + CF circularity for each ring, and as a percentage to its nominal size.

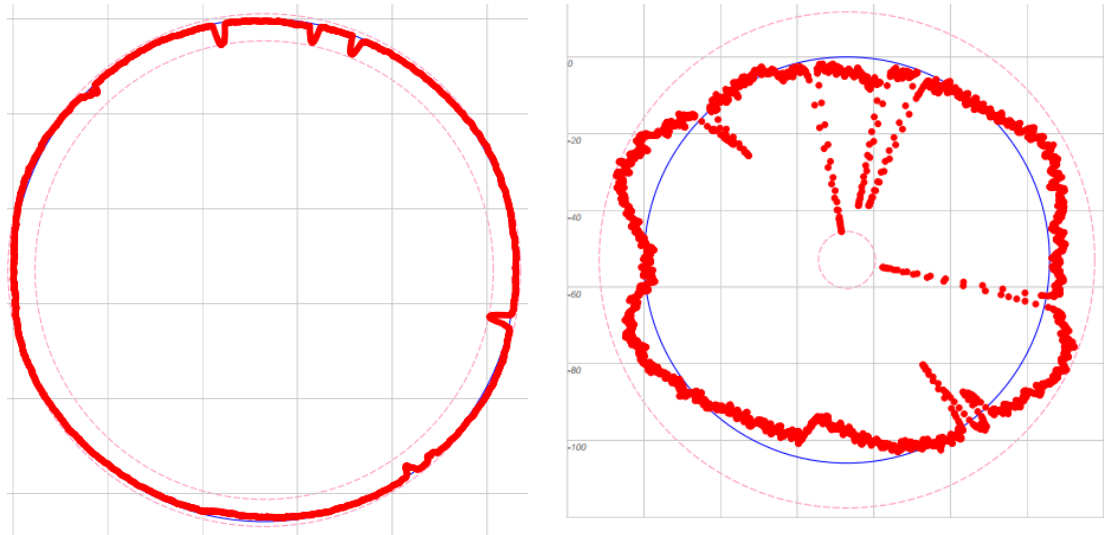


Figure 70. Plot showing Onyx + CF circularity for the largest diameter ring (number 5) inside measurement with 10X magnification, and 100X magnification, respectively.

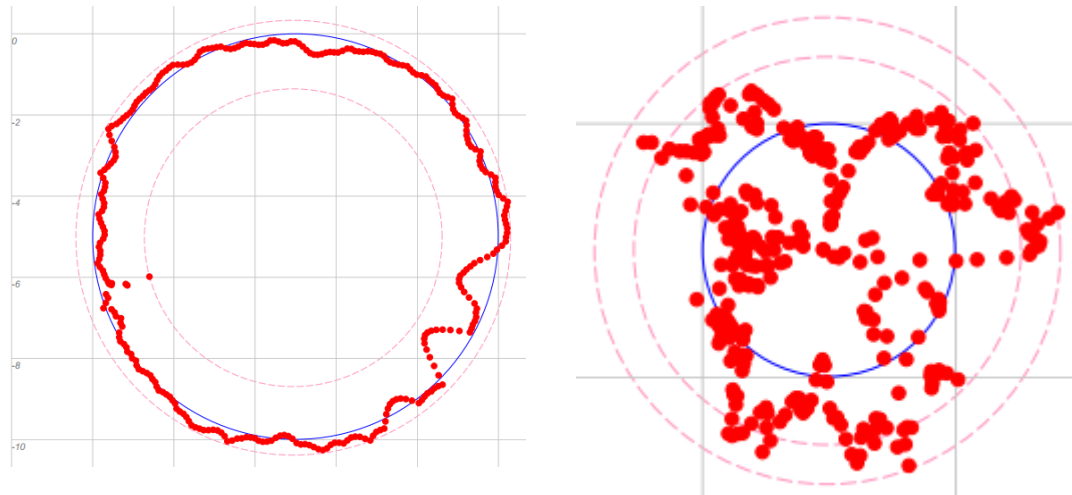


Figure 71. Plot showing Onyx + CF circularity for the smallest diameter ring (number 1) inside measurement with 10X magnification, and 100X magnification, respectively.

Concentricity issues on Figure 71 are shown to be the cause of printing issues on Figure 72. These problems are poor print optimisation caused by nozzle bleed at the start and stop of each layer. Figure 69 shows a higher circularity for the inside diameter of ring 5 which is caused by these defects.

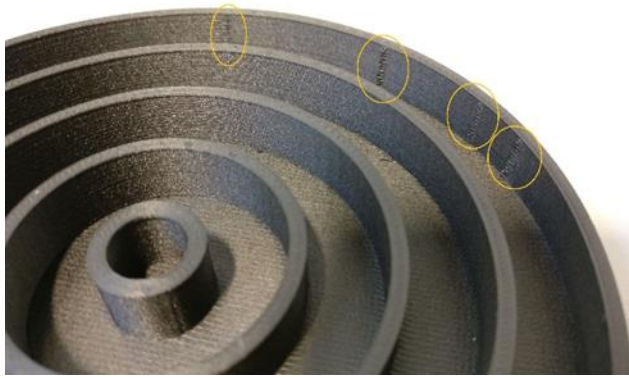


Figure 72. Onyx concentricity benchmark showing artefacts on ring five circled in yellow.

Analysis of the hollow cylinders diameter and circularity results

Plotting absolute deviation in diameter for the three materials against one another shows the difference in behaviour as the diameters increase. With the exception of ring 1, all diameters produce a negative deviation, meaning the diameter is smaller than intended. Onyx appears to have the closest diameters to nominal, but with the smaller print bed it is unable to print the larger diameter rings. Ti64Al is similar to PLA for the first few rings but can be seen to increase deviation as diameter increases whereas PLA and Onyx remain a set deviation from nominal regardless of diameter. Ti64Al maintains a window of between -0.7% to -0.4% of the nominal diameter for rings 2-10. For PLA it maintains a window of between -1.1% to -0.2% for rings 3-10. Analysing the increase in relative deviation for rings 1-3 in both materials shows that there is a minimum geometric deviation that exists independent of diameter. This shows that to produce a more accurate part with less deviation, increasing the diameter by the relative deviation percentage can produce a more accurate part. It is noticed that PLA experiences a greater difference between inside and outside diameter deviation indicating the wall thickness needs to be reduced by approximately 300 μ m when at 2mm.

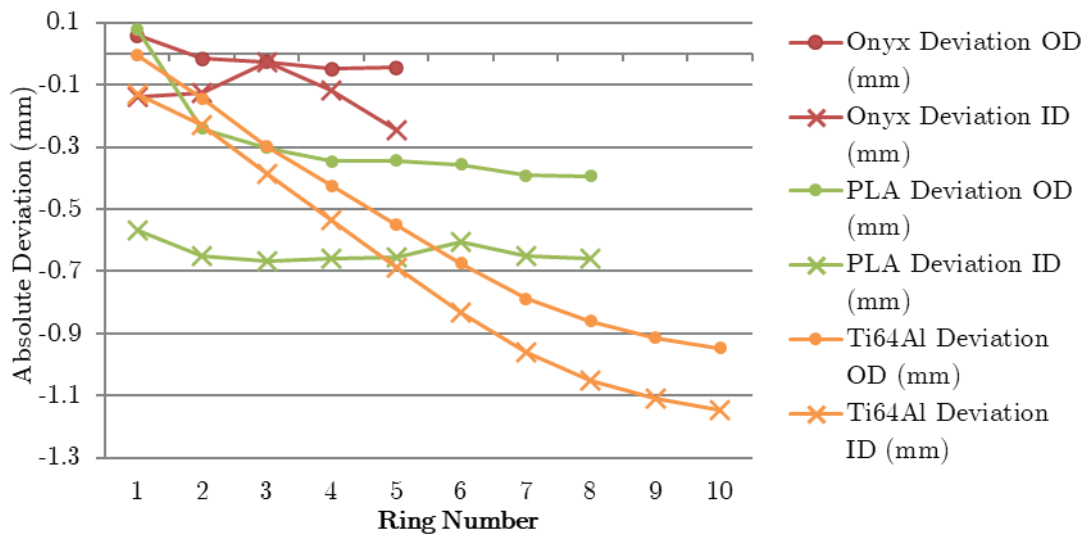


Figure 73. Comparison in diameter deviation between Ti64Al, PLA, and Onyx, printed on the AM400, Ultimaker 3, and Markforged Desktop Two respectively.

Similar results can be seen in Figure 74 for circularity. Looking at the plots for circularity, it can be seen that for the larger ring sizes in both PLA and Ti64Al there is a change in circularity whereby the extremity is larger in magnitude at the top and bottom, and second larger in magnitude at the left and right hand sides. This is only noticeable on the larger diameters and is present in both plastic and metal process types. This could be down to residual stresses in the material which creates a bending moment upon cooling. This is dependent on the thermal expansion co-efficient of the material and its scanning strategy. It has been shown that a higher CTE material has increased residual stress [140].

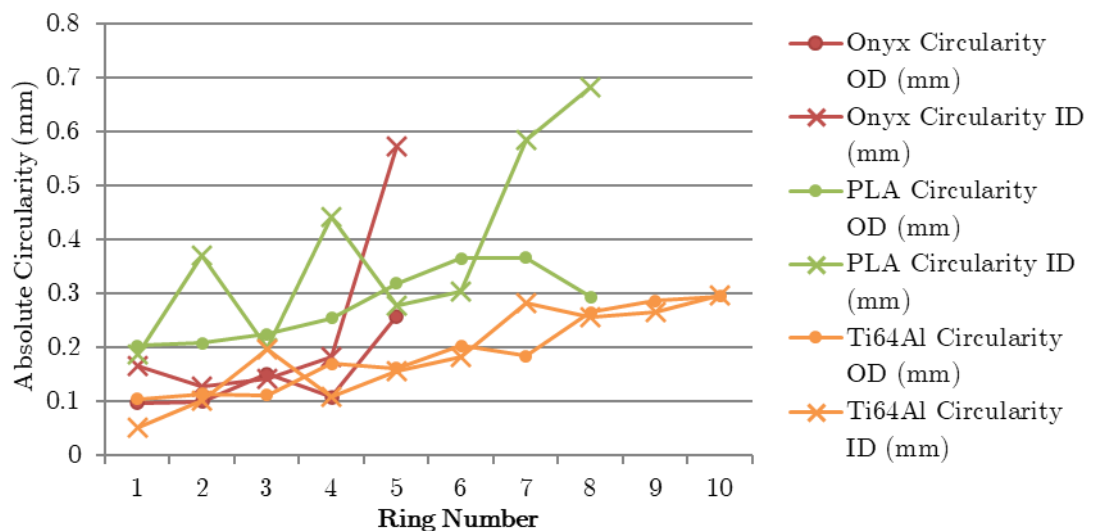


Figure 74. Comparison in circularity deviation between Ti64Al, PLA, and Onyx, printed on the AM400, Ultimaker 3, and Desktop Two respectively.

In literature an 85mm diameter outside cylinder was printed using LPBF to print parts in 316L. The cylinder had a circularity of between $95\mu\text{m}$ and $56\mu\text{m}$ depending on the repeat measured [138]. In the current work, ring 4 has a similar outside diameter to the literature of 84mm, and a circularity of $115\mu\text{m}$. With only a single diameter in literature, it is not possible to attain if the behaviour of increasing absolute circularity with increasing diameter for LPBF parts is indicative of the process as a whole.

3.4.9 Conclusions on the geometric tolerances of additive manufacturing

In conclusion, due to the tight tolerances required by the optical industry to ensure lens alignment, and accurate placement between lenses, additive manufacturing may not be suitable without further post-processes such as CNC milling to get the dimensions within tolerance. The requirements stated that Qioptiq would require a lens decentre of $\pm 0.02\text{mm}$ for a 50mm lens would be out of tolerance upon manufacture for all materials and all AM processes. Onyx on the Markforged machine would be closest to nominal at -0.11mm diameter deviation and $+0.15\text{mm}$ concentricity deviation for ring 2. Offsets can be made to the shape by inspecting the form of the component and adjusting by a percentage of the diameters size.

Recommendations can be made for the adjustment of nominal dimensions according to the benchmarks completed. These recommendations only stand true for the specific combination of; the machine manufacturer and model, the material type, and the orientation of the benchmark parts to the build direction and recoater. Literature shows that any changes to these three variables can produce different results [131]–[138]. The recommendations to be made using the configuration in the present work are the following.

- Rectangular slot resolution benchmarks recommend a fixed offset to the nominal gap for 316L, Ti64Al, PLA, and Onyx, of $+215\mu\text{m}$, $+110\mu\text{m}$, $+170\mu\text{m}$, and $+130\mu\text{m}$, respectively. Nylon requires a percentage offset of 15% and a 0.2mm fixed offset to every gap. Variation between gaps is higher for nylon than other materials.
- Cylinder slot resolution benchmarks recommends fixed offsets to nominal gap dimensions for 316L, Ti64Al, PLA, Nylon, and Onyx, of $+150\mu\text{m}$, $+110\mu\text{m}$, $+20\mu\text{m}$, $-60\mu\text{m}$, and $-420\mu\text{m}$, respectively.
- Wall thickness resolution benchmarks recommends fixed nominal offsets for 316L, Ti64Al, PLA, Nylon, and Onyx, of $-400\mu\text{m}$, $-210\mu\text{m}$, $-70\mu\text{m}$, $-40\mu\text{m}$, and $-85\mu\text{m}$, respectively.
- Hole diameter benchmarks recommend fixed nominal offsets for 316L, PLA, and Onyx of $+310\mu\text{m}$, $+550\mu\text{m}$, and $+200\mu\text{m}$, respectively. Nylon is difficult to make

a fixed recommendation for because the deviation has a wide range between +210 μ m and -500 μ m.

- Diameter deviations for a series of rings show that for Ti64Al an offset of 0.5% for the outside and 0.6% for the inside would be appropriate. Results for PLA show a fixed offset of 0.35mm for the inside and 0.06mm for the outside diameters. Onyx + CF is close to nominal, and only requires 0.1mm for the inside and 0.025mm for the outside diameters. Build defects cause by the fibre inclusions added a 0.4mm deviation on the last ring.
- Circularity plots for the form of the ring show that the largest rings are 'stretched' most likely caused by residual stresses across all materials. It would be recommended to heat treat all parts after removal.

4 Experimental Methods

4.1 Summary

To test the thermal expansion rates of a material there are several solutions available. To understand the linear thermal expansion rate of a sample, a commercially available Dilatometer can be used. For measuring the thermal expansion rate of a larger structure, a custom designed test rig is required. This section will explore the different approaches to measuring thermal expansion. It will also outline the equipment used to determine density, hardness, and tensile properties. The experimental methodology of orthogonal arrays will be described.

4.2 Dilatometer

The dilatometer is a commercially available and very accurate method of measuring CTE. It will be the main method for measuring the thermal expansion of a range of materials, from metals to plastics. The NETZSCH 402 Supreme pushrod cryogenic dilatometer uses liquid nitrogen to get measurements between -180 °C and 2000°C. One limitation is the sample size of only 25mm x 10mm, therefore this method is best suited to getting CTE results for the solid material constituents that will make up some of the CTE tailoring structures.

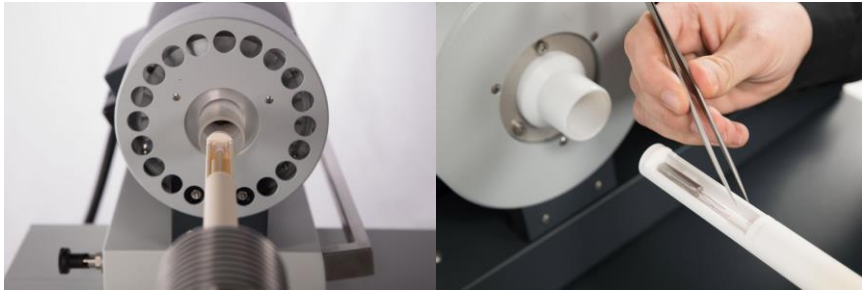


Figure 75. Netzsch 402 push-rod dilatometer photograph [148].

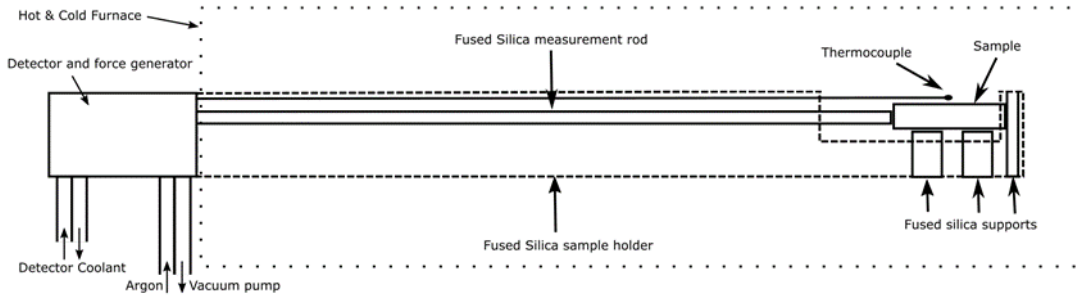


Figure 76. Schematic of the operation of a push-rod dilatometer.

Each test program must conform to the standard ASTM E228-17 which specifies the operating conditions for a push-rod dilatometer. The equipment outputs the change in length over the original length as a function of time or temperature. To analyse this data, two types of curves can be fitted. These are the Physical Alpha curves, and the Technical Alpha curves.

The Physical Alpha is calculated using equation 4.1.

$$\alpha_1(T) = \frac{1}{l_0} \left(\frac{\partial l}{\partial T} \right)_p \quad (4.1)$$

It is defined as the slope of the relative length-change curve at the respective temperature. Thus it corresponds to the first derivative of the dL/L_0 curve according to the temperature.

The Technical Alpha is calculated using equation 4.2.

$$\alpha(T_1, T_{ref.}) = \frac{\frac{dL}{l_0}(T_1) - \frac{dL}{l_0}(T_{ref.})}{T_1 - T_{ref.}} \quad (4.2)$$

l_0 = sample length and ambient temperature.

T_1 = upper temperature limit; $T_{ref.}$ = lower temperature limit.

It is used to calculate a CTE over a specified temperature range. Technical Alpha values are found in most materials data specification sheets. It can also be plotted, where $T_{ref.}$ is the lower temperature, thus a curve of this type is not accurate for any value below $T_{ref.}$.

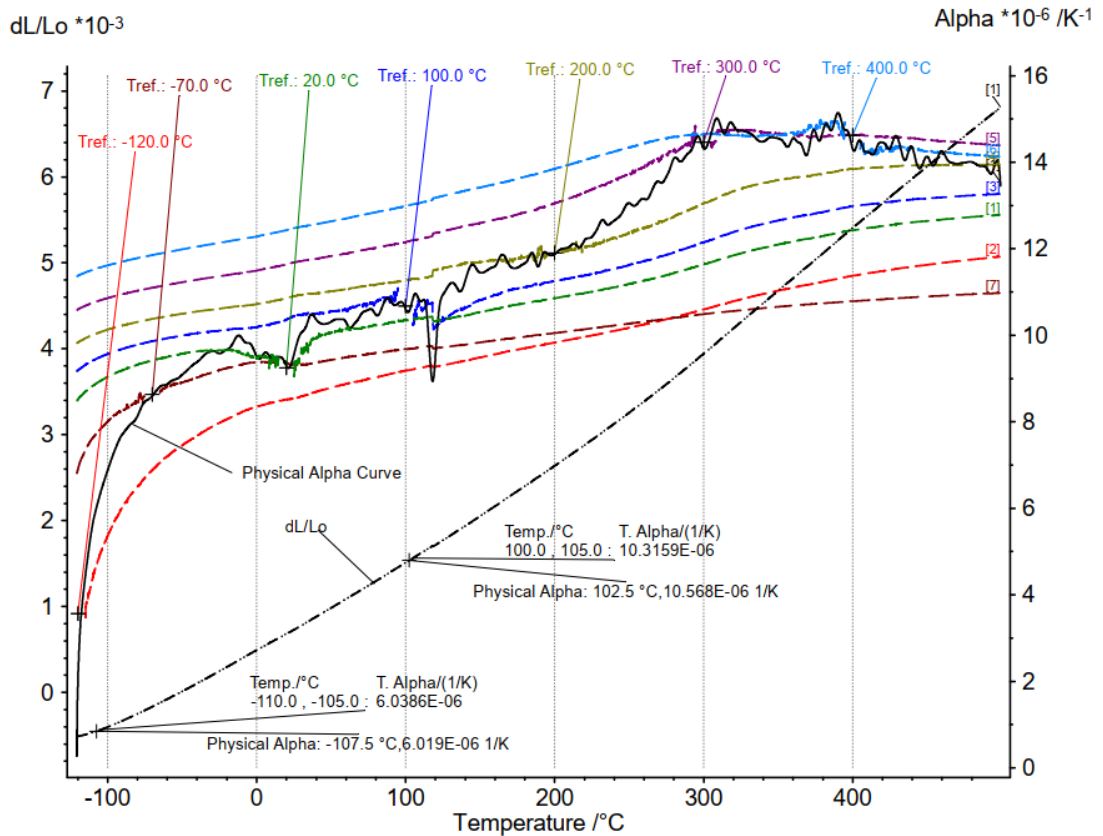


Figure 77. Graph comparing different methods of dilatometer thermal expansion analysis; physical and technical alpha curves. Physical Alpha is smoothed at a level 8.

Figure 77 shows how the Technical Alpha curves can vary depending on the Tref value. This method of CTE analysis will not be used. Instead the physical alpha curve will be used, and technical alpha values will be determined for a specified range. The temperature range must be narrow enough to keep the resolution of the physical alpha curve between two temperatures, but not so narrow that it picks up noise. The technical alpha values will be affected by the amount of smoothing applied. The types on smoothing available on the Netzsch proteus software are defined with levels 1-8, and A-H. Levels 1-8 apply a smoothing factor by reducing the height of all peaks. Smoothing factors A-H apply a different technique whereby the peaks are flattened by averaging the datapoints over an increasingly wider range.

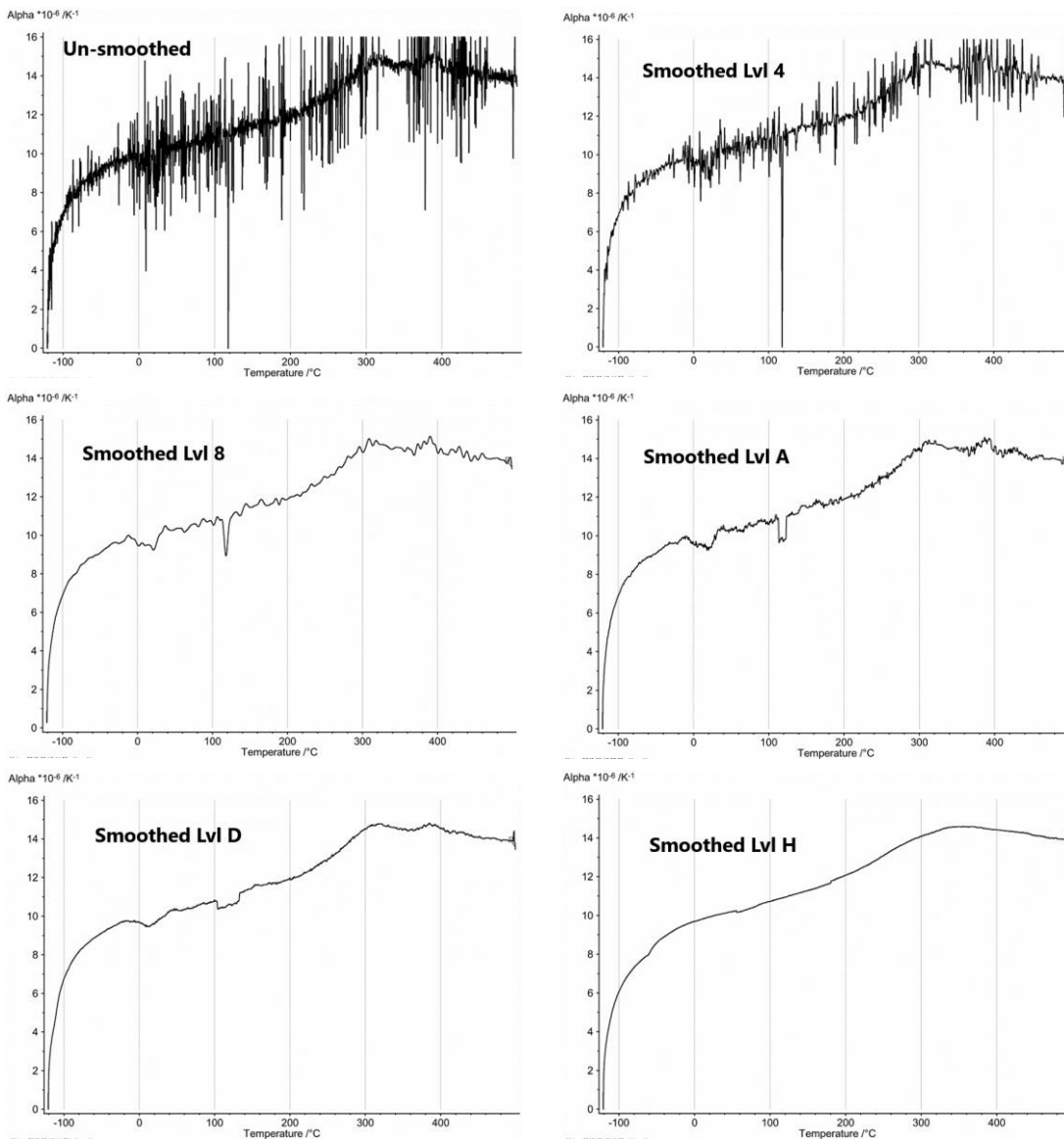


Figure 78. Graphs showing Physical Alpha smoothing levels from 1-8 and A-H in the Netzsch proteus software. Material used is AlSi10Mg from -120°C to 480°C.

To get an accurate result, a correction measurement must be performed. A correction measurement is necessary as the measured signal is the superposition of the sample and measurement systems expansion. The measured length change includes both the sample holder's thermal expansion, and the thermal expansion of the sample itself. The correction run measures the thermal expansion of a calibration standard material such as Al_2O_3 . The measured expansion curve is then compared against the expected expansion data for Al_2O_3 , and any deviations from the expected are subtracted from all future sample measurements. To include the correction curve in the result, an equation is outlined according to DIN-51045-1.

$$\begin{aligned}
dL_C(t) = & dL_{Sample}(t) - Offset_M(T_{Ref.}) \\
& - \left\{ dL_{Correction}(t) - Offset_{CAL.}(T_{Ref.}) \right. \\
& - [L_{0,Correction,20^\circ C} + Offset_{SL,CAL.}(T_{Ref.})] \\
& * \left. \left[\frac{\frac{dL}{L_{0 Std.,20^\circ C}}(T) - \frac{dL}{L_{0 Std.,20^\circ C}}(T_{Ref.})}{1 + \frac{dL}{L_{0 Std.,20^\circ C}}(T_{Ref.})} \right] \right\} \\
& + \{ [L_{0,Sample,20^\circ C} + Offset_{SL}(T_{Ref.})] \\
& - [L_{0,Correction,20^\circ C} + Offset_{SL,CAL.}(T_{Ref.})] \} \\
& * \left\{ \frac{\frac{dL}{L_{0 Sh,20^\circ C}}(T) - \frac{dL}{L_{0 Sh,20^\circ C}}(T_{Ref.})}{1 + \frac{dL}{L_{0 Sh,20^\circ C}}(T_{Ref.})} \right\}
\end{aligned} \tag{4.3}$$

Indexes; *C* - Corrected. *CAL* - Calibration, Calibration standard. *M* - Measured. *Ref* - Reference. *Sh* - Sample holder. *SL* - Sample length. *t* - measuring time of the temperature program.

$dL_C(t)$ - Calibration corrected expansion values at time *t* [s].

$dL_{Sample}(t)$ - uncorrected expansion signal of the sample [μm].

$Offset_M(T_{Ref.})$ - dL_{Offset} of the expansion of the sample [μm].

$dL_{Correction}(t)$ - Uncorrected expansion at time *t* of the calibration standard [μm].

$Offset_{CAL.}(T_{Ref.})$ - Offset of the expansion of the calibration standard at temperature $T_{Ref.}$ [μm].

$L_{0,Correction,20^\circ C}$ Length of the calibration standard at 20°C [mm].

$L_{0,Sample,20^\circ C}$ Sample length at 20°C [mm].

$Offset_{SL}(T_{Ref.})$ Offset applied on sample length [mm].

Correction for $T_{Ref.} \neq 20^\circ C$ or shrinkage of sample [μm].

$\frac{dL}{L_{0 Sh,20^\circ C}}(T)$ relative thermal expansion of the sample holder material with reference temperature 20°C.

$\frac{dL}{L_{0 Sh,20^\circ C}}(T_{Ref.})$ relative thermal expansion table of the sample holder material with the reference temperature 20°C.

To conform, the program must use a heating rate of 5°C/min, and apply a push rod force of 5cN to the sample. To assess the accuracy of the correction run and determine any error from reading to reading, the correction material Al_2O_3 is measured as a sample, in

combination with the established correction. The data is then compared against the expected dL/L_0 value to produce Table 17.

Al_2O_3 Literature		Al_2O_3 Results		Comparison	
Temperature (°C)	$\left(\frac{dL}{L_0} m^{-3}\right)$	Temperature (°C)	$\left(\frac{dL}{L_0} m^{-3}\right)$	Temperature Difference	$\left(\frac{dL}{L_0} m^{-3}\right)$ Difference
-100	-0.46342	-100.048	-0.45704	-0.05%	1.39%
-75	-0.3935	-75.049	-0.39057	-0.07%	0.75%
-50	-0.30781	-50.002	-0.30598	0.00%	0.60%
-25	-0.20631	-24.966	-0.20609	0.14%	0.11%
0	-0.0924	-0.035	-0.092651	-	-0.27%
25	0.0337	25.001	0.035091	0.00%	-4.04%
50	0.1693	50.041	0.17101	-0.08%	-1.00%
75	0.31395	74.977	0.31132	0.03%	0.84%
100	0.46645	100.021	0.4632	-0.02%	0.70%
125	0.62701	124.958	0.61793	0.03%	1.46%
150	0.79368	149.86501	0.77856	0.09%	1.92%

Table 17. Table showing the percentage difference in thermal expansion of the measured Al_2O_3 against reference values.

It can be seen that the difference between reading and expected reading is within the NETZSCH acceptable range of $\pm 5\%$ from the company's service team.

To determine the most accurate test program to run on the dilatometer, a study has been conducted measuring the thermal expansion of the low expansion metal invar. A lower expansion requires a program exhibiting less noise, since it will have a larger proportional effect. The constituents on the alloy are varied to increase the CTE. This provides samples for analysis on the effect of consistency between the various thermal expansion amounts. More information on this manufacturing process can be found in chapter 8.5.1. The first test program conducted went from -120°C to 150°C at 5k/min heating rate. This satisfies the requirement by Qioptiq for thermal solutions between -40°C and 70°C .

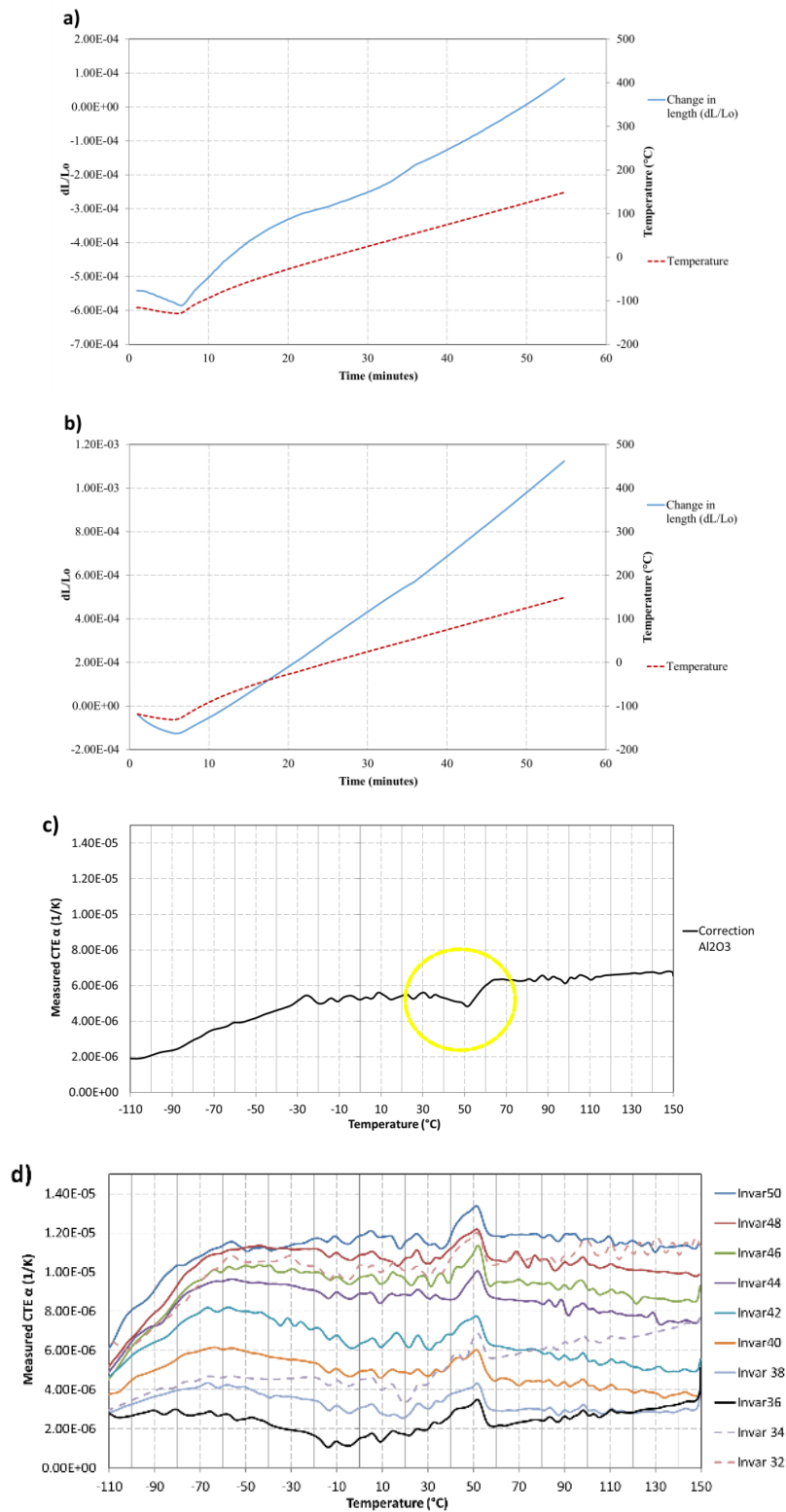


Figure 79. First dilatometer test run and analysis for a set of various FeNi alloys. a) Invar 36 temperature and change in length with correction applied, b) Al₂O₃ correction; temperature and change in length, c) Al₂O₃ correction; physical alpha curve with highlighted anomaly, d) the physical alpha curves for all invar variants. Physical alpha curves in graphs c and d have a smoothing level of 8.

It can be seen that at about 50°C there is a sudden increase in CTE on the physical alpha curves for all invar measurements shown in graph C. Analysis of the correction run in graph B shows an anomaly highlighted in yellow. This has applied an offset in the results in graph C. To obtain better results, the correction run will need to be run again until enough corrections have been tested to determine if the anomaly highlighted, repeatedly exist. If the anomaly highlighted is in every test, then the data is characteristic of the machine's behaviour, which needs to be accounted for in every sample. If the anomaly is not present in every correction run, it can be assumed the it is just an issue with the Al_2O_3 sample moving during testing, and the better correction run should be chosen.

Further analysis of graph A shows that the temperature does not maintain a linear increase overtime until approximately 20 minutes have passed. A linear increase is important to achieve, since the temperature reading is not of the sample itself but of the atmosphere alongside it. This is because of the location of the thermocouple, measuring the air temperature close to its vicinity. The assumption should be made that the thermocouple is not the exactly the same temperature as the sample. This is not an issue if both sample and the surrounding air increase at the specified rate of $5K/min$, because the CTE is calculated by the sample expansion at each temperature reading. It can be assumed that all readings below approximately $-50^\circ C$ are inaccurate.

To attempt to correct the issue, another test program was made whereby the furnace is held at $-120^\circ C$ for 30 mins, followed by heating at $5K/min$ up to $200^\circ C$. This will remove the overshoot exhibited in graph A where the temperature does not increase until 8 minutes has passed. An isotropic phase ensures both sample and furnace are at $-120^\circ C$ before increasing temperature. A suitable correction run with no anomalies was chosen from three correction samples test runs.

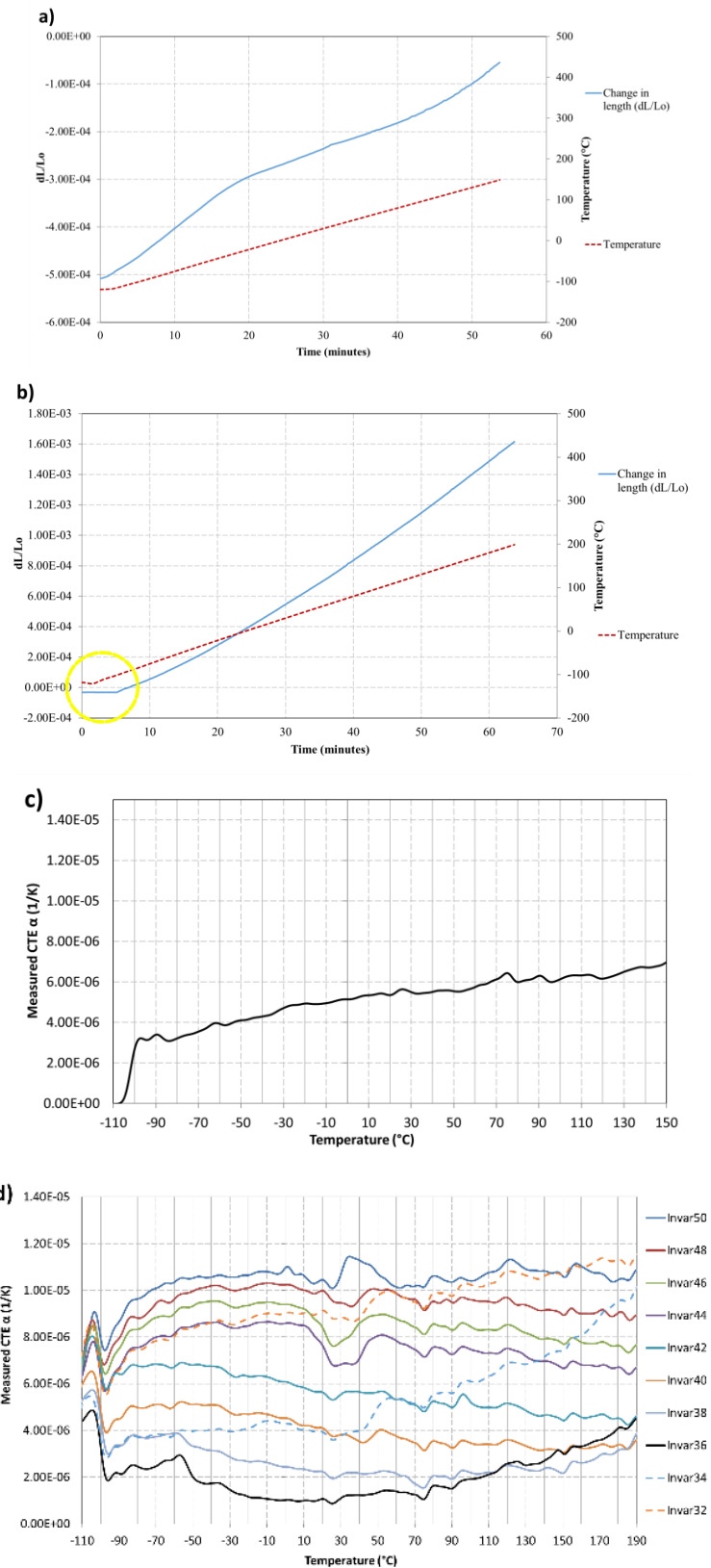


Figure 80. Second dilatometer test run and analysis for a set of various FeNi alloys. a) Invar 36 temperature against change in length with correction applied, b) Al_2O_3 correction; temperature and change in length c) Al_2O_3 correction; physical alpha curve, d) and the physical alpha curves for all invar variants. Alpha curves on graphs c and d have a smoothing level of 8.

It can be seen that the isotropic hold for 30 mins at -120°C has caused a fluctuation for all invar samples below -80°C shown on Figure 80d. This has been caused by a slower response from the sample to the increasing temperature surrounding it, as can be seen highlighted in Figure 80b. However, comparing the two graphs in Figure 79d and Figure 80d, it is clear that the isotropic stage for 30mins at -120°C has kept the consistent trend from max temperature to -70°C rather than from max temperature till 0°C as shown before. The anomaly shown previously in Figure 79c has been removed in the new data shown in Figure 80c and Figure 80d.

It is apparent that at the start of the cooling cycle, the discrepancy between the sample temperature and the ambient temperature will not be removed without a period of temperature change. This ensures that the rate of temperature change is the same in both sample and the surrounding air regardless of the specific values. To achieve a period of equalisation in the temperature rate of change, a test program will be used where the testing starts at a high temperature, and cools at $5\text{K}/\text{min}$ down to -120°C . Any inaccuracies should occur in the hotter region leaving the cryogenic region to be unaffected by inaccuracies at the start of the program. To compare the differences between measuring from low to high temperature and high to low temperature, the program will start reading at -120°C rising to 450°C where a 1hour isotropic phase will begin, before being cooled back down to -120°C again. An isotropic phase at -120°C has not been used because of only marginal improvement in the result, and the large amount of liquid nitrogen used of approximately 40 litres over the cycle, compared to 20 litres without it. In Figure 81 it can be seen that there are discrepancies in the heating and cooling curves for both temperature and change in length.

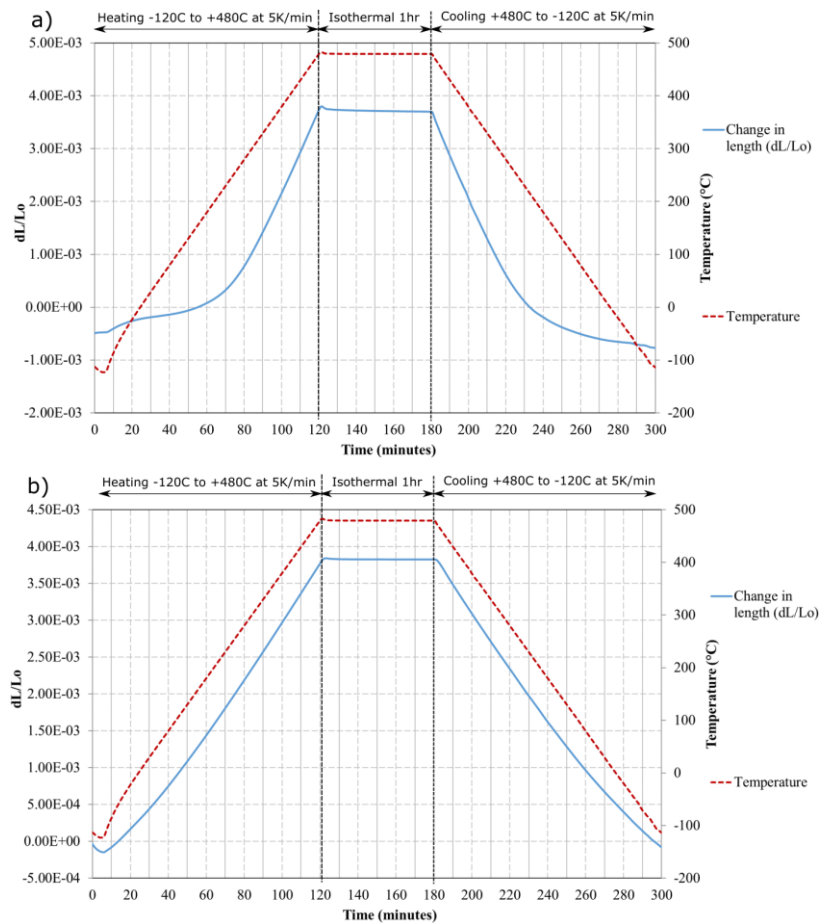


Figure 81. Final dilatometer test program showing change in length and temperature over time, for a) invar 36 with correction applied, and b) the Al₂O₃ correction run.

To determine the consistency of the temperature, both hot and cold cycles have been plotted against the target 5k/min.

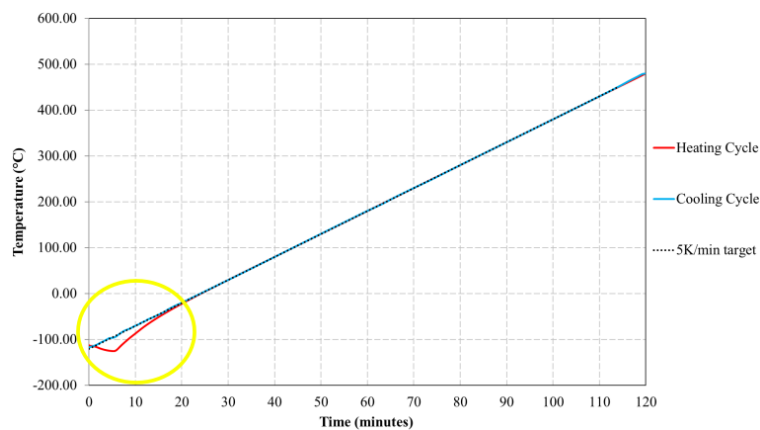


Figure 82. Temperature profile over time for the entire heating and cooling cycle, compared with the target 5k/min. Deviation is highlighted.

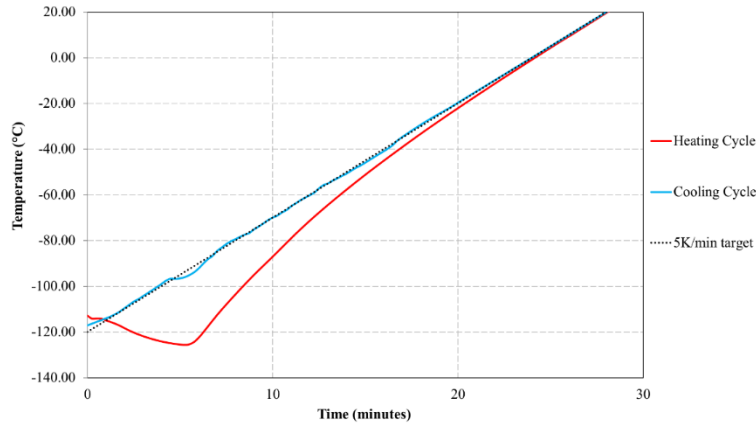


Figure 83. Temperature profile over time for the heating and cooling cycle from ambient to cryogenic temperatures. Target $5k/min$ compared.

It can be seen by analysing the temperature curves in Figure 83 it can be seen that the deviation on the heating cycle around sub ambient temperatures, creates a curve that does not conform to $5k/min$ target. There are no guidelines in ASTM E228-17 for the development of an accurate cryogenic measurement program, only overall guidelines defining the required outcome. The standard specifies that ‘the indicated temperature of the specimen shall not vary by more than $2^{\circ}C$. The cooling cycle does conform to within $2^{\circ}C$ of the $5k/min$ cooling rate, although with fluctuations where it exceeds by $2.8^{\circ}C$ at approximately 5.25 minutes for 1 minute before returning to within $\pm 0.6^{\circ}C$ of the $5k/min$ target. This is the largest fluctuation at about $-90^{\circ}C$, but the program slows down the cooling to compensate and reduce overall deviation. Due to these small fluctuations, the cooling cycles physical alpha curve may need a different level of smoothing to the level 8 applied previously.

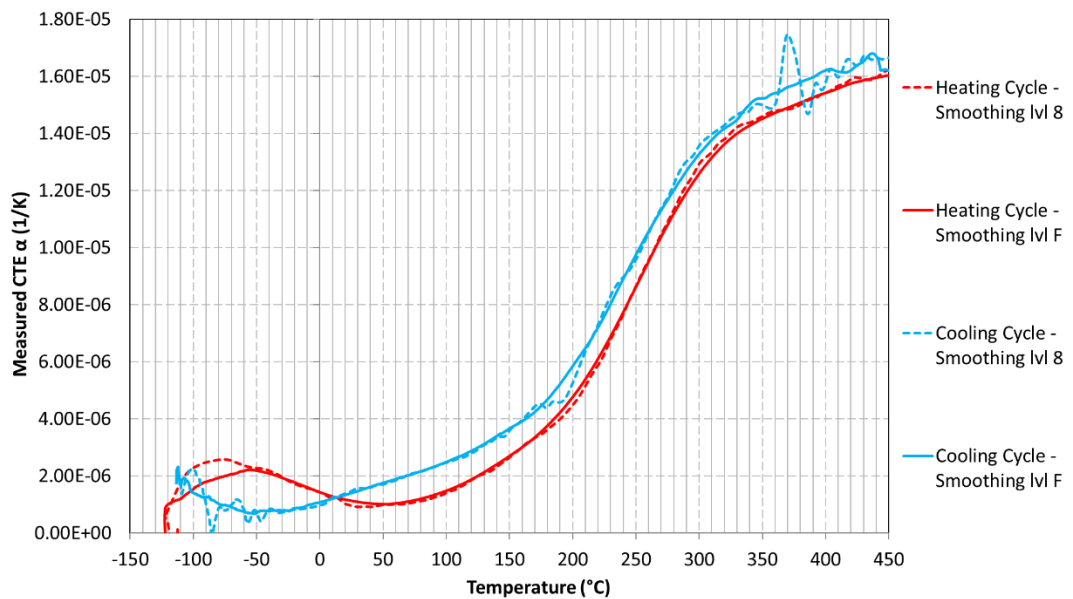


Figure 84. Dilatometer heating and cooling cycle showing physical alpha curves for invar 36 with level 8 and F smoothing.

By analysing the graph in Figure 84 it can be seen that a smoothing level of 8 applied to both heating and cooling cycles is adequate for the heating cycle, but not the cooling cycle. The smoothing level of F on the cooling cycle is able to take a best fit line through the cryogenic cycle, whereas for the heating cycle there were no fluctuations for a higher level of smoothing to be required. A level 8 on the heating cycle is sufficient to preserve the peak at the lower cryogenic temperatures.

Comparing dilatometer accuracy with literature using a DIL 805 A/D, shows that the heating and cooling curves of a specimen are different after an isothermal, and vary depending on pushrod materials. An alumina pushrod experiences a greater difference in change in length between heating and cooling cycles when compared with the silica pushrod [149]. The differences can be attributed to the different thermal conductivities between the two push-rod materials. At the beginning of isotropic heating phase, the starting temperature of the pushrod will be different to the temperature at the end of the isotropic heating phase. The variability can be attempted to be corrected by subtracting the differences using the DIN 51045 correction.

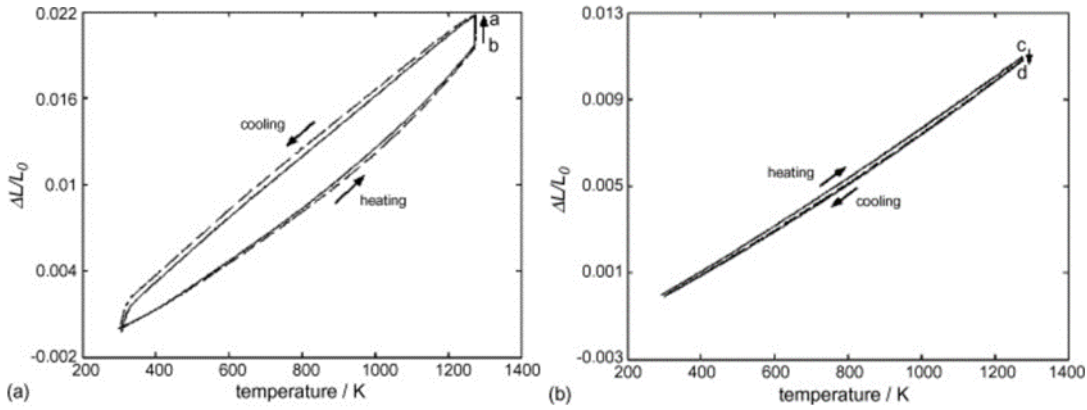


Figure 85. Measured length change as a function of temperature of a platinum reference specimen using a 20K/min rate interrupted by a 30min isothermal at 1273K for; a) alumina pushrods, b) fused silica pushrods. Measured with the DIL 805 A/D induction dilatometer from Texas Instruments [149].

Assessing the heating and cooling cycle for the Netzsch 402 CC induction heated and liquid nitrogen cooled cryogenic dilatometer shows a similar behaviour. The heating and cooling curves in Figure 86 show that some deviation maybe experienced between that two cycles.

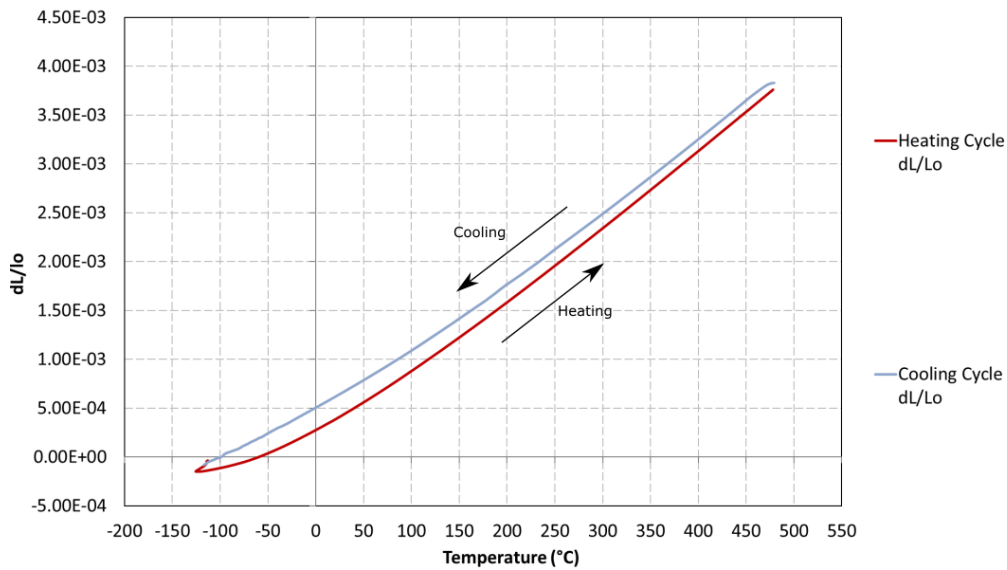


Figure 86. Measured length change as a function of temperature of Al_2O_3 specimen using a 5K/min rate interrupted by a 1hr isothermal at 480°C.

To conclude the study, it has been shown that the heating cycle is inaccurate due to the uncontrolled temperature as discussed earlier and should be ignored for cryogenic temperatures when a cooling cycle is able to provide better accuracy. For the cooling cycle, the increase in noise and smoothed CTE at temperatures less than -50°C leads to a questionable accuracy at this level. For the purposes of this thesis, it can be considered accurate enough to form a basis of comparison between one sample and another.

4.3 Density

The relative density of the component can be measured by obtaining the porosity. This has been achieved by optical porosity analysis, whereby the material is cross-sectioned, polished, and optical microscopy is performed. The Zeiss Smartzoom 5 was used with a 50-500x lens. The image is processed using ImageJ and the 'threshold', tool. This method will process the area dark in contrast as porosity and provide it as a percentage of the image. This method can provide a qualitative view of the distribution in location and size of porosity. Qualitative analysis of the size distributions can also be performed. The method has a level of human interaction when adjusting the threshold and therefore cannot be absolute in accuracy. Relative accuracy from one sample to the next depends on polishing quality such as scratches that will appear as porosity if not removed. Obtaining the density cannot be calculated as a percentage of the known material density, because the porosity may contain un-melted powder when manufactured with LPBF.

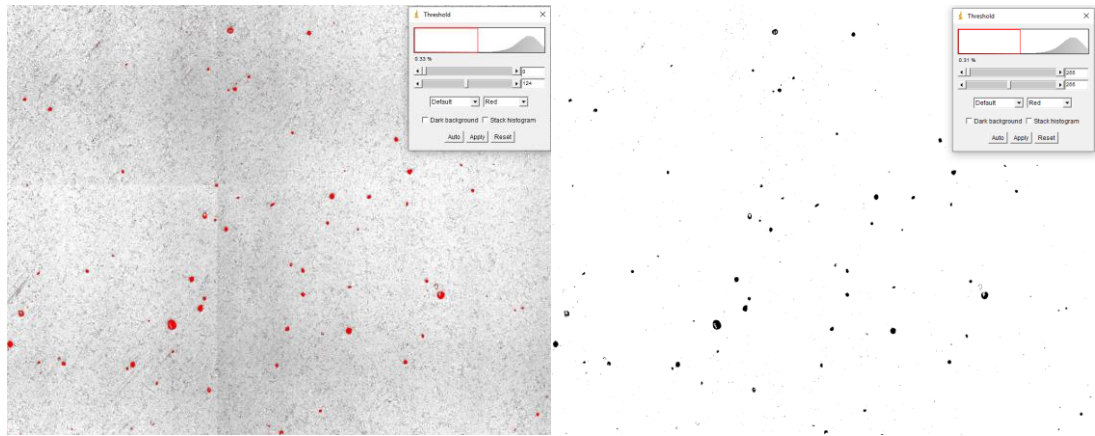


Figure 87. ImageJ threshold analysis.

Another method of obtaining density values relative to the known material density is to use Archimedes principles. The Attension tensiometer by Biolin Scientific works by measuring the sample mass before and after immersion in water. The sample is measured from a hook with the sample hanging with a piece of hydrophobic material.

$$\rho_{samp} = (\rho_w - ((T_w - T_a) * 0.00025)) \frac{M}{\Delta M} \quad (4.4)$$

Where ρ_w = water density, M = the initial sample mass, ΔM = the program output, T_w = water temperature. T_a = air temperature.

This method removes variables present in optical porosity analysis. The variables such as temperature and changes in water density due to surfactant do not significantly influence

the results. The type of fastening method used to attach the samples does affect the results and should be torn from the initial mass. Any knots tied must not be submerged.

4.4 Microhardness

The hardness of a material is the ability of the material to resist plastic deformation. To adjust the thermal expansion of a metal, the alloys constituents or manufacturing method will be adjusted. To understand the effect this has on mechanical properties, hardness values will be obtained. The Wilson VH3100 machine will be used to obtain the Vickers hardness of the materials tested. A diamond shape is indented into the surface of the material, and the length from one side to the other is measured. The load should be suitable to make a well-defined impression. The unit of hardness is known as the Vickers Pyramid Number (HV), and is determined by the load over the surface area of the indentation. It is expressed as; xxxHVyy, where xxx is the hardness number, and yy is the load used in *kgf*. A typical suitable force for most metallic alloys will range between 1-3 *kgf*. Brittle alloys will require less force to avoid cracking, whilst ductile alloys will require less force to achieve a suitable sized indent.

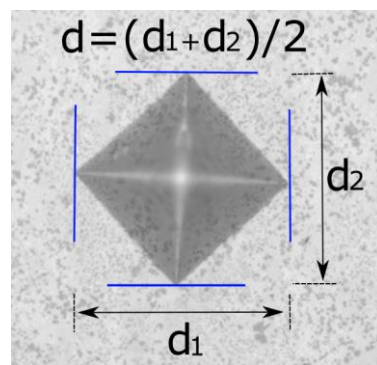


Figure 88. Vickers hardness indent showing where the measurements are taken.

The Wilson DiaMet automation software automatically calculates the HV in value in MPa using the following formula;

$$HV [kgf/mm^2] = 0.1891 \frac{F}{d^2} [N/mm^2] \quad (4.5)$$

4.5 Tensile

To supplement any hardness data, tensile data will also be gathered. To carry out the tensile testing, a Tinius Olsen H25KS 25KN tensile machine will be used, with an Epsilon extensometer with a gauge length of 16mm. Data output has been interpreted providing; tensile modulus, Ultimate Tensile Strength (UTS), and elongation till UTS, elongation till break.

4.6 Composition

The most frequently used method for determining composition is called energy-dispersive X-ray spectroscopy (EDS), which is performed on the Scanning Electron Microscope (SEM). It works by firing charged electrons at the sample and analysing the X-rays emitted from the sample. The x-rays emitted are characteristic of the atomic structure of the emitting element, so a determination can be made on the quantity of that element. A map scan can be produced which shows visually where the elements are located in the SEM image. The time taken for each reading depends on the resolution of the map required, or the number of single point quantitative data readings required. The EDS in this thesis has been conducted on the JOEL JSM-6010PLUS/LA Analysis SEM.

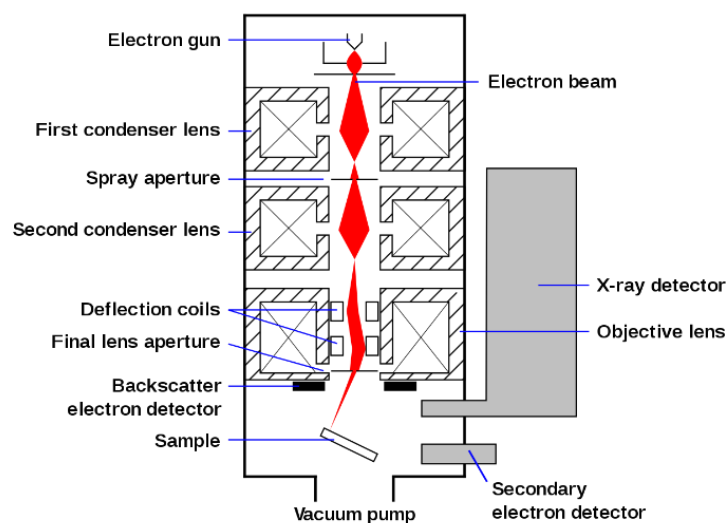


Figure 89. EDS operational diagram [150].

Choosing the correct EDS settings is very important to achieving good results. First the accelerating voltage ($<20\text{kV}$) and spot size ($<99\text{nm}$) need to be adjusted so that the counts per second (cps) places the dead time (DT) in the region of 20-50%. A higher voltage will penetrate deeper into the sample and will allow for detection of higher energies on the spectrum. For an iron-nickel alloy 20kV is required to detect the 6-9kV range adequately. As a general rule of thumb, the accelerating voltage should be twice that of the highest excitation. An increase in the cps will increase the DT due to the increase in data to process. Adjusting the spot size will increase the cps up to a limit, at which the cps will taper off. It is important to increase the spot size until the DT reaches in between 20-50%, approximately 35%. This is usually between 60-70nm. When conducting a study between different samples, the DT will change depending on the sample material. To maintain adequate cps the spot size can be changed without affecting the comparative compositional accuracy between samples.

There are several EDS specific variables to adjust when completing a map scan, these include; the map resolution, the spectral resolution, the number of sweeps, and the dwell time. The map resolution is simply the resolution of the image in pixels. The greater the map resolution the longer the scan time. The spectral resolution has four settings from T1-T4, where T1 provides a higher count rate, and T4 provides a higher resolution. Increasing the spectral resolution decreases the width of the detection band for all elements. If a composition features elements with excitations closer to one another, a higher spectral resolution should be chosen to limit crossover. Decreasing spectral resolution will increase available counts because a wider keV range will pick up a wider excitation range for the specified element. This can reduce noise in a map scan where there is no crossover between elements. Figure 90 shows an example of potential crossover where a T4 scan might be considered for quantitative accuracy. The difference in discernible map scan detail between a T4 and T2 map scan can be seen in Figure 91. In this map scan the higher count rate has improved the signal to noise (s/n) ratio.

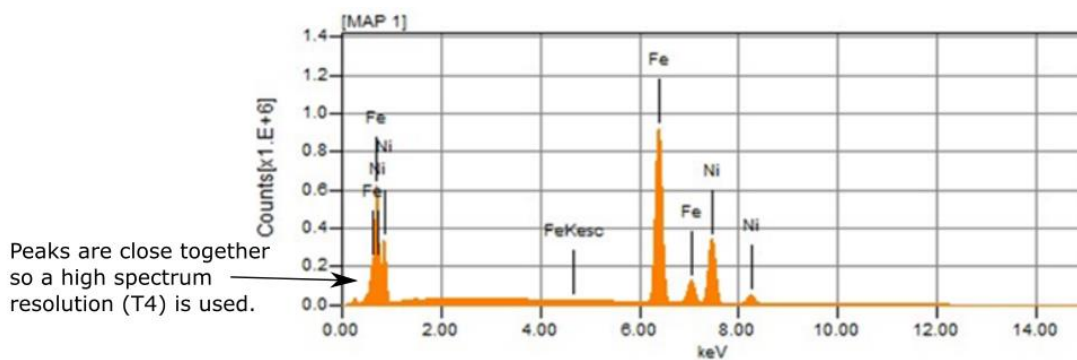


Figure 90. EDS Spectrum for an iron-nickel alloy.

The number of sweeps is the number of times the image is scanned. Scanning the image multiple times will improve s/n ratio. Dwell time is how long the electron beam dwells on a single point during a sweep. Increasing this value also improves s/n ratio. Increasing both the number of sweeps and the dwell time will also increase the scan time. A suggested optimum value is 5 sweeps and a dwell time of 1.0msec. This will take approximately 30mins to complete with a resolution of 512x384, and 2hrs with a resolution of 1024x768. A comparison of the differences between a low and high s/n ratio in and EDS map scan can be seen in Figure 91.

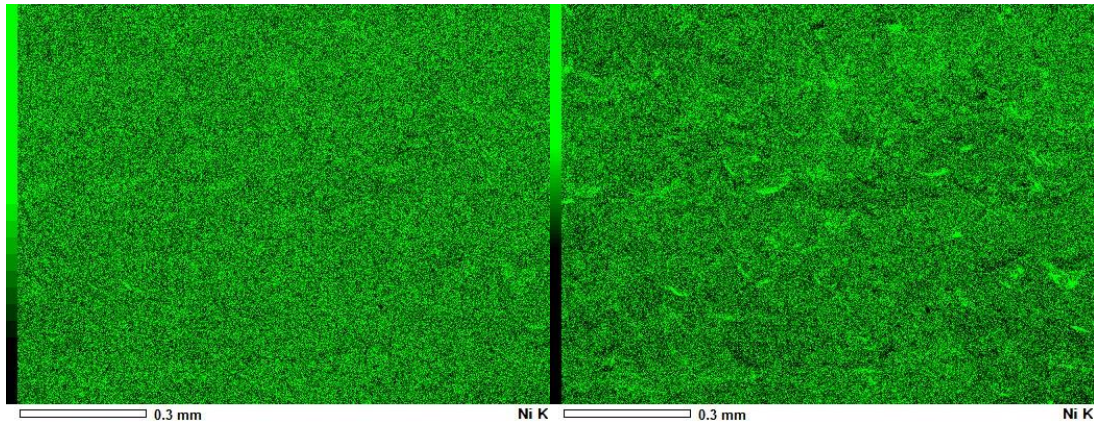


Figure 91. Comparison of a T4 EDS scan (left) and a T2 EDS scan (right) for an iron-nickel alloy. 512x384, 5 sweeps, dwell time 1.0msec, mag x100.

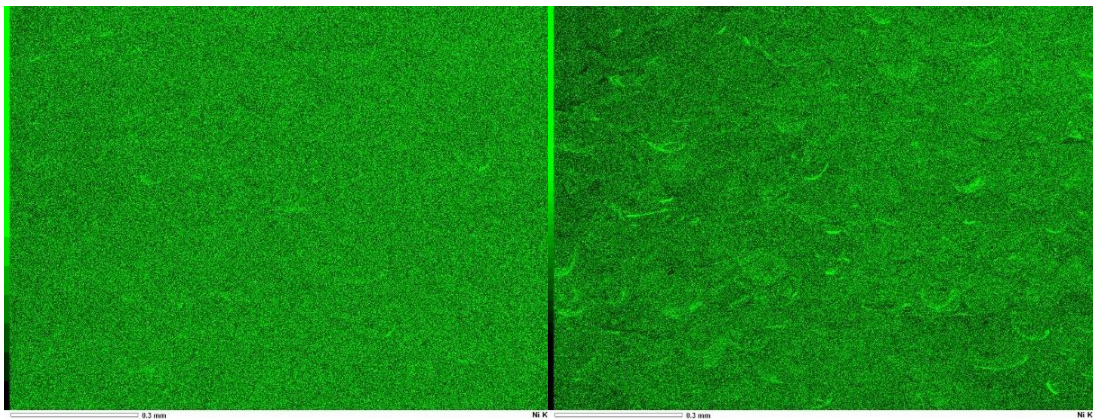


Figure 92. Comparison of a single sweep EDS scan (left) and a 5 sweep EDS scan (right) for an iron-nickel alloy. 1024x768, T2, dwell time 1.0msec, mag x100.

It is suggested that a high spectral resolution of T4 is used where quantitative compositional analysis is carried out for determining alloy constituents. For a high-quality map scan with low s/n ratio a higher count rate is suggested with a T2 scan. Five sweeps should always be used with a dwell time of 1.0msec and a resolution of 512x384 for a quick 30-minute scan. This is the best combination for an optimum quality with maximum throughput. For analysis of surface microcracking and porosity, it is best to use backscatter electron microscopy, since the secondary electron detector is at an angle.

4.7 Design of Experiments and Orthogonal Arrays

When manufacturing components using laser powder bed fusion, the laser parameter settings contribute to the overall densification of the part. In a Renishaw machine there is a pulse modulate laser, meaning the laser exposes in a fixed location for a set amount of time, before moving onto the next point of exposure. This is different compared to all other LPBF machines which use a continuous scanning laser, meaning there is an additional parameter to account for. To achieve full densification, there are several parameters that will require adjusting, these include; the laser power (PW), Point distance

(PD), the hatch spacing (HS), and the exposure time (ET). More information on what each parameter is can be found in the manufacturing section in 8.3.

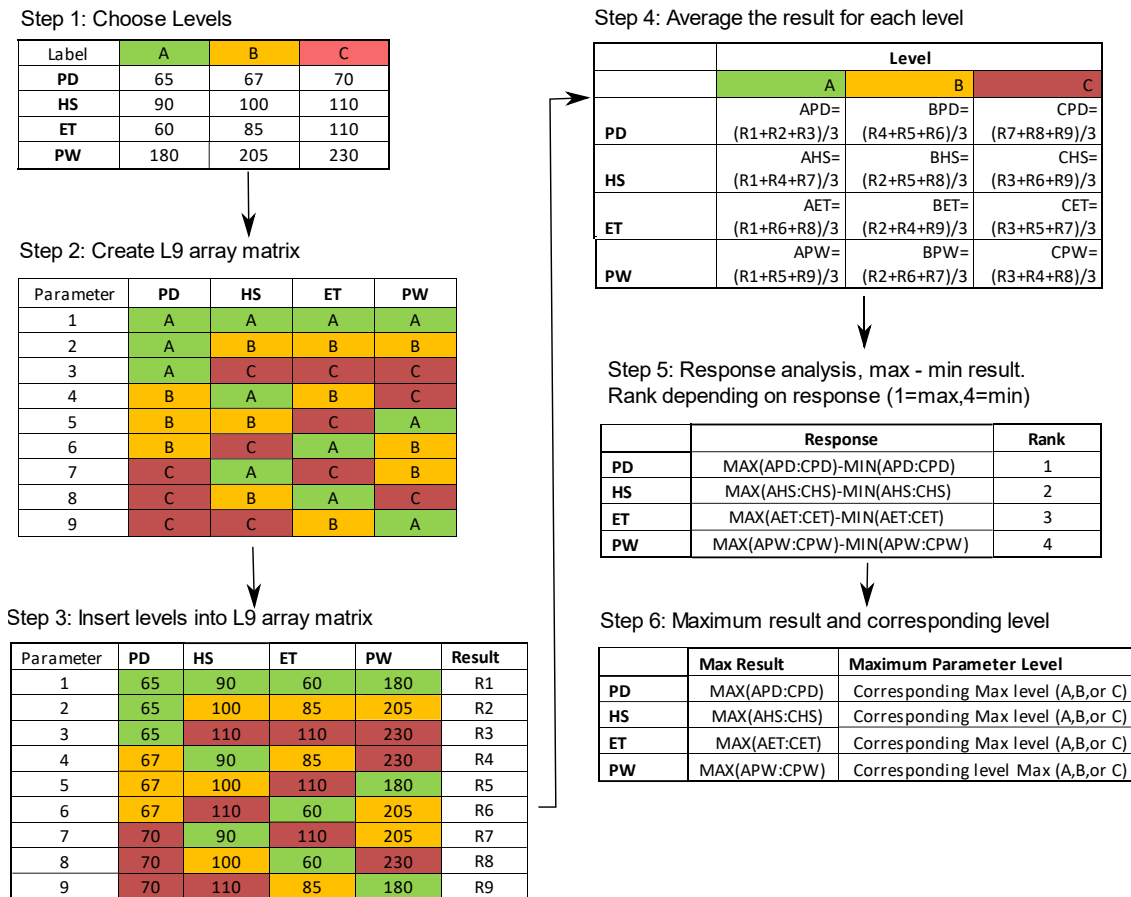


Figure 93. Step by step process for designing a L9 array. For density optimisation, the relative density percentage will be the result. Output in step 5 gives the response each laser parameter has on the density. Step 6 provides a rank for the maximum result.

The L9 orthogonal array provides the ability to individually analyse the effect of each laser parameter (PW,PD,HS, and ET) on the density. It also provides a rank for the maximum of each parameter to help with the selection of the optimum settings. Selection of the laser parameters with the densest components may not be the best approach, since some density measurements could be within the margin of error. Analysis of parameter response can help to understand which parameters can still be change to increase build speed, while maintaining density. Further mechanical tests need to be conducted on those samples above 99.8% dense to determine suitable parameters.

4.8 Thermal expansion test bench design

Understanding the amount of thermal expansion of an object is a very complex process that requires precise temperature control, coupled with accuracy capable of measuring small thermal expansions experienced by invar from 0.2 to 1µm/mK. Measurement of

CTE must be taken when the temperature is isotropic across all materials, removing other variables such as thermal conductivity / diffusivity of the different materials present.

The functions to be considered when designing a test rig are as follows;

1. To measure a CTE between $-40\text{ }^{\circ}\text{C}$ up to $+70\text{ }^{\circ}\text{C}$.
2. Measure the CTE of a 2D radial profile around a lens of 60mm in diameter.
3. Measure the CTE without affecting the CTE itself. In structures where stiffness is reduced, measurement by contact with the specimen could affect the measurement.

Two solutions have been identified for measuring the thermal expansion of large structures; Digital Image Correlation (DiC), whereby a camera is used to track the movement of the structure as it expands, and a Co-ordinate Measuring Machine (CMM), where a probe is used to touch the surface after its thermally expanded.

Both methods will require a hotplate with uniform temperature distribution as shown in Figure 94.

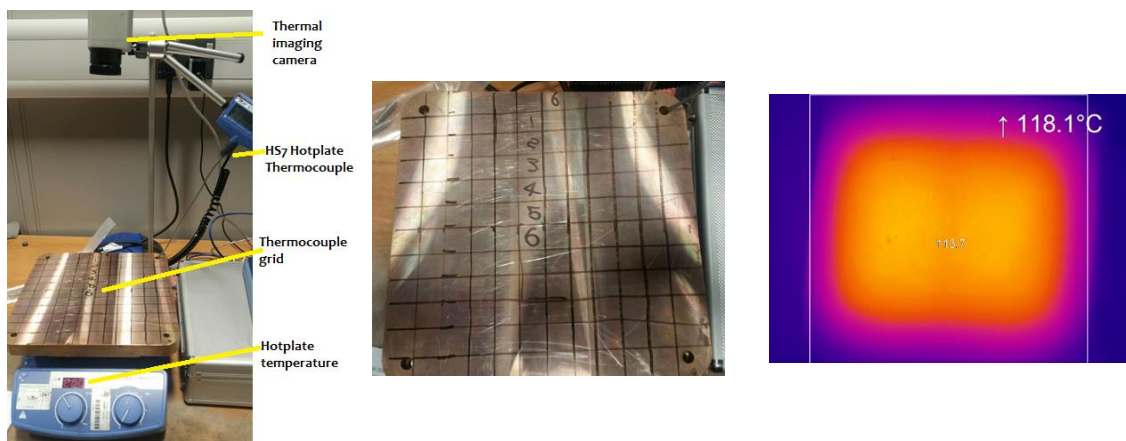


Figure 94. Heated baseplate featuring a grid array for analysis of temperature distribution. Image shows setup with IR camera, Baseplate with thermocouple reading locations, and IR image where the white box shows the plate boundary.

It is shown that the distribution of temperature over the hotplate is very consistent. After being left to heat soak for 1 hour, the temperature in the centre is approximately 2.8°C hotter than the very edge. Therefore, the structure should be placed in the centre at location 6, and the thermal expansion should be calculated using a thermocouple fixed as close to the sample as possible using copper tape.

Grid No.	6	5	4	3	2	1
1	161.6	161.6	162.48	162.15	161.4	163.16
2	161.7	162.6	161.28	163	163.02	163.2
3	161.74	162.3	163.56	161.72	164.5	163.4
4	162.4	162.3	163.6	163.48	164.8	163.04
5	162	162.3	162.47	164.27	163.5	164.5
6	161.42	161.7	162.8	163.38	164.2	164.4

Table 18. Table showing temperature uniformity from thermocouple readings across the baseplate. Hotplate temperature is set to 200°C, but the hotplate thermocouple reads a steady 156°C. 1:1 is at the top left edge, and 6:6 is at the centre.

4.8.1 Digital Image Correlation (DiC) camera system

Digital Image Correlation (DiC) can be used to measure the thermal expansion of a larger sample by using a camera and software to track a stochastic pattern on the sample. The stochastic pattern is either applied by paint, or present in the sample from surface roughness. This method was attempted for measuring the CTE of large structures. A matlab script called NCorr was tested against a software called GOM correlate to determine the most effective software. It was determined that GOM correlate was superior due to its ability to automatically resolve x and y displacements and overlay the results. The camera used is a Nikon D300 with a AF-S 60mm macro lens. The hotplate used is a Fisher scientific Isotemp. This method has many advantages and disadvantages.

Advantages include;

- Ability to measure a large sample of the required 2D 100mm x 100mm plane.
- Non-contact measurement means sample is not affected by a contact probe.
- Measurements can be resolved to find expansion rates independent of movement of the sample during heating.

Disadvantages included;

- Inaccuracies down to image resolution and compression.
- Stochastic pattern applied with a spray paint can needs to be fine enough in resolution for the application.
- Any movements of the camera or sample during heating will affect the accuracy of the results. A longer distance from the camera to the sample will create more movement in the image.
- Heat haze from the heated sample will be picked up by the camera.
- Change in ambient lighting conditions will affect the accuracy of the results.
- Cannot measure in 3D without a complex dual camera system carefully designed specifically for the task 3rd party vendor.

To test the suitability of DiC in determining the thermal expansion co-efficient of the system, a test bench was setup with a DSLR mounted camera and a hot plate.

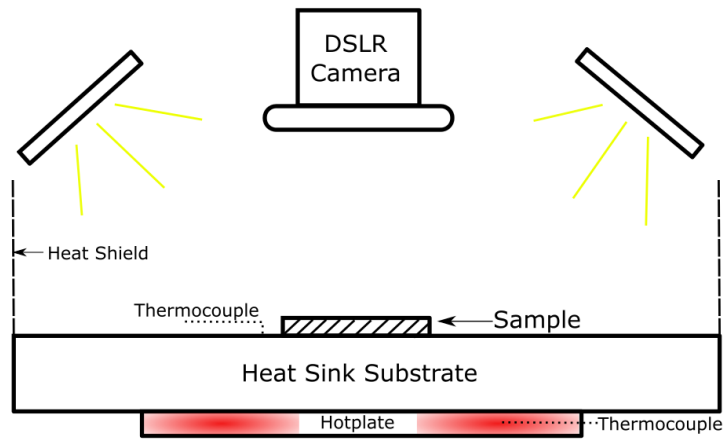


Figure 95. Schematic showing the DiC test rig setup.

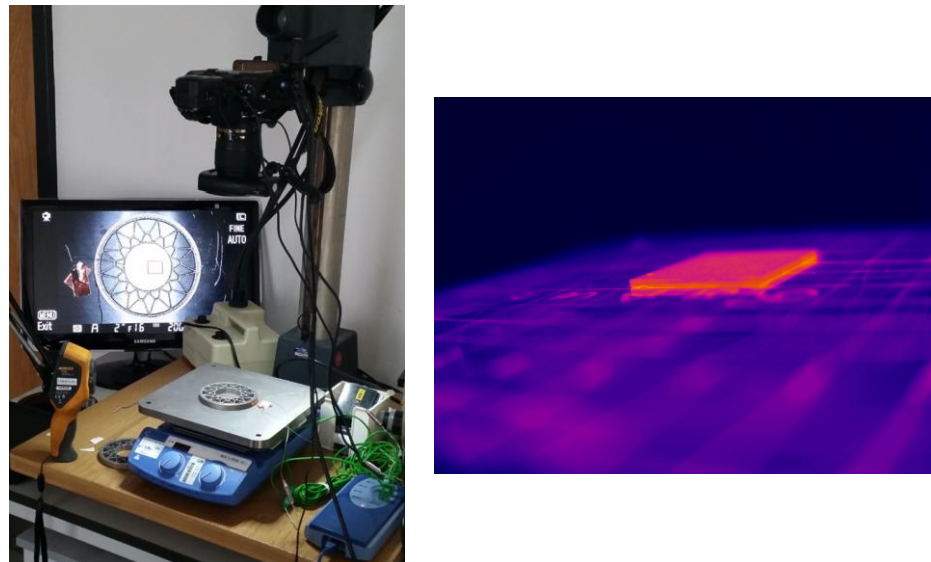


Figure 96. Image of the DiC test rig setup, and Infra-red image from the Ti64Al test plate.

The software GOM correlate is used to present the thermal expansion images in Figure 97 and Figure 98. The rough surface area and high magnification lens provides a good level of detail for the software to track. An initial image is taken at ambient, then another is taken after the temperature at the adjacent thermocouple has measured 100°C

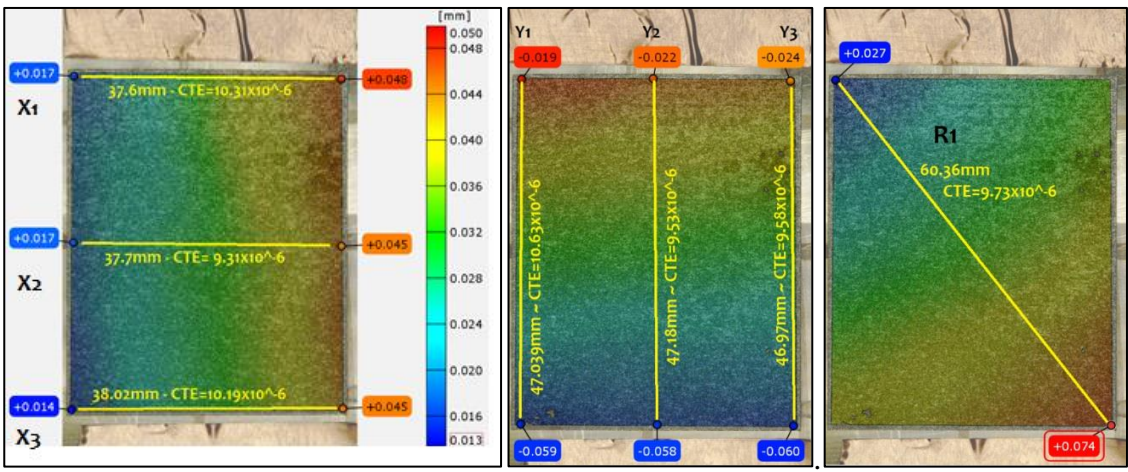


Figure 97. DiC images of a flat Ti64Al plate at 100°C showing the displacement contours for the X, Y, and XY combined directions respectively.

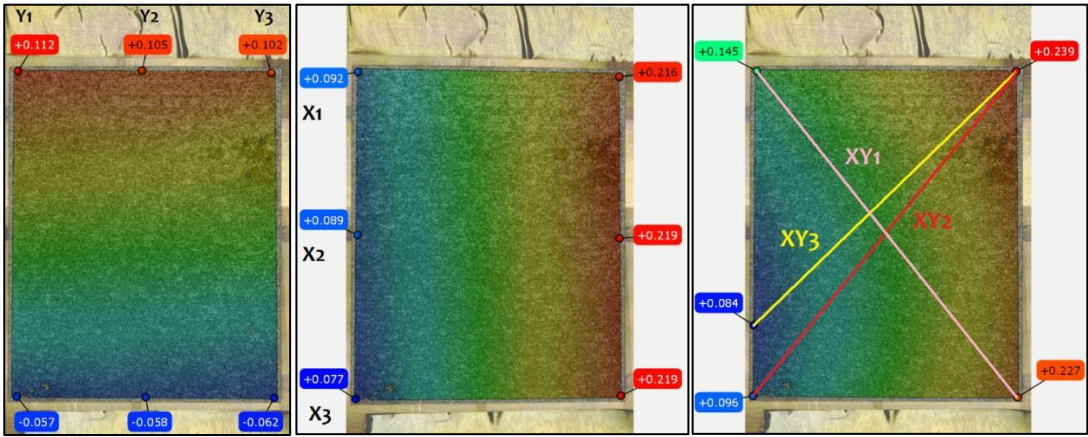


Figure 98. DiC images of a flat Ti64Al plate at 230°C showing the displacement contours for the X, Y, and XY combined directions respectively.

The thermal expansion is resolved in both XY directions, and can be seen to expand from the top left corner down to the bottom right corner after being heated from ambient to 100°C shown in Figure 97. As the temperature increases to 230°C, the place of expansion starts from the measured location ‘XY3’ in Figure 98. The selection of the minimum and maximum areas of displacement can be difficult and lead to inaccuracy. Automatic selection is effected by noise, and so cannot be used with averaging its neighbouring areas, a function that the software does not support. Table 19 shows the thermal expansion displacements at 230°C, with dimensions shown from Figure 98.

	Length (mm)	Change in Length (mm)	Temp (°C)	CTE (m/mK)
Y1	47.1687	0.169	230	1.55778E-05
Y2	47.3	0.163	230	1.4983E-05
Y3	47.102	0.164	230	1.51383E-05
X1	37.2165	0.124	230	1.44863E-05
X2	37.8034	0.13	230	1.49515E-05
X3	37.97	0.142	230	1.626E-05
XY1	60.5253	0.082	230	5.89046E-06
XY2	60.4667	0.143	230	1.02823E-05
XY3	52.94	0.155	230	1.27298E-05

Table 19. Table showing displacement and CTE data for a flat Ti64Al plate at 230°C from annotations in Figure 98.

The dimension XY3 shows a CTE of 12.73 μ m/mK for the Ti64Al part. The actual dilatometry gives Ti64Al a CTE of 10.3 μ m/mK in this temperature range. There are many variables that can affect the result. The disadvantages of the system have contributed to the high error percentage of 19.1%. The strains of the plate shown in Figure 99, are used to measure error since here should be no strains in the system. A maximum normalised strain is 1.2% after removing anomalies by adjusting the correlation co-efficient.

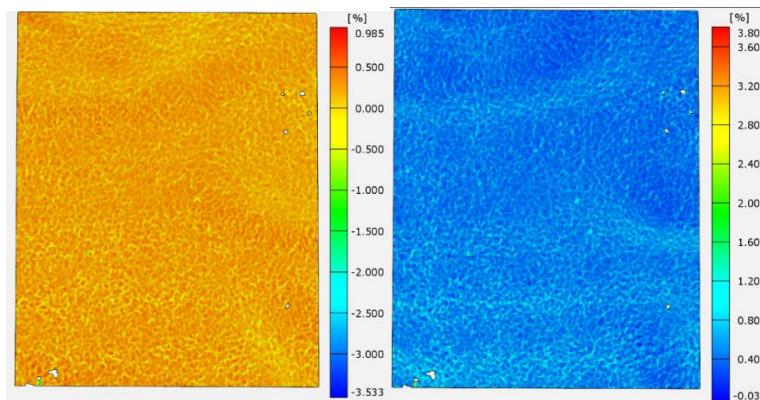


Figure 99. DiC images of a flat Ti64Al plate at 230°C showing the strain contours for the overall strain, and the normalised overall strain. Strain represents error.

When moving to larger ALM parts, the camera will not be able to pick up the stochastic pattern produced by the surface roughness due to reduced resolution. The surface roughness is also less on the top surface of any printed LPBF part, which is the critical surface that needs measuring. Surface roughness is also less on plastic components. For this reason, a stochastic spray pattern will need to be used in DiC to give the software many points to track. This is achieved with a white paint coating and a black spray can at a distance. This test looks to expand the structure to reduce resolution by 4 times whilst testing the spray pattern to be applied in all future testing.

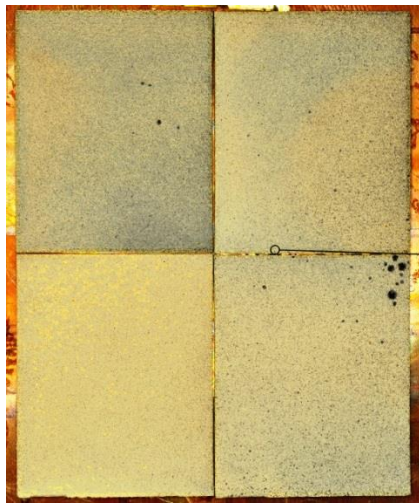


Figure 100. Four Ti64Al test plates with a Stochastic pattern applied with white and black spray paint.

The four speckled plates shown in Figure 100 are calculated for their displacement after heating at 220°C and the results shown in Figure 101.

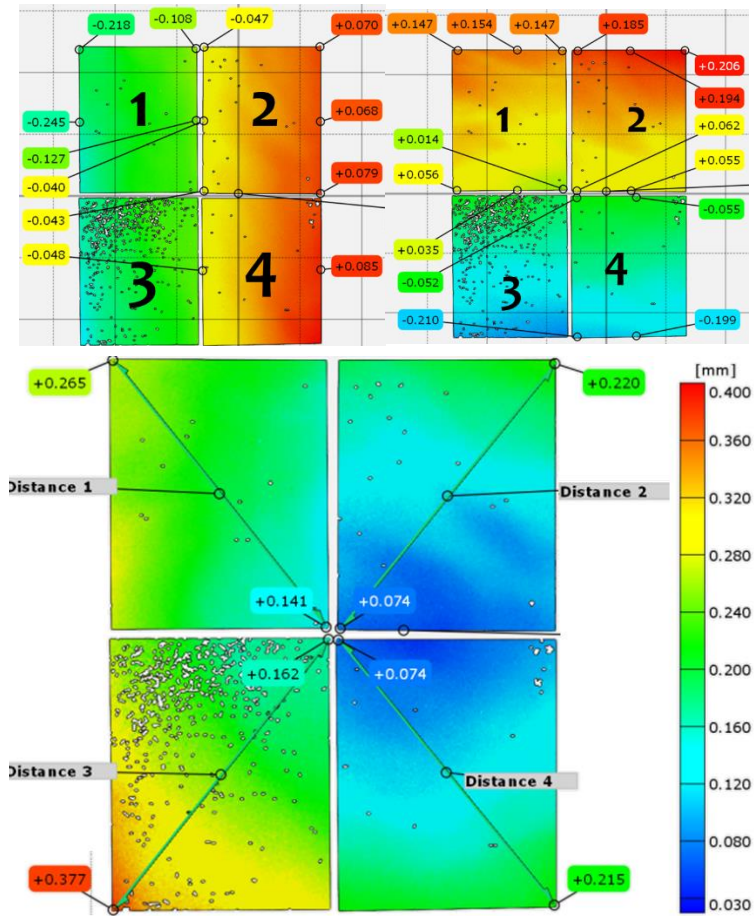


Figure 101. DiC images of a flat Ti64Al plate at 220°C showing the displacement contours and values(mm) for the four speckled plates in the X, Y, and combined XY direction, respectively.

Four independent squares have been used to mimic the effect of a moving lattice structure. The data is tabulated in Table 20.

	Length (mm)	Change in Length (mm)	Delta Temp(°C)	CTE ($\mu\text{m}/\text{mK}$)
X1	37.83	0.118	210	14.8131
X2	37.74	0.116	210	14.594
X3	-	-	-	-
X4	38.14	0.134	210	16.7708
Y1	46.86	0.11	210	11.6177
Y2	47.01	0.141	210	14.25
Y3	-	-	-	-
Y4	46.60	0.151	210	15.4302
XY1	60.03	0.124	210	9.83578
XY2	59.91	0.146	210	11.6047
XY3	60.75	0.215	210	16.8509
XY4	60.10	0.141	210	11.1724

Table 20. Table showing displacement and CTE data for a flat Ti64Al speckled plate at 220°C from annotations in Figure 101 above.

Once the resolution has been reduced by four times by using an increased sample size, the thermal expansion can be measured. It can be seen that the resolved XY thermal expansions from corner to corner on each sample has not been consistent at all. The CTE's ranged from 16.8 to 9.8 $\mu\text{m}/\text{mK}$. There are several reasons for this occurring, including heat haze, lower resolution, room lighting changes, and camera movement. The movement of each square individually has been resolved as a single unit, presenting challenges when resolving multiple moving lattice structures on larger parts.

Further testing was conducted on a range of structures designed later in the thesis. Unfortunately, although the methodology for the testing is correct, equipment and budget limitations meant that the results were not within an acceptable margin. To further improve on this test method, a higher resolution camera will be required, and a lightbox whereby no shadows can be cast. The heat haze can be removed by reducing the heat, but this would in-turn require higher resolution again. It would be preferable to use a 3rd party such as VIC-2D, which specialise is DiC, and have developed specialist software for detecting dimensional changes using a dual camera setup using a CCD sensor instead of a CMOS sensor for better pixel image tracking. Software support can provide the necessary knowledge to measure the unique structures.

4.8.2 Co-ordinate measuring machine

A co-ordinate measuring machine allows the user to accurately measure a component by touching or scanning a probe across its surface. This can be used to attain the co-efficient of thermal expansion by measuring before and after temperature change.

This is a useful tool to measure the diameter and circularity of optical components for benchmarking purposes. The setup consists of the Renishaw Revo 5-Axis CMM machine, with a 2mm ruby tipped probe head. The hotplate setup defined earlier is used, with a glass box around the edge to reduce the effect of wind on temperature stability, while keeping the sample visible for checking. The three metal plates are made of steel and hold the sample at three corners. Since the sample is expanding, the plates can move with the sample. The point measurements of the sample form an overall diameter, so the movement of the centre of the cylinder will not effect the overall thermal expansion measurement.

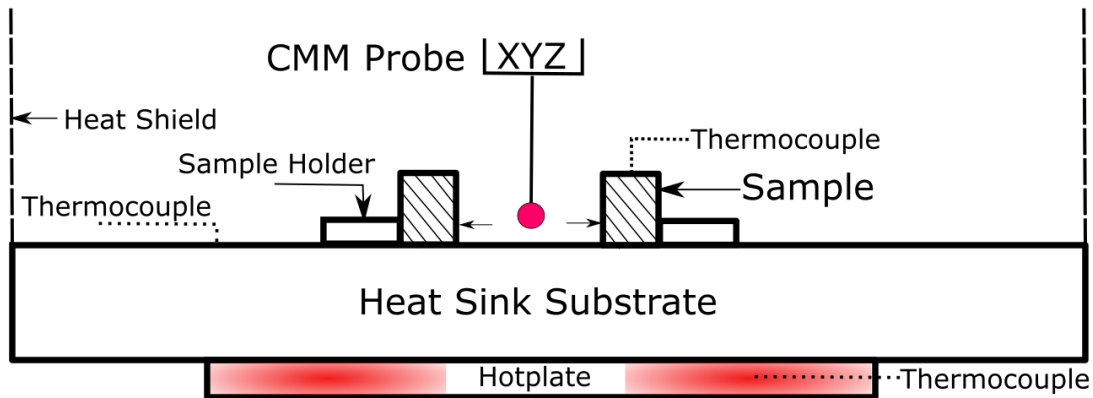


Figure 102. Schematic of CMM test bench setup.

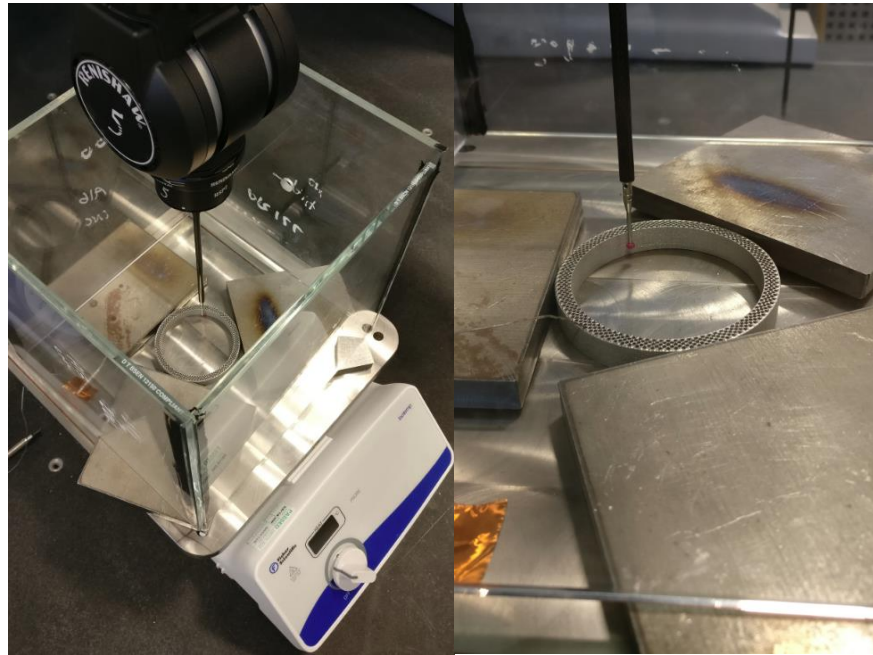


Figure 103. Image of the CMM test bench.

The co-ordinate measuring machine has been programmed to take a measurement of the diameter by touching each segment of the inside of the cylinder. A series of 30 data points will be taken to obtain one diameter reading. A total of 100 diameter readings is taken to analyse the variation between each diameter. This means a total of 3000 touches will be made. The following steps are taken to measure the co-efficient of thermal expansion with the correction run;

1. Measurement of a single material structure with a known thermal expansion at room temperature.
2. Measurement of the same structure at an elevated temperature measured from both the thermocouple and the hotplate. A heat soak cycle must be used to ensure all objects have uniformly heated for approximately 3 hours.
3. Replace the structure with the multi-material structure and repeat step 1 and 2, ensuring the hotplate has completely cooled to room temperature.

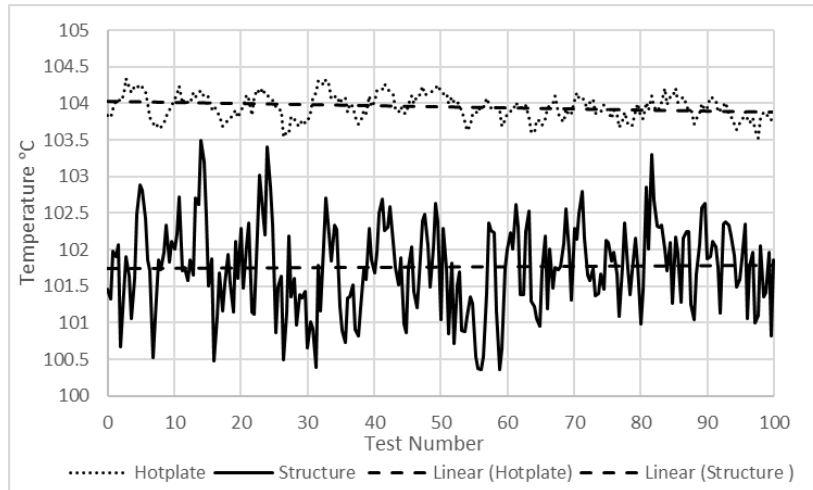


Figure 104. Temperature profile for hotplate and structure for the CMM test rig measuring a Ti64Al cylinder.

Figure 105 and Figure 106 show how accurate the measurement is from test to test. A single test number is one diameter reading. Over the 100 tests, the initial 15 tests is unstable, but stability improves after test 15. This could be due to loose powder being removed on the surface of the probe location. From 15 to 100 a trendline is drawn, which increases over the test by $1\mu\text{m}$ for ambient, and $1.8\mu\text{m}$ for 101.75°C . This means at an average of the given points the level of approximate difference is $0.8\mu\text{m}$. This equates to only a 1.7% level of stability related error when applied to the Ti64Al thermal expansion measured. The increase in diameter over the number of tests is attributed to the wear of the probes ruby tip, or the metal surface being measured.

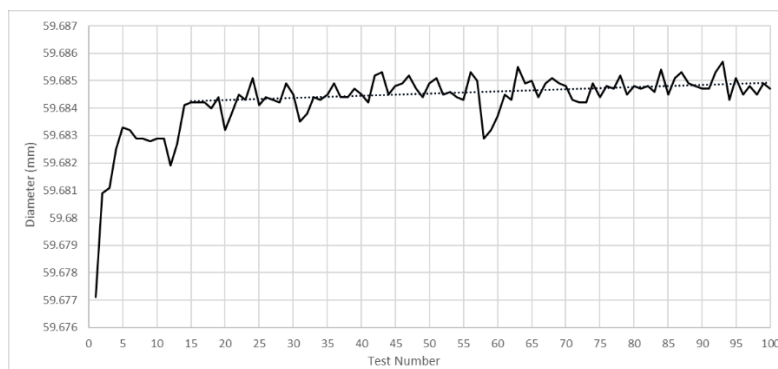


Figure 105. CMM Readings for the diameter of a Ti64Al cylinder at 24°C . Trendline shows increase of $1\mu\text{m}$ over 85 readings.

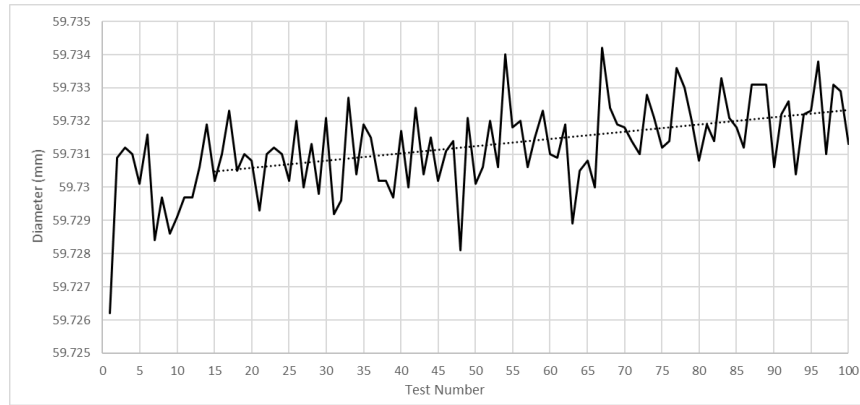


Figure 106. CMM Readings for the diameter of a Ti64Al cylinder at 101.75°C. Trendline shows increase of 1.8µm over 85 readings.

Calculating the thermal expansion co-efficient requires the overall increase in diameter after the temperature is raised. Figure 107 shows the increase in diameter when normalised for the average reading at 24°C. This data is used to calculate the CTE in Table 21. The experiment is run again for the lowest expansion metal, invar.

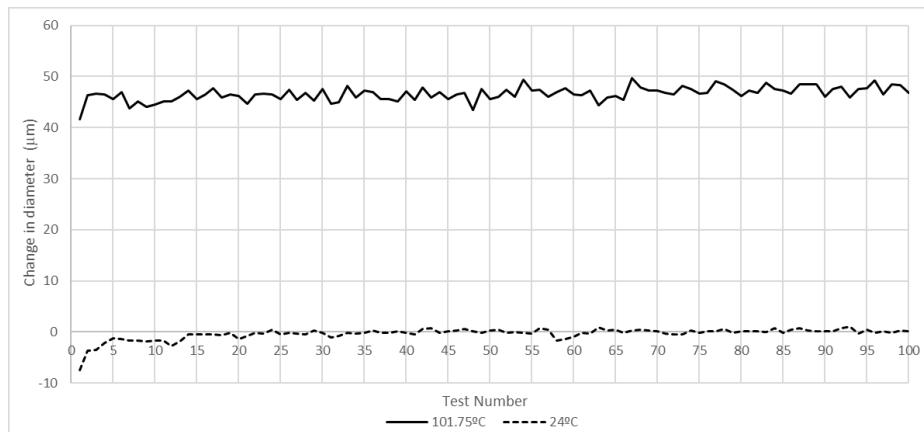


Figure 107. CMM readings comparing ambient against heated diameter for a Ti64Al cylinder. Change in diameter normalised against average ambient readings.

Material	Average Diameter (mm) at 22°C	Average Diameter (mm) at 101.75°C	Thermal expansion (µm)	Average Temperature Difference °C	Calculated CTE (µm /m K)	Reference CTE from Dilatometry (µm /m K)
Ti64Al	59.68459	59.73140	46.81	77.75	10.0343	10.6
Invar	59.43254	59.43860	6.06	81.5	1.2393	1.3

Table 21. CMM test bench measured CTE against reference CTE showing accurate thermal expansion measurement for Ti64Al and Invar.

Table 21 shows that the measured CTE's are very close to that of dilatometry. Ti64Al gives a reading of 10.0343 $\mu\text{m}/\text{mK}$, which is -5.34% away from the dilatometers result of 10.6 $\mu\text{m}/\text{mK}$. The invar result should be more sensitive to changes in accuracy since the thermal expansion is so low. The percentage difference is very similar to Ti64Al at -4.90%.

To conclude the CMM test bench is proven to be the best means of measuring the thermal expansion of large structures that cannot fit in the dilatometer. It has proven itself with high reliability between tests, and a similar CTE to that of dilatometry of between -4.9% and -5.34%.

5 Thermal Expansion Control in Metal AM by Design

5.1 Introduction

Controlling thermal expansion with a metallic additive manufacturing process is difficult because most processes are limited to a single material feedstock. Many thermal expansion-controlled structures require at least two materials, one with a higher CTE and one with a lower CTE. The combination of the two materials in a specific arrangement can produce a bending or stretching movement when constructed in lattice structures, some of which are outlined in chapter 3.

In this chapter a unique solution will be proposed which solves the design problem given by Qioptiq; to tailor the radial CTE of a cylindrical lens housing to match that of the internal lens material. The achieved design allows the engineer to adjust dimensional parameters which change the CTE in the design before manufacturing the solution. This is achieved by using two separate AM processes. The first process uses LPBF. This manufactured part includes the CTE tailoring structure. The secondary process applies a secondary metal directly to the outside of the cylinder using a Direct Energy Deposition (DED) process, also known as laser cladding. The combination of a high CTE and a low CTE metal in a cylinder provides a difference in expansion rates that will cause deformation of the inside geometry. Several designs have been considered for the geometry of the structure which will be covered in this chapter. These geometries include;

- Tuneable CTE auxetic structure designed for efficient transport of deformation over temperature with a wide range of CTE's.
- Tuneable designed porosity structure for a compact geometry but with a narrower tailorable CTE range.

The inside structure has been designed to be tuneable depending on variables such as the angle, and member thicknesses. The secondary material will be a different CTE to the first, creating an overall change in CTE across the inside diameter. This arrangement is only possible with a symmetric cylindrical cross-section, similar to the design of many optical systems. The primary lens housing and auxetic structure will be manufactured using LPBF with a single material, and the secondary material will be added using Direct Energy Deposition to the outside of the cylinder.

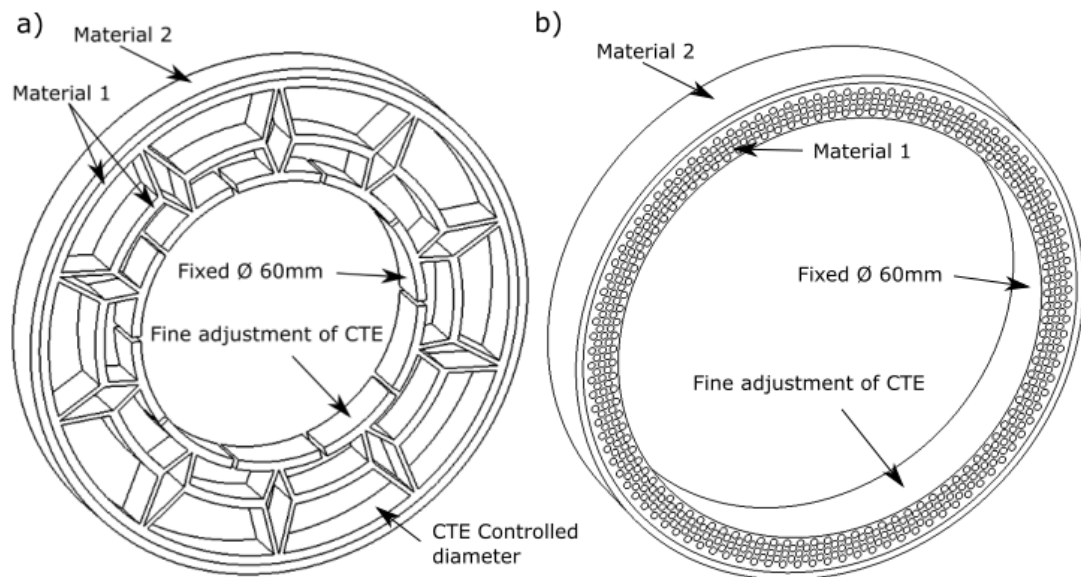


Figure 108. Figure showing the two arrangements, a) tuneable auxetic lattice type, and b) tuneable porosity type.

If material 2 is a lower CTE than material 1, as the part heats up, the inside structure will be in compression. As it cools, it will be in tension. The opposite is true for a clad material with a higher CTE.

The effectiveness at tailoring CTE has been determined from the ANSYS model, proving that in the maximum case, the CTE can be reduced by up to -160%, from $5\mu\text{m/mK}$ of the combined Ti64Al and invar ring, to $-3\mu\text{m/mK}$ on the inside annulus. The stiffness of the structure is also compared with different configurations, with alternatives proposed later in the chapter which provide greater stiffness whilst still maintaining a level of CTE control. The target CTE to obtain so that the casing matches the CTE of the lens material is $7.1\mu\text{m/mK}$ for a borosilicate glass lens, and $6.1\mu\text{m/mK}$ for a germanium lens.

To summarise the effectiveness of the manufacturing method, and its applicability to the simulation, the test benches outlined in chapter 6 have been used. The measured CTE has been compared to the simulation results.

5.2 Simulation setup

To determine the effect of various arrangements of materials and lattice structures on the radial CTE, a Finite Element Analysis (FEA) static-structural model has been designed using ANSYS 18.1 Mechanical. The simulation looks at a 2D cross-section through each cylindrical design. The model assumes the material is linear, and the temperature distribution is uniform throughout. The temperature will be raised by 100°C, and the deformations at key points will be obtained for later calculation of the CTE.

Material	Youngs Modulus (GPa)	Poisson's Ratio	UTS (MPa)	Density (kg/m ³)	CTE (μm/mK)
Ti64Al	113	0.34	970	4620	9.4
316L	193	0.25	558	7990	16
Invar	148	0.3	621	8050	1.24

Table 22. Linear material properties for determined ALM manufactured components and used in the simulation.

The contact edges between the inside and outside material of the cylinder have been set to 'bonded'. A cylindrical support is applied to the outermost circumference applying a fixed tangential, but free radial condition.

Depending on the design, the deformation probe will output the deformation as a function of the diameter for a full circle, or radius for an arc.

For a cylinder with no gaps, the deformation produced is relative to the whole cylinder, and thus the deformation result is with respect to the cylinders diameter;

$$\frac{\Delta\phi}{\Delta t \phi_o} = CTE (m/m.K) \quad (5.1)$$

For a cylinder with expansion gaps required for the introduction of an auxetic structure, the deformation results are with respect to the radius of the arc;

$$\frac{\Delta r}{\Delta t r_o} = CTE (m/m.K) \quad (5.2)$$

$\Delta\phi, \Delta r$ = deformation probe result for diameter, or radius.

Δt = change in temperature.

ϕ_o, r_o = Initial diameter or radius before thermal expansion change.

With each design, a mesh sensitivity study will be carried out to determine the most effective mesh element sizing depending on the geometry.

5.3 Bi-material bonded cylinder

If the optical system is cylindrical, the radial CTE can be controlled bonding two cylinders of different materials together. With a different thermal expansion rates for each material, a combination can be made to feature a different overall combined CTE. The CTE can be adjusted by changing the thickness of each ring. This is advantageous over any additional lattice structure because it requires less material, and the deformation is even across the inner surface requiring no expansion gaps which could interfere with mounting a lens. The disadvantages are that the thicknesses of each ring have to be tightly controlled. The exact thicknesses required to match that of germanium and glass will be determined through simulation, and the effect of tolerance on the CTE will be analysed.

The manufacturability of a bonded ring can be achieved easily with plastic AM by means of material jetting or dual extrusion FDM. Using this process type, the material can be added in situ. When it comes to metal-AM however, it is difficult because the material cannot be added in situ while printing. The metal AM method known as Direct Energy Deposition (DED) is routinely used in industry to ‘laser clad’ a material onto another. For the basic first assumption, this section aims to show the effect of a bonded ring and ignoring manufacturing method geometric variability.

The simulation will take the deformation of the inner surface and calculate the CTE at the lens interface. For an initial simplistic case, the outside ring will be assumed to be bonded. The mesh size function will be set to uniform, and the support type set to cylindrical with the tangential fixed and radial free. A mesh sensitivity study will be carried out, followed by a parametric study to determine the values of deformation at different internal and external ring thicknesses.

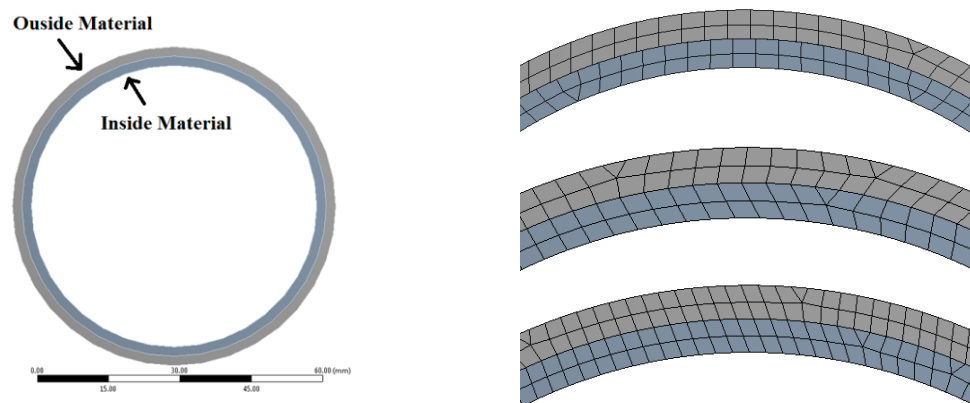


Figure 109. The bi-material ring arrangement, and mesh at 1.6mm body sizing (top image) followed by 1.4mm and 1mm body sizing.

A mesh sensitivity study has been carried out on the basic 2D symmetric profile to verify accuracy. It can be seen that for sizes less than 1.4mm there is little variance beyond what can be considered negligible. For sizes 1.6mm and above the CTE begins to vary by 0.001 $\mu\text{m}/\text{mK}$ possibly due to the mismatched mesh interface. With a uniform mesh size function 1.6mm body sizing does not provide a uniform spacing across both ring sizes. As a general rule of thumb, the body sizing used for further parametric studies will be set to half that of the smallest ring thickness.

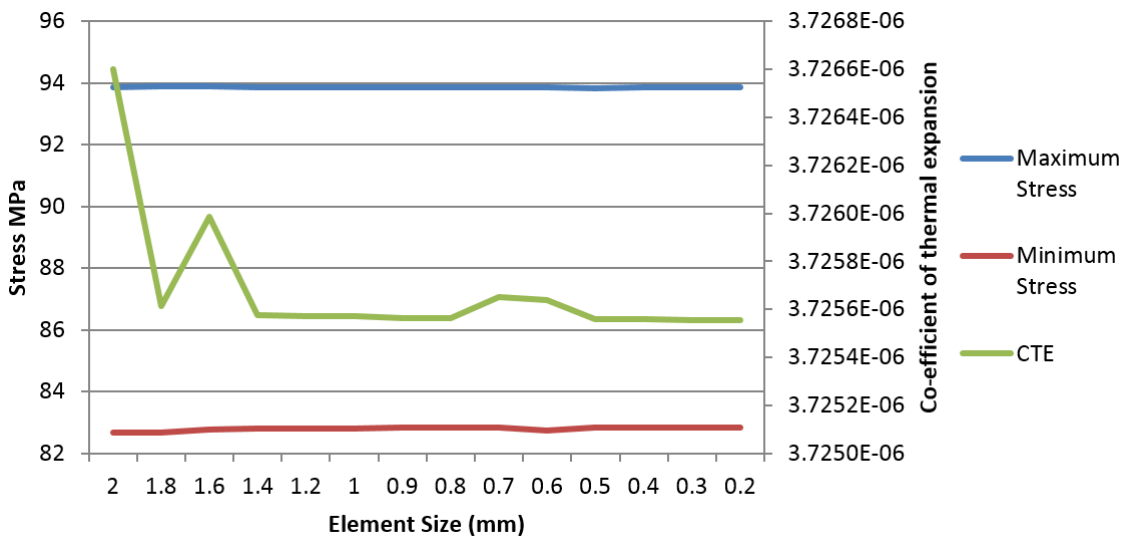


Figure 110. Graph showing sensitivity study for a bi-material ring of equal thickness ($T_o/T_i=1$) for Ti64Al inside and INVAR outside.

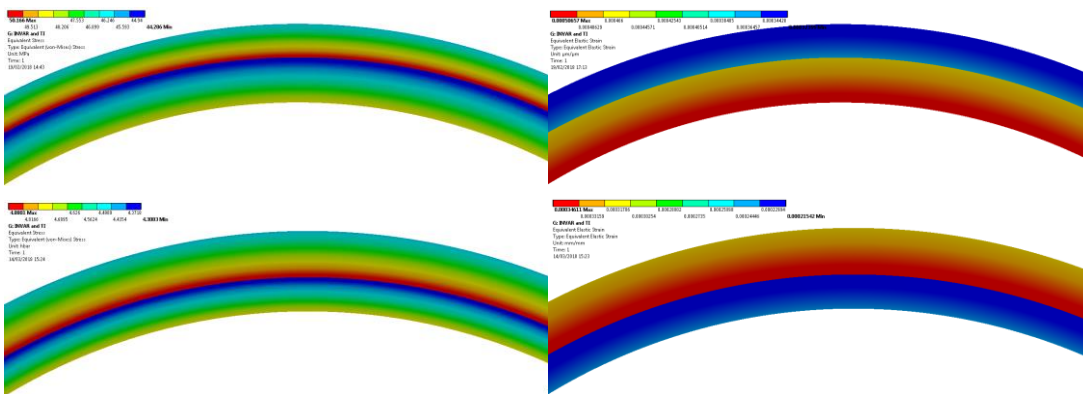


Figure 111. Simulation showing Stress on the left, and strains on the right. The outside material is INVAR whilst the inside is Ti64Al. The top two images simulate from 22°C to 70°C, whilst the bottom two simulate from -30°C to +22°C ($t_c/t_v=1$).

It can be seen that the maximum stresses in both hot and cold environments will be at the boundary between the two materials. At this point the stress differential is at its highest. This can also be seen for strains in the system; however, the inner ring has the highest

strains when above ambient, and the outer ring has the highest strains when below ambient. A parametric simulation was carried out over the range -30°C to $+70^{\circ}\text{C}$ for a range of ring thicknesses to attain the maximum and minimum bounds for CTE change given a realistic minimum thickness for manufacturability.

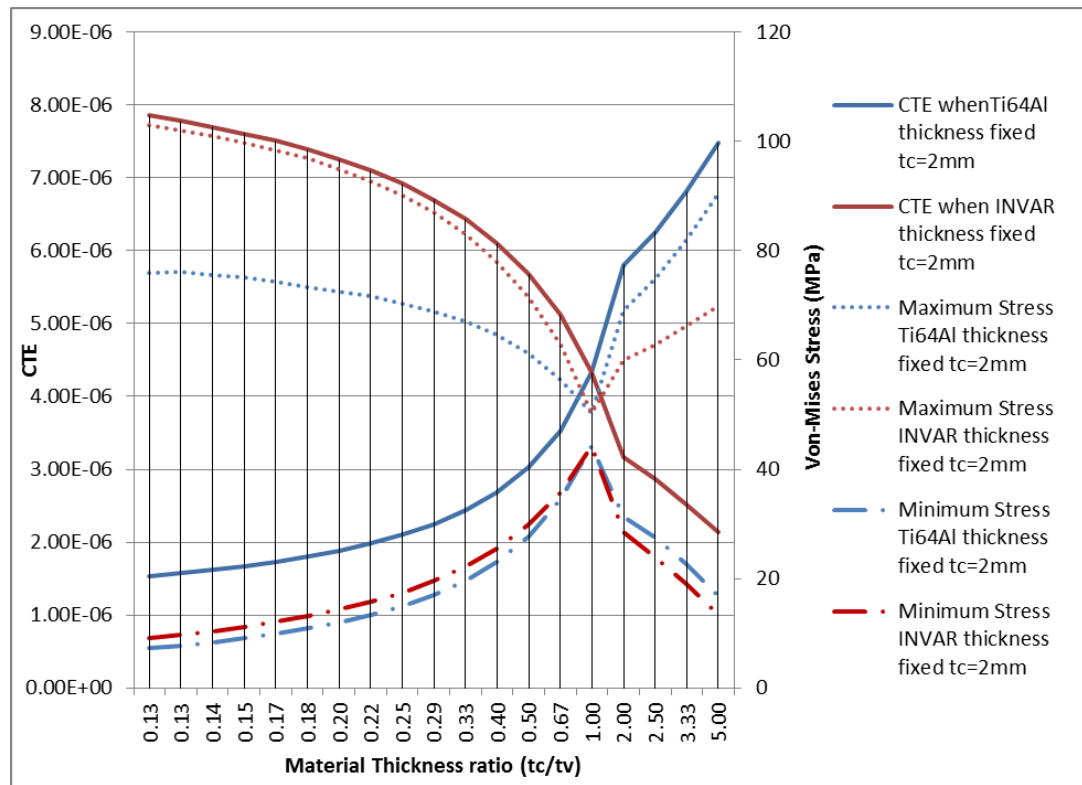


Figure 112. Graph showing CTE and Von-Mises strains as the INVAR to Ti64Al thickness ratio changes where t_c is the constant thickness material, and t_v is the thickness of the material being varied. Temperature range is $+100^{\circ}\text{C}$.

Figures 100-101 show that to acquire a CTE similar to that of a Borosilicate glass or germanium lens ($6-7\mu\text{m/mK}$), the material thickness ratio needs to be between 2 and 4. The variable thickness t_v needs to be between if t_c is 2mm. Benchmarking in chapter 6.2 shows a minimum wall thickness of 0.49mm in Ti64Al when the CAD specifies 0.1mm. Using DED for laser cladding INVAR onto any surface, the minimum deposition thickness on a single pass is between 0.4mm and 0.5mm. Therefore, it is not possible to get any further CTE changes outside of the bounds proposed without an additional milling operation. Stresses behaved as expected, with the change in magnitude corresponding with the change in CTE. A 3D plot has been constructed for visualisation purposes. This shows the extent of the thicknesses required to come close the CTE of either materials. To identify the different thickness combinations required to acquire a 6.1 or $7.1\mu\text{m/mK}$ CTE, a table has been created for 316L, Ti64Al, and Invar, where Invar and 316L have been used for the cladding material independently. To determine the effect of tolerance

on CTE, a $\pm 250\mu\text{m}$ adjustment to thickness has applied and its corresponding CTE calculated.

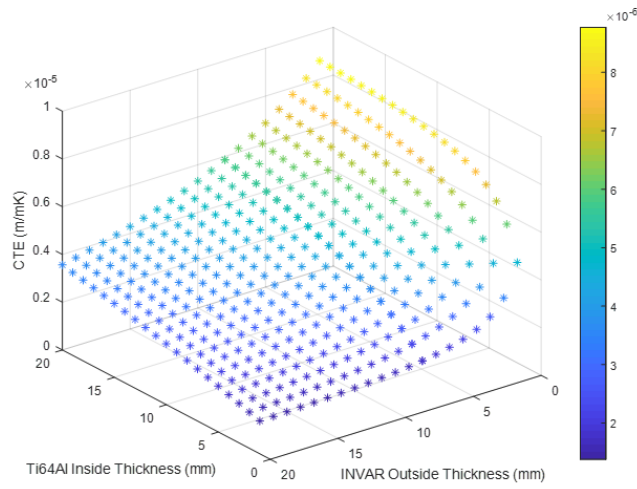


Figure 113. Scatter Plot showing FEA data for a bonded 2D ring of varying outside INVAR thickness and varying inside Ti64Al thickness and its corresponding CTE.

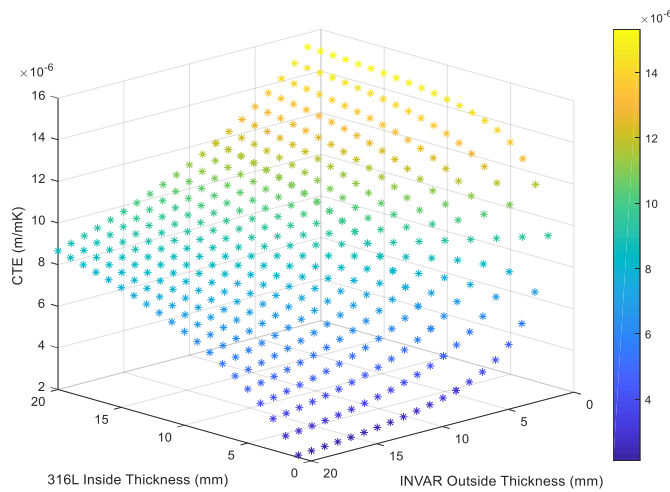


Figure 114. Scatter Plot showing FEA data for a bonded 2D ring of varying outside INVAR thickness and varying inside 316L thickness and its corresponding CTE.

Table 23. Data showing simulation results for 1-2mm bonded INVAR around a Ti64Al and 316L ring. Linear interpolation used to show required inside thickness to match the CTE of the lens material. Data showing simulation results for 1-2mm bonded 316L and Ti64Al around an Invar ring. Linear interpolation used to show required inside thickness to match the CTE of the lens material.

No.	INVAR Thickness (mm)	Ti64Al Thickness (mm)	316L Thickness (mm)	Simulated CTE ($\mu\text{m/mK}$)	Lens material	Lens material CTE ($\mu\text{m/mK}$)	Inside Thickness required to match lens material CTE (mm)	Tolerance effect on matched CTE for $\pm 250\mu\text{m}$ inside thickness ($\mu\text{m/mK}$)	Tolerance effect on matched CTE for $\pm 250\mu\text{m}$ outside thickness ($\mu\text{m/mK}$)
Location	Outside	Inside	Inside						
1	1	2-3	-	6.05-6.79	Germanium	6.1	2.068	± 0.185	± 0.487
2	2	4-5	-	5.94-6.35	Germanium	6.1	4.390	± 0.103	± 0.258
3	1	3-4	-	6.79-7.25	N-Bk7 Borosilicate Glass	7.1	3.674	± 0.115	± 0.434
4	2	7-8	-	6.92-7.13	N-Bk7 Borosilicate Glass	7.1	7.857	± 0.053	± 0.221
5	2	-	1-2	6.97-9.44	N-Bk7 Borosilicate Glass	7.1	1.053	± 0.618	± 0.454
Location	Inside	Outside	Outside						
6	2-3	-	1	7.28-5.95	Germanium	6.1	2.887	± 0.333	± 0.690
7	2-3	-	1	7.28-5.95	N-Bk7 Borosilicate Glass	7.1	2.135	± 0.333	± 0.690
8	1-2	1	-	4.82-6.22	Germanium	6.1	1.914	± 0.350	± 0.380

It can be seen from inspection of Table 23 that various combinations of materials and thicknesses can be used to create the desired CTE. The inside thickness can be varied with LPBF. The outside thickness can only be varied by approximately 0.5mm when applying the material with DED. For this reason, fixed thicknesses of 1 and 2mm have been used for the outside thickness.

Many of the proposed thicknesses for controlled CTE are outside what is capable with the manufacturing technique. Cladding onto a thickness of 1mm may present issues with warping, ruling out the feasibility of numbers 5 and 6. The larger inside thicknesses required when using Ti64Al with Invar means numbers 1-4 could provide an unwanted increase in mass. The CTE change from an applied tolerance to the inside thickness is the least with numbers 1-4 of between ± 0.053 and ± 0.185 . For the outside thickness an applied tolerance will have a greater effect on the thinner 1mm compared to the 2mm.

The optimum suggested arrangement for Germanium would be number 8, and number 7 for Borosilicate glass. These two arrangements use the least material, but display less CTE variance due to dimensional changes compared to their alternatives.

It can be seen that the variance in thicknesses of the bonded cylinder materials can have a large effect on the CTE, depending on the arrangement, material type, and thickness. It is difficult for the design engineer to tailor the CTE if the assumed tolerance can change the CTE by a significant amount. A new solution has been proposed by using an auxetic lattice structure inside the cylinder which can be tweaked in the CAD stage to produce a desired CTE which is less effected by the part tolerance due to a wider window. The design has been outlined and explored in the next part of this chapter.

5.4 Tuneable Auxetic Structure

Adjusting the co-efficient of thermal expansion (CTE) by using two bonded cylinders of different materials has been shown to be conceptually effective, however it has also outlined many problems. One problem identifies the effect of tolerance on CTE. A tolerance of only $\pm 250\mu\text{m}$ can produce a CTE that is $\pm 1.072\mu\text{m/mK}$ with arrangement number 5. This shows that changes in the thicknesses of either material will affect the CTE. It is proposed that an extruded 2D structure of an auxetic nature be placed inside the cylinder to provide additional material to the inner thickness.

An auxetic structure provides a negative Poisson's ratio meaning it can deform in on itself when compressed. This is useful for placing in a cylinder where the outside compression or extension applied from a material with a lower or higher CTE, will produce the opposite reaction on the auxetic structures inside radius.

Providing a design engineer with the ability to tailor CTE by making simple geometry changes in CAD is very advantageous. This means that the inner annulus can be adjusted to the same CTE as the lens material. Investigation of auxetic structures will allow for the forces created by the radial restriction to be converted into bending moments evenly across the radius, whilst maximising stiffness. The structure allows the most efficient distribution of thermal expansion forces as the structure changes temperature.

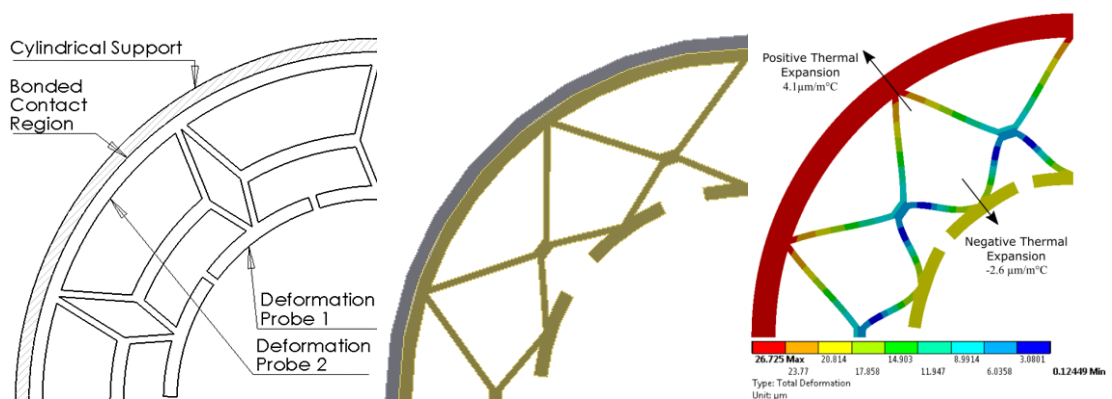


Figure 115. Demonstration of the greatest negative CTE the structure can produce. Simulation of Ti64Al Auxetic structure bonded with Invar showing before and after temperature change. Total Deformation image at 140x the true scale. Arrangement shown is at $\theta = 38^\circ$, $L_i = L_o = 1\text{mm}$, $L_a = 2\text{mm}$.

To fully define the auxetic structure, the variable and fixed dimensions need to be assigned. The shape of the auxetic structure is determined by a radius which changes depending on the angle of the tangent line appended to the radius. This allows for even distribution of force to the neighbouring auxetic structure. Every variable shown in Figure 116 (L_i , L_o , L_a , L_1 , L_2 , and L_3) will affect the CTE and stiffness; however, the angle θ is the desired variable for tailoring CTE since macro changes in thicknesses and diameters maybe hard to manufacture accurately. Studying Figure 116 it can be seen that the

adjoining member (L_a) is twice the thickness as each member it connects with ($L = \frac{L_a}{2}$). This ensures that the adjoining members are conserving force for application into the angle to create stretching of the structure, rather than deformation or bending of the adjoining members. The effect between every variable will be considered in an in-depth analysis using a static- structural model, whereby the deformations will be analysed before and after raising the temperature by 100°C . The model assumes that the temperature distribution is isotropic throughout both materials.

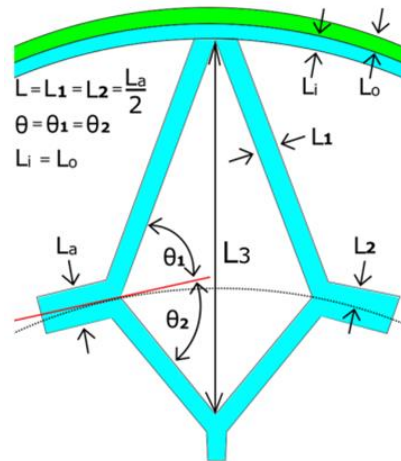


Figure 116. Shows both equal angles theta on its most efficient tangential line. All other variables are outlined.

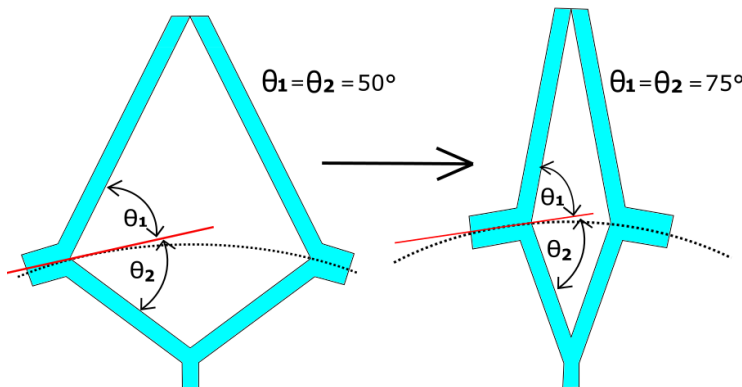


Figure 117. Diagram showing the angle change across the tangent line and its subsequent effect on the position of adjacent members.

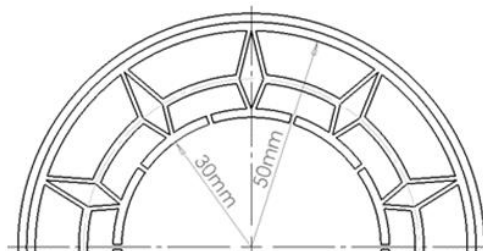


Figure 118. Fixed radius at both the inside and outside. These locations will be used determine the CTE in simulation and testing.

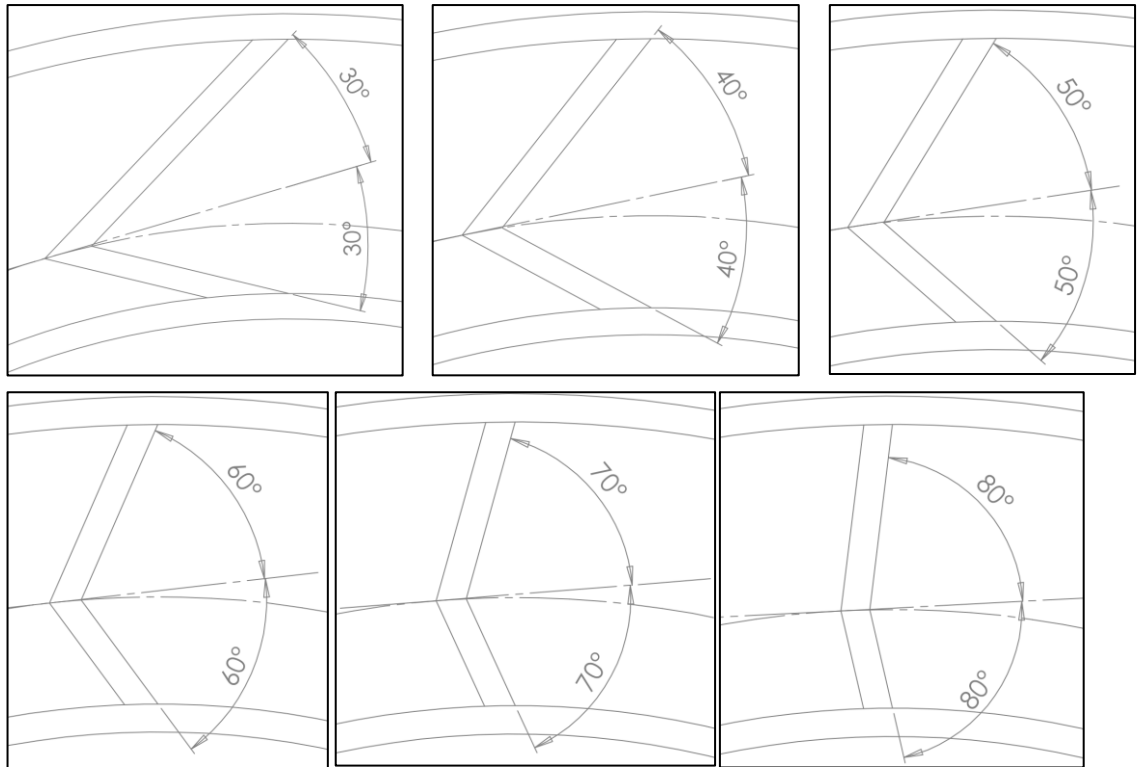


Figure 119. Series of CAD drawings showing the effect of angle change on the radius of the adjoining members.

The baseline simulation will set a standard design profile which can be tweaked in subsequent design iterations. The design will be manufactured in invar using LPBF on the AM400, and 316L stainless steel will be cladded to the outside. The material choice is down to manufacturing capabilities at the present time. For the purpose of the simulation it will be assumed that the two materials are bonded and will not separate.

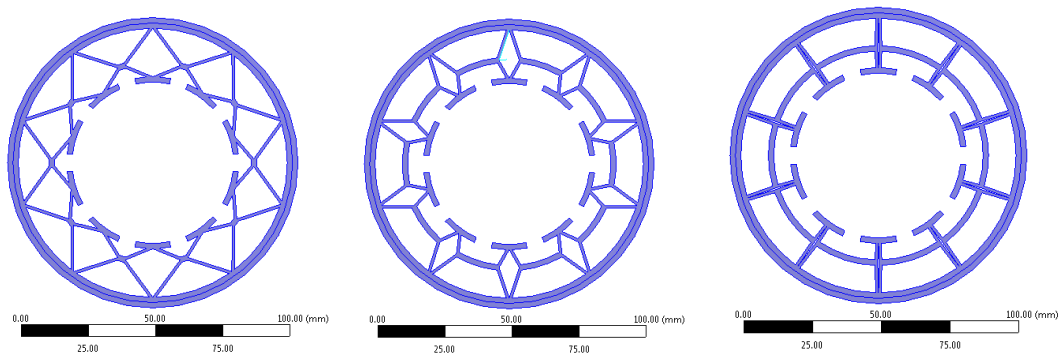


Figure 120. Series of CAD images showing the angle change for auxetic arrangement concept where the 38° minimum to 66° median and the 88° maximum angle.

5.4.1 Thermal Expansion Simulation

A parametric study has been carried out to assess the effectiveness of the structure at adjusting the co-efficient of thermal expansion. The simulation will be setup as outlined in chapter 8.2.

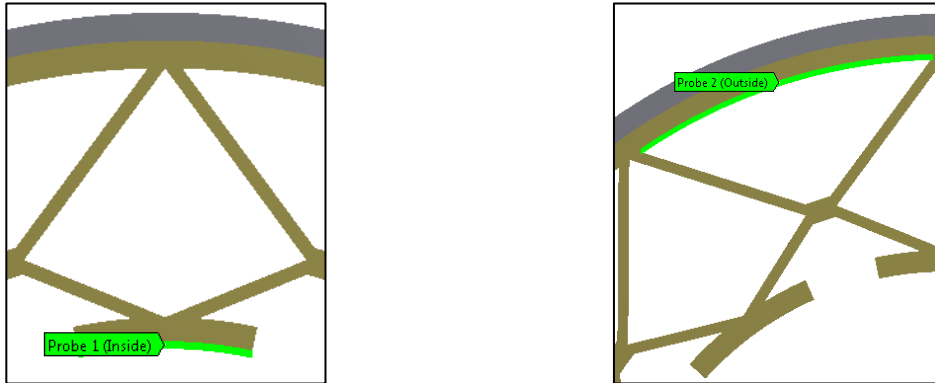


Figure 121. ANSYS Image showing the deformation probe location where the y-direction movement is measured.

The mesh sensitivity study was conducted to determine the effect of increasing the mesh density by adjusting the element sizing for Quadrilateral and Triangles from 0.5 to 0.25 and 0.2mm. These element sizes have been chosen to ensure there are a whole number of elements inside the minimum thickness of 1mm. It is assumed that $L_i = L_o = 1\text{mm}$. $L_a = 2\text{mm}$, and the material is invar with a 316L bonded ring.

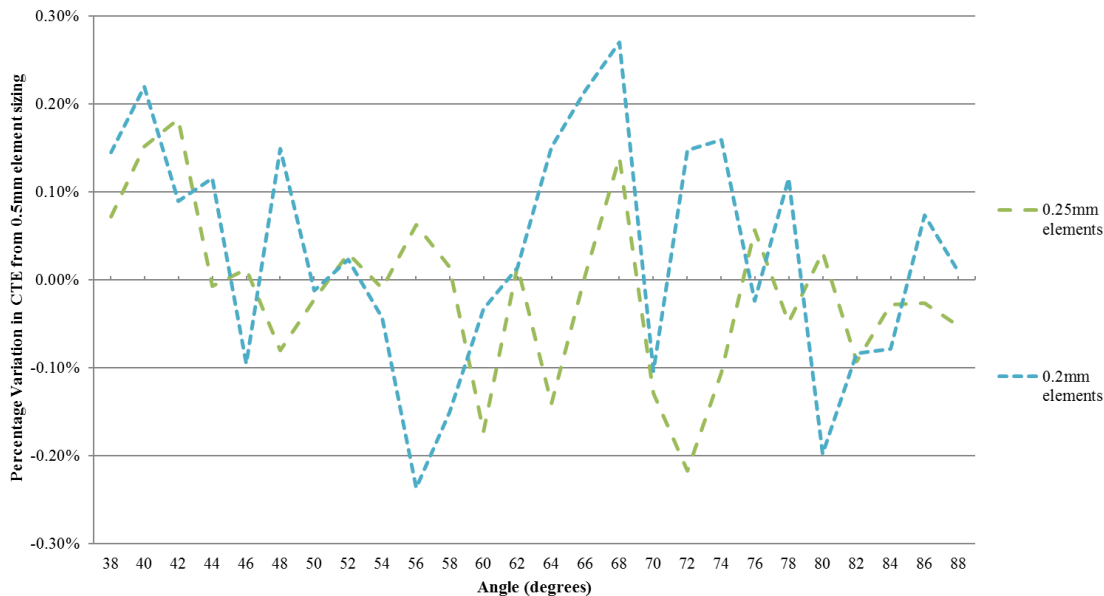


Figure 122. Mesh sensitivity study showing percentage change in deformation compared to a 0.5mm element size baseline. Invar structure with 316L clad.

The sensitivity study shows that 0.5mm element sizing can be used for determination of CTE within $\pm 0.2\%$. The simulation has been set to first determine the effect of adjusting

the angle θ on the CTE when applying in Invar clad to 316L (Figure 123) and Ti64Al (Figure 124), for different member thicknesses 1, 1.5, and 2mm.

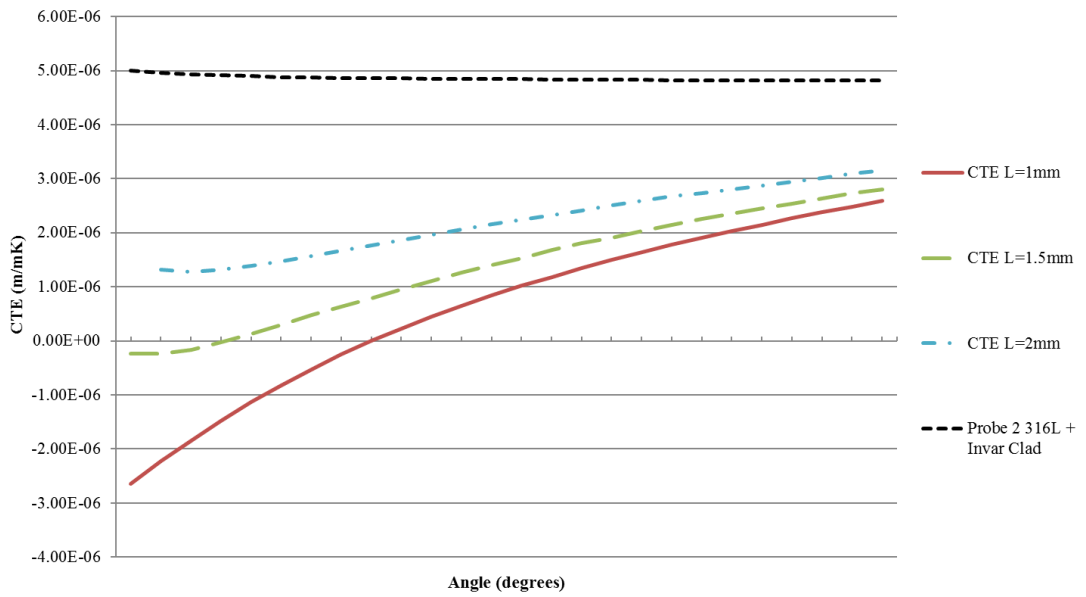


Figure 123. Graph displaying the simulated angle change against CTE for each member thickness L for materials **316L structure**, with an **Invar clad**. $L_i = L_o = 1mm$. $L_a = 2mm$.

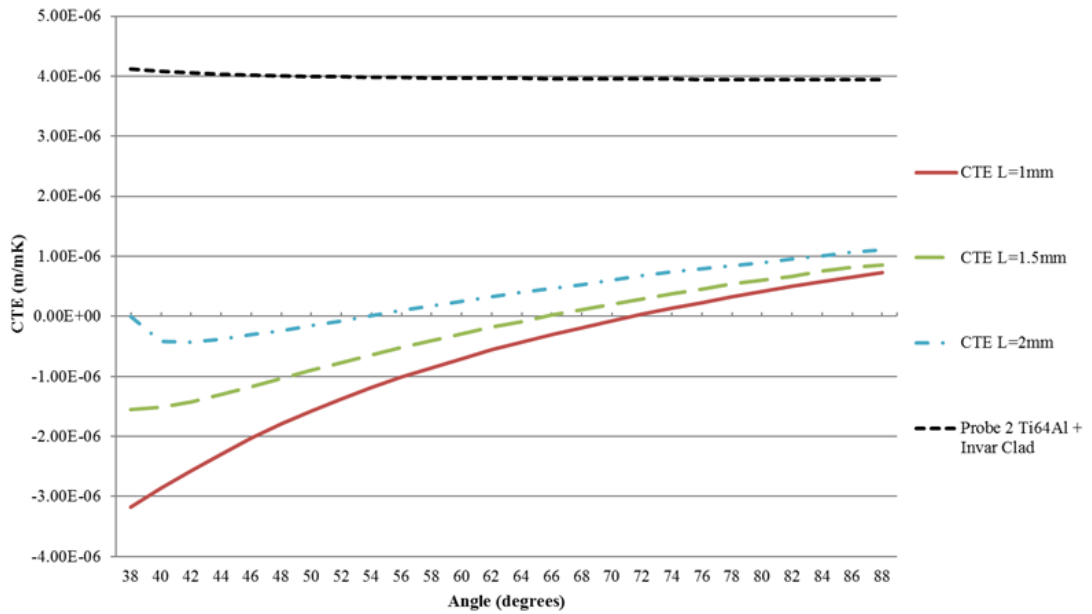


Figure 124. Graph displaying the simulated angle change against CTE for each member thickness L for materials **Ti64Al structure**, with an **Invar clad**. $L_i = L_o = 1mm$. $L_a = 2mm$.

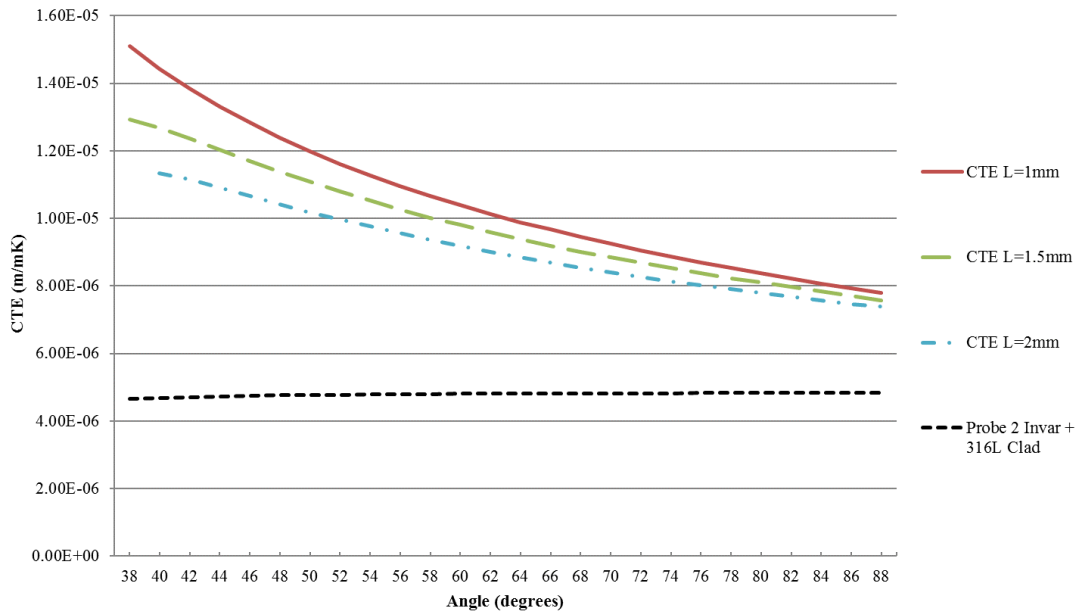


Figure 125. Graph displaying the simulated angle change against CTE for each member thickness L for materials **Invar structure**, with an **316L clad**. $L_i = L_o = 1mm$ $L_a = 2mm$.

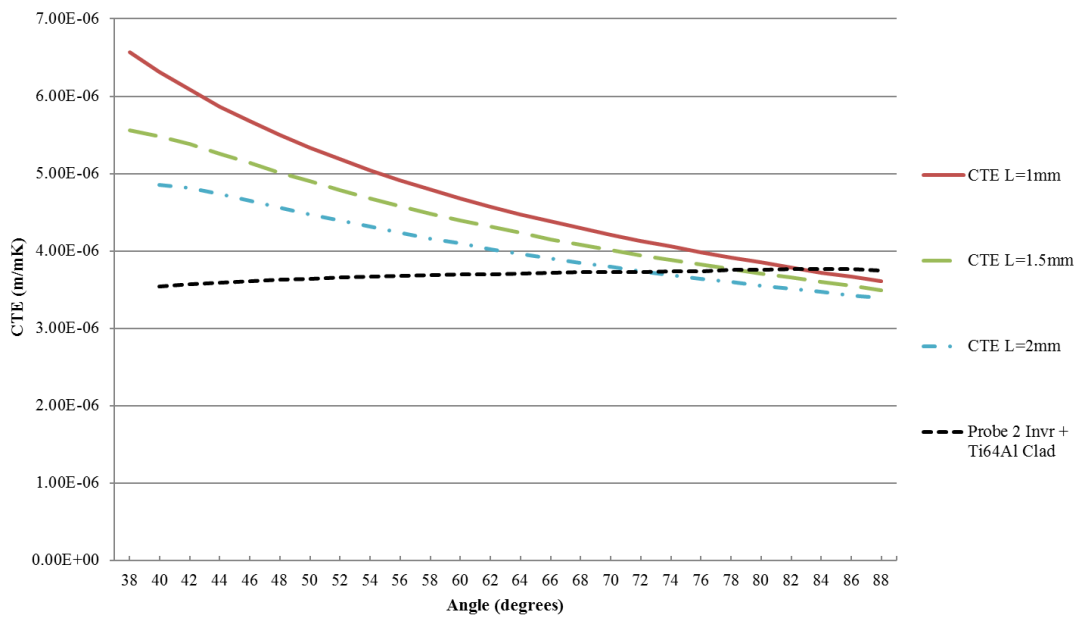


Figure 126. Graph displaying the simulated angle change against CTE for each member thickness L for materials **Invar structure**, with a **Ti64Al clad**. $L_i = L_o = 1mm$ $L_a = 2mm$.

It is shown from the simulation results that a significant range of thermal expansion can be tailored by adjusting the angle of the auxetic lattice structure. The range can be adjusted by selecting a material combination for the structure and the clad depending on the required CTE. As the member thickness increases, the tailorable range decreases as the stiffness and resistance to movement increases. To investigate the effect of the member thickness on stiffness, further simulation will be required.

5.4.2 Stiffness Simulation

To determine the effectiveness of the thermal expansion-controlled design, the stiffness will be analysed in ANSYS.

Calculating the stiffness of the lattice structure provides a means of comparing designs for their structural efficiency. Stiffness is calculated using the following equations;

$$k = \frac{F}{\delta} \quad (5.3)$$

Where; $k = \text{stiffness (N/m)}$ $F = \text{Force (N)}$, $\delta = \text{deflection(m)}$

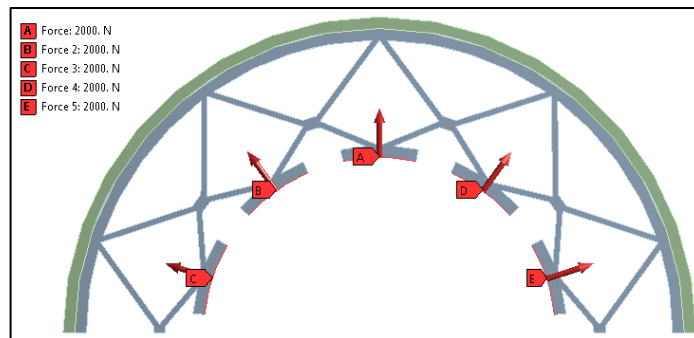


Figure 127. ANSYS Images showing radial forces applied to attain deformations for calculation of stiffness.

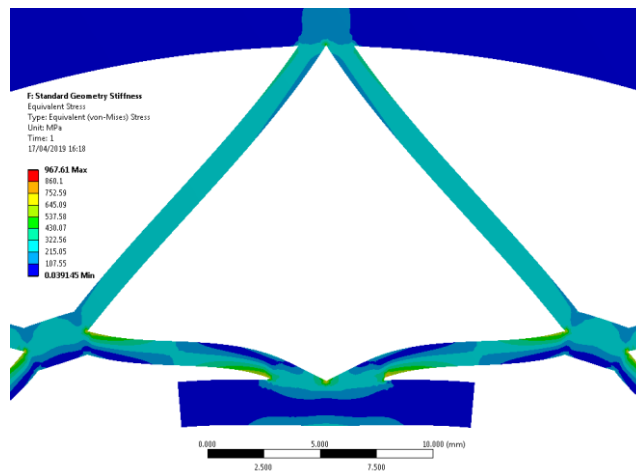


Figure 128. Simulation Image showing von-mises stresses and deformations at 22 times the true scale for visualisation purposes.

To analyse the model's stiffness sensitivity to changing force, the stiffness has been plotted for a range of forces. The linearity of stiffness with force shows the values for deflection scale with force. This shows that using any value for force in this range can be used to calculate the stiffness.

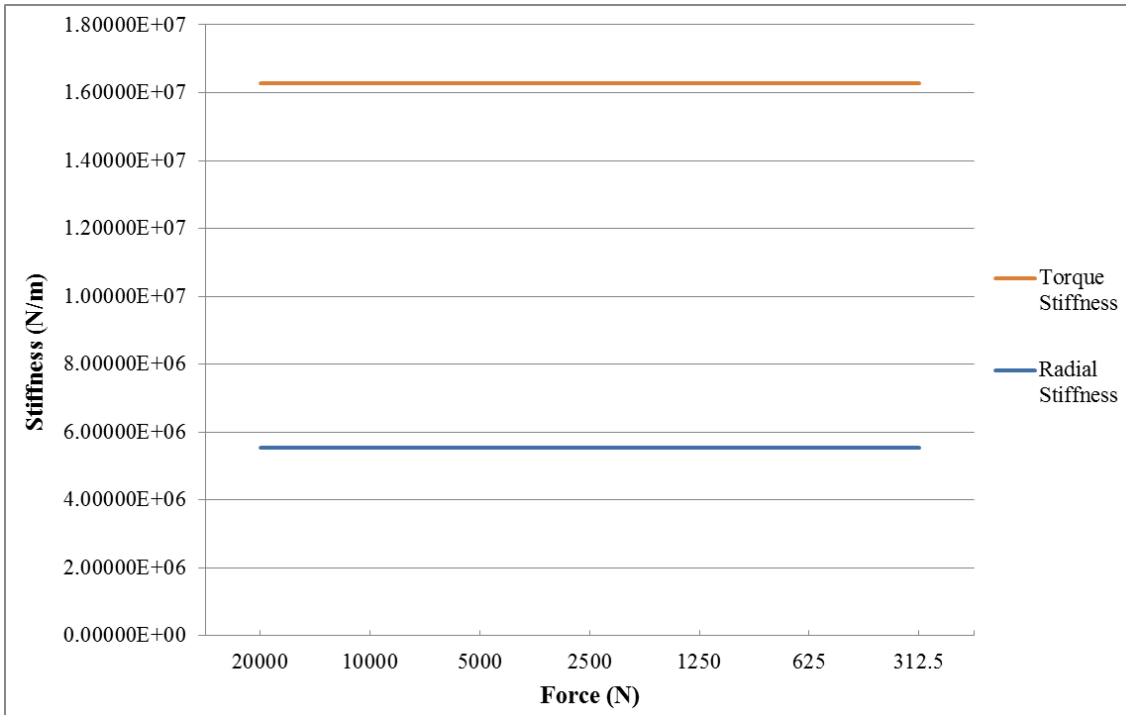


Figure 129. Plot of simulated results for stiffness against force applied for confirmation of force linearity with deformation result. $L = 1mm$, $\theta = 38^\circ$

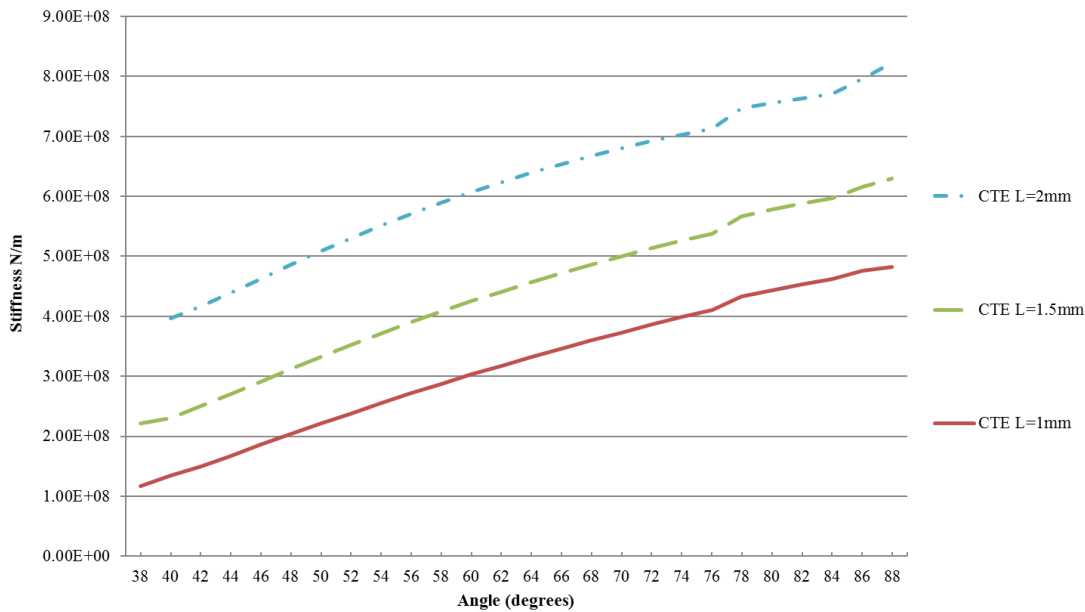


Figure 130. Graph showing the Stiffness for $L=1, 1.5,$ and $2mm$ for each possible angle for 316L clad invar structure.

It can be seen that the stiffness is very poor when compared to the solid bulk material. Stiffness can be directly compared directly as a ratio of the elasticity modulus for the material. The maximum stiffness achieved at 88° and $L = 2mm$ is approximately $0.81GPa$ compared with elasticity modulus of $148GPa$ for invar. Therefore, the maximum stiffness achieved is 0.548% of the original material. Under the same conditions, 316L

provides 1.07GPa of stiffness (0.554% of the original material) and Ti64Al provides 0.626GPa (0.553% of the original material).

5.4.3 Discussion on tuneable auxetic structure simulations

The tailorable auxetic structure provides a theoretical ability to tailor the thermal expansion of the inside annulus over a wide range. The choice of materials requires consideration whether the requirement is to tailor the CTE higher or lower than that of the material of the structure. For example, a 316L structure and a 1mm thick invar clad when $L = 1mm$ will produce a tailorable range from -2.8 to 2.5 $\mu\text{m/mK}$ depending on the angle. When the materials are switched around, the same arrangement produces a CTE of between 15.1 to 7.8 $\mu\text{m/mK}$. The choice of member thickness (L), will dictate the stiffness. The stiffness is expected to be much lower than the solid material. For an invar structure, the maximum stiffness achieved is approximately 0.81GPa at 88° where $L=2mm$, and 0.49GPa where $L=1mm$, which is only 0.548% and 0.333% of the solid materials stiffness.

5.5 Tuneable porosity structure

This section investigates the possibility of adding porosity by design into the cylindrical lens mount. The porosity has been procedurally designed across a 2D plane to tailor the CTE radially, similarly to the auxetic expansion designs. A tailored porosity solution will be analysed to determine its effectiveness compared with the auxetic solution. Two tailored porosity solutions will be proposed whereby one has a single array of 2D holes with the maximum number of holes for the given cross-section thickness, where the minimum wall thickness is still manufacturable. The second design will take the same cross-section thickness and place as many rows of 2D holes with 1mm diameter as possible, whilst still maintaining a manufacturable minimum wall thickness. Analysis will be performed using a thermo-mechanical simulation to determine the CTE for different hole diameters. It will analyse the deformations on the inner lens mount surface, to determine its effectiveness compared with the expansion gaps provided in the auxetic design.

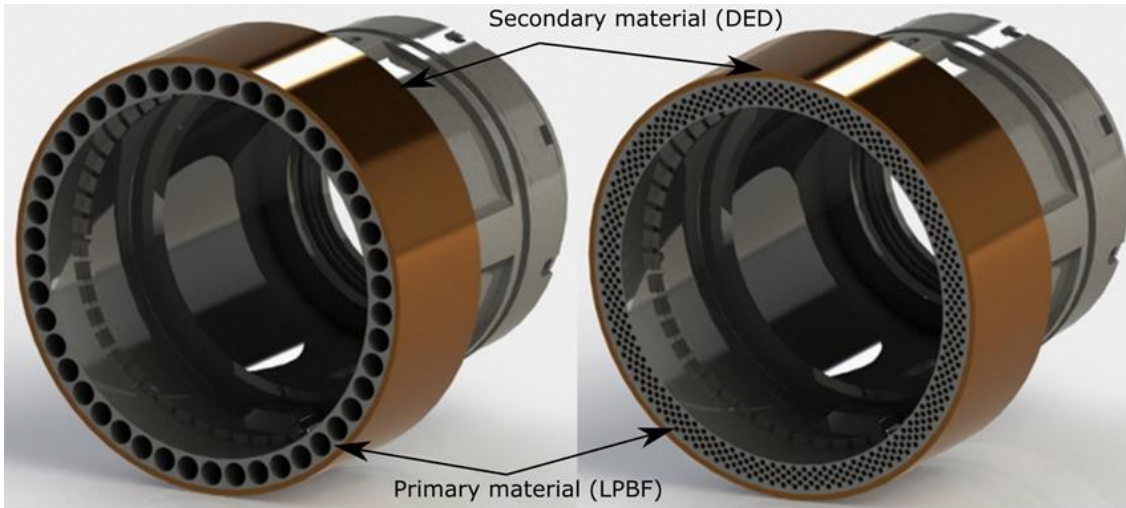


Figure 131. Rendered image of a single and multi-array tailored porosity structure fully integrated inside an optical system body.

Table 24 shows the material arrangements to be simulated, and their corresponding CTE's without the porosity added. These values have been obtained using the same thermo-mechanical simulation setup as outlined in section 8.2. These baseline values will be used to determine the effectiveness of the single and stacked porosity design visualised in Figure 131.

No.	Primary material	Secondary clad material	Clad thickness (mm)	CTE $\mu\text{m/mK}$
1	316L	Invar	1	13.90
2	316L	Invar	2	12.31
3	Invar	316L	1	4.55
4	Invar	316L	2	6.74
5	Ti64Al	Invar	1	7.57
6	Ti64Al	Invar	2	6.35
7	Invar	Ti64Al	1	2.40
8	Invar	Ti64Al	2	3.27

Table 24. Reference CTE for 5mm thick ring with clad material, without any porosity added

5.5.1 Design 1 – Single array

The single array of 2D holes has been designed to place as many 4mm diameter holes within the 5mm thickness. This provides a thickness of 0.5mm on the inside and outside to fit within the 5mm thickness. To maintain a similar thickness between each hole, 46 holes have been placed equally, giving a minimum thickness of 0.44mm between each hole. A drawing with all dimensions is show in Figure 132. Depending on the arrangement of materials, deformations will occur around the holes to create an overall

change in thermal expansion in the inner radius. The deformations will be uneven, and the difference between the maximum and minimum will be plotted. The average of maximum and minimum CTE will be plotted for a range of hole sizes between 4-2mm. The centroid will remain fixed while the diameter changes.

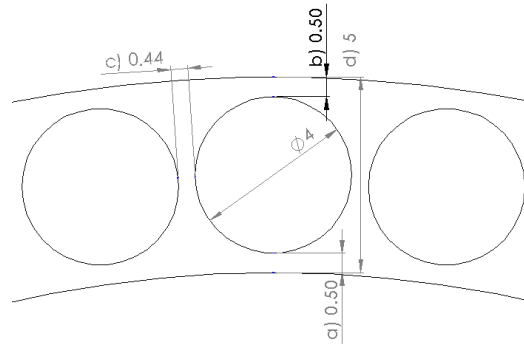


Figure 132. Dimensions for Single array in millimetres.

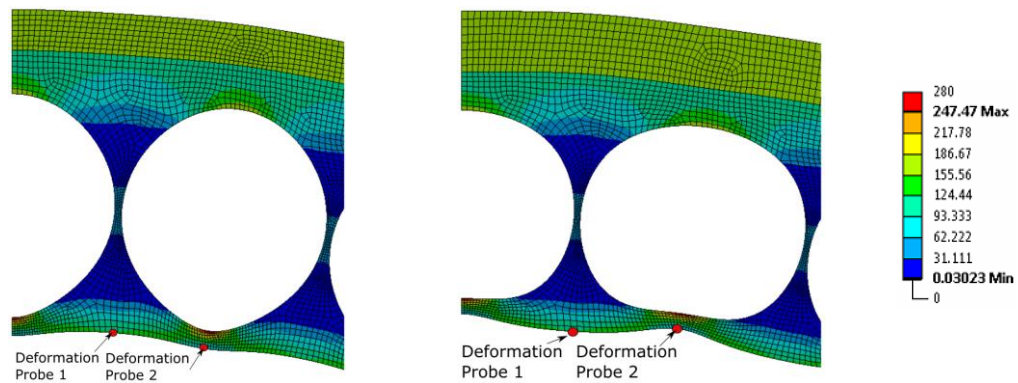


Figure 133. Von-mises stress plots in MPa with 130X scaled deformation, showing CTE probe locations with Invar cladded with 316L (left) and 316L cladded with Invar (right).

To analyse the effect of adjusting the holes diameter, an average of deformation probe 1 and 2 must be made. To understand the contribution to the maximum and minimum CTE, the differences between probe position 1 and 2 have been plotted in Figure 134.

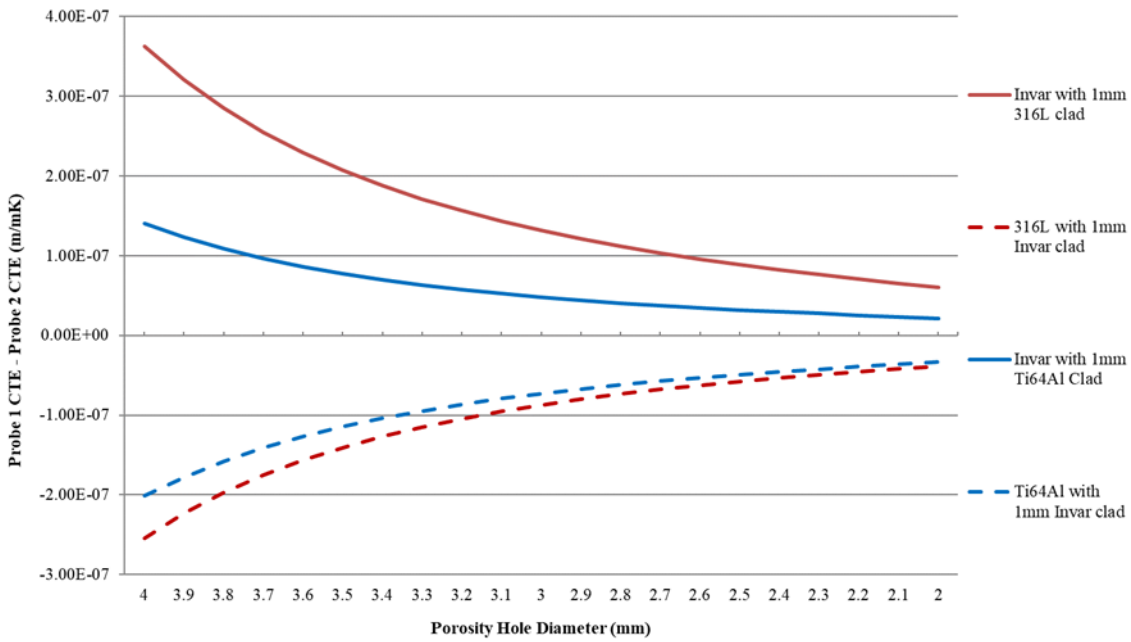


Figure 134. Simulated CTE difference caused by deformation differences between probes 1 and 2 for the single porosity array after a 100°C temperature change.

The differences between probe 1 and 2 and necessary to determine the amount change in CTE across the annulus of the lens. At the largest diameter of 4mm it can be seen that with Invar and a 1mm 316L clad there is approximately $0.365\mu\text{m}/\text{mK}$ difference. This means the CTE will be $\pm 0.1825\mu\text{m}/\text{mK}/\text{C}$, with a significant risk of lens decentre over many cycles. The thermal expansion for each array is plotted in Figure 135 and Figure 136, as a function of the hole diameter. Changing the hole diameter will change the thermal expansion of the inner radius by causing changes to the internal strains around the holes.

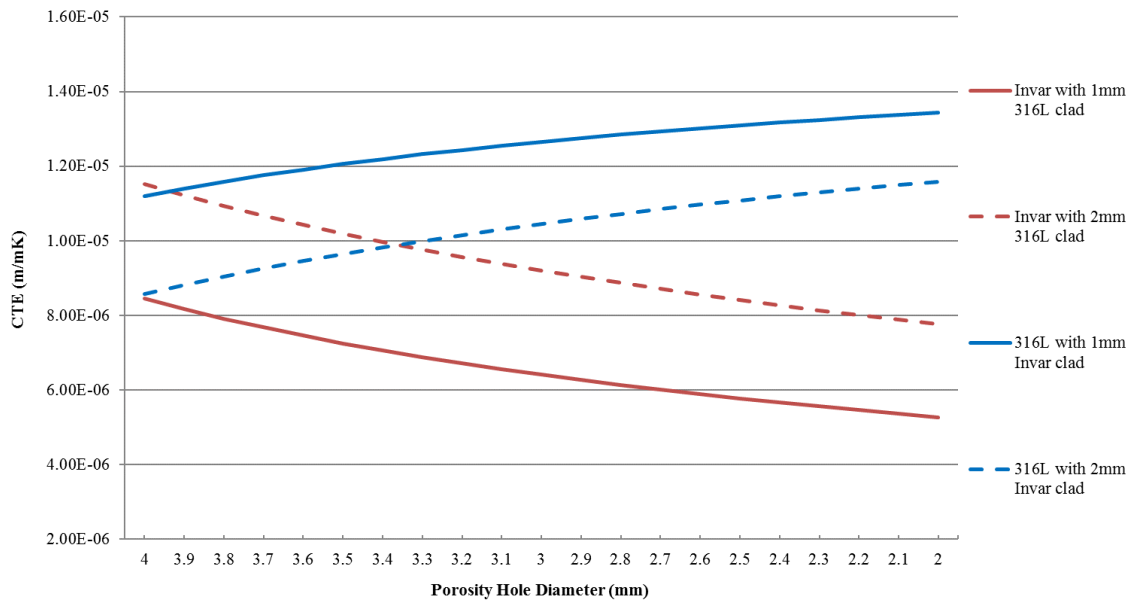


Figure 135. Thermal Expansion simulation for the **single array** for **Invar** and **316L** combinations.

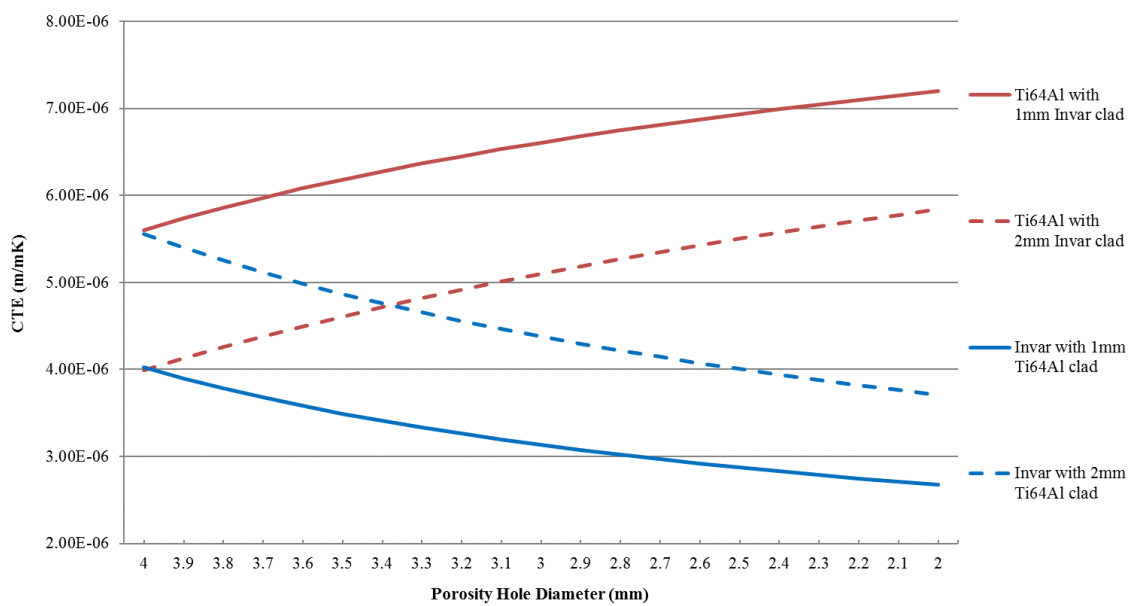


Figure 136. Thermal Expansion simulation for the **single array** for **Invar** and **Ti64Al** combinations.

To analyse the effectiveness of each arrangement, the percentage difference is taken for the maximum hole diameter (4mm), compared to that of the same structure and material arrangement with no porosity. The reference values with no porosity are found in Table 24. This value is then subtracted from the percentage difference for a hole diameter of half its size (2mm), to provide the effectiveness percentage. This represents the overall effectiveness of the structure and material arrangement at creating CTE change. It can be by equation 5.5.

$$Effectiveness \% = \left(\left(\frac{\alpha_o - \alpha_1}{\alpha_1} \right) - \left(\frac{\alpha_o - \alpha_2}{\alpha_2} \right) \right) * 100 \quad (5.5)$$

Where; α_o = reference CTE from table 16, α_1 = CTE for maximum hole diameter, α_2 = CTE for half the maximum hole diameter.

No.	Primary material	Secondary material	Clad thickness (mm)	CTE change		
				ø 4mm (%)	ø2mm (%)	Effectiveness (%)
1	316L	Invar	1	24.1	3.6	20.5
2	316L	Invar	2	43.8	6.3	37.6
3	Invar	316L	1	46.2	13.8	32.4
4	Invar	316L	2	41.5	13.2	28.3
5	Ti64Al	Invar	1	35.1	5.2	29.9
6	Ti64Al	Invar	2	59.2	8.8	50.4
7	Invar	Ti64Al	1	40.5	10.2	30.3
8	Invar	Ti64Al	2	41.2	11.8	29.3

Table 25. Simulated percentage CTE change for the single array design, compared with simulated values with no porosity.

By analysing the Figure 134 to Figure 136, it can be seen that as the hole size diameter approaches 2mm, the simulated CTE comes very close to the CTE in a system without any porosity. A system without any porosity has CTE values presented in table 21. At a hole diameter of 2mm for a 316L structure with an invar clad, the CTE is only 3.57% (1mm clad) and 6.26% (2mm clad) away from the maximum CTE obtainable without any porosity. With invar and a 316L clad there is a 13.19% and 13.78% difference under the same criteria. For Ti64Al and invar the maximum percentage difference is 11.81% for invar with a 2mm Ti64Al clad, all other configurations are less. This shows that further CTE tailoring by reducing hole size diameter maybe achievable, but with limited gain.

In the case where the diameter of the hole is 4mm, the diameter is in its maximum condition and cannot be built any larger due to material thickness constraints. At this diameter there is wide range of CTE change depending on the material arrangement, from 24.1% to 59.2%. The effectiveness of the arrangement at adjusting the CTE can be determined by the difference between the percentage difference at 4 and 2mm. This represents the percentage of the tailorable range. A greater effectiveness will provide a wider CTE range for the engineer to choose from, but this also means the dimensional tolerances need to be tighter to limit changes to the CTE.

To tailor the radial CTE the same as the CTE of the lens material, a suitable hole diameter has to be chosen. Linear interpolation has been used to obtain values within the 100 μ m range.

Primary Material	Outside Material	Outside Thickness (mm)	Lens Material	Lens CTE (μ m/mK)	Required Hole Diameter (mm)
Invar	316L	1	Germanium	6.1	2.77
Invar	316L	1	Borosilicate Glass	7.1	3.42
Ti64Al	Invar	1	Germanium	6.1	3.58
Ti64Al	Invar	1	Borosilicate Glass	7.1	2.2

Table 26. Proposed single array hole diameter to produce a matched CTE.

5.5.2 Design 2 –Stacked array

The stacked array has been designed to fit as many 1mm diameter holes into the 5mm thickness as possible, with an even distribution of material of approximately 250 μ m between each diameter. This thickness is maintained across the inside diameter with a minimum of 250 μ m thickness, with a 750 μ m outside thickness. To make a direct comparison with the single array, the thicknesses labelled (a) and (c) have been kept as close as possible in both cases. This ensures deformation is uniform across the holes. The outside dimension labelled (b) has an extra 250 μ m added compared to the single array. This will help preserve the geometry of the smaller holes on the stack array from weld penetration during laser cladding.

Looking at the benchmarking in chapter 5.1.4, a minimum nominal hole diameter with 316L is 0.7mm, but achieves approximately 0.3mm instead. Any specified diameter less than 0.7mm will not print. The simulation will run from 1mm down to 0.1mm diameter hole sizes, but anything below 0.3 cannot be printed.

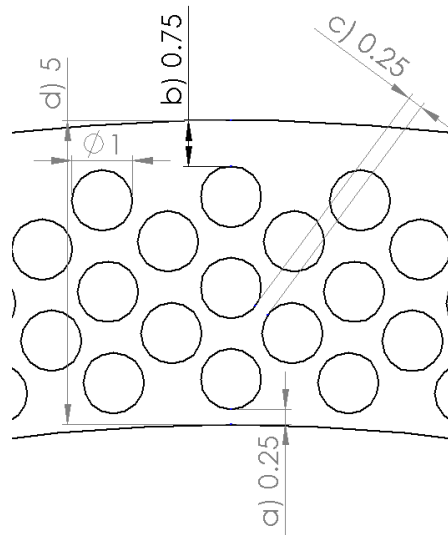


Figure 137. Dimensions for Stacked array in millimetres.

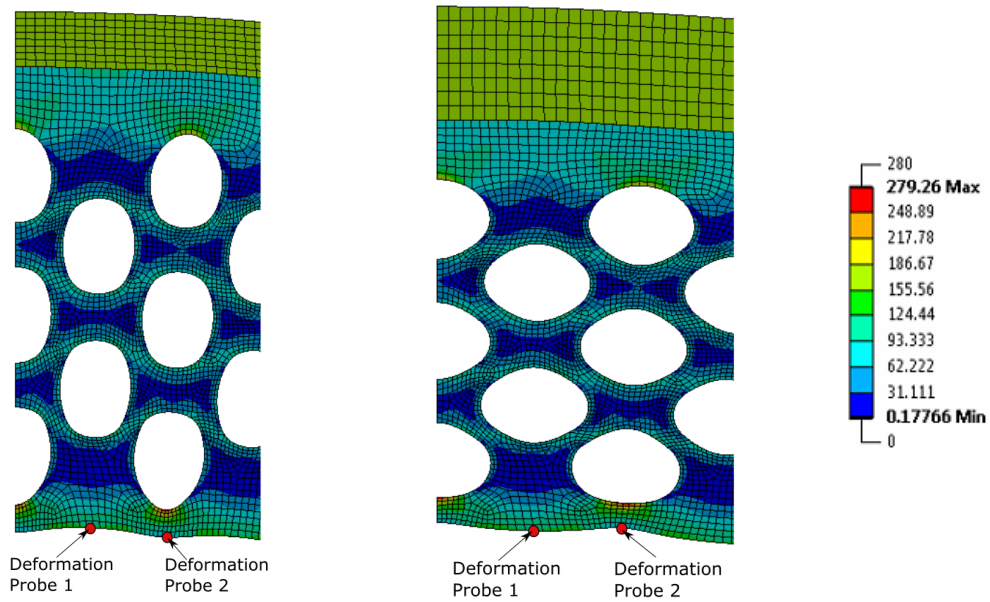


Figure 138. Von-mises stress plots with 130X scaled deformation, showing CTE probe locations with Invar cladded with 316L (left) and 316L cladded with Invar (right).

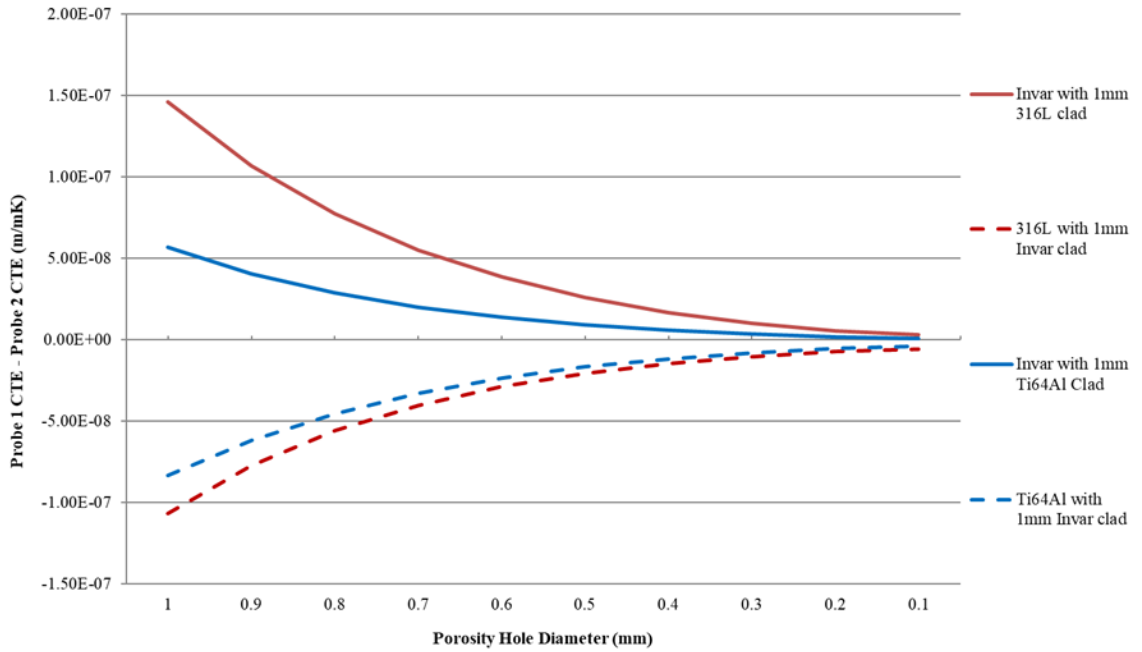


Figure 139. Simulated CTE difference caused by deformation differences between probes 1 and 2 for the stacked porosity array.

As discussed for the single array, the difference across probe 1 and 2 needs to be minimised as much as possible to reduce increase the stability of the required CTE. At a maximum hole diameter of 1mm for Invar with a 1mm 316L clad, a CTE difference of $0.149\mu\text{m/mK}$ will be experienced across the inside annulus. Moving toward smaller hole diameters in the stacked array, the difference can come down to as little as $0.026\mu\text{m/mK}$ for 0.5mm, which could be regarded as negligible. To adjust the thermal expansion of the inner radius, the hole diameter is adjusted. This causes a change in the strain rates around the holes, and a change in the overall, average CTE from probe 1 and 2.

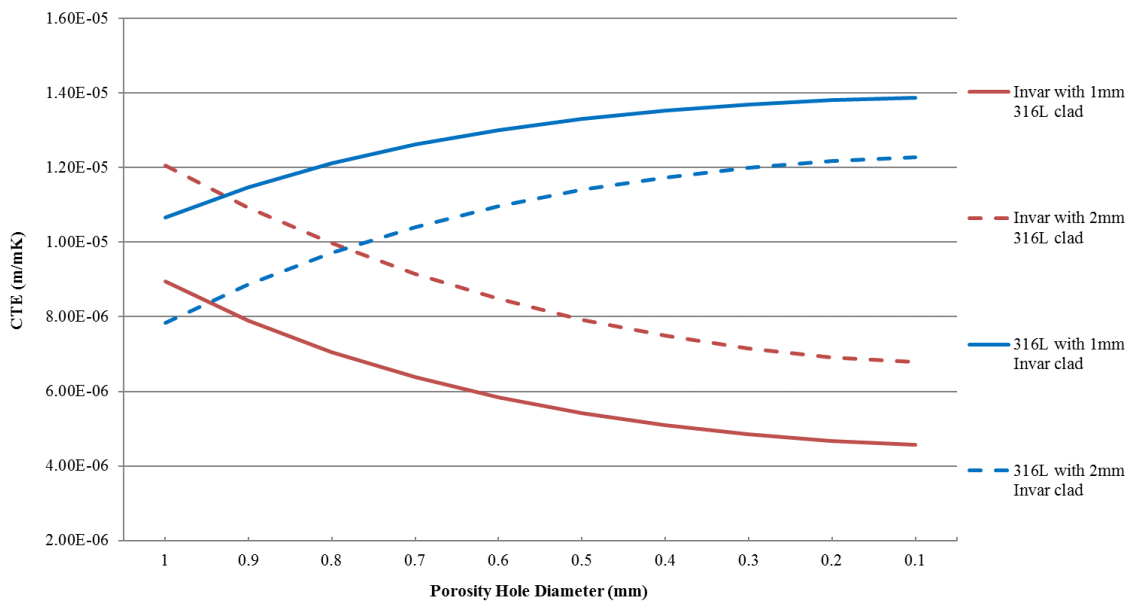


Figure 140. Thermal Expansion simulation for the **stacked array** for **Invar** and **316L** combinations.

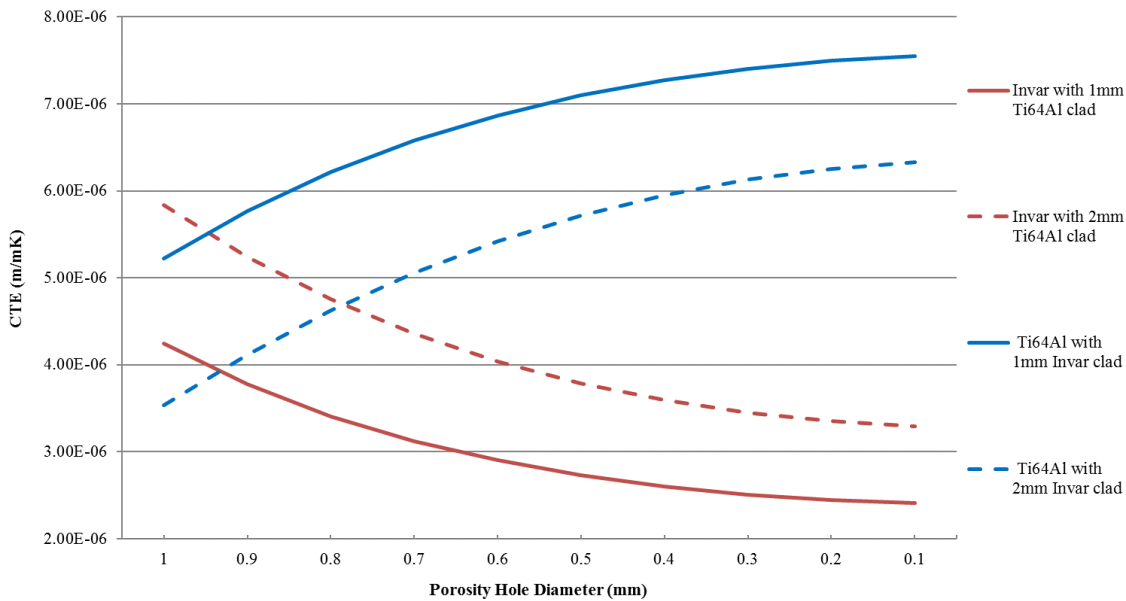


Figure 141. Thermal Expansion simulation for the **stacked array** for **Invar** and **Ti64Al** combinations.

No.	Primary material	Secondary material	Clad thickness (mm)	CTE change			Effectiveness (%)
				Ø1mm (%)	Ø0.5mm (%)	Ø0.1mm (%)	
1	316L	Invar	1	30.39	4.43	0.21	25.96
2	316L	Invar	2	57.04	8	0.26	49.04
3	Invar	316L	1	49.15	15.97	0.74	33.18
4	Invar	316L	2	44.09	15.05	0.64	29.05
5	Ti64Al	Invar	1	44.93	6.56	0.20	38.38
6	Ti64Al	Invar	2	79.93	11.23	0.34	68.69
7	Invar	Ti64Al	1	43.48	12.21	0.55	31.26
8	Invar	Ti64Al	2	43.88	13.68	0.56	30.21

Table 27. Simulated percentage CTE change for the stacked array design, compared with simulated values with no porosity.

If the hole size is reduced from 1mm to 0.1mm, the CTE change approaches zero. It has been established that hole sizes of less than 0.3mm cannot be manufactured. Half the diameter of 0.5mm experiences a similar percentage change in CTE as the half diameter of 2mm diameter in the single array. The trends are also similar, where the 316L with 1mm invar clad experiences the least change of only 4%, and the highest with 15.97% for the invar with 316L clad.

Similar to the single array, there are several arrangements that can create the desired CTE to match both borosilicate glass, and germanium. These are outlined in the Table 28.

Primary Material	Outside Material	Outside Thickness (mm)	Lens Material	Lens CTE ($\mu\text{m}/\text{mK}$)	Required Hole Diameter (mm)
Invar	316L	2	Borosilicate Glass	7.1	0.28
Ti64Al	Invar	1	Germanium	6.1	0.83
Ti64Al	Invar	1	Borosilicate Glass	7.1	0.5
Ti64Al	Invar	2	Borosilicate Glass	7.1	0.32

Table 28. Proposed stacked array hole diameter to produce a matched CTE.

5.5.3 Stiffness Simulation

To simulate the stiffness of the porous structures a 2D ANSYS mechanical model has been setup similarly to the stiffness simulation model in chapter 7.4.2. The same material parameters are used as outlined in table 13. The design is without the cladded material and only the primary material. This will enable analysis of just the structure alone. The pressure applied is uniformly applied to the inside diameter at 100MPa. Since the materials used are linear, the stiffness will remain constant regardless of the magnitude of the pressure. This has been demonstrated in section 7.4.2.

The mesh has been chosen to have 0.1mm minimum element sizing with proximity and curvature fitting functions activated.

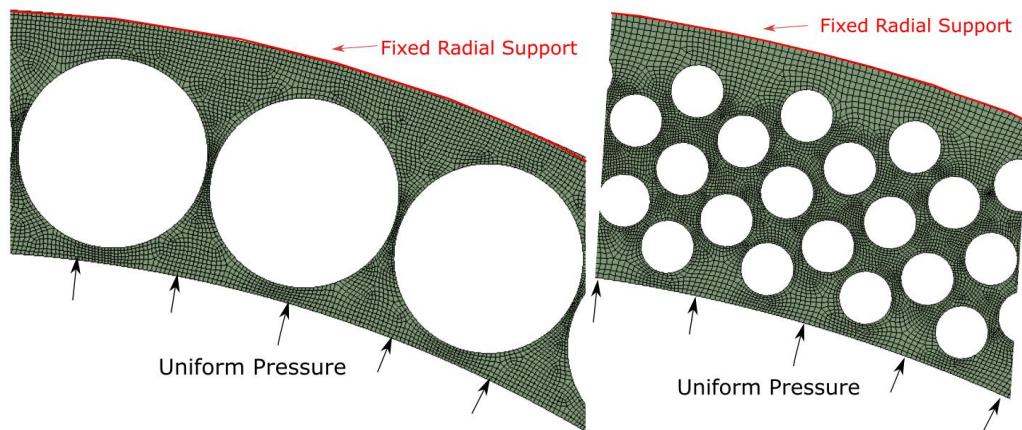


Figure 142. Ansys mech and support locations for the single array (left) and the stacked array (right).

The stiffness has been calculated with the following equation;

$$k = \frac{F}{\delta} \quad (5.6)$$

Where; $k = \text{stiffness (N/m)}$ $F = \text{Pressure (Pa)}$, $\delta = \text{deflection(m)}$

The stiffness values for both single and stacked arrays have been plotted in Figure 143 to Figure 146. Materials Invar, Ti64Al and 316L have been analysed. The probe 1 and 2 locations shown in Figure 133 and Figure Figure 138 have been used to obtain the deformation values used in the stiffness equation above. Figure 143 and Figure 145 show plots for these stiffness values in N/m for each hole diameter and material. Figure 144 and Figure 146 have plotting the stiffness as a percentage of the material's overall stiffness, also known as its elasticity modulus. This provides a way of determining which materials stiffnesses are affected most by the porosity.

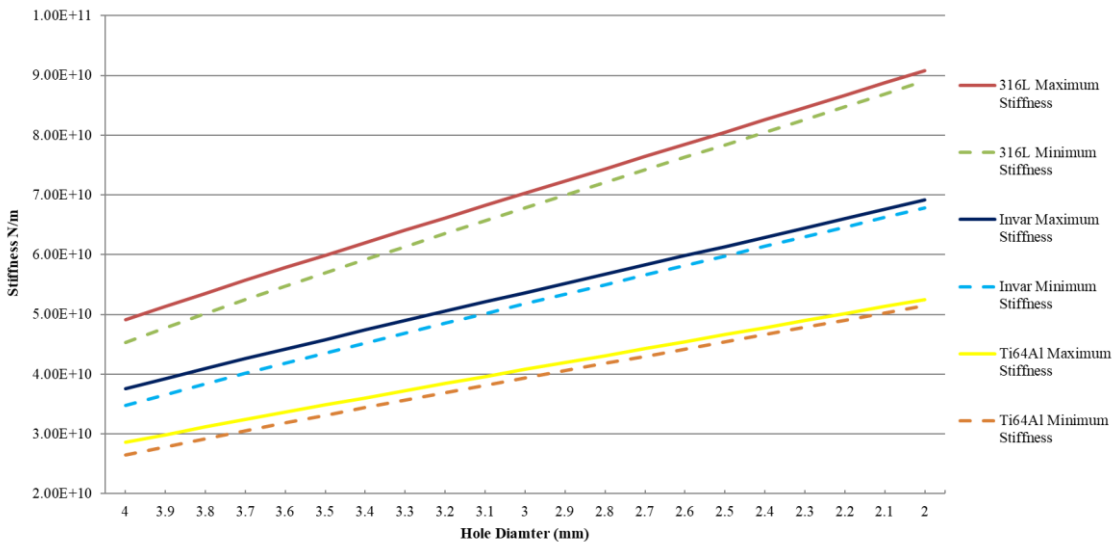


Figure 143. **Single array** stiffness for Invar, Ti64Al, and 316L.

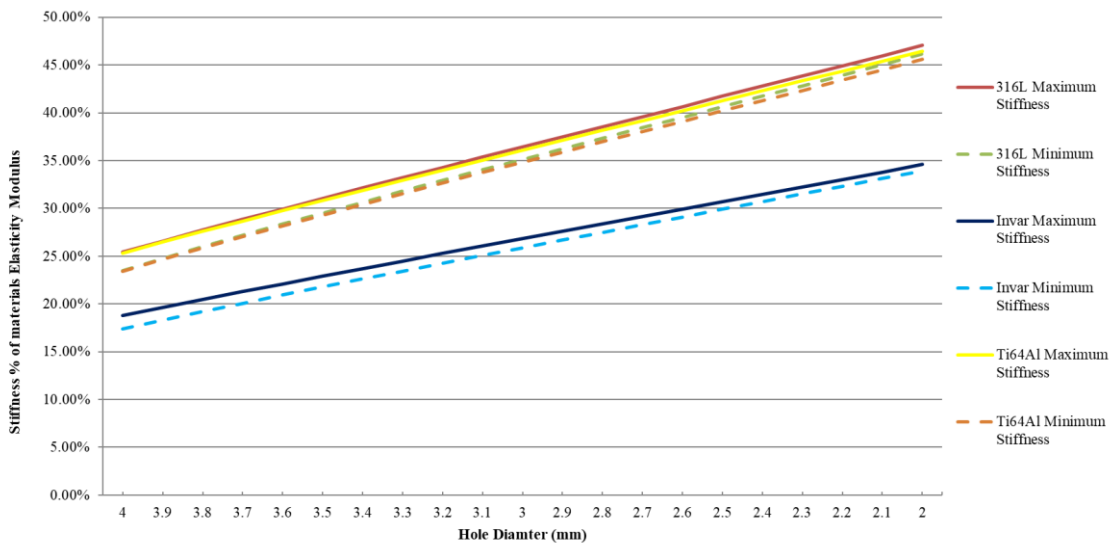


Figure 144. **Single array** stiffness for Invar, Ti64Al, and 316L, as a percentage of the materials elasticity modulus.

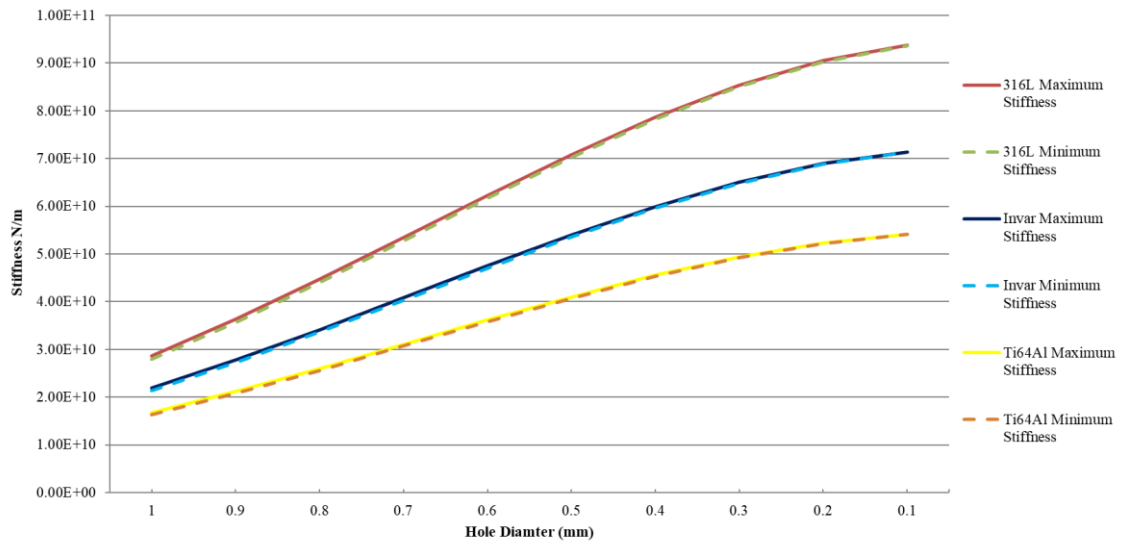


Figure 145. **Stacked array** stiffness for Invar, Ti64Al, and 316L.

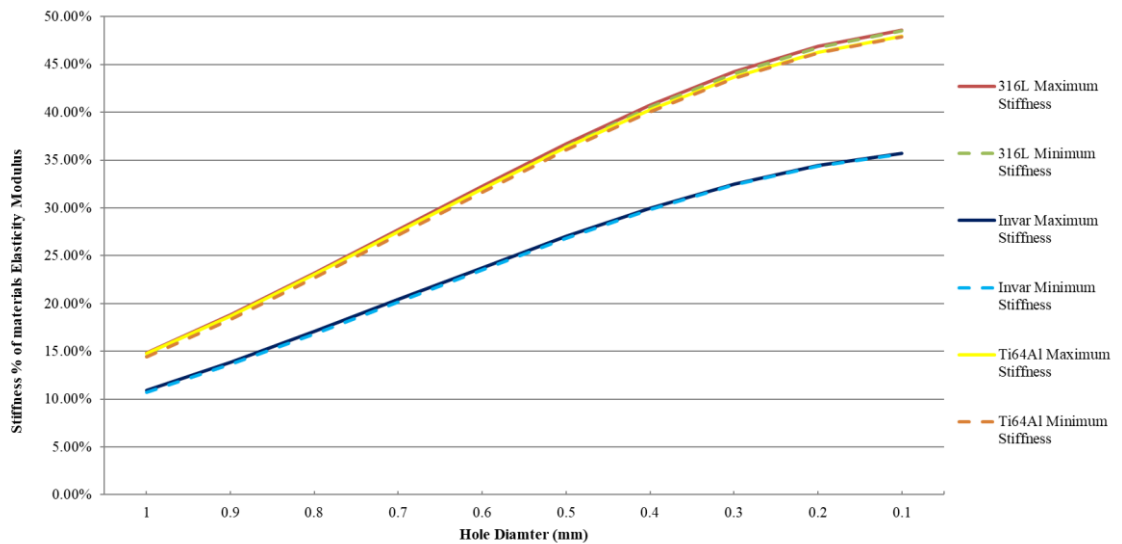


Figure 146. **Stacked array** stiffness for Invar, Ti64Al, and 316L, as a percentage of the materials elasticity modulus.

It is observed from the simulated stiffness that an increased hole diameter reduces overall stiffness. The added porosity shows that invar is significantly less stiff compared to 316L and Ti64Al in both stacked and single array designs after porosity is added.

5.5.4 Discussion on the tuneable porosity structure

It can be seen from the simulation results that both stacked and single array designs produce a variable CTE depending on the hole diameter. The available range to tailor the CTE is shown to depend on the material arrangement, and the thickness of the outside clad. With some arrangements there is a difference in the range of effectiveness at adjusting the CTE. A more effective structure and material arrangement will be able to

adjust the CTE over a wider range These are compared against one another graphically in Figure 147.

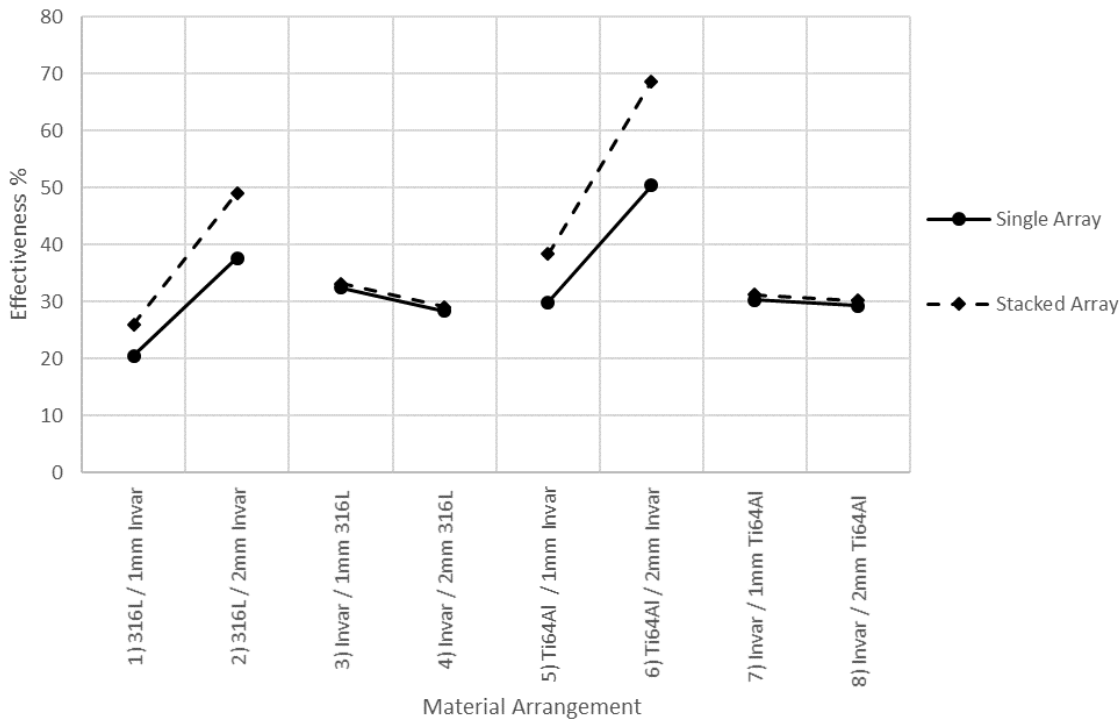


Figure 147. Single and stacked array designs showing percentage effectiveness for each material arrangement.

Figure 138 shows the effectiveness of each material arrangement with a 1mm and 2mm outside clad. Arrangements 1-2, and 5-6 place the primary material under radial compression as the temperature increases. Arrangements 3-4 and 7-8 place the primary material under radial tension as the temperature increases. It can be seen that when the arrangement provides radial compression (numbers 1-2 and 5-6), the stacked array provides an increased effectiveness over the single array. It also provides an increased effectiveness as the material thickness is increased from 1mm to 2mm. When the material arrangement provides radial tension (numbers 3-4 and 7-8) there is limited change between single and stacked arrays, and 1 and 2mm clad thickness. The material arrangements whereby the primary material (316L and Ti64Al) is in compression by the secondary material (invar) due to the lower CTE, there is a greater variation in effectiveness between the single and stacked array designs. The effectiveness increases with increasing clad thickness and has an overall effectiveness range of between 20%-70%. Where the primary material (invar) is in tension from the higher expansion secondary material (316L and Ti64Al) there is little difference in effectiveness between the two designs. There is also minimal change between clad thicknesses and materials. Overall the range only varies between 29%-32%.

5.6 Manufacture

The primary material has been manufactured using LPBF on the Renishaw AM400, with the secondary material added by a DED, also known as laser cladding. Laser cladding has been conducted by outside company Lase Ltd. This section look at the manufactured components and compare them to nominal dimensions.

5.6.1 Primary Material – LPBF

The auxetic structure and designed porosity structures have been printed in invar using LPBF on the AM400. Figure 148 shows the images, and measurements of the geometric accuracy compared to nominal. Dimensions were taken with calipers.

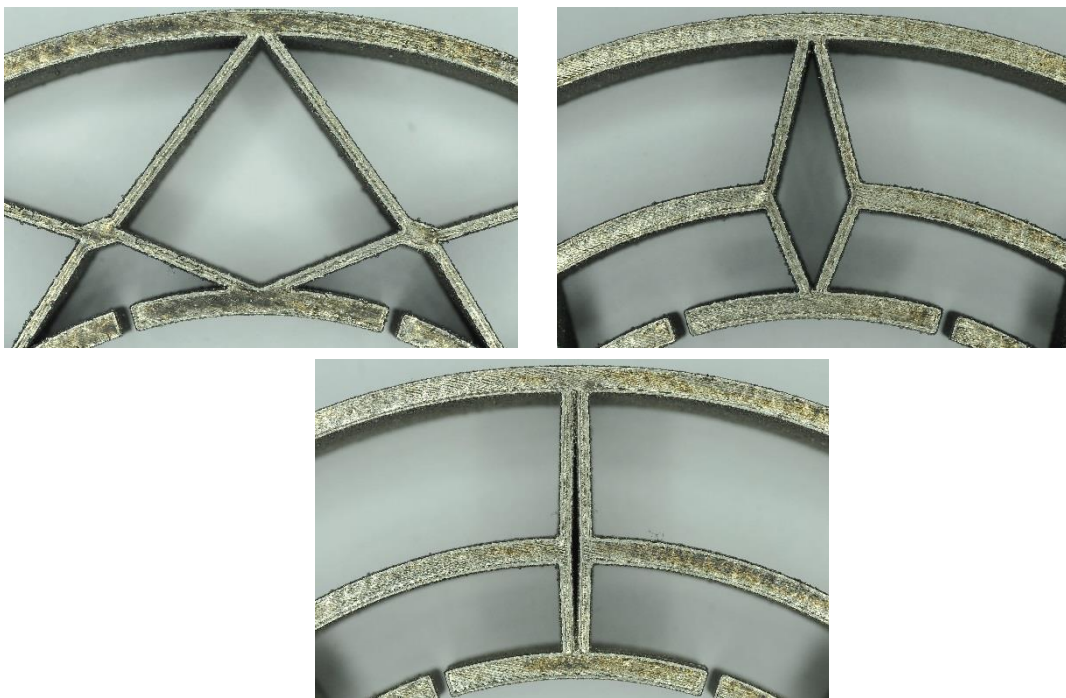


Figure 148. Manufactured tuneable auxetic structure in invar using LPBF. Angles shown are 38° , 66° , and 88° respectively.

38°			
Dimension	Nominal (mm)	Measured (mm)	Deviation (μm)
L_1	1	1.12	+120
L_a	2	2.18	+180
L_i	2	2.08	+80
66°			
Dimension	Nominal (mm)	Measured (mm)	Deviation (μm)
L_1	1	1.11	+110
L_a	2	2.19	+219
L_i	2	2.12	+212
88°			
Dimension	Nominal (mm)	Measured (mm)	Deviation (μm)
L_1	1	1.07	+70
L_a	2	2.08	+80
L_i	2	2.05	+50

Table 29. Geometric deviation from the nominal dimensions for the auxetic structure.

Figure 149 to Figure 151 shows the nominal dimensions in CAD and the optical microscopy images taken with the Zeiss Smartzoom 5 showing measurements of the geometric accuracy compared to nominal.

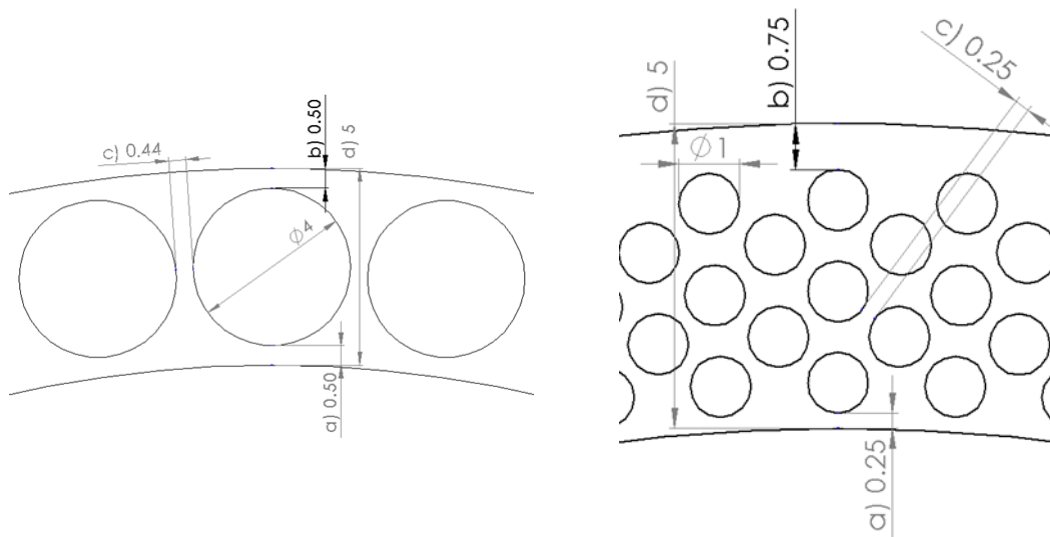


Figure 149. CAD drawings for single and stacked porosity designs.

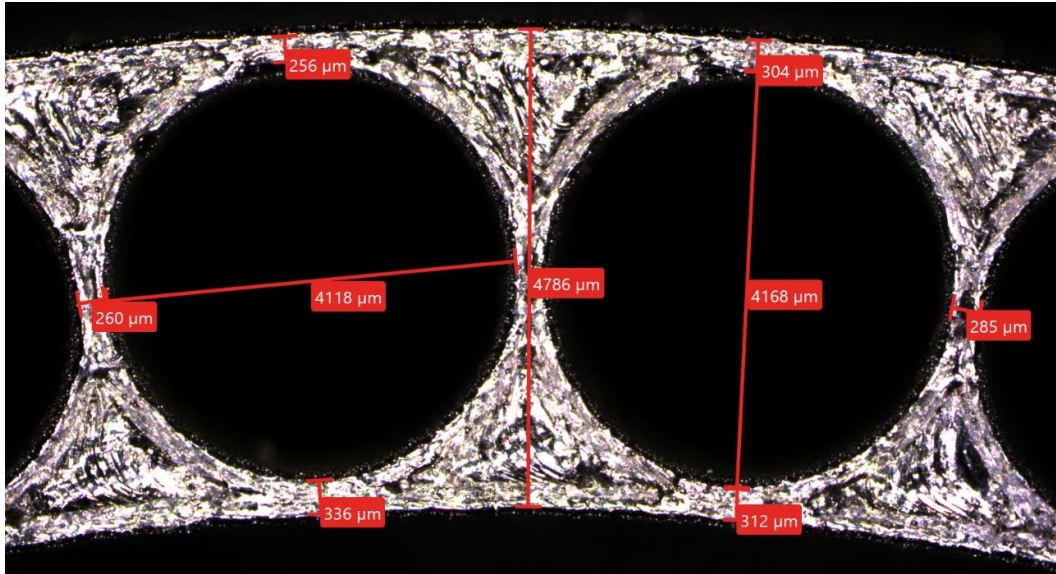


Figure 150. Optical microscopy of single array with 4mm diameter holes.

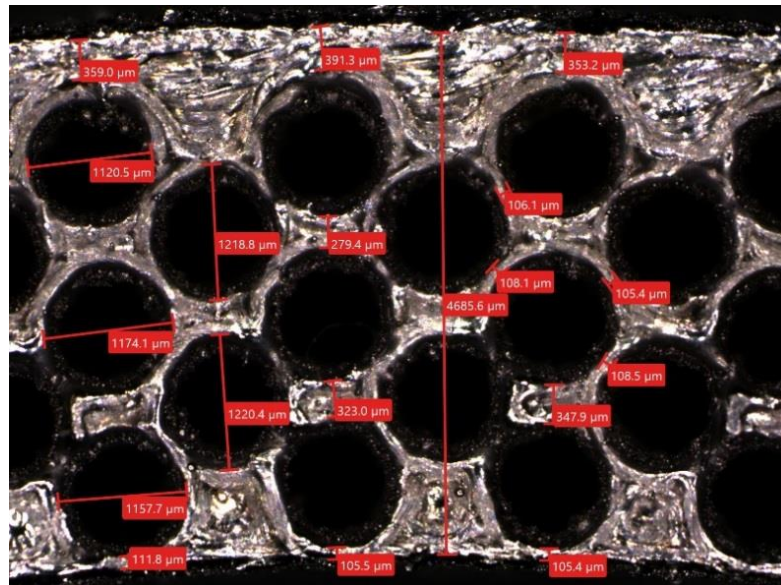


Figure 151. Optical microscopy of stacked array with 1mm diameter holes.

The measurements taken using optical microscopy are compiled in Table 30 for comparison.

Single Array			
Dimension	Nominal (mm)	Measured (mm)	Deviation (μm)
a)	0.5	0.324	-176
b)	0.5	0.28	-22
c)	0.44	0.285	-155
d)	5	4.786	-214
Hole Diameter	4	4.143	143
Stacked Array			
Dimension	Nominal (mm)	Measured (mm)	Deviation (μm)
a)	0.25	0.108	-142
b)	0.75	0.368	-382
c)	0.25	0.106	-144
d)	5	4.685	-315
Hole Diameter	1	1.183	183

Table 30. Nominal compared to measured dimensions for single and stacked arrays.

5.6.2 Secondary Material - DED

A Direct Energy Deposition (DED) machine will be used to add the secondary material. This is more commonly known as laser cladding. The metal powder is blown into the focus point of a laser while the cylinder rotates. A deposition of between 0.4-0.5mm will be applied on a single rotation. Laser cladding services provided by Lase Ltd. The processes used a deposition rate of 18g/min and power of 150W for the smaller tuneable porosity rings, and 30g/min and 200W for the larger auxetic structures. Reducing the power and deposition rate for the smaller cylinders reduces overheating. Surface speeds on both cylinders were the same at 17.6mm/s, but the overlap between each weld line was 1.5mm for the larger diameter auxetic design, and 1mm for the smaller tuneable porosity design. The LPBF material will be Invar, and cladded with 316L stainless steel. Both materials are immiscible with one another and will weld effectively. A trial run was conducted with cladding Ti64Al onto invar with success.

5.7 Thermal Expansion Test Bench Results

The thermal expansion of all cladded structures will be measured, and their accuracy to the simulations determined. To determine the thermal expansion, a specially designed test bench has been setup using a co-ordinate measuring machine. The test bench method outlined in chapter 7.6 will be used for the validation of the simulation results. In the this chapter it is outlined that the accuracy of the thermal expansion reading was between The co-ordinate measuring machine has been programmed to take a measurement of the diameter by touching each segment of the inside of the cylinder. A total of 10 readings

has been taken per diameter for each segment. A total of 100 diameter readings is taken to analyse the variation between each, totalling 1000 probe touches. The touch probe will become hot as it takes a reading of the diameter. The accuracy of the result will remain unaffected by the thermal expansion of the probe tip, because the probe will be expanding vertically downwards, which is the axis not being measured.

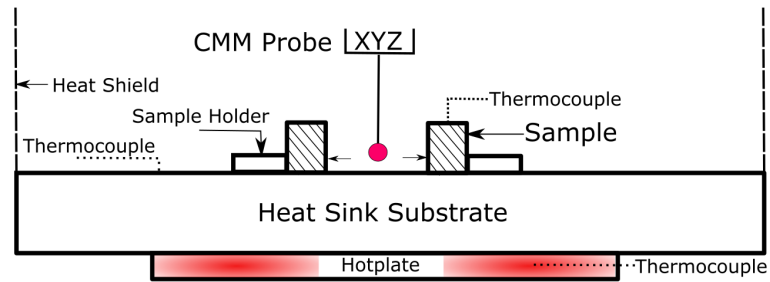


Figure 152. Schematic of CMM test bench setup.

To obtain the thermal expansion co-efficient, first the initial diameter must be measured. The three auxetic rings with lattice angles 38, 66, and 88° will be measured before and after cladding.

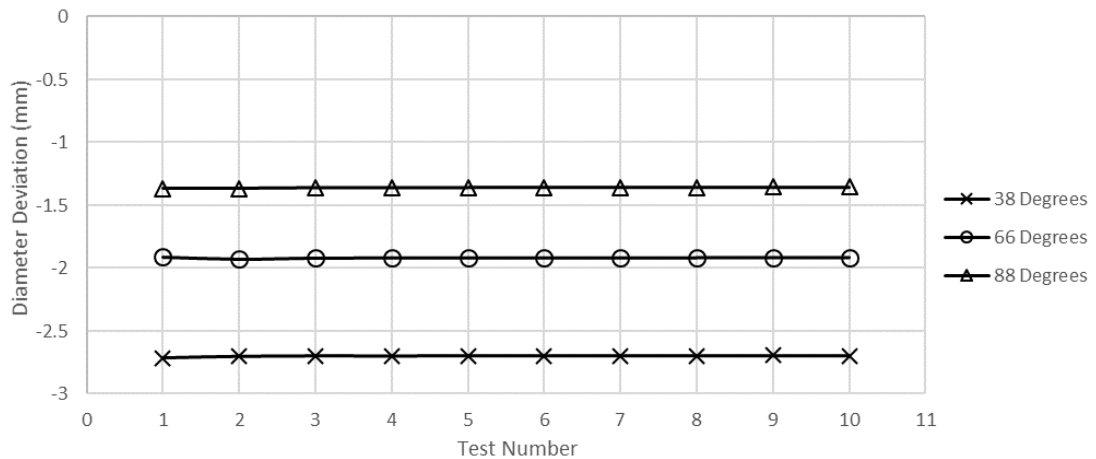


Figure 153. Deviation between cladded and un-cladded inside diameters.

Figure 153 shows that after cladding the invar auxetic structures with 316L, the inside diameter decreases across all three auxetic structure angles. It is shown that an increasing auxetic angle provides a decrease in the diameter deviation after cladding. In other words, the diameter gets smaller after cladding, but less so with higher angle auxetic structures. This could be due to the compression applied during cooling of the higher CTE 316L material. This shows that the auxetic is functioning correctly and reducing the inside thermal expansion with the higher auxetic angle in response to an outside circumferential compression.

To determine the thermal expansion of the cladded structure with temperature, the coordinate measuring machine test bench is used, as described in chapter 4.8.2. The measured CTE is compared to the simulated CTE. Auxetic angles 38° , 66° , and 88° are measured. The test bench provides two thermocouple readings, the structure temperature is used for the calculation of the CTE. The average diameter readings are taken at ambient and heated temperatures across 75 measurements, ignoring the first 25 for reasons explained in the experimental chapter 4.8.2. A single CTE value is produced for comparison to simulation. An example of the before and after temperatures at each test number is shown for auxetic structure 38° in Figure 154.

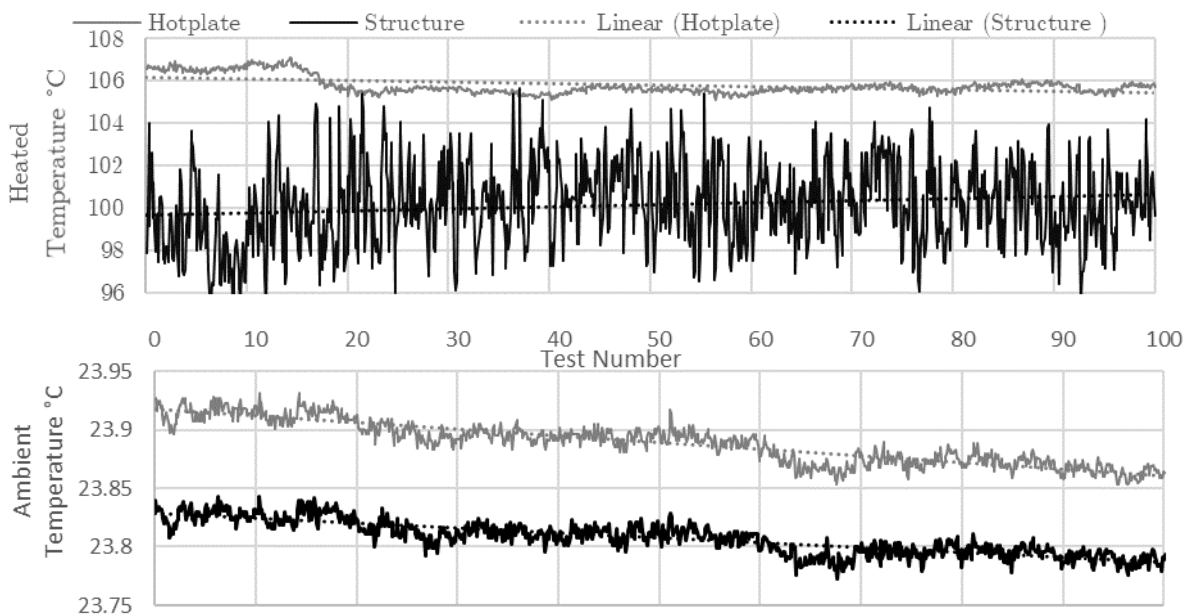


Figure 154. Thermocouple temperature readings over each test for the auxetic structure at 38°

The diameter is measured through 100 tests at ambient temperature and then at the heated temperature. Figure 155 shows a plot of the diameter for the auxetic structure at 38° .

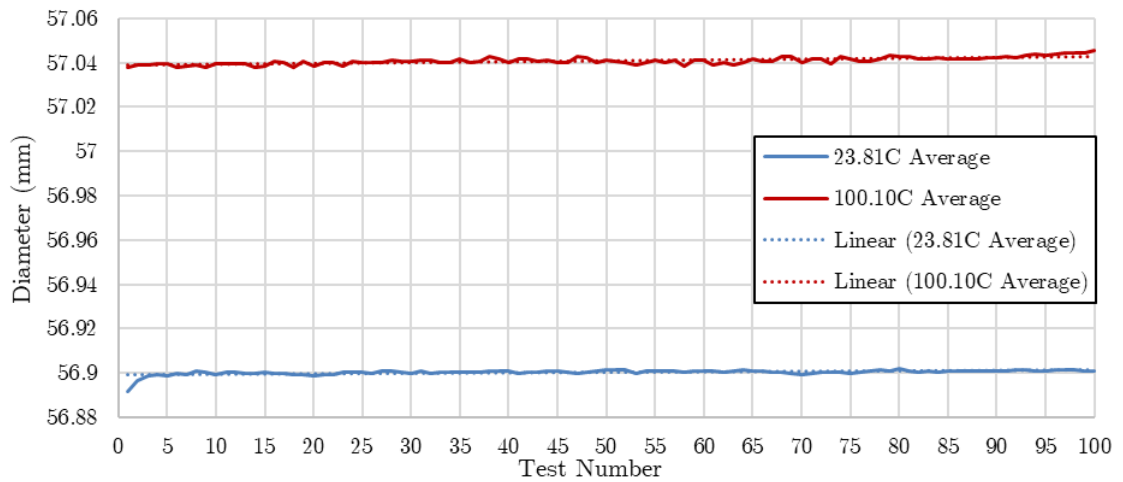


Figure 155. CMM diameter readings for the auxetic structure at 38°

The testing is carried out for the remaining structures using the same method, with a similar plot to those in Figure 154Figure 155. The difference in diameter is used to calculate the CTE, and plotted for comparison in Table 31.

5.8 Discussion on thermal expansion control in metal AM by design

The model has demonstrated an effective method of adjusting the CTE based upon geometry. The auxetic structure provides a wider range of CTE control, while the porosity array provides a more compact design, with a reasonable CTE tailor ability, but with a stiffness two orders of magnitude higher. It is observed that in the auxetic structures the measured CTE is different from the predicted CTE from modelling. However, the trend of a decreasing CTE with an increasing auxetic angle as predicted in the modelling is correct. With the designed porosity structures, the single array is closer to the simulated CTE, but the stacked array decreases by more than expected. The results are summarised in Table 31.

Structure	Measured CTE ($\mu\text{m}/\text{mK}$)	Simulated CTE ($\mu\text{m}/\text{mK}$)	Difference ($\mu\text{m}/\text{mK}$)
Auxetic 38°	29.33	15.1	14.23
Auxetic 66°	21.66	9.67	11.99
Auxetic 88°	15.57	7.8	7.77
Design 1 Single Array	10.05	11.2	1.15
Design 2 Stacked Array	4.99	10.7	5.71

Table 31. Simulated and measured CTE for the Auxetic and designed porosity structures manufactured in invar with a 316L clad, and measured with the CMM test bench.

The measured CTE shows a decrease as the auxetic lattice angle increases. This is as the model predicted, but the actual CTE values differ. The variation between measured and simulated CTE could be due to several reasons. The most plausible reason being the residual stress caused by the cooling of the higher CTE 316L clad material during the cladding process. This has increased the CTE for each auxetic lattice angle by relaxing the residual stresses at the higher temperatures. This is supported by the thermal expansion exceeding that of the highest CTE material 316L at $16\mu\text{m/mK}$. The porosity array has CTE measurements that agree with the model for the single array, but not with the stacked array. The residual stress theory could play less of a role in the porosity array compared to the auxetic array, because the outside diameter is smaller, and the structure is stiffer. The stacked array could differ due to geometric difficulties on the smaller porosity holes. The deviation from the nominal dimensions on key parameters is measured in chapter 5.6, and effects all structures.

5.9 Conclusion on thermal expansion control in metal AM by design

The simulation models show the capability to tailor thermal expansion of an annulus surrounding a hypothetical lens, depending on dimensional variables in the structure. The stiffness varies depending on the structure type, with the auxetic structures providing significantly less stiffness than the designed porosity structures. To conclude;

- The auxetic structures model demonstrates the ability to adjust the CTE over a wide range depending on the material configuration. Invar and a 316L clad can provide a maximum of 15.1 to $7.8\mu\text{m/mK}$ depending on the auxetic angle. It lacks stiffness however, providing only a maximum of 0.81GPa or 0.49% of the stiffness of the solid invar.
- The designed porosity structures model demonstrates the ability to adjust the CTE in a more compact form, while maintaining a much greater level of stiffness. Invar with a 316L clad provides a tailorable CTE range of between 8.1 to $5.7\mu\text{m/mK}$ for single and maximum of 9 to $4.4\mu\text{m/mK}$ for the stacked array, with a 69 to 71GPa maximum stiffness respectively.
- The auxetic structure CTE measurements demonstrate the structure as working effectively to decrease CTE with increasing auxetic angle. The CTE measurements are higher than predicted due to the relaxation of residual stresses in the clad material.
- The designed porosity array has a measured result that is correct to the model for the single array, but deviates in the stacked array.

6 Thermal Expansion Control in Metal AM by Alloy Selection

6.1 Summary

This chapter determines the effect of the LPBF manufacturing process on the thermal expansion of two controlled expansion alloys; invar and aluminium-silicon. It compares the mechanical and thermal properties of the manufactured components to that of conventionally manufactured parts, and proves their suitability to the LPBF process. By adjusting the laser settings, or component geometry, it has been shown that the thermal expansion can be adjusted by up to 30% for invar. Adjustment of the laser parameters in high silicon aluminium-silicon alloys, has shown to produce a finer superior microstructure to conventional spray-forming, with full densification and limited microcracking. Further tailoring of the CTE has been demonstrated by mixing Al-Si30 and Al-Si40 powders to achieve a tailored CTE between 17-12 $\mu\text{m}/\text{mK}$ with no adverse effects to mechanical performance or microstructure. For invar, fine elemental nickel and iron powders have been mixed with the invar alloy powder to adjust the nickel content of the manufactured part. Adjustment of the nickel content changes the CTE, allowing for 'fine tuning' of the CTE to obtain the critical 36% nickel for the lowest thermal expansion possible. Additions of up to 7% Ni have been investigated to tailor the CTE to that of glass for the optical industry. The manufactured parts are investigated using EDS to determine homogeneity.

6.2 Introduction

This chapter will form a comprehensive investigation into the use LPBF for the manufacture of controlled thermal expansion alloys. It will first investigate the manufacturability of the material invar, or FeNi36.

This will be achieved by adjusting the elemental constituents of the gas atomised powder, and adjusting the overall constituents of a blended powder. Mixing, or blending different elemental powders and melting in-situ is beneficial for an engineer looking to 'fine tune' the co-efficient of thermal expansion of an alloy by adjusting an already acquired powder. This could be due to several reasons. The powder can often be supplied $\pm 1\%$ of the nominal 36% nickel, and therefore exhibits a CTE higher than the specification. It can also be useful to acquire an exact CTE by increasing the nickel content to the corresponding amount.

AlSi7-10Mg and AlSi30-40 will be manufactured from fully alloyed gas atomised powders to determine the suitability of high silicon alloys to the LPBF process. Thermo-mechanical characterisation will be completed and compared against characterisation of induction melted, and spray formed components. This process will involve finding the

optimum laser processing parameters to minimise microcracking on the high silicon alloys.

Invar will be manufactured using LPBF. Several projects will be completed in this chapter, these include;

- The effect of part orientation on the CTE of Invar FeNi36 powder.
- The effect of laser processing parameters on CTE and microstructure.
- The effect of blending or mixing the fully alloyed gas atomised FeNi36 powder with incremental increases of nickel and iron powder. Determination of the suitability of blending powders in the AM process, and the effect on CTE and microstructure.

6.3 Manufacturing Setup

To additively manufacture the materials in this chapter, the Renishaw AM400 LPBF machine will be used. The machine features a 400W laser, and a 250x250x300mm build volume. For experimental powders, the Reduced Build Volume (RBV) will be used. This is a piece of equipment that is installed inside the chamber which allows the user to bypass the main material hopper for the machine and use a separate dosing system where the material is easily changed. It features a smaller build volume of 100x100x300mm, but due to design issues with powder spreading only a volume of 30x100x300mm can be used. The Al-Si and Fe-Ni alloy development in chapters 7.4, and 7.5 will use the RBV, whilst the main hopper will be used for geometry and laser parameter changes in chapters 7.6, and 7.7.

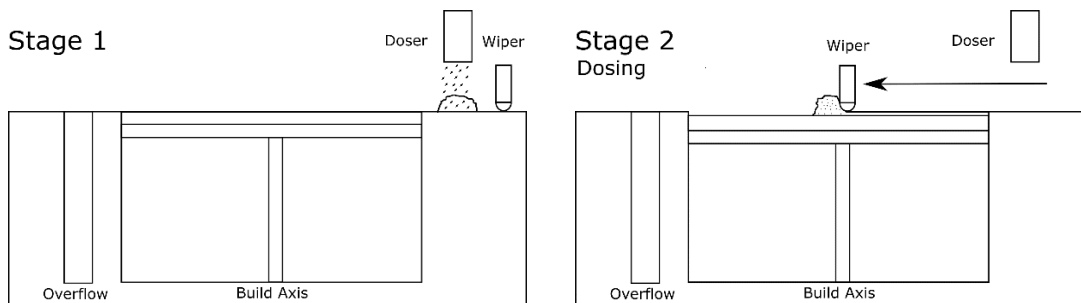


Figure 156. **Standard build volume** stages. Stage 1 shows the dosing of the powder from the hopper, stage 2 shows the machine applying the first layer of powder.

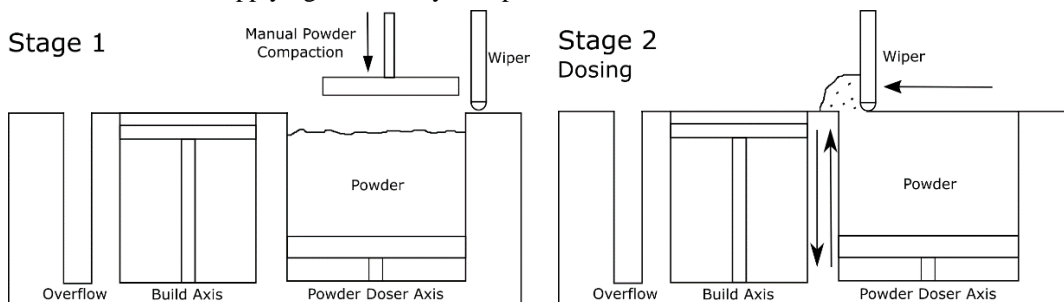


Figure 157. **Reduced Build Volume (RBV)** stages. Stage 1 shows the manual compaction of the powder, stage 2 shows the machine applying the first layer of powder.

The LPBF machines manufactured by Renishaw have a Pulse Width Modulated (PWM) laser compared to a continuous laser by other manufacturers. A continuous laser has a scanning velocity in mm/s, whereas a PWM laser has an Exposure Time (ET), and Point Distance (PD) instead. The ET identifies how long the laser is held on a single point in μs , and the PD defines the distance between each point in μm . These two variables can be combined to form a scanning velocity. There is also Hatch Spacing (HS) in μm and the Laser Power (LP) in W. The HS defines the distance between each laser scan for the internal volume of the part.

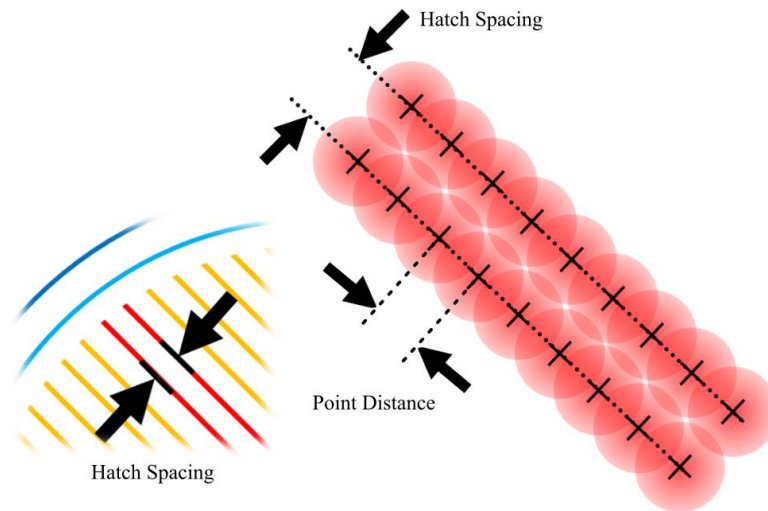


Figure 158. The configuration of the Renishaw LPBF pulse modulated laser scanning.

Varying the ET, PD, and LP will adjust the energy density which impacts the melt pool behaviour. Using a lower energy density, the weld will be in a conduction mode, and a higher energy density, it will be in a keyhole mode. Both low and high energy welds can cause porosity.

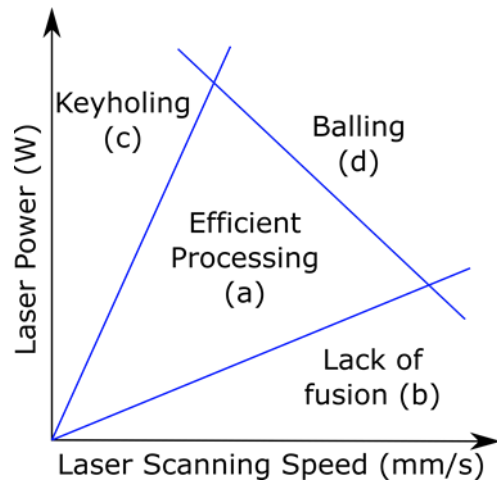


Figure 159. Laser power vs scanning speed graph – how process outcomes vary with laser parameters. Zones (a-d) relate to the weld-pool behaviour.

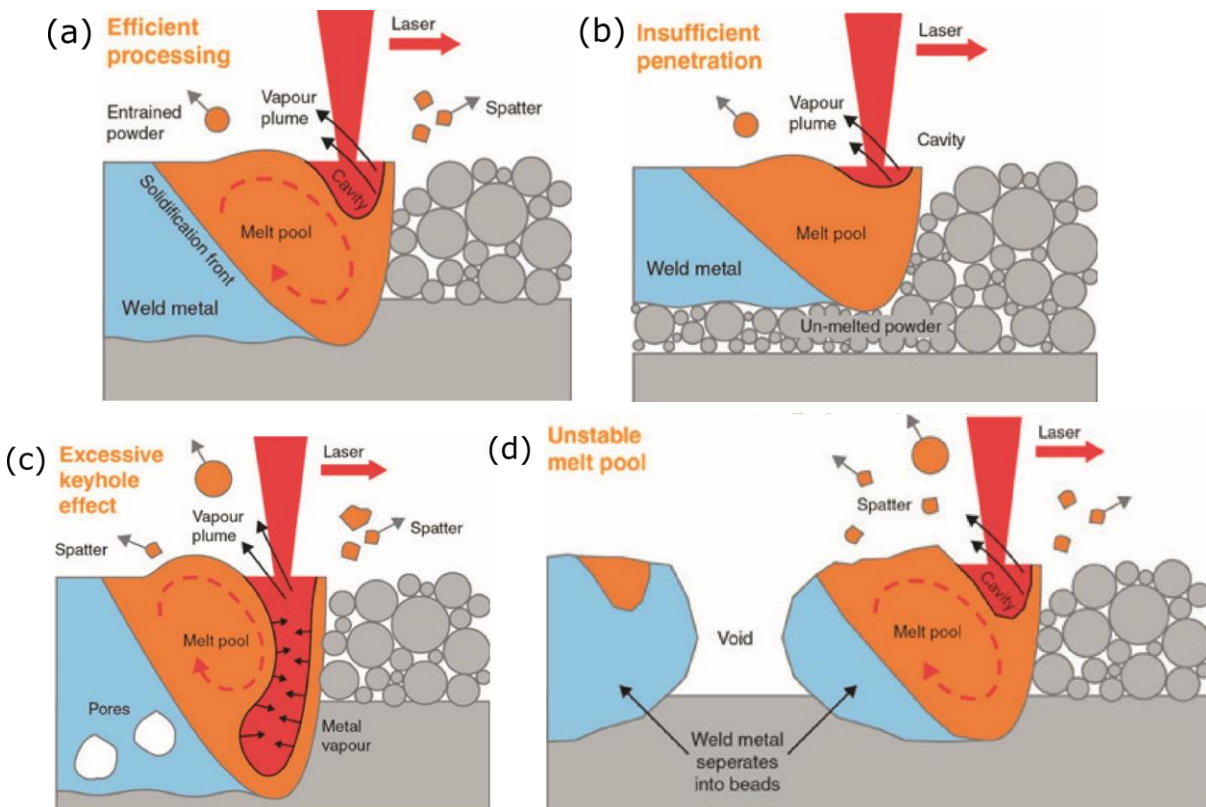


Figure 160. Cross-section diagram of laser weld behaviour.¹³

It is easiest to find a suitable laser parameter set if the ‘efficient processing’ window as wide as possible. Thicker layers will narrow the efficient processing window, so starting with a thinner layer is usually considered the best approach. The geometry can also affect the width of the processing window, by increasing or decreasing the heat conduction to

¹³ Renishaw Internal Product Development Memo - ‘X marks the spot - find the ideal process parameters for your metal AM parts’ [Accessed 01/09/2019].

the baseplate. A higher substrate temperature will narrow the efficient processing window, which is undesirable. It is best to keep samples a consistent geometry while experimenting with laser parameters.

The correct laser parameters will produce a fully dense component, with mechanical properties close to or exceeding that of a conventionally cast component. The parameter set will be unique for each material. Overall energy density is a good approximation to be used for achieving a fully dense part [151]. Energy density can be calculated with equation 6.1.

$$E_d (J/mm^3) = \frac{\text{Laser Power} \times \left(\frac{\text{exposure time}}{\text{hatch spacing} \times \text{point distance}} \right)}{\text{layer thickness}} \quad (6.1)$$

6.4 Powder Characterisation

It is important to understand the characteristics of the feedstock powder. The process requires the flow of powder through a narrow opening in front of the wiper blade, and the subsequent spreading of the powder over a 50µm layer thickness. To determine if the powder can fall through the opening, the flowability of the powder is determined. The particle size distribution is required to determine if it falls within the target 15-45µm target diameter range required for a 50µm layer thickness. The shape of the particle is also determined because its flowability improves with sphericity. The RBV requires a powder compaction step shown in Figure 157, so the tap density is obtained to understand the powders ability to compact.

To obtain this data, several methods are employed:

- Optical classification by visual inspection of a powder poured onto a surface, looking for agglomeration which will quickly indicate flowability in four categories.
- Scanning Electron Microscopy (JOEL) for determining particle shape and distribution, and the elemental constituents, using EDS.
- Rheometry (using Freeman RT4) for determining the Basic Flowability Energy (BFE) required, and the compaction percentage for each powder.
- Particle Size Distribution (PSD using Malvern Mastersizer) to determine particle size within three percentile ranges.
- Density measurements before and after tapping the powder on a surface. The force imparted can be used to determine a more packed state.

Alloy	Manufacturer	Manufacture Method	Atomisation Gas	PSD (μm)
Invar (FeNi36) Batch 1	TLS	Gas Atomisation	Argon	15-45
Invar (FeNi36) Batch 2	Sandvik	Gas Atomisation	Nitrogen	15-45
AlSi7Mg	Sandvik	Gas Atomisation	Argon	20-63
AlSi10Mg	Sandvik	Gas Atomisation	Nitrogen	20-63
AlSi30	TLS	Gas Atomisation	Nitrogen	20-63
AlSi40	TLS	Gas Atomisation	Nitrogen	20-63
Nickel	Goodfellow	Gas Atomisation	Nitrogen	15-45
Nickel	Goodfellow	Carbonyl	-	6-8
Iron	Goodfellow	Carbonyl	-	3-7

Table 32. Metal powders used - Manufacturing methodology and target PSD.

6.4.1 Optical Classification

Optical classification allows for quick identification of the powders flow characteristics by pouring a volume of the powder onto a surface. The nature of the agglomeration will determine whether it has sufficient flowability for the LPBF process [152]. Looking at the images provided in Figure 161 as a reference, the AlSi and FeNi powders shown in Figure 162 fall across three ranges of flowability.

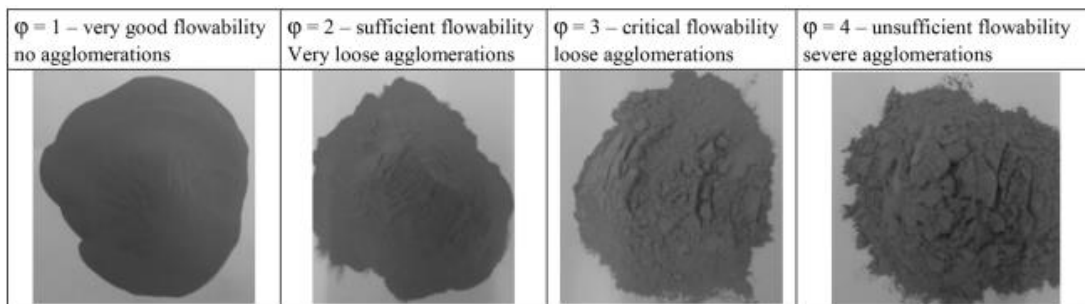


Figure 161. Reference for optical classification for flowability using LPBF [152].

Images of the powder have been taken so that they can be referenced against the scale shown in Figure 161.

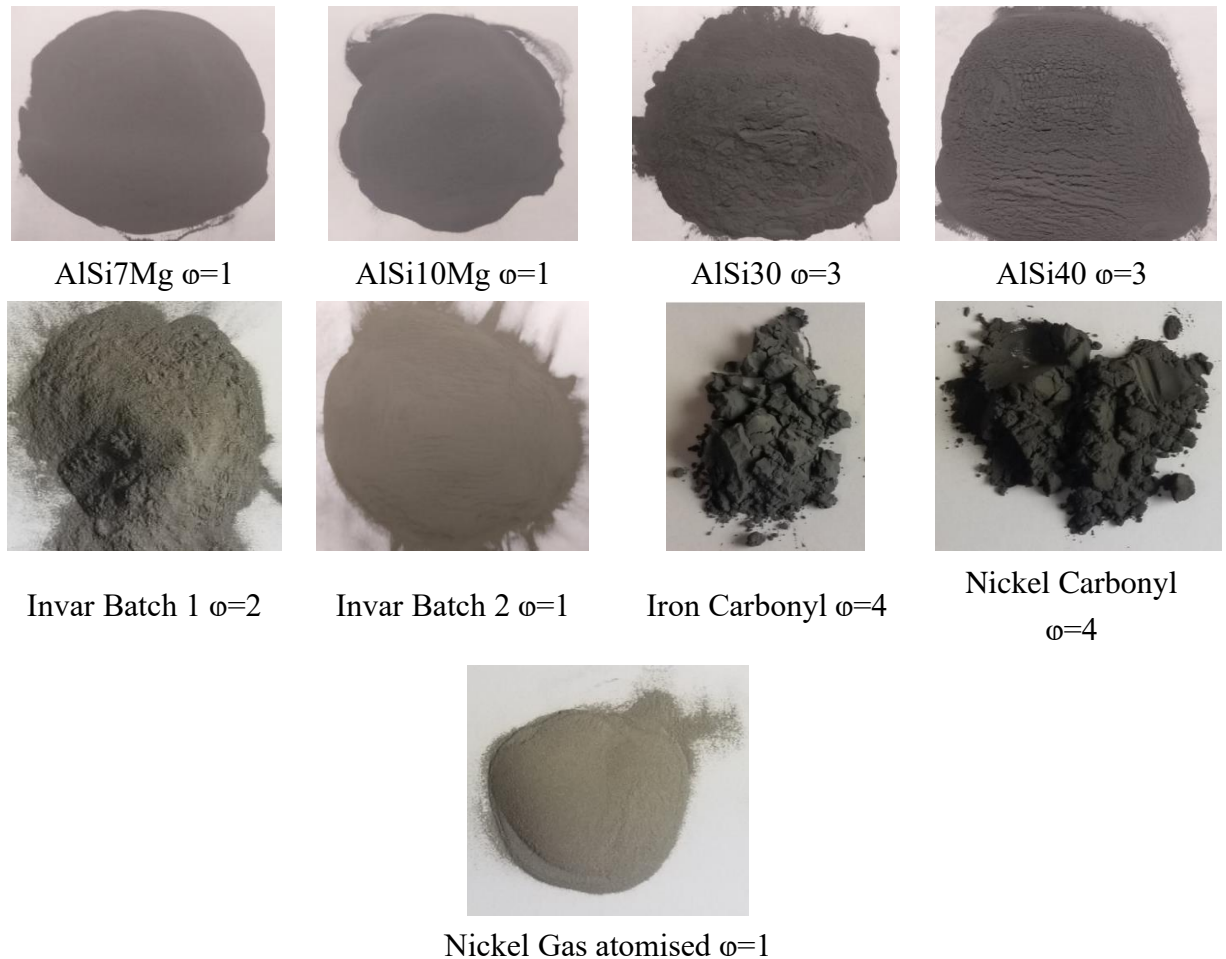


Figure 162. Optical classification of all used ALM powder feedstocks.

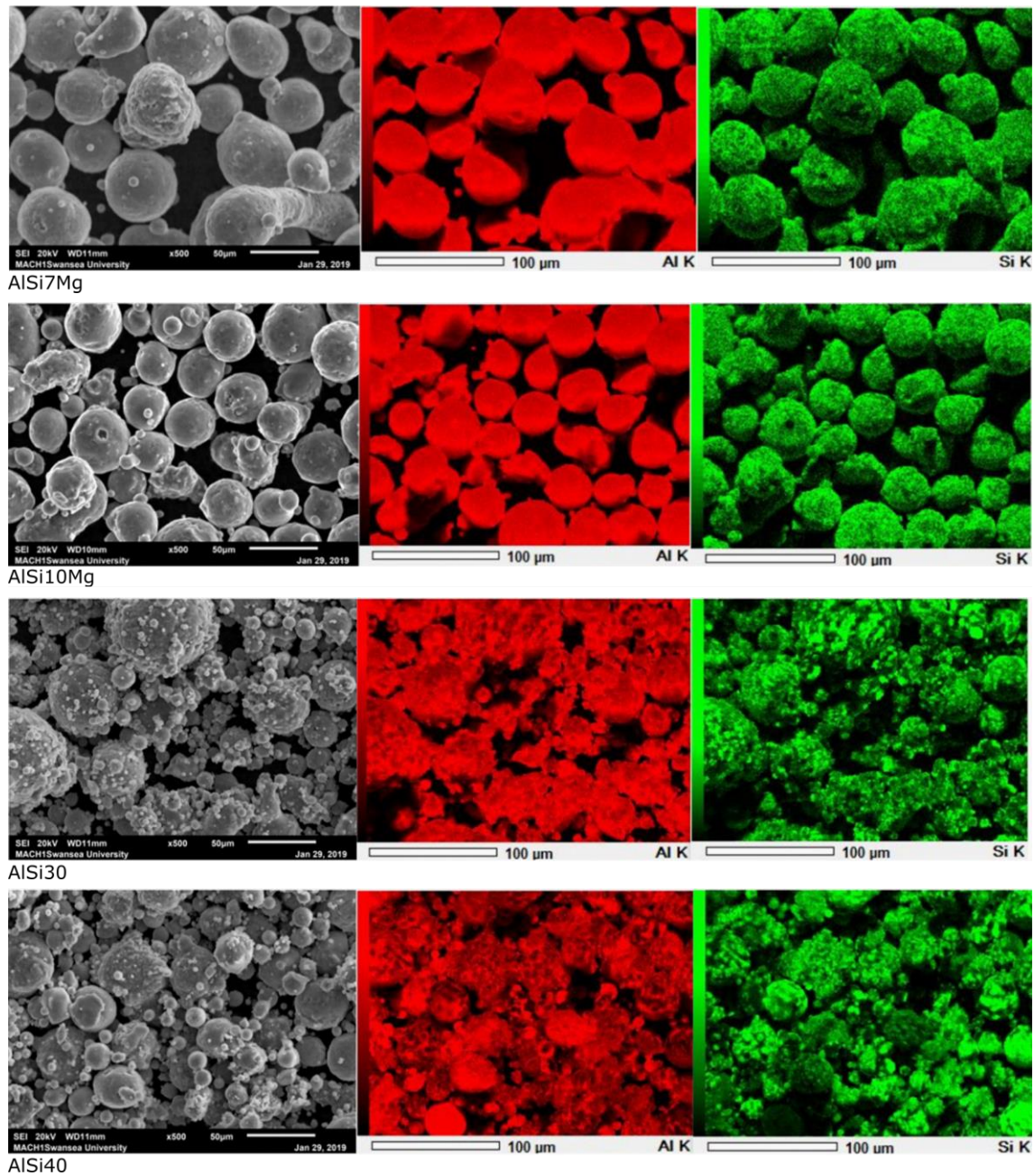
Figure 162 shows that AlSi7Mg, AlSi10Mg, invar batch 2, and gas atomised nickel, all exhibit excellent flowability. Invar batch 1 exhibits sufficient flowability, and AlSi30-40 exhibits critical flowability. Iron and nickel carbonyl powders exhibit insufficient flowability, as to be expected by their PSD and non-spherical carbonyl powder manufacturing method.

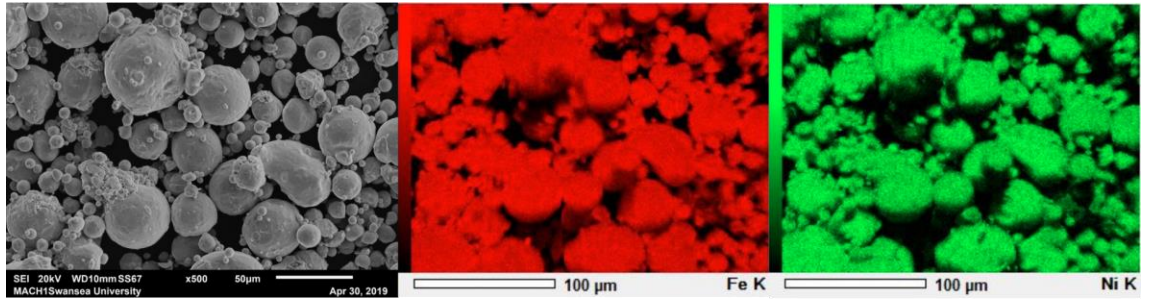
6.4.2 Scanning Electron Microscopy

Scanning Electron Microscopy can be used to determine the powder shape, distribution, and elemental composition. An image has been taken from AlSi7Mg, AlSi10Mg, AlSi30-40, and FeNi36 gas atomised powders. It can be seen that the higher silicon content alloys AlSi30-40 feature a larger number of satellite particles between 0.1 μm to 10 μm

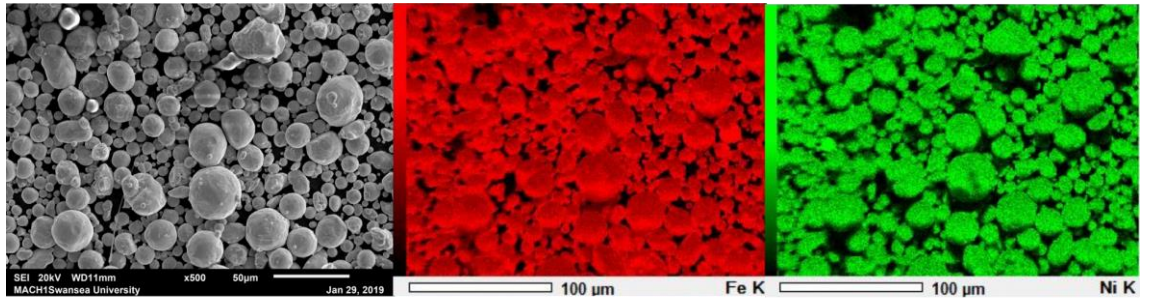
agglomerated around the larger 30-50µm particles. This could affect powder flowability and melting behaviour. EDS analysis shows silicon rich, and aluminium rich regions within the powder. This is to be expected from a hypereutectic AlSi alloy, and a similar behaviour maybe experienced in the final manufactured components. AlSi7-10Mg also experiences Al and Si rich areas, but does have such a high number of smaller satellite particles. Invar has the least number of satellite particles, and a limited number of Fe or Ni rich regions. Two batches of Invar were manufactured by Carpenter Additive.

Figure 163. SEM images of all metal powders used in manufacture. EDS maps show distribution of the two greatest elemental constituent.

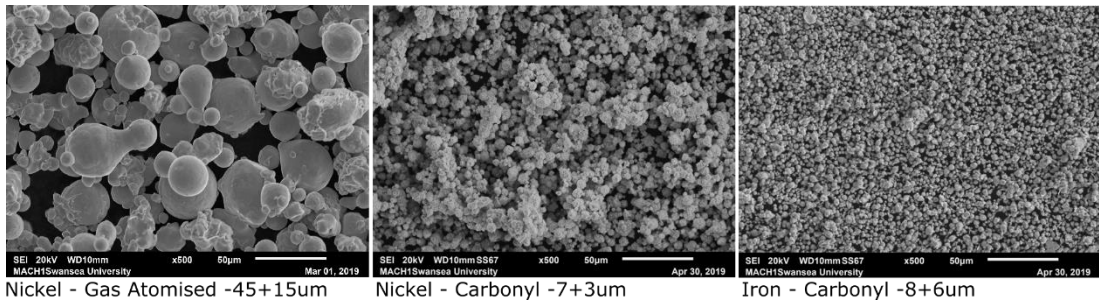




Invar Batch 1



Invar Batch 2



Nickel - Gas Atomised -45+15µm

Nickel - Carbonyl -7+3µm

Iron - Carbonyl -8+6µm

6.4.3 Particle Size Distribution (PSD)

The particle size distribution of any powder can be defined by the diameter of which 10, 50, and 90% of the of the samples mass is comprised of particles with a diameter less than the given value. For example, the D(10) of AlSi7Mg is 29.5µm, meaning 10% of the powders mass has particles of less than 29.5µm in diameter. This is useful for understanding the percentage of particles able to conform within a typical 60µm powder layer. A greater number of smaller particles may present problems with flowability.

Material	Atomisation Method	Nominal (μm)	D(10)(μm)	D(50)(μm)	D(90)(μm)
AlSi7Mg	Nitrogen	20-63	29.5	45	67.8
AlSi10Mg	Nitrogen	20-63	29.8	43.7	64
AlSi30	Nitrogen	20-63	13.5	35.3	71.6
AlSi35 (Blended)	Nitrogen	20-63	14.7	36.9	72.7
AlSi40	Nitrogen	20-63	16.2	37.2	67.1
Invar Batch 1	Argon	20-50	12.2	28.8	54.3
Invar Batch 2	Nitrogen	15-45	21.3	32	48.6
Nickel	Nitrogen	15-45	20.3	33.4	57.7
Nickel	Carbonyl	6-8	-	-	-
Iron	Carbonyl	3-7	-	-	-

Table 33. Particle Size Distribution for all gas atomised powders obtained using a Malvern Mastersizer. Powder sizes outside of nominal highlighted red.

It is observed that all powders are above the nominal maximum D(90). The aluminium powders were also under the nominal D(10). Agglomeration of powder particles will show as a larger single particle, and increasing the D(90) values.

6.4.4 Rheometry

The Freeman RT4 powder rheometer is used to measure flow energy in a defined amount of powder (25ml) according to the resistance of a rotating blade moving downwards and upwards within the powder bed using a helix motion. This method measures the pushing shearing behaviour of the powder. The motion is repeated 8 times at 100mm/s, and then reduced in increments to 70,40, and 10mm/s, as outlined in ASTM D7891 [153]. Mellin et al. [154] has found no correlation between the Gustavv flow meter (ISO 13517), and limited correlation with the hall flow meter (ISO 4490) for metallic powders. The compaction percentage is also tested whereby an increasing force is applied to the powder, and its displacement is measured. The invar tested is all from batch 2.

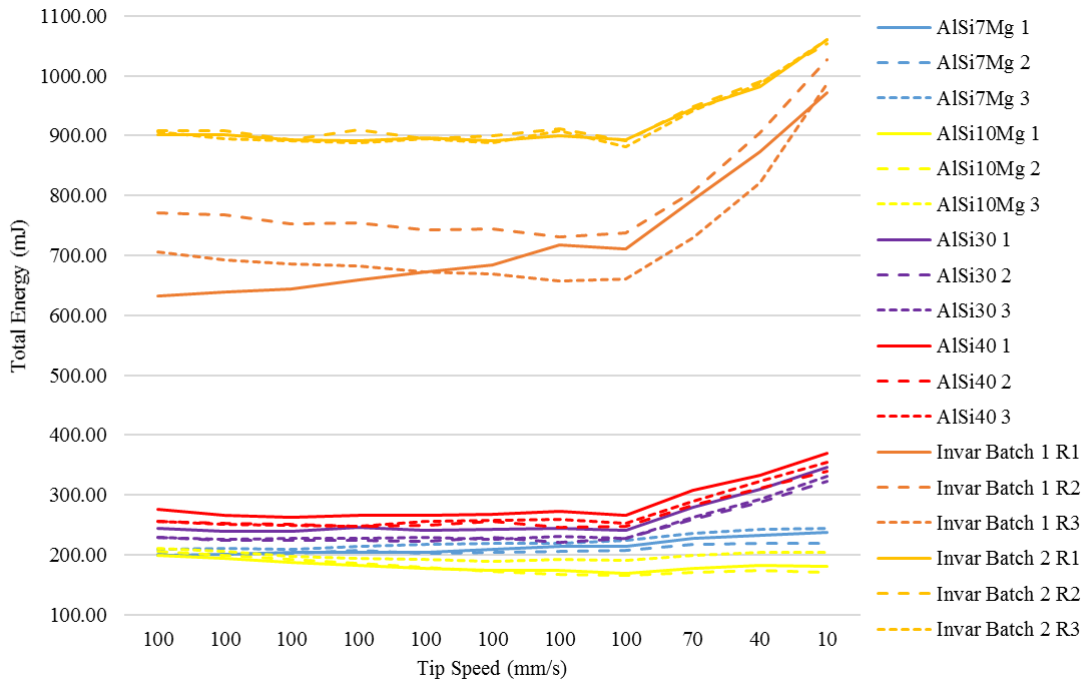


Figure 164. Graph of the basic flowability energy of the powder feedstock.

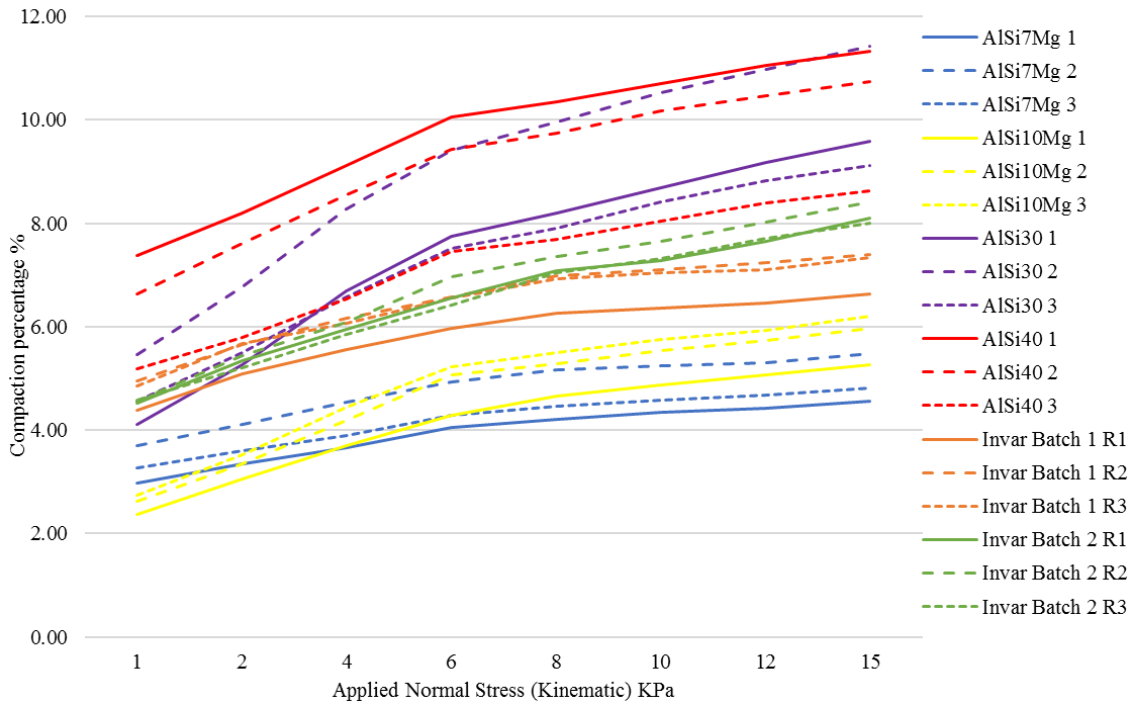


Figure 165. Graph of the compaction percentage of the powder feedstock.

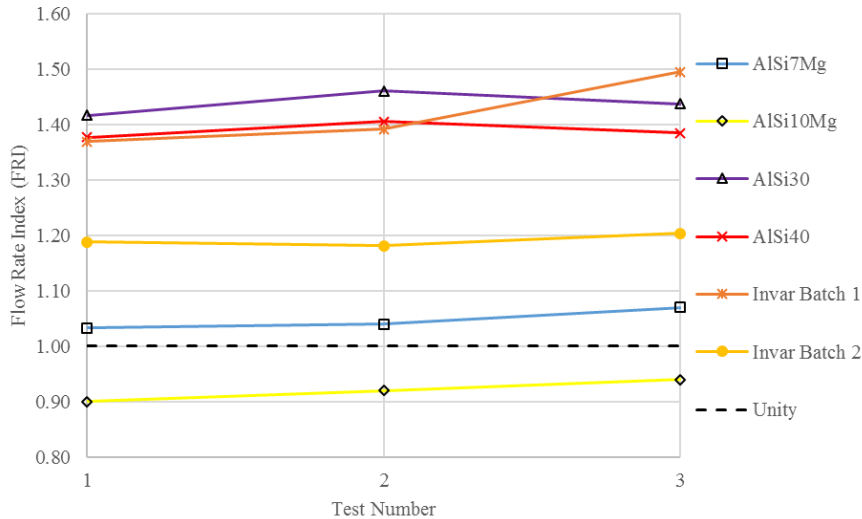


Figure 166. Flow Rate Index (FRI) for the powder feedstock.

The data shows that the denser powder invar (8.1kg. m^3) exhibits a higher required energy to flow of approx. 600-1000mJ compared with the lighter alloys ($2.8 - 2.5\text{kg. m}^3$). Invar batch 2 has more flowability energy than batch 1, but has less variability between tests. The powders with poor optical characteristics required an increased energy input as the tip speed decreased. This is also represented with a higher Flow rate index (FRI). The FRI is a dimensionless parameter to determine its ability to flow. It is defined as the ratio between the flow energy of the powder at anticlockwise blade motions of 10 and 100 mm/s, and the normalized fluidization energy, which is the energy required to move the blade through a gram of powder in an anti-clockwise motion at 100 mm/s tip speed, at the minimum fluidization velocity of each of the powders [155]. In practice this means that as the FRI increases from 1 onwards, the energy requirement increases to maintain flow rate, or in other words the angle required to pour the powder increases. As the FRI decreases below 1 more energy is required to produce flow, as the flow rate increases [156]. This is a desirable characteristic that provide smoother flow when pouring, with a reduction of agglomeration or ‘caking’ interrupting flow.

The compression data shows that AlSi30-40 can be compacted the most, SEM data would suggest this is down to a high number of smaller satellite particles. A greater compaction in the RBV will provide a consistent layer.

6.4.5 Tap Density

The density of the powder can be measured by obtaining the mass of a known volume. The tap density can be obtained by obtaining the mass after applying a specified number of taps of the vessel on a hard surface. The shock imparted will settle the powder into a denser state with a higher packing factor. ISO 3953 defines that the number of taps should be sufficient to provide no more volume change. For this experiment a vessel has been

used with 50ml of powder that can be split to provide exactly 25ml. Prior to the split, the vessel is tapped 50 times. After the split, the remaining 25ml is weighed and the tapped density is calculated.

Material	Solid Density	Powder Density	Powder Tapped Density	Packing Factor after tapping %
AlSi7Mg	2.7	1.42	1.56	57.78
AlSi10Mg	2.7	1.45	1.59	58.89
AlSi30	2.59	1.07	1.28	49.42
AlSi35 (Blended)	2.57	1.14	1.37	53.3
AlSi40	2.55	1.17	1.36	53.33
Invar Batch 1	8.1	4.75	5.42	66.95
Invar Batch 2	8.1	4.48	5.00	61.79

Table 34. Tap density results.

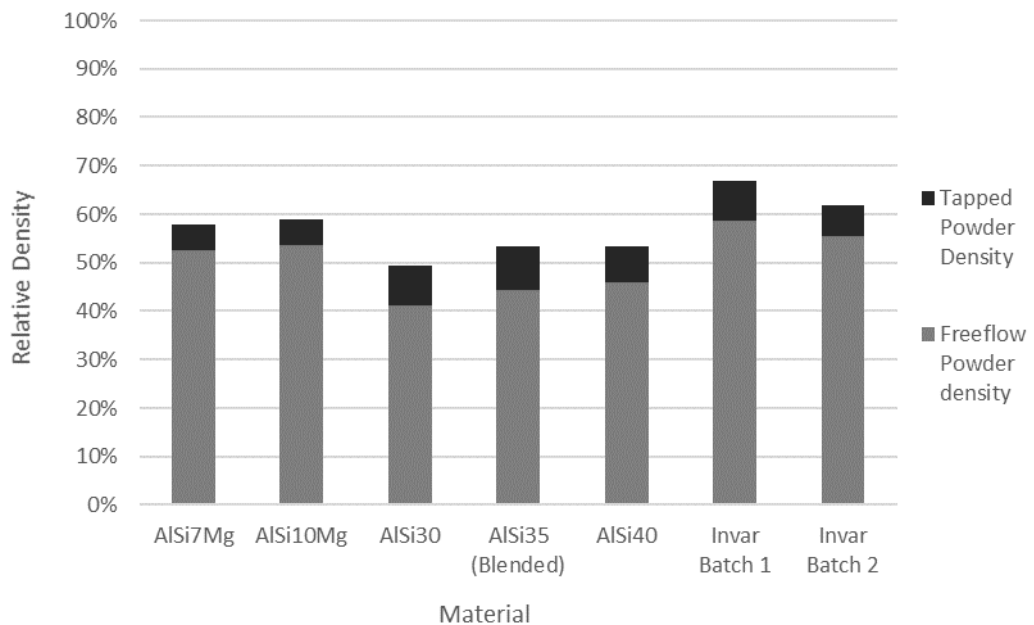


Figure 167. Tap density results for a selection of gas atomised powders.

6.4.6 Conclusion of powder characterisation

It is determined that significant flowability issues will be experienced when additively manufacturing with AlSi30-40 due to the high agglomerations in optical characterisation, the high number of satellite particles in the SEM, and increased energy response to a lower tip speed. The compaction data suggests that AlSi30-40 would offer a high packing factor in the RBV build volume, but it is unknown how this will affect the flowability over the build plate. Invar shows a high BFE response and also an increased energy at

lower tip speeds, with poor optical characterisation. It may also experience issues, but Invar has been widely demonstrated for its suitability in LPBF [151], [157], [158]. AlSi7-10Mg shows excellent optical characterisation with no agglomeration, no increased BFE response to a lower tip speed, and is widely used in LPBF [52], [53], [159], [160]. The Flow Rate Index (FRI) closely correlates with the optical classification.

A correlation can be made between the tap density and the quality of the powder observed through SEM. A powder which is more spherical and features less satellite particles is considered higher quality, and better for use with LPBF. The relative densities of the powders are higher when the particles are more spherical, with less agglomeration. The particles observed from Invar, AlSi7Mg, and AlSi10Mg are of a higher quality and feature higher relative densities, whilst AlSi30, AlSi35, and AlSi40 have a greater level of agglomeration and lower relative densities. AlSi30 has the poorest quality particles, and the lowest relative density. Invar has the highest quality particles, and the highest relative density.

6.5 Iron-Nickel (Fe-Ni) Alloys

Processing Invar with LPBF is very advantageous. The ability to create novel weight saving, topologically optimised structures, with a low coefficient of thermal expansion places it in a unique position within the aerospace industry. LPBF has been used to create several structures for satellites. Thales Alenia has sent over 80 3D printed parts into space, one included a LPBF manufactured antenna support measuring 480x378x364mm. Optimised process parameters were obtained through orthogonal array designs, analysing the effect of each parameter on density. Tensile testing was completed to obtain the optimum parameter.

Several studies improve the understanding of the effect of processing parameters on densification, microstructure, mechanical properties, and thermal properties. Yakout et al. (2017) obtained 99.87% dense components, and determined that volumetric energy density is only an approximation for full densification [161]. Qiu et al. (2016) provided a preliminary study of the mechanical properties. They reported that the as processed microstructure comprised of columnar vertically oriented γ grains, interspersed by nano precipitate α -phase. The material displayed anisotropic tensile behaviour, with specimens built in the horizontal orientation displaying superior yield strength and UTS to those built vertically; but elongation was superior in the vertical [157]. Harrison et al. (2017) followed this work and provided CTE measurements and mechanical testing for Invar 36 parts produced with a pulse modulated laser on a Renishaw SLM125. They determined an optimum 1D line energy density of between 0.35-0.40 J/mm , and maximum density at 0.33 J/mm (and 180.9 J/mm^3) with parameters of LP 190W, ET 120 μ s and PD 70 μ m

[162]. During the study, the layer thickness was fixed at 20 μ m and a HS of 90 μ m, based on the assumption from their previous study Harrison et al. (2015) from processing nickel-super alloys; that the parameters provided dense components [162]. This does not confirm the layer thickness at 20 μ m and HS at 90 μ m is optimum, only that it was a chosen fixed variable. The PSD of the powder is stated to be between 15-45 μ m meaning 20 μ m layer thickness may have not processed the entire distribution of powder. This should be avoided to reduce the likelihood of increasing the average particle size as the powder is recycled; therefore, optimising with a layer thickness of 50 μ m should be considered. There is a wide processing range when considering energy density alone, which is usually dependant on the machine and scanning strategy. Qui et al. produced fully dense parts between 10-25 J/mm^3 , Strauss and Stucky at 44 J/mm^3 , and Harrison et al. at 108.9 J/mm^3 . A new processing parameter set will need to be developed for use on the Renishaw AM400 with a layer thickness of 50 μ m.

Reference	Machine	Power (W)	Scanning Velocity (mm/s)	Layer Thickness (mm)	Hatch Spacing (mm)	Energy Density (J/mm^3)
Qui et al. (2016) [157]	Concept Laser M2	400	1800-4300	0.03	0.3	10-25
Yakout et al. (2017) [102],[106]	EOS M280	150-300	700-2200	0.040	0.08-032	23-93
Yakout et al. (2018) [163]	EOS M280	200-300	600-1000	0.04	0.08-0.12	42-156
Strauss and Stucky (2016) [165]	Phenix PXM (3D Systems)	300	2500	0.03	0.09	44
Harrison et al. (2017) [162]	Renishaw AM250	180-200	333-1000	0.02	0.09	100-333

Table 35. Laser parameters investigation ranges for LPBF of invar36.

Qui et al. (2016) determined that there is a difference in thermal expansion between components printed horizontally, and vertically when tested below the curie temperature of 300°C. Vertically printed samples exhibited higher thermal expansion than horizontally printed parts. The thermal expansion of a vertical component after heat treatment at 830°C for 30 minutes before water quenching, was reduced considerably to slightly higher than horizontal. CTE analysis conducted was not adequate to differentiate between results. Yakout et al. conducted a more comprehensive investigation, and found

CTE's exceptionally lower than that of cast. It was observed that after a stress-relieving heat treatment, the CTE increased from -0.355 and -0.471 to 0.76 and $1\mu\text{m}/\text{mK}$, concluding that the residual stress contributed to the lower CTE. This does not agree with Qui et al. who did not report on a lower CTE, but did report on lower change in expansion. Both heat treatments were at the same temperature 830°C except Yakout et al. held the material at 1h instead of 0.5h, which could be a more sufficient time to relieve residual stress.

Reference	Process	Temperature Range $^\circ\text{C}$	CTE $\mu\text{m}/\text{mK}$
Chapter 6.5.2	Induction Melted.	0-100	1.75
		100-200	3.79
		0-300	5.08
Yakout et al. (2017) [161], [163], [164]	LPBF aligned to build direction.	30-279	3.56
		30-100	-0.355
	LPBF normal to build direction.	30-279	3.34
		30-100	-0.471
	LPBF + Stress Relief aligned to build direction.	30-279	3.68
		30-100	1.00
	LPBF + Stress Relief normal to build direction.	30-279	3.36
		30-100	0.76
Qiu et al. (2016) [157]	LPBF as-built vertically, horizontally, and vertically heat treated.	0-300	3.5
		100-200	2.0
Asgari (2018) [151]	LPBF as-built to build direction.	0-300	3.0
		100-200	2.0

Table 36. CTE's for invar36 LPBF manufactured samples.

6.5.1 Optimum laser parameters for full densification

To obtain the best laser parameter set that creates full densification of gas atomised invar36 (batch 2), an L9 orthogonal array has been used to analyse the influence of the laser parameters on the density. The first setting chosen is placed in the level 1 column. 316L has been determined to be the closest in chemistry to invar36 and so will be used as a starting point. Layer thickness will be kept at $50\mu\text{m}$. The Renishaw provided 316L parameters are placed in column 1. A parameter increase for each level was; PW = 25W, ET = $25\mu\text{s}$, HS = $10\mu\text{m}$, and PD = $2.5\mu\text{m}$.

		Build 1			Build 2		
Parameter (units)	Label	1	2	3	1	2	3
Point distance (μm)	PD	65	67	70	60	65	70
Hatch Spacing (μm)	HS	90	100	110	95	100	105
Exposure time (μs)	ET	60	85	110	75	80	85
Power (W)	PW	180	205	230	200	210	220

Table 37. L9 input parameters for invar36 build 1. Level 1 build 1 is the settings for 316L provided by Renishaw. Level 1 build 2 is an estimated optimum setting from build 1.

<u>Build 1</u>						
Sample	PD	HS	ET	PW	Energy Density (J/mm^3)	Relative Density %
A1	65	90	60	180	36.92	99.11
A2	65	100	85	205	53.62	99.97
A3	65	110	110	230	70.77	100.09
A4	67	90	85	230	64.84	99.99
A5	67	100	110	180	59.10	99.96
A6	67	110	60	205	33.38	97.54
A7	70	90	110	205	71.59	100.10
A8	70	100	60	230	39.43	99.59
A9	70	110	85	180	39.74	99.09
<u>Build 2</u>						
A1	60	95	75	200	52.63	99.67
A2	60	100	80	210	56	100.02
A3	60	105	85	220	59.37	100.10
A4	65	95	80	220	57.00	99.98
A5	65	100	85	200	52.31	99.91
A6	65	105	75	210	46.15	99.61
A7	70	95	85	210	53.68	99.89
A8	70	100	75	220	47.14	99.86
A9	70	105	80	200	43.54	99.80

Table 38. Laser parameters and corresponding relative densities obtained. Red signifies higher energy density while green is lower.

Build 1								
	Step 4 – Average of relative densities at each level (%)			Step 5 – Response of each Laser Parameter		Step 6 – Maximum density		
Laser Parameter	1	2	3	Response (%)	Rank	Max Density (%)	Parameter Level	Value
PD	99.72	99.16	99.59	0.56	4	99.72	1	65
HS	99.73	99.84	98.90	0.94	2	99.84	2	100
ET	98.74	99.68	100.0	1.30	1	100.04	3	110
PW	99.38	99.20	99.88	0.68	3	99.88	3	230
Build 2								
PD	99.93	99.83	99.85	0.10	3	99.93	1	60
HS	99.84	99.93	99.83	0.10	3	99.93	2	105
ET	99.71	99.93	99.96	0.25	1	99.96	3	85
PW	99.79	99.84	99.98	0.19	2	99.98	3	220

Table 39. Response and density result analysis for steps 4,5 and 6 outlined in experimental Chapter 4.7.

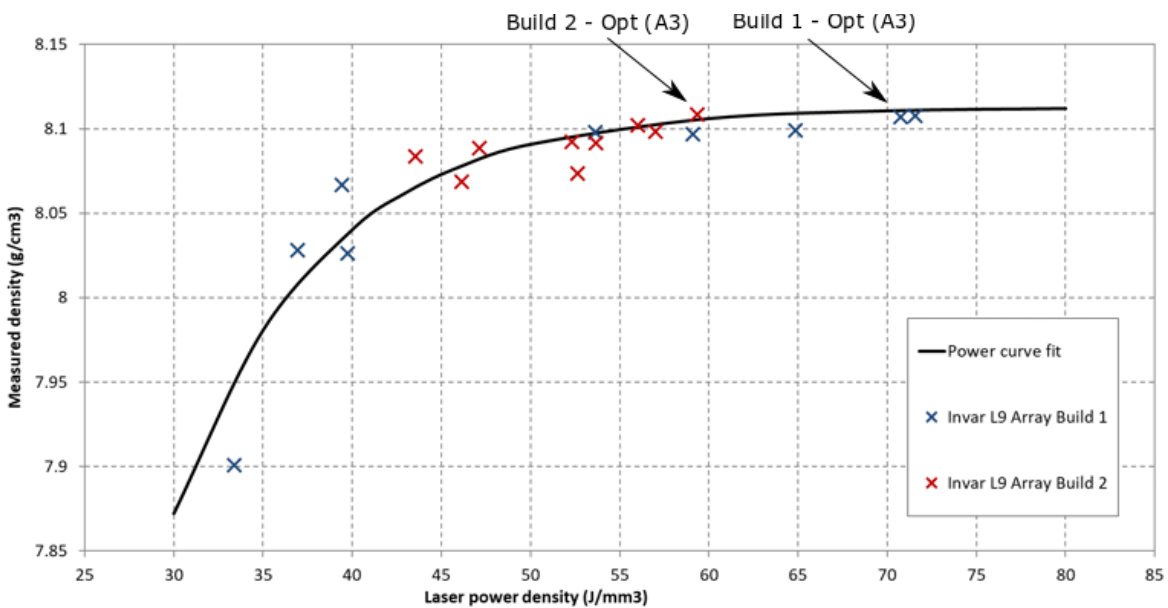


Figure 168. Invar36 build 1 and 2 Archimedes density plotted.

Looking at the wide range of variation in energy density, measured density (Table 38), and large response (Table 39) to each parameter in build 1, it was decided in build 2 to reduce the range of volumetric input energy. To achieve this a smaller value increase for each parameter set was used across levels 2 and 3, tightening the overall volumetric energy density as seen in Figure 168.

The optimum laser parameter setting for invar36 was determined to be; PW 220W, ET 85 μ s, HS 105 μ m, and PD 60 μ m. This is the component with the highest density in build 2. This provides an energy density of 59.36(J/mm³), which is well within the range reported in literature.

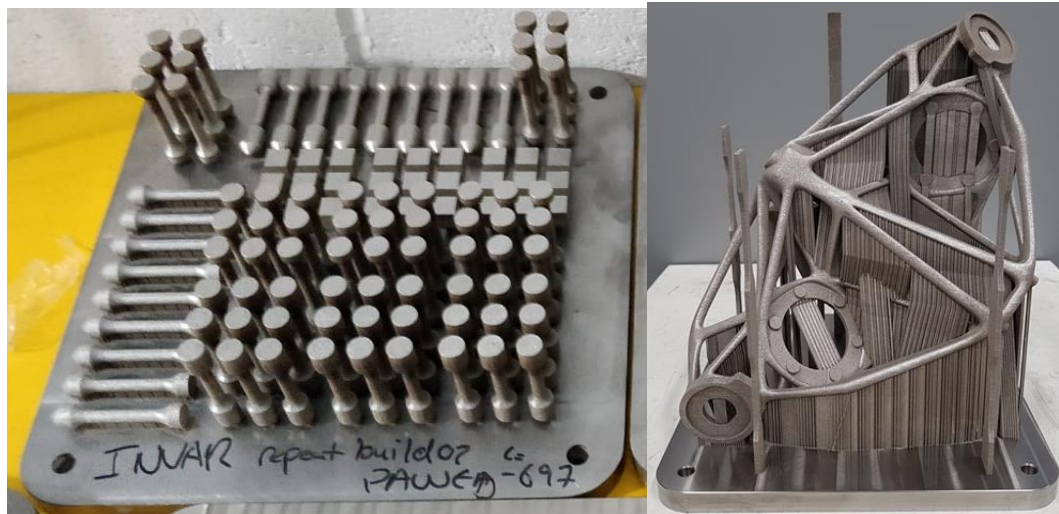


Figure 169. Tensile and density arrays used to determine optimum laser parameters (left), and the successful build completed using the parameters for Thales Alenia.

6.5.2 Invar induction melted compositional adjustments

This part of the chapter investigates the effect of adjusting the nickel content of invar (FeNi36) on the thermal expansion. For invar to have its lowest CTE, the alloy must have 36wt.% Ni, but the low CTE effect will be reduced if the nickel content is increased or decreased. The thermal expansion behaviour will be analysed to determine the differences when tailoring above or below the critical 36wt.%Ni and the range of CTE's available. This information will be a useful basis for comparison later in the thesis when comparing outcomes with the material manufactured using LPBF. Based on literature outlined in chapter 2.2.1 the CTE is less sensitive to nickel increases above 36% than decreases below it. To tailor the CTE to match that of glass or germanium ($6-7\mu\text{m}/\text{mK}$) it is easier to increase the nickel content and have a wider band of acceptable nickel content for the target CTE range. This increases the ease of targeting the specific nickel content required. To manufacture the samples for testing, iron and nickel powder has been mixed in the correct proportions to obtain a range of nickel content from 32-50% in increments of 2%. A total of 9 samples have been manufactured with the following ratios;

Sample No.	Iron wt. (g)	Nickel wt. (g)	Target Nickel wt. %	EDS Nickel wt. %
1	34.00	16.00	32	31.06
2	33.00	17.00	34	32.93
3	32.00	18.00	36	35.18
4	31.00	19.00	38	37.04
5	30.00	20.00	40	38.83
6	29.00	21.00	42	41.14
7	28.00	22.00	44	43.40
8	27.00	23.00	46	44.76
9	26.00	24.00	48	47.03
10	25.00	25.00	50	48.83

Table 40. Fe-Ni(x) induction melted alloy target and EDS measured composition.

The powders are thoroughly mixed by stirring for a full minute, and compacted 10g at a time using 20KN of force into 12.5mm diameter cylinders. This is completed five times and placed inside a 10x30mm cylindrical crucible. The samples are heated using an induction coil inside an argon environment. Every 20 seconds the power was increased by 200W up to 2.2KW and the held for 5 minutes until fully melted and combined. After casting, the samples have been turned on a lathe to manufacture the required 25x5mm rods for dilatometry. These samples will be used as a reference for the CTE from conventional casting techniques.

Composition

The composition of the iron-nickel alloys has been confirmed using EDS. The percentage of nickel is lower across all samples than what was intended. The measured nickel content ids to be used as the reference point for analysis against the CTE.

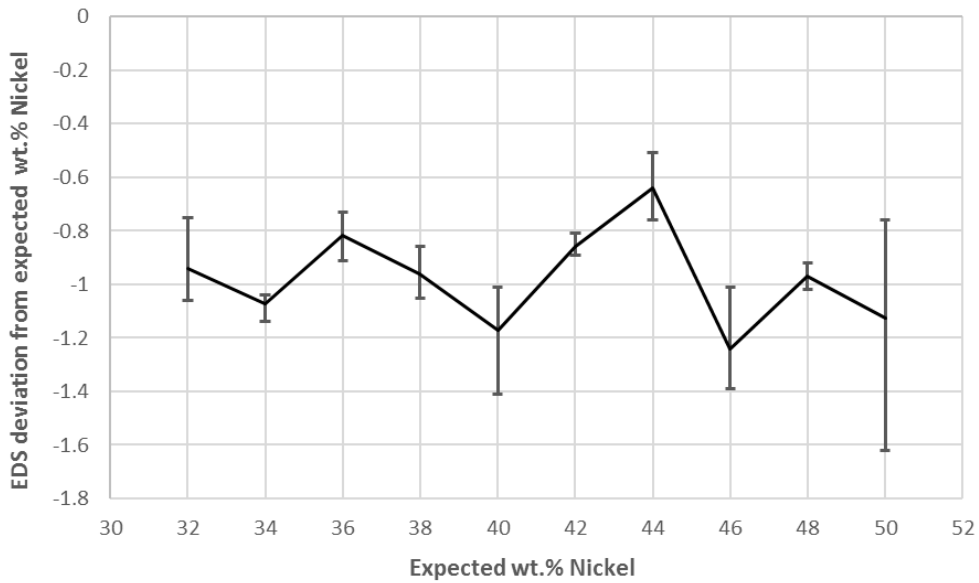


Figure 170. Fe-Ni(x) induction melted alloy deviation in target nickel composition.

Thermal Expansion

The thermal expansion will be measured using dilatometry from -120°C to 450°C at 5K/min with a 1-hour isothermal, then back down from 450°C to -120°C . This optimum program has been determined in the experimental methods chapter 4.2.

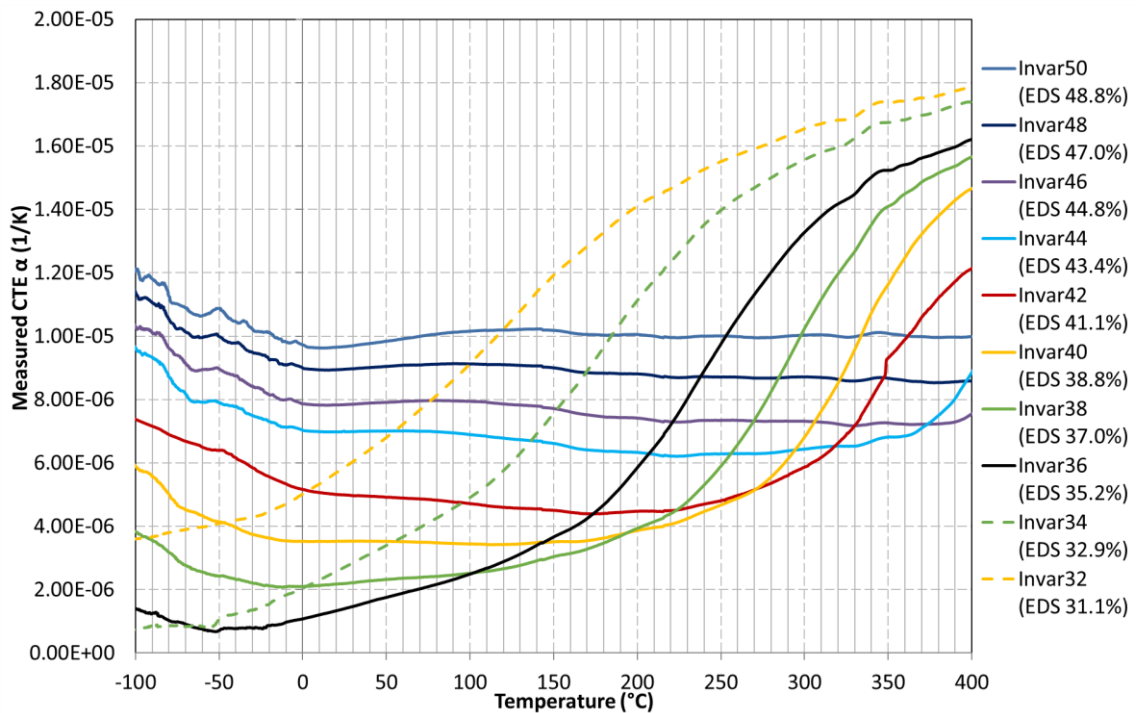


Figure 171. Dilatometry results showing physical alpha for induction melted Invar alloys **cooling** from 450°C to -120°C at 5K/min .

It is seen that the physical alpha curves increase rapidly with a sharper incline for nickel values below that of invar36. It can be seen that the temperature at which the low CTE

effect is observed becomes less as the nickel content is reduced. It can be seen that with 37% nickel, the sample experiences a lower CTE between 120 to 400°C, but invar with 35.2% Ni experiences the lowest from -60 to 120°C. It can even be seen that invar with 32.9% Ni experiences a lower CTE between -100 to -60°C. The curie temperature of Fe-Ni alloys decreases with nickel content, so this would explain the shift in the low CTE properties.

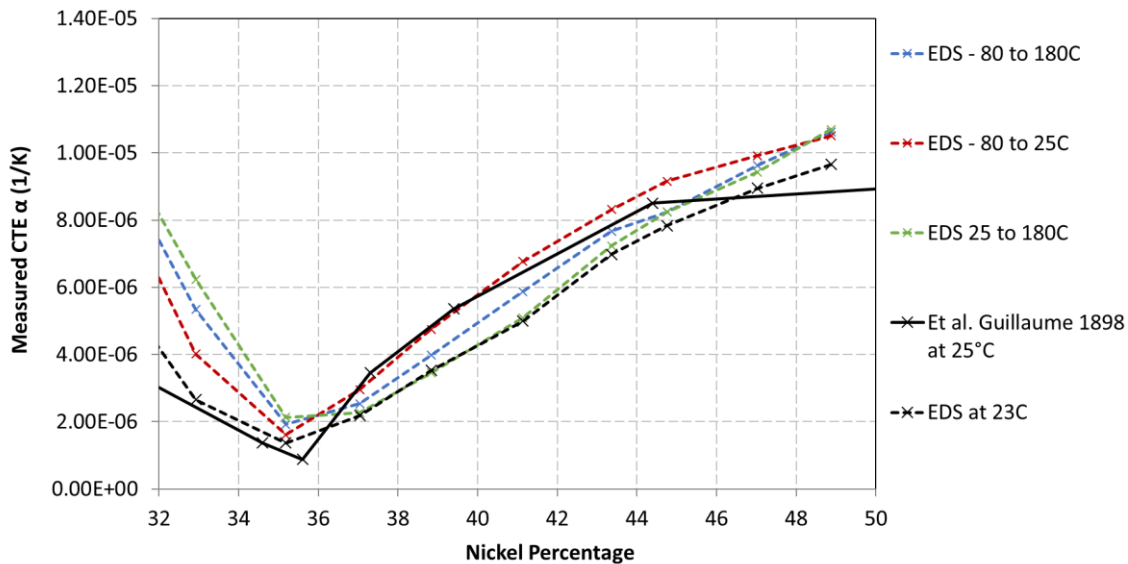


Figure 172. Dilatometry cooling cycle results. CTE's plotted for induction melted Invar alloys. Cryogenic and above ambient temperature ranges, as function of the nickel percentage measured using EDS.

It is seen that the CTE with reference to the EDS produces the lowest CTE effect at about the 35-36wt.% area for a useful temperature range. The CTE of glass or germanium (6-7 $\mu\text{m}/\text{mK}$) can be matched with approximately 40-42 wt.% nickel in the cryogenic region, and approximately 41-43wt.% nickel for -80°C to 180°C. The cast induction melted samples agree with the trends presented by Guillaume.

Conclusion on invar induction melted compositional adjustments

In the induction melted FeNi samples, the EDS measured values were consistently less than the targeted values for nickel. The EDS nickel wt.% tracked very well with the expected CTE results in comparison to Guillaume et al., with the lowest CTE is experienced between 35-36wt.% Ni, consistent with literature. It is observed that the CTE result tested at below ambient temperatures (-80 to 25°C), is lower than the CTE tested at above ambient temperatures (25 to 180°C), for nickel content of 36wt.% and below. The opposite is true for above 36wt.% nickel. This data provides a good basis for comparison against thermal expansion values obtained through LPBF.

6.5.3 Invar in-situ compositional adjustments

The thermal expansion of invar has been proven to be very sensitive to the percentage of nickel present in the iron-nickel alloy. It is observed in the induction melted invar samples that there is a point of very low CTE at approximately 35-36%. It has been established from sourcing of invar36 gas atomised powder that it is very difficult for the manufacturer to hit the critical 36wt.% Ni. In batch 1 of invar provided by TLS, the chemical analysis shows a nickel content of 35.1wt.%, while batch 2 provided by Sandvik shows a nickel content of 37.2wt.%. This part of the chapter investigates the feasibility of adding nickel powder to batch 1, and iron powder to batch 2 by 1 and 2wt.% of each. This aims to provide an overall composition of between 35.2 and 37.1wt.% Ni using both batches. The powder used will be fine carbonyl for easier mixing with the larger gas atomised powder. 1wt.% of Gas atomised nickel powder will be added to batch 2 to assess if a larger powder can be successfully mixed, then 7wt.% will also be added to try and get a similar CTE as germanium or borosilicate glass (6-7 μ m/mK). Gas atomised was decided to be used instead of carbonyl due to concerns about poorer flowability of the overall mixed powder after adding a large amount of finer carbonyl. PSD's can be found in chapter 8.4.3. If successfully alloyed, the ability to add powders in-situ and blend them together provides engineers with the ability to produce components with multiple CTE's from one powder source. This is an economic advantage, especially for limited production runs where only a small quantity of powder is required.

Similar research has been conducted into the use of blending elemental powders together and melting in-situ. A study conducted by Hua et al. [166] combined elemental powder of Ti, Al, and V to produce a bulk Ti64AlV component using a 2KW laser engineered net shaping (LENS) system with the powder injected into the melt pool. All three elemental powders were mixed homogeneously in the feedstock before being injected. It was demonstrated that the mechanical properties were found to be at least equal to those of parts produced with pre-alloyed powder. Several other authors have reported on the successful production of in situ metal matrix composites (MMC's) [167]–[172]. The melt behaviour of a LPBF system is different to that of a LENS based system. Research has been conducted showing the addition of Molybdenum powder to Ti64Al powder and processed using LPBF successfully achieves a Ti64Al+Mo MMC, providing improved ductility over Ti64Al using the same process [172].

Mixing Fe and Ni powders by blending in-situ has been researched, the first being Zhang et al. (2011) who mixed elemental iron and nickel powders and processed using LPBF. The initial overall composition in their first paper was Fe-30%Ni, which looks at the effect of adjusting laser power at intervals from 50,70,90, and 110W, and scanning velocities of 100, and 200 to 1600mm/s in 200mm/s increments for each laser power. The paper discovered correlations between larger crystallite sizes and with faster scanning

speeds and lower laser power. Its main focus was on the magnetic properties of the alloy. The paper did not assess densities, but did find that at 90W, and 100mm/s produced a dense part, but did not find a homogenous sample in any of the presented EDS map scans [173], [174]. His later work looked at Fe-Ni80wt.% found dense parts with 100W and 100,200,300, and 400mm/s scanning speeds with the same increasing crystalline size, no EDS map scans were presented. Research was also conducted by Gaard et al. (2006) shown that an MMC can be made by sintering TiC with a pre-alloyed invar36 gas atomised powder, with mixed success. Variations of 30,60,80wt.%Ni were added to the invar36, with 60 and 80% creating thermal cracks. Porosities were 10, 23, and 8% respectively. The low CTE effect was lost due to the dissolution of Ti and C in the invar36 matrix [175]. Strauss et la. (2016) has conducted a study to determine the feasibility of adding Fe and Ni36wt.% blended powder in-situ, to create invar36 components using LPBF. They used gas atomised Fe and Ni powders with a D(90) of 22.2 and 20.7 μ m each. They found that although they obtained fully dense parts, EDS map scans show nickel and iron rich regions around the cross-sectioned melt pools. They determined that after heat treatment at 1310°C for 90 minutes, the iron nickel rich regions diffused to form a homogeneous part.

Reference	Composition	PSD (μm)		Machine	Power (W)	Scanning Velocity (mm/s)	Layer Thickness (μm)
		Range (μm)	D(50) Mean Size (μm)				
Zhang et al. (2013)[173], [174], [176]	Fe-30%Ni Fe-80%Ni	Fe;<60 Ni;<58	Fe;35 Ni;30	LPBF MCP Realize II ^{SLM}	50-100	100-1600	50
Gaard et al. (2006) [175]	Fe-36%Ni& TiC (30,60,80wt. %) MMC	Fe-36%Ni &TiC; 1-50	Fe-36%Ni; 7 TiC; 30-50	DMLS EOSINT M 250	-	50	-
Strauss et al. (2016)[165]	Fe-36%Ni	D(5): Fe;3.6 Ni;3.9 D(90): Fe;22.2 Ni;20.7	Fe;11.7 Ni;11.7	Phenix PXM (3D Systems)	225-300	2500	30

Table 41. Literature references for in-situ LPBF composition, PSD, and manufacturing setup.

Method

To manufacture the components a Renshaw AM400 will be used with a Reduced Build Volume (RBV) with a 100x100x62mm build plate. More information on the setup of a RBV can be found in the manufacturing section 6.3. Enough powder will be mixed to obtain enough powder to fill the full height of the RBV axis. For the powder mixing a V-type blender will be used for 45 minutes. It is manufactured by LFA Tablet Presses, and has a barrel capacity of 8 litres, and an agitation speed of 60r/min. Components built will include; build density cubes, tensile bars, dilatometer rods, and LFA disks. Manufacturing is completed in a 99.999% pure argon atmosphere.

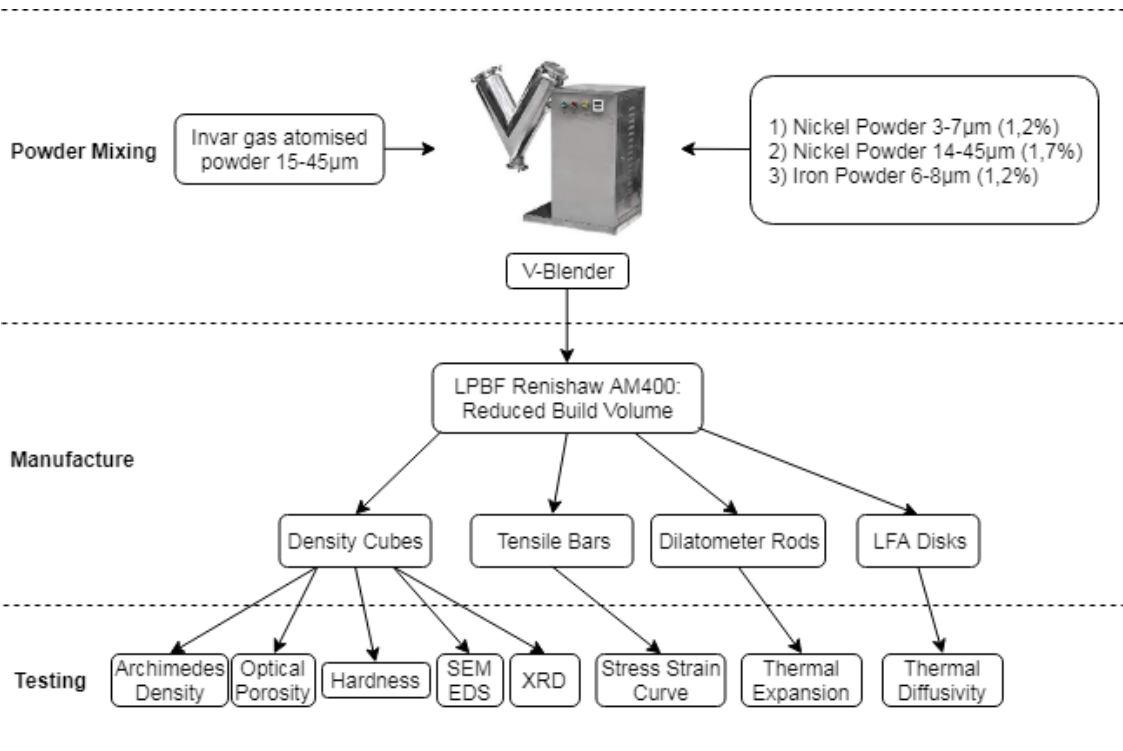


Figure 173. Process diagram for the experiment.

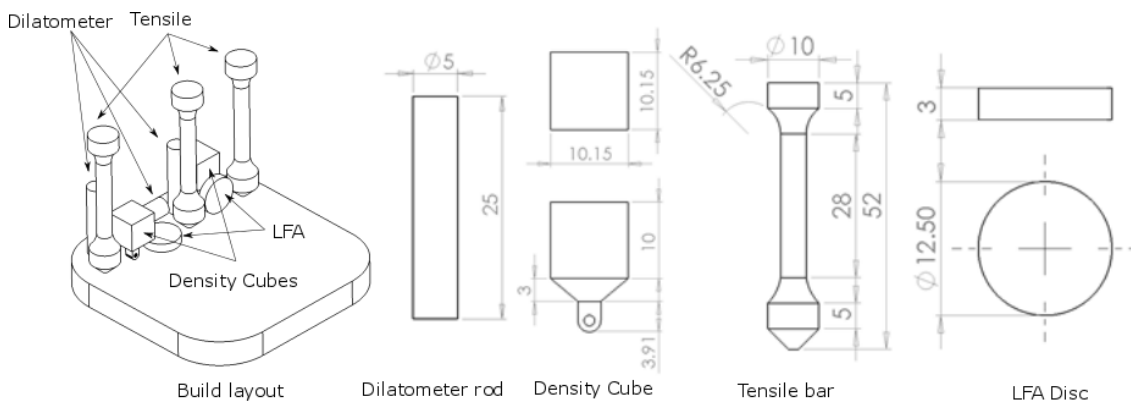


Figure 174. Build components and dimensions for in-situ blended powders.

One build will be completed per powder, featuring two vertical and one horizontally built dilatometer rod of dimensions 5x25mm, and two density cubes to measure any density variation across the powder blends. The cubes will be cross-sectioned to analysis of porosity and microstructure using microscopy. The composition will also be analysed with EDS on the SEM. The dilatometer rods will be used to measure the change in linear co-efficient of thermal expansion over each build. One vertical will be measured as-built, the other will be measured after heat treatment. Three vertical tensile bars have been custom designed within ASTM E8 to fit the reduced build volume with 10mm to spare. Two tensile bars will be heat treated, and the other will be tested as-built. The LFA discs have been printed should analysis need to be performed in the future, but for this study the thermal diffusivity data they provide is not needed to be determined.

The experiments will be conducted with 7 different blends of powders as outlined in Table 42.

Build No.	Invar Batch No.	Invar Powder wt.%Ni from ICPMS	Additions			Target Invar wt.%Ni after additions
			Quantity	Size (µm)	Type	
1	1	35.1	No additions (control)			35.1
2	1	35.1	+ 1% Ni	3-7	Carbonyl	36.1
3	1	35.1	+ 2% Ni	3-7	Carbonyl	37.1
4	2	37.2	No additions (control)			37.2
5	2	37.2	+ 1% Fe	6-8	Carbonyl	36.2
6	2	37.2	+ 2% Fe	6-8	Carbonyl	35.2
7	2	37.2	+ 1% Ni	14-45	Gas Atomised	38.2
8	2	37.2	+ 7% Ni	14-45	Gas Atomised	44.2

Table 42. Build plan showing percentage of in-situ Fe and Ni additions added.

These can be visualised easier in Figure 175 by plotting the original nickel content in invar36 powder against the target nickel content after the additions are made.

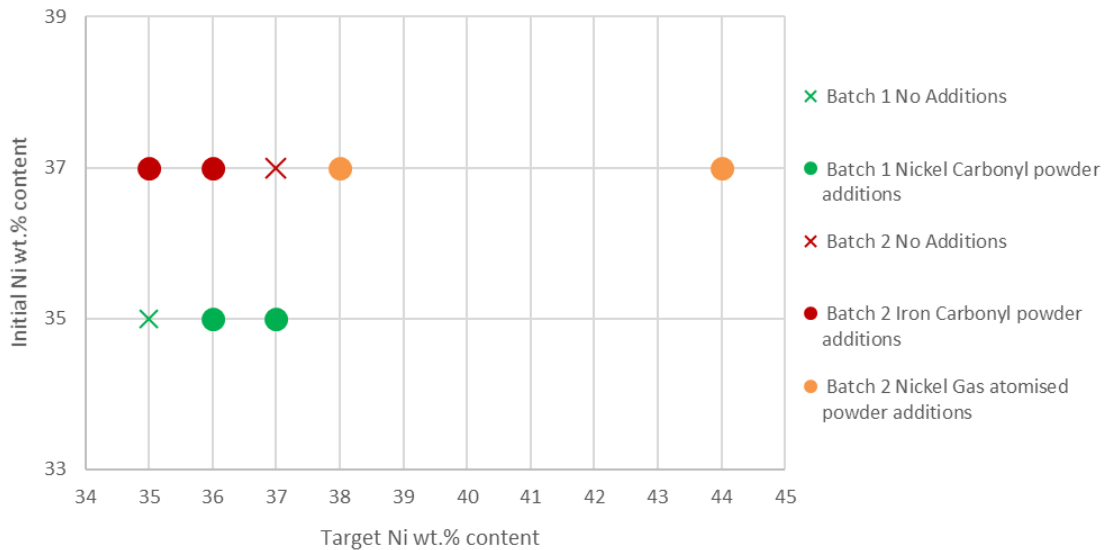


Figure 175. Plotted Ni wt.% target for each invar base alloy.

To start the experiment, the powders are mixed to obtain the full build volume of $0.0006m^3$. Assuming an invar density of $8100kg/m^3$ gives a weight of $5.022kg$. The packing factor (PF) for invar of 0.6 after compaction has been approximated from the tap density results in section 8.4.5. Adding the PF in and adding 20% for reserve, provides

an overall required weight of 3.616 kg. To simplify the weighing process 3.6 kg will be the required overall mass.

Build No.	Gas atomised invar 36 powder		Elemental additions (g)		New wt.% after additions		Confirm change in wt.%	Powder to weight out (g)		
	Fe	Ni	Fe	Ni	Fe	Ni	Ni	Invar	Fe	Ni
1	65	35	0	1.563	63.9 9968	36.0 0032	1.000315	3544.598	0	55.402
2	63	37	2.78	0	64.0 0078	35.9 9922	-1.00078	3502.627	97.373	0
3	63	37	5.7	0	64.9 9527	35.0 0473	-1.99527	3405.866	194.134	0
4	63	37	0	12.5	56	44	7	3200	0	400
5	63	37	0	1.615	61.9 9872	38.0 0128	1.001279	3542.784	0	57.216
6	63	37	0	3.28	60.9 9923	39.0 0077	2.000775	3485.67	0	114.330
7	65	35	0	3.18	62.9 967	37.0 033	2.003295	3489.048	0	110.952
8	63	37	0	10.53	56.9 981	43.0 019	6.0019	3257.034	0	342.966

Table 43. Invar in-situ blended powders mass proportions.

Analysis of the chemistry shows acceptably low levels of Mn, Si, C, N, and O. Carbon content needs to stay <0.05wt.% to ensure low CTE effect. Carbonyl powders will not increase the carbon above this level due to the high purity and low quantity used.

Powder	Fe %	Ni %	Mn %	Si %	C %	N %	O %
Invar Batch 1	Bal.	35.1	0.11	0.08	<0.1	<0.002	0.065
Invar Batch 2	Bal.	37.2	0.21	0.09	<0.1	-	0.042
Fe Carbonyl	Bal.	-	-	0.14	0.03	0.01	0.1-0.25
Ni Carbonyl	0.01	Bal.	-	0.001	0.02-0.06	-	0.1
Ni Gas Atom.	0.00	Bal.	-	0.22	0.01	<0.002	0.011

Table 44. Chemistry for the powders used measured using ICPMS.

After the components are built, two tensile bars and one vertical dilatometer rods will be subjected to a heat treatment of 850°C for 70 mins in an argon environment, with the cycle shown in Figure 176. The standard heat treatment for invar is 830°C for between 0.5hr to 1hr carried out by Qiu et al. and Yakout et al [157], [161], [163], [164], as established in J.Davies publication on alloying basics [177]. It is also the heat treatment requested by Thales Alenia performed by Renishaw for their invar components.

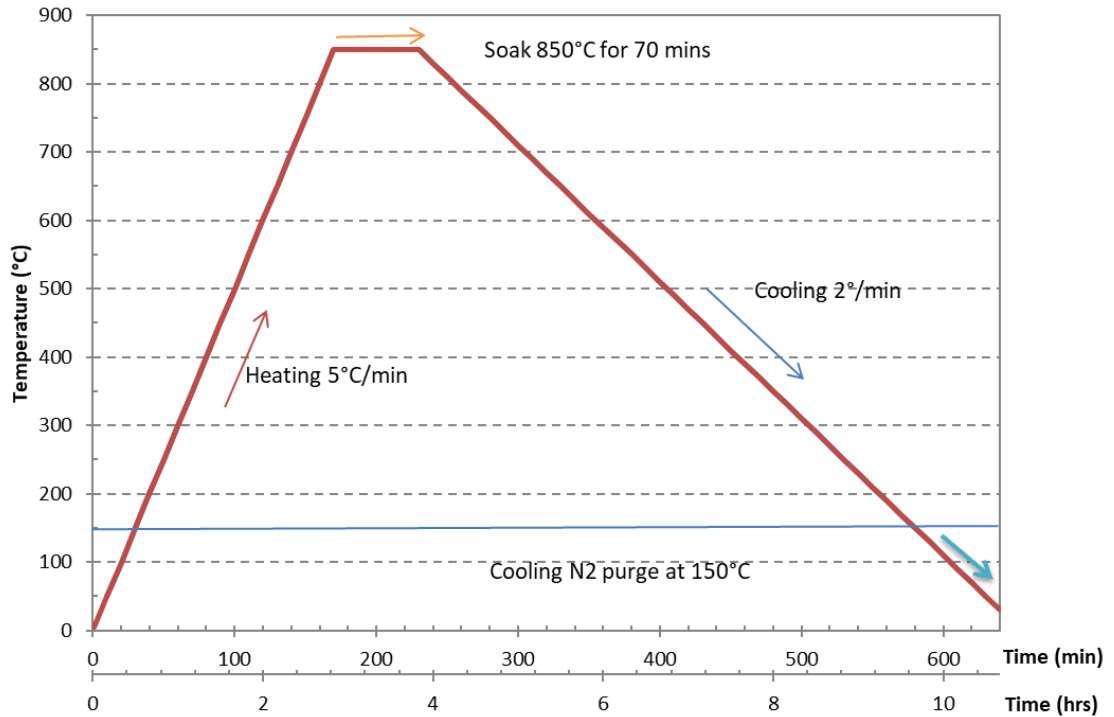
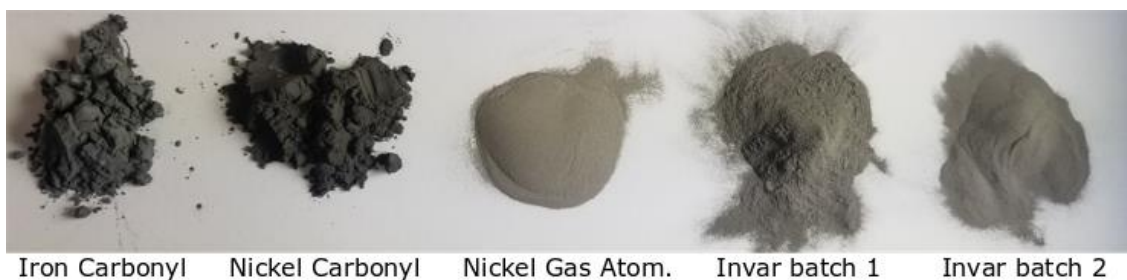


Figure 176. Heating and cooling cycle for Invar36 heat treatment.

Manufacture

To start manufacturing the blended powders, table 33 will be used to weigh out the quantities of additions. The powders mass is obtained from an Ohaus Pioneer precision balance scales, with a standard deviation of 0.0001g. Once measured, the powders are loosely mixed by stirring to avoid the additions adhering to the powder mixer by static forces. The V-Type blender used is manufactured by LFATabletPresses. It has a barrel capacity of 8litres, and an agitation speed of 60r/min. After purchasing, the inside of the powder mixed was polished by running a vibratory polishing fluid and ceramic chips inside for 2 hours. Smaller chips were later used to provide a mirror finish inside. This ensures minimal pickup of contaminants caused by abrasion caused by the powder to the inner surface during mixing. To start the powder mixing process, the full 3.6Kg of powders are added and mixed for 45 minutes. Powder is removed back into a container using an air tight seal. The seal is used to ensure smaller particles are not lost to the air.



Iron Carbonyl Nickel Carbonyl Nickel Gas Atom. Invar batch 1 Invar batch 2

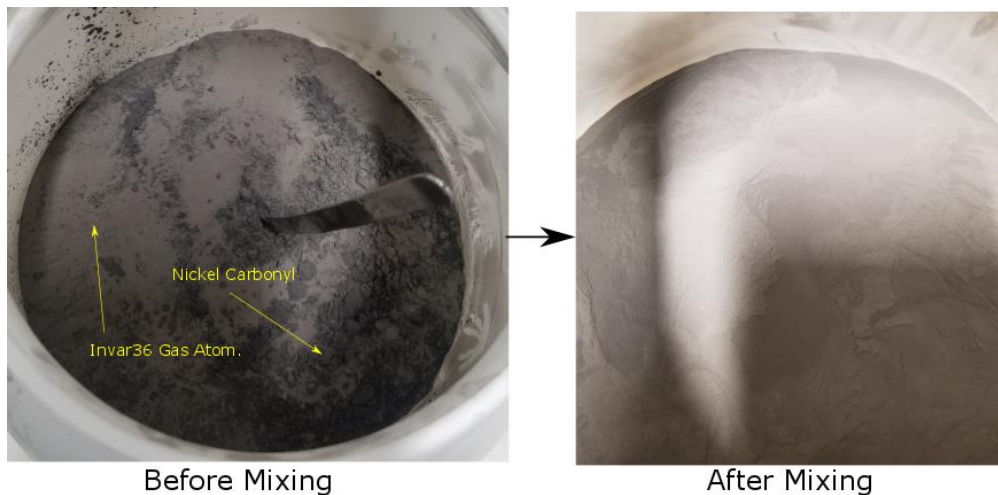


Figure 177. Images of powders before and after blending.

Once mixed, the powder is transferred to the RBV where it is compacted by hand into the dosing stage. The build is printed onto a stainless-steel plate. Pre-heating is not available on the RBV so it will likely remain at ambient temperature of 23°C. The optimal laser parameter settings were used for all builds, determined at the start of the chapter. The hatch pattern will be meander as it is considered optimal for reduced residual stresses. There is a limitation with the RBV meaning that builds can only be placed at the very front quarter of the plate. Any components further back have a higher likelihood of failure due to insufficient powder spreading.

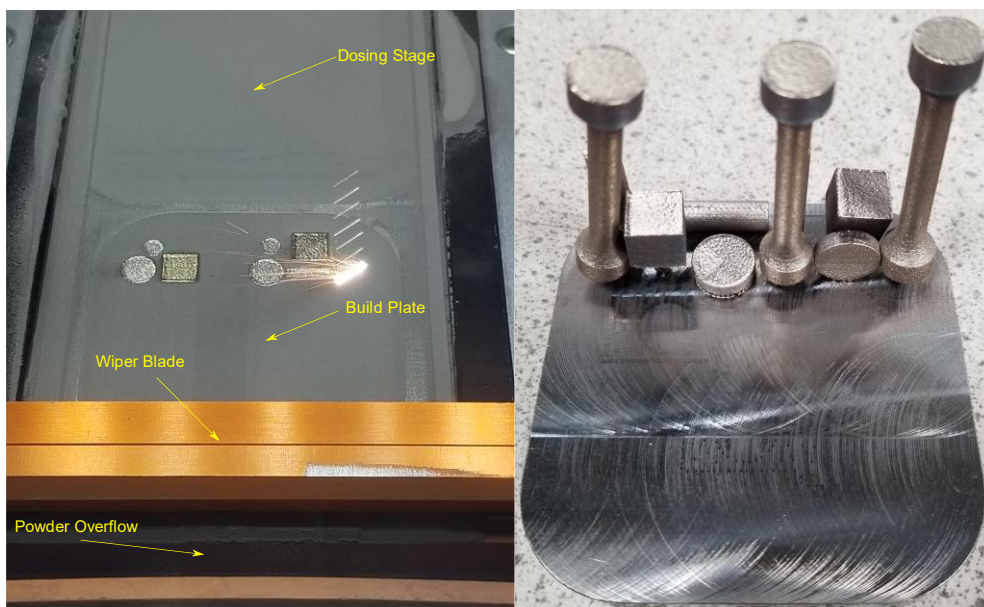


Figure 178. Image of RBV build in progress (left) and the finished build (right).

Once manufactured, the samples are removed from the plate, and the plate is ground down until flat, ready for the next build. All components printed successfully with no failed parts. Powder spreading was sufficient in all builds despite concerns that the finer

carbonyl powder would reduce flowability. It was noticed that the flowability was poorer whilst handling, but this did not affect the build quality.

Results

To understand the effect of the iron and nickel additions, the following data needs to be collected;

- Composition – To determine if the nickel and iron content deviate from the targeted values; and show homogeneity of alloy constituents.
- Density – To determine if fully dense parts have been made.
- Microhardness – determine if hardness changes across builds.
- Tensile – determine if UTS, elongation, and elasticity modulus changes across builds.

Composition

To determine if the additions have fully formed in with the invar alloy, EDS has been used to qualitatively determine its homogeneity throughout the alloy and quantify the overall nickel content. An EDS map scan has been performed on the side and top cut from a density cube, from locations shown in Figure 179. Two low resolution map scans have been completed on the top and side cross sections, and one high resolution scan. The nickel content over the three map scans has been averaged and plotted in Figure 180. The high-resolution scan has been used to visually determine the locations of any nickel or iron rich regions. More information about the range of EDS settings and their effect on measurement results can be found in the experimental methods chapter. All scans were conducted with the settings shown in Table 45.

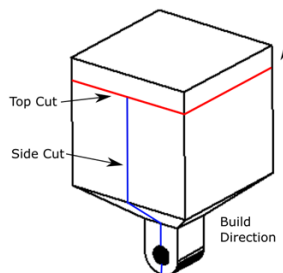


Figure 179. Density cube cut orientations for microscopy and EDS.

Resolution	Power	Spectrum Scan Resolution (T1-T4)	Number of sweeps	Spot Size	Dwell time	Scan Time
267x211	20KV	T4	5	65nm	1.0msec	15mins
1024x720	20KV	T2	5	65nm	1.0msec	70mins

Table 45. EDS scan settings used.

The additions of elemental powder to the two invar batches are manufactured, and the composition measured using EDS. The composition is measured and reported in Table 46.

Build No.	Invar Batch No.	Invar Powder wt.%Ni from ICPMS	Additions wt.%	Target wt.%Ni with additions	Component cross-section wt.%Ni from EDS		
					Side	Top	Average of side and top
1	1	35.1	No additions (control)		36.84	36.75	36.79
2	1	35.1	+ 1% Ni	36.1	37.83	37.83	37.83
3	1	35.1	+ 2% Ni	37.1	38.84	38.97	38.91
4	2	37.2	No additions (control)		36.98	36.96	36.97
5	2	37.2	+ 1% Fe	36.2	36.05	35.94	36.00
6	2	37.2	+ 2% Fe	35.2	35.02	35.03	35.02
7	2	37.2	+ 1% Ni	38.2	37.88	37.83	37.86
8	2	37.2	+ 7% Ni	44.2	46.59	41.69	44.14

Table 46. Build numbers with the EDS map wt.% of nickel for density cube side and top cross-sections.

For easier visualisation, the weight percentage nickel obtained from the EDS readings are normalised against the target values and plotted for the side and top cross-sections in Figure 180.

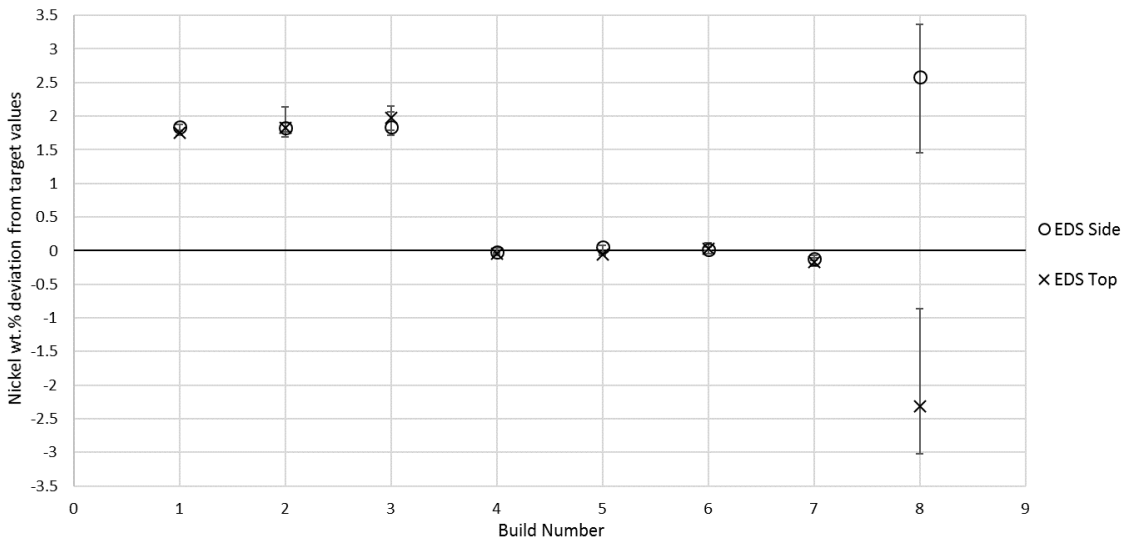


Figure 180. Deviation of nickel wt.% measured using EDS, from the target Ni content.

Figure 180 shows that build 1 is approximately 1.8wt.% above the intended nickel content. This is also true for builds 2 and 3, meaning that the nickel content added has increased by the intended amount. Invar batch 1 powder was shown to have a nickel

content of 35.1% measured using ICPMS, however the as built components are nearer to 36.79%. A 1.69% deviation is observed. The added nickel powder in builds 2-3 by 1-2% respectively were intended to increase the nickel content to 36-37%, providing data either side of the lowest CTE point at 36%. Builds 2 and 3 now show a nickel content of 37.8%, and 38.9% so a higher CTE would be expected from both builds compared to build 1. The ICPMS for invar batch 2 was shown to be 37.2% and the as-built component is shown to be 36.97%, confirming that the ICPMS was accurate for build 2. A map scan can be used to determine if there are any nickel or iron rich areas in the alloy. For comparison before and after the additions, presented first are the EDS scan of batch 1 and 2 with no additions.

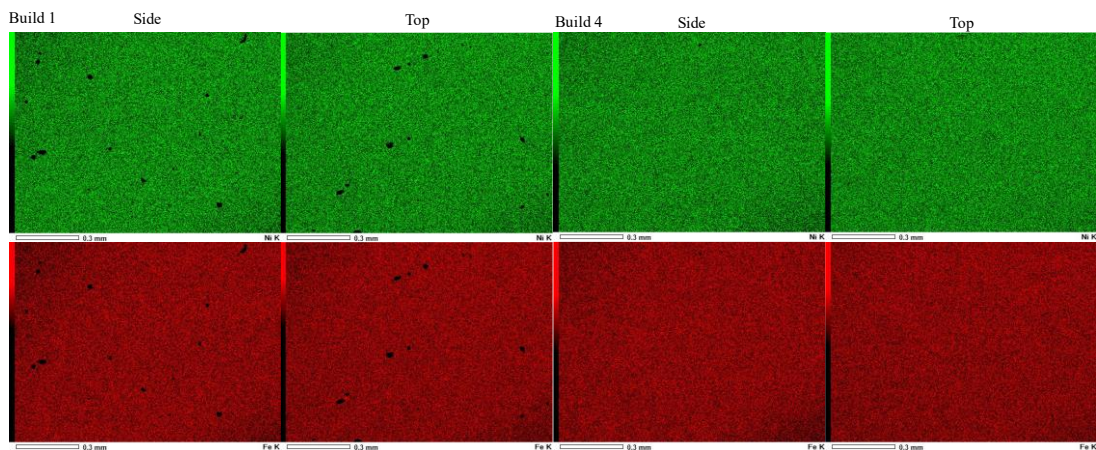


Figure 181. Build 1 & 4 – EDS map images for Invar batch 1 and 2 with no in-situ additions. It can be seen that for an alloy for no additions there is homogeneity throughout the map scan. The black spots seen in build 1 are porosity.

Figure 182 shows that with the addition of fine nickel powder, there is still homogeneity throughout. There is no difference compared to no additions in build 1.

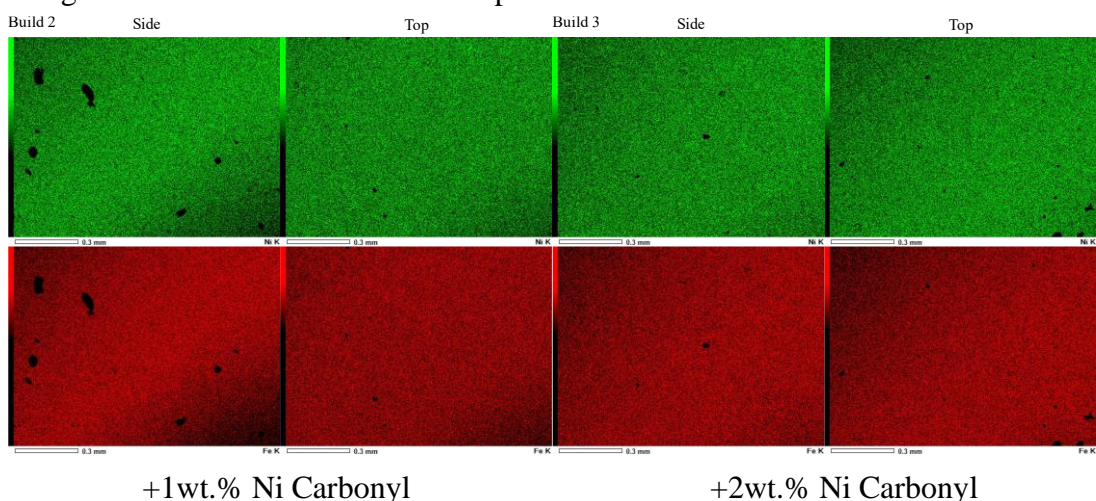


Figure 182. Builds 2 & 3 – EDS map images for invar batch 1, with 1 & 2wt.% Ni carbonyl fine powder (3-7 μ m diameter) added in-situ.

Figure 183 shows what with the addition of fine iron powder, there is still homogeneity, but there are a few small regions of nickel rich areas highlighted in yellow.

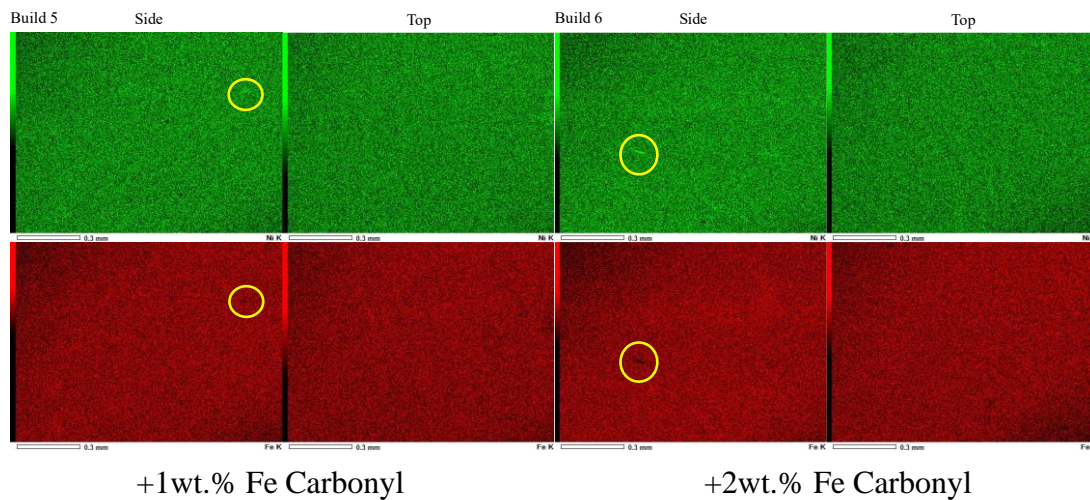
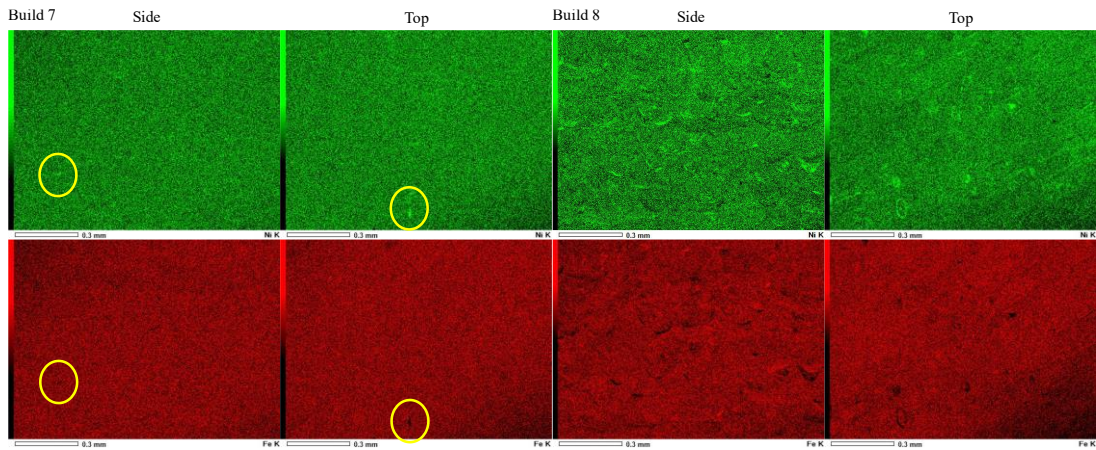


Figure 183. Builds 5 & 6 – EDS map images for invar batch 2, with 1 & 2wt.% Fe carbonyl fine powder (6-8 μ m diameter) added in-situ.

Figure 184 shows that with the addition of 1 and 7wt.% of nickel powder of a similar particle size as the invar (15-45 μ m diameter), by qualitative analysis the nickel rich region highlighted is larger than with 1% fine iron powder in build 5. Build 8 has the largest amount of nickel powder at 7wt.%. The nickel has many rich regions throughout, indicating it has not properly alloyed. The regions are located in the bottom shape of a typical weld pool region when inspecting the side cross-section. This indicates the nickel has not properly mixed during the laser weld. Strauss et al. [165] combined elemental Fe-Ni36wt.% and melting using LPBF and obtained similar nickel and iron rich areas shown using EDS. They demonstrated that heat treatment at 1310 $^{\circ}$ C for 90 minutes successfully homogenised the distribution of elemental constituents creating a fully alloyed part [165]. This shows that although adding +7wt.%Ni didn't fully alloy as-built, a heat treatment would improve the properties, bringing it closer to that of conventionally SLM'd material. The effects of heat treatment should be seen in the mechanical testing and thermal expansion data.



+1wt.% Ni Gas Atomised

+7wt.% Ni Gas Atomised

Figure 184. Builds 7 & 8 – EDS map images for invar batch 2, with 1 & 2wt.% Ni gas atomised powder (15-45µm diameter) added in-situ.

Density

To determine suitability of the in-situ blended powder additions to produce fully dense parts, the porosity has been measured using Archimedes and optically by cross-sectioning the density cube. Both methods of testing are outlined in section 5.4

To assess the porosity optically, an average of the porosity for the side and the top cross-section is taken as described in chapter 5.4. This data is presented in the graph shown in Figure 185.

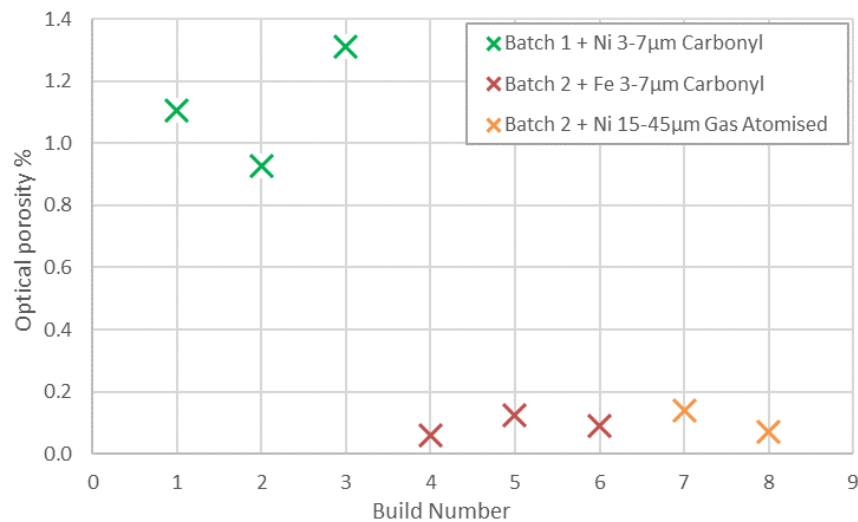


Figure 185. Optical porosity for invar builds with in-situ Fe and Ni additions.

The images from the optical porosity data have been cropped in Figure 186 to present a 1x1mm image in black and white showing porosity across all the cross-sections.

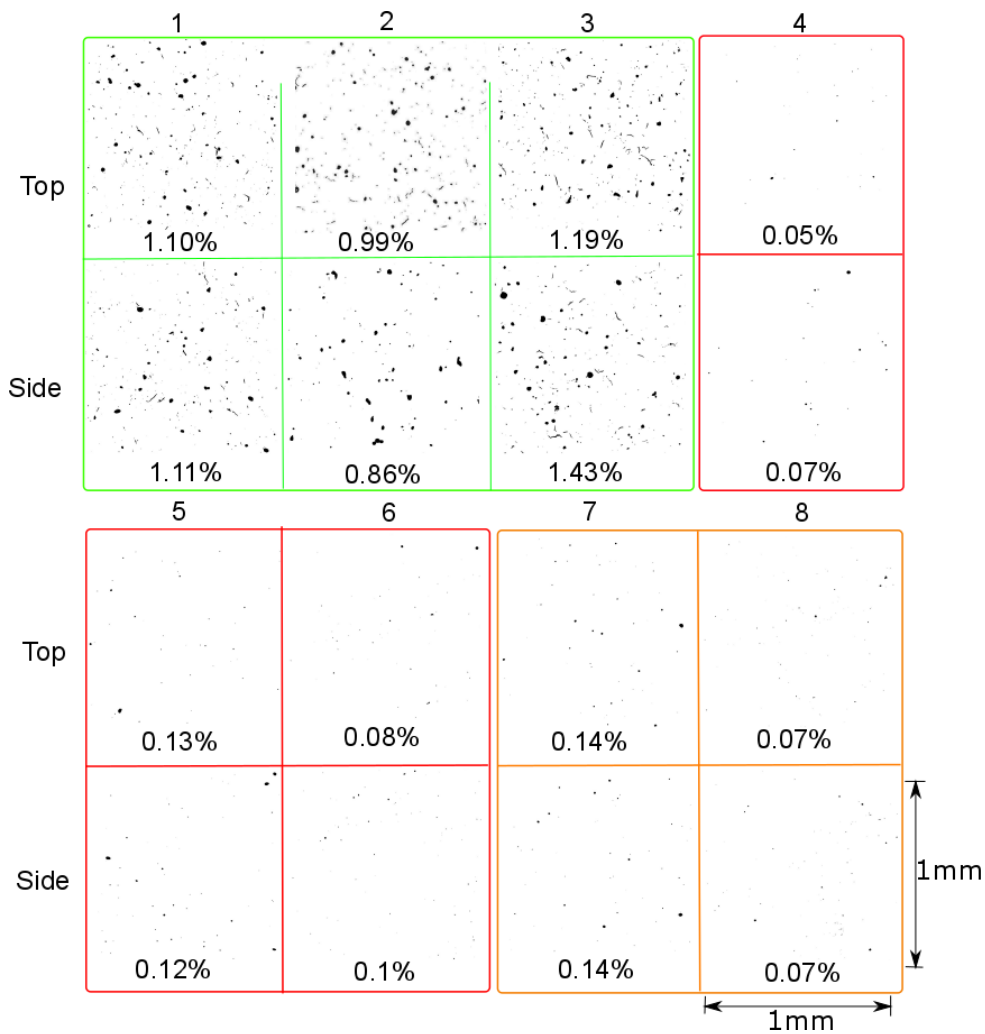


Figure 186. Optical porosity images showing porous locations for the in-situ blended compositions using the build number notation.

From the optical porosity data Figure 185 and Figure 186, there is a higher level of porosity in batch 1 compared to that of batch 2. Full densification is considered when densities of above 99.8% are achieved. All of batch 2 achieves above 99.87% density, with little noticeable effect from the additional powders. To verify the optical porosity, Archimedes has also been used to determine the density. This data has been plotted in Figure 187 as a function of the nickel content.

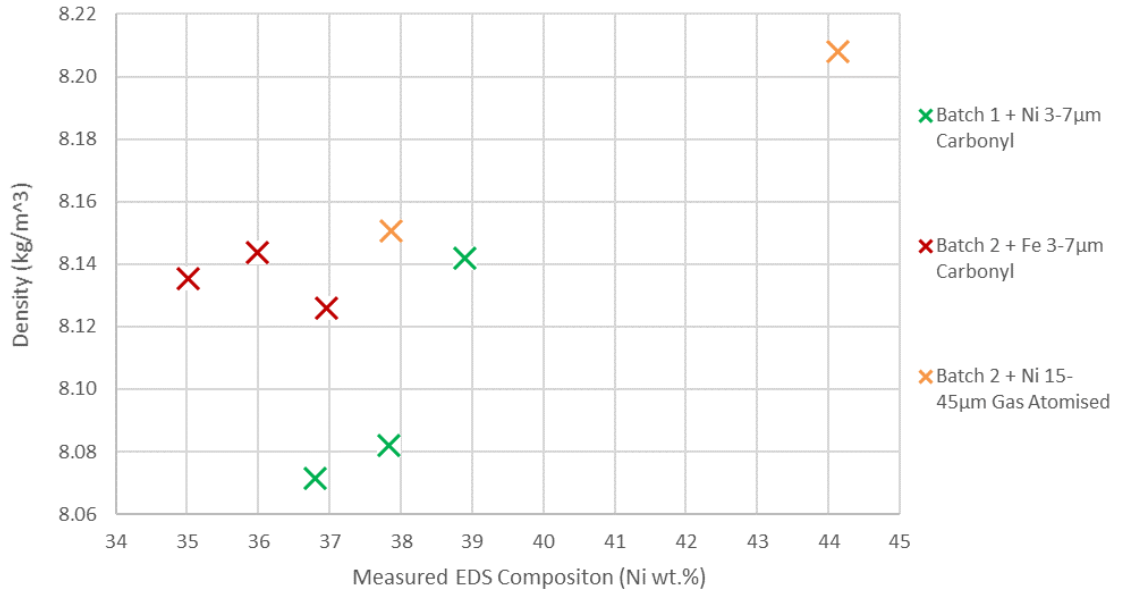


Figure 187. Archimedes density for increasing nickel content for the in-situ blended compositions.

Due to the higher density of nickel of 8.908 g/cm^3 compared to that of iron at 7.874 g/cm^3 , the density should increase with nickel content assuming full densification. An approximate trend of increasing density as nickel content increases can be seen when. To account for the changes in density depending on nickel content, the relative density has been used to plot both optical and Archimedes densities together.

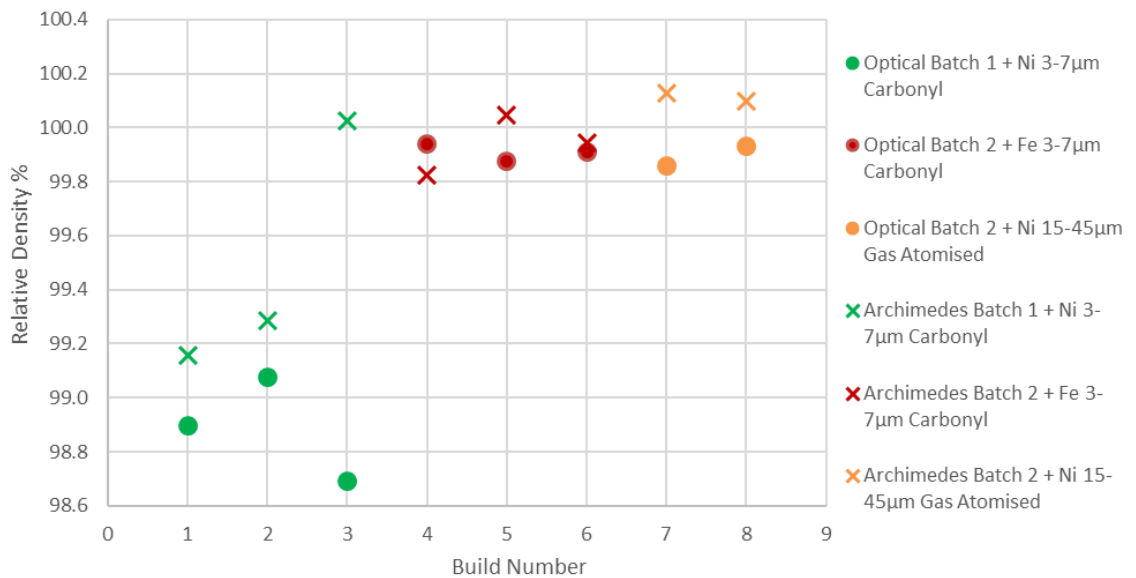


Figure 188. Optical and Archimedes density for each build in the in-situ blended compositions. Normalised against density for EDS measured composition.

It can be seen that the optical porosity is higher with all of batch 1 (0.9-1.3% porosity), but consistently low (0.02-0.15% porosity) for batch 2. This is due to a wider PSD with

more satellite particles, and higher agglomeration creating a different melt behaviour and resulting in an increase in porosity. The invar laser parameter set was developed for batch 2, and it is now clear that the laser parameters are dependent on the PSD. The PSD for batch 1 is between 12.2-54.3 μm whereas batch 2 is 21.3-48.6 μm , shown in chapter 8.4.3. SEM images showing higher agglomeration are in section 8.4.2, and poorer flowability is shown in the rheometry data in section 8.4.4. Rheometry provides a flow rate index (FRI) of 1.5 for batch 1 and 1.2 for batch 2, where a value closer to 1 is the most desirable. Poorer flow is an indication of the PSD.

The optical porosity of all of batch 2 low within 0.05 to 0.17%, with little noticeable change between builds as the elemental additions are added. Even when adding 7wt.% Ni powder it still achieved full densification. Archimedes data matches the optical porosity with the exception of build 3. It is believed that the Archimedes measurement is the anomaly due to the clear porosity seen optically to be the same as the rest of batch 1.

Microhardness

Microhardness testing was conducted using the Vickers method outlined in chapter 5.5. To prepare the samples, a density cube was taken from each build and cross-sectioned to show the side section of the cube. Figure 179 shows a diagram of the side cross section location. The side was chosen to conduct hardness testing on because it provides the thickest amount of material. Each cross-section was mounted and polished. The Vickers hardness indentations were made in a grid pattern of 5x5 producing 25 indents with 1mm gap in-between and placed in the centre of the cross section. A force of 2 *kgf* was found to produce a suitable indentation. Data was plotted using a box plot, and colour coded to match the experiment groups. Typical harness values for invar range between 150-200 [178].

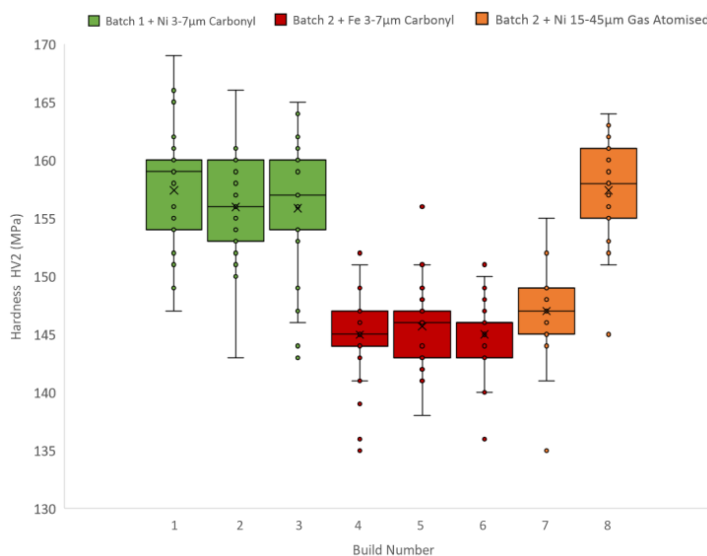


Figure 189. Box-plot for Vickers hardness values for invar in-situ additions.

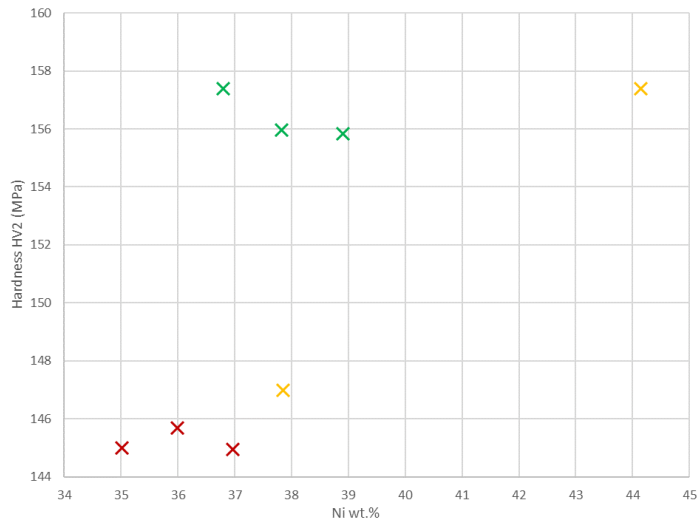


Figure 190. Scatter plot of Vickers hardness values against nickel content measured using EDS, for invar in-situ additions.

It can be seen from the hardness data that invar batch 1 is harder than invar batch 2 over builds 1-6. This can be seen by looking at builds 1-3 with a hardness average of 156 compared with builds 4-6 with an average hardness of 145. This is despite the introduction of Ni and Fe additions on builds 2-3 and 5-6 by 1-2% showing a negligible effect on the median and average hardness values.

The carbon content of invar must be strictly controlled (generally below 0.05wt.%) to keep the CTE low, but this also leads to low strength and hardness [179]. The ICPMS results for carbon shows both <0.1% for batches 1 and 2, which is not measuring low enough levels to determine the influence of a lower percentage of carbon.

Additions of Ni and Fe are made in builds 2-3 and 5-6 are shown to have a limited influence over the hardness. Adding gas atomised nickel powder by in builds 7 and 8 has increased the hardness however. The type of crystal structure will play an influence in the hardness values. FCC is more ductile and softer, whilst BCC is more brittle and harder. Nickel has an FCC crystal structure, so increasing the nickel content should reduce the hardness, but this is not observed with 1 and 2wt.% additions, and conversely observed with a 7% Ni addition. It is currently unclear the cause of deviation between batch 1 and batch 2 for the difference in hardness. It is speculated to be any combination of the following;

- Change in PSD causing a change in melt behaviour and corresponding microstructural changes.
- Change in melt behaviour caused by additions, adjusting proportional FCC to BCC.
- Change in invar gas atomisation gas between nitrogen and argon between batch 1 and batch 2.

- Change in carbon levels below 0.1wt.%.
- Porosity near to the indentation site.

To further confirm the hardness data, tensile testing has also been performed.

Tensile

To test the tensile performance with in-situ blended powders, one tensile bar has been pulled as-built, the other have been pulled after a heat treatment cycle specified at the start of the chapter. The tensile bars have been measured using an extensometer and pulled at a rate of 1mm/min using as outlined in chapter 5.6. All tensile bars failed within the gauge length.



Figure 191. Image of all tensile bars printed after pulling.

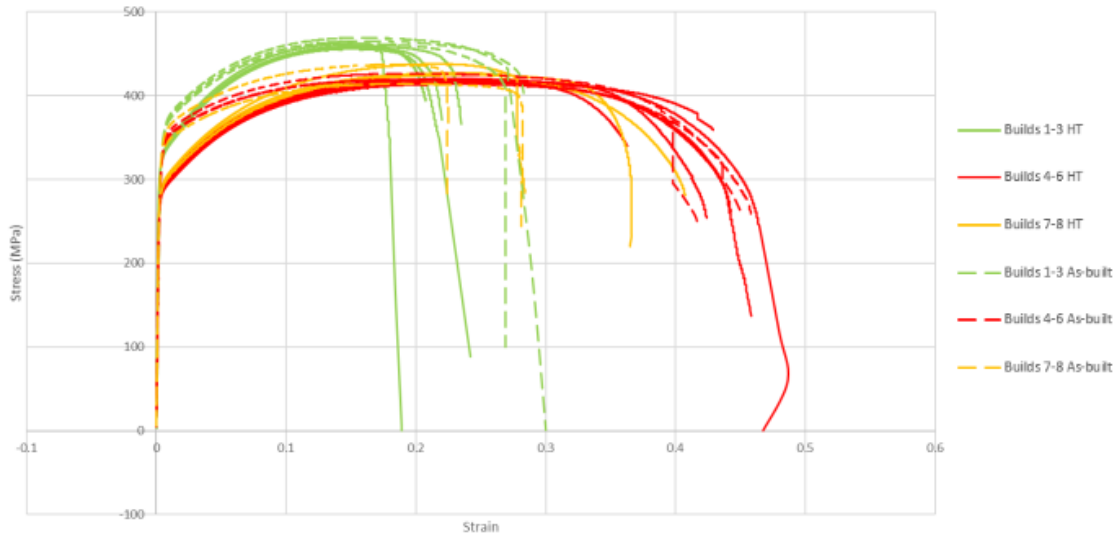


Figure 192. Stress against strain curves for all invar blended powders tensile pulls.

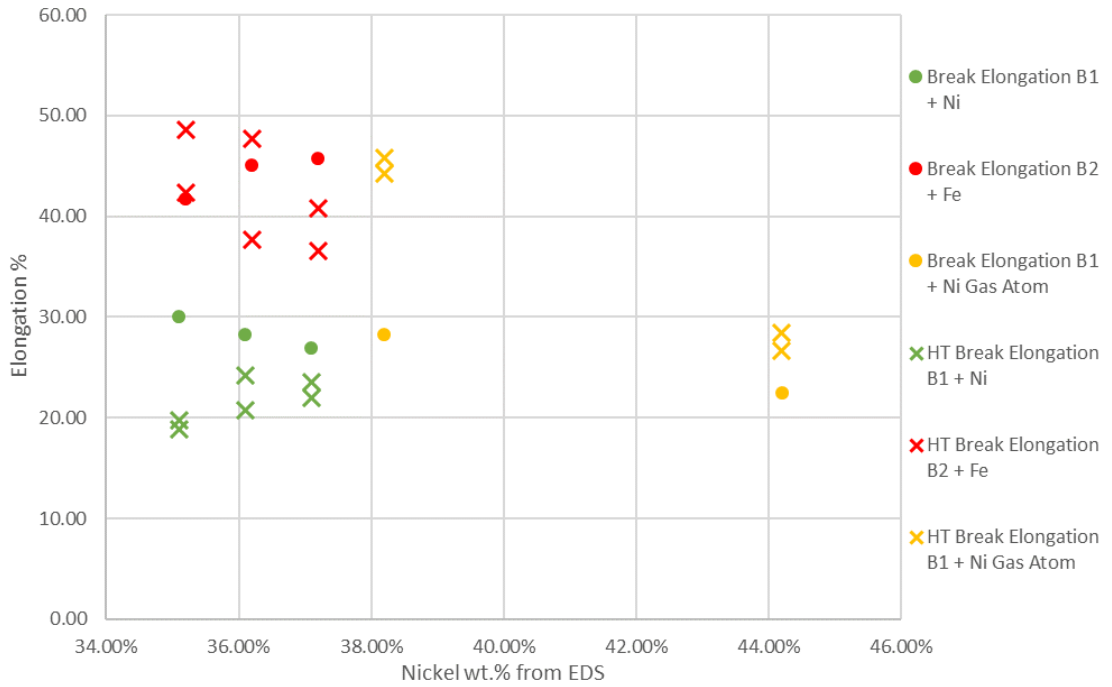


Figure 193. Blended in-situ invar additions tensile performance with and without heat treatment. Showing the percentage elongation until the tensile bar breaks for batch 1(B1) and batch 2 (B2).

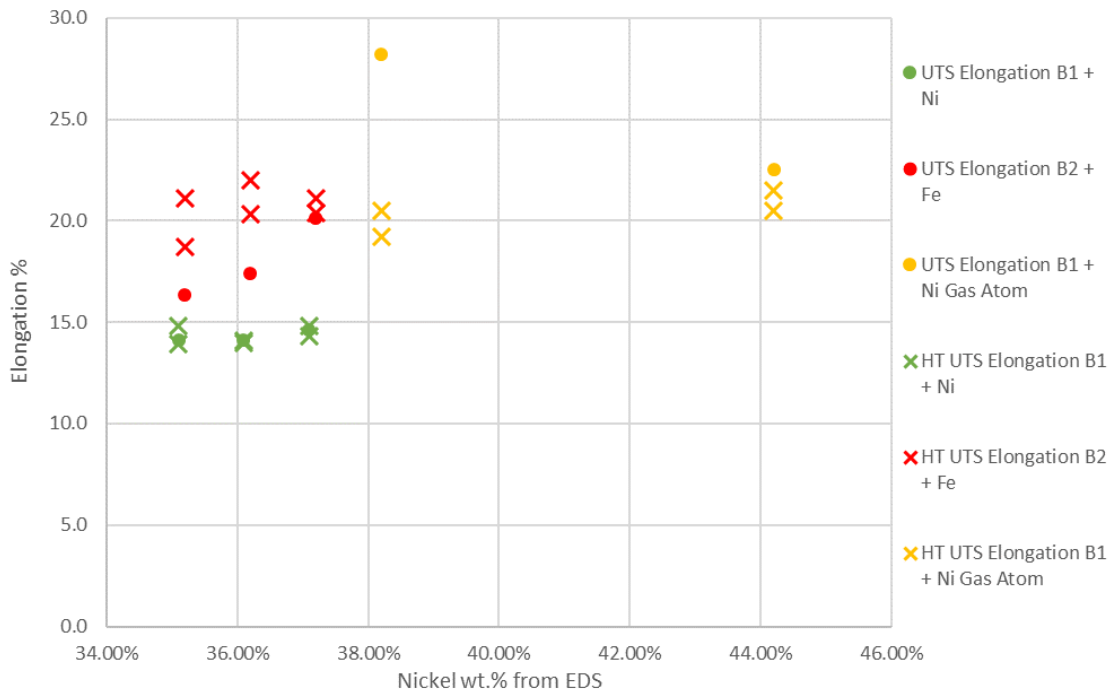


Figure 194. Blended in-situ invar additions tensile performance with and without heat treatment. Showing the percentage elongation until the ultimate tensile strength is achieved for batch 1(B1) and batch 2 (B2).

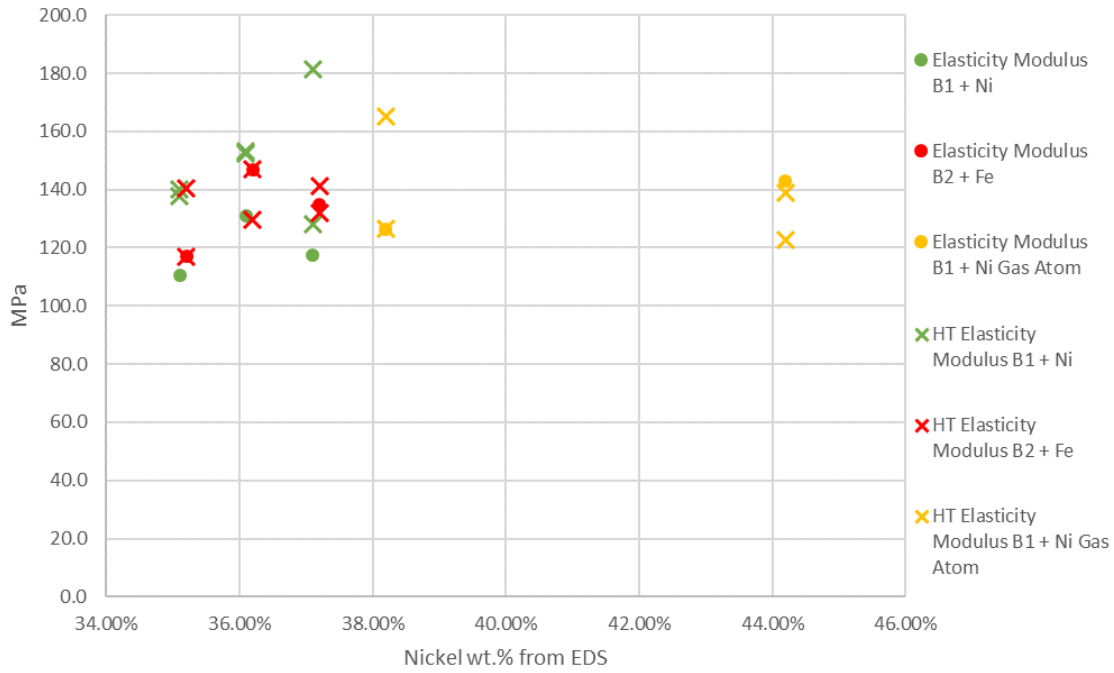


Figure 195. Blended in-situ invar additions tensile performance with and without heat treatment. Showing the elasticity modulus for batch 1(B1) and batch 2 (B2).

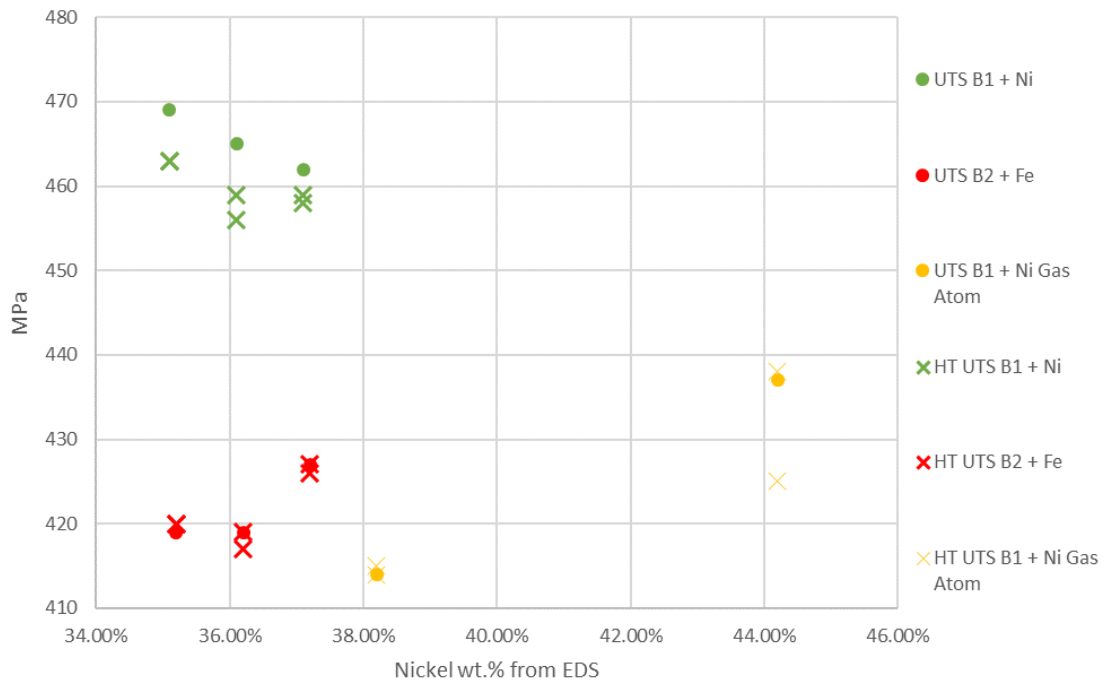


Figure 196. Blended in-situ invar additions tensile performance with and without heat treatment. Showing the ultimate tensile strength for batch 1(B1) and batch 2 (B2).

Build	E (MPa)	UTS (MPa)	Elongation at UTS (%)	Elongation at break (%)
1 HT	138.79	463.00	14.35	19.35
1 As-built	110.67	469.00	14.10	30.01
2 HT	152.79	457.50	14.05	22.47
2 As-built	130.87	465.00	14.10	28.30
3 HT	154.83	458.50	14.55	22.75
3 As-built	117.35	462.00	14.60	26.90
4 HT	136.59	426.50	20.75	38.68
4 As-built	135.04	427.00	20.10	45.80
5 HT	138.23	418.00	21.15	42.71
5 As-built	146.79	419.00	17.40	45.08
6 HT	128.66	420.00	19.90	45.53
6 As-built	116.97	419.00	16.30	41.76
7 HT	145.85	414.50	19.85	45.05
7 As-built	126.20	414.00	16.50	28.22
8 HT	130.85	431.50	21.00	27.50
8 As-built	143.10	437.00	16.50	22.50

Table 47. Tabulated tensile data for the blended in-situ invar additions.

It is observed that builds 1-3 using invar batch 1 were more brittle than that of builds 4-8 using batch 2 invar. This is seen by the higher UTS for batch 1, and lower UTS elongation and break elongation. The additions of nickel in builds 2-3 have created a reducing UTS from an as-built maximum of 469MPa on build 1 to a minimum of 463MPa on build 3. The heat-treated results follow the trend slightly lower. This is inversely proportional to batch 2 builds 5-6 where iron powder was added. It shows that build 6 with 2% Fe gave a larger UTS while build 5 remained the same as no additions on build 4. The elasticity modulus remained relatively stable across builds 1-8 with no noticeable trend. Looking at break elongation, it is particularly hard to draw a correlation, besides with clear differences between the two invar batches. It is seen that build 8 has a reduction in break elongation, and increase in UTS when 7% Ni is added, even after heat treatment.

Comparing the tensile data to literature, Qiu et al shows that the UTS of similar vertically printed round tensile bar tested as built are 422-455Mpa, and elongation at break of around 30% [157]. This places the data presented within a similar range.

Overall this shows that the additions have been a success, with limited change in tensile properties between the additions of 1-2wt.% Ni or Fe.

Thermal Expansion

To determine if the in-situ additions have been successful at adjusting the CTE, dilatometry will be used to measure the thermal expansion of a manufactured 25x5mm

cylinder. The thermal expansion of the in-situ LPBF builds will be compared with the thermal expansion of samples of cast invar at varying compositions.

The physical alpha curves have been plotted using the dilatometer test program as outlined in experimental chapter 5.3. This provides a heating curve, where the thermal expansion is measured as the machine is heating up, and a cooling curve, where the thermal expansion is measured whilst cooling down from a 1hr isotropic temperature hold at 500°C. Heating and cooling rates are set to 5K/min as required by ASTM E228-17, and the appropriate calibration curve is used and offset with the DIN-51045-1 equation.

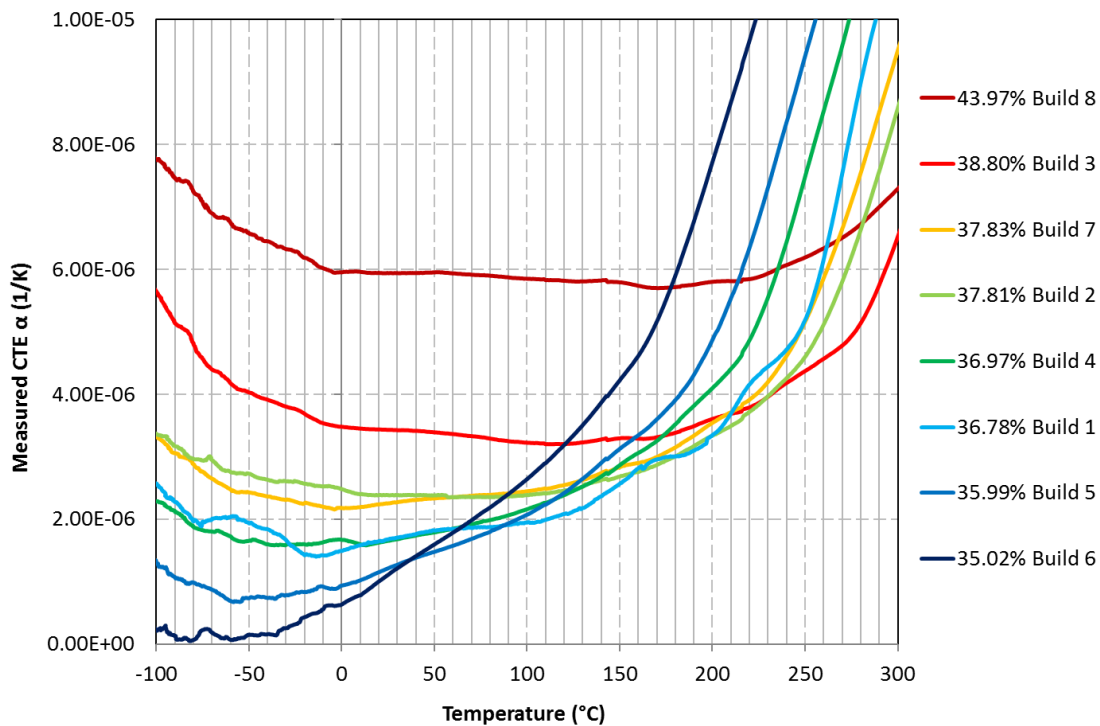


Figure 197. Physical alpha curves plotted for all in-situ compositionally adjusted invar alloys using the dilatometer **cooling cycle**. Nickel percentages taken from averaged EDS results.

The cooling curve in Figure 197 shows that the thermal expansion increases with increasing nickel content. Interestingly it is seen that 35.02% nickel has the lowest CTE from -100 to 35°C, whilst invar with 35.99% Ni has a lower CTE between 35 to 300°C. In literature there is no cryogenic thermal expansion data for LPBF invar36 manufactured samples. It would be useful to select invar35 for use in cryogenic applications only. The induction melted samples observe similar trends to that of those made using LPBF. The temperature at which the low CTE effect is observed becomes less as the nickel content is reduced. The target CTE of 6-7µm/mK is met with 43.97wt.% Ni giving just below 6µm/mK between 0 to 230°C. The compositional EDS scans showed the alloy had a non-homogenous elemental distribution with iron and nickel rich areas.

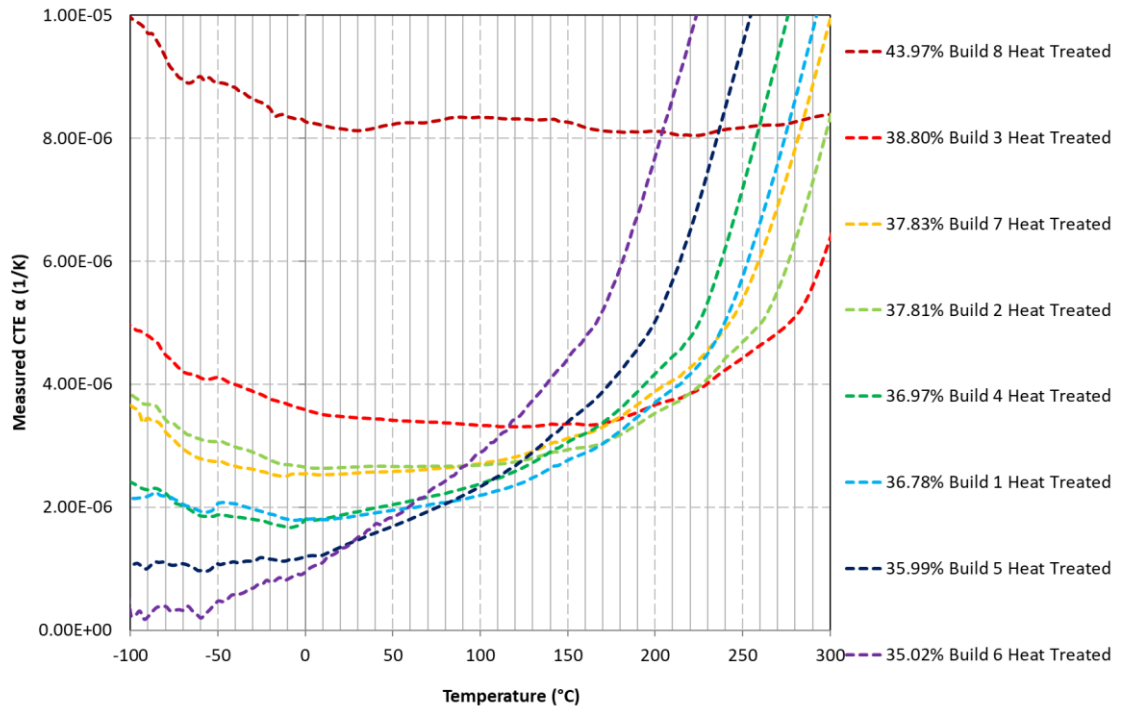


Figure 198. Physical alpha curves plotted for all **heat treated** in-situ compositionally adjusted Invar alloys using the dilatometer **cooling cycle**. Nickel percentages taken from averaged EDS results.

The samples were heat treated using the same temperature program used for the tensile bars. The heat treatment takes the Invar to 850°C at 5K/min and held for 70 minutes before it is cooled at 2k/min to ambient temperatures. The graph in Figure 199 shows the heat treated CTE against the as-built components. It is seen that Build 8 with the largest amount of nickel added at 7%, has had a dramatic increase in CTE. This can be attributed to better diffusion of the added nickel powder into the Invar alloy. This brings the overall CTE to above that of the targeted 6-7 $\mu\text{m}/\text{mK}$ at around 8.2 $\mu\text{m}/\text{mK}$ from 0-300°C required for the optical industry. This is above that of the cast components at 43.4wt.% Ni where a CTE of approx. 6.5 $\mu\text{m}/\text{mK}$ was obtained over the same temperature range. Overall it can be seen that heat treatment has increased the thermal expansion. This is also in line with literature that finds an increase in CTE after heat treatment of Invar36 pre-alloyed LPBF parts, although the CTE is still found to be lower than conventionally manufactured material [162].

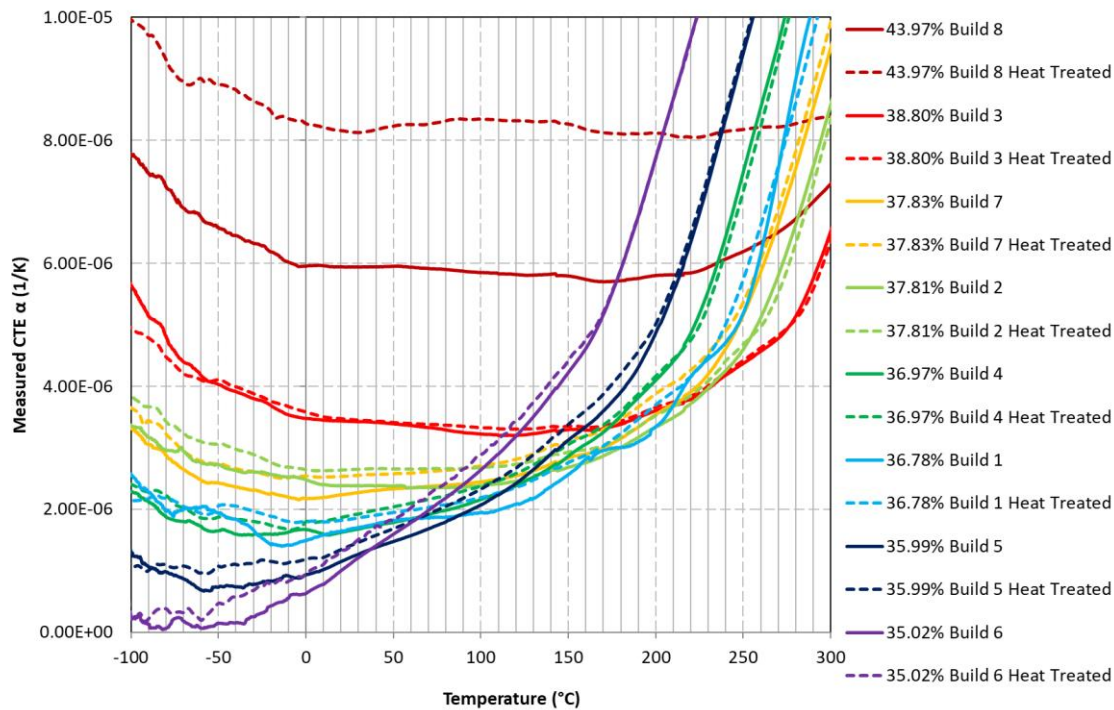


Figure 199. Physical alpha curves plotted for all **as-built and heat treated** in-situ compositionally adjusted Invar alloys using the dilatometer **cooling cycle**. Nickel percentages taken from averaged EDS results.

It can be seen from the graph in Figure 200 that at 25°C the thermal expansion of all the LPBF as-built before heat treatment, is lower than that of the cast material. The heat-treated parts are shown to have a higher CTE than the as-built. All thermal expansion data is lower than that of Guillaume et al.

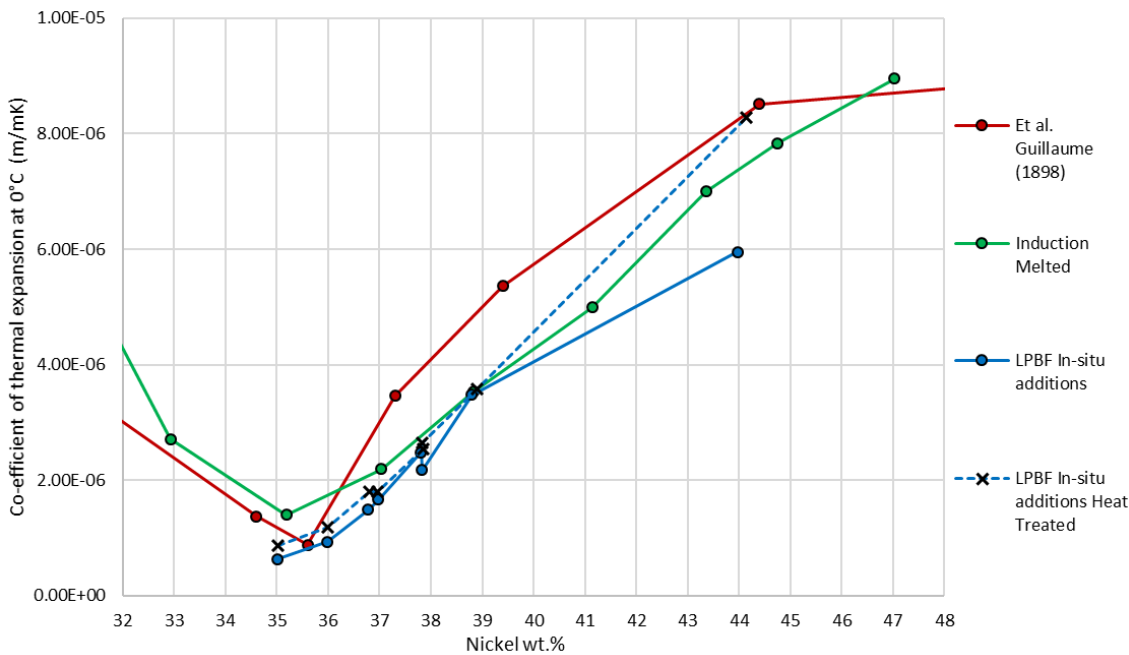


Figure 200. Physical alpha curves comparing instantaneous CTE at 25°C for a range of Ni content measured from EDS. Guillaume et al. added for reference.

Buil d No.	ED S wt. % Ni	- 100° C	- 50° C	0° C	50° C	100° C	150° C	200° C	250° C	300° C	350° C	400° C
8	44.0	7.8	6.6	6.0	6.0	5.9	5.8	5.8	6.2	7.3	9.1	11.7
8 HT	44.0	10.0	8.9	8.3	8.2	8.4	8.3	8.1	8.2	8.4	9.0	10.0
3	38.8	5.7	4.0	3.5	3.4	3.2	3.3	3.6	4.4	6.5	11.6	14.4
3 HT	38.8	4.9	4.1	3.6	3.4	3.3	3.4	3.7	4.4	6.4	11.5	14.6
7	37.8	3.3	2.4	2.2	2.3	2.5	2.8	3.5	5.2	9.5	13.1	14.5
7 HT	37.8	3.7	2.7	2.5	2.6	2.7	3.1	3.9	5.4	9.9	13.8	15.5
2	37.8	3.4	2.7	2.5	2.4	2.4	2.7	3.3	4.6	8.6	12.7	14.4
2 HT	37.8	3.9	3.1	2.7	2.7	2.7	2.9	3.5	4.7	8.3	13.3	15.3
4	37.0	2.3	1.7	1.7	1.8	2.2	2.9	4.1	7.5	12.7	15.2	16.2
4 HT	37.0	2.4	1.9	1.8	2.0	2.4	3.1	4.2	7.2	12.6	15.1	16.4
1	36.8	2.6	1.9	1.5	1.8	1.9	2.6	3.4	5.2	11.1	13.7	15.1
1 HT	36.8	2.2	2.1	1.8	2.0	2.2	2.8	3.7	5.7	10.8	14.1	15.5
5	36.0	1.3	0.7	0.9	1.5	2.1	3.1	4.9	9.4	13.3	15.3	16.2
5 HT	36.0	1.9	2.4	1.9	3.4	1.6	2.7	4.2	7.5	13.7	15.5	16.3
6	35.0	0.2	0.2	0.6	1.6	2.6	4.2	7.7	12.4	14.8	16.3	17.0
6 HT	35.0	0.2	0.5	1.0	1.8	2.9	4.4	7.7	12.7	15.2	16.5	17.3

Table 48. Invar blended powders instantaneous CTE's every 50°C for the whole temperature range, units are $\mu\text{m}/\text{mK}$.

Looking at Table 48 and Figure 61, 35.02wt.% nickel has a CTE of very close to zero at temperatures of -100 to -50°C.

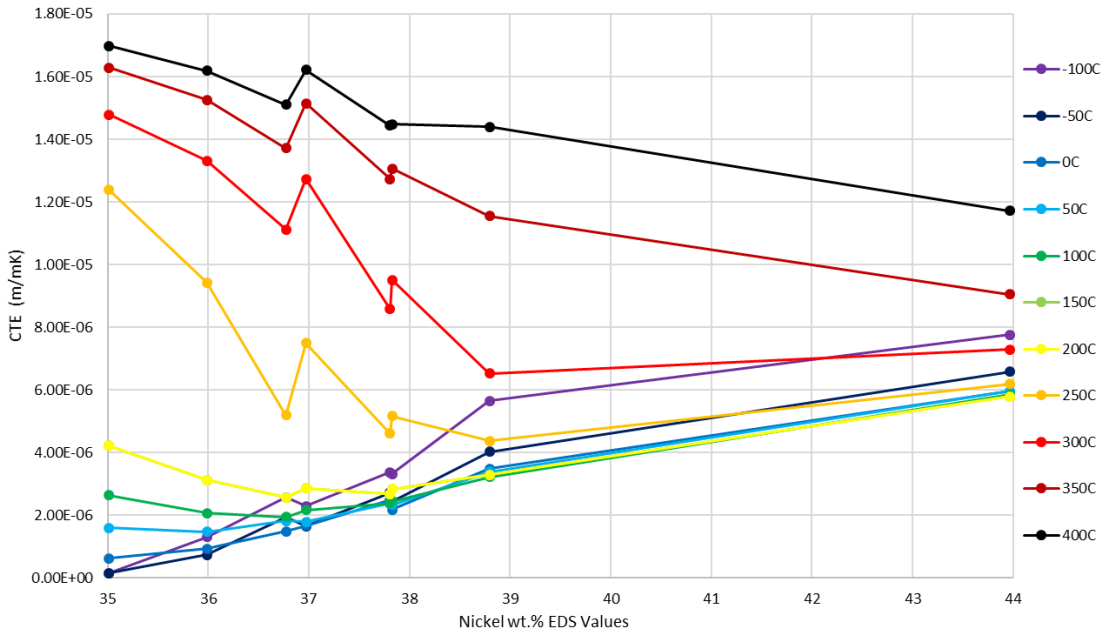


Table 49. Instantaneous CTE measurements for a range of temperatures for as-built parts for the invar blended powders.

Figure 201 shows good correlation between heat treated and as built. This increases confidence in the results.

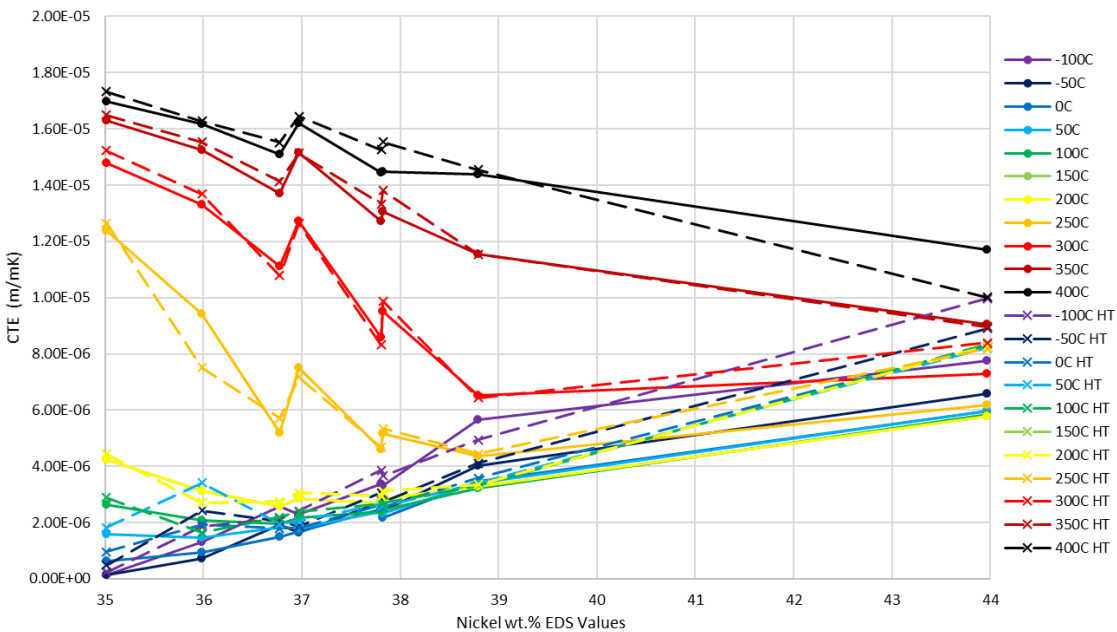


Figure 201. Instantaneous CTE measurements for a range of temperatures for as built and heat-treated parts for the invar blended powders.

Overall, it is observed that adding iron and nickel in-situ and blending the powders has been successful for adjusting the CTE. It is noticed that heat-treating increases the CTE, which can be a combination residual stress reduction, and improved homogeneity in the

samples with nickel added. Even in build 5 and 6 where iron was added, there is still an increase in CTE after heat treatment. This suggests either that the residual stress is the more dominant factor, or the iron was only fully alloyed after heat-treatment. In build 8 where 7% Ni is added, the improved nickel dispersion and alloying during heat-treatment was the overriding factor, since the overall thermal expansion change compared to as-built was much larger after heat treatment than other samples, bringing it in line with the cast material.

Discussion on in-situ compositional adjustments

It is observed that compositionally all samples with 1-2% additions have successfully alloyed. Build 8 which featured a large amount of nickel powder of 7%, found large amounts of nickel rich regions. It is observed that heat treatment had the biggest effect on this sample, with the thermal expansion increasing from 5.85 to 8.35 $\mu\text{m}/\text{mK}$ after heat treatment. The rest of the samples increase by only 0.09-0.43 $\mu\text{m}/\text{mK}$ depending on the temperature and sample. It is observed that builds 1-3 have significant porosity. This is due to a different PSD and chemical composition, requiring a new set of laser parameters, which was not realised at the start of the experiment. The mechanical testing reflects the increase in porosity for batch 1 invar, with builds 1-3 performing poorly in tensile testing. It is noticed that hardness remains consistent across builds 1-6, and is not impacted by the powder addition. Builds 7-8 are noticeably different, with increasing hardness for increasing nickel content.

Conclusion on in-situ compositional adjustments

To conclude it has been observed that adding 1-2wt.% of iron or nickel carbonyl fine powder and suitably mixing provides the ability to fine tune the thermal expansion of a pre-alloyed invar powder. The compositional data shows full alloying occurring, and the thermal expansion data shows the expected changes caused by adjustment of the Fe-Ni balance. It has been shown that the CTE's can be exceptionally low in the cryogenic region when reducing the nickel content past the conventionally understood 'optimal' of 36wt.%, down to 35.01%, where near zero expansion occurs between -100 and -30°C. The LPBF produced parts have been shown to have superior thermal expansion properties compared to conventionally cast parts, partly attributed to the residual stresses in the build. After heat-treatment, the residual stress is relieved, and the CTE increases, but still provides a lower thermal expansion than conventional. The 7wt.% Ni gas atomised powder addition did not fully alloy during processing. This is due to the increase in particle size and overall quantity. After heat-treatment the thermal expansion was in line with expected predictions and can be assumed to be fully alloyed. The mechanical data shows clear differences between the two pre-alloyed invar batches, mainly caused by improper laser parameters for batch 1, creating porosity. The sub optimal parameter set caused an increase in microhardness and brittleness. Comparing the differences between

the 1-2% additions compared to no additions shows limited change in overall tensile performance, with UTS of between 418-428Mpa for batch 2, correlating well with literature. The microhardness also shows limited change between the 1-2% additions, giving a microhardness of 145HV for batch 2 on average.

6.5.4 Adjustment of Invar laser processing parameters.

Laser powder bed fusion creates unique and often finer microstructures that are difficult to achieve by conventional manufacture [180]–[182]. The microstructure is directly affected by the four laser processing parameters. These are; the lasers power, exposure time, point distance, and hatch spacing. It is observed in literature that thermal expansion of parts is affected not only by build orientation, but by the laser energy density [162]. This is shown to occur with invar and 316L stainless steel. Yakout et al. has shown that the effect of processing parameters on invar has a great effect. Thermal expansion for invar can range from -3 to 18 $\mu\text{m}/\text{m}$, while 316L ranges from 400 to 440 $\mu\text{m}/\text{m}$ at 50 $^{\circ}\text{C}$ [163]. Their experiments were conducted with the following settings; laser power was 200, 250, and 300W, scanning speeds were 600, 800, and 1000mm/s, and hatch spacing was 80,100, and 120 μm . All parameters are tested with one another, giving an array of 3x3x3 =27 experiments. The team used an EOSINT M280 SLM machine to print vertical dilatometer rods. The thermal expansion values plotted in Figure 202 are measured by calculating the change in length after the sample reaches 50 $^{\circ}\text{C}$ divided by the original length before the samples was heated.

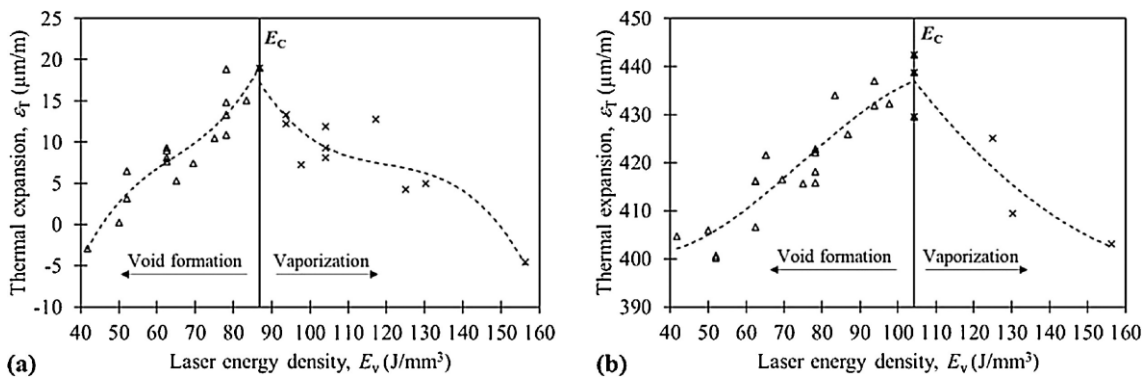


Figure 202. Thermal expansion of (a) Invar 36 and (b) stainless steel samples after increasing temperature to 50 $^{\circ}\text{C}$ [163].

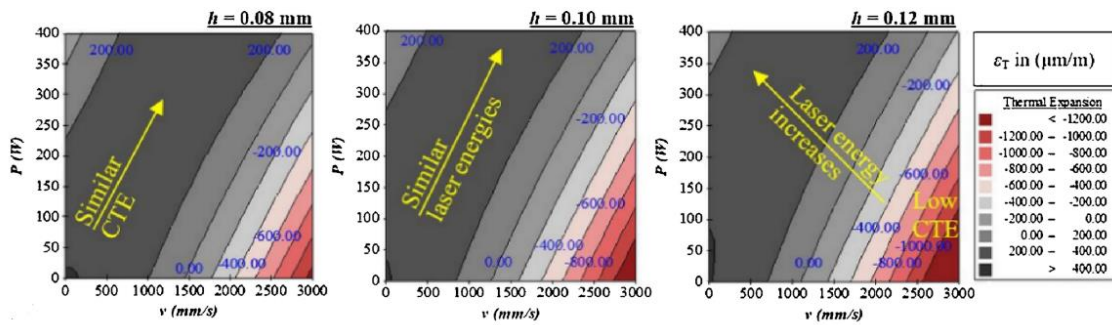


Figure 203. Contour plots for the thermal expansion of Invar 36 samples at temperature of 200 °C. The plots show the effect of laser power and scanning speed on thermal expansion at hatch spacings of 0.08, 0.10, and 0.12 mm [163].

From the contour plots in Figure 203 by Yakout et al. [163] it is seen that higher scanning speeds and lower laser power results in a lower thermal expansion. This is seen to be true across hatch spacings of 80, 100 and 120 μm , with lower thermal expansion in larger hatch spacings. It can be seen from the thermal expansion plotted against energy density that there are only a few data points to confirm the downwards trend in thermal expansion after the critical energy density E_C . It would be very advantageous to be able to decrease the thermal expansion of invar even further by increasing the overall energy density. Yakout et al. [163] suggests this downwards trend is caused by vapourisation. Vapourisation of one element over another can cause a change in the elemental constituents of the alloy. The boiling temperature of iron and nickel is very similar at 2862 and 2732 $^{\circ}\text{C}$, so the driving force behind vapourisation of these two elements is more likely to be caused by the thermal conductivity, which is 28.2W/mK for iron and 76.1W/mK for nickel when both at 927 $^{\circ}\text{C}$. It is unclear whether this difference is sufficient enough for vapourisation to occur, when existing in alloyed form as invar36. Yakout et al. [163] suggests that the vapourisation of trace elements which have higher coefficients of thermal expansion such as manganese (22 $\mu\text{m}/\text{mK}$) would cause a reduction in overall thermal expansion. They also suggest that the overall vapourisation of the main alloy constituents would increase the relative proportion of other trace elements with a lower coefficients of thermal expansion, such as molybdenum and silicon (4.8 and 0 $\mu\text{m}/\text{mK}$ respectively). It is stated that the magnetic dipole moments mainly depend on material composition, curie temperature, crystal structure, and thermal expansion. The authors have only hypothesised as to the potential cause of the decrease in thermal expansion. They do not provide any chemical analysis to determine if enough quantities of trace elements exist in their pre-alloyed invar36 powder, to be able to determine if they would change thermal expansion.

This section investigates the link between increasing energy densities and thermal expansion. It will expand upon work by Yakout et al. [163] producing more experiments

in the vapourisation zone at energy densities greater than the considered optimum. Looking at chapter 7.5.1 the optimum energy density for full densification was determined to be $59.36 J/mm^3$, however it was never established the maximum energy until keyhole formations occurred. Keyhole formations occur when the welds experiences rapid formation and collapse, caused by a high input energy, creating porosity at the weld root. The maximum input energy in the array of $71.16 J/mm^3$ still creates a fully dense part (99.98%). This study will only look at laser energy densities higher than the optimal of $59.36 J/mm^3$. This will help confirm or refute the trend proposed by Yakout et al. [163] from their 3 experiments in the vapourisation zone. This study will conduct 25 experiments by adjusting the laser power and exposure time. Each experiment will have a vertical and horizontal dilatometer rod for measuring linear thermal expansion, and a density cube for measuring density by Archimedes. Porosity will be analysed by cross-sectioning each dilatometer rod and using optical microscopy. Two repeats of each rod will be manufactured to allow a sample to be heat treated if required for publication.

Method

An experiment will be conducted to determine the effect of increasing the laser energy density in invar36 by adjusting only two parameters, the laser power, and laser exposure time. The two remaining parameters point distance and hatch spacing are kept the same at the considered optimal of $60\mu m$ and $110\mu m$, respectively. A full factorial orthogonal array has been constructed. The L25 array will consist two parameters at five levels, to create 25 experiments;

Parameter	1	2	3	4	5
Power (W)	220	265	310	355	400
Exposure time (ns)	85	141	198	254	310

Table 50. L25 array parameter variables.

To be able to compare the experiment to Yakout et al. [163], the exposure time and point distance used on the Renishaw pulse modulated laser need to be converted to scanning speeds in mm/s. To calculate scanning velocity it is; $\bar{v} = \text{Point Distance} / \text{Exposure Time}$. Figure 204 graphs the properties of each experiment.

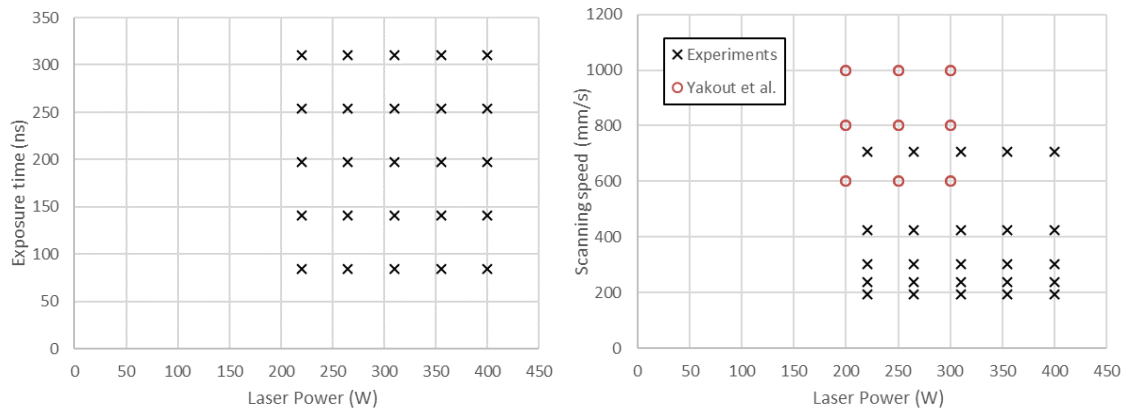


Figure 204. Each L25 parameter plotted for the experiment to be conducted (left), and the conversion to scanning speed plotted, and compared against those completed by Yakout et al. [163] (right).

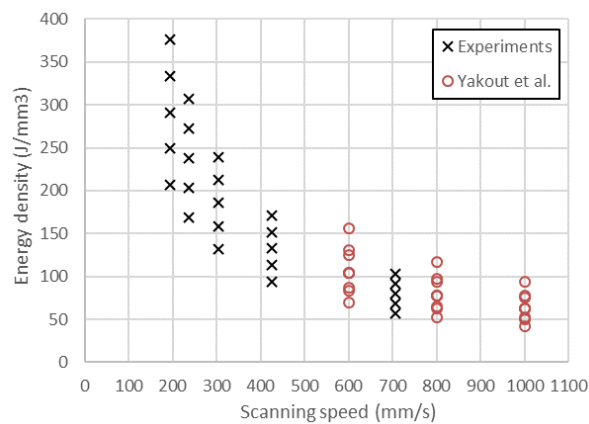


Figure 205. Comparison between energy density and scanning speeds for the experiment and Yakout et al.'s work.

It is observed that there is equal incremental spacing between the exposure time and the laser power for each experiment. When calculating the laser scanning speeds and plotting them against energy density, there is an un-even distribution. The higher scanning speeds provide less energy density across all experiments in the group. This is because the ET (or scan speed) is multiplied by all the laser power levels. Yakout et al. [163] has varied hatch spacing on each setting, so more datapoints are visible when plotting scanning speed against energy density than against laser power.

Manufacture

The build was completed on a Renishaw AM400 with a 250x250x300mm heated build plate at 160°C. Builds were processed in QuantAM slicing software. Dilatometer rods measured 25x5mm as specified in ASTM- E228-17, and density cubes are 10x10x10mm.

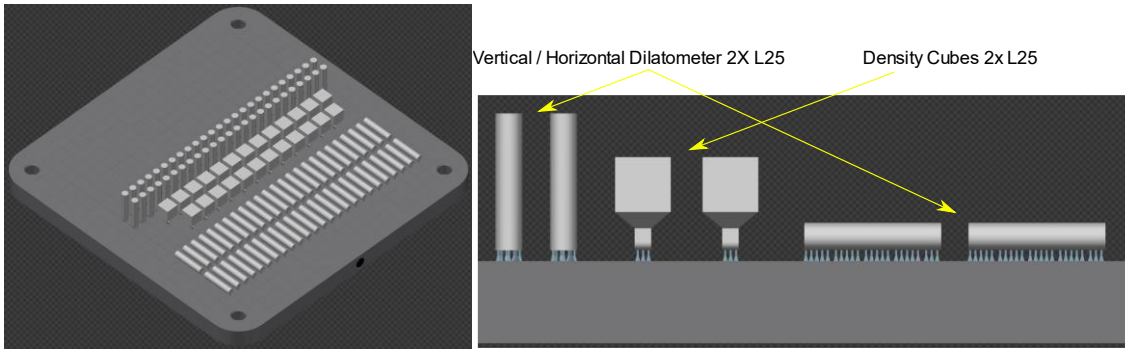


Figure 206. Invar high laser energy QuantAM build layout.

Results

To determine if porosity exists, each dilatometer rod is cross-sectioned to determine the porosity size, distribution, and location. The density cubes are also measured using Archimedes. The mechanical properties will be analysed by measuring Vickers hardness across the cross-sectioned dilatometer rod. The thermal expansion is measured using the vertically printed dilatometer rods normal to the build direction. Correlations are made between energy density, scanning speeds, and thermal expansion. The discussion section analyses any correlations between thermal expansion, porosity, and hardness. The effect of the laser parameters on all the results is also discussed.

Thermal Expansion

A relationship between the laser energy density and the thermal expansion of the invar parts has been established. The 25 dilatometer rods are measured over -120 to 200°C using a cooling cycle at $5\text{K}/\text{min}$. The coefficient of thermal expansion curves are plotted in Figure 207. The lowest CTE at approximately 75°C is between 1.62 and $1.26\mu\text{m}/\text{mK}$, a 22% difference.

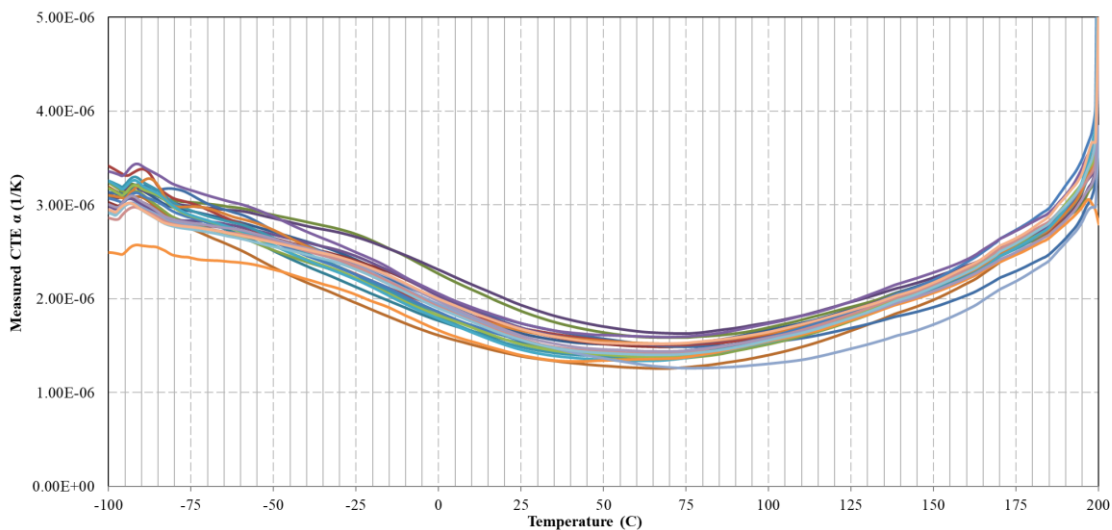


Figure 207. Physical CTE curve from -100°C to 200°C for invar as a function of volumetric laser energy density.

To try to correlate any changes with energy density, the cryogenic range from -80 to 25°C, the above ambient range from 25 to 180°C and the overall total range from -80 to 180°C have been averaged and plotted against its corresponding laser energy density. It is seen in the graph in Figure 208 that there seems to be a slight increase in the trendline as the energy density increases. There is also a slight increase in nickel content from EDS readings.

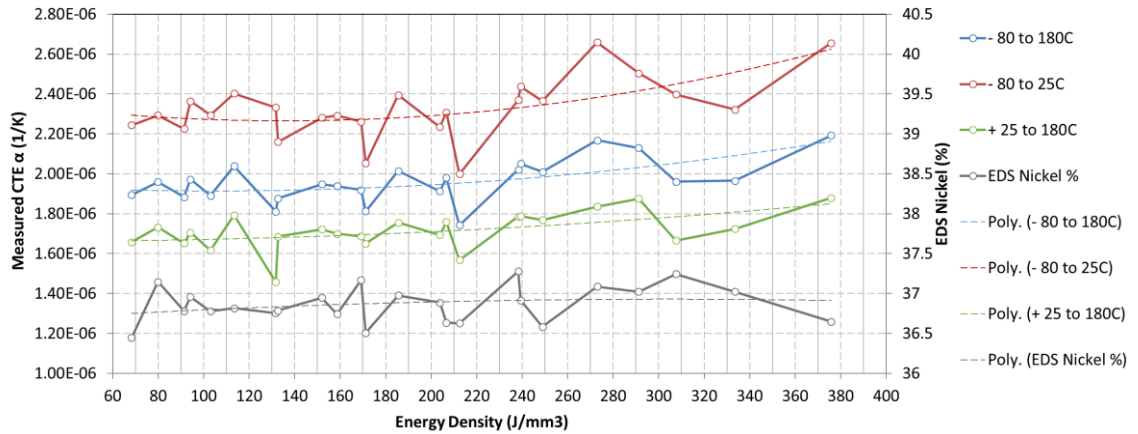


Figure 208. Graph showing the CTE and measured nickel content for 25 samples of increasing input energy density. Energy density is increased by adjusting both exposure time and power of the modulated laser.

The final change in length is determined after a 300°C change from -100 to 200°C. Yakout et al. [163] only tested from 23°C to 50°C, a range which would contain considerable noise without cooling to cryogenic temperatures first. For this reason, a direct comparison with Yakout et al.'s thermal expansion readings will not be completed, but instead the trends will be analysed. The max temperature of 200°C is well below the curie temperature and so the data will still be a close comparison. It can be seen that the CTE's lie in between 2.05 and 2.31 $\mu\text{m}/\text{mK}$, and that the correlation shows an increasing thermal expansion with an increasing laser energy density.

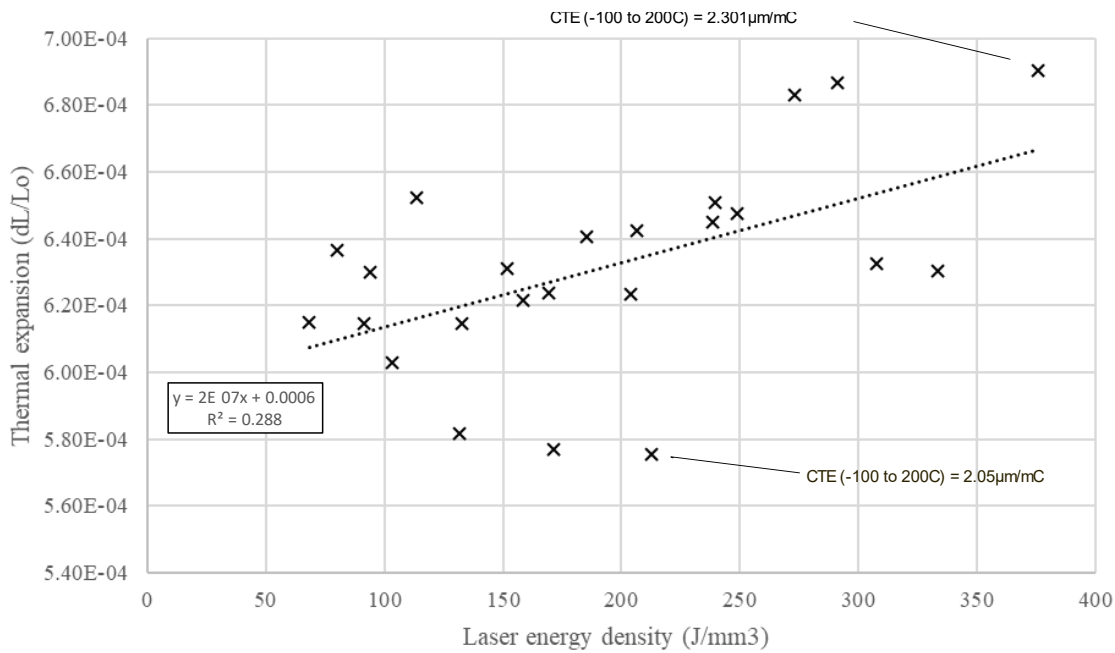


Figure 209. Final change in length over -100°C to 200°C for invar as a function of volumetric laser energy density.

Yakout et al. [163] presents work in Figure 210 which shows that as the laser energy density increases above the optimum value of approximately 87 J/mm^3 required for their machine to create a fully dense part, the thermal expansion of the part begins to decrease. For the work presented in Figure 209 this trend is not noticed. Increasing the laser energy density beyond the optimum value found for a fully dense part of 71.16 J/mm^3 shows a continual increase in thermal expansion. This disagrees with Yakout et al.'s [163] observation that the thermal expansion increases when entering the vapourisation regime. Differences could be due to the thermal expansion being measured over a wider temperature range in the present work from -100 to 200°C compared with Yakout et al.'s range of 23 to 50°C [163].

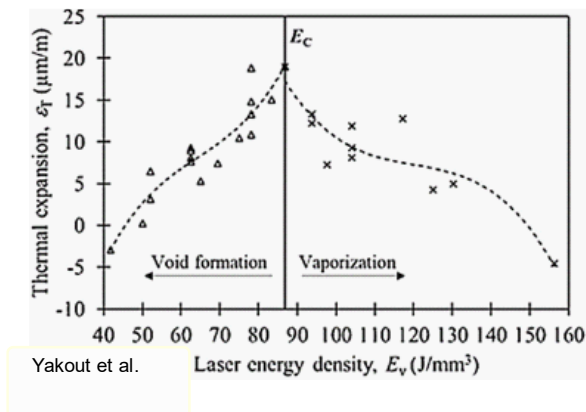


Figure 210. Yakout et al. comparison to Figure 209 over 23 to 50°C [163].

To examine the cause of the behaviour the nickel percentage for each sample measured by EDS is plotted with laser energy density in Figure 211. It can be seen that a small increase in nickel content is observed as the laser energy density increases. The linear shows a minimum of 36.8wt.% of nickel and a maximum of 37wt.%.

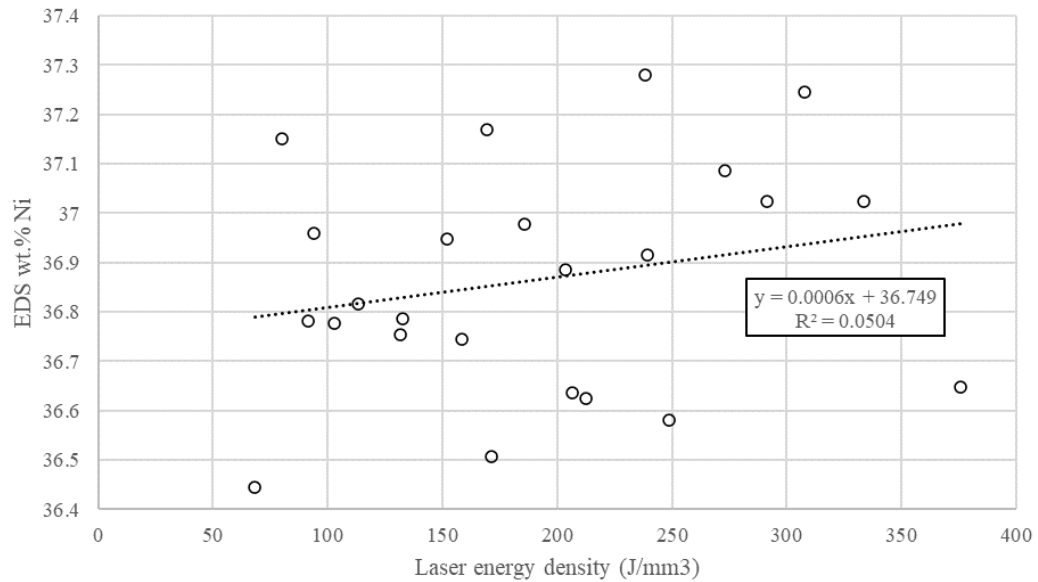


Figure 211. Measured nickel content using EDS for invar as a function of volumetric laser energy density.

By plotting the thermal expansion and the nickel content on the same graph with laser energy density in Figure 212 it is observable that an increasing linear trend can be made between for both as laser energy density increases.

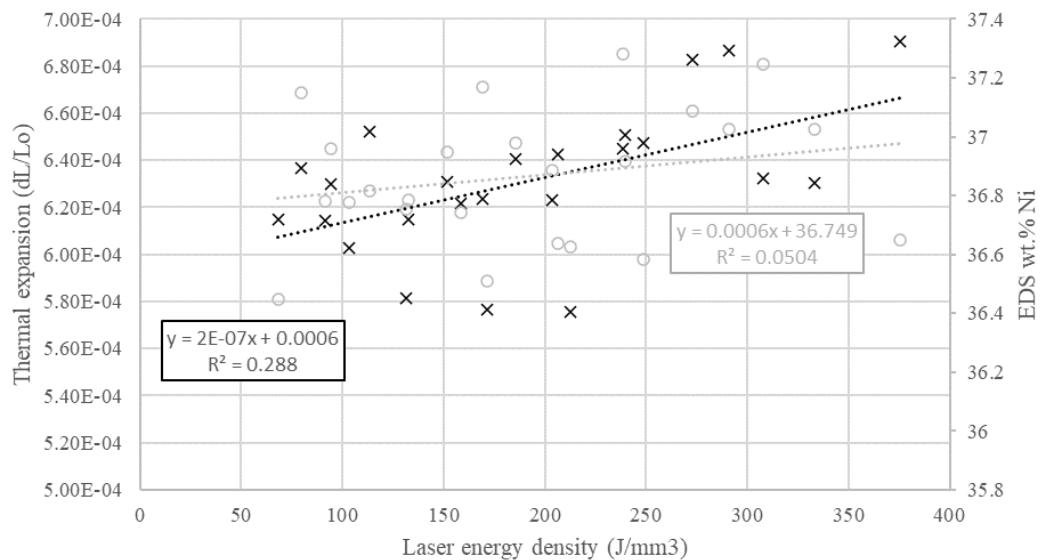


Figure 212. Thermal expansion and EDS compared over -100°C to 200°C. Crosses represent thermal expansion, circles represent EDS measurements.

Increasing laser energy density has a corresponding increase on thermal expansion over -100 to 200°C. The boiling points of both elements are similar at 2862°C for iron and 2730°C for nickel. Since iron has a higher boiling point, vapourisation seems implausible because the higher energy density would lead to more vapourisation of nickel, not less. As discussed earlier, Yakout et al. made the hypothesis that other trace elements featuring different CTE's, could increase or decrease relative to the rest of the constituents, due to vapourisation [163].

The most plausible theory is that the higher energy density has created larger melt pools that stay hotter for longer as they solidify. If the laser energy density is lower, a higher number of non-equilibrium microstructures are created from shallower narrower faster cooling weld pools. The faster cooling rate creates residual stresses that reduce the thermal expansion of invar. The effect of residual stress reducing thermal expansion in invar is well document occurrence in LPBF [96], [102], [108]–[111]. This is in conflict with Yakout at al's. original observation that as the energy density is increased beyond the optimum parameters and into the area labelled 'vapourisation' on Figure 210, a decrease in thermal expansion is observed. Their data is very limited in this region, with only 3 measurement points used to confirm the downwards trend in thermal expansion over 105 to 160 J/mm^3 .

Figure 213 shows there is an increase in thermal expansion with increasing exposure times when comparing with a series of fixed laser powers. This also remains true when comparing increasing laser power with the fixed exposure times 198, 254, and 310 μs shown in Figure 214.

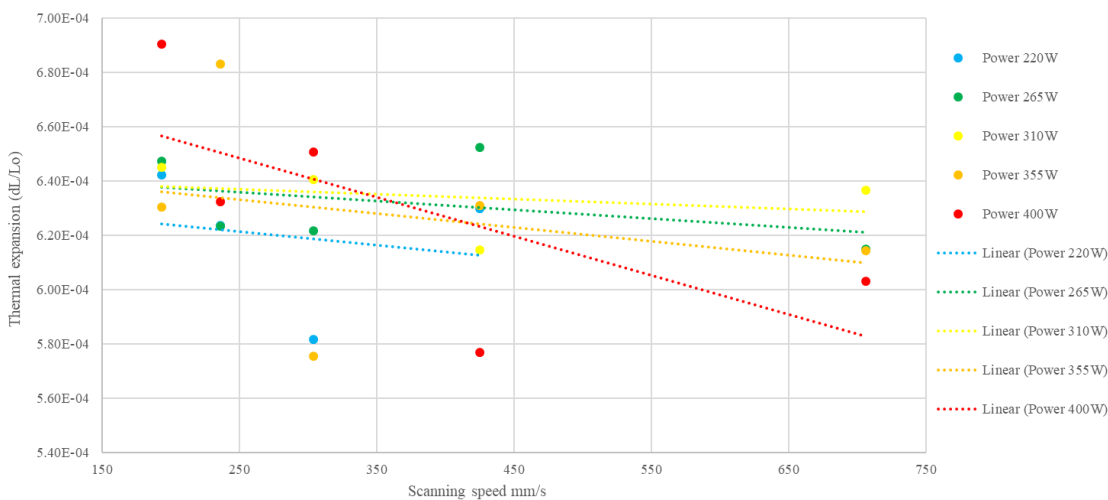


Figure 213. Final change in length over -100°C to 200°C for invar against scanning speed.

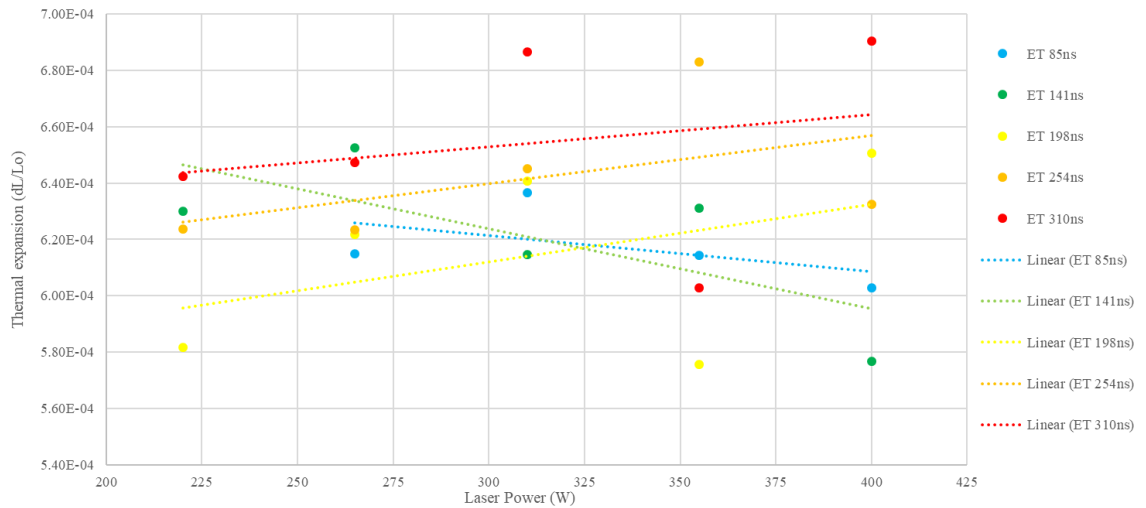


Figure 214. Final change in length over -100°C to 200°C for invar against laser power.

The two lowest exposure times 85 μ s and 141 μ s experience a significant reduction in thermal expansion as the power increases. It is hypothesised that a short exposure time creates finer microstructure. Longer ET creates larger melt pools reducing cooling rate, creating larger microstructures. It is known that greater cooling rates and higher residual stresses in LPBF yield lower thermal expansion in invar. Increasing the energy input into the melt pool reduces residual stress due to an increase in overall localised energy input and reducing thermal expansion.

In Figure 215 the contour plots show that an increase in scanning speed reduces thermal expansion, and an increasing laser power increases thermal expansion. This is in agreement with Yakout et al’s [163] findings.

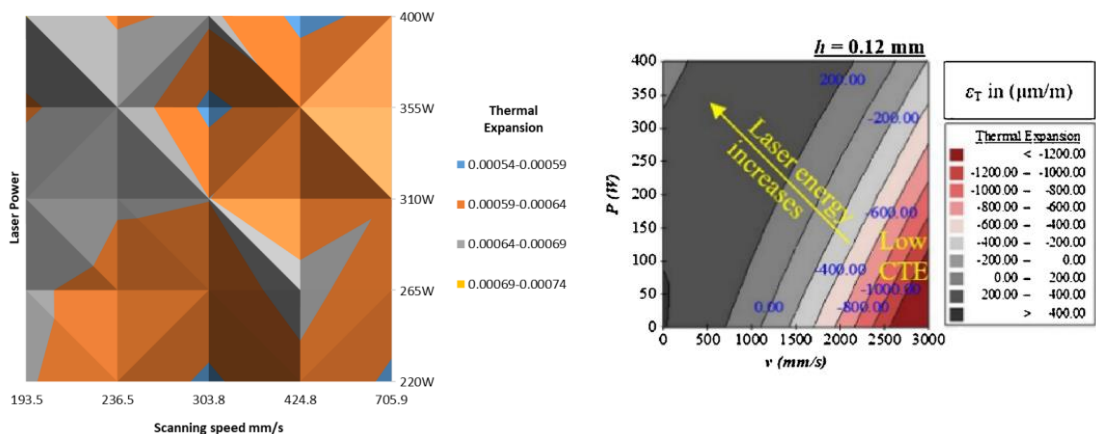


Figure 215. Contour plot of scanning speed against power for thermal expansion ranges in the present work (left). Yakout et al. contour plot (right) [163].

Density

The density has been measured with Archimedes using the density cubes printed, and by cross-sectioning the dilatometer rods and measuring the distribution of porosity optically. It can be seen in Figure 216 that there is reasonable correlation between optical and Archimedes measurements. Inspecting the graph for the lowest porosity levels suggest the optimum energy density should be between $125 - 175 \text{ J/mm}^3$ providing porosity of between 0.05 - 0.4%. A few readings show full densification at 76.24 and 152.2 J/mm^3 .

The increase in porosity as the energy density increases is due to the transition from conductive to keyhole weld. There are also other contributing factors to porosity such as the ejaculated matter from the weld pool, referred to as spatter. The spatter can land on other components increasing porosity [42]. A change in component residual heat can also affect whether a keyhole is created, which is dependent on how long the laser is scanning other areas [184].

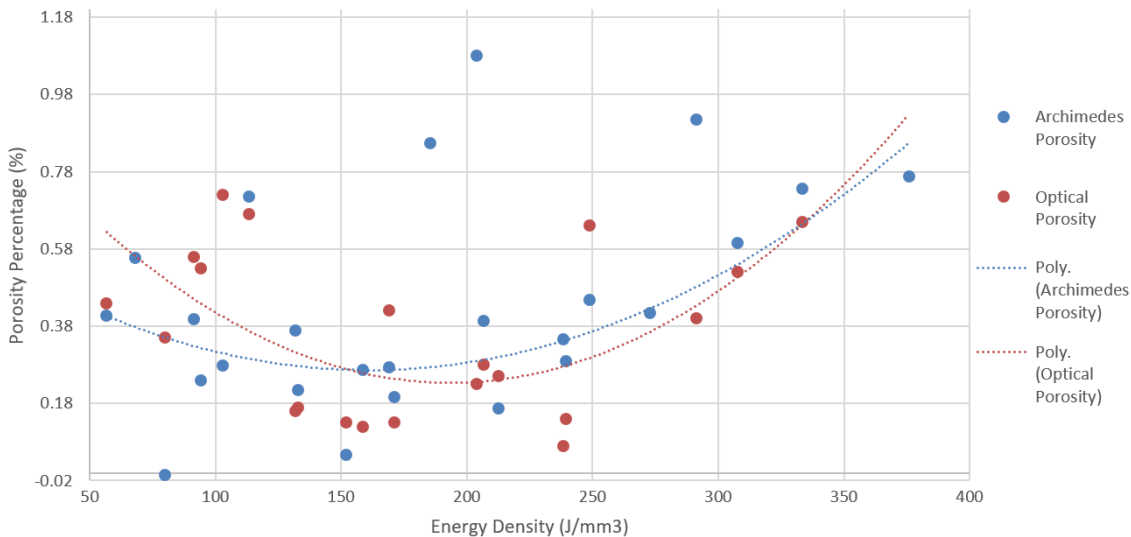


Figure 216. Graph showing the density measured by Archimedes and by optical microscopy. Optical porosity outliers for 3.12, 3.16, and 4.42% are not plotted and excluded from the polynomial curve. Archimedes outliers 0.85, 0.92, and 1.08% are also ignored from the polynomial curve.

Looking at the cross-sections in Table 51, it can be seen that there are regions of increased and decreased porosity at different heights in the build. These are in line with other components on the plate, such as the density cube and horizontal dilatometer rod.

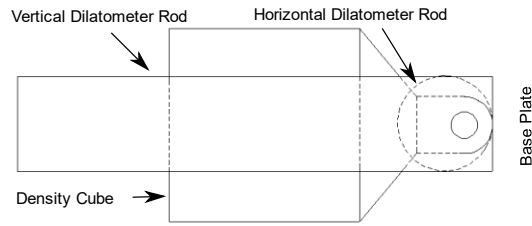



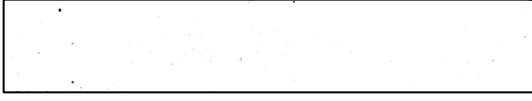
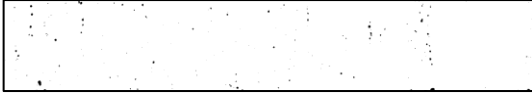


Figure 217. Build layout showing where the other components are in relation to the dilatometers cross-section.

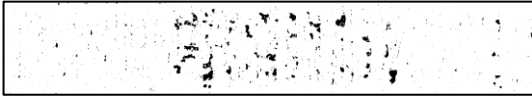
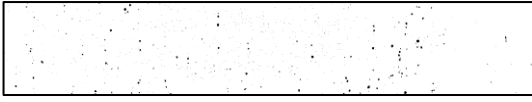

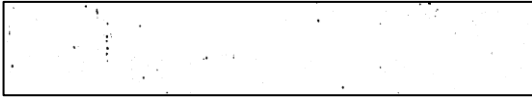
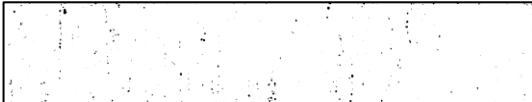
Looking at the optical porosity images in Table 51, arrays such as 8, 10, 12, and 15 experience less porosity where the layer cooling time is increased by the horizontal dilatometer rod being built. This matches up with the locations of the components in Figure 217. Array 11 is unaffected by the horizontal rod but increases porosity when the density cube is being built. This suggests that the keyhole behaviour in this high energy vapourisation zone is very sensitive to the latent heat remaining in the component from the previous layer.

Table 51. High laser energy input invar - optical porosity data.

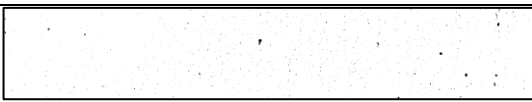
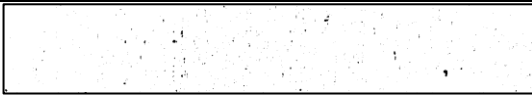
400W				
Array no.	Exposure Time μs	Build Energy J/mm^3	Optical Porosity	Optical Porosity %
1	85	103		0.72%
2	141	171		0.13%
3	198	240		0.14%
4	254	308		0.52%
5	310	376	Too porous to polish without significant scratches.	
310W				
Array no.	Exposure Time μs	Build Energy J/mm^3	Optical Porosity	Optical Porosity %


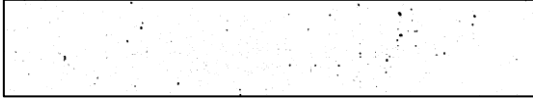

6	85	80		0.35%
7	141	133		0.17%
8	198	186		4.42%
9	254	238		0.07%
10	310	291		0.4%

265W

Array no.	Exposure Time μs	Build Energy J/mm^3	Optical Porosity	Optical Porosity %
11	85	68		3.16%
12	141	113		0.67%
13	198	159		0.12%
14	254	204		0.23%
15	310	249		0.64%

220W

Array no.	Exposure Time μs	Build Energy J/mm^3	Optical Porosity	Optical Porosity %
16	85	57		0.44%
17	141	94		0.53%

18	198	132		0.16%
19	254	169		0.42%
20	310	207		0.28%

Hardness

Hardness is measured using Vickers hardness HV2 indentations. 24 indentations were made from the bottom to the top of the dilatometer cross-section, and the data plotted and analysed for trends in Figure 218.

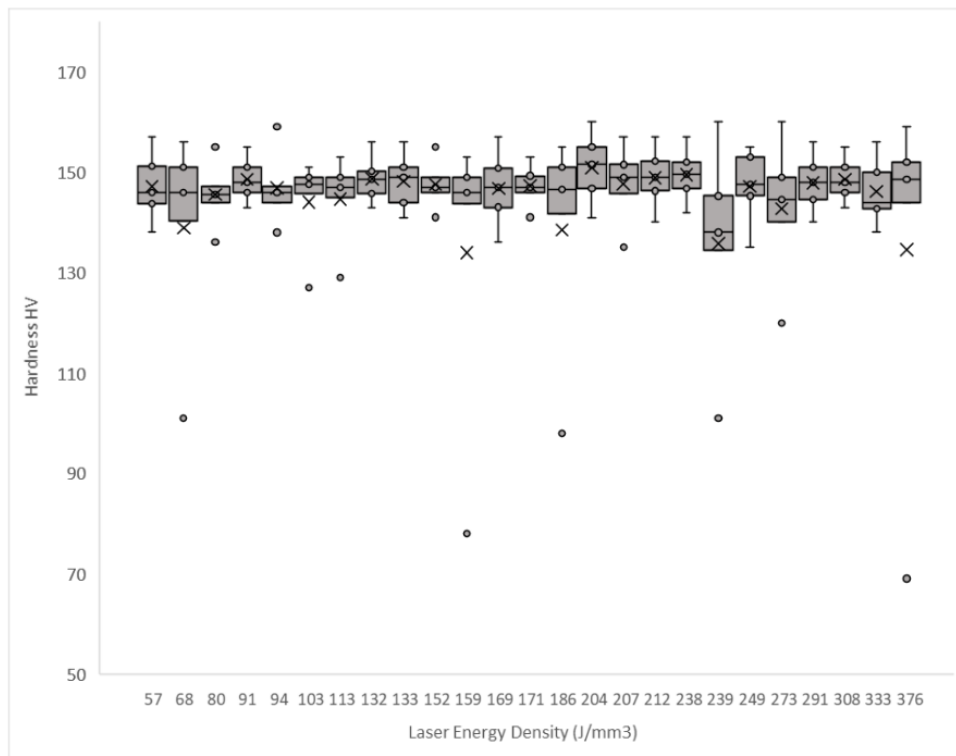


Figure 218. Hardness box plot for 24 linear points on a cross-section of each invar dilatometer rod against its corresponding laser energy density.

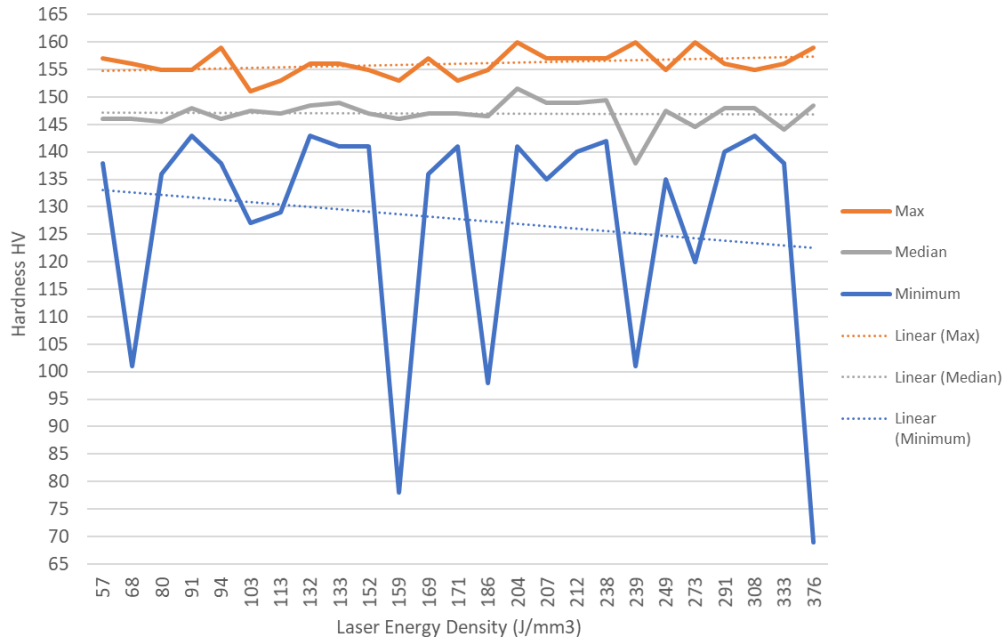


Figure 219. Hardness max, median, and minimum, for 24 linear points on a cross-section of each invar dilatometer rod against its corresponding laser energy density.

The hardness median values are approximately 147MPa across all laser energy densities. There is a reducing minimum hardness as energy density increases seen by the linear trendline, from 135 to 121MPa. Across the maximum trendline a slight increase of 2.5MPa is seen. Literature shows that hardness can range between 125 and 186MPa for invar36 manufactured using LPBF depending on the laser energy density [185].

This data shows that hardness remains relatively unaffected by the higher laser energy densities. The only noticeable trend is in the reducing minimum hardness values as energy density increases. The indentations for these lower values have been inspected and determined to be caused by an increase in porosity in the regions shown in Table 51. The bulk material where porosity does not exist is determined to be the same by the stable median result.

Conclusion for the adjustment of invar laser processing parameters.

To conclude, varying the laser energy density while manufacturing invar36 has the following outcomes;

- Thermal expansion increases with laser energy density, disagreeing with the original observation by Yakout et al. that thermal expansion decreases after the critical energy density. CTE increased by a maximum of 0.32µm/mK from 57 to 376 J/mm³.
- It is observed that as the 2D laser energy increases, so does the thermal expansion. This is observed with both increasing scan speed and decreasing laser power. This agrees with findings by Yakout et al [161], [163], [164].

- When processing in the vapourisation regime, on average component density continues to reduce with energy density, but is very sensitive to changes in component layer heat differences caused by other components on the baseplate.
- Vickers hardness median remains unchanged across all energy densities. Minimum hardness decreases with porosity, as energy density increases.

6.5.5 Discussion on the Iron-Nickel alloys

Invar36 gas atomised powder by Sandvik has been printed successfully with 99.98% relative density. It is observed that the invar effect outlined by Et al. Guillaume, was found to match the thermal expansion curve in the induction melted Fe-Ni alloys. The thermal expansion follows the trends of the curve, although some loss of nickel from 0.8%-1.6% over the range was shown by EDS. The in-situ additions have the promising prospect of allowing the gas atomised invar36 powder to have the nickel content adjusted by additions of either iron or nickel powder to ‘fine tune’ the CTE to the lowest possible value, it to increase the CTE to a value aimed to match with that of glass or germanium. The ‘fine tuning’ of the CTE in invar is shown to be necessary since the nickel content of the gas atomised powder can vary from the target composition. The two batches of invar received from two different suppliers had a nickel wt.% of 35.1 and 37.2 respectively, missing the 36% target. The in-situ additions show that fine carbonyl iron and nickel powder can adjust the CTE to the target values. EDS scans show homogenous distribution of Fe and Ni within the components. Problems occurred when adding large amounts of gas atomised nickel powder of 7wt.% to attempt to create an alloy that matches the CTE of glass. The thermal expansion was low compared to cast equivalent, and EDS scans show distributions of iron and nickel rich areas. Heat treatment of the 7wt.% Ni sample showed an increase in CTE for the sample from 5.85 to 8.35 $\mu\text{m}/\text{mK}$. The rest of the samples increase by only 0.09-0.43 $\mu\text{m}/\text{mK}$. This indicates that heat treatment should be an essential step for high amounts of in-situ additions. Smaller CTE changes were also noted in minor $\pm 1\text{-}2\%$ additions after heat treatment. The mechanical performance of the alloys is affected the most by the batch of invar, rather than the amount of $\pm 1\text{-}2\%$ additions of the fine carbonyl powder. It is observed that for batch 1 invar by TLS, these additions provide a Vickers hardness of 156-158, and for batch 2 by Sandvik they provide a hardness of 145-146. In tensile testing, batch 1 has a higher UTS, with lower break and UTS elongation compared to batch 2. There are many variables that can affect the mechanical performance between the two invar batches, these include;

- Change in PSD causing a change in melt behaviour and corresponding microstructural changes.
- Change in invar gas atomisation gas between nitrogen and argon between batch 1 and batch 2.

The laser parameter set was optimised for maximum density using invar batch 2. When manufacturing parts with invar batch 1 using the same laser parameters the parts became porous. If a batch of invar powder has the same composition, particle size distribution, and ICPMS results, as another batch of invar powder, that laser parameters can still not be optimal. There are practical implications of this finding because it shows that the laser parameters provided by the machine manufacture or in journal publications cannot be assumed to provide maximum density, even if the machine is the same and the powder composition is similar. The in-situ additions have shown successfully that an addition of carbonyl 3-7 μm nickel or iron powder effects the mechanical properties very little but adjusts the CTE as expected. Gas atomised 15-45 μm nickel powder does deviate the mechanical properties away from the properties of the components without the addition. It was successful at adjusting the CTE to the expected range after heat treatment. This shows that the CTE of the lens housing can be tailored to match the CTE of the lens material by increasing the amount of nickel using either carbonyl or gas atomised metal nickel powder.

The adjustment of the laser processing parameters has been shown in literature to adjust the thermal expansion of invar36. Yakout et al. shows the CTE increases if the combination of the laser scanning speed, and laser power create a higher laser energy over the 2D area. This agrees with the findings of the study conducted in this chapter. Yakout et al. also shows that the thermal expansion decreases past an optimum laser energy density, however this was not discovered in the experiment. It was discovered that there is a *linear increasing* relationship between laser energy density, and thermal expansion. As the laser energy density increases, so does the thermal expansion. The CTE increased by a maximum of 0.32 $\mu\text{m}/\text{mK}$ from 57 to 376 J/mm^3 . The optimum energy density is considered to be 59.36 J/mm^3 , so energy densities above and towards 376 J/mm^3 will have entered the vapourisation regime. The increasing laser energy density corresponds with an increasing trend of nickel content, suggesting the higher energy densities are evaporating iron in a higher relative proportion. The increase in nickel content could be responsible for the increase in CTE, with a maximum change in CTE of 0.32 $\mu\text{m}/\text{mK}$. With an overall nickel change from 36.44 to 37.28% or a 0.74% difference, this is within the range possible for a 0.32 $\mu\text{m}/\text{mK}$ CTE variability. Looking at the in-situ additions, builds 1 and 5 had a difference of 0.97wt.%Ni and a CTE difference of 0.56 $\mu\text{m}/\text{mK}$ at 150°C. This places the CTE change within the expected region.

Overall the method of tailoring the thermal expansion of an optical system body by adjusting the laser parameters is not an optimal choice to get the desired thermal expansion values. The change achieved of only 0.32 $\mu\text{m}/\text{mK}$ is only useful for tailoring to a very specific CTE value. The trend line plotted is a function of lots of measurements sometimes lower or higher than the trend line, and therefore unpredictable. The method

of vaporising nickel to adjust the CTE will increase porosity, which is undesirable. The best approach to adjusting the thermal expansion of Fe-Ni gas atomised alloy powder is to adjust the chemical composition of the powder through adding in-situ additions of either Fe or Ni powder in fine carbonyl form. The laser parameters after the addition have shown to produce the same densities and mechanical properties as that without the additions.

6.5.6 Conclusion on the Iron-Nickel alloys

To conclude, it is shown that the thermal expansion of an invar alloy can be tailored by in-situ additions of either Fe or Ni powder. The alloys ranging from $\pm 1-2\%$ Fe or Ni fine $3-7\mu\text{m}$ carbonyl powder added to gas atomised $15-45\mu\text{m}$ invar36 powder shows the expected change in CTE with minimal deviation on hardness and tensile performance. Thermal expansion has been shown to be tailored between Adding 1% and 7% of $15-45\mu\text{m}$ gas atomised nickel powder shows variation in mechanical properties, and Ni and Fe rich areas in EDS scans. Subsequent heat treatment improved the performance of both, however it would be recommended to use a finer powder to improve reliability of expected results. To summarise the technical outcomes of the in-situ additions;

- The thermal expansion on invar was found to be lowest at 35.01wt.% Ni between -100 and 0°C , but lowest at 35.99wt.% Ni above 0°C . This is supplementary to Guillaume et al. prediction that 36wt.% Ni produces the lowest thermal expansion, as they did not test cryogenic temperatures.
- Overall nickel content of between 35 to 38wt.% Ni varies the CTE from 0.63 to $3.48\mu\text{m}/\text{mK}$ at 0°C . The CTE is shown to be highly responsive of temperature as the nickel content varies.
- The microhardness shows limited change between the 1-2% additions, giving a microhardness of 154-157HV for batch 1 and 144-145HV for batch 2.
- The tensile performance also shows limited change between the 1-2% additions, giving a UTS of between 475-463MPa for batch 1 and 418-427MPa for batch 2.
- The relative density remains consistent when additions are added, with batch 2 invar at 99.95-99.87% relative density after +1-2wt.% Fe.
- Thermal expansion of 7wt.% Ni addition provides a CTE of $8.35\mu\text{m}/\text{mK}$ after heat treatment, demonstrating the possibility to tailor invar to the same CTE as glass or germanium ($6-7\mu\text{m}/\text{mK}$) with a slightly low nickel addition.

The thermal expansion of invar powder as also been shown to be adjustable by a maximum of around $0.32\mu\text{m}/\text{mK}$ by varying the laser parameters energy density. The experimental data disagrees with Yakout et al.'s original observation that thermal

expansion decreases past an optimal energy density, instead the relationship is increasing thermal expansion with increasing energy density from 57 to 376 J/mm^3 . Experimentation has not been conducted to determine the cause of this relationship. The practical use of these findings for tailoring thermal expansion are limited. A maximum increase of 0.32 $\mu m/mK$ is achievable, but not predictable. There is also a sacrifice of the increased porosity past the optimum laser energy density of 59.36 J/mm^3 . To summarise the technical outcomes of the invar laser parameter tailoring;

- Thermal expansion increases with laser energy density, disagreeing with the original observation by Yakout et al. that thermal expansion decreases after the critical energy density. CTE increased by a maximum of 0.32 $\mu m/mK$ from 57 to 376 J/mm^3 .
- Nickel content increased from 36.44 to 37.28wt.% representing a 0.74wt.% maximum increase due to vaporisation as the laser energy increases.
- Vickers hardness median values remain unchanged across all energy densities. Minimum hardness decreases with porosity, as energy density increases.
- Findings agree with Yakout et al. that increasing scanning speed reduces thermal expansion and increasing laser power increases thermal expansion.

In conclusion, the adjustment of the thermal expansion of invar is best achieved by adjusting the elemental constituents of the powder. This method allows a wide range of thermal expansions by adding a quantity of fine elemental iron or nickel powder and mixing thoroughly. The thermal expansion can be adjusted using this method to provide a CTE that is matched with that of a glass or germanium lens material aimed at the optical industry. Heat treatment is effective at combining FeNi rich regions for higher percentage elemental additions. The addition of $\pm 1-2\%$ carbonyl powder produces components with little variation in hardness and tensile properties, producing results similar to that of gas atomised invar without the additions. The density also only varies by 0.07% over the additions. The method of adjusting invar's thermal expansion by varying the laser energy density has no practical use. It has achieved a very small range of thermal expansion adjustment of 0.32 $\mu m/mK$, but also induces significant porosity in the process.

6.6 Aluminium-Silicon Alloys

6.6.1 Introduction

This chapter will investigate the manufacturability of controlled thermal expansion AlSi alloys with 30 to 40wt.% Si using LPBF. Literature shows that there has been mixed success with processing high silicon aluminium alloys using LPBF, with some reporting significant issues with cracking, and others not mentioning cracking but reporting high densification [50], [52]–[55], [181], [186]–[189]. This chapter will investigate the suitability of processing high silicon aluminium alloys with LPBF as a means of controlling thermal expansion. An investigation will be conducted where pre-alloyed AlSi30 and AlSi40 gas atomised powders are blended to make AlSi35. The hardness, thermal expansion, and microstructural properties of all the alloys will be compared to its industry leading method of manufacture called spray forming.

6.6.2 Method

To compare the thermo-mechanical effect of adding silicon to aluminium and processing with LPBF, AlSi30 and AlSi40 gas atomised powders from Carpenter Additive have been chosen. The PSD and SEM images of the powders can be found in chapter 6.4. Both powders will be printed by the Renishaw AM400 in the Reduced Build Volume using the setup outlined in chapter 6.3. In another build, both powders will be mixed at a 50% ratio to create AlSi35. The powders will be mixed in a V-type blender for 1hr at 60rpm.

The AlSi10Mg laser parameters provided by Renishaw will be used, and the exposure time will be varied six times from 10, 20, 30, 40, 80, 120 μ s. This will be useful to determine the effect of varied slice energy and scanning speeds. It has been shown in literature that faster scanning speeds create a finer microstructure [50]. This should result in a higher UTS, but lower ductility. It is unknown what effect the laser parameters have on thermal expansion of high silicon aluminium alloys. The parameters will be 350W LP, 90 μ m HS, 90 μ m PD, and 30 μ m LT, which are considered optimal for AlSi10Mg when using 40 μ s ET.

Sandvik Osprey have supplied high silicon aluminium alloys ranging from 42-87wt.% silicon manufactured by spray forming. These will be used to compare microstructure, hardness, and thermal expansion with that of LPBF parts. The alloys are manufactured into 5x5x25mm samples for measurement of thermal expansion using dilatometry. It was not possible to manufacture the cylindrical rod of dimensions 5 \varnothing x 25mm required by ASTM- E228-17, so the nearest equivalent square shape was manufactured. To ensure

the thermal expansion and microstructure can be directly compared to LPBF, the same sample shape of 5x5x25mm is also used for the samples manufactured using LPBF.

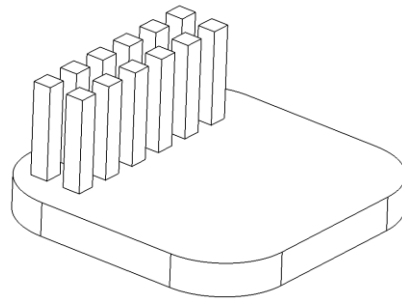


Figure 220. AlSi LPBF Build plate.







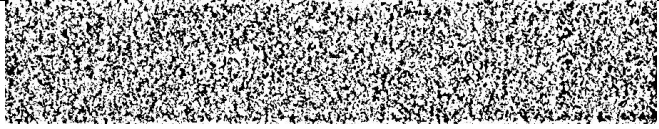



6.6.3 Results








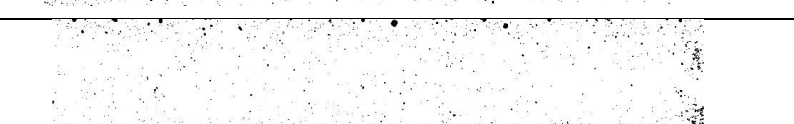



All samples manufactured by laser powder bed fusion and spray forming are measured for their linear thermal expansion. The thermal expansion can determine if processing by LPBF changes the thermal expansion of the alloy compared to spray forming. The samples are cross sectioned and mounted. After polishing, optical microscopy is performed to determine the porosity percentage. Microstructure images are also taken using light microscopy. SEM BEC is performed to see the phases of the material and their location. The determination of the phase constituents is achieved using EDS. Microhardness indentations are made down the centreline of all the samples to assess the process parameters on the mechanical properties. A diagram of the locations of the indentations can be found in Figure 222.


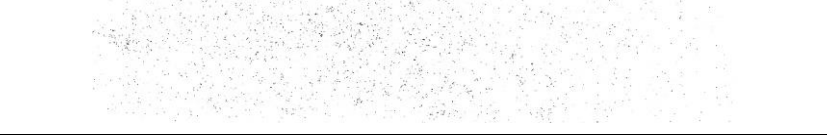
Density

A porous component can be produced if the laser parameters are not optimal. To determine the density, both laser powder bed fusion and spray formed samples have been cross-sectioned and analysed for porosity using the methodology outlined in the experimental chapter 5. The density will be compared with spray formed components to determine if densification is equal with conventional methods.

Table 52. AlSi Optical porosity results table. The black dots are the porosity in the optical of the cross-section of the dilatometer rod.

LPBF - AlSi30		
Exposure Time	Optical Porosity	Porosity
10 μ s		31.32%
20 μ s		5.33%
30 μ s		0.74%
40 μ s		0.37%
80 μ s		1.14%
120 μ s		1.49%
LPBF - AlSi35 (Blended 50% AlSi30 powder with 50% AlSi40 powder)		
Exposure Time	Optical Porosity	Porosity
10 μ s		35.98%
20 μ s		8.65%
30 μ s		1.78%
40 μ s		0.44%

80 μ s		0.66%
120 μ s		0.89%
LPBF - AlSi40		
Exposure Time	Optical Porosity	Porosity
10 μ s		36.57%
20 μ s		3.48%
30 μ s		2.96%
40 μ s		0.23%
80 μ s		0.9%
120 μ s		1.63%
Spray Formed		
Material	Optical Porosity	Porosity
AlSi42		0.35%
AlSi60		0.57%
AlSi70		1.21%

AlSi80		0.23%
AlSi87		0.86%

The optimum exposure time of 40 μ s for AlSi10Mg also appears to be the best for AlSi30,35, and 40, with porosities of 0.37, 0.44, and 0.23% respectively. Porosity could be reduced by further refinement with an L9 array. It is also clear that some samples manufactured with spray forming have a higher porosity than samples made by LPBF. AlSi42 is the spray formed component with a silicon quantity closest to AlSi30-40 LPBF parts, and has a porosity of 0.35%, close to AlSi40 LPBF with 0.37%.

Figure 221 shows the porosity trends. As exposure time increases above 40 μ s ET, keyhole welds appear, increasing porosity. As the energy drops below 40 μ s ET, there is insufficient energy to fully melt the powder.

The density of all AlSi components manufactured using optimum laser exposure time in LPBF are considered equivalent or better than the most common, conventionally manufactured parts using spray forming.

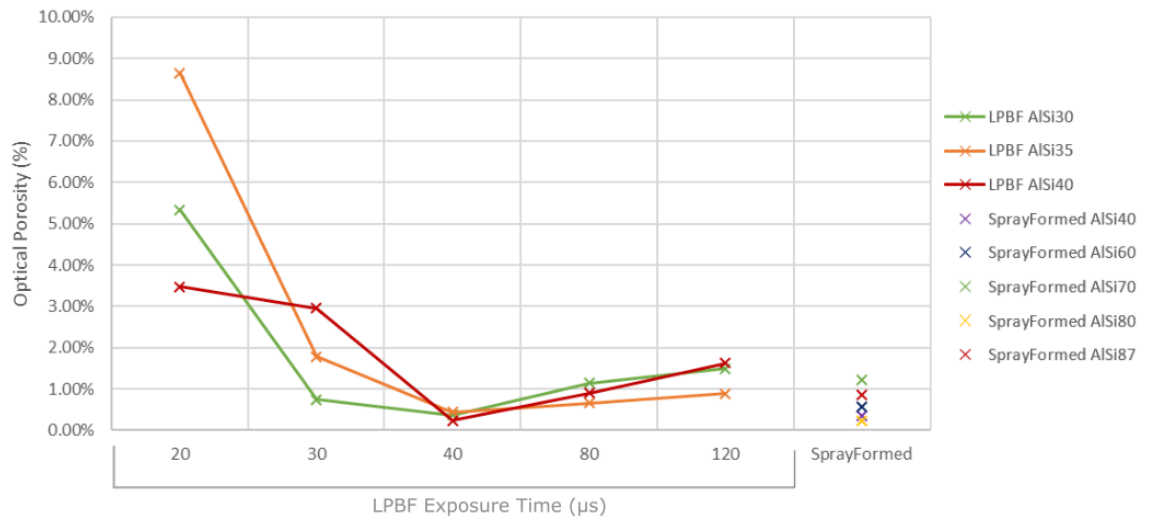


Figure 221. Optical porosity for each AlSi alloy manufactured by LPBF and spray forming. LPBF exposure time of 10 μ s has been omitted to make results comparable.

Metallography

It is important to understand the microstructure of any AlSi controlled expansion alloy printed using LPBF, compared with manufacturing by spray forming. The microstructures size and homogeneity are important factors in the isotropy of thermo-mechanical properties. A cross-section has been made through the center of each sample, and the very centre is imaged with white light microscopy using a Zeiss Axio Observer Z1m, and captured with an AxioCamHR3. Magnification was kept at a constant ensuring each image is 275 μ m in width.

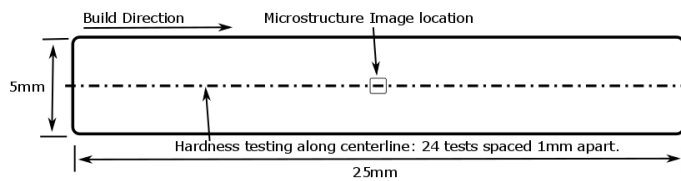
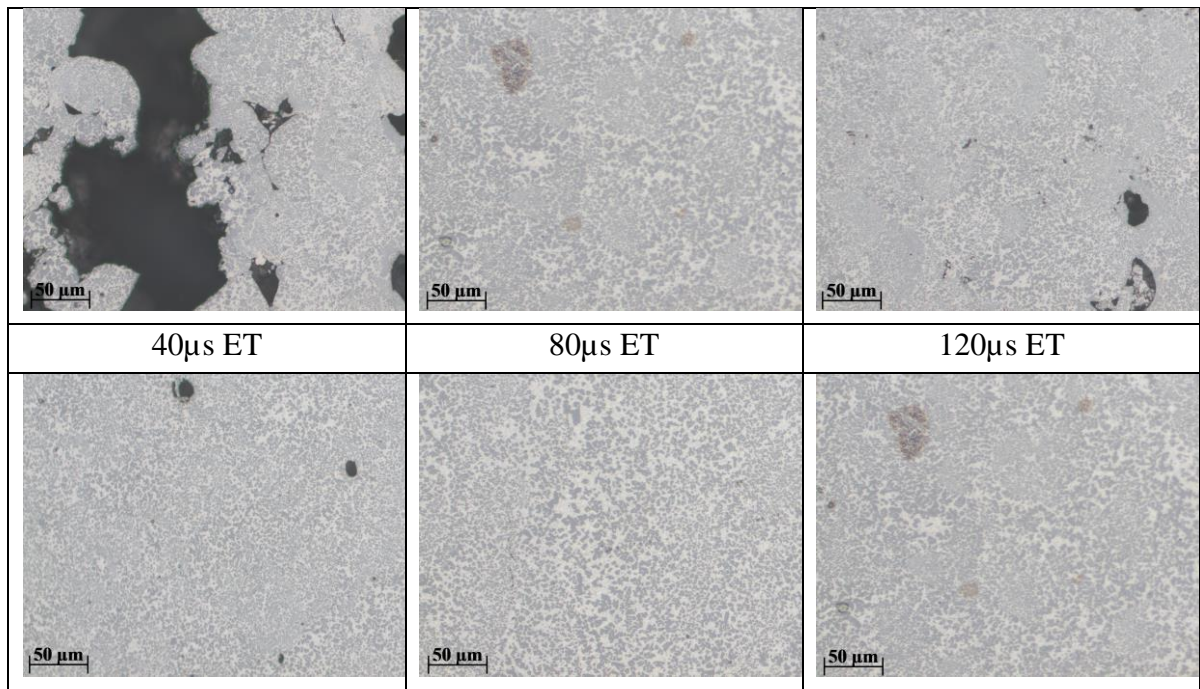


Figure 222. Dilatometer rod showing hardness indent locations and imaging location.

The captured images in Table 53 show the aluminium phase in white, and silicon phase in grey. Any black space is porosity.

Table 53. Microstructure of spray formed AlSi alloys. Centreline images compared.

AlSi87 Spray Formed	AlSi80 Spray Formed	AlSi70 Spray Formed
AlSi60 Spray Formed	AlSi42 Spray Formed	
AlSi40 LPBF		
10 μ s ET	20 μ s ET	30 μ s ET



Looking at the micrographs in Table 53 the microstructure is finer on laser powder bed fusion samples compared with spray formed samples. In the spray formed components, the silicon phase becomes continuous from 60% Si and higher, and the Al phase is continuous at 42%. The micrographs show that the laser powder bed fusion samples also have a continuous Al phase at 40%, although there are zones of finer Si regions which would count as continuous. The variation between exposure times also changes the microstructure sizing. Exposure times near to the optimum of 40 μ s experience a much finer microstructure. Exposure times 10, 20, 80, and 120 μ s all have larger Al and Si phases compared to 30, and 40 μ s ET. It is also observed that the distribution of sizing in the microstructure is less consistent on the LPBF samples than in the spray formed samples. Figure 223 show the average Si phase area for the images in Table 53. It is observed in Figure 223 that the average phase area and phase count is highest for the optimum density 40 μ s exposure time. Reducing and increasing the exposure times either side of 40 μ s reduces the phase count and increase the average phase sizing.

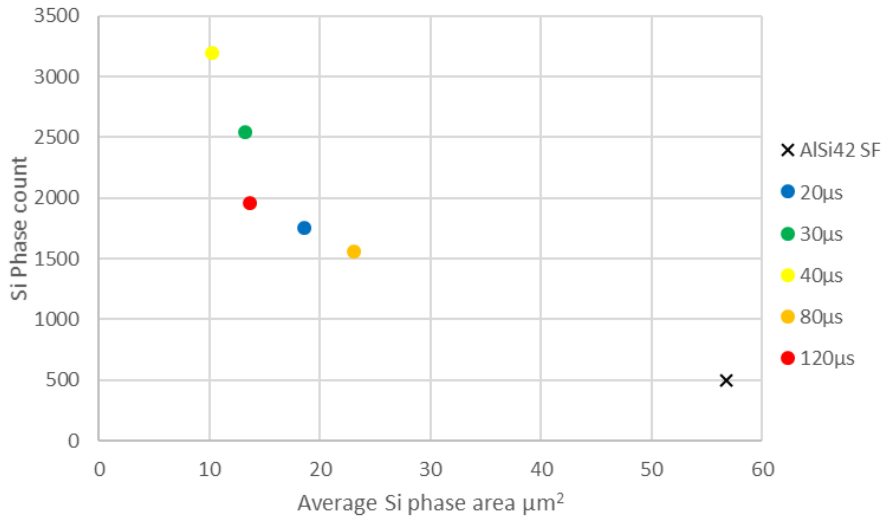


Figure 223. AlSi40 phase area compared to the quantity of phases.

Comparing the SEM images shown in Table 54, in the spray formed parts there are very distinct Al and Si phases, which are much larger than the LPBF phases. The microstructure size spacing is more uniform across the cross-section in SF compared to LPBF. In the LPBF cross-sections the microstructure size distribution is much wider, with very fine, and large phases.

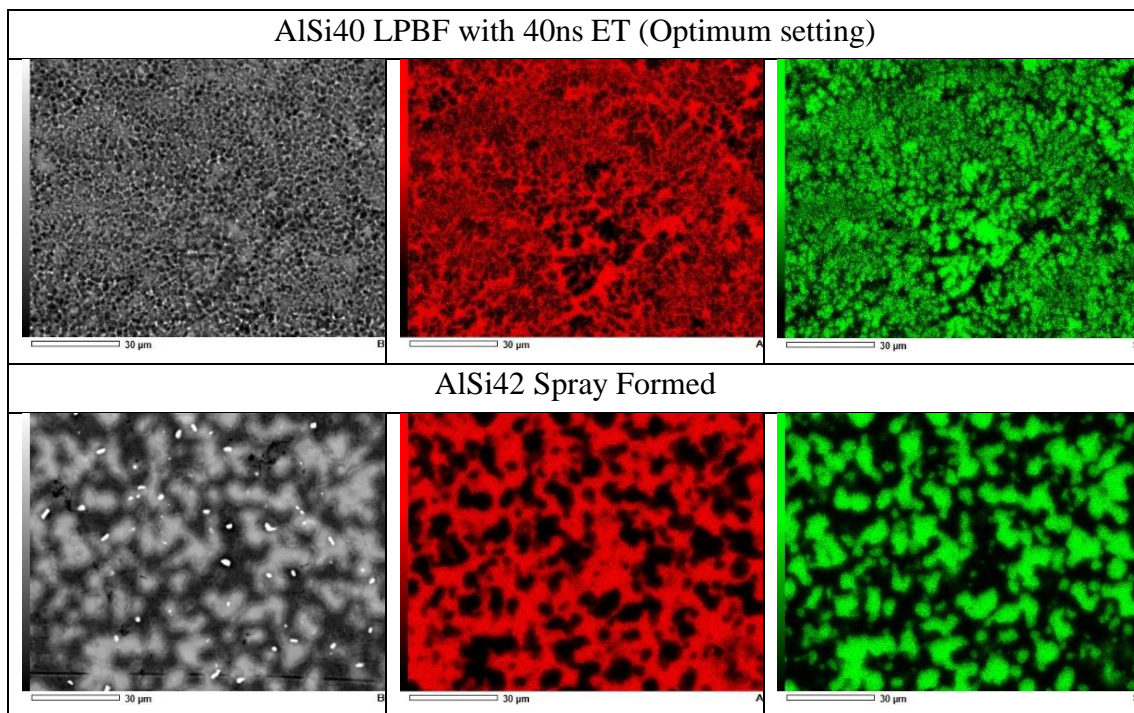


Table 54. SEM BEC & EDS images showing phase sizes and distribution for AlSi40 manufactured with LPBF with 40ns ET, and AlSi42 spray formed. Magnification is x1000.

To improve the visual distinction between Al and Si phases, both EDS red and green images can be overlaid in one image. Figure 224 shows AlSi40 manufactured using LPBF

at a two times lower magnification compared to the images in Table 54 of x500. The SEM BEC images show difficulty in separating phases, but the overlaid EDS image provides a qualitative understanding of phase size distribution between aluminium and silicon.

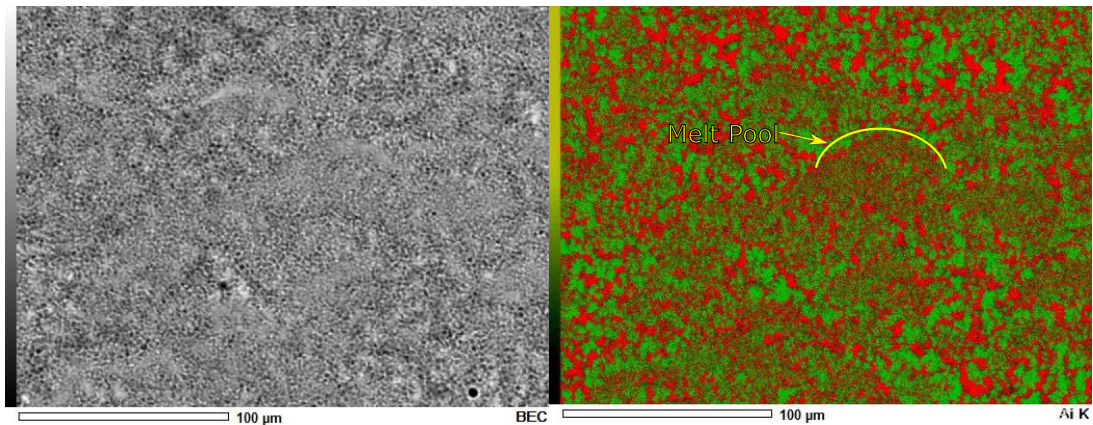


Figure 224. AlSi40 LPBF x500 SEM BEC & EDS overlaid showing finer microstructure around weld melt pools. Red is Al, green is Si, overlaid using 50% transparency.

It is possible to see that there is significant refining of microstructure around the weld pool regions. It is important to get an equal distribution in phases sizes to ensure that internal residual stresses do not increase when thermal cycling the material. Larger phases of low thermal expansion silicon or high thermal expansion aluminium could exert more force onto the surrounding finer microstructure creating anisotropic internal forces, leading to thermally induced mechanical fatigue. The thermal expansion could be anisotropic if the distribution is uneven in one direction.

Microhardness

Vickers microhardness has been obtained for each sample. The centreline hardness was plotted by taking 25 indentations spaced 1mm apart, as shown in Figure 222. Indentation force was found to be optimum at 2 kgf/mm^2 . Silicon contents higher than 60% and higher cracked upon testing and so were not included in the results. An example image showing cracking during indentation is seen in Figure 225. An acceptable reading of the dimensions of the crack cannot be obtained from this image.



Figure 225. HV2 indent in AlSi30 producing clear shape (left). HV2 indent applied to AlSi80 showing significant cracking (right).

The hardness for each exposure time is plotted using a box plot to best represent the 25 indentations made per sample. Figure 226 to Figure 228 show the box plots for AlSi30, AlSi35, and AlSi40 manufactured using LPBF. The optimum exposure time for maximum density is 40 μ s across all AlSi30, AlSi35, and AlSi40 samples. Figure 226 shows consistent median hardness values for 20, 30, and 40 μ s exposure times of 185, 188, and 180MPa respectively, but a reduction in median hardness for exposure times greater than 40 μ s, of 117MPa for 80 μ s and 146MPa for 120 μ s.

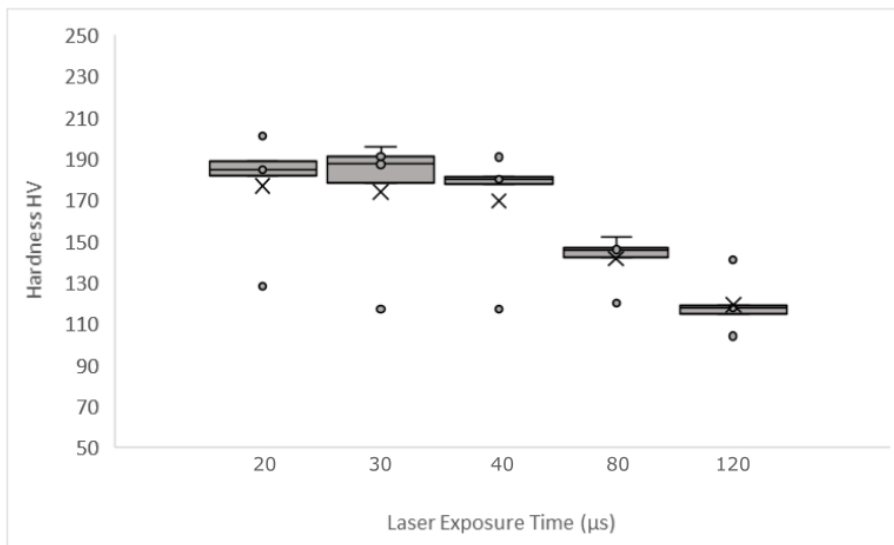


Figure 226. AlSi30 Vickers HV2 hardness data for a LPBF component at various laser exposure times.

Similar trends continue for AlSi35 in Figure 227 where similar median hardness values are given for exposure times for the optimal 40 μ s, but lower values for exposure times below. The overall hardness has increased due to the increased silicon content. For exposure times of 20, 30, and 40 μ s, median hardness values of 193, 195, and 193MPa are found, respectively. For those of 80 μ s and 120 μ s, hardness values of 148 and 123MPa are found, respectively.

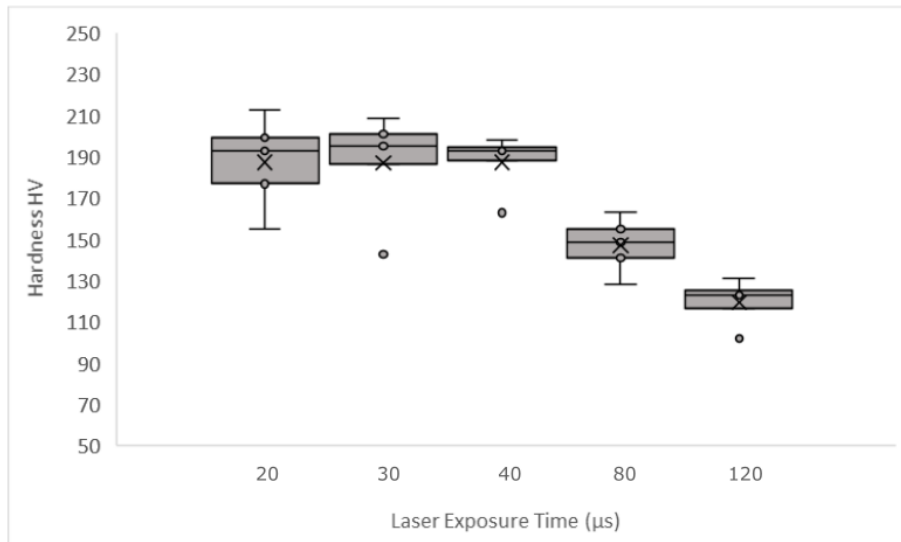


Figure 227. AlSi35 blended Vickers HV2 hardness data for a LPBF component at various laser exposure times.

Figure 228 includes an added sample of AlSi42 manufactured using the spray forming technique for comparison alongside the AlSi40 samples manufactured using the LPBF method. The similar silicon content makes direct comparisons of the manufacturing method easier. It is observed that the median hardness values for 20, 30, 40, 80, and 120μs exposure times are 233, 223, 217, 165, and 166MPa, respectively. For the spray formed AlSi42 a median hardness of 98MPa is measured.

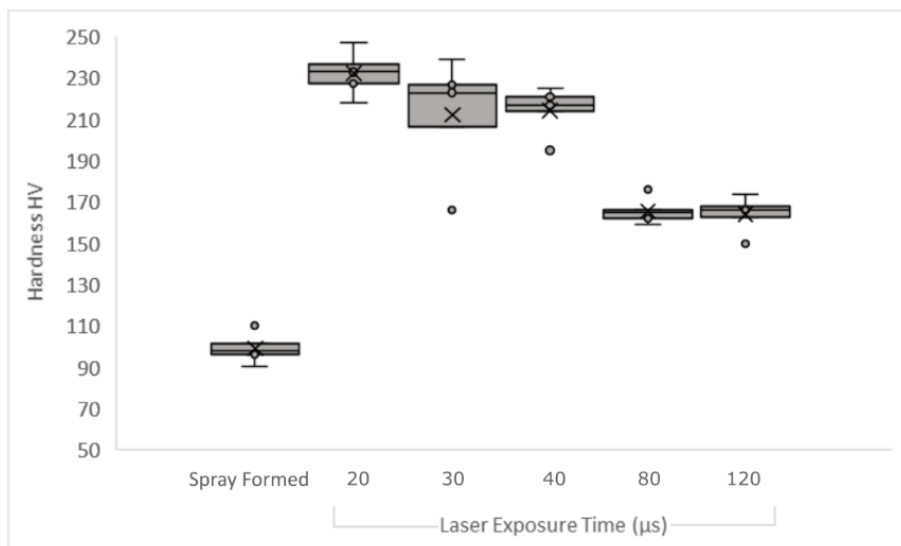


Figure 228. Vickers HV2 hardness data for a spray formed component AlSi42, and a LPBF AlSi40 component at various laser exposure times.

At the optimum exposure time of 40μs, there is a hardness median value of 217, 193, and 180MPa for AlSi40, AlSi35, and AlSi30 respectively. This shows hardness decreases as silicon decreases. The blended AlSi35 made from half AlSi30 and half AlSi40 has produced a hardness value approximately halfway between both. Figure 229 shows that

when the exposure time increases from 40 μ s to 80 μ s and 120 μ s, the hardness values are close to that of the lower percentage silicon powder (AlSi30). This observation is repeated in the lower exposure times, with 30 μ s, and 20 μ s becoming closer to the hardness of AlSi30 the further the exposure time reduces from its optimal of 40 μ s. This indicates the increased silicon from AlSi40 has not been sufficiently distributed within the microstructure to exhibit the same characteristics as pre-alloyed AlSi35, when outside of the optimum laser exposure time.

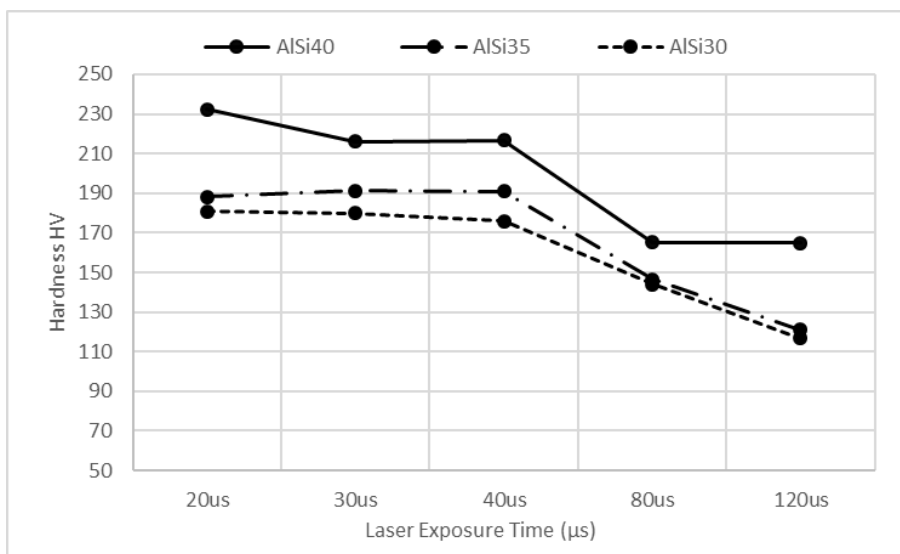


Figure 229. AlSi30, AlSi35, and AlSi40 median Vickers hardness comparison over a range of exposure times.

It is also observed that there is an overall decrease in hardness for the higher exposure times of 80 and 120 μ s. This cannot be attributed to the density, because a high porosity of between 3.5 and 8.7% is observed in the lower ET of 20 and 30 μ s with no significant change in hardness. It is known that lower energy density, and faster scanning speeds create finer microstructures and phase sizes within AlSi alloys manufactured with LPBF [50], [52], [53], [56], [190], [191]. The lower hardness in these higher energies can be attributed to the larger individual phase sizes. This conclusion is backed up by the metallography which shows that there are larger areas of aluminium and silicon for 80 and 120 μ s compared to 40, 30, and 20 μ s as shown in Figure 223 and Table 53. It is also seen that the spray formed AlSi42 component exhibits significantly less hardness at a median of 98MPa compared to AlSi40 manufactured with LPBF at 218MPa. Spray forming produces significantly larger phase sizes of Al and Si compared to all LPBF samples, as seen by the metallography. This improvement in hardness compared to the conventional spray forming method is a very significant and presents a potential benefit for parts manufactured using LPBF.

Thermal Expansion

The thermal expansion has been measured using a heating cycle from -120°C to 200°C at $5\text{k}/\text{min}$. The temperature was held at -120°C for 30 minutes to ensure even temperature distribution. This test program is slightly different to the heating and cooling cycle used to measure invar and outlined in the experimental chapter 5. This method stabilises the temperature using a cryogenic hold, rather than a high temperature hold. This method avoids any stress-relieving high temperatures that may affect the result.

Figure 230 shows the change in length divided by the original length, for a LPBF samples with ET from the lowest $10\mu\text{s}$, to the optimum $40\mu\text{s}$, and to the highest $120\mu\text{s}$.

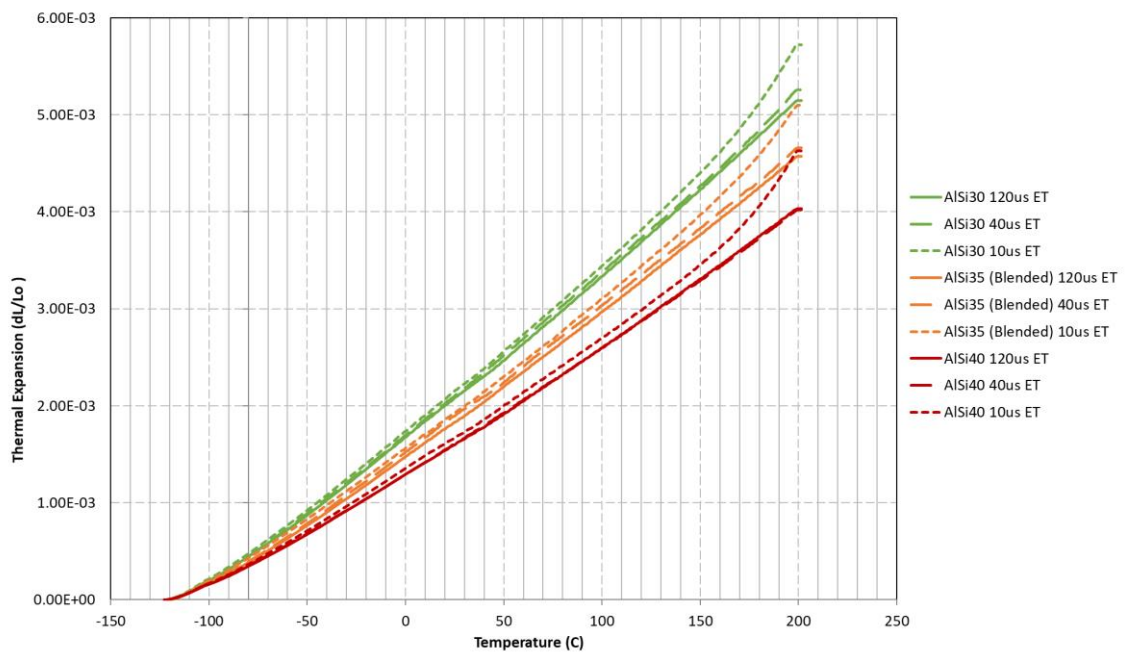


Figure 230. Thermal expansion for all AlSi LPBF printed materials, showing the effect of exposure time and silicon content.

It is observed that the AlSi35 blended alloy has obtained an expansion rate in-between AlSi30 and AlSi40 which is to be expected and confirms that the AlSi35 has been successfully manufactured and produces the desired thermal expansion. It is also seen that the $10\mu\text{s}$ ET has maintained a stabled temperature increase until approximately 150°C where the thermal expansion increases. To better visualise this, the co-efficient of thermal expansion is plotted in Figure 231.

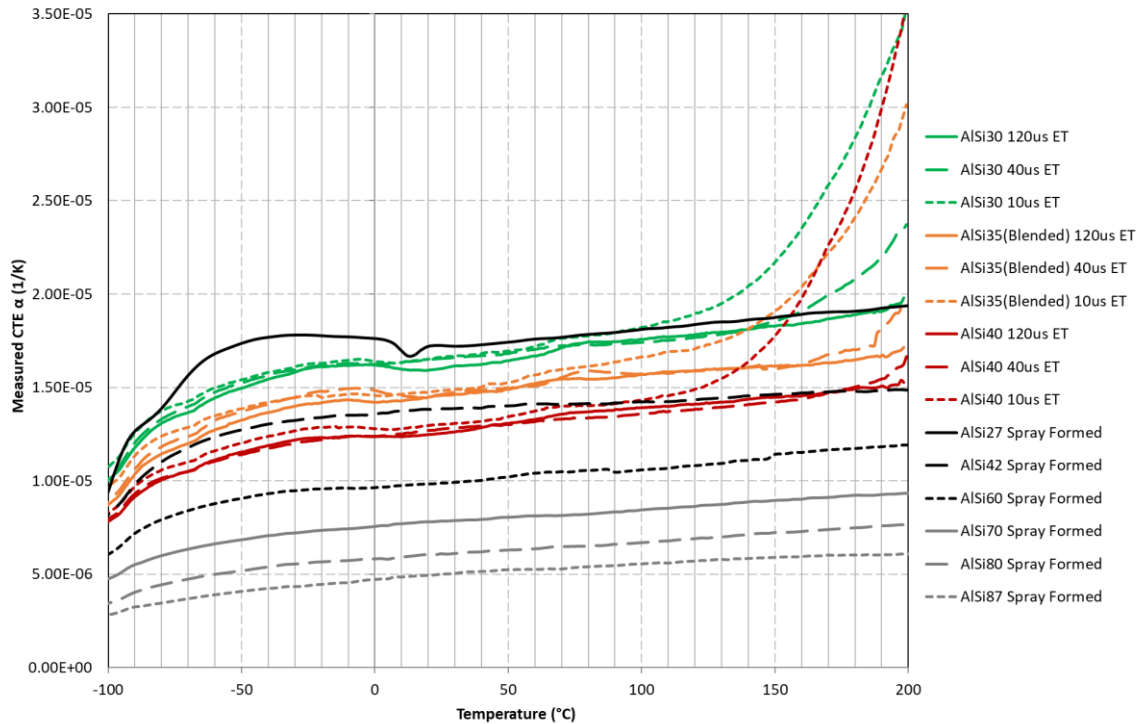


Figure 231. Physical alpha values for all AlSi LPBF printed materials, and spray formed materials.

The physical alpha values plotted in Figure 231 show a rapid increase in CTE for the 10µs ET samples, at approximately 110°C. This could be due to weak bonding between the Al and Si meaning the higher expansion aluminium becomes free to move within the matrix. It is observed that even at 40µs ET, an increase in expansion starts to occur at approximately 150-160°C depending on the alloy. This is not observed within the temperature range for 120µs ET. To further study the thermal stability of the AlSi LPBF samples, a higher temperature range would be needed. The testing range is adequate for the optical industry which specified a working temperature range of between -40 and +70°C. The spray formed alloys exhibit a similar CTE curve to that of the nearest equivalent LPBF alloy. For example, SF AlSi42 is very similar to LPBF AlSi40. The AlSi40 LPBF component has exhibited slightly less thermal expansion than its spray formed counterpart, even though the SF part has 2% more silicon. Table 55 provides the CTE values for all AlSi alloys at all exposure times and for all spray formed alloys over the working temperature range required by Qioptiq of -40 to 70°C.

Si wt.%	Process	Exposure Time (μs)	CTE ($\mu\text{m/m K}$)
30	LPBF	10	16.8
30	LPBF	40	16.6
30	LPBF	120	16.4
35	LPBF	10	15.1
35	LPBF	40	14.9
35	LPBF	120	14.6
40	LPBF	10	13.2
40	LPBF	40	12.7
40	LPBF	120	12.8
27	SF	-	17.8
42	SF	-	13.8
60	SF	-	9.95
70	SF	-	7.76
80	SF	-	6.10
87	SF	-	4.91

Table 55. Co-efficient of thermal expansion of the aluminium-silicon alloys averaged over -40 to 70°C.

Overall it is determined that the low CTE characteristics of high silicon aluminium alloys are realised with LPBF. It is shown that additional CTE tailoring can be achieved by blending two gas atomised powders of AlSi40 and AlSi30 to produce a blended AlSi35 and successfully print and measure a CTE value in-between both alloys. The optimum exposure time of 40 μs produces sufficiently stable thermal expansion from -120 to 150°C, in-line with that of their spray formed counterparts.

6.6.4 Discussion

The manufacture of AlSi30, AlSi35, and AlSi40 with LPBF has produced properties that are equal or better than those manufactured using the conventional spray forming method. It has been observed that the default laser parameter settings for AlSi10Mg provided by Renishaw the machine manufacturer, have provided close to optimal part densities of between 0.23 and 0.44% for alloys AlSi30-40. Kimura et al. achieved porosities of up to 0.5% for AlSi20, close to that achieved here [50]. The metallography shows that the Al and Si phases are much finer than that of spray formed parts. This also agrees with literature on LPBF that indicates most metallic material, including Al-Si alloys, processed with LPBF have a finer microstructure due to the high cooling rates [48], [50]–[53]. The finer microstructure leads to a higher hardness with most materials processed by LPBF, including Al-Si alloys [186], [188], [189]. The relationship between laser exposure time or laser scanning speeds on microstructure is related to the cooling rates, a faster scanning

speed will increase cooling rate, and therefore create a finer microstructure. The relationship between exposure times in Al-Si alloys, and microstructure has not been sufficiently studied in literature. The relationship presented here shows both Al and Si phase sizes increase, with increasing and decreasing exposure times past the considered optimal for the lowest porosity. A lower exposure time should increase cooling rate, and therefore reduce phase sizes, but here it is observed that the microstructure average sizes have increases from $10.1\mu\text{m}^2$ at the optimal ET of $40\mu\text{s}$ to $13.3\mu\text{m}^2$ at $30\mu\text{s}$ ET, and $18.5\mu\text{m}^2$ at $20\mu\text{s}$ ET. This could be due to insufficient melting. Conversely it is observed that at the higher exposure times of 80 and $120\mu\text{s}$, the average phase size increases to $23.1\mu\text{m}^2$ and $13.6.1\mu\text{m}^2$ respectively. This is due to a reduction in cooling rates. It is interesting to note that although the Si phase sizes have increased for 20 and $30\mu\text{s}$ ET compared to the optimal of $40\mu\text{s}$ ET, the median hardness values remain consistent and do not decrease. This is in contrast to literature that states that as microstructure size increases, hardness decreases [180], [181], [193], [194]. Increasing the exposure time for AlSi30 above $40\mu\text{s}$ to 80 and $120\mu\text{s}$, shows an agreement with this literature with a reduction in hardness from 180HV_2 , to 146 , and 118HV_2 respectively. Comparing the hardness between spray formed and LPBF also shows agreement with the literature. Spray forming with AlSi40-42 produced average Si phase areas of $56.7\mu\text{m}^2$ and hardness 97HV_2 , compared to $10.2\mu\text{m}^2$ and a hardness of 217HV_2 for LPBF.

The thermal expansion for all AlSi30-40 printed by LPBF are within the expected range for the silicon content they contain. The physical alpha is at its most stable between -50 to 100°C , so this range will be used for comparing the technical alpha values. Over this temperature range, and at the optimum laser parameters, AlSi40 has the highest CTE at $12.7\mu\text{m}/\text{mK}$, lower than the SF AlSi42 which had $13.8\mu\text{m}/\text{mK}$. This agrees with most literature that shows lower thermal expansion in LPBF components, which is mainly attributed to residual stresses present in LPBF that are not present in conventional methods of manufacture [151], [157], [162], [163]. The AlSi35 blended composition has a CTE of $14.9\mu\text{m}/\text{mK}$, and AlSi30 has a CTE of $16.6\mu\text{m}/\text{mK}$. AlSi35 obtaining a CTE approximately halfway between AlSi30 and 40 shows that the alloy can be tailored by blending pre-alloyed powders to obtain a CTE required. All three alloys manufactured with a $10\mu\text{s}$ exposure time, and 31.3 - 36.6% porosity, experience a rapid increase in thermal expansion above 150°C . This is could be attributed to insufficient melting and weak bonds between the Al and Si phases, which would allow the continuous phase Al to expand around the Si.

6.6.5 Conclusions on Al-Si alloys

The manufacture of high silicon Al-Si alloys has been successful with no cracks immediately visible across all exposure times, for AlSi30, AlSi35 (blended) and AlSi40.

To conclude;

- Printing in AlSi30, 35, and 40 can produce close to full densification with porosities between 0.23-0.44%, an improvement compared to conventional spray forming with porosities between 0.35 – 1.21%
- Printing in AlSi30-40 in LPBF creates a finer, but less homogenous microstructure compared to spray forming.
- The finer microstructure in LPBF increases hardness compared to spray forming by about double, from 97 to 218 HV2 for AlSi40-42 components.
- The low thermal expansion property of AlSi30-40 printed by LPBF is fully realised, and slightly lower than the conventionally manufactured spray formed components.
- Al-Si 30 and 40 powder can be blended to obtain an alloy with a silicon content between 30 and 40%. The new blended alloy has a CTE in between both, at the targeted ratio. The blended alloy features the same thermal expansion stability as its pre-blended constituents.
- The hardness of the AlSi30&40 blended powder components are more susceptible to the laser processing parameters, and requires the optimum laser parameters to achieve expected hardness. Variation outside optimum parameters lowers hardness nearer to the blended alloy that features the lowest hardness. The densities are as expected, and in-line with AlSi30 and AlSi40.

6.7 Conclusions on thermal expansion control with metal AM using alloy selection

This chapter has shown that the thermal expansion of parts produced by metal base AM, using LPBF can be tailored by adjusting the alloys elemental constituents. To the best of the authors knowledge this is the first time that a pre-alloyed invar powder has been blended with additions of iron and nickel powder and manufactured using LPBF. It is also believed to be the first time that two aluminium-silicon pre-alloyed powders have been blended together and manufactured using LPBF.

Chapter 6.5 conducted a study where the adjustment of the nickel content of FeNi36 was attempted by means of blending the FeNi36 powder with iron or nickel powder to adjust the overall nickel content in the alloy. Increasing the nickel content above 36wt.% increases the thermal expansion of the alloy and opening up opportunities for thermal

expansion tailoring depending on the nickel content. The blended material is manufactured using laser powder bed fusion and the parts produced are characterised.

The study was conducted by blending ± 1 , and 2wt.% of iron and nickel in fine carbonyl form with a particle size diameter of between 3 and 7 μm into an FeNi36 gas-atomised powder. The blended powder was manufactured using laser powder bed fusion and the manufactured parts were determined to have fully alloyed and shown to provide the expected adjustment in thermal expansion considering its nickel content. This is useful in the optical industry because the gas atomised invar has been shown to be as much as ± 1 wt.% nickel away from the intended target. Adding 7wt.% of nickel has shown to increase coefficient of thermal expansion to 8.35 $\mu\text{m}/\text{mK}$. The wide range of tailorability from 0.68 to 6.35 $\mu\text{m}/\text{mK}$ provides opportunities to match the coefficient of thermal expansion of the FeNi alloy with that of glass or germanium (6-7 $\mu\text{m}/\text{mK}$). The blended powders produce fully dense parts and a homogenous distribution of iron and nickel within the alloy. The mechanical testing shows that the additions have little effect, achieving only ± 9 MPa deviation in UTS, and ± 1 HV2 deviation in vickers hardness. Increasing the volumetric laser energy density by up to five times optimal has shown to increase thermal expansion by 0.32 $\mu\text{m}/\text{mK}$ in invar. This is a relatively small amount and is not a practical way of adjusting thermal expansion because it creates porosity.

Chapter 6.6 conducts a study into the processability of AlSi30 and AlSi40 pre-alloyed gas atomised powders using laser powder bed fusion. Both powders have parts manufactured with the LPBF process separately, but also blended together in equal proportions to make a blended powder and component with an overall silicon content of 35wt.%. The components made undergone density measurements and determined that they were of a higher density than parts made using the conventional method of spray forming. The microstructure was finer which produced an increase hardness for alloys AlSi40-42 from 97HV2 in the spray formed parts to 218HV2 in the LPBF parts. No macro cracking was observed on the printed parts, which is a concern due to the high silicon content. The blended AlSi35 powder experienced a thermal expansion halfway between AlSi40 (12.7 $\mu\text{m}/\text{mK}$) and AlSi30 (16.6 $\mu\text{m}/\text{mK}$) at a value of 14.9 $\mu\text{m}/\text{mK}$ which was as expected. All the components printed had a high densification of between 99.56 and 99.77% compared to the spray formed parts which had a lower densification of between 97.79 and 99.65%. The ability to tune the thermal expansion of an aluminium alloy is useful because aluminium is very lightweight is used extensively in optical systems. The conventional method of spray forming requires the alloy to be manufactured and machined by the company Sandvik-Osprey. This could be expensive for companies such as Qioptiq that already have their own machining facilities and do not require it to be outsourced. The ability to manufacture high silicon aluminium alloys using laser powder

bed fusion means the manufacturing can be done in-house, saving cost. The capital investment of a large 60Kg batch of pre-alloyed aluminium-silicon powder could be more appealing if it is understood that it can be blended with future batches to achieve a tailored silicon content. This is also true for iron-nickel alloys, where the large capital investment of a batch of pre-alloyed invar powder can be re-purposed with the addition of some iron or nickel powder.

7 Thermal Expansion Control in Plastic AM

7.1 Summary

This chapter explores the ability to control thermal expansion using a multi-material plastic FDM printer. It provides a method of tailoring a plastic material feedstock CTE from $98\mu\text{m}/\text{mK}$ down to $18.6\mu\text{m}/\text{mK}$. Several multi-material combinations are graded within a component to provide a thermal expansion change.

7.2 Introduction

Plastics have a higher co-efficient of thermal expansion than metals. Metals can have a CTE of between $1\text{-}24\mu\text{m}/\text{mK}$, while plastics can range between $50\text{-}110\mu\text{m}/\text{mK}$. This can make them very difficult to use in the optical industry for housing glass or germanium lenses with CTE's of between $6\text{-}7\mu\text{m}/\text{mK}$. This chapter will understand the thermal expansion behaviour of plastics printed using the FDM process. It will investigate the effect on the thermal expansion when adding different types of particles and fibres into the plastics. These particles or fibres can restrict the thermal expansion of the material, lowering the overall CTE. They can also improve the stability of the thermal expansion over a range of temperatures. Multi-material FDM printing will also be investigated, where two different types of plastics are printed together, and their combined thermal expansion is measured. This can provide engineers with a method of tailoring thermal expansion at the design level, instead of at the material feedstock.

7.3 Plastic feedstock material

There is an extensive range of plastics available that can be printed with FDM techniques. The most common materials include; PLA, ABS, PETG, and Nylon. Others include PEEK, PEKK, PC, PET, and ULTEM, which are more difficult to process, but possess a higher performance [195]. This chapter will look at the industry leading materials provided by the company Ultimaker. The thermal expansion will be measured using cryogenic dilatometry on 3D printed samples of PLA, CPE (PETG), CPE+ (PETG), ABS, and Nylon. An assessment will be made to determine and quantify the effect of build orientation on thermal expansion of the printed components.

Table 56. Plastic mechanical data as printed from Ultimaker technical data sheets.

Material	Tensile modulus MPa	Tensile stress at yield MPa	Tensile stress at break MPa	Elongation at yield %	Elongation at break %	Flexural strength MPa	Flexural modulus MPa	Izod impact strength, notched kJ/m^3	Hardness Shore D
	ISO 527 (1 mm/min)	ISO 527 (50 mm/min)			ISO 178		ISO 180	Durometer	
Poly-lactic Acid (PLA)	1820	37	37	3.1	3.1	78	2490	9	79
Acrylonitrile Butadiene Styrene (ABS)	1618	39	33.9	3.5	4.8	70.5	2070	10.5	76
Copolyester (CPE)	1537	41.1	37.7	4.7	5.1	79.5	1990	4	72
Copolyester (CPE+)	1128	35.2	33	6	6.6	65	1555	6.2	75
Nylon	579	27.8	34.4	20	210	24	463.5	34	74

Table 57. Plastic thermal data from Ultimaker technical data sheets

Material	Melt mass-flow rate	Heat detection (at 0.455 MPa)	Heat deflection (at 1.82 MPa)	Vicat softening temperature	Glass transition temperature T_g	CTE (mm/mm °C)	Melting temperature	Specific gravity
	ISO 1133	ASTM D648	ASTM D648	ISO 306			ISO 11357	ISO 1183
Poly-lactic Acid (PLA)	6-7 g/10 min	-	-	63 °C	62 °C	-	151 °C	1.22
Acrylonitrile Butadiene Styrene (ABS)	41 g/10 min	-	-	97 °C	-	-	225 - 245 °C	1.24
Copolyester (CPE)	13 g/10 min	70 °C	62 °C	-	82 °C	$7 \cdot 10^{-5}$	Not relevant (amorphous)	1.27
Copolyester (CPE+)	8.5 g/10 min	94 °C	81 °C	-	-	-	Not relevant (amorphous)	1.18
Nylon	6.2 g/10 min	-	-	-	50 °C	-	185 - 195 °C	1.14

7.3.1 Manufacture

Manufacture of the materials provided by Ultimaker has been completed on their own machine the Ultimaker 3. A single 0.4mm diameter nozzle has been used to print the materials. The build software used was Cura V3.3.1 using default material and build parameters. The samples were printed with 100% infill with a raster pattern of 45° by default. A range of plastics have been tested including the most common grade FDM materials such as PLA and ABS, and other materials such as Nylon and the co-polyester (CPE, CPE+) groups, which are more commonly known as PETG (Polyethylene terephthalate glycol). The CPE+ co-polyester is advertised to have a higher temperature resistance and improved mechanical properties over CPE. The materials PLA and PETG will have additions such as carbon fibre and metal particles added to them in chapters 7.4 and 8, so its important to get a baseline coefficient of thermal expansion first. A dilatometer sample is required by ASTM E831 standards to be 5mm diameter and 25mm in length. For this experiment the samples will be made to be square with dimensions of 5x5x25mm. This ensures that there is minimum manufacturing variability due to the influence of support structures and build orientation.

Figure 232 shows an image from the Cura build software that shows the final top slice of both vertical and horizontal build orientations.

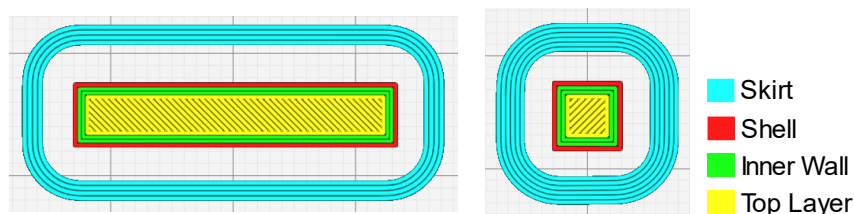


Figure 232. Image from the Cura build software showing the extrusion paths for a horizontal sample (left) and a vertical sample (right).

Table 58 shows the default material profile parameters specified by Cura for use with Ultimakers own 2.85mm filament.

Cura material profile	Nozzle temp. °C	Plate temp. °C	Print speed mm/s	Wall thickness mm	Top/bottom thickness mm	Top/bottom number of layers	Cooling fan %
PLA	200	60	70	1	1	12	100
ABS	230	80	55	1.3	1.2	12	5
Nylon	245	60	70	1.3	1.2	12	40
CPE	240	70	55	1.3	1.2	12	50
CPE+	265	107	40	1.3	1.2	12	1

Table 58. Cura default material profile parameters for a 0.1mm layer thickness.

7.3.2 Thermal Expansion

To measure the coefficient of thermal expansion, two horizontal and two vertical dilatometer rods measuring 5x5x25mm in dimension were printed. The manufacturing and testing is completed in accordance with ASTM E831. The equipment used was a NETZSCH 401 Cryogenic dilatometer has been used to measure over the range of -110°C to +90°C. The temperature program starts with an isothermal for 15 minutes at -110°C, before increasing the temperature by 5°C/min. The temperature range adequately captures the -40°C to +70°C range outlined by Qioptiq. Figure 233 to Figure 237 show the CTE curves for each material printed vertically and horizontally with two repeats of each, and a linear CTE value calculated from the stable range.

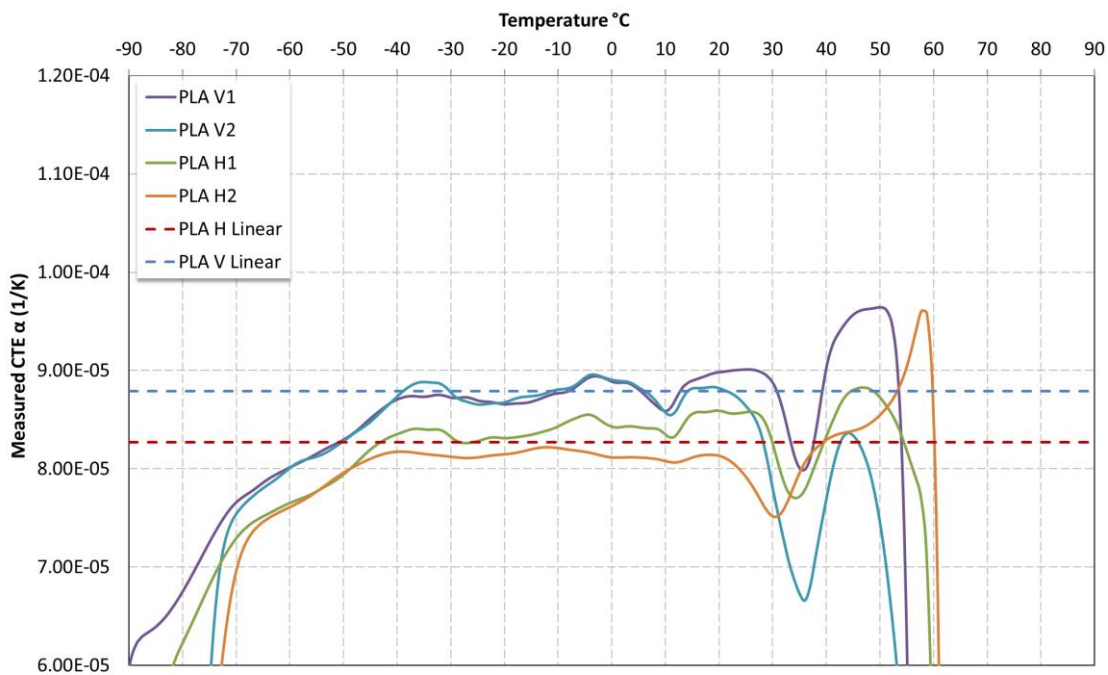


Figure 233. PLA dilatometer results showing CTE and averaged linear expansion rates.

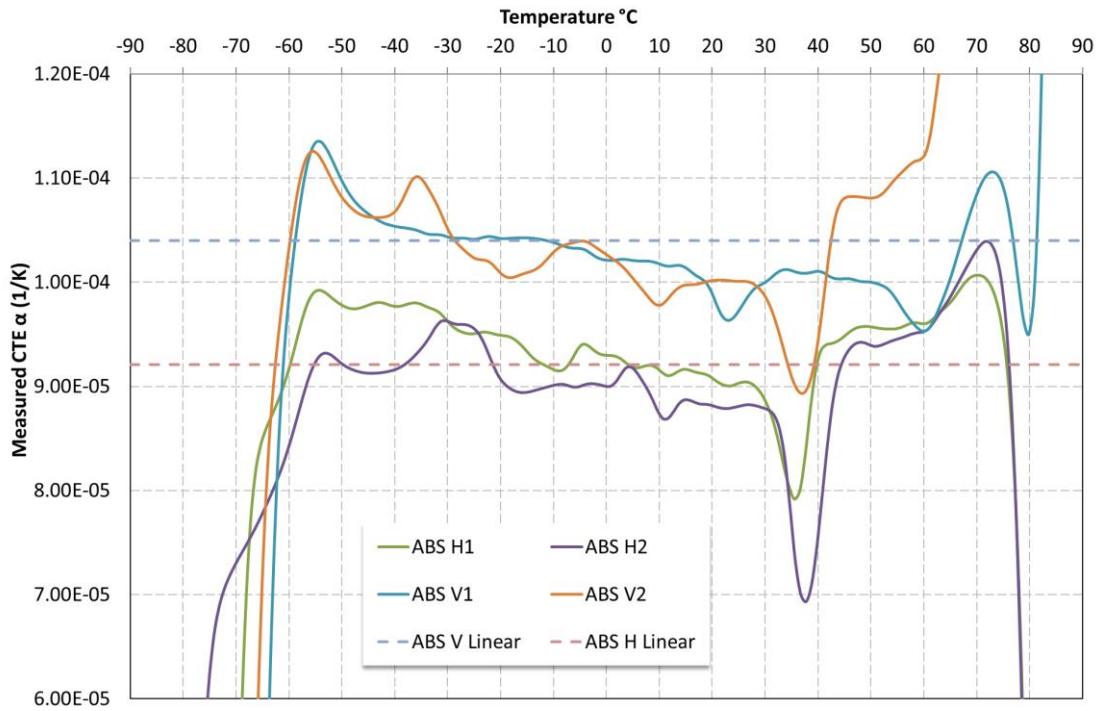


Figure 234. ABS dilatometer results showing CTE and averaged linear expansion rates.

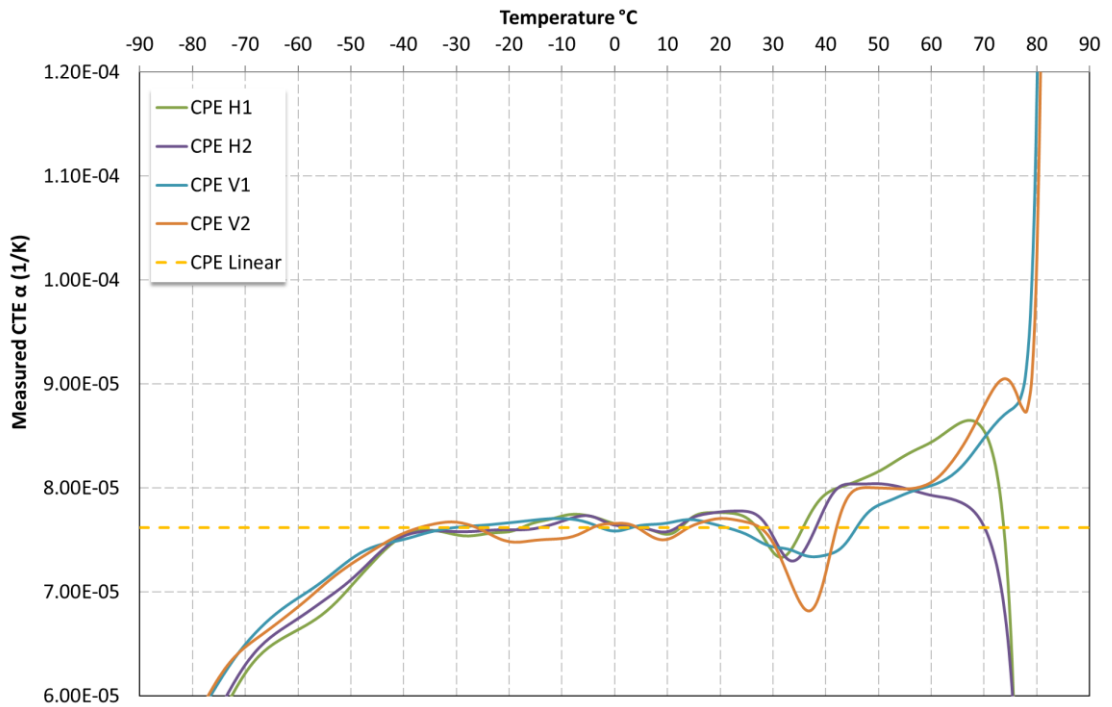


Figure 235. CPE dilatometer results showing CTE and averaged linear expansion rates.

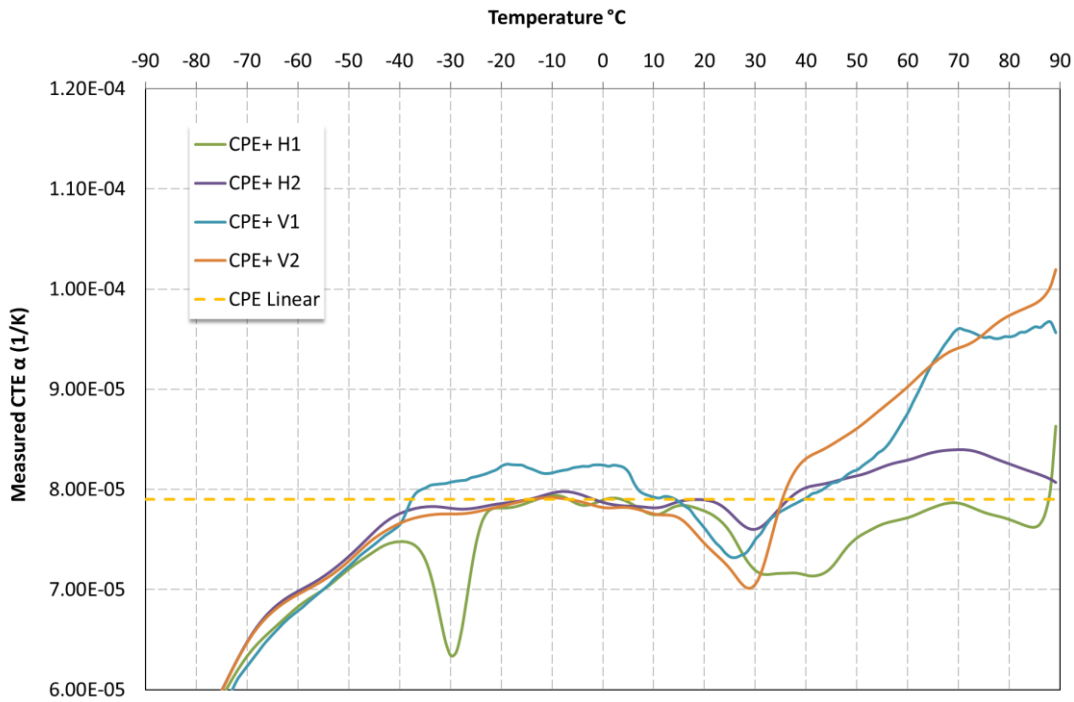


Figure 236. CPE+ dilatometer results showing CTE and averaged linear expansion rates.

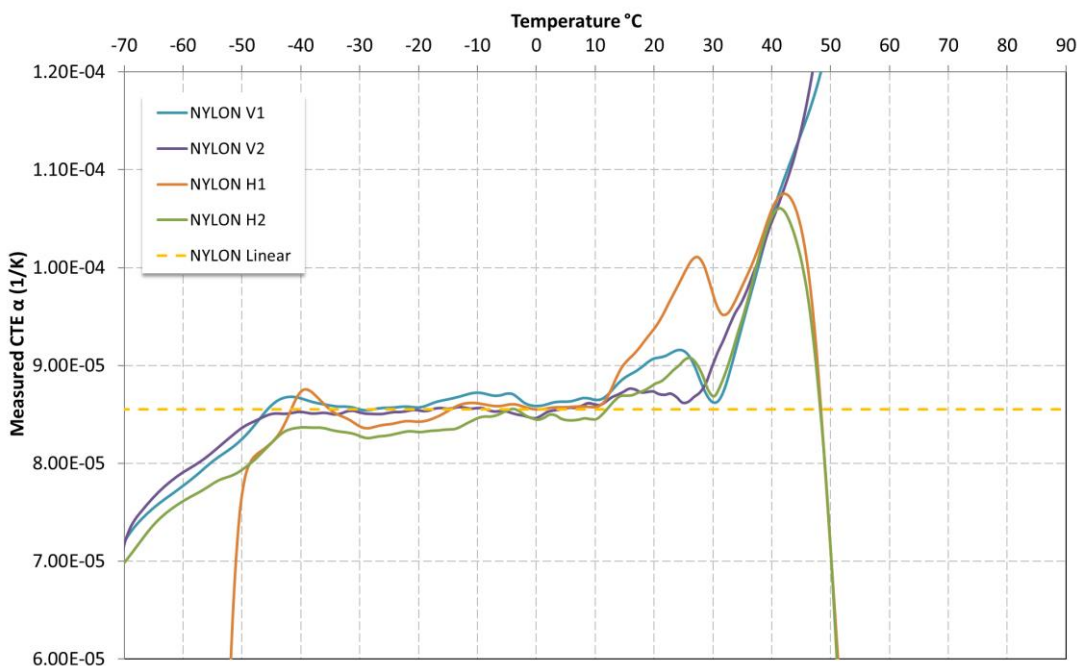


Figure 237. Nylon dilatometer results showing CTE and averaged linear expansion rates.

The coefficient of thermal expansion curves plotted in Figure 233 to Figure 237 show a similar linear zone roughly positioned between -40°C and $+50^{\circ}\text{C}$. In this zone the average CTE has been taken for the horizontal and vertical samples and plotted. For plastics such as nylon and CPE, a single average is taken since there are no differences between the two build directions. It is also observed that for materials ABS, CPE, and Nylon, all

experience a different failure mechanism at the point of softening. The horizontally printed parts contract, while the vertically printed parts expand. For PLA both build orientation contract at the point of softening. For CPE+ there is more expansion in the vertically printed samples at the point of softening, but both directions avoid material failure up to 90°C. The CTE data has been tabulated in Table 59 and compared to its CTE in plastic injection moulded parts.

Material	Temp. range °C	Average Vertical CTE (µm/mK)	Average Horizontal CTE (µm/mK)	Average CTE (µm/mK)	Dilatometer yield temp. (°C)	Glass transition temp. (T_g °C) ¹⁴	Injection moulded CTE (µm/mK) ¹⁵
PLA	-40 to 20	87.9	82.7	85.3	~45	62	85
ABS	-40 to 20	104	92.1	98.05	-55	90-102	72-108
CPE	-40 to 20	76.2	76.2	76.2	~65	82	70
CPE+	-40 to 20	79	79	79	-	82	-
Nylon	-40 to 20	85.5	85.5	85.5	~30-40	50	50-90

Table 59. Dilatometer results for thermal expansion of FDM plastics.

7.3.3 Discussion on plastic feedstock material

It is observed that the range between -40°C and +50°C is where the results the most linear and stable. In this range ABS has the greatest difference between vertical and horizontal samples. ABS is widely known to have a large residual stress after cooling, resulting in warping and cracking of large parts [196], [197]. The shrinkage factor of ABS could have played a part in the differences observed between the CTE in horizontal and vertical samples. The change in raster orientation for horizontal and vertical samples has resulted in a change in distribution of internal forces as the sample is heated. It is also observed for ABS, CPE, CPE+, and Nylon; the horizontally built samples became shorter in length as the glass transition temperature (T_g) of the plastic is reached, whilst the vertically built samples increased in length. It is observed that the T_g is always much higher than the point as yield temperature, suggesting that the crystalline structure is highly amorphous. This is observed that nylon, CPE, and ABS, both build directions show a large decrease in CTE for horizontally built samples as T_g is approached, and an increase in CTE for vertically built samples as T_g is approached. This is due to the length of each deposited track shrinking, causing each sample to contract across the layer. The horizontally built sample features longer tracks and fewer layers which will cause it to shrink in length, whilst the vertically built sample will contract in diameter and increase its length.

¹⁴ Ultimaker material specification sheets

¹⁵ https://www.engineeringtoolbox.com/linear-expansion-coefficients-d_95.html

For the optimum choice of materials, CPE has the lowest CTE whilst ABS have the highest. This combination of materials would be best for a multi-material configuration because the objective is to find the largest ratio between the two materials. A higher ratio allows for greater tune-ability of structures such as those by Steeves et al. [2], [3], [10].

7.3.4 Conclusion on plastic feedstock material

To conclude this chapter, the observations made testing the thermal expansion of Ultimakers common FDM plastics shows us the following;

- The plastic featuring the highest CTE is ABS at 104 to 91.4 $\mu\text{m}/\text{mK}$, while the lowest thermal expansion is CPE (PETG) at 76 $\mu\text{m}/\text{mK}$.
- PLA and ABS have a lower CTE in horizontally printed samples, compared to vertically printed ones. PLA is 5.92% lower, and ABS is 11.44% lower. All other materials experience no significant change depending on build orientation.
- At the glass transition temperature of ABS, CPE, CPE+, and Nylon, the horizontally printed samples contract across the length of the sample, while the vertically printed samples expand. For PLA both print orientations contract across the length of the sample.
- The target CTE of 60 $\mu\text{m}/\text{mK}$ to match a ZEONEX[®] lens is not achieved with any of the polymers, which all have a higher thermal expansion.

7.4 Controlled thermal expansion plastic feedstock

Many studies have been conducted analysing the manufacturability, tensile, and hardness performance of the 3D printed components with many different types of inclusions added into the plastic feedstock [18], [150], [206]–[208], [198]–[205]. The inclusions are added into the plastic filament by the manufacturer and can be printed on a typical FDM printer setup.

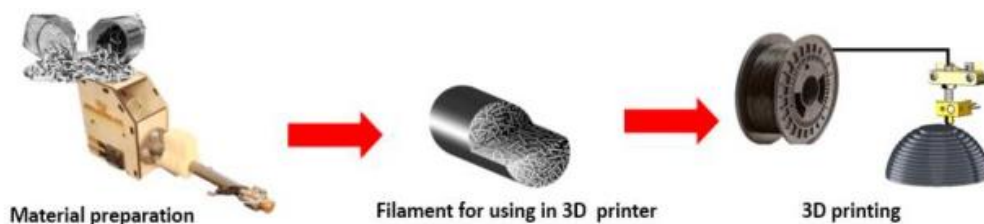


Figure 238. Image showing process for plastic impregnation with inclusions.

Poly-Lactic Acid (PLA) is the most common 3D printed material due to its ease of processability, high print quality, and low residual stresses. Reinforcements of PLA ranging from synthetic fibres, metals, and ceramics, have been shown to be manufacturable with increased mechanical performance [18], [150], [198]–[205].

Polyethylene Terephthalate-Glycol (PETG) is the newest material onto the scene, seeing a rapid adoption amongst companies utilising 3D printing due to its similar characteristics to ABS but with less residual stresses. It is the second most common material on the market featuring inclusions, after PLA. Most of the commercially available PETG filaments to feature inclusions, have carbon or glass fibres in due to the plastics use as a structural material. Only a few studies have examined the mechanical performance of 3D printed PETG, and a smaller number have studied the effect of adding inclusions into the plastic [206]–[208]. Studies into the thermal expansion characteristics of PLA and PETG are difficult to find. This is most likely due to the requirement for cryogenic test equipment because most plastics soften at low temperatures.

This chapter will investigate the thermal expansion properties of PLA and PETG with many different types of commercially available inclusions. These inclusions should restrict the thermal expansion properties of the plastic by different amounts depending on the type of inclusion, the quantity of the inclusion, and the bond between the plastic and the inclusion.

The plastic with the largest assortment of commercially available inclusions is PLA, from metallic alloy powders such as brass and bronze, to natural fibres such as wood. These filaments are mostly used to aesthetic purposes, to provide 3D printed parts with an appearance similar to that of its inclusion after polishing. Other inclusions such as glass and carbon fibres are included in PLA to improve its mechanical strength and performance. It is more common to see glass and carbon fibres included in PETG over PLA, due to the improved mechanical performance of PETG. A summary of the features for each filament is presented in Table 60.

Plastic	Inclusion	Manufacturer	Features
PLA	-	Ultimaker®	Standard PLA, material parameters tuned by Ultimaker for optimal performance on their own machines.
PLA	Iron	Proto-Pasta	Aesthetics, fine iron powder, magnetic, not conductive, can provide rust appearance, weaker than PLA.
PLA	Bronze	Filaprint®	Aesthetics, 80% bronze content, metal feed & touch, 3x heavier than PLA, can be polished, weaker than PLA.
PLA	Glass Fibre	3D Fuel®	1.4x stronger than PLA(UTS 57Mpa), 1.9x more flexible (Tensile Elongation 3.4%)
PLA	Brass	Filaprint®	Aesthetics, 70% bronze content, metal feed & touch, 2.2x heavier than PLA, can be polished, weaker than PLA.
PLA	Wood	Filaprint®	Aesthetics, can be polished, weaker than PLA.
PLA	Carbon Fibre	Proto-Pasta	Stronger than PLA, as easy to print as standard PLA.
CPE (PETG)	-	Ultimaker®	CPE (PETG), material parameters tuned by Ultimaker for optimal performance on their own machines.
PETG	Carbon Fibre	CarbonP	20% carbon fibre, 2x stiffness over PETG. E-modulus 3800Mpa, Density 1.19g/cc
PETG	Carbon Fibre	3DXTech® CarbonX™	2.6x stiffness over PETG, E-modulus 4928Mpa, Density 1.34g/cc

Table 60. Plastics with inclusions and their claimed features.

To get a qualitative understanding of these materials an image has been taken of each 2.85mm diameter filament with the Ziess Smartzoom 5 and presented in Figure 239.



Figure 239. Image of 2.85mm diameter filaments used to manufacture dilatometer rods using Ultimaker 3.

7.4.1 Manufacture

To manufacture the filaments with inclusions, the Ultimaker 3 was used. The standard AA 0.4mm diameter print core included with the Ultimaker was switched with one from Solex3D, designed to have swappable hardened steel and ruby tipped nozzles. This is a requirement when printing inclusions which can wear away at the nozzles. In the Ultimaker 3 it is impossible to replace the nozzle without replacing the entire print core, so it is a necessity to purchase a 3rd party print core that features changeable nozzles. The print parameters will be kept the same as the Ultimaker default for the plastic, which are found in Table 60. This ensures consistency across all materials. The samples will be the same dimensions as before, at 5x5x25mm. The build orientation will be horizontal only because the outcome of the experiment is to determine differences between inclusions rather than build orientation.

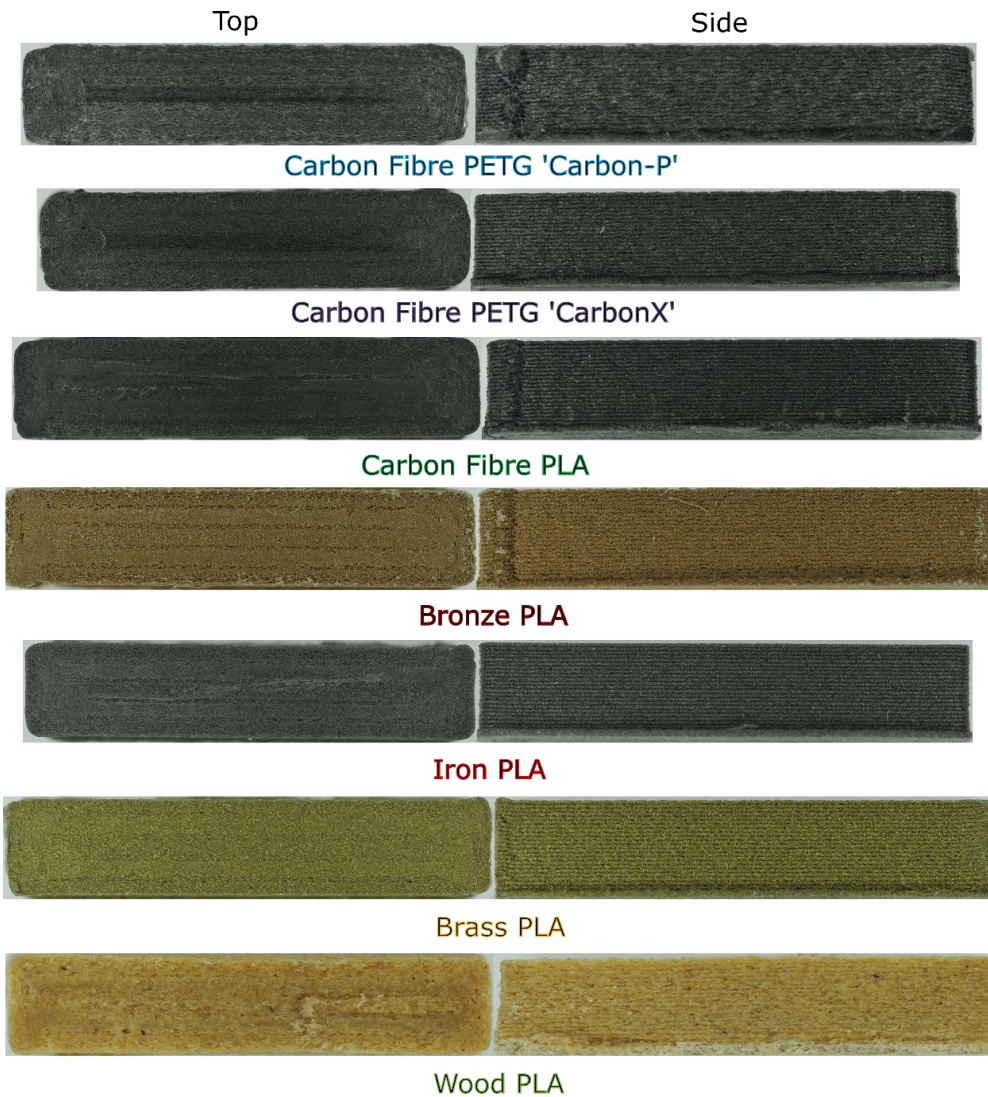
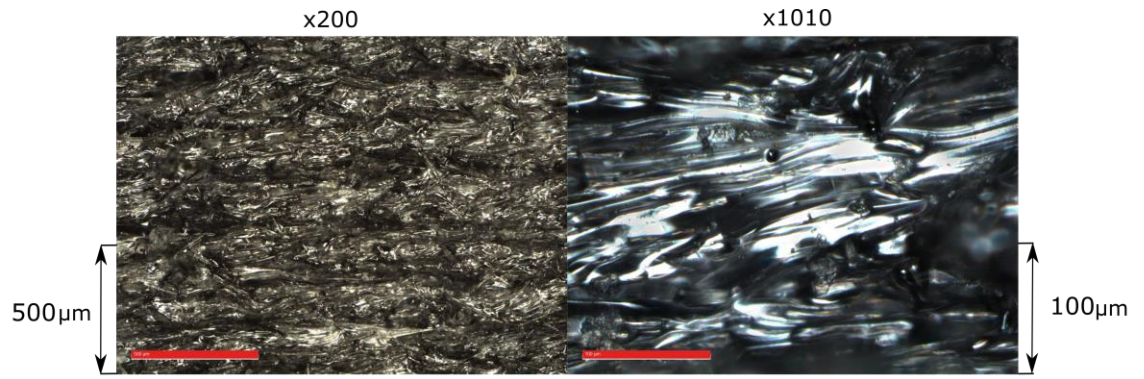
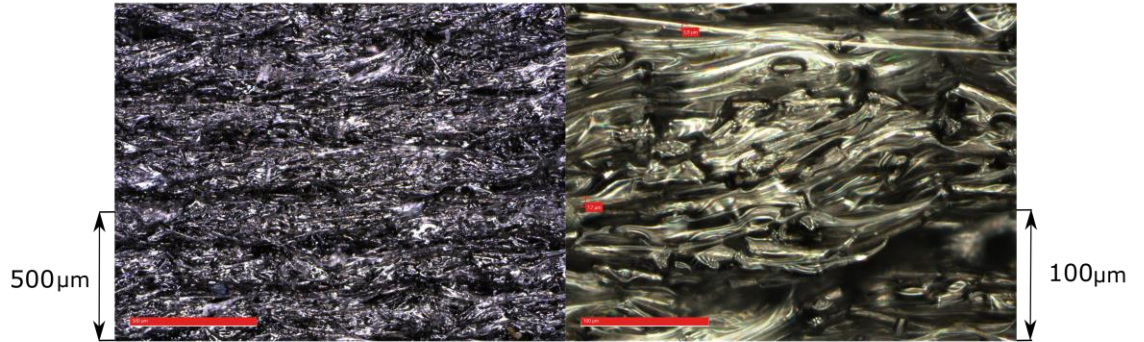


Figure 240. Optical images taken with a DSLR camera of the horizontally printed samples, from the top (left) and side (right).

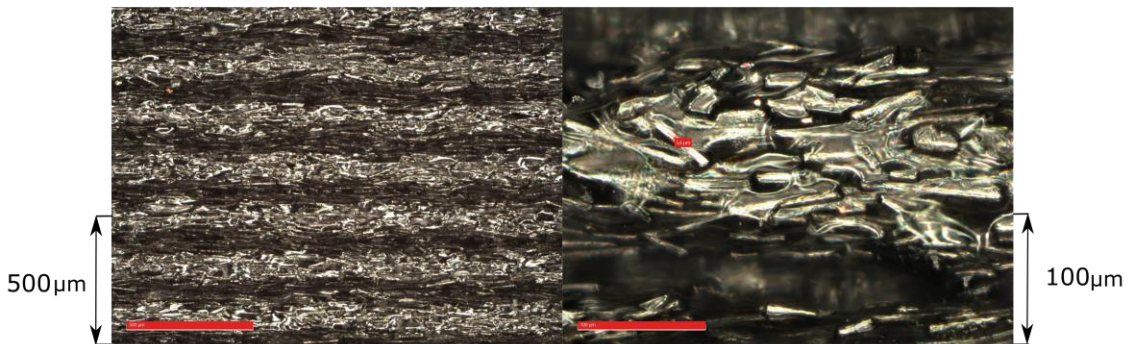
To determine the orientation of the fibres, and the size and distribution of the particles, white light optical microscopy has been used to observe the side of a printed sample. Each sample has been looked at under 200x and 1010x using the Zeiss Smartzoom 5.



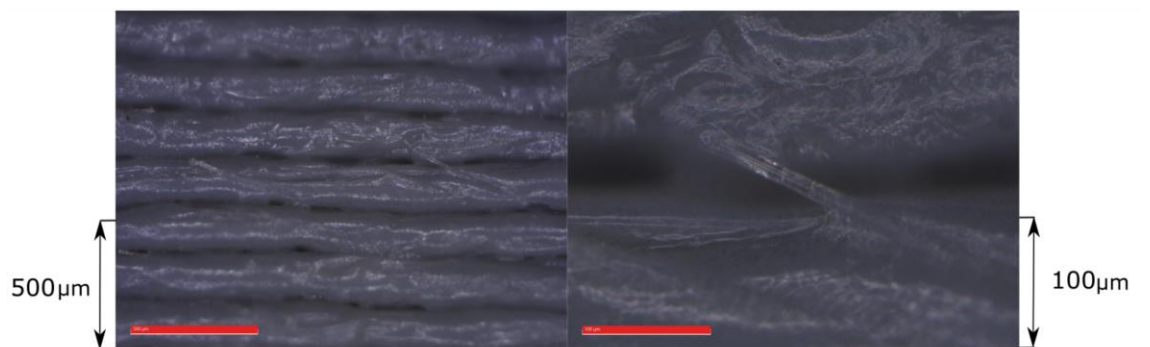
Carbon Fibre PETG 'Carbon-P'



Carbon Fibre PETG 'CarbonX'



Carbon Fibre PLA



Glass Fibre PLA

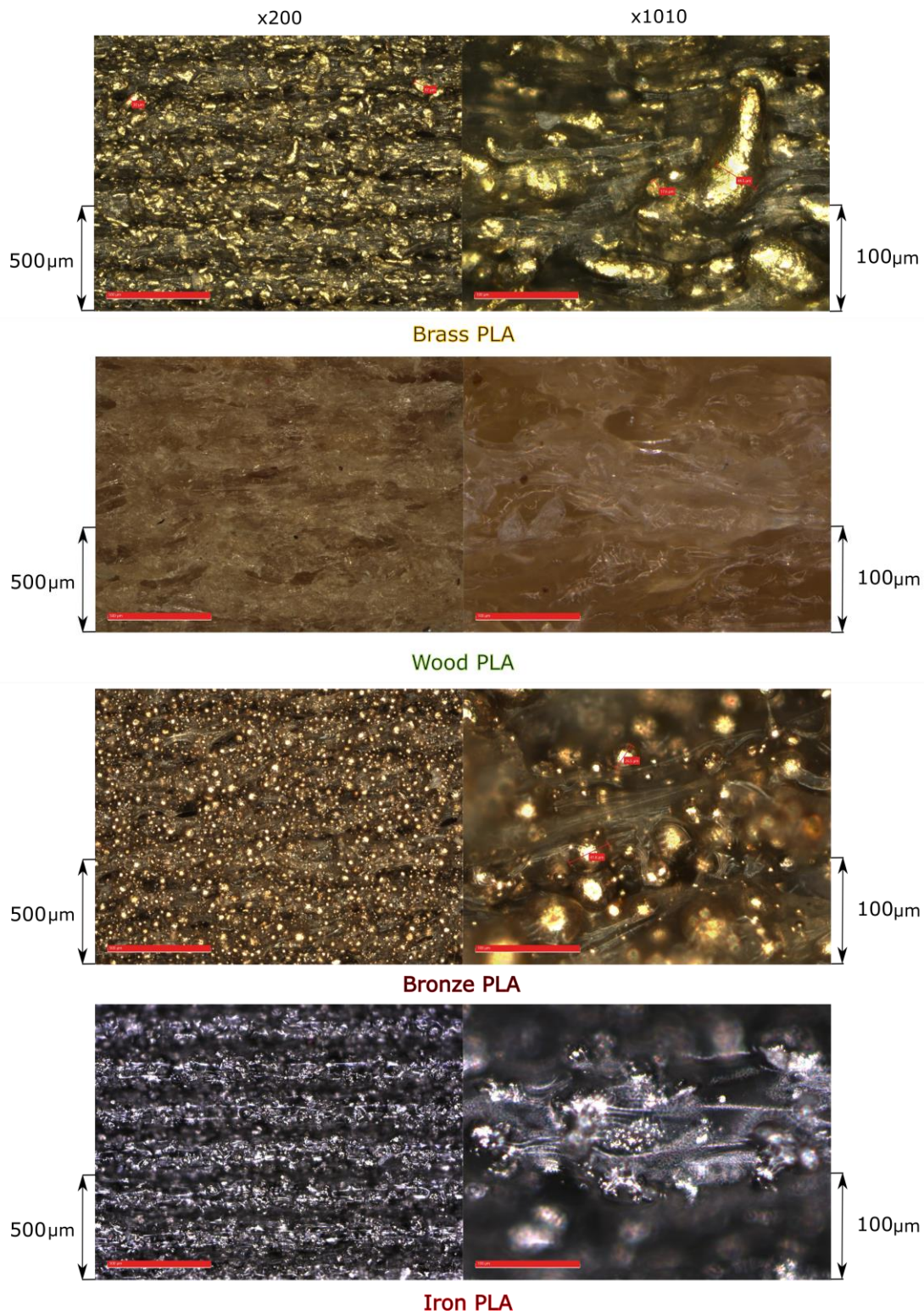


Figure 241. Optical microscopy images of the side of a printed 7x7x25mm sample showing the layers and inclusions at x1010 and x200

Material	Inclusion Dimension
PLA	-
PLA Iron	18 – 45µm Spherical, lots of smaller satellite particles attached
PLA Bronze	16-66µm, large volume of finer particles
PLA Glass Fibre	~15µm diameter glass fibres, 400-550µm in length
PLA Brass	17.6 - 120µm Non-spherical
PLA Wood	12-14µm diameter wood fibres
PLA Carbon Fibre	5.5-7.5µm diameter carbon fibres, 90-110µm in length
CPE (PETG)	-
PETG Carbon Fibre 'CarbonP'	4.1-8.4µm diameter carbon fibres, 180-330µm in length
PETG Carbon Fibre 'CarbonX'	5-11µm diameter carbon fibres, 155-290µm in length

Table 61. Filament inclusion measurements from optical microscopy.

Studying the dimensional variance of metal powder inclusions, iron and bronze and spherical, whilst brass too irregular to be called spherical. The method of manufacture of the powders is not stated by the filament producer, but the particles appear to have a smooth surface and would suggest gas atomisation. Iron appears to have a higher distribution of small particles but has a similar minimum and maximum diameter as bronze. The irregular shaped brass particles vary from 2-3 times the maximum of either iron or bronze. The carbon-fibres appear to have a similar diameter to each other but possess a difference in observed length. Longer filaments should create orientation of the fibres towards the print direction, while shorter fibres would promote better mixing with the layer below. It is observed that the PETG carbon fibre filaments have roughly the same length, while the PLA has slightly shorter lengths. The PLA with glass fibre has much longer fibres with the longest measured being 550µm, but the fibres could be longer and obscured by encapsulation inside the PLA. The observed layers have almost no cross-over of fibres with the lower layers. This suggests the glass-fibre PLA to be more oriented to the raster orientation across the XY axis than the Z axis.

7.4.2 Thermal Expansion

To test the thermal expansion, the same dilatometer test program was used as in the previous plastics chapter 7.3. The temperature range is across -110°C to 90°C , starting from an isothermal hold at -110°C for 15 minutes, and increasing to 90°C at $5^{\circ}\text{C}/\text{min}$. This test program conforms with ASTM E831.

Studying the co-efficient of thermal expansion plots in Figure 242, there are several inclusions which are superior at lowering the overall thermal expansion, and several that perform better at maintaining a stable thermal expansion curve across the temperature range. Looking at the effect of inclusions in PLA, there is a wide range of variance from a 22.8% reduction with iron inclusions, down to a 54.6% reduction with carbon fibre. It is observed that the iron inclusions have provided a similar drop in CTE compared to that of bronze and brass inclusions. Iron inclusions have a significant advantage in the stability of the rate of thermal expansion compared to bronze and brass. The variance across the CTE curve is much less. It is observed that for the remaining inclusions; glass fibre, carbon fibre, and wood, wood provides the least stability, while carbon and glass fibres remain similar, with glass performing better. It is observed that for temperatures higher than -10°C the wood and carbon fibre samples become unstable with fluctuations in the CTE. The two PETG carbon fibres tested from different manufactures have a similar CTE between $18.6 - 19.5\mu\text{m}/\text{mK}$, presenting a 74.9 - 76.1% reduction compared to matrix material alone. This is the highest percentage reduction in CTE, which can be attributed to a better cohesion between matrix and inclusion, demonstrated by the increased stability of the material.

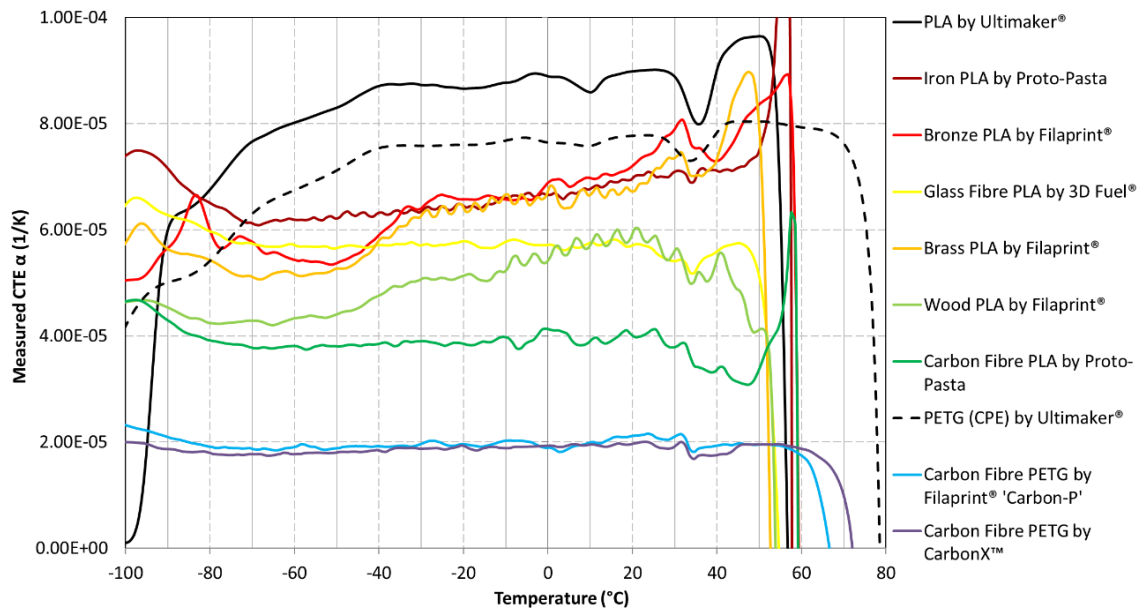


Figure 242. CTE curves for a PLA and PETG with a range of inclusions. Printed on the Ultimaker 3 with Cura's predefined PLA and PETG material parameters. 3rd party Solex3D heating core and hardened steel nozzle used.

The co-efficient of thermal expansion from Figure 242 is averaged over the temperature range of -80 to 40°C and added into Table 62. The temperature range has been chosen because below -80°C is noisy, and above 40°C the polymer composites begin to soften.

Matrix Material	Inclusion	Manufacturer	CTE ($\mu\text{m}/\text{m K}$) -80°C to 40°C	CTE reduction %
PLA	-	Ultimaker®	84.9	-
PLA	Iron	Proto-Pasta	65.5	22.8
PLA	Bronze	Filaprint®	64.6	23.8
PLA	Glass Fibre	3D Fuel®	56.9	33.0
PLA	Brass	Filaprint®	61.7	27.2
PLA	Wood	Filaprint®	50.4	40.6
PLA	Carbon Fibre	Proto-Pasta	38.5	54.6
PETG	-	Ultimaker®	78.0	-
PETG	Carbon Fibre	Filaprint®	19.5	74.9
PETG	Carbon Fibre	CarbonX™	18.6	76.1

Table 62. Plastic CTE values and corresponding percentage reduction from inclusions.

7.4.3 Discussion on controlled thermal expansion plastic feedstock

It is observed that there is a wide range of differences in the thermal expansion depending on the type of inclusion. The PLA metal powder inclusions were designed with aesthetics in mind, rather than as a usable structural material and hence their strength is less. These materials all exhibit an increase in CTE as the temperature increases. This could signify that the plastic matrix is expanding around the particles at an increasing rate as the amorphous plastic continues to soften above -10°C . This is also noticed in wood fibre. This occurs due to a rapid release of energy caused by movement of the matrix around the inclusions. This could be caused by lack of cohesion between matrix and inclusion, exacerbated by the low thermal expansion of both inclusions. Due to the smoothing applied to the physical alpha curves, these sudden releases in energy appear as smoothed peaks.

7.4.4 Conclusions on controlled thermal expansion plastic feedstock

To conclude, the findings in this chapter on plastic inclusions are outlined as follows;

- The printing of all inclusions in PLA and PETG successfully produced the required component using default cura print settings for the respective plastic.
- PLA displays a wide range of tailorable CTE's depending on the inclusion, from 84.9 to $38.5\mu\text{m/mK}$.
- Thermal expansion of PETG with carbon fibre inclusions had the largest reduction overall in CTE of 74.9-76.1% ($19.5 - 18.6\mu\text{m/mK}$) compared to PETG with no inclusions. Carbon fibre in PLA had the largest reduction out of all PLA inclusions on 54.6% ($38.5\mu\text{m/mK}$)
- All fibres produced the lowest thermal expansion, with the most linear CTE's across the temperature range when compared to metal particles, which had an increasing CTE as temperature increased.
- All samples printed samples have reached a softening point at about 50°C where they contract.

The effect of manufacture variance and inclusion percentage has could not be accounted for in this study, as manufactures do not publish the percentage of inclusions in their formulations. Further work would need to be conducted to determine the influence on percentage of inclusions and manufacturing method variability of both inclusions, plastic, and the mixing of both inclusion and plastic.

7.5 Multi-material triangular concept

Printing using Fused Deposition Modelling allows for two materials to be selectively placed on each layer. Allowing two different plastics to be printed simultaneously means each material can be placed in any location required within the build volume, which is not currently possible with metal ALM. This chapter will focus on the effectiveness of the triangular structure proposed by Steeves et al. Literature shows it to be the most structurally efficient tailorable CTE metastructure. There is limited research into its effectiveness when manufactured with multi-material FDM [2][53][68]. For additively manufacturing such a design, a multi-material printer will be required that can print in two materials. The Ultimaker 3 was selected due to its ability to print in two materials by lifting one nozzle above the other depending on the material being printed. This unique patented feature means the secondary nozzle does not drag over the first damaging the print. This is an issue with all multi-material FDM printers using multiple extruders, and is the first to solve the engineering limitation. The materials used are manufactured by Ultimaker. Each material comes with a datasheet outlining its mechanical properties, and come with a pre-configured material profile for optimised printing. This setup gives the most reliable and repeatable data. The materials provided by Ultimaker included; ABS, PLA, CPE, CPE+, and Nylon, which have been characterised in chapter 6.3.2, and determined that ABS is the best material to use for the high CTE material ($98\mu\text{m}/\text{mK}$), and CPE for the low CTE material ($76\mu\text{m}/\text{mK}$). These two materials provide a stable mostly linear CTE between -40°C to 50°C .

As outlined by the equations in chapter 2.3.2, the CTE can be calculated for a pin-jointed arrangement by Steeves et al. [2] where there is no resistance to rotation. This has been calculated and plotted in Figure 243.

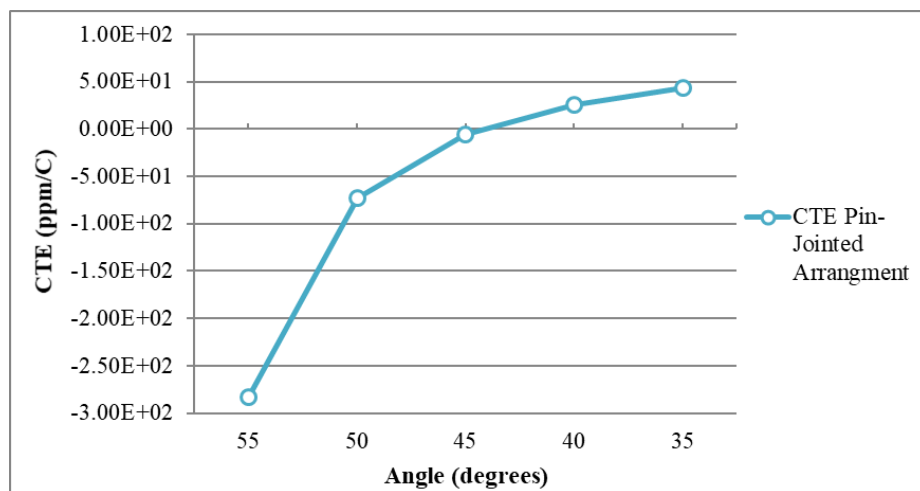


Figure 243. Triangular concept structure showing calculated CTE as the angle changes for a pin-jointed arrangement for CPE (low CTE constituent) and ABS (high CTE constituent).

To create a structure that can be printed, it will need to have a bonded joint, rather than a pin-jointed one. The design in Figure 244 shows the connection method of a radius at tip of the triangle, which connects with the secondary material of the outside member.

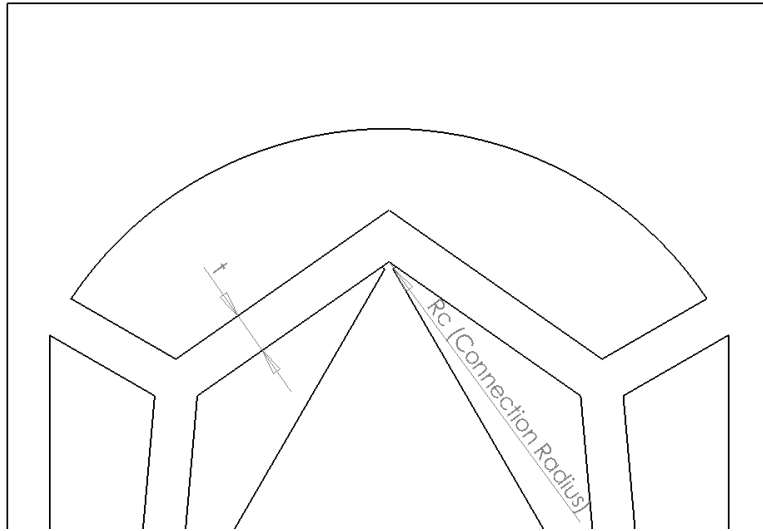


Figure 244. Figure showing the location of the connection radius.

Simulating this structure using finite element method provides a range of thermal expansion depending on the member thickness and the member angle. The simulated results for various member thicknesses from 2 to 5mm across 35 to 57° is plotted in Figure 245. The member length L is kept constant at 50mm and the connection radius R_c shown in

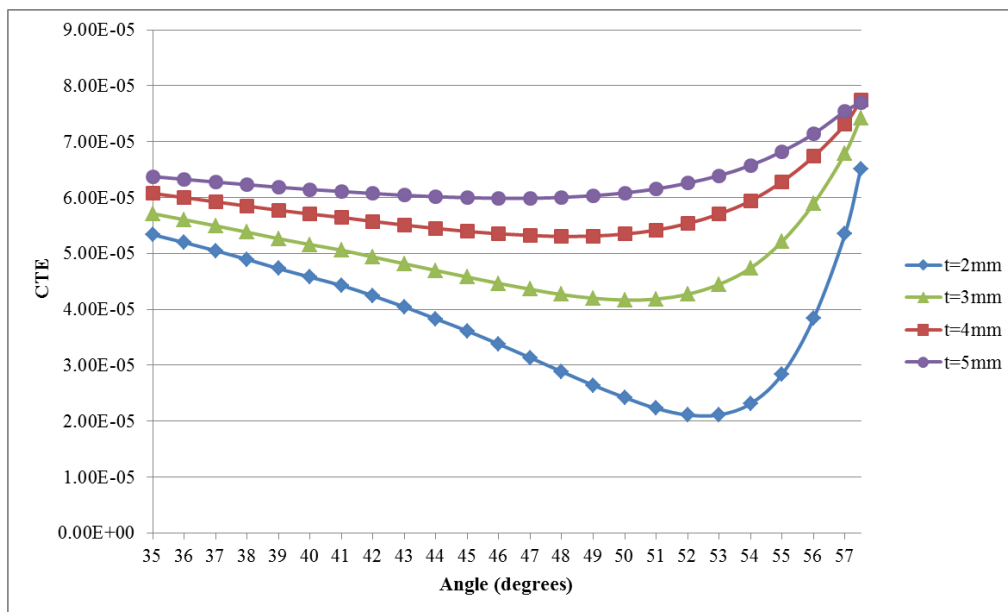


Figure 245. Triangular concept structure showing simulated CTE as the angle changes for varying outside member thicknesses, where $r=2\text{mm}$, $L=50\text{mm}$.

Comparing a theoretical pin-jointed arrangement (Figure 243) and simulation (Figure 245) it is clear that the simulation model follows a similar trend, but shows an increase in overall thermal expansion caused by the resistance to rotation at the joint location. When 3D printing, the connection radius cannot be maintained as the angle increases. As the angle increases the gap between the triangle and the members decreases, with a very narrow gap closer to the triangle corner. At these small distances the two materials can become fused, and therefore the model must account for this. The samples printed in Table 63 show the dimensions of the fused material. To replicate this, the simulation will increase the size of the connection radius to that of the measured value, to determine the effect of an increased connection radius at greater angles.

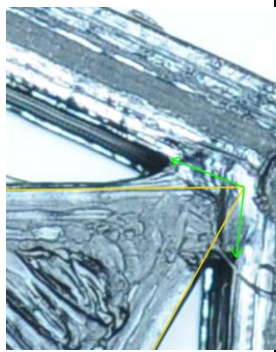
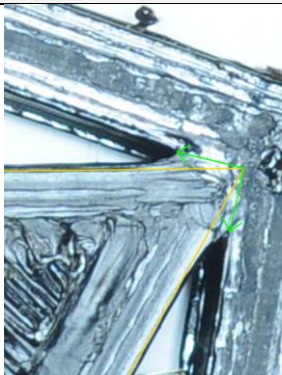
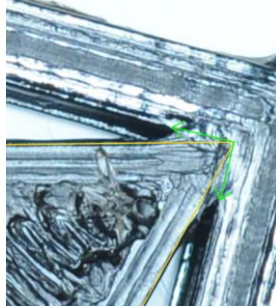
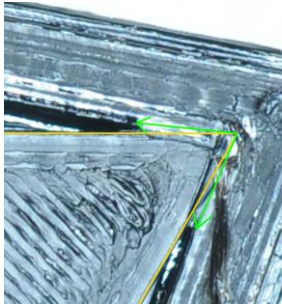
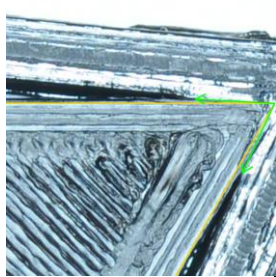
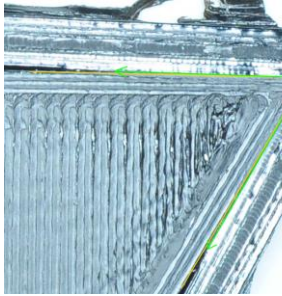
Angle	Image	Average Connection Radius Deviation from 1mm	Angle	Image	Average Connection Radius Deviation from 1mm
35°		+0.45mm	40°		+0.64mm
45°		+0.9mm	50°		+1.65mm
55°		+3.11mm	57.5°		+10.41mm

Table 63. Table of figures displaying Triangular lattice concept manufactured in CPE and ABS at different angles. The connected interface is measured and compared to the nominal value.

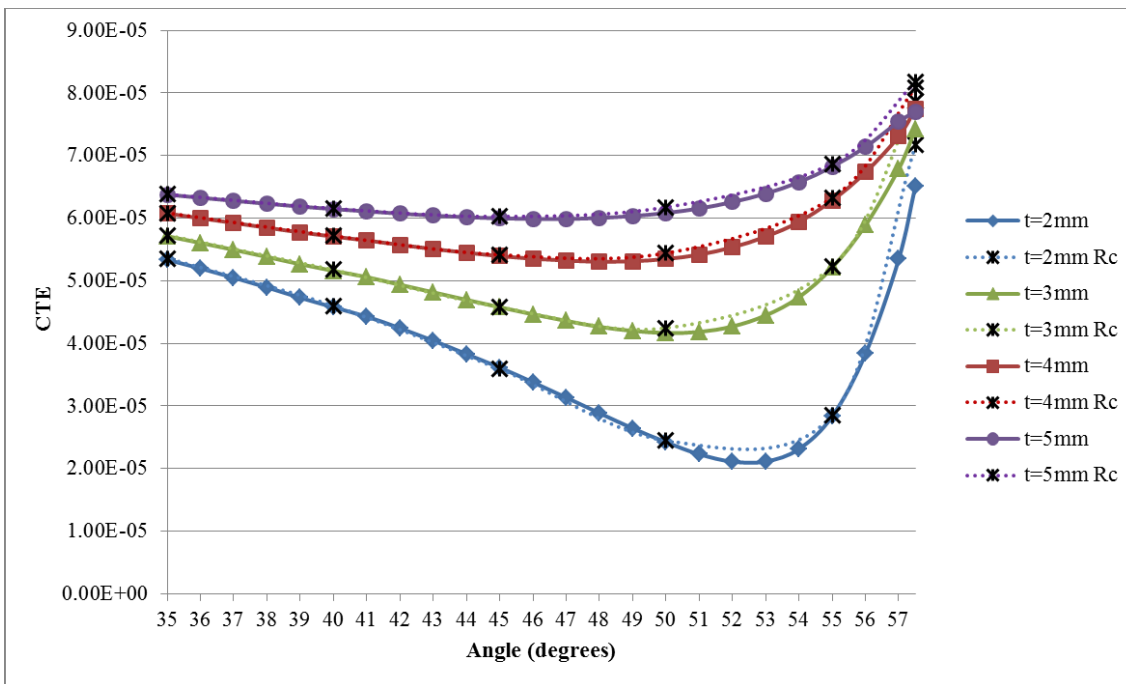


Figure 246. Simulation results showing comparison between the measured connection radius (R_c) from the values on Table 63, and where the connection radius is kept at 1mm.

The simulation data plotted in Figure 246 shows that the 3D printing of the triangular CTE controlled structure developed by Steeves et.al, would not impede on the performance of the structure due to an increasing connection radius.

It was attempted to measure the CTE of the structures using DiC and a hotplate using the test setup as outlined in the experimental chapter, but it was not successful. This is due to the aforementioned problems with the DiC test method setup caused by larger structures. Another problem was caused by ‘bowing’ of the structure, as the inside expands more than the outside, the centre of the structure expanded towards the camera, effecting the ability to track the stochastic black and white speckled pattern applied. The CMM test bench also cannot be used on a plastic, because they become softer as the temperature increases and will compress when probed.

7.6 Multi-material polymer combinations

The composite plastic concept is a means of investigating the CTE of two bonded plastics printed in situ together. This can be used to tailor the CTE between the two lenses. It is known that in this arrangement, the maximum CTE change can only be in-between that of both materials;

$$a_1 < a_{net} < a_2$$

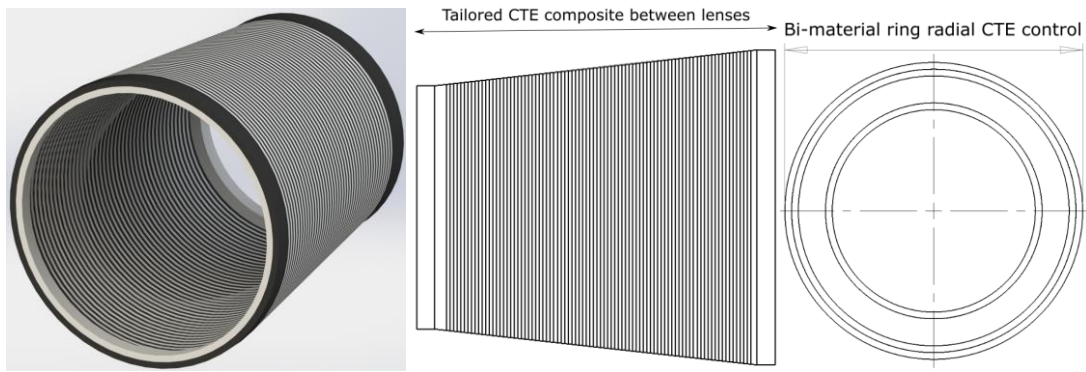


Figure 247. Images showing a potential arrangement for a graded composite plastic material in the form of an optical system body. The overall thermal expansion would be a value in between both materials.

The combination of materials will be printed using the Ultimaker 3 with materials tested in chapter 7.3. The highest and lowest expansion plastics have been chosen, the most expansive is ABS at $92.1\mu\text{m/mK}$ and the least is CPE at $76.2\mu\text{m/mK}$. The composites will be printed in $25\times 5\times 5\text{mm}$ samples for measurement of the linear CTE using the dilatometer. The designs are repeatable periodic structures, designed to utilise the printer’s high-resolution capabilities.

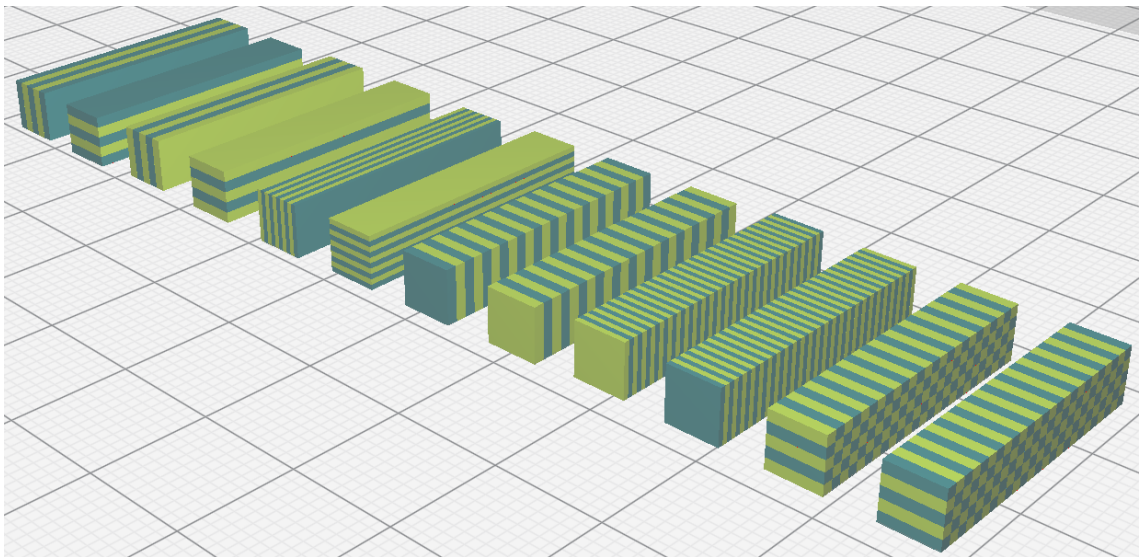


Figure 248. Build image showing the orientation of each patterned dilatometer rod. Light green represents ABS while dark green represents CPE.

The naming convention for each sample is; (Build Direction)(Pattern Number)_(Part Number). So going from left to right in Figure 248 above, there are H1_1, H1_2, H1_3, H1_4, followed by H2_1 where a new pattern is used, the H2_2, H3_1, H3_2, H4_1, H4_2, H5_1, and H5_2. The build direction ‘H’ stands for horizontal. Only horizontal samples have been printed due to manufacturing complexity. White ABS has been used Figure 249 to differentiated between materials. In thermal testing black ABS was used to remove any influence of the pigment on the results.

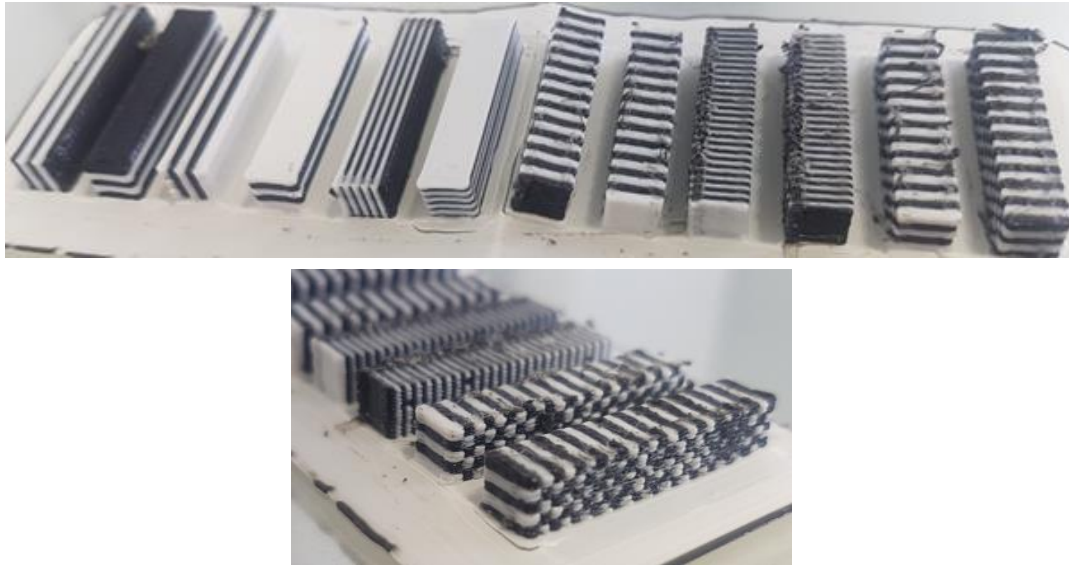


Figure 249. Images of the completed lattices in black CPE and white ABS.

Name	Pattern CAD - 2D extruded.	Material Volume Ratio (CPE:ABS)	Material Volume Decimal Ratio (CPE:ABS)	Print Rate ($mm^3/hour$)
H1_1 H1_2		3:2	0.6:0.4	3125
H1_3 H1_4		2:3	0.4:0.6	3125
H2_1 H2_2		1:1	0.5:0.5	2500
H3_1 H3_2		13:12 12:13	0.52:0.48 0.48:0.52	2083
H4_1 H4_2		1:1	0.5:0.5	1500
H5_1 H5_2		63:62 62:63	0.504:0.496 0.496:0.504	2083

Table 64. Plastic experimental composite layouts and their corresponding CTE ratio.

7.6.1 Manufacture

To manufacture each sample, the Ultimaker 3 has been used due to its robust approach to printing two materials at once. The method of lifting one nozzle above the other depending on the nozzle in use means the nozzle will not drag over the print and cause build failure and quality issues. The approach of the Ultimaker design team ensures that the Ultimaker materials come pre-registered in the build software Cura for a higher probability of build success. The repeatability of any experiments can be achieved easier with a matched manufacturer for both materials and machine.

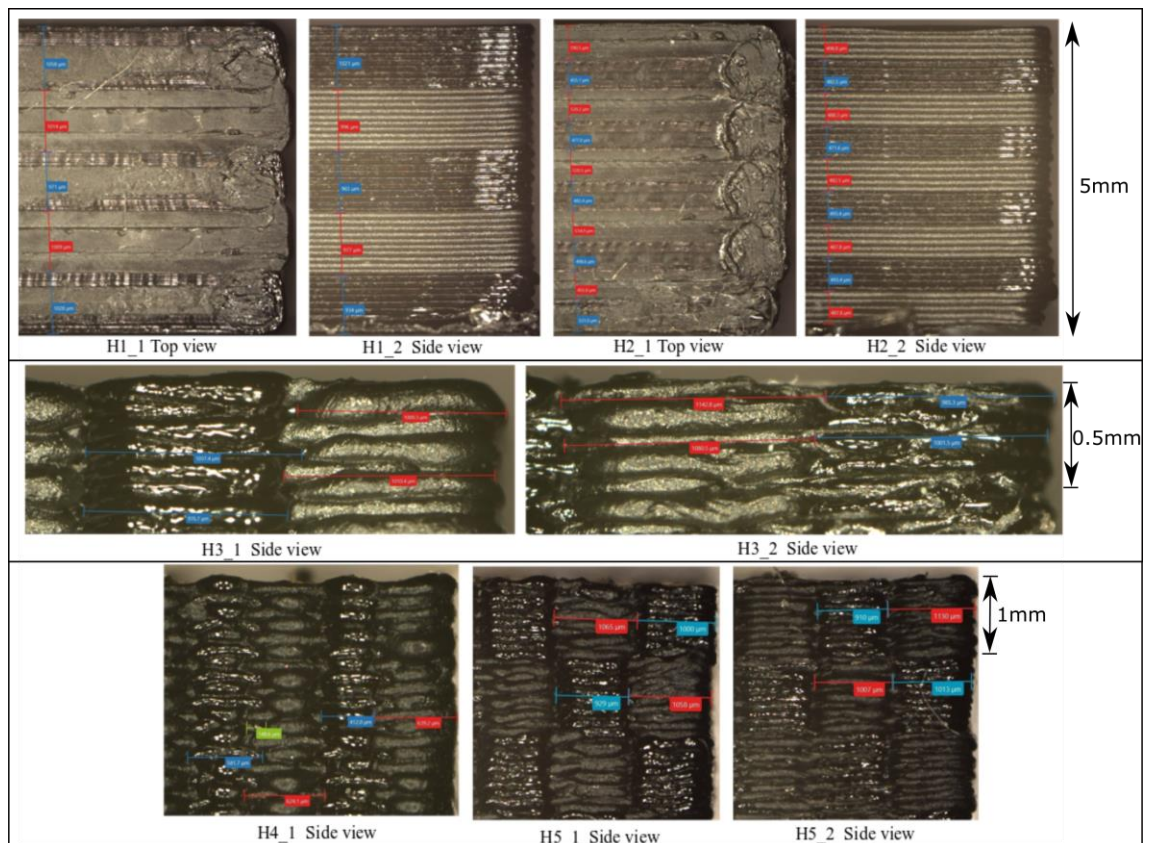


Figure 250. Selection of images and measurements of the dilatometer plastic composites. The reflective black is CPE whilst the matte black is ABS.

7.6.2 Curvature Calculations

Calculating the CTE of each arrangement will require analysis of layout of each composite. It can be seen that H3 and H4 are stacked linearly such that the CTEs can simply be summed together by their ratios. This provides the easiest and most structurally efficient method of tailoring CTE to a value between the two materials, since there are no forces restricting movement along the axis of measurement. This means elastic constants can be neglected. This relationship can be defined simply as;

$$[r_1 a_1 + r_2 a_2] = a_{H3} = a_{H4} \quad (7.1)$$

Where; a_1, a_2 = the CTE for materials 1 and 2; r_1, r_2 = the corresponding ratio of material volume.

Name	$r_1 a_1$	$r_2 a_2$	$a_{Calculated}$
H3_1	$(0.52)X(92.1E - 06)$	$(0.48)X(76.2E - 06)$	8.45E-05
H3_2	$(0.48)X(92.1E - 06)$	$(0.52)X(76.2E - 06)$	8.38E-05
H4_1	$(0.5)X(92.1E - 06)$	$(0.5)X(76.2E - 06)$	8.42E-05
H4_2	$(0.5)X(76.2E - 06)$	$(0.5)X(92.1E - 06)$	8.42E-05

Table 65. Homogenised CTE's for composite dilatometer rods H3 H4.

Looking at H1 and H2 it can be seen that the thermal expansion will be a function of the CTE of each material and its elastic properties. When two bonded layers with different CTE's and elastic properties change in temperature, a bending moment is observed. This has been outlined by Timoshenko and developed further to include a model for multiple material laminates by M. Vasudevan and W. Johnson [210][211][212]. The model allows for calculation of curvature for any number of laminate strips.

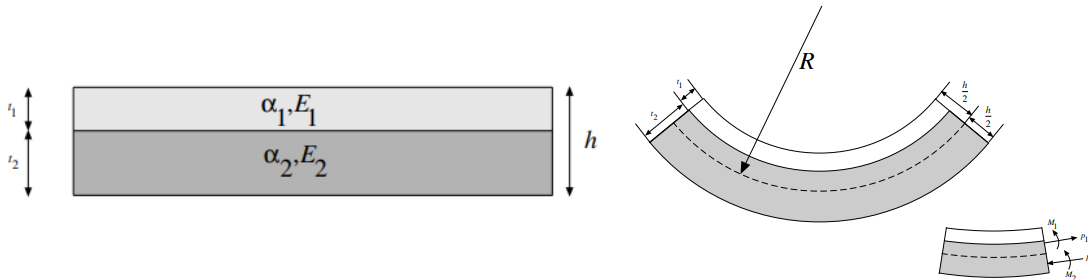


Figure 251. Two bonded layers with different elastic properties and their mechanical behaviour [213].

$$\Gamma = \frac{1}{R} = \frac{(a_2 - a_1)T}{\frac{h}{2} + \frac{2(E_1 I_1 + E_2 I_2)}{h} \left(\frac{1}{t_1 E_1} + \frac{1}{t_2 E_2} \right)} \quad (7.2)$$

Where T is temperature, w is the width and;

$$I_i = \frac{t_i^3}{12} \quad i = 1,2 \quad (7.3)$$

Thickness		Γ
t_1	t_2	
0.5mm	0.5mm	1748.6 μ m
1mm	1mm	874 μ m

Table 66. Curvature and radius for a bi-material strip composed of CPE and ABS.

Due to the curvature calculated, the layout in H1 and H2 has been designed such that no curvature is theoretically possible, since it is symmetric down the central axis. Any bending occurring during testing will be caused by manufacturing geometries being from the nominal value. To determine the linear CTE of such an arrangement, FEA will be the most accurate since the boundary interface distance will cause deformation and strain leading to uneven distributions of deformation.

7.6.3 Rule of Mixtures analysis

The rule of mixtures can be used to determine the CTE of a composite when it can be assumed that there is a homogeneous mixture of matrix and re-enforcement particles. [214]

The bulk modulus upper bound is represented as:

$$K_{upper} = K_m V_m + K_p V_p \quad (7.4)$$

And the lower bound as;

$$K_{lower} = \frac{(K_m K_p)}{(V_m K_p) + (V_p K_m)} \quad (7.5)$$

Where; $K_m K_p$ $V_m V_p$ represent the bulk modulus and volume fraction for both the matrix and the reinforcement particles.

P.Turner et al. [41] created an equation that can be used to calculate the CTE of a composite. This includes the material specific properties;

$$\alpha_c = \frac{(V_m \alpha_m K_m + V_p \alpha_p K_p)}{(K_m V_m + V_p K_p)} \quad (7.6)$$

To include estimations for upper and lower bound, the following equation can be used;

$$\alpha_c = \alpha_p + \frac{K_m(a_m - a_p)(K_p - K_{composite})}{K_{composite}(K_p - K_m)} \quad (7.7)$$

Where $K_{composite}$ represents either the upper or lower bounds.

There are no re-reinforcement particles, instead the material has two materials in unique orientations, this calculation will only provide theoretical bounds should geometry not be relevant and both materials are evenly dispersed. The matrix and re-reinforcement particles will be alternated between each plastic to attain two values for both upper and lower. The volume fraction will be defined from the material ratio of the composite layout.

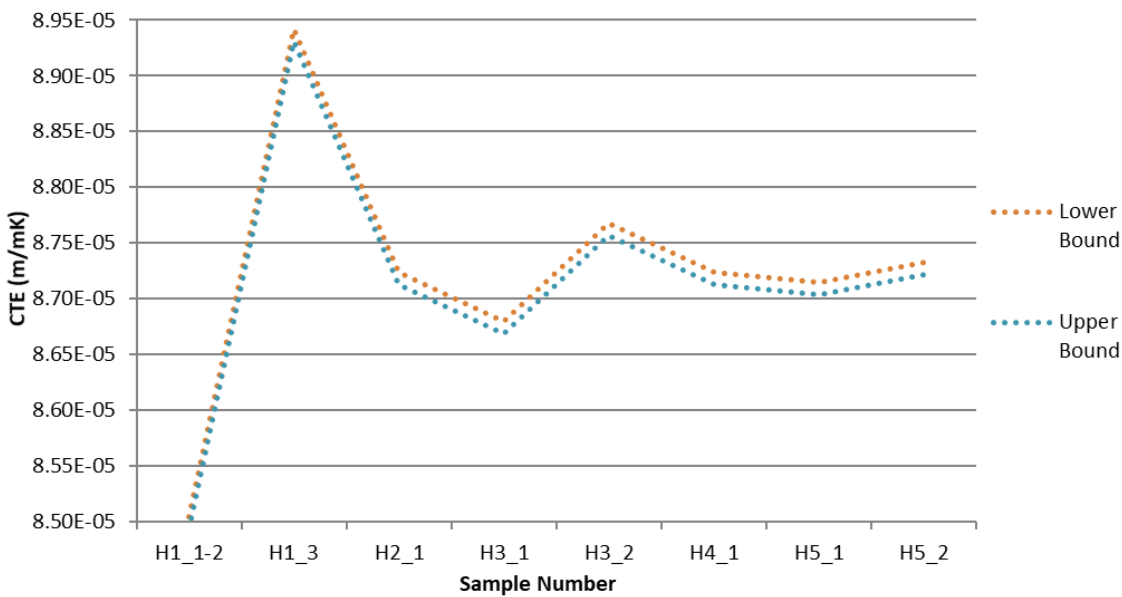


Figure 252. Calculated upper and lower bounds of thermal expansion.

7.6.4 Simulation

To understand the linear CTE value such an arrangement has, it will be easiest to perform finite element analysis since the thickness away from the boundary interface will affect deformation. A static structural simulation has been performed with boundary conditions holding nodes A and B shown in Figure 253a). The conditions are such that A is a fixed displacement, while B is fixed in Y and Z but not in the X-direction. This allows for the free expansion of all sides for accurate analysis of any deformations due to swelling between each layer. In Figure 253b) the boundary conditions are applied to produce the same circumstance.

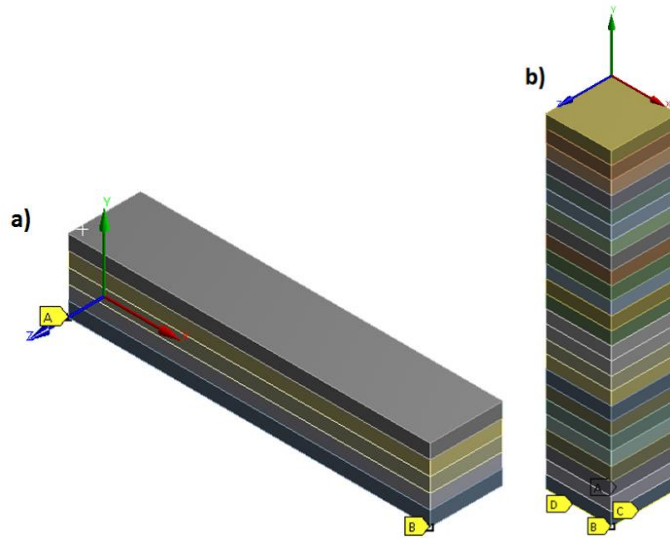


Figure 253. a) Showing boundary conditions to be applied to the H1, H2, and H5 composite dilatometer samples. A and B are nodes held at a fixed displacement. A is fixed in XYZ, B is fixed in YZ. b) boundary conditions to be applied to H3 and H4 composite dilatometer sample.

Boundary Conditions				
	A	B	C	D
H1, H2, H5	Node (0,0,0)	Node (Free,0,0)	Frictionless Surface (Free,0,Free)	
H3, H4	Frictionless Surface (Free,0,Free)	Node (0,0,0)	Line (0,Free,0)	Line (Free,0,0)

Table 67. Boundary conditions for simulated composites.

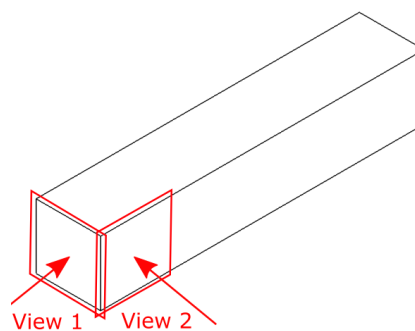


Figure 254. Simulation views for all dilatometer composite rods

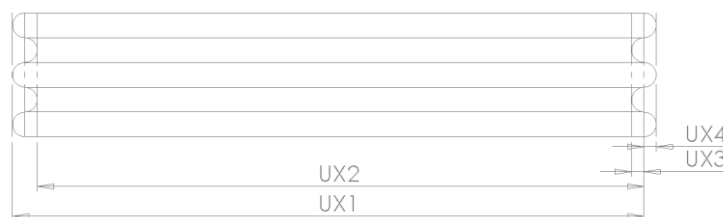
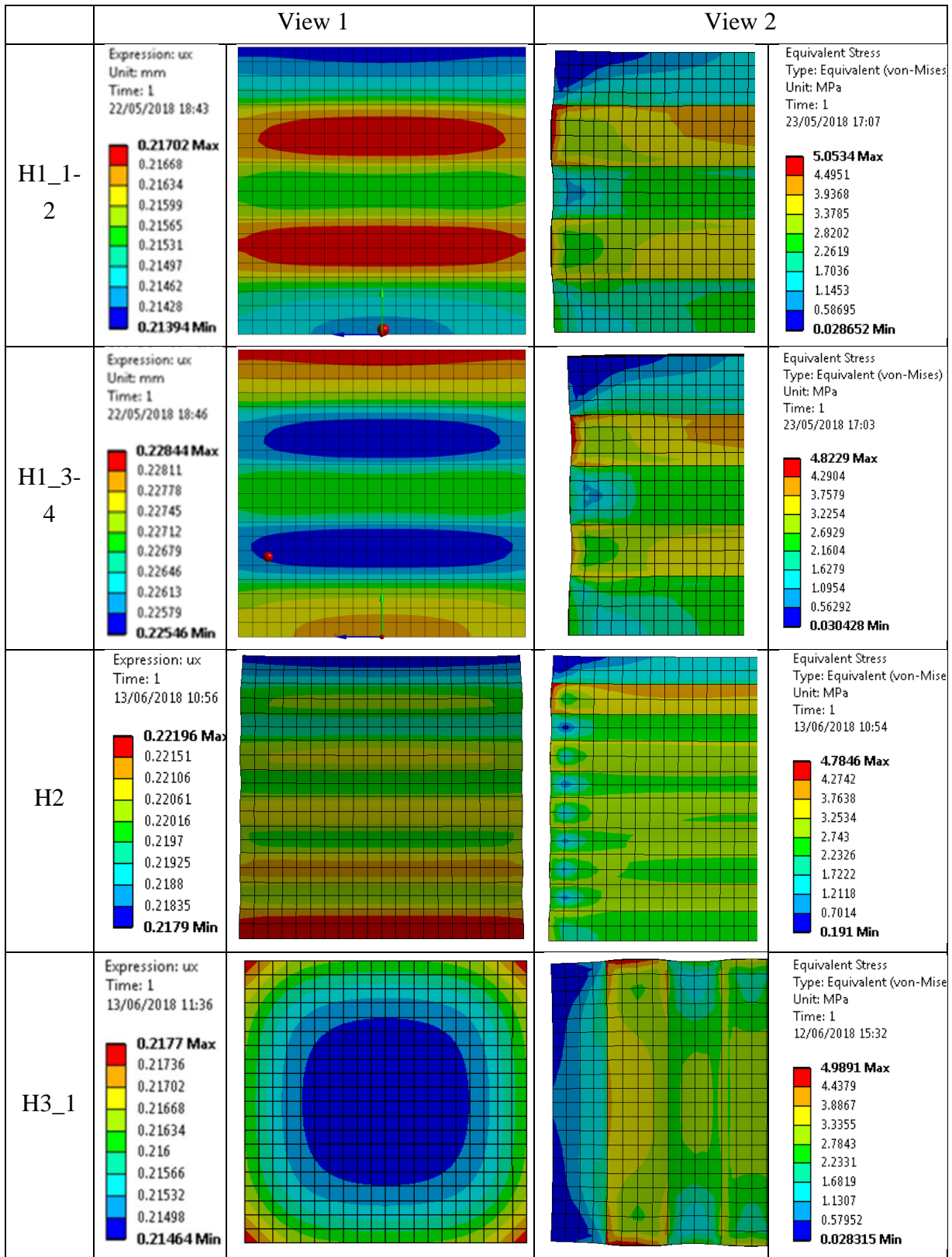
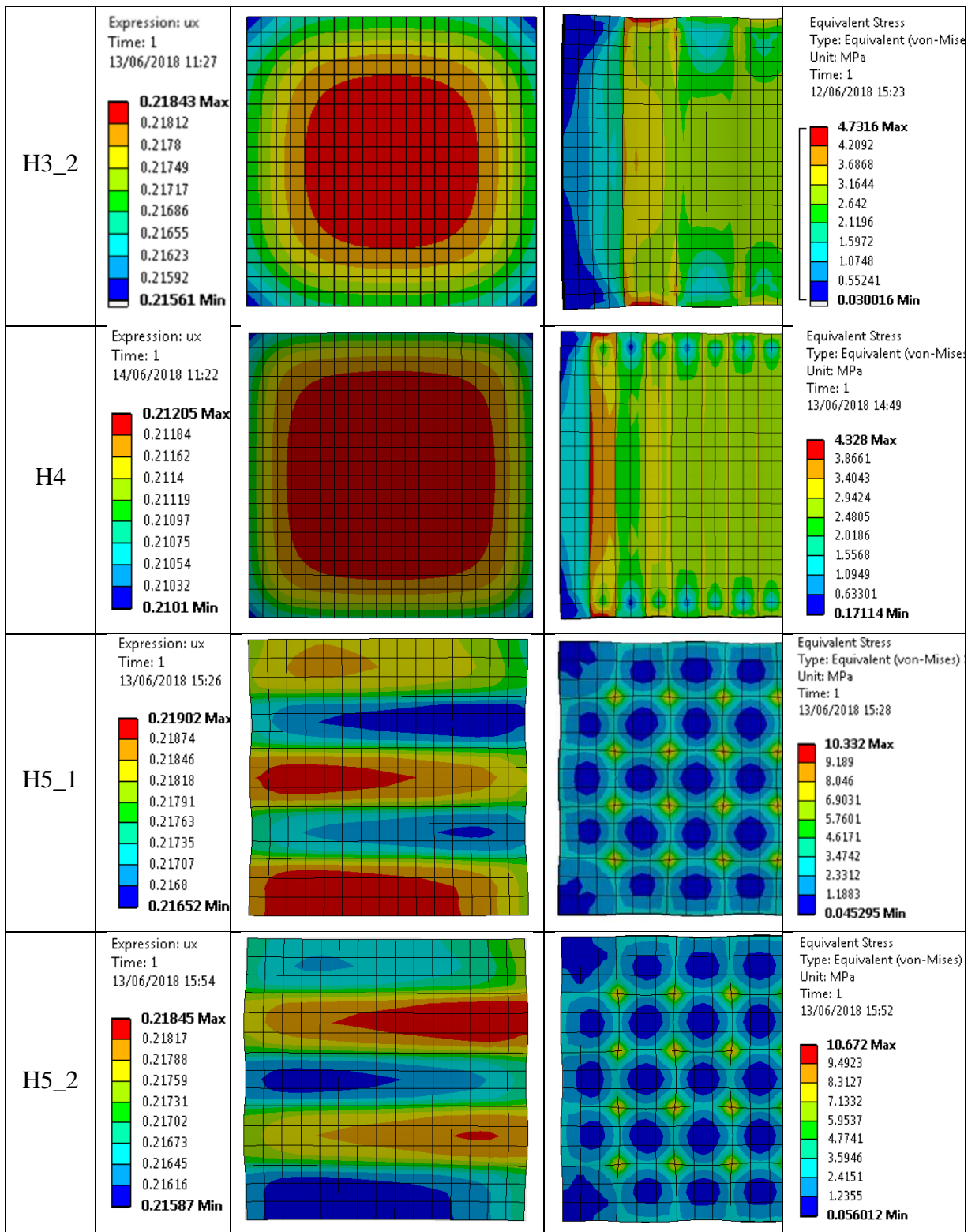


Figure 255. Displacement locations and notation example for the composite dilatometer rod H1_1-2.

Figure 256. Simulations showing deformation with 30x scaler to visibly show swelling locations. View 1 shows displacement values whilst view 2 shows Von-mises stresses.





Sample	UX1 (mm)	UX2 (mm)	UX4 (mm)	UX1 CTE (m/m°C)	UX2 CTE (m/m°C)	UX1+UX4 CTE (m/m°C)
H1_1 H1_2	0.21702	0.21394	-0.0027411	8.68E-05	8.56E-05	8.6640E-05
H1_3 H1_4	0.22844	0.22546	-0.0010699	9.14E-05	9.02E-05	9.1424E-05
H2	0.22196	0.2179	- 0.00023245	8.88E-05	8.72E-05	8.8877E-05
H3_1	0.2177	0.21464	-0.0018306	8.71E-05	8.59E-05	8.7676E-05
H3_2	0.21843	0.21561	- 0.00098009	8.74E-05	8.62E-05	8.7968E-05
H4_1	0.21314	0.21101	- 0.00072701	8.53E-05	8.44E-05	8.5939E-05
H5_1	0.21902	0.21652	- 0.00086359	8.76E-05	8.66E-05	8.7953E-05
H5_2	0.21845	0.21587	-0.0015855	8.74E-05	8.63E-05	8.8014E-05

Table 68. Table of simulated deformation data and calculated CTE's for the dilatometer composite samples.

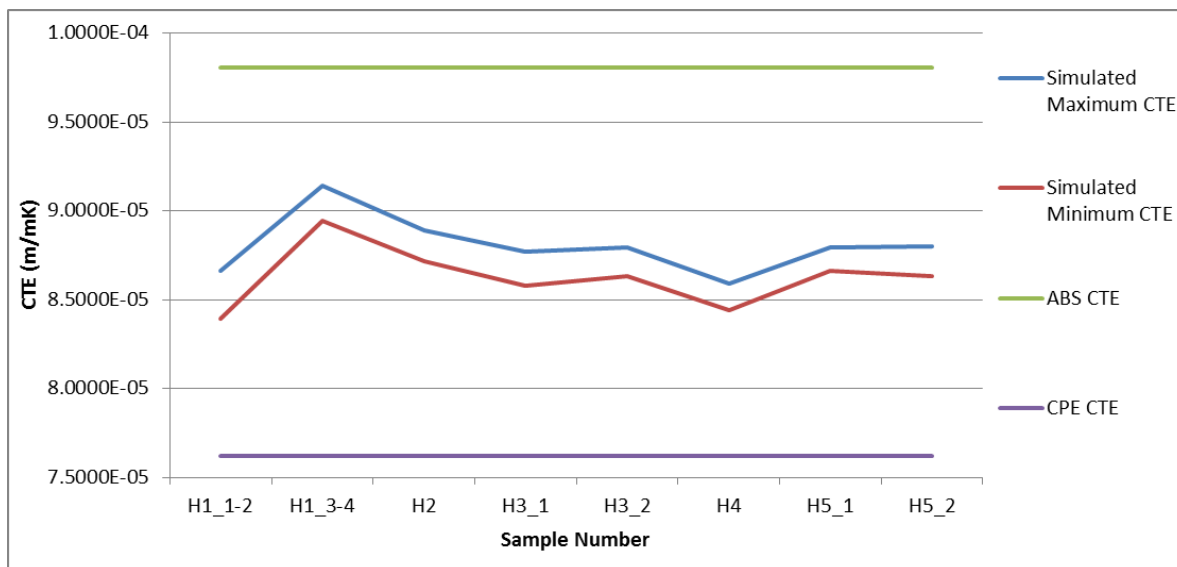


Figure 257. Simulated CTE results for dilatometer composites.

From the perspective of view 1 in Figure 254, the simulated displacement contours in Figure 256 show differences through the cross section. Composite sample H3 shows that the deformation is consistent in the centre, whereas all other samples show multiple increases and decrease locations across the surface. This will be more challenging to

introduce into a tailored CTE design since the consistency, and predictability of the location of deformation is important for placement of the part on the object surface. View 2 shows the Von-mises stresses and deformation plot showing the swelling of the laminates. This swelling causes stresses between 4-5MPa for H1 to H4, and between 10-11MPa for H5. The Yield Stress for CPE is 41.1MPa and ABS is 39MPa, meaning that over a 100°C temperature ranges, the stresses are within the materials ability.

7.6.5 Thermal Expansion

The composites have been tested using the dilatometry procedure and test program outlined in chapter 6.3.2. Two of every composite sample has been printed to give a total number of 16 composite samples.

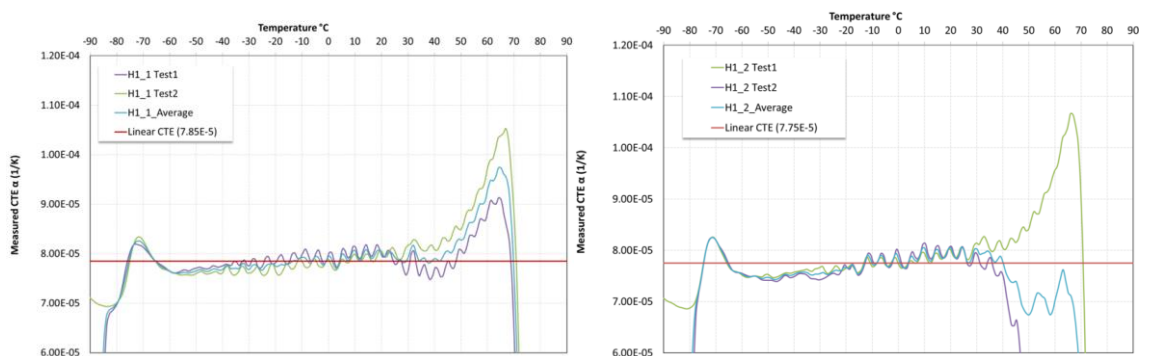


Figure 258. Dilatometer Results for H1_1, and H1_2 Composite Samples.

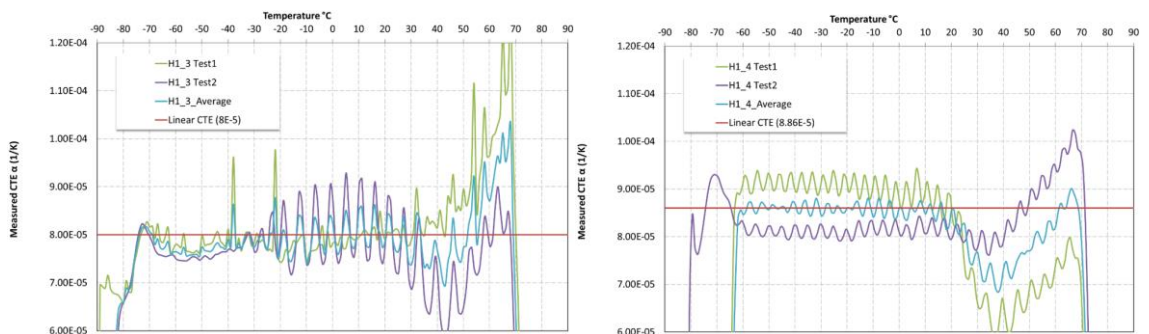


Figure 259. Dilatometer results for H1_3, and H1_4 Composite Sample.

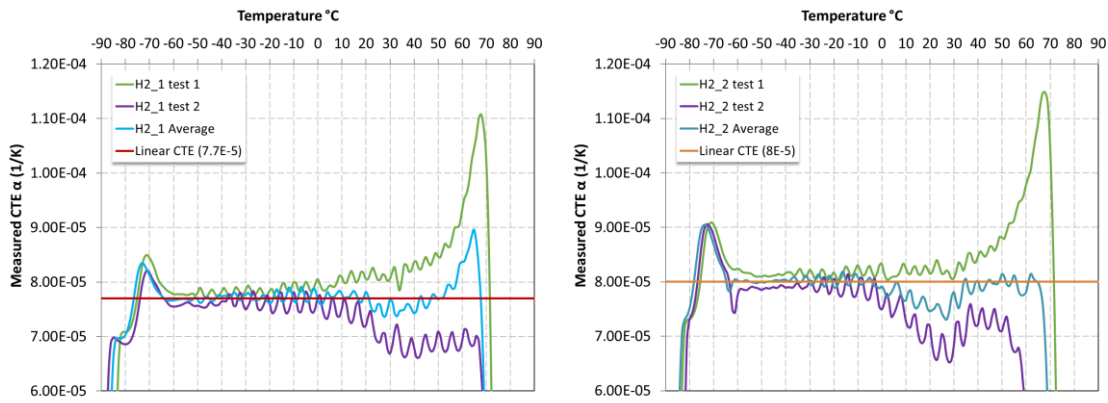


Figure 260. Dilatometer results for H2_1, and H2_2 Composite Sample.

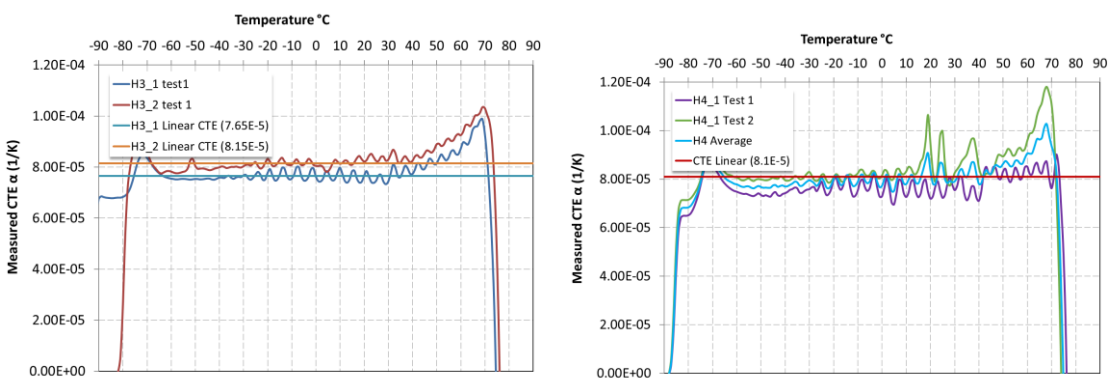


Figure 261. Dilatometer results for H3_1-2 and H4_1 Composite Sample.

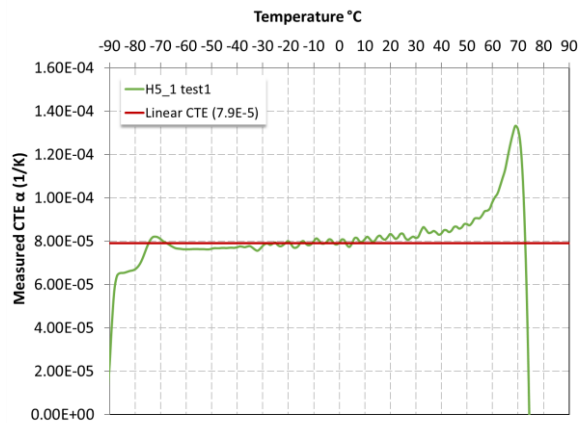


Figure 262. Dilatometer results for H5_1 Composite Sample.

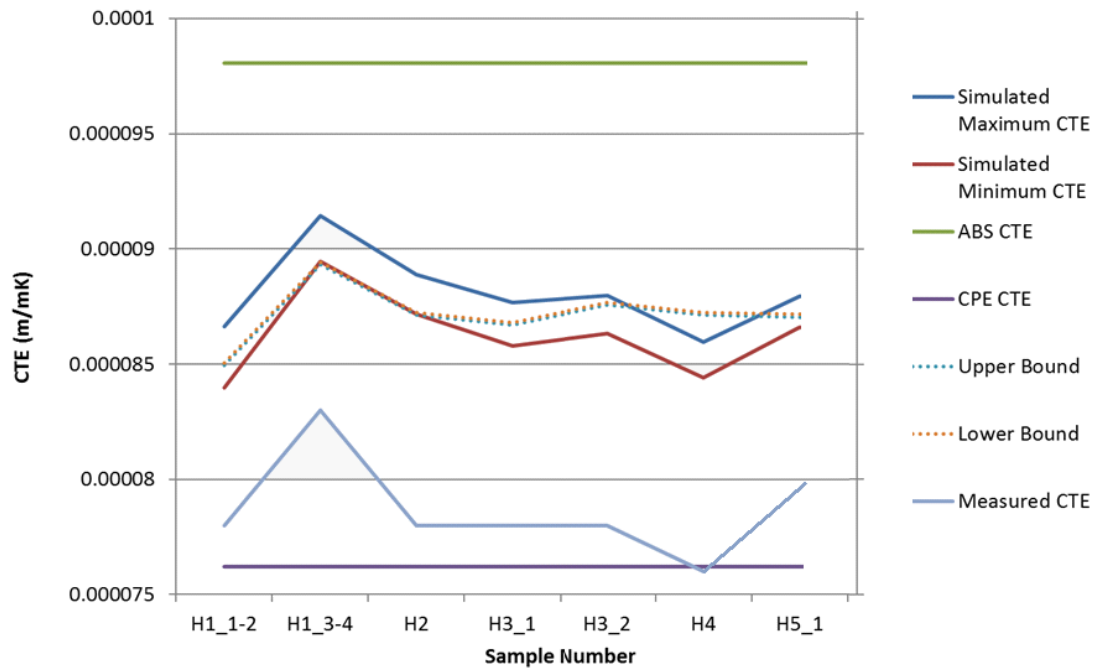


Figure 263. Co-efficient of thermal expansion results for all printed plastic composites compared against simulated expansion, and theoretical upper and lower bounds.

7.6.6 Discussion on multi-material polymer combinations

This chapter shows that it has been possible to 3D print a dual material plastic in arrangements that combine to feature a CTE in-between both plastics. The arrangements have been simulated and determined to approximately follow the upper and lower bounds of thermal expansion using the turner equation (Eqn. 7.6). Dilatometry shows that the thermal expansion followed the trends of both the theoretical and simulation-based estimates, but was much closer to the thermal expansion of the CPE rather than the centre range predicted. The measured CTE's from dilatometry ranged between 82.5 to 75 $\mu\text{m}/\text{mK}$, instead of the intended 91.5 to 86 $\mu\text{m}/\text{mK}$. This could be due to a change in the elasticity modulus for both materials depending on the temperature. The elasticity modulus was assumed to be a steady state condition in the simulation. Inter-layer fatigue between the two materials could present a problem over many cycles and would need to be tested further on a suitably chosen design. It would be most effective to choose a design to minimise the surface area, and strain rates on the two material connections.

As a solution to tailoring thermal expansion in a plastic, this solution provides only a limited range. To improve on the method further, a better understanding of the behaviour of each plastic over a wide range of temperatures is required. A transient thermo-mechanical simulation with the variable young's modulus and thermal expansion values can be used for a more accurate prediction. Plastics with a higher or lower CTE can open up a wider range of thermal expansion tailoring. The practical applications of a

constructed composite using the designs proposed would not be the most effective method of controlling thermal expansion in its current form.

7.6.7 Conclusion on multi-material polymer combinations

To conclude the simulation, and manufacture and testing of multi-material plastic combinations has provided a tailored thermal expansion to a value between both ABS and CPE materials. Its accuracy to the models shows a correlation to the trend, but not the absolute values. The summarise the technical conclusions below;

- The manufacture of fine dual material plastic lattice structures has been completed with an exceptionally high accuracy of down to $\pm 30\mu\text{m}$ across a 2mm section with two different 1mm sections in the finest composite H5.
- The thermal expansion of the structures varies between the CTE of ABS ($97.5\mu\text{m/mK}$) and CPE ($76\mu\text{m/mK}$) to within the range of 82.5 to $75\mu\text{m/mK}$, but not the predicted range of 91.5 to $86\mu\text{m/mK}$.

7.7 Discussion on thermal expansion control in polymer AM

Reducing the thermal expansion of a plastics printed using FDM could be very useful considering the polymers relatively high thermal expansion of plastics and polymers ($76\text{--}98\mu\text{m/mK}$) compared to metals. R makes them challenging to use with glass or germanium lenses ($6\text{--}7\mu\text{m/mK}$). The polymer lens named ZEONEX[®] has a CTE in the region of $60\mu\text{m/mK}$ and therefore would be an ideal candidate to find a method of tailoring the thermal expansion of a plastic 3D printed material to match.

The thermal expansion of the Ultimaker branded plastics printed using the Ultimaker 3 is measured using cryogenic dilatometry and determined to be in the range of between $76\text{--}98\mu\text{m/mK}$ when averaged between horizontally built and vertically built. PLA and ABS plastics were found to exhibit higher CTE's in the when printed vertically, whilst CPE, CPE+, and Nylon had no noticeable change in CTE with build orientation. It is important to have thermal expansion isotropy across the part to ensure the optical system body does not cause distort the lens alignment. To reduce the thermal expansion of the polymers, additions have been added into the polymer, such as carbon, glass, wood, and synthetic fibre, as well as metal powders. These have shown to provide a thermal expansion range of between $65.5\text{--}18.6\mu\text{m/mK}$. Inclusions such as carbon and glass fibre with PLA and PETG matrix material have provided the most stable and linear CTE across the temperature range, and would be considered the best candidates for varying the volume fraction of the fibre to achieve the desired CTE. It is also well documented in literature that in the introduction of carbon fibres into a plastic or polymer matrix improves the mechanical performance [18], [60]. The volume fraction of the inclusions is not disclosed by the manufacturer, but it is known that an increased volume of lower expansion carbon

fibre will reduce thermal expansion of the carbon fibre reinforced polymer [18], [21], [23]. For future work, it would be necessary to manufacture PETG with varying volume fractions of carbon fibre to tailor the thermal expansion to that of ZEONEX® or even glass or germanium.

The multi-material printing ability of the Ultimaker 3 has opened up the possibility of printing novel low thermal expansion structures, where the higher thermal expansion structures can produce a movement in the structure to reduce the overall thermal expansion of the structure. This chapter looks at designs by Craig.A.Steeves et al. and prints the proposed structures with the Ultimaker 3 in ABS and CPE. The structures have been simulated to provide a tuneable thermal expansion behaviour depending on the angle of the structure. During manufacture it was discovered that as the angle of the members increases, the gap between the two materials at the member joint decreases, thus increasing the connection between the two materials. When simulating this behaviour, the thermal expansion results were unaffected by the printing geometry issue. This demonstrates the viability of the design for 3D printing. For future work, it would be important to measure the thermal expansion of the structure through experimental methods. An attempt was made to use a DiC test bench outlined in chapter 4.8.1 but experienced too many issues with its accuracy, and would require a redesign to ensure a higher resolution, with improved lighting conditions. The distortion of the plastic caused the structure to bend upwards while heating, causing issues with focus and particle tracking in the DiC software.

The multi-material composites have been printed to tailor the thermal expansion between that of the two materials used. This is different to the tailored CTE structures by Craig.A.Steeves et al. that are larger, and can produce thermal expansions of the structure that are lower than both materials. These composites have been printed into a dilatometer rod and feature a range of patterns designed to investigate the thermal expansion of different locations and proportions of high and low CTE polymers. The thermal expansion of the structures varies between the CTE of ABS ($97.5\mu\text{m/mK}$) and CPE ($76\mu\text{m/mK}$) to within the range of 82.5 to $75\mu\text{m/mK}$. The simulation of the designs predicted the trend of increasing and decreasing CTE's between the designs, but did not predict the actual values which were much lower towards that of CPE. The predicted range of the simulations was between 91.5 to $86\mu\text{m/mK}$. To improve on the method further, a better understanding of the behaviour of each plastic over a wide range of temperatures is required. A transient thermo-mechanical simulation with the variable young's modulus and thermal expansion values can be used for a more accurate prediction. Plastics with a higher or lower CTE can open up a wider range of thermal expansion tailoring. The practical applications of a constructed composite using the

designs proposed would not be the most effective method of controlling thermal expansion in its current form.

7.8 Conclusion on thermal expansion control in polymer AM

To conclude, this chapter has demonstrated the viability of thermal expansion tailoring through adjusting the material polymer feedstocks constituents with additions of various fibres and powders, but also through the design of multi-material structures. To summarise, the technical outcomes of this chapter are as follows;

- Thermal expansion ranges for PLA, ABS, CPE, CPE+, and nylon, are between 76-98 $\mu\text{m}/\text{mK}$.
- The addition of carbon, glass and wood fibre, including brass, bronze, and iron powders into PETG and PLA provide an adjustable range of between 65.5-18.6 $\mu\text{m}/\text{mK}$.
- Carbon and glass fibres provide superior linear CTE behaviour from -100 to 90°C proving the best inclusions for varying volume fraction to tailor CTE in future work.
- PLA with brass inclusions provides the closest match with the polymer lens ZEONEX[®], featuring a CTE of 61.7 $\mu\text{m}/\text{mK}$, to the lenses 60 $\mu\text{m}/\text{mK}$.
- The triangular thermal expansion tailoring structures were manufactured and simulated to show that the surface area in connection between the two materials is not critical to the low CTE effect. This proves the structures viability in polymer FDM. Future work requires improved experimental measurement techniques.
- Multi-material polymer composites manufactured with exceptionally low deviation of down to $\pm 30\mu\text{m}$ across a 2mm dual material section on H5. CTE's achieved between 82.5 to 75 $\mu\text{m}/\text{mK}$, although simulation data matched the trend but not the values correctly. Needs further research into viability due to elastic modulus variability with temperature.

To conclude, the tailoring of thermal expansion using FDM polymers has been shown to be the most successful by adding inclusions into the polymer material feedstock. This process can produce the widest tailorable range of thermal expansion co-efficient. Adjustment of the volume fraction of carbon or glass fibre in PETG should be attempted to tailor the CTE in future work. This is the most practical approach to matching the thermal expansion for industrial applications. The polymer lens ZEONEX which features a CTE of 60 $\mu\text{m}/\text{mK}$ could be matched by a PETG with only a small volume fraction of carbon fibres, due to the fibres low expansion property as shown by the CF-PETG at only

18.6 $\mu\text{m}/\text{mK}$. The inclusion with the closes CTE to that of ZEONEX in its current form is PLA with brass powder, providing a well matched 61.7 $\mu\text{m}/\text{mK}$.

8 Thermal Expansion Control in Polymer AM using Fibre Reinforced Material

8.1 Summary

This chapter investigates the capabilities of continuous fibre reinforced polymer additive manufacturing. It looks at the effect of the matrix polymer, fibre material, and fibre orientation on the linear co-efficient of thermal expansion. It will understand the thermal expansion behaviour of carbon fibre, glass fibre, and Kevlar fibres printed with nylon, and a nylon mixed with short-chopped carbon fibres called ‘Onyx’. The thermal expansion will be measured for fibres orientated along the test direction, transverse to the test direction, and the with both along, transverse, and at 45° to the test direction. Tailoring the CTE by adjusting the type of fibre, and the angle its oriented at is highly advantageous for the optical systems industry. This provides the company with the ability to change the thermal expansion to exhibit a pre-determined CTE at a specific orientation and location within the optical system body.

8.2 Introduction

This chapter will investigate a new field of fused deposition modelling called fibre reinforced polymer additive manufacturing. The technology uses a dual nozzle system where a layer of nylon matrix material is deposited, followed by a continuous fibre strand from the second nozzle. The continuous strand of fibre is deposited at a predetermined path inside a nylon matrix to form a composite. The technology patent holder belongs to Markforged. The Markforged Desktop 2 system has been used for manufacture.

The introduction of glass or carbon fibres has shown to reduce thermal expansion of the polymer matrix [20], [59]. Other inclusions such as wood, metal powders, and synthetic fibres have also been shown in chapter 7 to reduce the thermal expansion. This allows for adjustment of the CTE by varying the volume fraction (V_f) of short-chopped inclusions. The method presented in this chapter has the capacity to control thermal expansion by adding a continuous unbroken fibre filament directly into the printed layer. This works by feeding carbon, glass, or kevlar fibres directly into the previously laid polymer layer from a secondary nozzle. This is known as Continuous Filament Fabrication (CFF) and allows fibres to be laid in a specified direction to produce a composite that can be stronger and less thermally expansive in one direction than the other [25]–[27]. The printer has a choice of Nylon or Onyx as the printing material. Onyx is nylon, impregnated with short-

chopped carbon fibres. The feed filament consists of woven thin hairs of continuous fibres encased in nylon, instead of a thicker single continuous strand. This enables the filament to be more flexible and less brittle, and provides it with a means to adhere to the substrate [28].

This chapter will investigate the effect of orientating a continuous fibre inside a nylon sample. The orientations will be printed inside a 25x7x7mm dilatometer rod. Longitudinally printed samples will have orientations towards the test direction, transverse will be across the test direction, and isotropic will be both along, transverse, and at 45° to the test direction. All fibres will be printed in a nylon matrix material, and then again separately using the ‘Onyx’ matrix material. Onyx is the Markforged brand name for nylon with a percentage of short-chopped carbon fibres evenly mixed within the material. Three fibres will be tested, these include carbon fibres, glass fibres, and Kevlar fibres. To the best of the authors knowledge there is no available literature on the effect of thermal expansion on composites printed using continuous fibre filament fabrication.

8.3 Design

The test samples will be designed to be measured for their linear thermal expansion using a dilatometer. The design of the samples has been considered to fit an optimum amount of orientated fibre within the limited width available for a dilatometer sample. The standard ASTM E228-17 specifies that the dilatometer samples should be a cylindrical 25x5mm rod, but this is not possible when adding fibres into the sample. Instead the sample has been designed to be rectangular at 25x7x7mm. A width of 7mm was the minimum width found to be manufacturable whereby a fibre can be orientated across the test direction as well as transverse to it. Figure 264 shows the three orientations to be printed in both nylon and onyx in the Eiger print software. This gives a total of three orientations, three fibre types, and two polymers, making a total of 18 samples. An additional two samples will be added for pure nylon and onyx with no fibres, making 20 samples total.

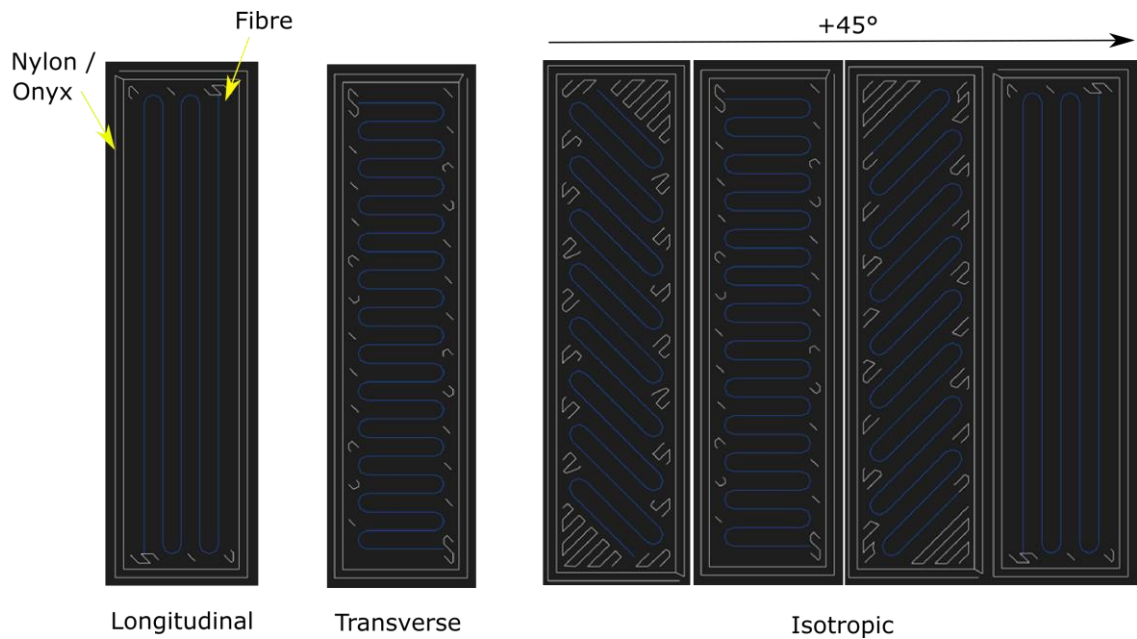


Figure 264. Fibre orientations for the three samples. Images from Markforged's Eiger.io print software.

8.4 Manufacture

Manufacturing a continuous fibre reinforced polymer with a Markforged 2 machine is a simple process. The STL is imported into the slicing software Eiger.io, where the fibre orientations and layup are selected. The number of fibre layers can be tailored by a ratio of fibre to nylon, for example; 1 layer of nylon to 1 layer of fibre would have a ratio of 1:1. The dilatometer samples printed here have a 1:0 layup, meaning every layer is a layer of fibre. This provides the most consistent thermal expansion through the cross-section. Each fibre layer is printed within a nylon layer to fill in the gaps between the fibres. In total the height of a single layer of filament with nylon is 50µm. A series of images as been taken showing the build after layer 1 has completed, and then again after layer 2 has been printed on top of layer 1.

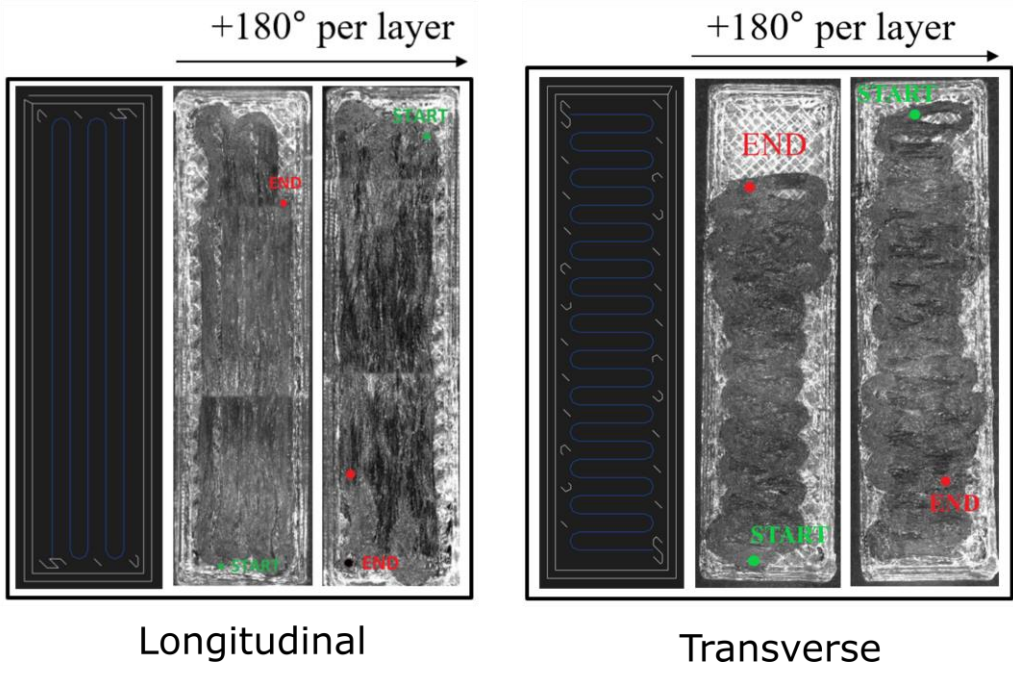


Figure 265. Top down view of two dilatometer samples with the fibre laid **longitudinally**, and **transverse** to the test direction. Image shows the CAD, then layer 1, and layer 2 respectively.

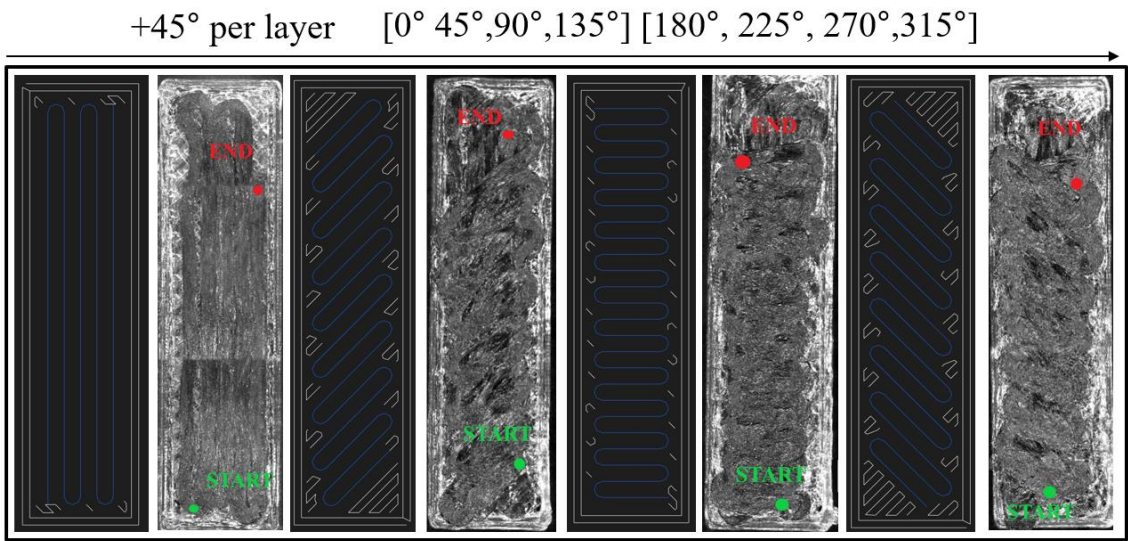


Figure 266. Top down view of a dilatometer sample with the fibre rotated at 45° each layer. This is to attempt to make a material with **isotropic** thermal expansion. Image shows the CAD, then layer 1, layer 2, layer3, and layer 4, respectively.

One manufacturing issue that can be seen in the images in Figure 265 to Figure 266 is the early cut off point for the fibre. The fibre does not extend to the end of the sample. To maintain coverage in this area, the start point for the fibre extrusion on the proceeding layer is set to the previous layers fibre end point. For the isotropic orientations, the +45° on every start point will cover the previous end point after 4 layers. Figure 267 shows an image of each dilatometer rod printed with longitudinal, transverse, and isotropically oriented fibres.

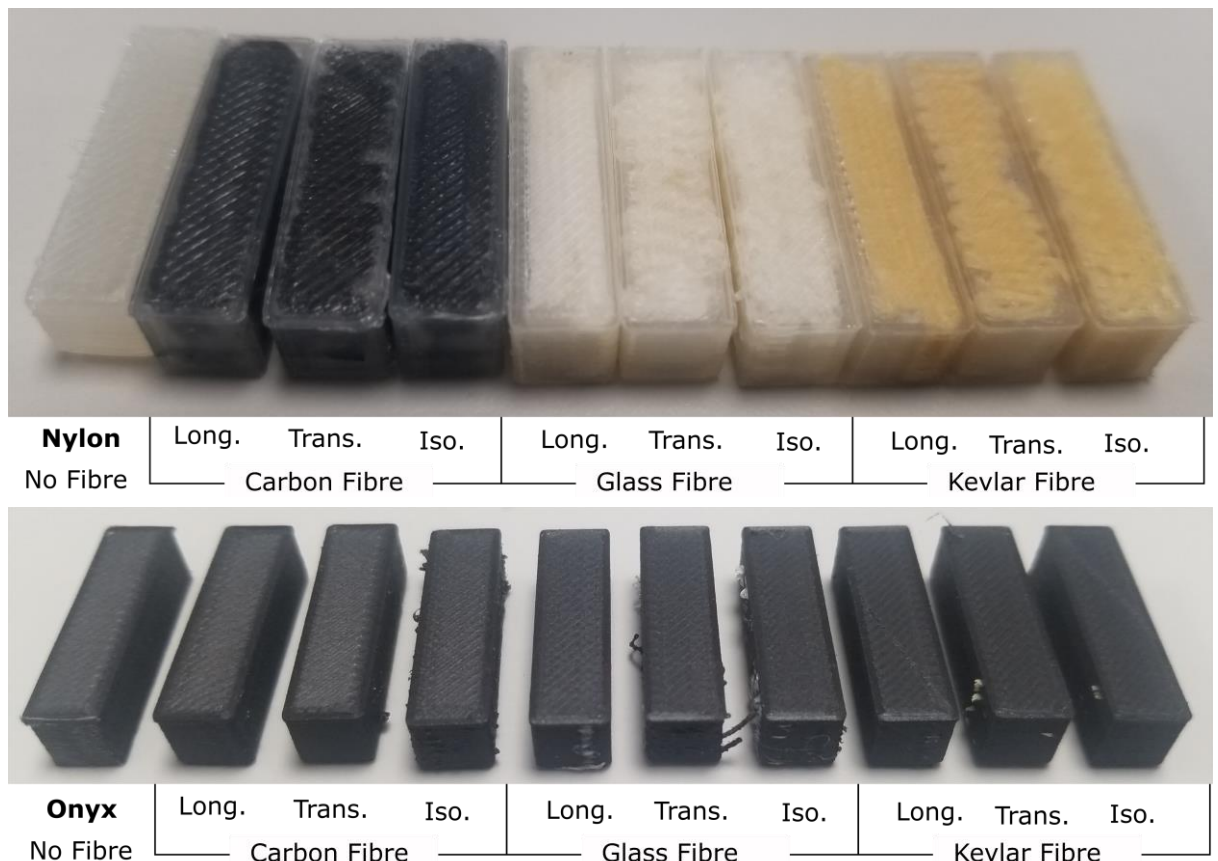


Figure 267. Images of 3D printed continuous fibre composites showing fibre orientation.

The nylon samples show the fibre orientations visibly, whereas the Onyx contains the short-chopped carbon fibres which are so fine that they block all light transmission through the nylon. Overall the samples have manufactured well, with little stringing of the polymer. There is a slight intrusion of the fibre into the outside wall on some locations depending on the orientation. The tolerances in sample length are incredibly tight, to within 25 ± 0.02 mm on the onyx, and 25 ± 0.05 mm on the nylon samples. The actual sample length is used in the dilatometry, to account for any comparative inaccuracies due to thermal expansion change.

8.5 Results

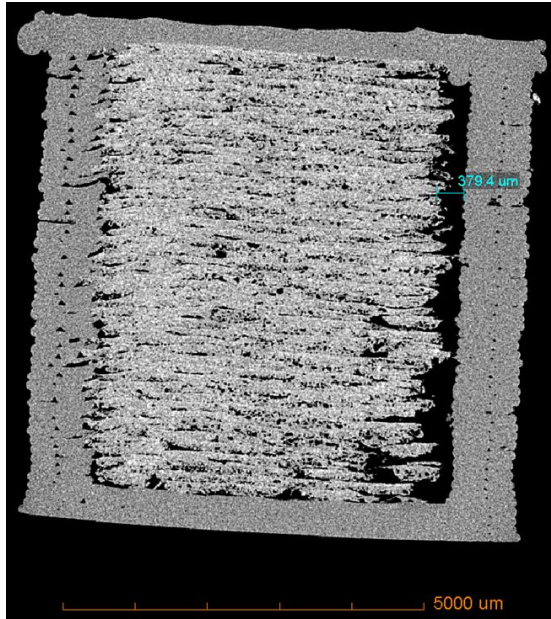
To determine any manufacturing defects in the part, a nylon sample with longitudinally oriented carbon-fibre has been scanned using computerized tomography (CT). This has been used to determine porosity locations between the layers, within the fibres, and within the nylon. It also helps to visualise the fibre orientation layer by layer which will help understand the fibre interaction between the layers.

The thermal expansion will be measured using the Netzsch 402 dilatometer with a cryogenic liquid nitrogen stage. The temperature will go down to -120°C and up to 90°C

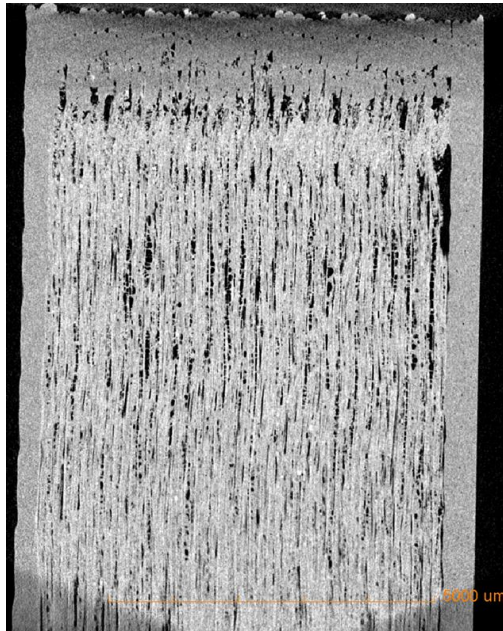
at 5°C/min and determine the physical and technical alpha curves and values respectively. This is the same test program and correction run used for the polymers in chapter 7, meaning a direct comparison is very accurate.

8.5.1 CT Scans

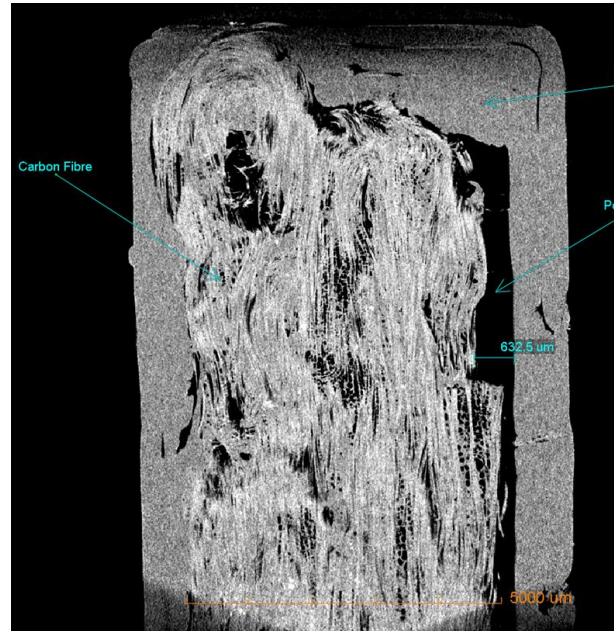
The CT scanning has been provided by the Advanced Imaging of Materials (AIM) facility. The scanning resolution between constituents can be approximated by the densities of each. The density of carbon fibre is twice that of nylon at $2g/cm^3$ compared to $1.15g/cm^3$ respectively. This provides an adequate level of determination between the two. Two scans have been performed, the first at a lower resolution encompassing the end of the sample with an imaging dimension of 7x7x10mm, and the second at a higher resolution focusing on a 1mm diameter x 1mm depth scan inside a section of fibres.



End View



Side View



Top View

Figure 268. CT scan of a nylon polymer with longitudinally oriented carbon-fibre filament. All views are taken from a middle cross-section.

The first images presented are of the first scan of the end of the sample. Here it is seen there is substantial porosity within the sample, as seen by the black space. The higher densities are lighter in colour, so the carbon fibre appears a lighter shade of grey compared to the nylon. Combining the image into a rendered solid and cutting a 3.5x3.5x7mm block out of the sample can visually emphasise where the fibre and porosity is located. The outside nylon can also be selectively removed to show just the fibre layers inside.

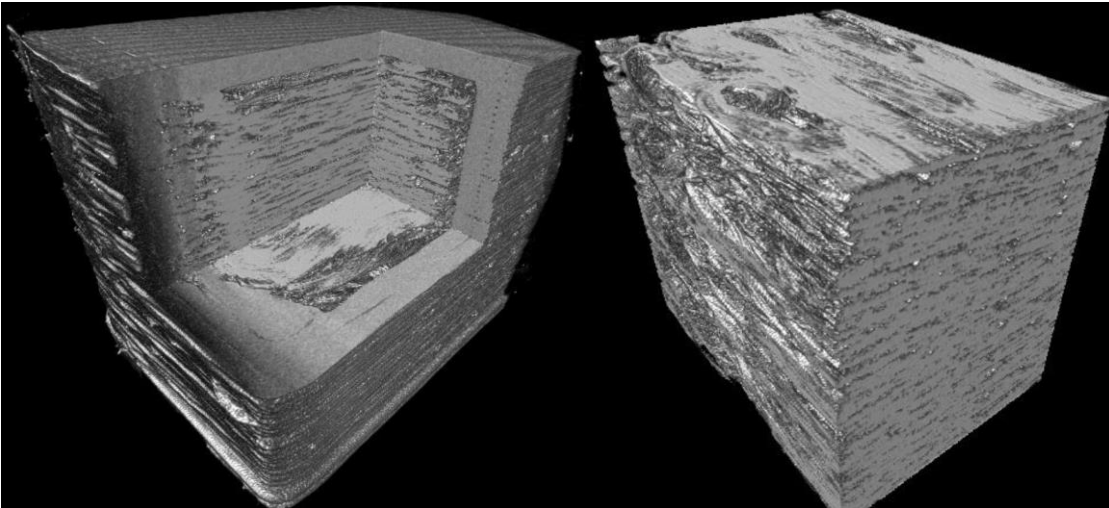


Figure 269. CT scan showing a rendered 3D view outside with a 3.5x3.5x7mm block removed (left) and the inside layers of carbon-fibre and nylon with the walls removed (right) of the longitudinally oriented carbon-fibre nylon dilatometer sample.

To better understand the behaviour inside a length of fibre, a 1mm diameter by 1mm length section of fibres has been scanned at a higher resolution. The length captures approximately 5 layers of nylon and fibre.

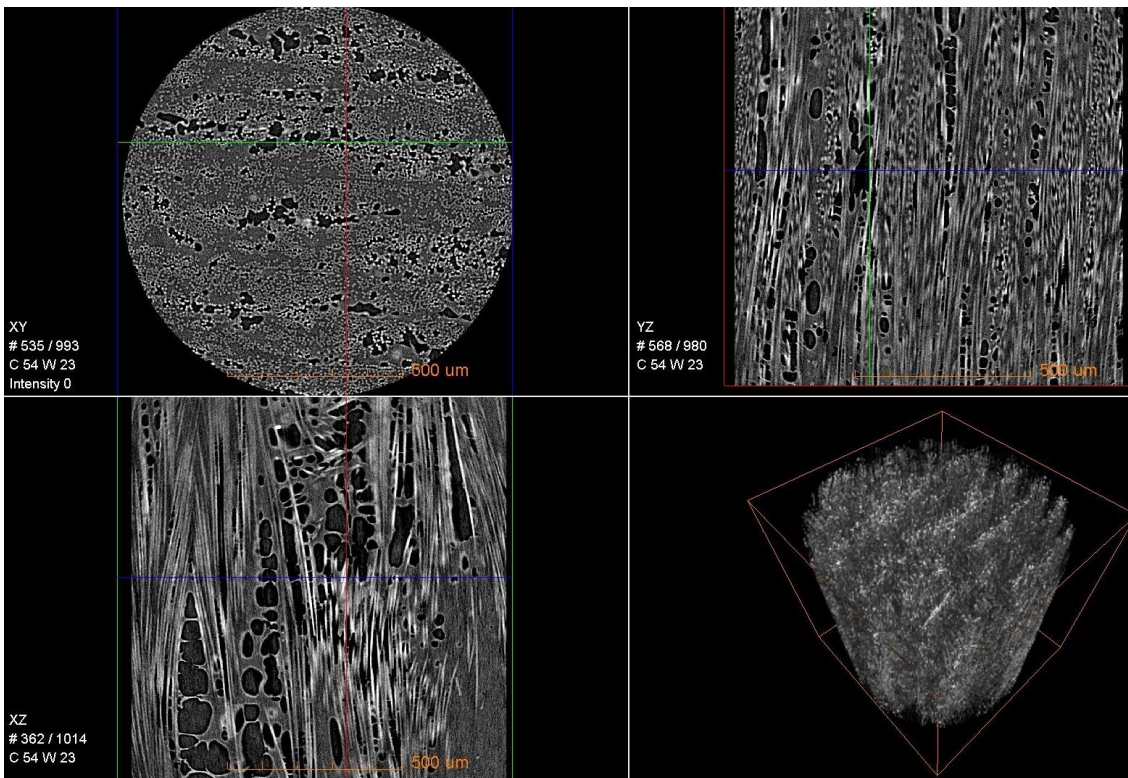


Figure 270. High resolution CT scan imagery of a 1mm diameter by 1mm length section of fibres in the centre of the longitudinally oriented carbon-fibre nylon dilatometer sample.

Inspecting the CT scan views in Figure 270. High resolution CT scan imagery of a 1mm diameter by 1mm length section of fibres in the centre of the longitudinally oriented carbon-fibre nylon dilatometer sample. it is observed that the carbon fibres themselves are surrounded by nylon, with areas of porosity. Looking at view XZ there is significant porosity in the nylon when the distance between the neighbouring carbon fibres become wider. This is also observed in view XY where the lighter shade signifies the location of the higher density carbon fibres, there is also black holes indicating porosity next to the fibres. Above and below these locations is the medium shade grey indicating the nylon is present in this region, which features limited porosity. This indicates that the porosity is more localised to the regions where the fibre is laid, and the subsequent layer is nylon applied with the primary nozzle does not penetrate the previous layer adequately to fill the voids between the fibres. It is also observed in Figure 268 that there are large voids around the outer wall at the end of the sample.

8.5.2 Thermal Expansion

To determine the thermal expansion of the polymer composite, the 25x7x7mm samples will be measured in the dilatometer over a temperature range of -120°C to 90°C using the same temperature program used to measure the polymers in chapter 7. All physical alpha curves will be smoothed to a level 8. Level 8 maintains any spikes caused by rapid expansion of the polymer, where the higher lettered levels will attempt to smooth these out over a wider temperature range creating inaccuracies. More information on the effect of smoothing can be found in the experimental method Chapter 4.2 and examples found on Figure 78.



Figure 271. Image of the Nylon Kevlar fibre orientated transverse to the test direction.

Nylon matrix material

The matrix material nylon has been used to print two of each fibre material and orientation. The sample will be discarded after the first test, and a new one printed for the repeat test. After the first test, the sample will be heat treated and no longer representative of the as-built condition. Presented is a physical alpha graph for each orientation, and a new graph for each fibre material.

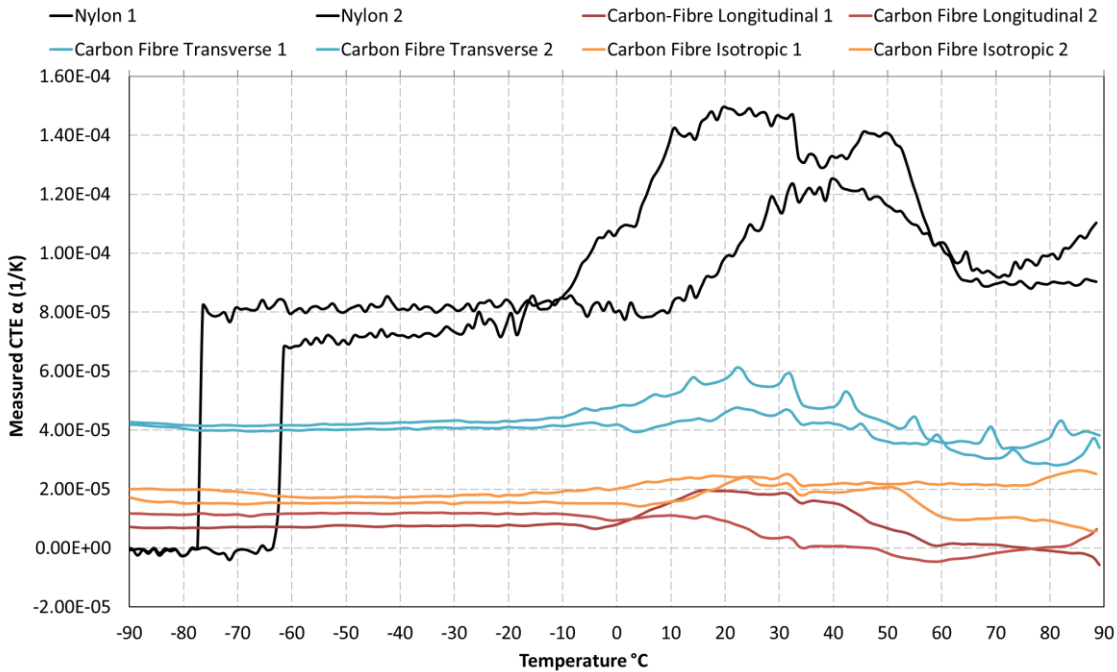


Figure 272. CTE curves for **nylon** matrix material and orientated **carbon-fibre**.

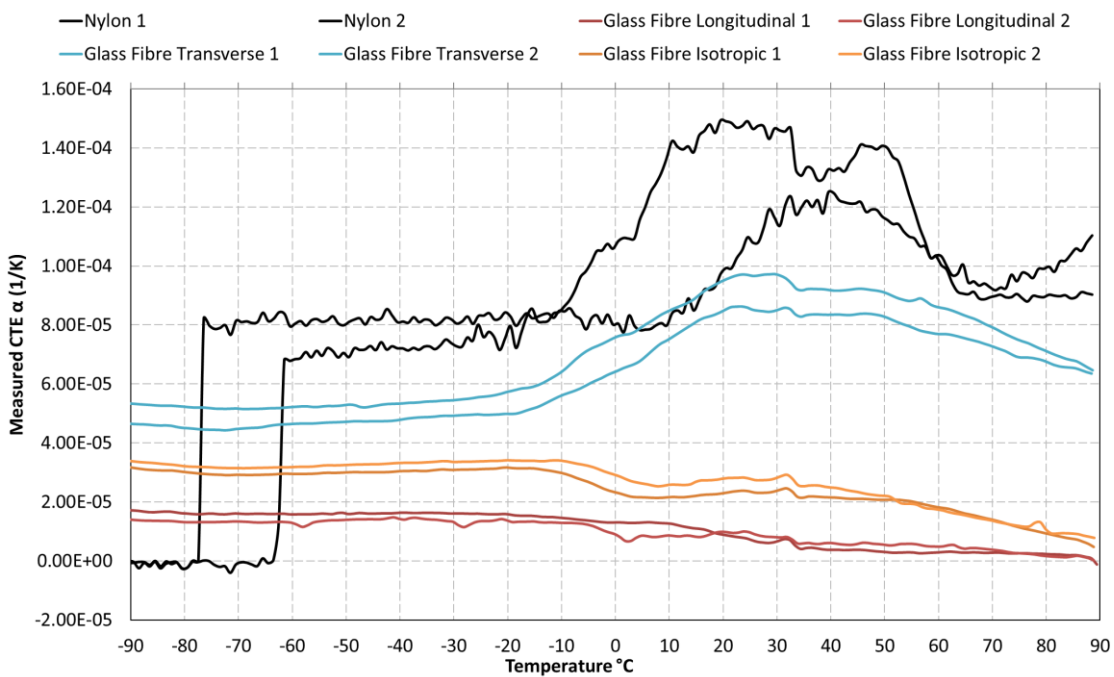


Figure 273. CTE curves for **nylon** matrix material and orientated **glass-fibre**.

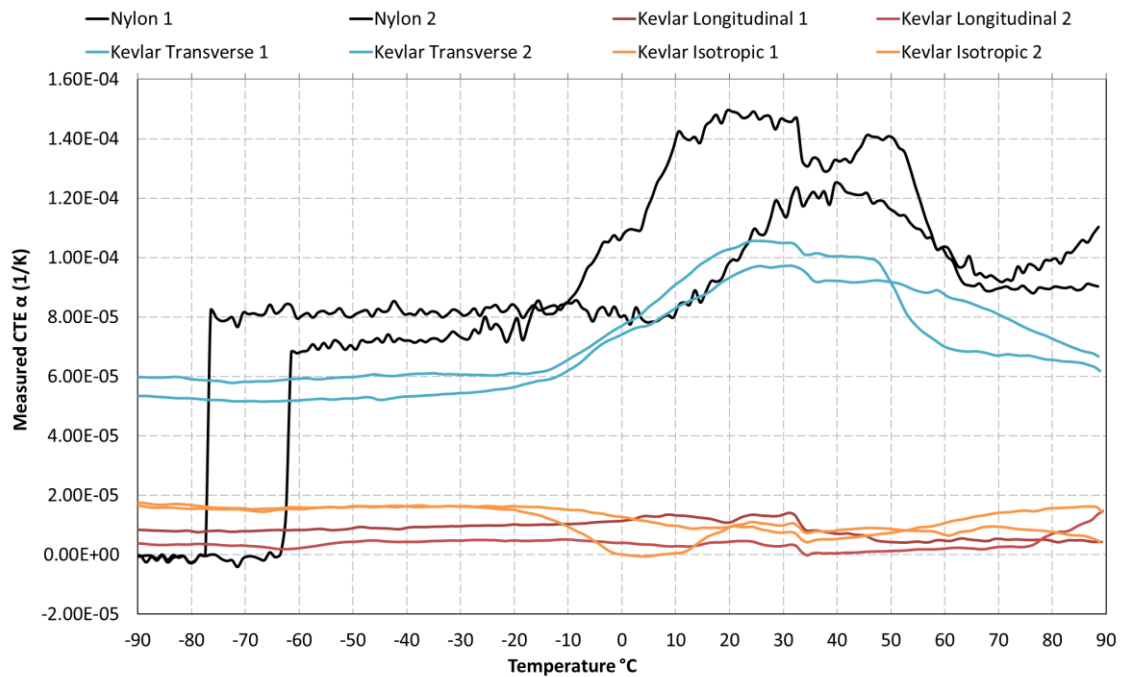


Figure 274. CTE curves for **nylon** matrix material and orientated **Kevlar fibre**.

Analysing the physical alpha thermal expansions, it is determined that at -40°C there is the most consistency across all orientations and material to obtain a value to be tabulated and used for comparison in Table 69 below. The average is taken across both readings at -40°C . The percentage decrease caused by the fibre introduction was calculated from the averaged reading for nylon without fibre at -40°C .

Polymer	Fibre	Fibre Orientation	Average CTE at -40°C ($\mu\text{m}/\text{mK}$)	CTE decrease with orientated fibre inclusion %
Nylon	-	-	76.7	-
Nylon	Carbon	Longitudinal	9.68	87.4
Nylon	Carbon	Transverse	41.7	45.6
Nylon	Carbon	Isotropic	16.3	78.7
Nylon	Glass	Longitudinal	15.3	80.1
Nylon	Glass	Transverse	50.8	33.8
Nylon	Glass	Isotropic	31.9	58.4
Nylon	Kevlar	Longitudinal	6.78	91.2
Nylon	Kevlar	Transverse	57.1	25.6
Nylon	Kevlar	Isotropic	16.4	78.6

Table 69. CTE's for oriented fibre reinforced nylon and the percentage reduction compared to the matrix polymer without the orientated fibres.

There is a wide range of thermal expansions available for nylon depending on the type and orientation of the fibre. It is observed that the tailorable range varies between 57.1 and 6.78 $\mu\text{m}/^\circ\text{C}$ at -40°C .

Onyx matrix material

Onyx is the material name given by Markforged for a nylon material with fine short chopped carbon fibres distributed evenly within the nylon matrix material. Data on the volume fraction is not provided by Markforged. To determine the behaviour of the material Onyx, nine dilatometer test measurements have been conducted with three samples, each tested three times. The first run shows a reduction in thermal expansion above 40°C , which is not seen on the second and third run. This can be attributed to stress relief after printing and improvements in crystallinity from the heat treatment. It is observed that onyx has a CTE of approximately 36-38 $\mu\text{m}/\text{mK}$ between -90 to -10°C , rising to a peak of 50-55 $\mu\text{m}/\text{mK}$ at 20°C where it largely remains.

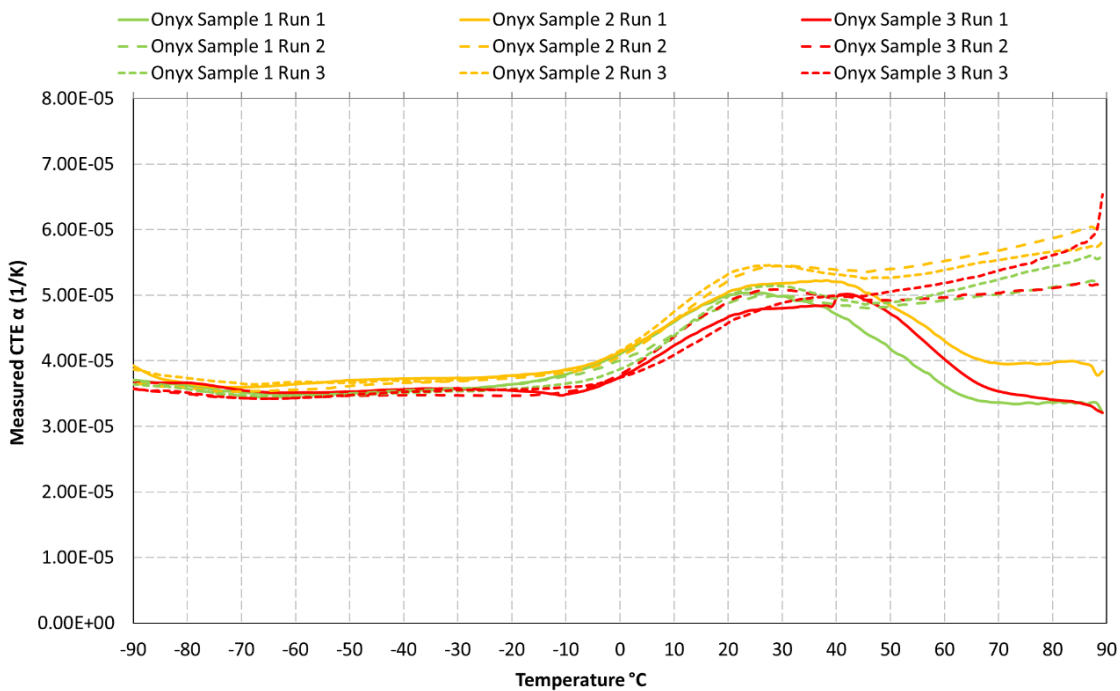


Figure 275. CTE curves showing thermal expansion for three identical Onyx samples, tested three times each. Shows stability of material over multiple temperature cycles.

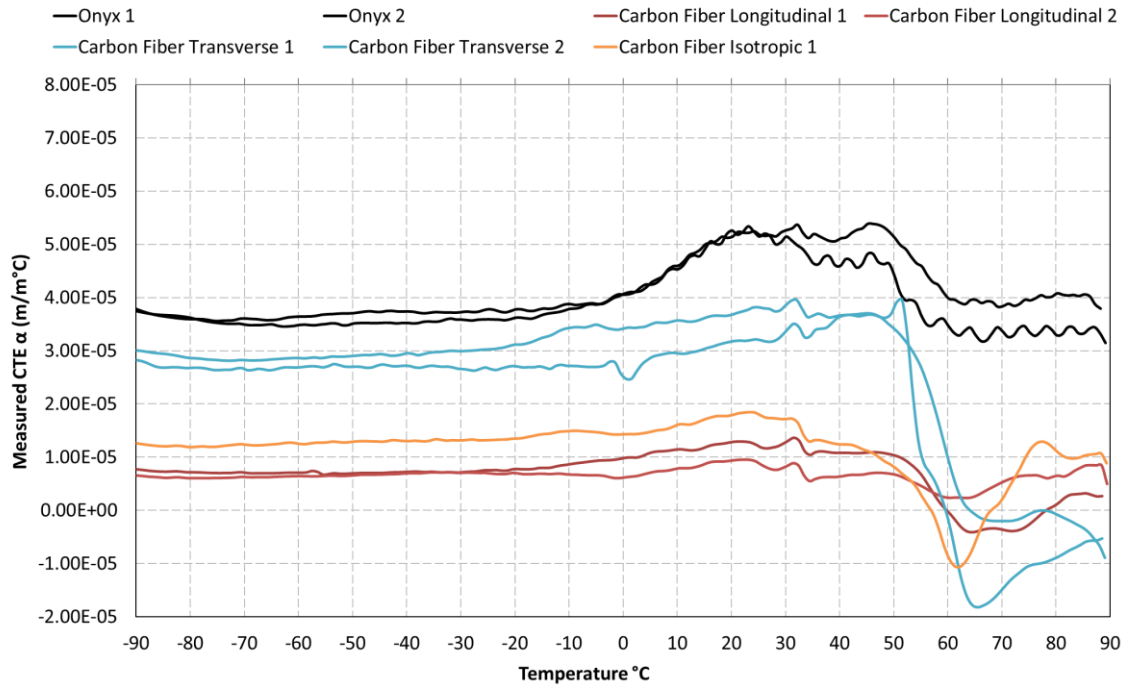


Figure 276. CTE curves for **Onyx** matrix material and orientated **carbon-fibre**.

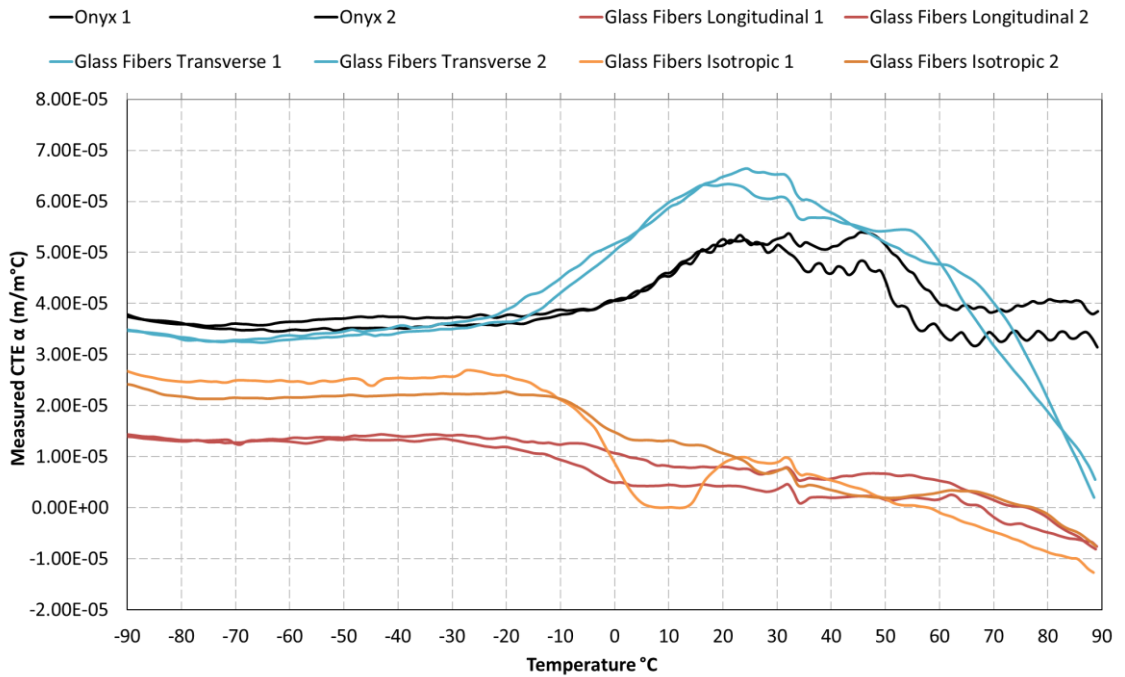


Figure 277. CTE curves for **Onyx** matrix material and orientated **glass-fibre**.

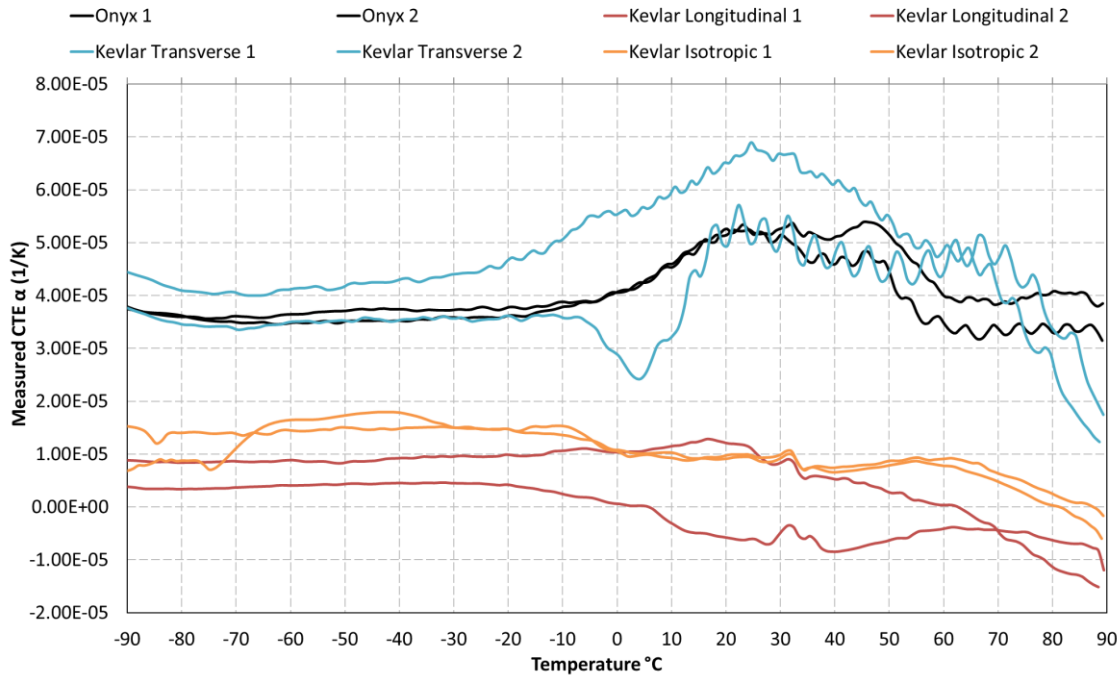


Figure 278. CTE curves for **Onyx** matrix material and orientated **Kevlar fibre**.

Analysing the physical alpha thermal expansions, it is determined that at -40°C there is the most consistency across all orientations and material to obtain a value to be tabulated and used for comparison in Table 70 below. The average is taken across both readings at -40°C . The percentage decrease caused by the fibre introduction was calculated from the averaged reading for nylon without fibre at -40°C .

Matrix material	Fibre	Fibre Orientation	Average CTE at -40°C ($\mu\text{m}/\text{mK}$)	CTE decrease with orientated fibre inclusion %
Onyx	-	-	36.3	-
Onyx	Carbon	Longitudinal	6.96	80.8
Onyx	Carbon	Transverse	28.3	22.0
Onyx	Carbon	Isotropic	6.5	82.1
Onyx	Glass	Longitudinal	13.6	62.5
Onyx	Glass	Transverse	35.1	3.3
Onyx	Glass	Isotropic	23.8	34.4
Onyx	Kevlar	Longitudinal	6.89	81.0
Onyx	Kevlar	Transverse	38.9	-7.2
Onyx	Kevlar	Isotropic	16.4	54.8

Table 70. CTE's for oriented fibre reinforced onyx and the percentage reduction compared to the matrix polymer without the orientated fibres.

There is a wide range of thermal expansions available for onyx depending on the type and orientation of the fibre. It is observed that the tailorable range varies between 38.9 and 6.5 $\mu\text{m}/^\circ\text{C}$ at -40°C .

8.6 Discussion on thermal expansion control in polymer AM using fibre reinforced material

This chapter has demonstrated that the manufacture of 3D printed polymer composites with continuous fibres can be achieved with a wide range of thermal expansions. The thermal expansions varying drastically depending on the orientation of the fibres, with longitudinally orientated fibres reducing thermal expansion the most, and transversely orientated fibres reducing the thermal expansion the least. To compare all the fibre orientation, fibre material, and matrix material together, a plot has been made from the CTE values at -40°C . The error bars plot both results, while the cross indicates the average of both results.

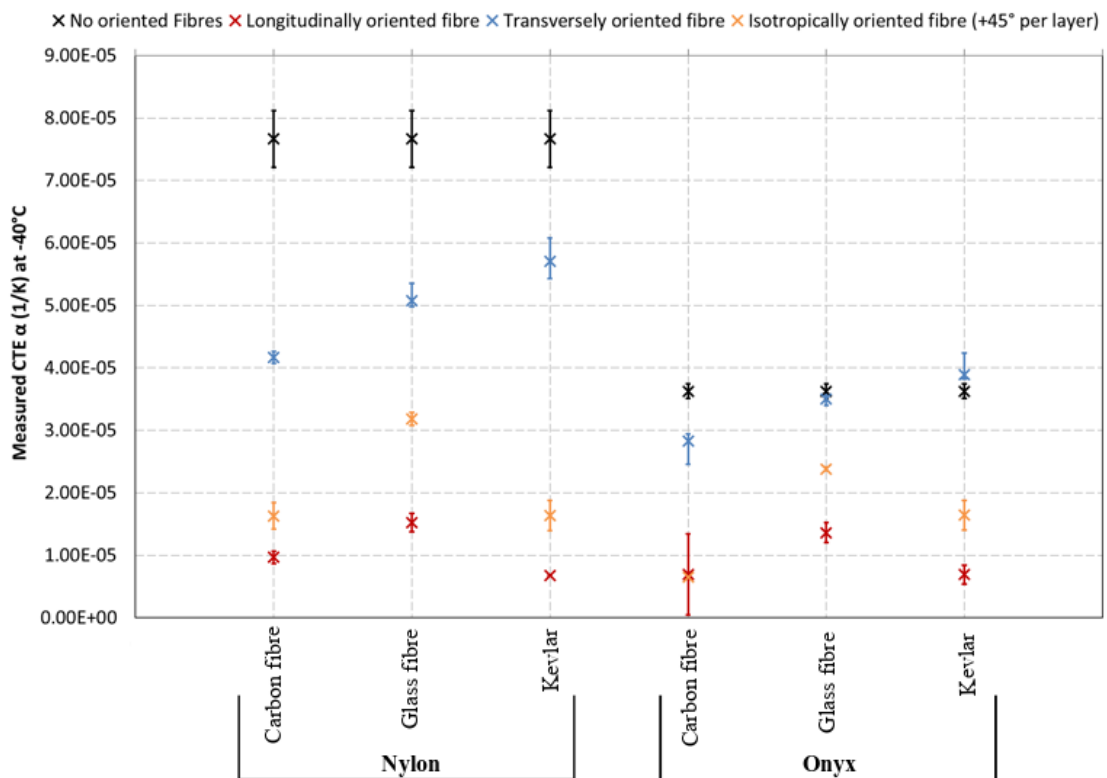


Figure 279. CTE values for instantaneous CTE at -40°C for all nylon and onyx with all fibre types and orientations.

By observing Figure 279 it is seen that the trends based on orientation apply to both nylon and onyx. Longitudinally oriented fibres remain approximately the same CTE regardless of the matrix material, whereas transversely oriented fibres do not. Kevlar exhibits the widest range of thermal expansion with orientation, featuring a lower CTE than glass

fibre longitudinally, but a higher CTE than glass fibre when oriented transversely. Carbon fibre remains the lowest thermal expansion across all orientations. Glass fibre produces the highest CTE when fibres are orientated longitudinally and isotopically, but not transversely. An interesting observation is that the sample with glass fibres orientated isotopically are approximately half the CTE of longitudinal and transverse orientations. This is not observed with carbon fibre and Kevlar where the CTE is very close to the longitudinal result. This shows that for equal thermal expansion in all directions, the isotropic orientation should be used with carbon fibre, or Kevlar, but not glass fibre. The onyx material with the isotopically oriented carbon fibre, shows the same CTE as the longitudinally oriented one. Therefore, onyx with isotopically orientated carbon fibre would be the ultimate choice for tailoring to near glass or germanium, featuring a CTE of $6.5\mu\text{m}/\text{mK}$. With longitudinally oriented fibre in onyx a negative thermal expansion can be achieved, but with greater

The CTE stability has been shown to increase in onyx when running a second and third dilatometer test run on the same sample compared to the as-built first test run. This is due to the heat treatment from cycling the material to 90°C and back to room temperature, relieving some of the residual stresses, and increasing the crystallinity of the semi-crystalline nylon. It is observed that in all test runs 1-3 a CTE increase from between -10°C to 20°C occurs from approximately 35 to $50\mu\text{m}/\text{mK}$. At 40°C after the as-built condition decreases in CTE back to its previous value, whereas tests 2 and 3 remain at $50\mu\text{m}/\text{mK}$ until the test ends. This indicates that for better thermal expansion rate stability above 40°C heat treatment is required. Although this experiment has only been carried out on onyx, it can be assumed a similar heat treatment behaviour will be observed for straight nylon.

The lowest thermal expansions achieved were between $6.5-7\mu\text{m}/\text{mK}$ meaning that several orientations can be used to match the CTE of glass or germanium with a CTE of between $6-7\mu\text{m}/\text{mK}$. With the ZEONEX[®] polymer lens featuring a CTE of $60\mu\text{m}/\text{mK}$, only the transversely oriented glass fibre in nylon provides a close CTE of $57.1\mu\text{m}/\text{mK}$.

The CT scans show reasonable cohesion between nylon and carbon fibre, although some porosity was observed within the fibre itself, and a lot of porosity was discovered on the outer wall of the end of the sample. This could be due to the expectation of a fibre which was expected to be in this region, but unfortunately was terminated before the end of the sample due to firmware issues. This early termination should be of limited influence on structural properties as the component scales up to a full optical system body, since the void becomes a smaller proportion of the actual part. The porosity amongst the fibres could affect the mechanical performance over time. Improvements to the process to

reduce these voids can be achieved by ensuring all moisture is removed from the nylon, the that the extrusion temperatures and feed rates are optimal.

8.7 Conclusions on thermal expansion control in polymer AM using fibre reinforced material

To conclude this chapter has been successful in 3D printing a continuous fibre polymer composite with a tailored thermal expansion based on the fibre material, orientation, and matrix material. To summarise;

- The orientation of the fibre has a significant impact on the thermal expansion, with longitudinal reducing thermal expansion the most, and transverse the least.
- Orientating at increments of 45° produces low thermal expansion close to that of longitudinal orientation in carbon and Kevlar fibre.
- In nylon, the CTE has been reduced by a maximum average of 91.2% from 76.7 to $6.78\mu\text{m}/\text{mK}$ in longitudinally oriented Kevlar.
- In onyx, the CTE has been reduced by a maximum average of 82.1% from 36.3 to $6.5\mu\text{m}/\text{K}$ in isotopically oriented carbon fibre.
- Selected configurations can be chosen to approach a similar CTE to that of glass or germanium ($6\text{-}7\mu\text{m}/\text{mK}$), which is highly unique for a polymer.
- The matrix material nylon and onyx benefits from a heat treatment cycle to improve thermal expansion stabilise thermal expansion rate above 40°C .
- CT scans show porosity in the regions around the outer walls of the part. Smaller regions of porosity are found inside the fibre layer, where the fibres separate.

9 Final Discussion

9.1 Thermal expansion control by design

Thermal expansion control of an optical system has been achieved by designing a unique multi-material structure that exists around a cylindrical lens. The featured designs consist of extruded 2D profiles that tailor thermal expansion radially to match the thermal expansion of the lens material. The designs all have a secondary material featuring a different CTE, which is laser cladded around the outside circumference of the first material. The structure of the first material is manufactured with LPBF, and features either an auxetic structure, or a holed structure depending on the design. The auxetic structure occupies 20mm radially, whereas the holed structure occupies only 5mm radially, making it more compact. Each variation of the auxetic lattice angle is simulated, with the results showing a variable thermal expansion from 15.1 to $7.8\mu\text{m}/\text{mK}$ with an invar structure

and 316L clad. With the same materials, the stacked array of holes can vary from 9 to $4.4\mu\text{m}/\text{mK}$, by adjusting hole diameter. The stacked array of holes has a higher simulated maximum stiffness of 71GPa rather than the auxetic structures has a much lower 0.81GPa. The measurement results for thermal expansion do not match those from the simulation but do support the conclusion that increasing the auxetic angle reduces thermal expansion radially. The measured CTE is higher in every design compared to the simulated CTE. This is potentially caused by the clad material cooling and shrinking around the structure, due to its higher CTE. The cooling effect has compressed the structure, and measuring the CTE with the application of heat has released some of the residual stresses creating an observed increase in CTE.

To conclude; this method has been shown to be viable from a theoretical standpoint but not from a practical one. The lack of concentricity shown in chapter 2 in LPBF produced parts means the manufactured components will require additional post processing to ensure lenses are aligned. More research is needed to mitigate the residual compression stresses caused by the cooling of the clad 316L. This could be achieved with future multi-metallic AM processes that have the possibility to print the structure in one process, eliminating internal stresses. This will bring the measured CTE in line with the simulated CTE. Future work should look into designs that tailor CTE across each lens, in the third dimension. In its current design, the clad material would create a bowing effect across the third dimension, unless compensated for with a graded thickness of clad secondary material.

9.2 Thermal expansion control using metal AM

The control of thermal expansion using metal AM has been achieved by varying the elemental constituents of the components produced. Chapter 6 demonstrates the effectiveness of adjusting the nickel content of invar to produce CTE's ranging from 0.68 to $8.35\mu\text{m}/\text{mK}$ by adding iron or nickel powder to the gas atomised invar powder and mixing together. The resulting components experienced similar tensile and hardness performance after +1-2wt.% additions. Higher percentage additions such as 7wt.% nickel experiences a CTE of $8.35\mu\text{m}/\text{mK}$ after heat treatment, demonstrating the ability to slightly reduce the nickel content in future work to achieve a CTE closer to glass or germanium at $6-7\mu\text{m}/\text{mK}$. Adjusting the thermal expansion with laser parameters was achieved, but only by a maximum of $0.32\mu\text{m}/\text{mK}$. The corresponding increase of porosity made this method impractical.

AlSi-30 and AlSi40 were printed, and despite the high silicon content, no microcracking was observed. The finer microstructure produces harder components than traditionally

manufactured spray formed parts at 218 compared to 92 HV2. The density is also slightly higher, and the low expansion property slightly improved. The thermal expansion can be reduced by increasing the silicon content, so to show that CTE tailoring is possible, AlSi35 was made by mixing AlSi30 and AlSi40 together with a 50% ratio. The resulting CTE was in between that of both. AlSi30, 35, and 40, exhibited 16.6, 14.9, and 12.7 $\mu\text{m}/\text{mK}$. Increasing the silicon to 70-80wt.% can tailor the CTE from 7.76 to 6.1 $\mu\text{m}/\text{mK}$ when manufactured with spray forming. For future work, it would be useful to attempt to print an AlSi alloy with a higher silicon content using LPBF to create parts can match the CTE of glass or germanium. It would also be useful to print larger components and look for cracking caused by the component size increase.

9.3 Thermal expansion control using polymer AM

Methods of controlling thermal expansion using a multi-material polymer FDM printers has been investigated. The most successful method introduces inclusion of carbon and glass fibres, with wood, bronze, brass, and iron metal particles, into the PETG or PLA polymer. These have tailored the CTE within a wide range of between 65.5 and 18.6 $\mu\text{m}/\text{mK}$. The control of the volume fraction of carbon fibres is considered to be the best method of tailoring thermal expansion to that of glass, germanium, or ZEONEX lens material. Further work would need to be conducted to determine the volume fractions required, and manufacture of these materials is required in-house, as manufacturers do not disclose volume fraction content. Attempts to print with multi-material composite structures using ABS and CPE have shown a tailorable range between 82.5 to 75 $\mu\text{m}/\text{mK}$. This method will require future work to further define material parameters at a range of temperatures, and a transient simulation model used to better predict the thermal expansion values. The geometric tolerances shown in chapter 5 show that FDM provides a relative circularity of 0.25% and relative deviation from nominal diameter of 650 μm . It is important to get high tolerances in polymer AM parts since post process machining is more challenging compared with metals.

9.4 Thermal expansion control using fibre-reinforced polymer AM

The control of thermal expansion using AM fibre-reinforced polymer composites has provided the ability to adjust thermal expansion depending on the fibre orientation within the composite. This is useful as it provides the engineer with the ability to tune the thermal expansion of an optical system in the direction required. The material of the fibre has an effect on the overall thermal expansion of the composite, but the orientation of those fibres in the composite effect the thermal expansion the most. The fibres oriented longitudinally to the test direction show a large reduction in the thermal expansion, closely followed by the isotropic arrangement, and then the transverse arrangement.

When selecting a configuration of fibre orientation, material, and matrix material, Figure 279 can be used for an approximate comparison, with greater detail gained for specific temperature ranges from the physical alpha graphs in chapter 8.5.2. It is observed that a CTE of less than $7\mu\text{m}/\text{mK}$ can be achieved with specific arrangements, opening the possibility to tailoring the material to the same CTE as glass or germanium. The use of carbon fibre and Kevlar has produced some of the lowest CTE arrangements in onyx and nylon. The polymer lens ZEONEX[®] has a higher CTE than any metal ($60\mu\text{m}/\text{mK}$) so polymers are the only material that can be used to match the high thermal expansion. One combination with transverse glass fibre and nylon comes closest to the ZEONEX[®] polymer lens with a CTE of $57.1\mu\text{m}/\text{mK}$.

The use of AM fibre-reinforced polymers may produce highly anisotropic thermal expansion if all fibres are orientated in one direction. The isotropic arrangement with its 45° orientation change on each layer provides a means to obtain better isotropy. The dilatometer results in Figure 279 show that the low CTE effect of a longitudinally oriented fibre is maintained when adding subsequent 45° oriented fibres on top, but only for certain materials. Carbon fibre isotropic orientation provides the closest similarity to longitudinally oriented samples in both nylon and especially in onyx, while Kevlar comes in a close second place. Glass fibre does not conform to the observed behaviour and instead expands at a value of halfway in-between transverse and longitudinal orientations. For improved thermal expansion stability past 40°C , heat treatment was found to be effective at keeping the matrix material at a steady physical alpha. CT scans show regions of porosity around any separated fibres, and larger voids around the outer wall at the sample ends.

9.5 Controlling thermal expansion in optical applications

The technical objectives for the investigation are to obtain a method of adjustable CTE to match that of glass, germanium, and Zeonex at 6.1 , 7.1 , and $60\mu\text{m}/\text{mK}$ respectively. There have been several methods attempted to achieve this, including design, and material tailoring. The designs, manufacture and testing of designed solutions has provided a range of solutions in theory, with testing displaying accurate trends, but not exact values. Further work needs to be carried out to improve modelling and increase the feasibility of such designs. The material tailoring is the most promising avenue for further exploration, showing FeNi and AlSi to be tailorable by mixing powders and printing in-situ. To match glass and germanium, a 5-6wt.% addition of nickel is proposed for future work. The CTE control with fibre-reinforced polymers has provided a wide range of CTE's to choose from, with material arrangements and fibre orientations to tailor to glass, germanium, and Zeonex. The polymers have shown that with inclusions of carbon fibre, the CTE can be drastically reduced, and controlling the volume fraction can allow for the tailoring of the

CTE, although a specific volume fraction requires further work to obtain to match that of the lens material.

Another technical objective was to achieve 10 μ m tolerances on the inner radius. The benchmark results in chapter 5 suggest that this will be a difficult task to achieve with all forms of additive manufacturing. The relative deviation with respect to the diameter for metal, polymer, and polymer-fibre, are 700, 650, and 250 μ m. It is observed however, that with changing diameter, the percentage deviation relative to the diameter remains consistent, meaning the nominal diameter can be offset to match the relative percentage deviation. Circularity varies depending on the process type with relative circularity percentages of metal, polymer, and polymer-fibre of 0.14, 0.29, 0.22%. The circularity mismatch would need to be offset in CAD, with CMM used to verify. Without post processing, and fine tuning through multiple builds, the parts produced using all process types would not match the \pm 10 μ m tolerance.

10 Conclusions

10.1 Summary of outcome of work

The objectives of this thesis are outlined, and work completed summarised;

- Investigate the latest advancements in additive manufacturing for deployment of tailored thermal expansion solutions.

In this work various materials and additive manufacturing processes have been investigated through literature. The possible application of these additive processes to the manufacture of optical lens systems has been explored, with the main design criteria being the control of thermal expansion. This has been achieved by adjusting the material feedstock for the AM processes, and through the design of dual material structures.

- Benchmarking current additive manufacturing processes to assess feasibility for production of components in the optical industry.

Benchmarking has been completed on a metal laser powder bed fusion machine, polymer fused deposition modelling machine, and a state-of-the-art polymer continuous fibre fabrication fused deposition modelling machine. The geometric variations in concentricity, diameter, wall thicknesses, and gap resolution have been obtained. The conclusion has been made that the technology is currently not in a position to manufacture parts with \pm 10 μ m tolerances. The parts can be designed with the geometric tolerances provided to be adjusted by a percentage to make the nominal deviation less. The processes

would require a secondary milling operation on critical surfaces, where circularity, nominal dimension, or surface finish are important.

- Investigate thermal expansion control structures with multi-material additive manufacturing techniques.

The control of thermal expansion through design with two materials is a novel theory applicable to the area of physics and mathematics. Through modelling and simple experiments in this work it has been verified that at least in principle it is possible to control thermal expansion depending on key geometric design variations. Most current metal AM systems work with only one material, and the application of laser cladding for the second material introduces high residual stresses due to the CTE differences between the materials. This effects the overall thermal expansion and deviates the measured result away from that of the static-thermomechanical model. Furthermore, the geometrical tolerances are also an issue, since the dimensions of the structures are directly driving the thermal expansion. With the polymer AM printing on the other hand it is possible to combine more than one material, but the overall thermal expansion and stiffness are a function of temperature and not necessarily those required by the optical lens application.

- Investigate methods of controlling thermal expansion with laser powder bed fusion using controlled expansion alloys.

Thermal expansion of the metal printed using LPBF can be tuned by adjusting the elemental constituents of the metal powder. This is achieved with gas atomised FeNi36, AlSi30 and AlSi40. Fine Fe or Ni powder can be added to FeNi36 to adjust its thermal expansion with minimal effect on mechanical performance. Higher additions of up to 7% nickel have been fully alloyed after heat treatment and proved that the CTE can be matched with glass or germanium. AlSi 30 and AlSi40 were successfully printed despite the difficulty of manufacture due to brittleness, higher densification than convention spray forming was achieved, with lower thermal expansion and higher hardness. AlSi 30 and AlSi40 were mixed together in an even ratio to show the ability to tailor the thermal expansion to that of halfway in-between both, demonstrating the ability to tailor CTE in-situ.

- Investigate controlled expansion polymers for printing using fused deposition modelling.

Thermal expansion of polymer printed using FDM can be tuned by adding inclusions into the polymer PLA or PETG feedstock material. Carbon and glass fibre have been added,

including organic and metal particles. Carbon and glass fibre produced the most stable linear CTE behaviour, while all others increased with temperature. Brass particle inclusions provided the nearest CTE to that of Zeonex polymer lens material, and carbon fibre provided the lowest CTE. Carbon fibre inclusion is the most suitable as a practical material as it's the strongest out of all the materials. Varying the volume fraction of the carbon fibre can be used as a method to adjust the CTE. The percentage volume fraction of the fibre is undisclosed by the manufacturer, so to tailor thermal expansion based on volume fraction the material would need to be commissioned or made in house specifically at the fraction required to obtain a specified CTE.

- Investigate additively manufactured controlled expansion fibre reinforced polymers.

Thermal expansion of fibre-reinforced polymers using state-of-the-art FDM techniques have been tailored over the widest range of thermal expansions out of all process methods tested. It provides direct arrangements of fibre orientation and materials to produce tailored CTE's for glass, germanium, and Zeonex. The thermal expansion can be designed to be either isotropic or anisotropic depending on the requirements. This is highly novel, and not published in literature to the best of the authors knowledge.

10.2 Future work requirements

There are areas in each chapter that can be expanded upon to improve on the solutions offered to Qioptiq. There was significant work carried out to obtain a digital image correlation test bench in chapter 4.8.1 which had the aim of determining thermal expansion of structures using a hotplate and a camera to track the image as the structure expands. The setup was successful in measuring the thermal expansion changes on a 60x40mm rectangle but was unable track the speckled pattern on the surface of a larger structure of 100x100mm. Further work to replace the 12-megapixel camera with a higher resolution camera would improve the capability for measuring larger samples. Current DSLR cameras on the market can achieve up to 61-megapixels which would provide more pixels for the software to track. The speckled pattern applied to the surface of the structure turned from brilliant white to an off white with a yellow tint as the temperature increased past 150°C. A higher resolution camera would also provide the ability to track smaller changes to the image, requiring a lower temperature change across the sample to determine the thermal expansion. The lighting needed improving to ensure a consistent source was present. This could be achieved through a light box surrounding the sample and hotplate, ensuring ambient light is not present. The mounting of the camera to the stand could be re-designed to reduce the vibrations from ambient sources. If all of these

changes are made, the DiC test rig would be able to measure the thermal expansion of the bi-material structure and all its members.

An investigation was carried out to determine if blending iron and nickel powder into invar36 powder and manufacturing with LPBF would result in a homogeneous distribution of the elements in the alloy, with the expected thermal expansion for the composition. This was successful for $\pm 2\%$ additions, but unsuccessful for a $+7\%$ nickel addition. The alloy was discovered to be non-homogenous in elemental distribution throughout a cross-section. Further work determining the elemental homogeneity after a heat treatment cycle would be beneficial to understanding if heat treatment could be used as a method of dissipating iron and nickel rich areas within the alloy. The heat treatment of the alloy was shown to increase the thermal expansion of the alloy, indicating some dissipation of iron and nickel had occurred, but this was not verified with EDS. Further work should include manufacturing with invar36 powder that includes a series of nickel additions between $+6-8\text{wt.}\%$ nickel, to determine the quantity required to match germanium's CTE of $6.1\mu\text{m/mK}$.

Aluminium-silicon alloys with between 30 and 40wt.% silicon were manufactured using LPBF instead of the conventional method of spray forming. The high silicon content in the alloy has shown in dilatometer results have thermal expansion of $12.7\mu\text{m/mK}$ for 40wt.% silicon. Spray formed parts AlSi80wt.%, and AlSi87wt.% manufactured by Sandvik-osprey can produce CTE's of $6.5\mu\text{m/mK}$ and $5.1\mu\text{m/mK}$ close to that of germanium and glass. Future work needs to be completed to investigate whether its possible to print these high silicon AlSi80-87wt.% alloys and obtain similar thermal expansions as their spray formed counterparts.

In chapter 7 polymer printing materials were found that had inclusions thought to lower the co-efficient of thermal expansion. The polymer feedstock material had been mixed with various particles by the manufacturer of the product. Results shown that short chopped carbon fibres mixed into PETG were particularly effective at lowing the thermal expansion from 78 to $18.6\mu\text{m/mK}$. It is not known what the volume fraction of carbon fibre is because the manufacturer regards it as a trade secret. Further work is needed to manufacture materials in-house with various volume fractions of short-chopped carbon fibres. Understanding the effect of the volume fraction on the thermal expansion will provide a robust means of tailoring to produce a the CTE required for the component.

References

- [1] Wohlers, “Wohlers Report,” 2020.
- [2] C. A. Steeves, S. L. dos Santos e Lucato, M. He, E. Antinucci, J. W. Hutchinson, and A. G. Evans, “Concepts for structurally robust materials that combine low thermal expansion with high stiffness,” *J. Mech. Phys. Solids*, vol. 55, no. 9, pp. 1803–1822, 2007.
- [3] C. A. Steeves, C. Mercer, E. Antinucci, M. Y. He, and A. G. Evans, “Experimental investigation of the thermal properties of tailored expansion lattices,” *Int. J. Mech. Mater. Des.*, vol. 5, no. 2, pp. 195–202, 2009.
- [4] O. Sigmund and S. Torquato, “Design of Materials With Extreme Thermal Expansion Using a Three-Phase Topology,” *J. Mech. Phys. Solids*, vol. 45, no. 6, pp. 1037–1067, 1997.
- [5] O. Sigmund and S. Torquato, “Composites with extremal thermal expansion coefficients,” *Appl. Phys. Lett.*, vol. 69, no. 21, pp. 3203–3205, 1996.
- [6] G. Jefferson, T. A. Parthasarathy, and R. J. Kerans, “Tailorable thermal expansion hybrid structures,” *Int. J. Solids Struct.*, vol. 46, no. 11–12, pp. 2372–2387, Jun. 2009.
- [7] R. Lakes, “Cellular solid structures with unbounded thermal expansion,” *J. Mater. Sci. Lett.*, vol. 15, no. 6, pp. 475–477, 1996.
- [8] J. Lehman and R. Lakes, “Stiff lattices with zero thermal expansion,” *J. Intell. Mater. Syst. Struct.*, vol. 23, no. 11, pp. 1263–1268, 2012.
- [9] H. Xu, A. Farag, and D. Pasini, “Multilevel hierarchy in bi-material lattices with high specific stiffness and unbounded thermal expansion,” *Acta Mater.*, vol. 134, pp. 155–166, Aug. 2017.
- [10] C. A. Steeves and A. G. Evans, “Optimization of thermal protection systems utilizing sandwich structures with low coefficient of thermal expansion lattice hot faces,” *J. Am. Ceram. Soc.*, vol. 94, no. SUPPL. 1, pp. s55–s61, Jun. 2011.
- [11] J. Berger, C. Mercer, R. M. McMeeking, and A. G. Evans, “The design of bonded bimaterial lattices that combine low thermal expansion with high stiffness,” *J. Am. Ceram. Soc.*, vol. 94, no. SUPPL. 1, pp. s42–s54, Jun. 2011.
- [12] S. C. Daminabo, S. Goel, S. A. Grammatikos, H. Y. Nezhad, and V. K. Thakur, “Fused deposition modeling-based additive manufacturing (3D printing): techniques for polymer material systems,” *Materials Today Chemistry*, vol. 16. Elsevier Ltd, p. 100248, 01-Jun-2020.
- [13] A. P. Valerga, M. Batista, R. Puyana, A. Sambruno, C. Wendt, and M. Marcos, “Preliminary study of PLA wire colour effects on geometric characteristics of parts manufactured by FDM,” *Procedia Manuf.*, vol. 13, pp. 924–931, Jan. 2017.
- [14] T. Singh, S. Kumar, and S. Sehgal, “3D printing of engineering materials: A state of the art review,” *Mater. Today Proc.*, vol. 28, pp. 1927–1931, Jun. 2020.
- [15] V. Mazzanti, L. Malagutti, and F. Mollica, “FDM 3D Printing of Polymers Containing Natural Fillers: A Review of their Mechanical Properties,” *Polymers (Basel)*, vol. 11, no. 7, p. 1094, Jun. 2019.
- [16] K. Salonitis, J. Pandremenos, J. Paralikas, and G. Chryssolouris, “Multifunctional materials: Engineering applications and processing challenges,” *Int. J. Adv. Manuf. Technol.*, vol. 49, no. 5–8, pp. 803–826, Jul. 2010.
- [17] E. M. Palmero *et al.*, “Composites based on metallic particles and tuned filling factor for 3D-printing by Fused Deposition Modeling,” *Compos. Part A Appl. Sci. Manuf.*, vol. 124, p. 105497, Sep. 2019.
- [18] L. G. Blok, M. L. Longana, H. Yu, and B. K. S. Woods, “An investigation into 3D printing of fibre reinforced thermoplastic composites,” *Addit. Manuf.*, vol. 22, pp. 176–186, Aug. 2018.
- [19] Deborah D.L. Chung, *Carbon Fiber Composites*. Butterworth-Heinemann, Newton, MA, 1994.
- [20] R. Kulkarni and O. Ochoa, “Transverse and longitudinal CTE measurements of carbon fibers and their impact on interfacial residual stresses in composites,” *J. Compos. Mater.*, vol. 40, no. 8, pp. 733–754, Apr. 2006.
- [21] G. Korb, J. Koráb, and G. Groboth, “Thermal expansion behaviour of unidirectional carbon-fibre-reinforced copper-matrix composites,” *Compos. Part A Appl. Sci. Manuf.*, vol. 29, no. 12, pp. 1563–1567, Dec. 1998.
- [22] M. yan Zhang, K. zhi Li, X. hong Shi, L. jun Guo, L. Feng, and T. Duan, “Influence of cryogenic thermal cycling treatment on the thermophysical properties of carbon/carbon composites between room temperature and 1900 °C,” *J. Mater. Sci. Technol.*, vol. 34, no. 2, pp. 409–415, Feb. 2018.
- [23] B. Yates *et al.*, “The thermal expansion of carbon fibre-reinforced plastics - Part 2 The influence of fibre volume fraction,” *J. Mater. Sci.*, vol. 13, no. 2, pp. 433–440, Feb. 1978.
- [24] M. Barucci, G. Bianchini, T. Del Rosso, E. Gottardi, I. Peroni, and G. Ventura, “Thermal expansion and thermal conductivity of glass-fibre reinforced nylon at low temperature,” *Cryogenics (Guildf)*,

- vol. 40, no. 7, pp. 465–467, Jan. 2000.
- [25] R. Matsuzaki *et al.*, “Three-dimensional printing of continuous-fiber composites by in-nozzle impregnation,” *Sci. Rep.*, vol. 6, no. 1, p. 23058, Sep. 2016.
- [26] T. D. Ngo, A. Kashani, G. Imbalzano, K. T. Q. Nguyen, and D. Hui, “Additive manufacturing (3D printing): A review of materials, methods, applications and challenges,” *Compos. Part B Eng.*, vol. 143, pp. 172–196, Jun. 2018.
- [27] D. Espalin, J. A. Ramirez, F. Medina, and R. Wicker, “Multi-material, multi-technology FDM: Exploring build process variations,” *Rapid Prototyp. J.*, vol. 20, no. 3, pp. 236–244, Apr. 2014.
- [28] M. Chapiro, “Current achievements and future outlook for composites in 3D printing,” *Reinf. Plast.*, vol. 60, no. 6, pp. 372–375, Nov. 2016.
- [29] A. Le Duigou, A. Barbé, E. Guillou, and M. Castro, “3D printing of continuous flax fibre reinforced biocomposites for structural applications,” *Mater. Des.*, vol. 180, p. 107884, Oct. 2019.
- [30] S. S. Milward, H. Swygart, L. Eccles, S. G. R. Brown, and N. P. Lavery, “Controlling thermal expansion with lattice structures using laser powder bed fusion,” in *Solid Freeform Fabrication Symposium*, 2017.
- [31] J. H. Burge, T. Peper, and S. F. Jacobs, “Thermal Expansion of Borosilicate Glass, Zerodur, Zerodur M, and Uncer amized Zerodur at Low Temperatures,” *Appl. Opt.*, vol. 38, no. 34, p. 7161, Dec. 1999.
- [32] D. Luo and Z. Shen, “Wetting and spreading behavior of borosilicate glass on Kovar,” *J. Alloys Compd.*, vol. 477, no. 1–2, pp. 407–413, May 2009.
- [33] A. K. Tyagi and S. N. Achary, “Tailored Thermal Expansion Material for High-Temperature Applications,” in *Materials Under Extreme Conditions: Recent Trends and Future Prospects*, Elsevier, 2017, pp. 471–500.
- [34] C.-É. Guillaume, “Recherches sur les aciers au nickel,” *J. Phys. Théorique Appliquée*, vol. 7, no. 1, pp. 262–274, 1898.
- [35] “I. Magnetic properties of alloys of Nickel and iron,” *Proc. R. Soc. London*, vol. 48, no. 292–295, pp. 1–13, Jan. 1891.
- [36] Y. Nakamura, “The Invar Problem,” *IEEE Trans. Magn.*, vol. 12, no. 4, pp. 278–291, Jul. 1976.
- [37] E. P. Wohlfarth, “Invar behaviour in crystalline and amorphous alloys,” *J. Magn. Magn. Mater.*, vol. 10, no. 2–3, pp. 120–125, Feb. 1979.
- [38] V. L. Moruzzi, J. F. Janak, and K. Schwarz, “Calculated thermal properties of metals,” *Phys. Rev. B*, vol. 37, no. 2, pp. 790–799, Jan. 1988.
- [39] F. Liot and C. A. Hooley, “A simple theory of the Invar effect in iron-nickel alloys,” 2008.
- [40] S. Y. TANJI Yasunori, “Thermal Expansion Coefficient of Fe-Ni(fcc)Alloys,” 1970.
- [41] P. S. Turner, “Thermal-expansion stresses in reinforced plastics,” *J. Res. Natl. Bur. Stand. (1934)*, vol. 37, no. 4, p. 239, 1946.
- [42] M. T. Sijo and K. R. Jayadevan, “Characterization of Stir Cast Aluminium Silicon Carbide Metal Matrix Composite,” in *Materials Today: Proceedings*, 2018, vol. 5, no. 11, pp. 23844–23852.
- [43] A. O. Inegbenebor, C. A. Bolu, P. O. Babalola, A. I. Inegbenebor, and O. S. I. Fayomi, “Aluminum Silicon Carbide Particulate Metal Matrix Composite Development Via Stir Casting Processing,” *Silicon*, vol. 10, no. 2, pp. 343–347, Mar. 2018.
- [44] M. H. Rahman and H. M. M. Al Rashed, “Characterization of silicon carbide reinforced aluminum matrix Composites,” in *Procedia Engineering*, 2014, vol. 90, pp. 103–109.
- [45] A. R. Chambers, “The machinability of light alloy MMCs,” *Compos. Part A Appl. Sci. Manuf.*, vol. 27, no. 2, pp. 143–147, Jan. 1996.
- [46] S. P. S. Sangha, D. M. Jacobson, A. J. W. Ogilvy, M. Azema, A. A. Junai, and E. Botter, “Novel aluminium-silicon alloys for electronics packaging,” *Eng. Sci. Educ. J.*, vol. 6, no. 5, pp. 195–201, Oct. 1997.
- [47] J. Joel and M. Anthony Xavier, “Aluminium Alloy Composites and its Machinability studies; A Review,” in *Materials Today: Proceedings*, 2018, vol. 5, no. 5, pp. 13556–13562.
- [48] “SupremEX® Metal Matrix Composites (MMCs) for Aerospace Components.” [Online]. Available: <https://materion.com/products/metal-matrix-composites/supremex/commercial-and-military-aerospace>. [Accessed: 27-Jan-2019].
- [49] “Controlled expansion alloy properties — Sandvik Materials Technology.” [Online]. Available: <https://www.materials.sandvik/en/products/ce-alloys/product-properties/#tab-alloys-range>. [Accessed: 27-Jan-2019].
- [50] T. Kimura, T. Nakamoto, M. Mizuno, and H. Araki, “Effect of silicon content on densification, mechanical and thermal properties of Al-xSi binary alloys fabricated using selective laser melting,” *Mater. Sci. Eng. A*, vol. 682, pp. 593–602, Jan. 2017.
- [51] “Materials and processes in manufacturing,” *J. Manuf. Syst.*, vol. 17, no. 3, p. 235, 1998.

- [52] B. Chen *et al.*, “Strength and strain hardening of a selective laser melted AlSi10Mg alloy,” *Scr. Mater.*, vol. 141, pp. 45–49, Dec. 2017.
- [53] N. Read, W. Wang, K. Essa, and M. M. Attallah, “Selective laser melting of AlSi10Mg alloy: Process optimisation and mechanical properties development,” *Mater. Des.*, vol. 65, pp. 417–424, Jan. 2015.
- [54] N. Kang, P. Coddet, C. Chen, Y. Wang, H. Liao, and C. Coddet, “Microstructure and wear behavior of in-situ hypereutectic Al-high Si alloys produced by selective laser melting,” *Mater. Des.*, vol. 99, pp. 120–126, Jun. 2016.
- [55] N. Kang, P. Coddet, H. Liao, and C. Coddet, *Macrosegregation mechanism of primary silicon phase in selective laser melting hypereutectic Al - High Si alloy*, vol. 662. Elsevier, 2016, pp. 259–262.
- [56] A. Salmi, G. Piscopo, E. Atzeni, P. Minetola, and L. Iuliano, “On the Effect of Part Orientation on Stress Distribution in AlSi10Mg Specimens Fabricated by Laser Powder Bed Fusion (L-PBF),” in *Procedia CIRP*, 2018, vol. 67, pp. 191–196.
- [57] M. Mueller *et al.*, “Microstructural, mechanical, and thermo-physical characterization of hypereutectic AlSi40 fabricated by selective laser melting,” *J. Laser Appl.*, vol. 31, no. 2, p. 022321, May 2019.
- [58] S. Eberle *et al.*, “Additive manufacturing of an AlSi40 mirror coated with electroless nickel for cryogenic space applications,” in *International Conference on Space Optics — ICSO 2018*, 2019, vol. 11180, p. 40.
- [59] R. Joven, A. Ahmed, B. Tavakol, R. Das, P. Roozbehjavan, and B. Minaie, “Study of Thermal Expansion in Carbon Fiber Reinforced Polymer Composites,” *“SAMPE” Int. Symp. Proceedings. 2012.*, 2012.
- [60] A. N. Dickson, J. N. Barry, K. A. McDonnell, and D. P. Dowling, “Fabrication of continuous carbon, glass and Kevlar fibre reinforced polymer composites using additive manufacturing,” *Addit. Manuf.*, vol. 16, pp. 146–152, Aug. 2017.
- [61] B. Brenken, E. Barocio, A. Favaloro, V. Kunc, and R. B. Pipes, “Fused filament fabrication of fiber-reinforced polymers: A review,” *Addit. Manuf.*, vol. 21, pp. 1–16, May 2018.
- [62] “MarkForged develops 3D printer for carbon fibre,” *Reinforced Plastics*, vol. 59, no. 1. Elsevier Advanced Technology, p. 12, 01-Jan-2015.
- [63] J. Mazumder, “Laser-aided direct metal deposition of metals and alloys,” *Laser Addit. Manuf. Mater. Des. Technol. Appl.*, pp. 21–53, 2017.
- [64] A. Takezawa, M. Kobashi, and M. Kitamura, “Porous composite with negative thermal expansion obtained by photopolymer additive manufacturing,” *APL Mater.*, vol. 3, no. 7, p. 076103, Jul. 2015.
- [65] C. S. Ha, E. Hestekin, J. Li, M. E. Plesha, and R. S. Lakes, “Controllable thermal expansion of large magnitude in chiral negative Poisson’s ratio lattices,” *Phys. Status Solidi Basic Res.*, vol. 252, no. 7, pp. 1431–1434, 2015.
- [66] L. V. Gibiansky and S. Torquato, “Thermal expansion of isotropic multiphase composites and polycrystals,” *J. Mech. Phys. Solids*, vol. 45, no. 7, pp. 1223–1252, 1997.
- [67] B. E. Carroll *et al.*, “Functionally graded material of 304L stainless steel and inconel 625 fabricated by directed energy deposition: Characterization and thermodynamic modeling,” *Acta Mater.*, vol. 108, pp. 46–54, Apr. 2016.
- [68] T. Mukherjee, J. S. Zuback, A. De, and T. DebRoy, “Printability of alloys for additive manufacturing,” *Sci. Rep.*, vol. 6, no. 1, p. 19717, Apr. 2016.
- [69] H. Sahasrabudhe, R. Harrison, C. Carpenter, and A. Bandyopadhyay, “Stainless steel to titanium bimetallic structure using LENS™,” *Addit. Manuf.*, vol. 5, pp. 1–8, Jan. 2015.
- [70] A. Bandyopadhyay and B. Heer, “Additive manufacturing of multi-material structures,” *Mater. Sci. Eng. R Reports*, vol. 129, pp. 1–16, Jul. 2018.
- [71] M. Hannibal and G. Knight, “Additive manufacturing and the global factory: Disruptive technologies and the location of international business,” *Int. Bus. Rev.*, vol. 27, no. 6, pp. 1116–1127, Dec. 2018.
- [72] I. A. Segura *et al.*, “Characterization and mechanical properties of clad stainless steel 316L with nuclear applications fabricated using electron beam melting,” *J. Nucl. Mater.*, vol. 507, pp. 164–176, Aug. 2018.
- [73] C. K. Chua, C. H. Wong, and W. Y. Yeong, “Roadmap on Additive Manufacturing Standards,” in *Standards, Quality Control, and Measurement Sciences in 3D Printing and Additive Manufacturing*, Elsevier, 2017, pp. 31–55.
- [74] H. Bikas, P. Stavropoulos, and G. Chryssoulouris, “Additive manufacturing methods and modelling approaches: a critical review,” *Int. J. Adv. Manuf. Technol.*, vol. 83, no. 1–4, pp. 389–405, Mar. 2016.

- [75] D. D. Gu and Y. F. Shen, "Development and characterisation of direct laser sintering multicomponent Cu based metal powder," *Powder Metall.*, vol. 49, no. 3, pp. 258–264, 2006.
- [76] K. A. Mumtaz and N. Hopkinson, "Selective Laser Melting of thin wall parts using pulse shaping," *J. Mater. Process. Technol.*, vol. 210, no. 2, pp. 279–287, 2010.
- [77] J. C. Fox, S. P. Moylan, and B. M. Lane, "Effect of Process Parameters on the Surface Roughness of Overhanging Structures in Laser Powder Bed Fusion Additive Manufacturing," in *Procedia CIRP*, 2016, vol. 45, pp. 131–134.
- [78] J. Wroe, "Introduction to Additive Manufacturing Technology: A Guide for Designers and Engineers," *Eur. Powder Metall. Assoc.*, pp. 28–34, 2015.
- [79] Daniel Thomas, "The Development of Design Rules for Selective Laser Melting," *Univ. Wales Institute, Cardiff, PhD Thesis*, 2009.
- [80] V. Petrovic and R. Niñerola, "Powder recyclability in electron beam melting for aeronautical use," *Aircr. Eng. Aerosp. Technol.*, vol. 87, no. 2, pp. 147–155, Mar. 2015.
- [81] L. E. Murr *et al.*, "Metal Fabrication by Additive Manufacturing Using Laser and Electron Beam Melting Technologies," *Journal of Materials Science and Technology*, vol. 28, no. 1. Elsevier, pp. 1–14, 01-Jan-2012.
- [82] S. P. Narra, R. Cunningham, J. Beuth, and A. D. Rollett, "Location specific solidification microstructure control in electron beam melting of Ti-6Al-4V," *Addit. Manuf.*, vol. 19, pp. 160–166, Jan. 2018.
- [83] H. Helmer, A. Bauereiß, R. F. Singer, and C. Körner, "Grain structure evolution in Inconel 718 during selective electron beam melting," *Mater. Sci. Eng. A*, vol. 668, pp. 180–187, Jun. 2016.
- [84] S. Momeni, R. Guschlbauer, F. Osmanlic, and C. Körner, "Selective electron beam melting of a copper-chrome powder mixture," *Mater. Lett.*, vol. 223, pp. 250–252, Jul. 2018.
- [85] V. Bhavar, P. Kattire, V. Patil, S. Khot, K. Gujar, and R. Singh, "A Review on Powder Bed Fusion Technology of Metal Additive Manufacturing," *Mater. Sci. Technol. 2014*, no. April 2016, 2014.
- [86] A. Essop, "Freemelt raises \$1.6 million in investment round for open-source EBM 3D printer," 2019. [Online]. Available: <https://3dprintingindustry.com/news/freemelt-raises-1-6-million-in-investment-round-for-open-source-ebm-3d-printer-161493/>. [Accessed: 06-Jul-2020].
- [87] J. K. Algardh *et al.*, "Thickness dependency of mechanical properties for thin-walled titanium parts manufactured by Electron Beam Melting (EBM) ®," *Addit. Manuf.*, vol. 12, pp. 45–50, 2016.
- [88] N. Hrabe, T. Gnäupel-Herold, and T. Quinn, "Fatigue properties of a titanium alloy (Ti-6Al-4V) fabricated via electron beam melting (EBM): Effects of internal defects and residual stress," *Int. J. Fatigue*, vol. 94, pp. 202–210, 2017.
- [89] M. T. Stawovy, "Comparison of LCAC and PM Mo deposited using Sciaky EBAM™," *Int. J. Refract. Met. Hard Mater.*, vol. 73, pp. 162–167, Jun. 2018.
- [90] D. M. Keicher *et al.*, "Free Form Fabrication Using the Laser Engineered Net Shaping (LENS) Process." Albuquerque, NM, and Livermore, CA (United States), pp. 1–8, 31-Dec-1996.
- [91] D. Ding, Z. Pan, D. Cuiuri, and H. Li, "Wire-feed additive manufacturing of metal components: technologies, developments and future interests," *International Journal of Advanced Manufacturing Technology*, vol. 81, no. 1–4. pp. 465–481, 2015.
- [92] A. Pugalendhi, R. Ranganathan, and S. Ganesan, "Impact of process parameters on mechanical behaviour in multi-material jetting," *Mater. Today Proc.*, Jan. 2020.
- [93] M. Molitch-Hou, "XJet Demos Metal Jet 3D Printing Live at RAPID 2016 & ENGINEERING.com," *Engineering.com*, 2016. [Online]. Available: <https://www.engineering.com/3DPrinting/3DPrintingArticles/ArticleID/12207/XJet-Demos-Metal-Jet-3D-Printing-Live-at-RAPID-2016.aspx>. [Accessed: 06-Nov-2017].
- [94] D. Gilmer *et al.*, "An in-situ crosslinking binder for binder jet additive manufacturing," *Addit. Manuf.*, vol. 35, p. 101341, Oct. 2020.
- [95] A. Mostafaei *et al.*, "Binder jet 3D printing – process parameters, materials, properties, and challenges," *Prog. Mater. Sci.*, p. 100707, Jun. 2020.
- [96] E. Stevens, S. Schloder, E. Bono, D. Schmidt, and M. Chmielus, "Density variation in binder jetting 3D-printed and sintered Ti-6Al-4V," *Addit. Manuf.*, vol. 22, pp. 746–752, Aug. 2018.
- [97] Y. Wang and Y. F. Zhao, "Investigation of Sintering Shrinkage in Binder Jetting Additive Manufacturing Process," *Procedia Manuf.*, vol. 10, pp. 779–790, Jan. 2017.
- [98] T. Do, P. Kwon, and C. S. Shin, "Process development toward full-density stainless steel parts with binder jetting printing," *Int. J. Mach. Tools Manuf.*, vol. 121, pp. 50–60, Oct. 2017.
- [99] S. Vangapally, K. Agarwal, A. Sheldon, and S. Cai, "Effect of Lattice Design and Process Parameters on Dimensional and Mechanical Properties of Binder Jet Additively Manufactured Stainless Steel 316 for Bone Scaffolds," *Procedia Manuf.*, vol. 10, pp. 750–759, Jan. 2017.
- [100] T. Do, P. Kwon, and C. S. Shin, "Process development toward full-density stainless steel parts with

- binder jetting printing,” *Int. J. Mach. Tools Manuf.*, vol. 121, pp. 50–60, Oct. 2017.
- [101] D. L. Bourell, “Perspectives on Additive Manufacturing,” *Annu. Rev. Mater. Res.*, vol. 46, no. 1, pp. 1–18, Jul. 2016.
- [102] Markforged Inc., “US20180154438A1- Additive manufacturing with continuous debinding,” 04-Jan-2018.
- [103] M. R. Razfar, P. Sarvi, and M. M. A. Zarchi, “Experimental investigation of the surface roughness in ultrasonic-assisted milling,” in *Proceedings of the Institution of Mechanical Engineers, Part B: Journal of Engineering Manufacture*, 2011, vol. 225, no. 9, pp. 1615–1620.
- [104] R. Goodridge and S. Ziegelmeier, “Powder bed fusion of polymers,” in *Laser Additive Manufacturing: Materials, Design, Technologies, and Applications*, Woodhead Publishing, 2017, pp. 181–204.
- [105] J. P. Kruth, G. Levy, F. Klocke, and T. H. C. Childs, “Consolidation phenomena in laser and powder-bed based layered manufacturing,” *CIRP Ann. - Manuf. Technol.*, vol. 56, no. 2, pp. 730–759, Jan. 2007.
- [106] M. Sachs, A. Schmitt, J. Schmidt, W. Peukert, and K. E. Wirth, “Functionalization of polymer powders for SLS-processes using an atmospheric plasma jet in a fluidized bed reactor,” in *AIP Conference Proceedings*, 2015, vol. 1664, p. 100004.
- [107] M. Baumers, C. Tuck, and R. Hague, “Selective Heat Sintering Versus Laser Sintering: Comparison of Deposition Rate, Process Energy Consumption and Cost Performance,” *Proc. 26th Solid Free. Fabr. Symp.*, pp. 109–121, 2015.
- [108] J. W. Stansbury and M. J. Idacavage, “3D printing with polymers: Challenges among expanding options and opportunities,” in *Dental Materials*, 2016, vol. 32, no. 1, pp. 54–64.
- [109] D. Ibrahim *et al.*, “Dimensional error of selective laser sintering, three-dimensional printing and PolyJet™ models in the reproduction of mandibular anatomy,” *J. Cranio-Maxillofacial Surg.*, vol. 37, no. 3, pp. 167–173, Apr. 2009.
- [110] B. Haldar *et al.*, “Present status and some critical issues of abrasive jet materials processing: A review,” in *Procedia Manufacturing*, 2018, vol. 20, pp. 523–529.
- [111] M. Baumers, C. Tuck, P. Dickens, and R. Hague, “How Can Material Jetting Systems be Upgraded for More Efficient Multi-Material Additive Manufacturing?,” in *Proceedings of Solid Freeform Fabrication Symposium*, 2014, pp. 170–184.
- [112] M. Ziaee and N. B. Crane, “Binder jetting: A review of process, materials, and methods,” *Additive Manufacturing*, vol. 28. Elsevier B.V., pp. 781–801, 01-Aug-2019.
- [113] B. M. Wu, S. W. Borland, R. A. Giordano, L. G. Cima, E. M. Sachs, and M. J. Cima, “Solid free-form fabrication of drug delivery devices,” *J. Control. Release*, vol. 40, no. 1–2, pp. 77–87, Jun. 1996.
- [114] C. Polzin, S. Spath, and H. Seitz, “Characterization and evaluation of a PMMA-based 3D printing process,” *Rapid Prototyp. J.*, vol. 19, no. 1, pp. 37–43, 2013.
- [115] J. Carballo, Q. Ni, J. Vasquez, S. Chatzisavas, and N. Crane, “Micro-scale part manipulation on a liquid interface through interface curvature effects,” in *ASME International Mechanical Engineering Congress and Exposition, Proceedings (IMECE)*, 2012, vol. 9, no. PARTS A AND B, pp. 731–733.
- [116] L. H. Han, G. Mapili, S. Chen, and K. Roy, “Projection microfabrication of three-dimensional scaffolds for tissue engineering,” *J. Manuf. Sci. Eng. Trans. ASME*, vol. 130, no. 2, pp. 0210051–0210054, Apr. 2008.
- [117] J. W. Choi, R. Wicker, S. H. Lee, K. H. Choi, C. S. Ha, and I. Chung, “Fabrication of 3D biocompatible/biodegradable micro-scaffolds using dynamic mask projection microstereolithography,” *J. Mater. Process. Technol.*, vol. 209, no. 15–16, pp. 5494–5503, Aug. 2009.
- [118] F. P. W. Melchels, J. Feijen, and D. W. Grijpma, “A poly(d,l-lactide) resin for the preparation of tissue engineering scaffolds by stereolithography,” *Biomaterials*, vol. 30, no. 23–24, pp. 3801–3809, Aug. 2009.
- [119] F. P. W. Melchels, J. Feijen, and D. W. Grijpma, “A review on stereolithography and its applications in biomedical engineering,” *Biomaterials*, vol. 31, no. 24. Elsevier, pp. 6121–6130, 01-Aug-2010.
- [120] Y. Lu, G. Mapili, G. Suhali, S. Chen, and K. Roy, “A digital micro-mirror device-based system for the microfabrication of complex, spatially patterned tissue engineering scaffolds,” *J. Biomed. Mater. Res. - Part A*, vol. 77, no. 2, pp. 396–405, May 2006.
- [121] T. Instruments, “DLP9500UV DLP ® 0.95 UV 1080p 2x LVDS Type A DMD,” 2012. [Online]. Available: www.ti.com. [Accessed: 08-Aug-2018].
- [122] B. Mueller, “Additive Manufacturing Technologies – Rapid Prototyping to Direct Digital

- Manufacturing,” *Assem. Autom.*, vol. 32, no. 2, pp. 151–154, Apr. 2012.
- [123] F. Lucklum and M. J. Vellekoop, “Rapid prototyping of 3D phononic crystals using high-resolution stereolithography fabrication,” in *Procedia Engineering*, 2015, vol. 120, pp. 1095–1098.
- [124] F. Lucklum, S. Janssen, W. Lang, and M. J. Vellekoop, “Miniature 3D gas chromatography columns with integrated fluidic connectors using high-resolution stereolithography fabrication,” in *Procedia Engineering*, 2015, vol. 120, pp. 703–706.
- [125] R. Liska *et al.*, “Photopolymers for rapid prototyping,” *J. Coatings Technol. Res.*, vol. 4, no. 4, pp. 505–510, 2007.
- [126] N. Martelli *et al.*, “Advantages and disadvantages of 3-dimensional printing in surgery: A systematic review,” *Surg. (United States)*, vol. 159, no. 6, pp. 1485–1500, Jun. 2016.
- [127] D. A. Roberson, D. Espalin, and R. B. Wicker, “3D printer selection: A decision-making evaluation and ranking model,” *Virtual Phys. Prototyp.*, vol. 8, no. 3, pp. 201–212, 2013.
- [128] U. K. Debnath, M. A. Chowdhury, M. A. Kowser, and M. S. Mia, “Study of erosion characterization of carbon fiber reinforced composite material,” in *AIP Conference Proceedings*, 2017, vol. 1851, p. 020098.
- [129] G. T. Mark and A. S. Gozdz, “US20160361869A1 - Three dimensional printer for fiber reinforced composite filament fabrication,” 03-May-2016.
- [130] ISO/ASTM, “ISO/ASTM DIS 52902 - Additive Manufacturing - Test artefacts - Standard guideline for geometric capability assessment of additive manufacturing systems (in development),” 2018. [Online]. Available: <https://www.iso.org/standard/67287.html>. [Accessed: 23-Mar-2018].
- [131] Y. L. Yap, C. Wang, S. L. Sing, V. Dikshit, W. Y. Yeong, and J. Wei, “Material jetting additive manufacturing: An experimental study using designed metrological benchmarks,” *Precis. Eng.*, vol. 50, pp. 275–285, Oct. 2017.
- [132] V. Matilainen, “Benchmarking of Laser Additive Manufacturing Process,” 2012.
- [133] D. Thomas Thesis, “The Development of Design Rules for Selective Laser Melting,” University of Wales, 2009.
- [134] J.-P. Kruth, B. Vandenbroucke, J. Vaerenbergh, and P. Mercelis, “Benchmarking of different SLS/SLM processes as rapid manufacturing techniques,” in *Int. Conf. Polymers & Moulds Innovations (PMI), Gent, Belgium, April 20-23, 2005*, 2005, pp. 1–7.
- [135] J. Kranz, D. Herzog, and C. Emmelmann, “Design guidelines for laser additive manufacturing of lightweight structures in TiAl6V4,” *J. Laser Appl.*, vol. 27, no. S1, p. S14001, Feb. 2015.
- [136] M. G. Teeter, A. J. Kopacz, H. N. Nikolov, and D. W. Holdsworth, “Metrology test object for dimensional verification in additive manufacturing of metals for biomedical applications,” *Proc. Inst. Mech. Eng. H.*, vol. 229, no. 1, pp. 20–7, Jan. 2015.
- [137] K. Kamarudin, M. S. Wahab, A. A. Raus, A. Ahmed, and S. Shamsudin, “Benchmarking of dimensional accuracy and surface roughness for AlSi10Mg part by selective laser melting (SLM),” in *AIP Conference Proceedings*, 2017, vol. 1831, no. 1, p. 020047.
- [138] A. L. Cooke and J. A. Soons, “Variability in the Geometric Accuracy of Additively Manufactured Test Parts.”
- [139] “AIA/NAS - NAS979: Uniform cutting tests - NAS series metal cutting equipment specifications.” 2013.
- [140] S. A. Sillars, C. J. Sutcliffe, A. M. Philo, S. G. R. Brown, J. Sienez, and N. P. Lavery, “The three-prong method: a novel assessment of residual stress in laser powder bed fusion,” *Virtual Phys. Prototyp.*, vol. 13, no. 1, pp. 20–25, Jan. 2018.
- [141] R. K. Ganeriwala *et al.*, “Corrigendum to ‘Evaluation of a thermomechanical model for prediction of residual stress during laser powder bed fusion of Ti-6Al-4V’ [Addit. Manuf. 27 May (2019) 489–502] (Additive Manufacturing (2019) 27 (489–502), (S2214860418308741), (10.1016/j.addma.2019.03.034)),” *Additive Manufacturing*, vol. 32. Elsevier B.V., 01-Mar-2020.
- [142] C. Casavola, A. Cazzato, V. Moramarco, and G. Pappalettera, “Residual stress measurement in Fused Deposition Modelling parts,” *Polym. Test.*, vol. 58, pp. 249–255, Apr. 2017.
- [143] T. Mukherjee, W. Zhang, and T. DebRoy, “An improved prediction of residual stresses and distortion in additive manufacturing,” *Comput. Mater. Sci.*, vol. 126, pp. 360–372, Jan. 2017.
- [144] J. Cao, M. A. Gharghoury, and P. Nash, “Finite-element analysis and experimental validation of thermal residual stress and distortion in electron beam additive manufactured Ti-6Al-4V build plates,” *J. Mater. Process. Technol.*, vol. 237, pp. 409–419, Nov. 2016.
- [145] M. Ghasri-Khouzani *et al.*, “Experimental measurement of residual stress and distortion in additively manufactured stainless steel components with various dimensions,” *Mater. Sci. Eng. A*, vol. 707, pp. 689–700, Nov. 2017.
- [146] X. Song *et al.*, “Advances in additive manufacturing process simulation: Residual stresses and distortion predictions in complex metallic components,” *Mater. Des.*, vol. 193, p. 108779, Aug.

- 2020.
- [147] C. Y. Lee and C. Y. Liu, "The influence of forced-air cooling on a 3D printed PLA part manufactured by fused filament fabrication," *Addit. Manuf.*, vol. 25, pp. 196–203, Jan. 2019.
- [148] N. Saba and M. Jawaid, "A review on thermomechanical properties of polymers and fibers reinforced polymer composites," *J. Ind. Eng. Chem.*, vol. 67, pp. 1–11, Jun. 2018.
- [149] G. Mohapatra, F. Sommer, and E. J. Mittemeijer, "Calibration of a quenching and deformation differential dilatometer upon heating and cooling: Thermal expansion of Fe and Fe-Ni alloys," *Thermochim. Acta*, vol. 453, no. 1, pp. 31–41, Jan. 2007.
- [150] Y. Song, Y. Li, W. Song, K. Yee, K. Y. Lee, and V. L. Tagarielli, "Measurements of the mechanical response of unidirectional 3D-printed PLA," *Mater. Des.*, vol. 123, pp. 154–164, Jun. 2017.
- [151] H. Asgari, M. Salarian, H. Ma, A. Olubamiji, and M. Vlasea, "On thermal expansion behavior of invar alloy fabricated by modulated laser powder bed fusion," *Mater. Des.*, vol. 160, pp. 895–905, Dec. 2018.
- [152] A. B. Spierings, M. Voegtlin, T. Bauer, and K. Wegener, "Powder flowability characterisation methodology for powder-bed-based metal additive manufacturing," *Prog. Addit. Manuf.*, vol. 1, no. 1–2, pp. 9–20, 2016.
- [153] O. D. Neikov and N. A. Yefimov, "Powder Characterization and Testing," in *Handbook of Non-Ferrous Metal Powders*, Elsevier, 2019, pp. 3–62.
- [154] P. Mellin, O. Lyckfeldt, P. Harlin, H. Brodin, H. Blom, and A. Strondl, "Evaluating flowability of additive manufacturing powders, using the Gustavsson flow meter," *Met. Powder Rep.*, vol. 72, no. 5, pp. 322–326, Sep. 2017.
- [155] H. Kinnunen, G. Hebbink, H. Peters, J. Shur, and R. Price, "An investigation into the effect of fine lactose particles on the fluidization behaviour and aerosolization performance of carrier-based dry powder inhaler formulations," *AAPS PharmSciTech*, vol. 15, no. 4, pp. 898–909, Aug. 2014.
- [156] N. O. Lindberg *et al.*, "Flowability measurements of pharmaceutical powder mixtures with poor flow using five different techniques," *Drug Dev. Ind. Pharm.*, vol. 30, no. 7, pp. 785–791, Jan. 2004.
- [157] C. Qiu, N. J. E. Adkins, and M. M. Attallah, "Selective laser melting of Invar 36: Microstructure and properties," *Acta Mater.*, vol. 103, pp. 382–395, Jan. 2016.
- [158] X. C. Li, J. Stampfl, and F. B. Prinz, "Mechanical and thermal expansion behavior of laser deposited metal matrix composites of Invar and TiC," *Mater. Sci. Eng. A*, vol. 282, no. 1–2, pp. 86–90, Apr. 2000.
- [159] E. Brandl, U. Heckenberger, V. Holzinger, and D. Buchbinder, "Additive manufactured AlSi10Mg samples using Selective Laser Melting (SLM): Microstructure, high cycle fatigue, and fracture behavior," *Mater. Des.*, vol. 34, pp. 159–169, 2012.
- [160] H. Asgari, C. Baxter, K. Hosseinkhani, and M. Mohammadi, "On microstructure and mechanical properties of additively manufactured AlSi10Mg_200C using recycled powder," *Mater. Sci. Eng. A*, vol. 707, pp. 148–158, Nov. 2017.
- [161] M. Yakout, A. Cadamuro, M. A. Elbestawi, and S. C. Veldhuis, "The selection of process parameters in additive manufacturing for aerospace alloys," *Int. J. Adv. Manuf. Technol.*, vol. 92, no. 5–8, pp. 2081–2098, Sep. 2017.
- [162] N. J. Harrison, I. Todd, and K. Mumtaz, "Thermal expansion coefficients in Invar processed by selective laser melting," *J. Mater. Sci.*, vol. 52, no. 17, pp. 10517–10525, Sep. 2017.
- [163] M. Yakout, M. A. Elbestawi, and S. C. Veldhuis, "A study of thermal expansion coefficients and microstructure during selective laser melting of Invar 36 and stainless steel 316L," *Addit. Manuf.*, vol. 24, pp. 405–418, Dec. 2018.
- [164] M. Yakout, M. A. Elbestawi, and S. C. Veldhuis, "Density and mechanical properties in selective laser melting of Invar 36 and stainless steel 316L," *J. Mater. Process. Technol.*, vol. 266, pp. 397–420, Apr. 2019.
- [165] J. Strauss and S. Michael, "Laser Additive Manufacturing Processing of a Mixture of Iron and Nickel Powders," *27th Annu. Int. Solid Free. Fabr. Symp.*, no. 3, p. 12, 2016.
- [166] H. Tan, J. Chen, F. Zhang, X. Lin, and W. Huang, "Microstructure and mechanical properties of laser solid formed Ti-6Al-4V from blended elemental powders," *Xiyou Jinshu Cailiao Yu Gongcheng/Rare Met. Mater. Eng.*, vol. 38, no. 4, pp. 574–578, Apr. 2009.
- [167] R. Banerjee, P. C. Collins, A. Genç, and H. L. Fraser, "Direct laser deposition of in situ Ti-6Al-4V-TiB composites," *Mater. Sci. Eng. A*, vol. 358, no. 1–2, pp. 343–349, Oct. 2003.
- [168] R. Banerjee, D. Bhattacharyya, P. C. Collins, G. B. Viswanathan, and H. L. Fraser, "Precipitation of grain boundary α in a laser deposited compositionally graded Ti-8Al-xV alloy - An orientation microscopy study," *Acta Mater.*, vol. 52, no. 2, pp. 377–385, Jan. 2004.
- [169] D. Gu, G. Meng, C. Li, W. Meiners, and R. Poprawe, "Selective laser melting of TiC/Ti bulk

- nanocomposites: Influence of nanoscale reinforcement,” *Scr. Mater.*, vol. 67, no. 2, pp. 185–188, Jul. 2012.
- [170] D. Gu and W. Meiners, “Microstructure characteristics and formation mechanisms of in situ WC cemented carbide based hardmetals prepared by Selective Laser Melting,” *Mater. Sci. Eng. A*, vol. 527, no. 29–30, pp. 7585–7592, Nov. 2010.
- [171] D. Gu, Y. C. Hagedorn, W. Meiners, K. Wissenbach, and R. Poprawe, “Selective Laser Melting of in-situ TiC/Ti5Si3 composites with novel reinforcement architecture and elevated performance,” *Surf. Coatings Technol.*, vol. 205, no. 10, pp. 3285–3292, Feb. 2011.
- [172] B. Vrancken, L. Thijs, J. P. Kruth, and J. Van Humbeeck, “Microstructure and mechanical properties of a novel β titanium metallic composite by selective laser melting,” *Acta Mater.*, vol. 68, pp. 150–158, Apr. 2014.
- [173] B. Zhang, N. E. Fenineche, H. Liao, and C. Coddet, “Microstructure and magnetic properties of Fe-Ni alloy fabricated by selective laser melting Fe/Ni mixed powders,” *J. Mater. Sci. Technol.*, vol. 29, no. 8, pp. 757–760, Aug. 2013.
- [174] B. Zhang, N. E. Fenineche, L. Zhu, H. Liao, and C. Coddet, “Studies of magnetic properties of permalloy (Fe30%Ni) prepared by SLM technology,” *J. Magn. Magn. Mater.*, vol. 324, no. 4, pp. 495–500, Feb. 2012.
- [175] A. Gård, P. Krakhmalev, and J. Bergström, “Microstructural characterization and wear behavior of (Fe,Ni)–TiC MMC prepared by DMLS,” *J. Alloys Compd.*, vol. 421, no. 1–2, pp. 166–171, Sep. 2006.
- [176] B. Zhang, N. E. Fenineche, H. Liao, and C. Coddet, “Magnetic properties of in-situ synthesized FeNi3 by selective laser melting Fe-80%Ni powders,” *J. Magn. Magn. Mater.*, vol. 336, pp. 49–54, Jun. 2013.
- [177] J. R. (Joseph R. . Davis, “Alloying: understanding the basics,” *Choice Rev. Online*, vol. 39, no. 09, pp. 39-5209-39–5209, 2002.
- [178] W. Martienssen and H. Warlimont, *Springer handbook of condensed matter and materials data*. Springer, 2005.
- [179] C. E. Guillaume, “The anomaly of the nickel-steels,” in *Proceedings of the Physical Society of London*, 1919, vol. 32, no. 1, pp. 374–404.
- [180] A. Keshavarzkermani *et al.*, “An investigation into the effect of process parameters on melt pool geometry, cell spacing, and grain refinement during laser powder bed fusion,” *Opt. Laser Technol.*, vol. 116, pp. 83–91, Aug. 2019.
- [181] H. Qin, V. Fallah, Q. Dong, M. Brochu, M. R. Daymond, and M. Gallemeault, “Solidification pattern, microstructure and texture development in Laser Powder Bed Fusion (LPBF) of Al10SiMg alloy,” *Mater. Charact.*, vol. 145, pp. 29–38, Nov. 2018.
- [182] D. J. Newell *et al.*, “Mitigation of scan strategy effects and material anisotropy through supersolvus annealing in LPBF IN718,” *Mater. Sci. Eng. A*, vol. 764, p. 138230, Sep. 2019.
- [183] X. Zhan, Y. Meng, J. Zhou, C. Qi, C. Zhang, and D. Gu, “Quantitative research on microstructure and thermal physical mechanism in laser melting deposition for Invar alloy,” *J. Manuf. Process.*, vol. 31, pp. 221–231, Jan. 2018.
- [184] J. P. Oliveira, A. D. LaLonde, and J. Ma, “Processing parameters in laser powder bed fusion metal additive manufacturing,” *Mater. Des.*, vol. 193, p. 108762, Aug. 2020.
- [185] K. Wei *et al.*, “Mechanical properties of Invar 36 alloy additively manufactured by selective laser melting,” *Mater. Sci. Eng. A*, vol. 772, p. 138799, Jan. 2020.
- [186] K. G. Prashanth *et al.*, “Microstructure and mechanical properties of Al-12Si produced by selective laser melting: Effect of heat treatment,” 2013.
- [187] P. Vora, K. Mumtaz, I. Todd, and N. Hopkinson, “AlSi12 in-situ alloy formation and residual stress reduction using anchorless selective laser melting,” *Addit. Manuf.*, vol. 7, pp. 12–19, 2015.
- [188] T. Ullsperger *et al.*, “Selective laser melting of hypereutectic Al-Si40-powder using ultra-short laser pulses,” *Appl. Phys. A Mater. Sci. Process.*, vol. 123, no. 12, p. 798, Dec. 2017.
- [189] J. Suryawanshi, K. G. Prashanth, S. Scudino, J. Eckert, O. Prakash, and U. Ramamurty, “Simultaneous enhancements of strength and toughness in an Al-12Si alloy synthesized using selective laser melting,” *Acta Mater.*, vol. 115, pp. 285–294, Aug. 2016.
- [190] J. Zhang, B. Song, Q. Wei, D. Bourell, and Y. Shi, “A review of selective laser melting of aluminum alloys: Processing, microstructure, property and developing trends,” *J. Mater. Sci. Technol.*, vol. 35, no. 2, pp. 270–284, Feb. 2019.
- [191] M. Wang, B. Song, Q. Wei, Y. Zhang, and Y. Shi, “Effects of annealing on the microstructure and mechanical properties of selective laser melted AlSi7Mg alloy,” *Mater. Sci. Eng. A*, vol. 739, pp. 463–472, Jan. 2019.
- [192] Y. Jia *et al.*, “Microstructure and thermal expansion behavior of spray-deposited Al-50Si,” *Mater.*

- Des.*, vol. 57, pp. 585–591, May 2014.
- [193] S. Shakerin, A. Hadadzadeh, B. S. Amirkhiz, S. Shamsdini, J. Li, and M. Mohammadi, “Additive manufacturing of maraging steel-H13 bimetal using laser powder bed fusion technique,” *Addit. Manuf.*, vol. 29, p. 100797, Oct. 2019.
- [194] A. Keshavarzkermani *et al.*, “Controlling mechanical properties of additively manufactured hastelloy X by altering solidification pattern during laser powder-bed fusion,” *Mater. Sci. Eng. A*, vol. 762, p. 138081, Aug. 2019.
- [195] J. Herzberger, J. M. Serrine, C. B. Williams, and T. E. Long, “Polymer Design for 3D Printing Elastomers: Recent Advances in Structure, Properties, and Printing,” *Progress in Polymer Science*, vol. 97. Elsevier BV, p. 101144, Oct-2019.
- [196] H. Rahman, T. D. John, M. Sivadasan, and N. K. Singh, “Investigation on the Scale Factor applicable to ABS based FDM Additive Manufacturing,” in *Materials Today: Proceedings*, 2018, vol. 5, no. 1, pp. 1640–1648.
- [197] A. Armillotta, M. Bellotti, and M. Cavallaro, “Warpage of FDM parts: Experimental tests and analytic model,” *Robot. Comput. Integr. Manuf.*, vol. 50, pp. 140–152, Apr. 2018.
- [198] R. T. L. Ferreira, I. C. Amatte, T. A. Dutra, and D. Bürger, “Experimental characterization and micrography of 3D printed PLA and PLA reinforced with short carbon fibers,” *Compos. Part B Eng.*, vol. 124, pp. 88–100, Sep. 2017.
- [199] S. Chaitanya and I. Singh, “Ecofriendly treatment of aloe vera fibers for PLA based green composites,” *Int. J. Precis. Eng. Manuf. - Green Technol.*, vol. 5, no. 1, pp. 143–150, Jan. 2018.
- [200] “Fused Deposition Modelling of Natural Fibre/Polylactic Acid Composites,” *J. Compos. Sci.*, vol. 1, no. 2, p. 8, Aug. 2017.
- [201] Z. Liu, Q. Lei, and S. Xing, “Mechanical characteristics of wood, ceramic, metal and carbon fiber-based PLA composites fabricated by FDM,” *J. Mater. Res. Technol.*, vol. 8, no. 5, pp. 3743–3753, Jul. 2019.
- [202] M. O. Montjovent *et al.*, “Human fetal bone cells associated with ceramic reinforced PLA scaffolds for tissue engineering,” *Bone*, vol. 42, no. 3, pp. 554–564, Mar. 2008.
- [203] N. Ayrimis, M. Kariz, J. H. Kwon, and M. Kitek Kuzman, “Effect of printing layer thickness on water absorption and mechanical properties of 3D-printed wood/PLA composite materials,” *Int. J. Adv. Manuf. Technol.*, vol. 102, no. 5–8, pp. 2195–2200, Jun. 2019.
- [204] S. M. Lebedev, O. S. Gefle, E. T. Amitov, D. V. Zhuravlev, D. Y. Berchuk, and E. A. Mikutskiy, “Mechanical properties of PLA-based composites for fused deposition modeling technology,” *Int. J. Adv. Manuf. Technol.*, vol. 97, no. 1–4, pp. 511–518, Jul. 2018.
- [205] Y. Tao, H. Wang, Z. Li, P. Li, and S. Q. Shi, “Development and application of wood flour-filled polylactic acid composite filament for 3d printing,” *Materials (Basel)*, vol. 10, no. 4, Mar. 2017.
- [206] K. Durgashyam, M. Indra Reddy, A. Balakrishna, and K. Satyanarayana, “Experimental investigation on mechanical properties of PETG material processed by fused deposition modeling method,” in *Materials Today: Proceedings*, 2019, vol. 18, pp. 2052–2059.
- [207] A. Hamidi and Y. Tadesse, “Single step 3D printing of bioinspired structures via metal reinforced thermoplastic and highly stretchable elastomer,” *Compos. Struct.*, vol. 210, pp. 250–261, Feb. 2019.
- [208] K. Szykiedans, W. Credo, and D. Osiński, “Selected Mechanical Properties of PETG 3-D Prints,” in *Procedia Engineering*, 2017, vol. 177, pp. 455–461.
- [209] M. M. Toropova and C. A. Steeves, “Adaptive bimaterial lattices to mitigate thermal expansion mismatch stresses in satellite structures,” *Acta Astronaut.*, vol. 113, pp. 132–141, Aug. 2015.
- [210] S. Timoshenko, “Analysis of Bi-Metal Thermostats,” *J. Opt. Soc. Am.*, vol. 11, no. 3, p. 233, Sep. 1925.
- [211] M. Vasudevan and W. Johnson, “On multi-metal thermostats,” *Appl. Sci. Res. Sect. B*, vol. 9, no. 6, pp. 420–430, Dec. 1961.
- [212] M. Vasudevan and W. Johnson, “Thermal Bending of a Tri-Metal Strip,” *J. R. Aeronaut. Soc.*, vol. 65, no. 607, pp. 507–509, Jul. 1961.
- [213] A. T. Abawi, “The Bending of Bonded Layers Due to Thermal Stress,” 2004.
- [214] J. R. Vinson, “Plate and panel structures of isotropic, composite and piezoelectric materials, including sandwich construction,” *Solid Mech. its Appl.*, vol. 120, pp. 1–434, 2005.

